Investigating the Function of Coding Polymorphisms within the *TBX15-WARS2* Locus Associated with Waist-Hip Ratio as a Risk Factor for Metabolic Syndrome

Louisa Zolkiewski

2023

Department of Physiology, Anatomy and Genetics
Trinity College, University of Oxford

Genetics of Type 2 Diabetes
MRC Mammalian Genetic Unit, MRC Harwell Institute

TRINITY COLLEGE
UNIVERSITY of OXFORD

Memorandum

The work presented in this thesis is the original work of the author; no work herein has been submitted for assessment for a degree at this, or any other, university. This work was carried out independently under the supervision of Professor Roger Cox, Dr. Liz Bentley, and Dr. Rebecca Dumbell (MRC Harwell Institute), with input from Professor Clive Wilson (DPAG, University of Oxford). All work presented here was performed independently; collaborative work has been clearly stated throughout the thesis and my independent contribution clearly indicated. The following contributions were integral to the completion of this DPhil project:

The Medical Research Council Harwell (MRCH) molecular and cell biology (MCB) facility generated the *Tbx15*^{H156N} and *Tbx15*^{M566R} mouse lines described in this thesis. Dr. Rebecca Dumbell designed the *Tbx15*^{H156N} mouse line, and I designed the *Tbx15*^{M566R} mouse line with assistance from Dr. Gemma Codner in the MCB.

The Mary Lyon Centre (MLC) facility carried out all husbandry and welfare assessments in accordance with UK Home Office regulations. Staff in Ward 4 and Ward 5 set up mating trios to generate all *Tbx15* mouse lines detailed in this thesis. MLC staff took ear biopsies for genotyping and randomised mice into same-sex cages as required. The MRCH genotyping facility isolated DNA from ear biopsies, designed all *Tbx15* allele discrimination PCR assays and performed all genotyping. The MLC clinical chemistry facility performed all blood plasma analyte analysis.

Dr. Liz Bentley performed terminal retro-orbital bleeds, DEXA and X-Ray on all *Tbx15*^{H156N} mice. Dr. Liz Bentley, and the MLC phenotyping team, performed echo-MRI and IPGTT phenotyping on *Tbx15*^{H156N} and *Tbx15*$^{+/-}$ mice during the initial COVID-19 lockdown and during a short period of recovery following surgery in 2021. The MLC necropsy facility performed terminal retro-orbital bleeds and assisted with tissue dissections for *Tbx15*$^{+/-}$ and *Tbx15*^{M566R} mouse lines.

Dr. Sara Pulit (Big Data Institute, University of Oxford, UK) performed posterior probability analysis and Nasa Sinnott-Armstrong (Broad Institute, MIT, USA) performed epi-PMCA to predict functionality of genetic variants outlined in this thesis. All *in silico* protein homology modelling and protein-protein docking was performed under the guidance of Professor Kimberley Watson (University of Reading, UK).

RNA-sequencing library preparation and genome sequencing were performed by the Oxford Genomics Centre (Oxford, UK). Dr. Michelle Simon (MRCH biocomputing group) processed all raw data files, performed initial quality control analysis, analysed differential gene expression, and produced selected gene-expression graphs (as indicated in figure legends). Dr. Michelle Simon further provided input for functional enrichment analysis. ChIP-sequencing library preparation and genome sequencing, quality control and basic data analysis were performed by Active Motif Inc.

~ word count: approximately 50,000 ~

Acknowledgements

The past four years of my DPhil have been a rollercoaster experience, for which I am grateful to have had support from so many people. First and foremost, I would like to thank my supervisors Professor Roger Cox and Professor Clive Wilson for their support, direction, and encouragement throughout my project. I am grateful to Roger for his continued enthusiasm for my work, for encouraging me to think critically and for keeping the question *"What's the hypothesis?"* at the forefront of all my experimental endeavours. With his support, I was afforded the opportunity to attend several training courses and present my work at national and international conferences. I am thankful for Clive's input into my project, for all the engaging discussions and for encouraging me to consider the overall scope of my work. I would not have started my DPhil without my past supervisors, Professor Mike Briggs, Professor Ray Boot-Handford, Dr. Natalie Gardiner and Dr. Richard Unwin, who ignited my passion for scientific research and cultivated my "green-fingered" nature in the lab.

I am eternally grateful to Dr. Liz Bentley and Dr. Rebecca Dumbell in the Cox group, for welcoming me into the lab and for giving me the confidence to work independently. To Liz, for her invaluable help in setting up my mouse colonies, training me in several metabolic phenotyping procedures and for her guidance, even when I was asking incessant questions. Liz was integral to ensuring my mouse phenotyping continued, undisrupted, throughout the COVID-19 lockdowns, and whilst I was recovering from elbow surgery, for which I am eternally indebted to her. To Rebecca, who went from a mentor to a close friend, for keeping an eye on me in the lab and being a wealth of knowledge, discipline, and guidance, and of course, for the endless pep-talks whenever I doubted myself. Special thanks go to all past members of the Cox group, especially Dr. Milan Mušo, Dr. Ying Bai, Dr. Grace Yu, and Dr. Yixing Wu for their training, advice and scientific discussions. Thank you to all the DPhil friends I made at Harwell, for sharing the general ups and downs of DPhil life, for pre-COVID lunchtime get-togethers and all the college adventures. In particular, my dear friends Amy Southern and Gurpreet Bharj, for the friendship, support, laughter and endless snacks they have provided over the past four years, I am grateful we shared this experience together.

I owe a debt of gratitude to the Mary Lyon Centre staff who carried out routine colony maintenance and breeding of my mice, trained me in metabolic phenotyping and assisted with necropsy and pathology. Specifically, Lucie Vizor and the Ward 4 staff, Jackie Harrison and the Ward 5 staff, Dr. Marianne Yon, Dr. Lee Moir, Lynn Beresford, Alexandra Rodriguez and all the phenotyping team. Not only did they instil a sound working knowledge of *in vivo* techniques and colony management skills, they offered a wealth of advice, support and a shoulder to cry on.

Much of this work would not have been possible without initial prioritisation efforts of our collaborators Dr. Sara Pulit (Professor Cecilia Lindgren research group, Big Data Institute, University of Oxford, UK) and Nasa Sinnott-Armstrong (Professor Melina

Claussnitzer research group, Broad Institute, MIT, USA). I am further thankful to Professor Kimberley Watson (University of Reading, UK) for her valuable direction with all *in silico* protein-homology and protein-protein docking analysis, and for her input into interpretation of these results. Additionally, I am extremely grateful for Dr. Michelle Simon's ongoing analysis of all RNA-sequencing data and guidance with functional analysis. I have learnt the ins and outs of handling large data sets, and without her input I would inevitably still be stuck attempting the most basic of bioinformatics analysis.

To my extended family at TMBSC masters, for sharing the highs and lows of this journey from 200 miles aways. For the endless hugs, pep talks and the excuse to escape DPhil life for a weekend of swimming competitions. To my OUSC swimming friend Zoé, for making sure I made it to early-morning training sessions, proof-reading my chapters and being a wonderful friend.

One of the most important people I must thank is Richard Ford, for being there through every step of this journey. For supporting me through every failed application and interview that got me here today; helping me to brush myself off and focus on the next opportunity. Your endless encouragement throughout has kept me going; you've reminded me to laugh daily and made sure I haven't had to worry about anything. Thank you for your patience, and for preparing and eating some very late dinners when I've been working late.

Finally, to my parents George and Judy, to whom I dedicate this thesis, for their love and support. Thank you for exemplifying working hard to achieve your dreams and never giving up despite life's hurdles. Thank you for providing me with the opportunities to explore what I love doing, without which I would not be where I am today.

~ Na koniec moim rodzicom Jerzemu i Judy, którym dedykuję tę rozprawę doktorską, za ich miłość i wsparcie. To Wy własnym przykładem pokazaliście mi, że trzeba ciężkiej pracy, aby spełniać swoje marzenia i że nie wolno się poddawać mimo życiowych przeszkód. Dziękuję Wam za możliwości, które mi stworzyliście abym zgłębiała dziedzinę, którą kocham - bez Was nie doszłabym do punktu, w którym jestem dzisiaj ~

Table of contents

Memorandum i
Acknowledgements ii
Table of contents iv
List of figures xiii
List of tables xvii
Abstract xxi
Common abbreviations xxii
1. Introduction 1
1.1. Obesity 1
1.2. Metabolic Syndrome 3
1.2.1. Adipose tissue expandability hypothesis 4
1.3. Fat mass distribution and disease risk 6
1.4. Adipose tissue biology 8
1.4.1. White, brown and beige adipocytes 8
1.4.2. Adipogenesis 11
1.4.3. Adipose tissue expansion 13
1.4.4. Adipose tissues in rodents 16
1.5. Genome-wide association studies as a tool to identify adiposity genes 18
1.5.1. Type 2 diabetes mellitus 20
1.5.2. Body mass index 20
1.5.3. Waist-to-hip ratio and BMI association 21
1.5.4. Identifying functional variants 25
1.6. *TBX15-WARS2* locus 28
1.6.1. *TBX15-WARS2* locus associations with WHRadjBMI 28
1.6.2. Identifying candidate genes in the *TBX15-WARS2* locus 30
1.6.2.1. *SPAG17* 32
1.6.2.2. *WARS2* 34
1.6.2.3. *TBX15* 35
1.7. Prioritising functional SNPs in the *TBX15-WARS2 locus* 41
1.7.1. Epi-phylogenetic module complexity analysis 41
1.7.2. Posterior probability analysis 43

1.8. Thesis aims and hypotheses 44
2. Methods 46
2.1. Cell culture 46
2.1.1. General cell culture and consumables 46
2.1.1.1. Immortalised cell line procurement 46
2.1.1.2. Maintenance of immortalised cell lines 48
2.1.1.3. Primary murine SVF isolation 48
2.1.1.4. Thawing cells 50
2.1.1.5. Cell counting 50
2.1.1.6. Freezing cells 50
2.1.2. Transfections 51
2.1.2.1. Poly-D-Lysine coating 51
2.1.2.2. Seeding densities 52
2.1.2.3. Lipofectamine 3000™ reagent 52
2.1.3. Adipogenic differentiation 53
2.1.3.1. Differentiation media stocks 53
2.1.3.1. hWAT cells 54
2.1.3.2. 3T3-L1 cells 54
2.1.3.3. Primary murine SVF cells 55
2.1.3.4. OilRedO stain 56
2.2. Animal studies 57
2.2.1. Ethical statement 57
2.2.2. Mouse husbandry 58
2.2.3. Mouse lines 59
2.2.3.1. Stock line generation 59
2.2.3.1.1. TBX15-KO-B6N mouse line 59
2.2.3.1.2. TBX15-H156N-EM2-B6N and TBX15-M566R-EM3-B6N mouse lines 59
2.2.3.2. Genotyping 60
2.2.3.3. Experimental cohorts 60
2.2.3.3.1. TBX15-KO-B6N 60
2.2.3.3.2. TBX15-H156N-EM2-B6N 61
2.2.3.3.3. TBX15-M566R-EM3-B6N 62

2.2.4. Metabolic phenotyping 63
2.2.4.1. Metabolic phenotyping pipeline 63
2.2.4.2. Body composition analysis 64
2.2.4.3. Intraperitoneal glucose tolerance test 65
2.2.4.4. Intraperitoneal insulin tolerance test 65
2.2.4.5. DEXA and X-Ray 66
2.2.5. Terminal procedures 67
2.2.5.1. Terminal retro-orbital bleeds 67
2.2.5.2. Terminal dissections for tissue weights 67
2.2.5.3. Terminal dissections for RNA and protein isolation 68
2.2.6. Histology 68
2.2.6.1. Tissue processing and H&E staining 68
2.2.6.2. Adipocyte size analysis 69
2.2.7. Pathology 69
2.2.7.1. Clinical chemistry analysis 69
2.3. Molecular Biology 70
2.3.1. DNA applications 70
2.3.1.1. Deoxynucleoside triphosphate stocks 70
2.3.1.2. Oligonucleotide sequences and primers 70
2.3.1.3. Polymerase chain reaction amplification 71
2.3.1.4. Site-directed mutagenesis 72
2.3.1.5. Agarose gels 73
2.3.1.6. DNA extraction from agarose gels 74
2.3.1.7. Restriction enzyme digestion 75
2.3.1.8. DNA ligation 75
2.3.1.9. DNA quantification 75
2.3.1.10. Sanger Sequencing 76
2.3.2. RNA applications 77
2.3.2.1. RNA extraction 77
2.3.2.1.1. Primary murine cells 77
2.3.2.1.2. Adipose tissues 77
2.3.2.2. RNA concentration and purity analysis 79
2.3.2.3. RNA quality analysis 79

2.3.2.4. cDNA synthesis 80
2.3.2.5. Real-time quantitative PCR 81
2.3.2.5.1. House-keeping genes assays 81
2.3.2.5.2. TaqMan® gene assays 81
2.3.2.5.3. Real-time quantitative PCR reactions 82
2.3.2.6. RNA-Sequencing 82
2.3.2.6.1. Sample preparation and RNA-sequencing 82
2.3.2.6.2. Functional analysis 83
2.3.3. Protein applications 83
2.3.3.1. Protein extraction 83
2.3.3.1.1. Immortalised cell lines 83
2.3.3.1.2. Mouse tissues 84
2.3.3.2. Protein quantification 85
2.3.3.3. Immunoprecipitation 85
2.3.3.3.1. Sepharose G bead immunoprecipitations 86
2.3.3.3.2. Magnetic bead immunoprecipitations 87
2.3.3.4. Immunoblot analysis 89
2.3.3.5. DNA binding assays 91
2.3.3.6. ChIP-sequencing 93
2.3.3.6.1. Sample fixation 93
2.3.3.6.2. ChIP-sequencing 95
2.3.3.6.3. Functional analysis 95
2.4. Bacterial work 95
2.4.1. General bacterial work 95
2.4.1.1. Vector construct procurement 96
2.4.1.2. Vector construct design 96
2.4.1.3. Lysogeny broth and antibiotics selection plates 97
2.4.1.4. Transformation of competent Escherichia coli (*E. Coli*) cells 97
2.4.1.5. Glycerol stocks 98
2.4.2. DNA isolation 98
2.4.2.1. Miniprep 98
2.4.2.2. Maxiprep 99
2.5. *In silico* applications 100

2.5.1. ATAC-sequencing analysis 100
2.5.2. Transcription factor binding motif analysis 101
2.5.3. Protein sequence alignments 101
2.5.4. Nuclear localisation sequence analysis 102
2.5.5. Mutation predictions 102
2.5.6. Protein sequence modelling 103
2.5.7. Dimer modelling 103
2.6. Statistical analysis 104
3. Prioritising the role of potentially functional coding SNPs within the *TBX15* gene 106
3.1. Introduction 106
3.1.1. Chapter hypothesis 109
3.1.2. Chapter aims 109
3.2. Results 110
3.2.1. *In silico* analysis of the regulatory role of *TBX15* coding SNPs 110
3.2.1.1. rs10494217 and rs61730011 overlapped minimal epigenetic marks in differentiating hWAT cells 110
3.2.1.2. Transcription factor binding motifs altered by rs10494217 and rs61730011 114
3.2.2. *In silico* analysis of the protein-coding role of TBX15 coding SNPs 117
3.2.2.1. TBX15 protein sequence was conserved across vertebrate species 117
3.2.2.2. Human and mouse had two full-length consensus TBX15 transcripts 120
3.2.2.3. p.M566R was predicted to have a more severe impact on TBX15 protein sequence than p.H156N 126
3.2.2.4. p.H156N predicted to alter TBX15 T-box region loop structure 127
3.2.2.5. p.H156N was predicted to alter conformation of TBX15-TBX15 and TBX15-TBX18 dimers 133
3.2.3. *In vitro* validation of the impact of p.H156N and p.M566R on TBX15 transcription factor function 140
3.2.3.1. Generation and validation of HA- and Myc-tagged TBX15 and TBX18 cDNA constructs in HEK293T cells 140
3.2.3.2. TBX15 immunoprecipitations using sepharose G beads showed non-specific binding in IgG control 143

3.2.3.3. Optimisation of magnetic co-immunoprecipitation systems for quantification of TBX15 protein dimers 144
3.2.3.4. Protein dimerisation was not significantly altered by p.H50N or p.M460R substitutions in the TBX15-2 protein 151
3.2.3.5. DNA binding was not significantly altered by p.H156N or p.M566R substitutions in the TBX15-1 protein 153
3.3. Discussion 155
3.3.1. *In silico* analysis of the regulatory role of *TBX15* coding SNPs 155
3.3.2. *In silico* analysis of the protein-coding role of *TBX15* coding SNPs 157
3.3.3. *In vitro* validation of protein-protein and protein-DNA binding effects of *TBX15* coding SNPs 161
4. Characterising the function of *Tbx15 in vivo* 165
4.1. Introduction 165
4.1.1. Chapter hypothesis 166
4.1.2. Chapter aims 167
4.2. Results 167
4.2.1. Initial viability assessment 167
4.2.2. Metabolic phenotyping pipeline and sample size calculations 169
4.2.3. *Tbx15*$^{+/-}$ and *Tbx15*^{H156N} lines exhibit sexually dimorphic sub-viability post-weaning 170
4.2.4. Echo-MRI body composition analysis over time 173
4.2.4.1. *Tbx15*$^{+/-}$ mice fed a low-fat-diet had lower bodyweight and less fat mass 173
4.2.4.2. *Tbx15*$^{+/H156N}$ mice had increased lean mass on high-fat diet 176
4.2.4.3. *Tbx15*^{M556R} did not exhibit body composition differences over time 178
4.2.5. Glucose response 180
4.2.5.1. Female *Tbx15*$^{+/-}$ mice fed LFD had impaired glucose tolerance 180
4.2.5.2. *Tbx15*^{H156N} mice did not exhibit a differential glucose response 182
4.2.5.3. *Tbx15*$^{+/M566R}$ male mice fed a HFD had improved glucose clearance 183
4.2.6. DEXA body composition at early adulthood 187
4.2.6.1. *Tbx15*$^{+/-}$ mice on LFD exhibit sexually dimorphic body composition 187
4.2.6.2. *Tbx15*$^{H156N/H156N}$ male mice fed a HFD exhibited less fat mass 189
4.2.6.3. *Tbx15*$^{M566R/M566R}$ female mice fed a LFD had less fat mass 191
4.2.7. Adipose depot distribution 193

4.2.7.1. *Tbx15*$^{+/-}$ mice on LFD had smaller adipose tissues....193
4.2.7.2. *Tbx15*^{H156N} male mice had decreased WAT weights....194
4.2.7.3. *Tbx15*^{M566R} mice did not have altered tissue distribution....195
4.2.8. Terminal blood plasma clinical chemistry....202
4.2.8.1. *Tbx15*$^{+/-}$ mice had decreased LDH and glycerol levels....202
4.2.8.2. *Tbx15*$^{+/H156N}$ mice had increased blood plasma analytes....204
4.2.8.3. *Tbx15*$^{+/M566R}$ and *Tbx15*$^{M566R/M566R}$ mice had altered blood plasma analytes....205
4.2.9. Terminal adipose tissue cell analysis....208
4.2.9.1. *Tbx15*$^{+/-}$ mice on HFD had altered cell size distribution in WAT....208
4.3. Discussion....213
4.3.1. *Tbx15*$^{+/-}$ mice....216
4.3.2. *Tbx15*^{H156N} mice....220
4.3.3. *Tbx15*^{M566R} mice....223
5. Identifying the TBX15 transcriptional network....229
5.1. Introduction....229
5.1.1. Chapter hypothesis....231
5.1.2. Chapter aims....231
5.2. Results....232
5.2.1. Determining TBX15 target genes in 3T3-L1 and hWAT cells using ChIP-sequencing....232
5.2.1.1. Quality control and method optimisation....232
5.2.1.1.1. TBX15 antibodies exhibited cross-reactivity in muscle tissues and hWAT cell samples....232
5.2.1.1.2. Optimisation of sample collection for accessibility of target binding sites....234
5.2.1.1.3. Sample quality control and validation for ChIP-sequencing....236
5.2.1.2. TBX15 binding network *in vitro*....240
5.2.2. Determining the *Tbx15* regulatory network in adipose tissues using RNA-sequencing....243
5.2.2.1. Sample quality control for *Tbx15*$^{-/-}$ tissues....243
5.2.2.2. *Tbx15*$^{-/-}$ RNA regulatory network in adipose tissues....246
5.2.3. The core TBX15 regulatory network consists of 236 genes....252
5.3. Discussion....255

5.3.1. Possible novel regulatory roles for TBX15 256
5.3.1.1. Lineage determination 256
5.3.1.2. Adipocyte Differentiation 261
5.3.1.3. Immune regulation/inflammation 263
6. Identifying p.H156N perturbations of the TBX15 transcriptional network 269
6.1. Introduction 269
6.1.1. Chapter hypothesis 270
6.1.2. Chapter aims 270
6.2. Results 271
6.2.1. Determining the *Tbx15*^{H156N} regulatory network using RNA-sequencing 271
6.2.1.1. *Tbx15*^{H156N} regulatory network in adipose tissue 271
6.2.1.2. *Tbx15*^{H156N} regulatory network in differentiating primary adipocytes 275
6.2.1.2.1. Optimisation of primary SVF isolation and differentiation 275
6.2.1.2.2. *TBX15*$^{H156N/H156N}$ did not have altered total lipid accumulation in differentiated iWAT-derived SVF cells 277
6.2.1.2.3. *Tbx15*$^{H156N/H156N}$ regulatory network 278
6.3. Discussion 283
6.3.1. The p.H156N polymorphism directly perturbed the TBX15 regulatory network 283
7. General discussion and future perspectives 288
7.1. Summary 288
7.2. Dissecting the functional role of polymorphisms within complex WHRadjBMI loci 289
7.3. *In silico* prioritisation of DNA-regulatory or protein-coding mechanisms of potential effector SNPs in the *TBX15-WARS2* locus 292
7.4. Modelling WHR and metabolic phenotypes associated with *Tbx15* alleles *in vivo* 297
7.4.1. TBX15 regulatory network 302
7.5. Future perspectives 306
7.6. Final impact and conclusions 307
8. References 309
9. Appendix 335
9.1. Methods 335

9.1.1. Animal Studies 335
9.1.1.1. TBX15-H156N-EM2-B6N and TBX15-M566R-EM3-B6N stock line generation using CRISPR/Cas9 335
9.1.1.2. Genotyping 337
9.1.1.3. Clinical chemistry analysis 339
9.1.2. Molecular biology studies 341
9.1.2.1. RNA-sequencing 341
9.1.2.1.1. Sample preparation and RNA-sequencing 341
9.1.2.1.2. Differential gene expression analysis 342
9.1.2.2. ChIP-sequencing 342
9.1.2.2.1. Sample preparation 342
9.1.2.2.2. ChIP-sequencing 343
9.1.2.2.3. HA antibody validation 344
9.2. Results 345
9.2.1. Chapter 3 – Prioritising the role of potentially functional coding SNPs within the *TBX15* gene 345
9.2.2. Chapter 4 – Characterising the function of *Tbx15 in vivo* 349
9.2.3. Chapter 5 – Identifying the TBX15 transcriptional network 391
9.2.4. Chapter 6 – Identifying p.H156N perturbations of the TBX15 transcriptional network 394

List of figures

Figure 1.1. Share of adults that were overweight or obese from 1975 to 2016 across the world. 1
Figure 1.2. Metabolically healthy versus unhealthy obesity.. 4
Figure 1.3. Adipose tissue expandability hypothesis. 5
Figure 1.4. Adipogenesis of white, brown and beige adipocytes. 11
Figure 1.5. PPARγ and C/EBPα positive feedback loop drives adipogenesis. 12
Figure 1.6. Mechanisms of adipose tissue expansion during obesity. 14
Figure 1.7. Major white, brown and beige adipose depots in mouse and human. 17
Figure 1.8 Variant-to-function analyses to investigate potentially functional SNPs. 27
Figure 1.9. Regional association plot showing four independent association signals in the *TBX15-WARS2* locus. 30
Figure 1.10. Associations between gene expression levels and cardiometabolic traits.. 31
Figure 1.11. Epi-phylogenetic module complexity analysis (epi-PMCA) of *TBX15-WARS2* locus SNPs 42
Figure 2.1. Adipose depots of the neck region. 47
Figure 2.2. *Tbx15* metabolic phenotyping pipeline. 64
Figure 2.3. Schematic representation of protein sepharose G and magnetic bead co-IP systems. 86
Figure 3.1. Chromosome map of the *TBX15-WARS2* locus SNPs identified by GWAS meta-analyses. 107
Figure 3.2. TBX15 protein domain map. 108
Figure 3.3 ATAC-sequencing data for hWAT cells at different adipocyte differentiation time points. 111
Figure 3.4. Altered transcription factor binding motifs (TFBMs) for rs10494217 and rs61730011. 116
Figure 3.5. TBX15 taxonomy tree in 205 vertebrate species. 118
Figure 3.6. Multiple sequence alignment of TBX15 protein between eight vertebrate species (next page). 118
Figure 3.7. Schematic of human and mouse TBX15 protein transcripts. 122
Figure 3.8. Alignment of full-length TBX15 protein transcripts between human and mouse. 123
Figure 3.9. Alignment of full-length TBX15 transcripts between human and mouse. 125
Figure 3.10. Amino acid substitutions for rs10494217 and rs61730011 in TBX15 protein-coding transcripts. 126
Figure 3.11. Comparison of 3D TBX15 T-box protein models between several homology modelling servers. 130
Figure 3.12. Comparative 3D protein models of TBX15 T-box structure with both alleles of rs10494217 (p.H156N). 132
Figure 3.13. Example HADDOCK protein-protein docking strategy. 134

Figure 3.14. Optimisation of *in silico* protein-protein docking TBX15 and TBX18 T-box dimerisation models....135
Figure 3.15. Impact of p.H156N on TBX15-TBX15 and TBX15-TBX18 dimers in silico. 138
Figure 3.16. Schematic representation of cloning strategies for TBX15-2. 141
Figure 3.17. Validation of TBX15-2 and TBX18 target expression in HEK293T cells by immunoblotting.....142
Figure 3.18. Representative immunoblot for sepharose G bead immunoprecipitation. 144
Figure 3.19. Initial magnetic co-immunoprecipitation optimisation. 146
Figure 3.20. Magnetic co-immunoprecipitation optimisation for protein lysate input. 147
Figure 3.21. Magnetic co-immunoprecipitation optimisation for SDS-PAGE.....149
Figure 3.22. TBX15 magnetic co-immunoprecipitation primary antibody detection optimisation. 150
Figure 3.23. Non-synonymous amino acid substitutions p.H50N and p.M460R do not affect TBX15 protein dimerisation in vitro. 152
Figure 3.24. Non-synonymous amino acid substitutions p.H156N and p.M566R do not alter TBX15 protein-DNA binding in vitro. 154
Figure 4.1. χ^2 analysis of observed versus expected genotype ratios in *Tbx15* mouse line viability cohorts....168
Figure 4.2. *Tbx15* metabolic phenotyping cohort experimental pipeline.. 170
Figure 4.3. χ^2 analysis of observed versus expected genotype ratios for *Tbx15*$^{+/-}$, *Tbx15*^{H156N} and *Tbx15*^{M566R} mice post-weaning. 172
Figure 4.4. *Tbx15*$^{+/-}$ echo-MRI body composition over 4 to 24 weeks. 175
Figure 4.5. *Tbx15*^{H156N} echo-MRI body composition over 4 to 24 weeks. 177
Figure 4.6. *Tbx15*^{M566R} echo-MRI body composition over 4 to 24 weeks....179
Figure 4.7. *Tbx15*$^{+/-}$ intraperitoneal glucose tolerance tests (IPGTT) at 13 weeks....181
Figure 4.8. *Tbx15*$^{+/-}$ intraperitoneal insulin sensitivity tests (IPIST) at 17 weeks. 182
Figure 4.9. *Tbx15*^{H156N} intraperitoneal glucose tolerance tests (IPGTT) at 13 weeks184
Figure 4.10. *Tbx15*^{H156N} intraperitoneal insulin sensitivity test (IPIST) at 17 weeks 185
Figure 4.11. *Tbx15*^{M566R} intraperitoneal glucose tolerance tests (IPGTT) at 13 weeks. 186
Figure 4.12. *Tbx15*$^{+/-}$ DEXA at 23 weeks under recoverable anaesthesia.. 188
Figure 4.13. *Tbx15*^{H156N} DEXA at 24 weeks under terminal anaesthesia. 190
Figure 4.14. *Tbx15*^{M566R} DEXA at 23 weeks under recoverable anaesthesia. 192
Figure 4.15. Female *Tbx15*$^{+/-}$ terminal adipose depot measurements and distribution. 196
Figure 4.16. Male *Tbx15*$^{+/-}$ terminal adipose depot measurements and distribution. 197
Figure 4.17. Female *Tbx15*^{H156N} terminal adipose depot measurements and distribution.. 198

Figure 4.18. Male *Tbx15*^{H156N} terminal adipose depot measurements and distribution.. 199
Figure 4.19. Female *Tbx15*^{M566R} terminal adipose depot measurements and distribution. 200
Figure 4.20. Male *Tbx15*^{M566R} terminal adipose depot measurements and distribution. 201
Figure 4.21. *Tbx15*$^{+/-}$ mice had decreased LDH and glycerol levels. 203
Figure 4.22. *Tbx15*$^{+/H156N}$ mice had increased blood plasma analytes. 206
Figure 4.23. *Tbx15*$^{+/M566R}$ and *Tbx15*$^{M566R/M566R}$ mice had altered blood plasma analytes. 207
Figure 4.24. Female *Tbx15*$^{+/-}$ terminal adipocyte cell area. 209
Figure 4.25. Female *Tbx15*$^{+/-}$ adipocyte cell area distribution for white adipose tissues (WAT) 210
Figure 4.26. Male *Tbx15*$^{+/-}$ terminal adipocyte cell area. 211
Figure 4.27. Male *Tbx15*$^{+/-}$ adipocyte cell area distribution for white adipose tissues (WAT). 212
Figure 4.28. Summary of metabolic phenotypes in *Tbx15* mouse lines. 213
Figure 5.1. TBX15 adipose tissue expression in human and mouse. 230
Figure 5.2. TBX15 antibody validation. 233
Figure 5.3. Optimisation of transfection for TBX15 for ChIP-sequencing. 235
Figure 5.4. Example ChIP-sequencing infographics for 3T3-L1 cells. 238
Figure 5.5. Example ChIP-sequencing infographics for hWAT cells. 239
Figure 5.6. *Tbx15*$^{-/-}$ RNA-sequencing cohort experimental pipeline and sample collection. 245
Figure 5.7. Total number of significantly differentially expressed genes in adipose tissues. 248
Figure 5.8. STRING network of TBX15 common network genes. 254
Figure 5.9. TBX15 regulation of mesenchymal stem cell differentiation. 258
Figure 5.10. The role of TBX15 in regulating the PPARγ-CEBPα adipogenesis feedback loop. 262
Figure 6.1. *Tbx15*^{H156N} RNA-sequencing cohort.. 272
Figure 6.2. Total number of significantly differentially expressed genes in *Tbx15*^{H156N} adipose tissues. 273
Figure 6.3. Optimisation of differentiation protocol for stromal-vascular fraction (SVF) cells derived from inguinal white adipose tissue (iWAT). 276
Figure 6.4. Differentiation of stromal-vascular fraction (SVF) cells derived from inguinal white adipose tissue from female *Tbx15*$^{+/+}$ and *Tbx15*$^{H156N/H156N}$ mice. 277
Figure 6.5. Total number of significantly differentially expressed genes in *Tbx15*^{H156N} stroma-vascular fraction cells. 278
Figure 7.1. *TBX15-WARS2* locus expression quantitative trait loci plots. 291
Figure 7.2. Proposed variant to function approach to prioritise multiple SNPs associated with complex traits. 296

Figure 7.3. Topologically associated domain (TAD) architecture for human and mouse *TBX15*-*WARS2* locus. 299
Figure 7.4. Potential transcription factor role for TBX15 in adipose tissues. 304
Figure 9.1 Comparison of full-length 3D TBX15 protein models between several homology modelling servers. 345
Figure 9.2. Comparison of 3D TBX15 N- and C-terminal protein models between several homology modelling servers. 347
Figure 9.3. TBX15-HA ChIP-sequencing sample validation. 391
Figure 9.4. FactorPath qPCR validation of TBX15-HA samples 392
Figure 9.5. Principal component analysis of female *Tbx15*$^{-/-}$ adipose tissues. 393
Figure 9.6. Principal component analysis of *Tbx15*$^{H156N/H156N}$ adipose tissues. 394

List of tables

Table 1.1. Clinical body mass index classification. 2
Table 1.2. Genome-wide association study meta-analyses for anthropometric body composition measurements. 23
Table 1.3. Genome-wide association data for representative set of SNPs in the *TBX15-WARS2* locus associated with WHRadjBMI. 33
Table 1.4. Models of *Tbx15* expression in vitro and in vivo. 40
Table 1.5. Posterior probability analysis of *TBX15-WARS2* locus SNPs. 43
Table 2.1. Maintenance of immortalised and primary cell lines 49
Table 2.2. Freezing media components for immortalised cell lines. 51
Table 2.3. Adipocyte differentiation media supplement stocks. 53
Table 2.4. hWAT differentiation media composition. 54
Table 2.5. 3T3-L1 differentiation cocktail and maintenance media composition. 55
Table 2.6. Primary murine SVF differentiation and maintenance media composition.. 56
Table 2.7. Mouse diet composition details. 58
Table 2.8. Total number of mice bred for TBX15-KO-B6N mouse line experimental cohorts. 61
Table 2.9. Total number of mice bred for TBX15-H156N-EM2-B6N-IC mouse line experimental cohorts. 62
Table 2.10. Total number of mice bred for TBX15-M566R-EM3-B6N-IC mouse line experimental cohorts. 63
Table 2.11. Insulin working stock dilutions for intraperitoneal injections 66
Table 2.12. Preparation of 10 mM dNTP stock. 70
Table 2.13. PCR amplification primers for sub-cloning, site-directed mutagenesis, and template amplification. 71
Table 2.14. Polymerase chain reaction amplification reactions.. 72
Table 2.15. Thermocycler parameters for PCR amplification 72
Table 2.16. Site-directed mutagenesis amplification reactions. 73
Table 2.17. Thermocycler parameters for site-directed mutagenesis 73
Table 2.18. Kinase, Ligase & DpnI (KLD) treatment reactions. 73
Table 2.19. Restriction enzymes for digestion of DNA inserts and vectors for sub-cloning applications.. 75
Table 2.20. Custom and stock sequencing primers used for Sanger Sequencing at Source Bioscience. 76
Table 2.21. cDNA synthesis reactions and thermocycler conditions. 81
Table 2.22. TaqMAN® assay qPCR primers for mouse genes. 82
Table 2.23. Default thermocycler parameters for qPCR reactions using 7500 v2.3 software. 82
Table 2.24. Protein lysis buffers. 84
Table 2.25. Primary and secondary antibodies used in immumoblotting applications.. 91
Table 2.26. DNA oligonucleotide sequences for TBX15 DNA binding assay. 92

Table 2.27. Oligonucleotide annealing buffer stocks. 93
Table 2.28. Thermocycler parameters for DNA oligonucleotide annealing. 93
Table 2.29. Primary antibody dilutions for DNA binding assay. 93
Table 2.30. Reagents required for cell fixation for ChIP-sequencing analysis. 94
Table 2.31. T-box protein transcript sequences used for alignments. 102
Table 2.32. Crystallographic structures available in the protein data bank for T-box family members. 104
Table 2.33. Power calculation parameters to calculate the required sample sizes for metabolic phenotyping cohorts. 105
Table 3.1. Haplotype blocks for the *TBX15-WARS2* locus SNPs associated with WHRadjBMI. 108
Table 3.2. Regulatory marks for *TBX15-WARS2* SNPs. 115
Table 3.3. Alignment of amino acid residues in human TBX15 protein transcripts between NCBI and Ensembl annotations. 121
Table 3.4. Alignment of amino acid residues in mouse TBX15 protein transcripts between NCBI and Ensembl annotations. 121
Table 3.5. Exon 1 read counts for human *TBX15* and mouse *Tbx15* transcripts. 125
Table 3.6. Prediction scores for non-synonymous coding SNPs in TBX15 protein-coding transcripts using SIFT, PolyPhen2 and Condel. 127
Table 3.7. Associated scores for TBX15 3D T-box protein models. 131
Table 3.8. Protein-protein interacting residues for T-box family proteins. 135
Table 3.9. Optimised TBX15-TBX15 T-box homodimer models *in silico*. 136
Table 3.10. Optimised TBX15-TBX18 T-box heterodimer models *in silico*. 137
Table 3.11. Impact of p.H156N on TBX15-TBX15 and TBX15-TBX18 dimers *in silico.* 139
Table 4.1. Calculated sample sizes using *a priori* power analysis to detect an effect with α=0.95 power and $p<0.05$ significance (two-sided). 169
Table 4.2. Total numbers of mice weaned per sex and diet group for *Tbx15* metabolic phenotyping cohorts. 173
Table 4.3. Summary of metabolic phenotypes in *Tbx15* mouse lines. 214
Table 4.4. Diet composition between *Tbx15* mouse studies. 217
Table 4.5. HaploReg v4.1 regulatory associations for SNPs in high LD ($r^2 \geq 0.8$) with rs61730011. 228
Table 5.2. Total number of peaks detected in ChIP-sequencing samples. 240
Table 5.3. Enriched WikiPathways terms for TBX15 target binding sites in 3T3-L1 and hWAT cells. 241
Table 5.4. Enriched WikiPathways terms for common TBX15 target binding sites in 3T3-L1 and hWAT cells. 242
Table 5.5. Female and male *Tbx15*$^{-/-}$ bodyweights at 12 weeks of age. 246
Table 5.6. Top common upregulated and downregulated genes in *Tbx15*$^{-/-}$ and *Tbx15*$^{+/-}$ inguinal white adipose tissue. 249
Table 5.7. Top common upregulated and downregulated genes in *Tbx15*$^{-/-}$ and *Tbx15*$^{+/-}$ brown adipose tissue 250

Table 5.8. Top enriched terms in *Tbx15*$^{-/-}$ inguinal white adipose tissue. 252
Table 5.9. Top enriched terms in *Tbx15*$^{-/-}$ brown adipose tissue. 253
Table 5.10. Top enriched terms in TBX15 common network genes. 255
Table 5.11. TBX15 regulation of mesenchymal stem cell lineage determination genes. 259
Table 5.12. TBX15 regulation of key adipogenesis genes. 263
Table 5.13. TBX15 regulation of immune response genes. 265
Table 6.1. Female and male *Tbx15*^{H156N} bodyweight at 12 weeks of age. 272
Table 6.2. Top common upregulated and downregulated genes in *Tbx15*^{H156N} and *Tbx15*$^{-/-}$ inguinal white adipose tissue. 274
Table 6.3. Top common enriched terms between *Tbx15*$^{H156N/H156N}$ and *Tbx15*$^{-/-}$ inguinal white adipose tissue. 275
Table 6.4. Top common upregulated genes in *Tbx15*^{H156N} differentiating stromal-vascular fraction cells. 279
Table 6.5. Top common downregulated genes in *Tbx15*^{H156N} differentiating stromal-vascular fraction cells. 280
Table 6.6. Top common enriched terms in *Tbx15*^{H156N} differentiating stromal-vascular fraction cells. 282
Table 7.1. *TBX15-WARS2* locus expression quantitative trait loci. 292
Table 9.1. sgRNA sequence used for TBX15-H156N and TBX15-M566R CRISPR/Cas9 repair to generate mouse models. 335
Table 9.2. Homology directed repair donor sequence for TBX15-H156N and TBX15-M566R CRISPR/Cas9 repair compared to wildtype sequence. 336
Table 9.3. qPCR reaction mixes for *Tbx15* allele specific FAM assays. 337
Table 9.4. *Tbx15* mouse line genotyping assay details. 338
Table 9.5. qPCR reaction mixes for Dot1l VIC internal control assay. 339
Table 9.6 Beckman Coulter calibration material information. 339
Table 9.7. Beckman Coulter Assay information. 340
Table 9.8. Beckman Coulter quality control material information. 341
Table 9.9. Associated scores for full-length 3D TBX15 protein models. 346
Table 9.10. Associated scores for 3D TBX15 N-terminal and C-terminal protein models 348
Table 9.11. Female *Tbx15*$^{+/-}$ echo-MRI body composition over 4 to 24 weeks. 349
Table 9.12. Male *Tbx15*$^{+/-}$ echo-MRI body composition over 4 to 24 weeks. 350
Table 9.13. Female *Tbx15*^{H156N} echo-MRI body composition over 4 to 24 weeks. 351
Table 9.14. Male *Tbx15*^{H156N} echo-MRI body composition over 4 to 24 weeks. 353
Table 9.15. Female *Tbx15*^{M566R} echo-MRI body composition over 4 to 24 weeks. 355
Table 9.16. Male *Tbx15*^{M566R} echo-MRI body composition over 4 to 24 weeks. 357
Table 9.17. *Tbx15*$^{+/-}$ intraperitoneal glucose tolerance tests at 13 weeks. 359
Table 9.18. *Tbx15*$^{+/-}$ fasted blood glucose and area under the curve from intraperitoneal glucose tolerance tests. 359
Table 9.19. *Tbx15*$^{+/-}$ intraperitoneal insulin sensitivity tests at 17 weeks. 360

Table 9.20. *Tbx15*$^{+/-}$ area under the curve from intraperitoneal insulin sensitivity tests.. 360
Table 9.21. *Tbx15*^{H156N} intraperitoneal glucose tolerance tests at 13 weeks.....361
Table 9.22. *Tbx15*^{H156N} fasted blood glucose and area under the curve analysis from intraperitoneal glucose tolerance tests....362
Table 9.23. *Tbx15*^{H156N} intraperitoneal insulin sensitivity tests at 17 weeks. 363
Table 9.24. *Tbx15*^{H156N} area above the curve analysis from intraperitoneal insulin sensitivity tests. 364
Table 9.25. *Tbx15*^{M566R} intraperitoneal glucose tolerance tests at 13 weeks.....365
Table 9.26. *Tbx15*^{M566R} fasted blood glucose and area under the curve from intraperitoneal glucose tolerance tests....366
Table 9.27. *Tbx15*$^{+/-}$ DEXA at 23 weeks under recoverable anaesthesia. 367
Table 9.28. Female *Tbx15*^{H156N} DEXA at 24 weeks under terminal anaesthesia. 368
Table 9.29. Male *Tbx15*^{H156N} DEXA at 24 weeks under terminal anaesthesia.. 369
Table 9.30. Female *Tbx15*^{M566R} DEXA at 23 weeks under recoverable anaesthesia. .370
Table 9.31 Male *Tbx15*^{M566R} DEXA at 23 weeks under recoverable anaesthesia. 371
Table 9.32. *Tbx15*$^{+/-}$ terminal measurements. 372
Table 9.33. *Tbx15*$^{+/-}$ terminal depot weights....372
Table 9.34. Female *Tbx15*^{H156N} terminal measurements. 373
Table 9.35. Male *Tbx15*^{H156N} terminal measurements....373
Table 9.36. *Tbx15*^{H156N} terminal depot weights....374
Table 9.37. Female *Tbx15*^{M566R} terminal measurements. 376
Table 9.38. Male *Tbx15*^{M566R} terminal measurements....376
Table 9.39. *Tbx15*^{M566R} terminal depot measurements.. 377
Table 9.40. *Tbx15*$^{+/-}$ blood plasma clinical chemistry. 379
Table 9.41. *Tbx15*^{H156N} blood plasma clinical chemistry. 380
Table 9.42. *Tbx15*^{M566R} blood plasma clinical chemistry analysis. 383
Table 9.43. *Tbx15*$^{+/-}$ average adipocyte cell area. 386
Table 9.44. Female *Tbx15*$^{+/-}$ high-fat diet adipocyte cell area distribution. 387
Table 9.45. Female *Tbx15*$^{+/-}$ low-fat diet adipocyte cell area distribution. 388
Table 9.46. Male *Tbx15*$^{+/-}$ high-fat diet adipocyte cell area distribution. 389
Table 9.47. Male *Tbx15*$^{+/-}$ low-fat diet adipocyte cell area distribution. 390

Investigating the Function of Coding Polymorphisms within the *TBX15-WARS2* Locus Associated with Waist-Hip Ratio as a Risk Factor for Metabolic Syndrome

Louisa Zolkiewski

Department of Physiology, Anatomy and Genetics; Trinity College, University of Oxford
Genetics of Type 2 Diabetes; MRC Mammalian Genetic Unit, MRC Harwell Institute
A thesis presented for the degree of Doctor of Philosophy; Trinity Term 2022

Abstract

As prevalence of obesity and metabolic disorders increase, it is necessary to elucidate mechanisms driving body mass, body composition and energy homeostasis. Elevated waist-hip ratio (WHR) increases type 2 diabetes and cardiovascular disease risk. The *TBX15-WARS2* locus contains several independent association signals for WHR adjusted for BMI (WHRadjBMI). However, whether these risk variants are functional remains to be determined. The aim of my DPhil was to characterise two potentially functional *TBX15*-coding polymorphisms, rs10494217 (p.H156N) and rs61730011 (p.M566R), at a cellular and organismal level to investigate their impact on TBX15 function in adipose tissue biology.

Firstly, I prioritised the mechanism-of-action of these two polymorphisms at either a DNA-regulatory or protein-coding level *in silico.* I showed the most likely mode-of-action was at the protein-coding level with p.H156N predicted to alter a loop structure in the T-box of TBX15, further implicated in altered protein-protein dimerisation. However, this was not recapitulated *in vitro* (within assay sensitivity limits).

TBX15-WARS2 signals were associated with differential *TBX15* and *WARS2* expression, and several *Tbx15* and *Wars2* mouse models had altered body composition phenotypes. I metabolically characterised heterozygous knock-out ($Tbx15^{+/-}$) mice and mice carrying orthologous human polymorphisms p.H156N ($Tbx15^{H156N}$) or p.M566R ($Tbx15^{M566R}$) and showed all three alleles conferred resistance to fat mass gain.

Finally, to evaluate the effect of TBX15 on gene expression, I generated a TBX15 regulatory network using ChIP-sequencing of preadipocyte cell lines, and RNA-sequencing of adipose tissues from homozygous knock-out ($Tbx15^{-/-}$) and $Tbx15^{H156N}$ mice. Functional enrichment of differentially expressed genes implicated TBX15 in regulating lineage determination, adipogenesis of committed preadipocyte cells and immune response. In summary, these results suggest TBX15 regulates adipose tissue biology and body composition and shows a novel functional role for two human WHRadjBMI risk variants. Further work is needed to elucidate underlying mechanisms of action that can be targeted therapeutically.

Common abbreviations

3T3-L1	Swiss-albino "3-day transfer, inoculum 3 x 10^5" (3T3) subclone L1; murine preadipocyte cell line
aa	Amino acids
ALP	Alkaline phosphatase
ALT	Alanine aminotransferase
ANOVA	Analysis of variance
AST	Aspartate aminotransferase
ATP	Adenosine triphosphate
AUC	Area under the curve
BAT	Brown adipose tissue
BDNF	Brain-derived neurotrophic factor
BMC	Bone mineral content
BMD	Bone mineral density
BMI	Body mass index
BMP7	Bone morphogenic factor 7
BSA	Bovine serum albumin
BSdir	Direct repeat of the T-half site consensus binding sequence
BSinv	Inverse repeat of the T-half site consensus binding sequence
BSp	Palindromic repeat of the T-half site consensus binding sequence
°C	Degrees Celsius
CD137	CD137 antigen (gene: TNFRSF9)
C/EBP	CCAAT/enhancer-binding protein
ChIP-sequencing	Chromatin immunoprecipitation with next generation sequencing
CIDEA	Cell death inducing DFFA-like effector A
CK	Creatine kinase
cm	Centimetre
CO_2	Carbon dioxide
Co-IP	Co-immunoprecipitation
COX7A	Cytochrome c oxidase subunit VIIa
COX8B	Cytochrome c oxidase subunit VIIIb
CREB	cAMP-response element binding protein
CRISPR	Clustered regularly interspaced short palindromic repeats
CRM	Cis-regulatory module
CT	Computer tomography
CtBP1	C-terminal binding protein 1
CtBP2	C-terminal binding protein 2
CVD	Cardiovascular disease
ddH_2O	Double distilled water
DEG	Differentially expressed gene

DEXA	Dual-energy X-ray absorptiometry
diH_2O	Deionised water
DIO2	Deiodinase iodothyronine 2
DMEM	Dulbecco's modified eagle medium
DMSO	Dimethyl sulfoxide
DNA	Deoxyribonucleic acid
dNTP	Deoxynucleoside triphosphate
DPBS	Dulbecco's phospho-buffered saline
dWAT	Dermal white adipose tissue
E	Embryonic day
EBF2	Early B-cell factor 2
ECM	Extracellular matrix
E. Coli	Escherichia coli
EDTA	Ethylenediaminetetraacetic acid
EGR2	Early growth response protein 2
EMSA	Electromobility shift assay
ENU	N-ethyl-N-nitrosourea
eQTL	Expression quantitative trait loci
FABP4	Fatty acid binding protein 4
FBS	Foetal bovine serum
FDR	False discovery rate
FFA	Free fatty acid
FGF21	Fibroblast growth factor 21
FTO	Fat mass and obesity associated gene
GFD15	Growth differentiation factor 15
GWAS	Genome wide association study
gWAT	Gonadal white adipose tissue
gWAT:iWAT	Ratio of gonadal white adipose tissue to inguinal white adipose tissue
H_2O	Water
HADDOCK	High ambiguity driven protein-protein docking
HbA1c	haemoglobin A1c
HC	Hip circumference
HCl	Hydrochloric acid
HDL	High-density lipoprotein
H&E	haematoxylin and eosin
HEK293T	Human embryonic kidney 293 cells immortalised using SV40 T antigen
HFD	High-fat diet
HOMA-β	Homeostasis model assessment of β-cell function
HOMA-IR	Homeostatic model assessment for insulin resistance
HOXC8	Homeobox C8
HOXC9	Homeobox C9

HRP	Horseradish peroxidase
hWAT	Human white adipose tissue preadipocyte cells
JNK	c-Jun N-terminal kinases
IBMX	Isobutyl methylxanthine
IgG	Immunoglobulin G
IL-1B	Interleukin 1 beta
IL-6	Interleukin 6
IL-18	Interleukin 18
IP	Immunoprecipitation
IRF3	Interferon regulatory factor 3
IRF4	Interferon regulatory factor 4
IPGTT	Intraperitoneal glucose tolerance test
IPIST	Intraperitoneal insulin sensitivity test
IU	International units
iWAT	Inguinal white adipose tissue
KLD	Kinase, Ligase & DpnI
KLF4	Krüppel-like factor 4
KLF5	Krüppel-like factor 5
KLF15	Krüppel-like factor 15
KOH	Potassium hydroxide
LB	Lysogeny broth
LD	Linkage disequilibrium
LDH	Lactate dehydrogenase
LDL	Low-density lipoprotein
LEP	Leptin
LFD	Low-fat diet
LPL	Lipoprotein lipase
LN_2	Liquid nitrogen
MAF	Minor allele frequency
MAFG	Maf bZIP transcription factor G
MetS	Metabolic syndrome
MHO	Metabolically healthy obesity
MLC	Mary Lyon centre
MRCH	Medical Research Council Harwell institute
MRI	Magnetic resonance imaging
MSC	Mesenchymal stem cell
MUO	Metabolically unhealthy obesity
mWAT	Mesenteric white adipose tissue
MYF5	Myogenic factor 5
NaCl	Sodium chloride
NAFLD	Non-alcoholic fatty liver disease
NANOG	Homeobox transcription factor
NLS	Nuclear localisation sequence

NaOH	Sodium hydroxide
NBCS	New-born calf serum
NCBI	National centre for biotechnology information
NEB	New England Biolabs
NF-H_2O	Nuclease-free water
NF-κB	Nuclear factor kappa-light-chain-enhancer of activated B cells
ng	Nanogram
NRSF	Neuron restrictive silencer factor
OCT-4	Octamer-binding transcription factor 4
PAGE	Polyacrylamide gel electrophoresis
PCR	Polymerase chain reaction
PDB	Protein data bank
PDL	Poly-D-lysine
PGC1α	PPARγ coactivator 1α
POU2F2	POU class 2 transcription factor 2
PPA	Posterior probability analysis
PPAR	Peroxisome proliferator-activated receptor
Ppm	Parts per million
PRDM16	PR/SET domain 16
PVDF	Polyvinylidene difluoride
pWAT	Perirenal white adipose tissue
QC	Quality control
qPCR	Quantitative polymerase chain reaction
RNA	Ribonucleic acid
RM3	Rat and mouse no. 3 breeding diet
Rpm	Revolutions per minute
RSPO3	R-spondin 3
SAT	Subcutaneous adipose tissue
SD	Standard deviation
SDS	Sodium dodecyl sulphate
SEM	Standard error mean
SHOX2	Short stature homeobox 2
SIFT	Sorting intolerant from tolerant
SMAD	Suppressor of mothers against decapentaplegic
SNP	Single nucleotide polymorphism
SOX2	SRY-box transcription factor 2
SPAG17	Sperm-associated antigen-17
SREBP1	Sterol regulatory element-binding protein 1
SVF	Stromal vascular fraction
T2DM	Type 2 diabetes mellitus
T3	3,3′,5-Triiodo-L-thyronine
T	Brachyury
TAE	Tris-Acetate-EDTA

TBS	Tris-buffered saline
TBST	Tris-buffered saline containing 0.1% Tween-20
TBX1	T-box 1
TBX3	T-box 3
TBX5	T-box 5
TBX15	T-box 15
TBX18	T-box 18
***Tbx15*$^{+/+}$**	Wild-type *Tbx15* mouse
***Tbx15*$^{+/-}$**	Heterozygous *Tbx15* knockout mouse
***Tbx15*$^{-/-}$**	Homozygous *Tbx15* knockout mouse
***Tbx15*$^{+/H156N}$**	Heterozygous *Tbx15* p.H156N mouse
***Tbx15*$^{H156N/H156N}$**	Homozygous *Tbx15* p.H156N mouse
***Tbx15*$^{+/M566R}$**	Heterozygous *Tbx15* p.M566R mouse
***Tbx15*$^{M566R/M566R}$**	Homozygous *Tbx15* p.M566R mouse
TCF12	Transcription factor 12
TCF21	Transcription factor 21
TF	Transcription factor
TFBM	Transcription factor binding motif
TFBS	Transcription factor binding site
TFS	ThermoFisher Scientific
TGFβ	Transforming growth factor beta
TLE3	Transducin-like enhancer protein 3
TMEM26	Transmembrane domain protein 26
TNF	Tumour necrosis factor
TNFRSF9	Tumour necrosis factor receptor family member 9
TWIST1	Twist Family basic helix loop helix Transcription Factor 1
µg	Microgram
µL	Microliter
UCP1	Uncoupling protein 1
V	Volts
VAT	Visceral adipose tissue
v/v	Volume/volume
WARS2	Tryptophanyl-tRNA synthetase 2
WAT	White adipose tissues
WC	Waist circumference
WHR	Waist-to-hip ratio
WHRadjBMI	Waist-to-hip ratio adjusted for body mass index
WNT5A	Wingless family member 5A
WNT5B	Wingless family member 5B
WNT10B	Wingless family member 10B
w/v	Weight/volume

1

Introduction

1.1. Obesity

Adipose tissue is central to healthy metabolic homeostasis, acting as both an energy store and an endocrine organ to regulate signals associated with satiety. Increased fat accumulation is influenced by a range of factors including age, sex, low socio-economic status and African or Asian ethnicity (Chooi, Ding and Magkos, 2019; WHO, 2021). Obesity is one of the largest risk factors for developing metabolic diseases, cancer and depression (De Pergola and Silvestris, 2013; Chooi, Ding and Magkos, 2019; Blasco *et al.*, 2020). Globally, the prevalence of overweight and obese individuals has been rising rapidly, over three-fold from 1975 to 2016, and we are now facing a pandemic of epic proportions (Figure 1.1) (WHO, 2021).

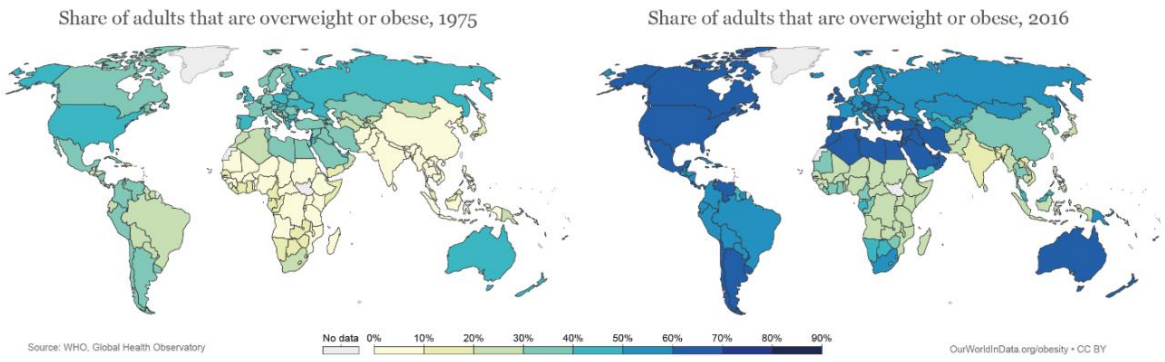

Figure 1.1. Share of adults that were overweight or obese from 1975 to 2016 across the world. Left hand panel 1975, right hand panel 2016. Figure reproduced from https://ourworldindata.org/obesity (Ritchie and Roser, 2017) (under creative commons licence: CC BY 4.0); data was collated from the World Health Organisation "obesity and overweight factsheet".

An accepted and simple proxy used to measure fat accumulation is body mass index (BMI), calculated as weight divided by height squared (kg/m^2). BMIs of ≥25.0, ≥30.0 and ≥40.0 are used to define overweight, obese and morbidly obese individuals, respectively, with a BMI ≥50.0 recommended for extreme obesity (Sturm, 2007; WHO, 2021). In 2016, 39% of the adult population (1.9 billion individuals) were classified as overweight and 13% (650 million) were classified as obese; while 25% (442 million) of children and adolescents were obese (Chooi, Ding and Magkos, 2019; WHO, 2021). In the UK, it is predicted that by 2050 ~60% of males and 50% of females will be obese, while 1% and 4%, respectively, will be morbidly obese (McPherson, Marsh and Brown, 2007).

Table 1.1. Clinical body mass index classification. Abbreviations: BMI (body mass index).

Weight category	BMI (kg/m^2)
Underweight	<18.5
Normal weight	18.5 – 24.9
Overweight	25.0 – 29.0
Obese (class I)	30.0 – 34.9
Obese (class II); severe	35.0 – 39.9
Obese (class III); morbid	40.0 – 49.9
Obese (class IV); extreme	≥50.0

Obesity is an important risk factor for cardiovascular disease (CVD), metabolic syndrome (MetS), type 2 diabetes mellitus (T2DM), cancer, osteoarthritis and reduced life expectancy (McPherson, Marsh and Brown, 2007; Agha and Agha, 2017). In 2012, 3.7 million deaths worldwide were attributed to T2DM and high blood glucose-induced CVD (WHO, 2016). UK incidence of T2DM, coronary heart disease and stroke are predicted to increase 70%, 28% and 20%, respectively, by 2035 as a consequence of obesity (McPherson, Marsh and Brown, 2007). This is associated with a predicted

increase in NHS costs to £49.9 billion in 2050 to treat BMI-related diseases. However, a decrease of -8.0 BMI units across the population could reduce these treatment costs to £17.6 billion in 2050 (McPherson, Marsh and Brown, 2007), highlighting the need to better understand the underlying genetics of overall adiposity so that targeted treatments can be developed.

1.2. Metabolic Syndrome

MetS encompasses five main factors: hypertension (high blood pressure), raised plasma glucose, high serum triglycerides, low high-density lipoprotein (HDL) cholesterol, and abdominal obesity. Other contributing factors include insulin resistance, altered liver function, altered adipokine and cytokine expression, elevated urinary albumin levels, and inflammatory abnormalities (Srivastava, 2012; Katsiki *et al.*, 2014; Dommermuth and Ewing, 2018). MetS affects one quarter of adults globally and increases the risk of developing CVD and T2DM two- and four-fold, respectively (Srivastava, 2012; Katsiki *et al.*, 2014; Dommermuth and Ewing, 2018).

The first mention of metabolically healthy obesity (MHO) appeared during the 1950s, where the incidence of diabetes and atherosclerosis differed between subpopulations of obese individuals with altered body fat distribution (Vague, 1956). Clinically, MHO is defined as an absence of CVD, T2DM, dyslipidaemia and hypertension with specific criteria for serum triglycerides, HDL-cholesterol, blood pressure and fasting glucose levels (Figure 1.2) (Blüher, 2020). Further, individuals can transition between MHO and metabolically unhealthy obesity (MUO) states over time as a result of factors such as diet, medication, surgical intervention and physical exercise suggesting individuals can have a metabolically favourable profile whilst clinically obese (Blüher, 2020).

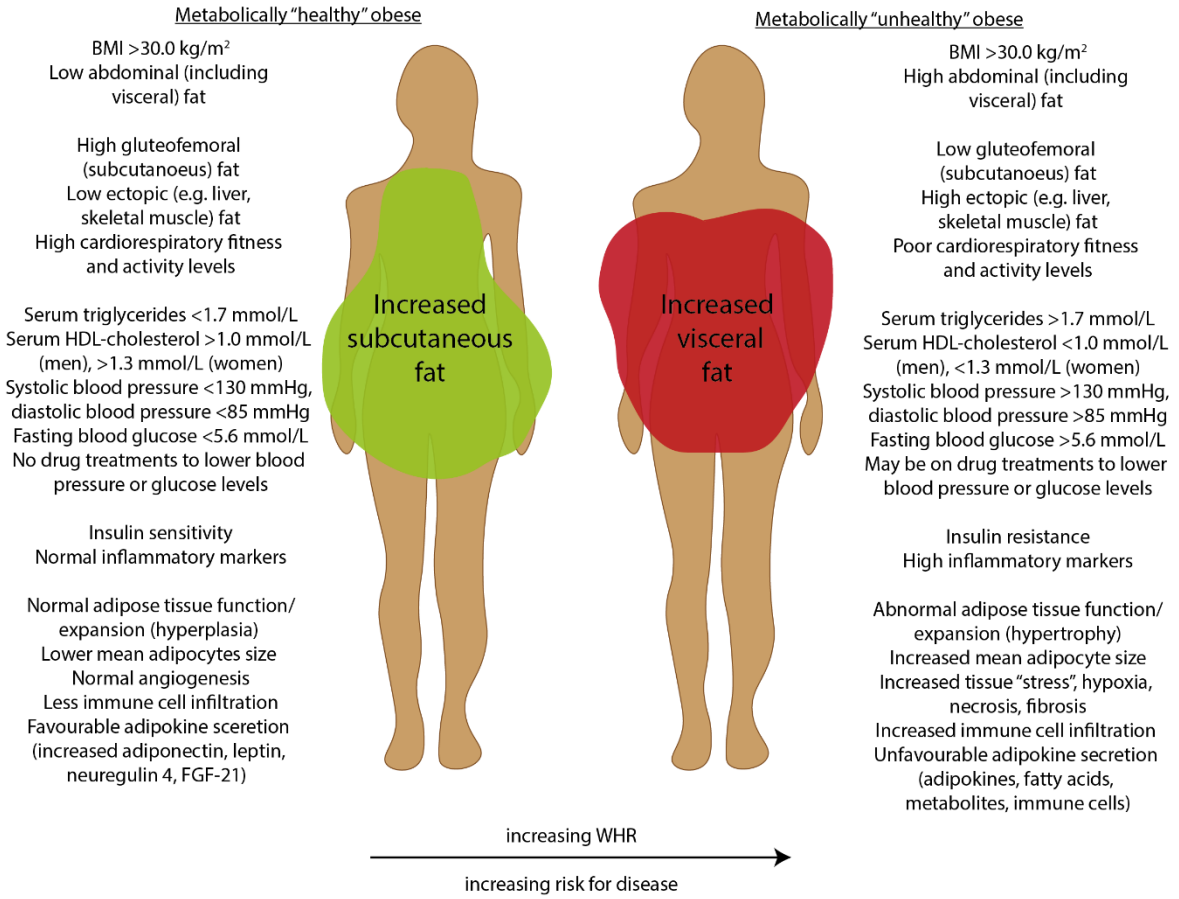

Figure 1.2. Metabolically healthy versus unhealthy obesity. Obesity is defined as a BMI ≥30.0 kg/m², within this there are subpopulations of individuals classified as metabolically "healthy" or "unhealthy" obese based on a range of criteria including fat distribution, fitness levels, blood pressure and serum glucose levels. Further, insulin sensitivity and adipose expansion (either through hyperplasia or hypertrophy), infiltration of immune cells and adipokine secretion all influence this categorisation. Abbreviations: WHR (waist-to-hip ratio), FGF-21 (fibroblast growth factor 21). Figure adapted from (Blüher, 2020) (under creative commons licence: CC BY 4.0).

1.2.1. Adipose tissue expandability hypothesis

Adipose tissue expansion is a key factor in distinguishing MHO and MUO individuals. The adipose tissue expandability hypothesis states that white adipose tissues (WAT) have a maximal expansion limit influenced by genetic and environmental factors (Unger and Scherer, 2010; Vegiopoulos, Rohm and Herzig, 2017). When this limit is reached, excess lipids are stored ectopically, in tissues such as muscles, pancreatic β cells and the liver, resulting in lipotoxicity, β cell dysfunction and insulin resistance (Figure 1.3) (Virtue and Vidal-Puig, 2008; Vegiopoulos, Rohm and Herzig, 2017). Both

obese and lipodystrophic individuals are susceptible to this lipotoxic insulin resistance, suggesting that MetS is not a direct cause of obesity, rather, an imbalance in excess lipid storage (Virtue and Vidal-Puig, 2008; Unger and Scherer, 2010).

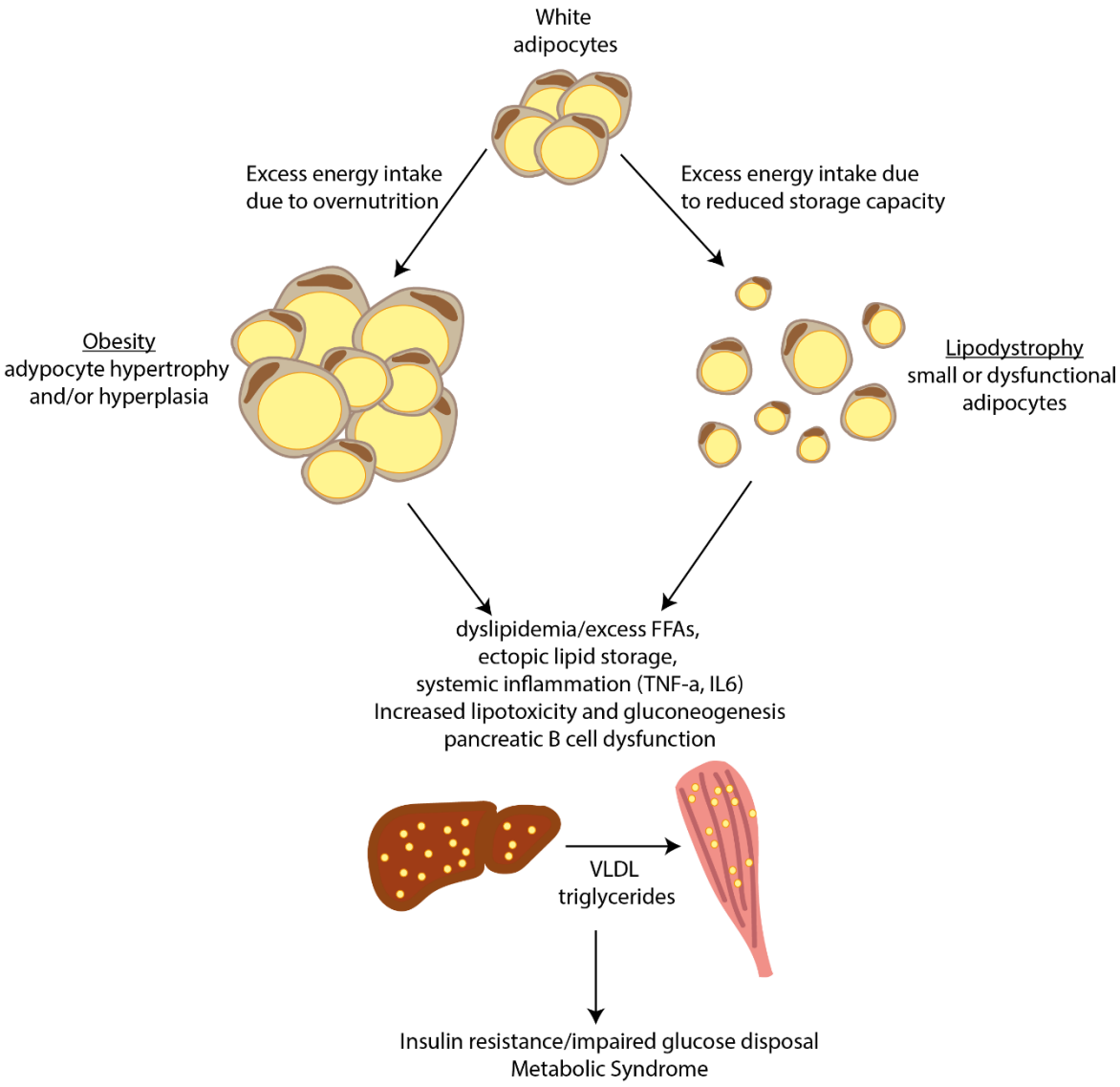

Figure 1.3. Adipose tissue expandability hypothesis. White adipocytes store excess lipids, and white adipose tissue expands in response to this by hyperplasia (production of new adipocytes) or hypertrophy (enlargement of existing adipocytes). Individuals have a maximum adipose tissue expandability limit in response to excess energy intake. Once this is reached, excess lipids travel systemically and are stored ectopically in muscle, liver and pancreatic β cells. This results in systemic inflammation and increased lipotoxicity which results in insulin resistance and ultimately metabolic syndrome. Abbreviations: IL-6 (interleukin 6), FFAs (free fatty acids), TNF-α (tumour necrosis factor α) and VLDL (very low density lipid cholesterol). Adapted from (Vegiopoulos, Rohm and Herzig, 2017) with permission from John Wiley and Sons (licence number: 5342990964694).

1.3. Fat mass distribution and disease risk

BMI is a simple and non-invasive tool for measuring fat accumulation that correlates at a population level with adverse metabolic health. However, it fails to account for factors such as age, sex, ethnicity and body composition (Gallagher *et al.*, 1996). Further, it does not distinguish adipose tissue distribution, nor individuals with increased muscle mass or decreased bone density. Several more advanced methods such as computer tomography (CT), magnetic resonance imaging (MRI), dual energy X-ray absorptiometry (DEXA) and electrical bio-impedance analysis can be exploited to examine body composition (Lemos and Gallagher, 2017). Techniques such as MRI and CT are more appropriate than DEXA for estimating adipose tissue distribution, specifically enabling the quantification of subcutaneous and visceral WAT (SAT and VAT, respectively) (Lane *et al.*, 2005; Kullberg *et al.*, 2009).

Adipose distribution is associated with disease risk, independent of obesity. For example, increased VAT:SAT ratio was significantly associated with increased blood pressure, impaired glucose metabolism, decreased HDL-cholesterol levels, atherosclerosis, diabetes and MetS (Kaess *et al.*, 2012; Katsuyama, Kawaguchi and Yanai, 2015; Elffers *et al.*, 2017; Storz *et al.*, 2018). More recently, increased VAT:SAT ratio was associated with poorer prognosis following intensive care unit admission for COVID-19 patients, indicating body composition may prove a useful tool in clinical settings (Bunnell *et al.*, 2021).

However, routine use of these methods in clinical practice is impeded by high purchase and maintenance costs of the associated equipment. A common, and importantly simple and inexpensive, method to analyse body fat distribution is waist-to-hip ratio (WHR), a ratio of waist circumference (WC) and hip circumference (HC). A high WHR,

defined as ≥0.9 in men and ≥0.85 in women (WHO, 2011), was considered a better indicator of disease development for cardiometabolic disorders compared to BMI and WC alone (Cheng *et al.*, 2010; Søgaard *et al.*, 2015; Jafari-Koshki *et al.*, 2016; Rashiti *et al.*, 2016; Andreasson *et al.*, 2017; Emdin *et al.*, 2017; Morris, 2017; Tang *et al.*, 2017). In particular, a decreased HC increased risk for CVD and mortality, independent of WC and BMI (Heitmann and Lissner, 2011; Cameron *et al.*, 2012). For example, the relative risk for T2DM increases approximately 2-fold for each increase in standard deviation (SD) of WHR (Vazquez *et al.*, 2007; Czernichow *et al.*, 2011). Further, mortality and CVD incidence were significantly correlated with increased BMI and WHR but not total fat percentage (Myint *et al.*, 2014). These adiposity traits are highly correlated, with WC and WHR increasing with BMI (r^2 ~0.9 and ~0.6, respectively) (Lindgren *et al.*, 2009). Therefore, adjusted-model approaches can be used to distinguish correlated traits, for example WC adjusted for BMI (WCadjBMI) and WHR adjusted for BMI (WHRadjBMI). Whilst it has been suggested that these adjusted models introduce bias towards false positive results in genome-wide association studies (GWAS) (Aschard *et al.*, 2015), WHRadjBMI is considered a more robust surrogate measure of fat distribution than WHR alone (Winkler *et al.*, 2018).

Twin and heritability studies have indicated that heritability accounts for 40-70% of an individual's BMI (Speliotes *et al.*, 2010; Berndt *et al.*, 2013), and 22-61% for WHRadjBMI (Zillikens *et al.*, 2008; Schleinitz *et al.*, 2014). The genetic drivers of these traits remain elusive; however, GWAS have identified genomic regions that may be involved in this regulation. Currently, over 300 loci have been associated with WHRadjBMI (discussed in more detail in section 1.5.3) (Heid *et al.*, 2010; Shungin *et al.*, 2015; Justice *et al.*, 2019; Pulit *et al.*, 2019). Further, Mendelian randomisation studies have leveraged GWAS data to determine causality between variants and traits.

For example, 48 single nucleotide polymorphisms (SNPs) identified across six GWAS (~770,000 total individuals) accounted for 1.5% of WHRadjBMI variance observed in the sampled individuals (Emdin *et al.*, 2017). One SD increase (0.09 units) in WHRadjBMI was associated with decreased HC (4.1 cm) and BMI (1.0 kg/m^2), increased WC (2 cm) and WHR (0.068 units), and increased systolic blood pressure (3 mmHg), cholesterol (7.3 mg/dl), fasting insulin levels (0.078 mg/dl), and increased incidence of T2DM (2.0x) and CVD (1.6x), suggesting a causal influence of these SNPs on cardiometabolic traits (Emdin *et al.*, 2017). Interestingly, BMI-associated genes were enriched in brain tissue, while WHRadjBMI signals were expressed in adipocytes indicating that WHR is more likely regulated intrinsically within adipose tissues (Heid *et al.*, 2010; Shungin *et al.*, 2015).

1.4. Adipose tissue biology

1.4.1. White, brown and beige adipocytes

Adipose tissue is well-established as an insulating and protective layer. More recently it has been identified as a paracrine and endocrine organ, secreting numerous factors that regulate appetite, immune function, insulin sensitivity, lipid accumulation and inflammation (Ali *et al.*, 2013; Chen and Tong, 2013). Nominally there are two types of adipocytes – white and brown – both with different functions.

White adipocytes primarily store excess energy as triglycerides within a unilocular lipid droplet which expands in response to excess lipids. White adipocytes regulate systemic metabolism by inducing lipolysis of triglyceride stores into constituent free fatty acids (FFAs) and glycerol for metabolism (Lo and Sun, 2013; Park, Kim and Bae, 2014). White adipocytes are characterised by expression of markers such as fatty acid

binding protein 4 (*FABP4*), homeobox C8 and C9 (*HOXC8* and *HOCX9*), lipoprotein lipase (*LPL*), leptin (*LEP*) and transcription factor 21 (*TCF21*) (Lo and Sun, 2013; Park, Kim and Bae, 2014; Pilkington, Paz and Wankhade, 2021).

Brown adipocytes have multilocular lipid droplets and high numbers of mitochondria giving them a characteristic reddish-brown colour. Brown adipocytes use their own lipid stores to produce heat in response to cold exposure, dependent on uncoupling protein 1 (*UCP1*) expression (Lo and Sun, 2013; Park, Kim and Bae, 2014). Additional brown adipocyte markers include cell death inducing DFFA-like effector A (*CIDEA*), deiodinase iodothyronine 2 (*DIO2*), bone morphogenic protein 7 (*BMP7*), cytochrome c oxidase subunits VIIIb and VIIa (*COX8B* and *COX7A*) and PR/SET domain 16 (*PRDM16*) (Lo and Sun, 2013; Park, Kim and Bae, 2014; Pilkington, Paz and Wankhade, 2021).

A third type of beige adipocyte has been described more recently; these appear classically white with a single lipid droplet, however, upon cold exposure can be stimulated to take on a brown-like phenotype expressing greater numbers of mitochondria, and markers such as *UCP1, CIDEA* and *DIO2* (Chen and Tong, 2013; Lo and Sun, 2013; Park, Kim and Bae, 2014). It is unclear whether beige adipocytes are their own population or occur through transdifferentiation of white adipocytes. They have their own gene expression markers including tumor necrosis factor receptor family member 9 (*CD137*), T-box 1 (*TBX1*), transmembrane domain protein 26 (*TMEM26*) and short stature homeobox 2 (*SHOX2*). Although, they express both white (*HOXC8* and *HOXC9*) and brown (*CIDEA, COX7A, PRDM16* and *UCP1*) adipocyte markers (Lo and Sun, 2013; Park, Kim and Bae, 2014; Pilkington, Paz and Wankhade, 2021).

Mesenchymal stem cells (MSCs) are the major source of adipocyte progenitor cells. The differentiation process of these cells requires a complex communication between individual adipocytes and the surrounding extracellular environment (Ali *et al.*, 2013). MSCs give rise to distinct myogenic factor 5 positive (*MYF5*$^{+}$) or negative (*MYF5*$^{-}$) precursor cells which differentiate into brown, and white and beige lineages, respectively (Figure 1.4) (Chen and Tong, 2013; Park, Kim and Bae, 2014). In mice and humans, WAT develops during mid-gestation, continuing to expand during late gestation and after birth (Symonds *et al.*, 2012; Park, Kim and Bae, 2014; Ghaben and Scherer, 2019). Lineage tracing in mouse models has shown that white adipocytes in inguinal WAT (iWAT) develop at embryonic day 14 (E14) and numbers of adipocytes are genetically predetermined at this stage (Wang *et al.*, 2013). Conversely, adipocytes from gonadal WAT (gWAT) begin to form at P1, with *de novo* adipocytes forming post-weaning (Wang *et al.*, 2013). In humans, total numbers of adipocytes in WAT remain fairly constant throughout adulthood with a cell turnover rate of ~10% reported for both lean and obese individuals, despite obese individuals having overall higher numbers of adipocytes compared to lean individuals (Spalding *et al.*, 2008).

In comparison, brown adipose tissue (BAT) develops during the latter stages of gestation and rapidly declines in humans postnatally, while remaining more prominent in rodents particularly in the interscapular BAT (Symonds *et al.*, 2012; Park, Kim and Bae, 2014; Ghaben and Scherer, 2019). This suggests that developmental transcription factors (TFs) could be important regulators of adipose tissue biology in later life. It has been suggested that adipogenesis occurs bi-directionally, with mature adipocytes capable of returning to their undifferentiated state, although it remains unclear what is driving this process (Ghaben and Scherer, 2019).

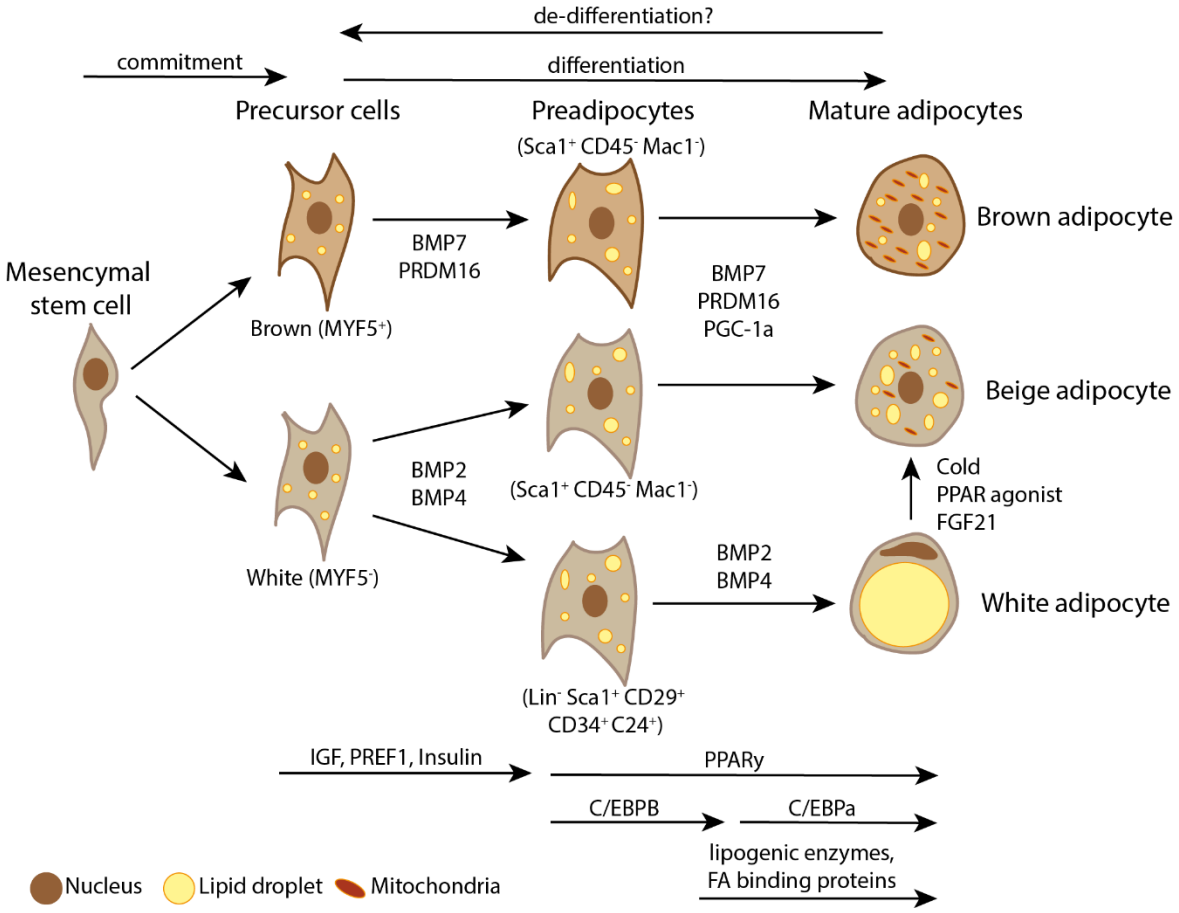

Figure 1.4. Adipogenesis of white, brown and beige adipocytes. Mesenchymal stem cells undergo an irreversible determination to the adipocyte lineage, transforming from a fibroblast-like cell to a committed preadipocyte, remaining in this preadipocyte phase until growth stops. At this point, preadipocytes undergo mitotic clonal expansion and begin to resemble adipocytes. Terminal differentiation results in mature adipocytes which contain either a single lipid droplet with a thin cytoplasm layer surrounding it and the nucleus at the edge of the cell (white adipocytes), or a combination of smaller lipid droplets and mitochondria (brown and beige adipocytes). Abbreviations: IGF (insulin growth factor), PREFf-1 (preadipocyte factor 1), C/EBP (CCAAT-enhancer-binding protein), PPARγ (Peroxisome proliferator-activated receptor gamma), FA (fatty acid). Adapted from (Chen and Tong, 2013) with permission from Elsevier (licence number: 4664281430725).

1.4.2. Adipogenesis

Despite arising from different precursor lineages, differentiation of brown and white adipocytes is regulated by a common cascade of factors. Peroxisome proliferator-activated receptor (PPAR) and CCAAT/enhancer-binding protein (C/EBP) family members act in a positive feedback loop at the core of this process, regulated by pro- and anti-adipogenic factors, to promote lipid and glucose homeostasis in mature

white adipocytes (Figure 1.5) (Ali *et al.*, 2013; Chen and Tong, 2013; Giralt and Villarroya, 2013; Park, Kim and Bae, 2014).

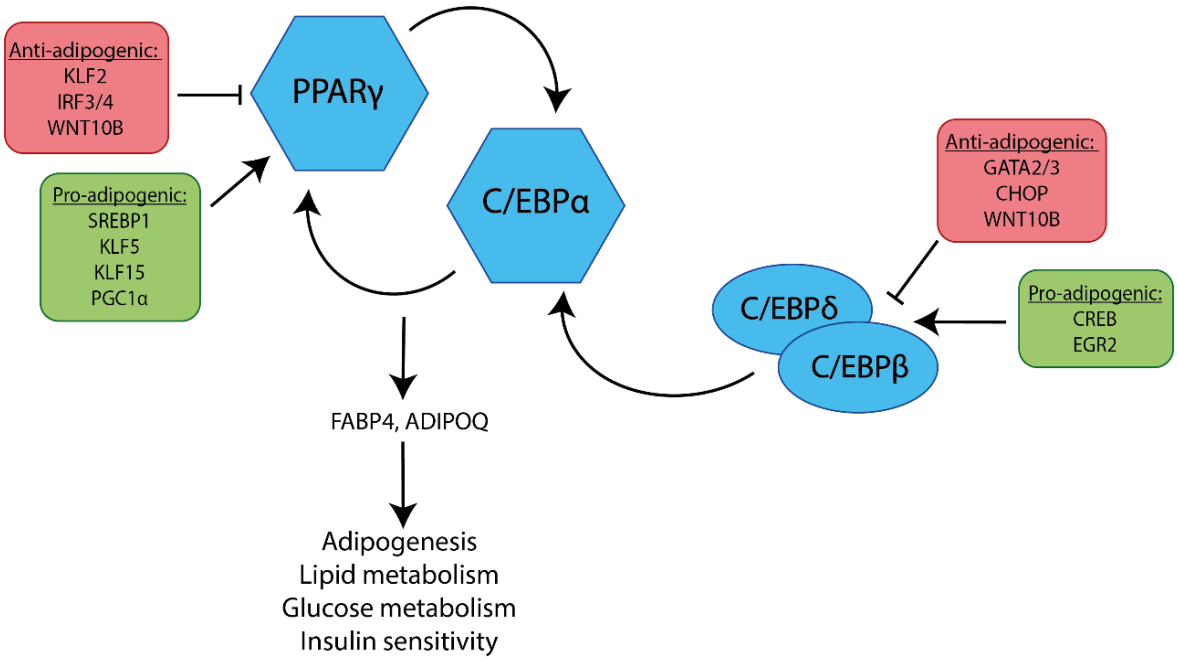

Figure 1.5. PPARγ and C/EBPα positive feedback loop drives adipogenesis. Peroxisome proliferator-activated receptor gamma (PPARγ) and CCAAT/enhancer-binding protein alpha (C/EBPα) are at the centre of a positive feedback loop which is stimulated and inhibited by several factors. Factors such as sterol regulatory element-binding protein 1 (SREBP1), Krüppel-like factors 5 and 15 (KLF5, KLF15) and PPARγ coactivator 1 alpha (PGC1α) stimulate PPARγ, whilst KLF2, interferon regulatory factors 3 and 4 (IRF3, IRF4) and wingless family member 10B (WNT10B) act to inhibit PPARγ. cAMP-response element binding protein (CREB), early growth response protein 2 (EGR2), GATA-binding factors 2 and 3 (GATA2, GATA3), C/EBP homologous protein (CHOP) and WNT10B act through C/EBPβ and C/EBPδ to regulate C/EBPα in the feedback loop. When PPARγ and C/EBPα are activated, they drive the differentiation of pre-adipocytes into mature adipocytes. Adapted from (Ali *et al.*, 2013) with permission from Elsevier (licence number: 4664301278198).

Additionally, during brown adipocyte differentiation PRDM16, norepinephrine, leptin, brain-derived neurotrophic factor (BDNF) and PPARγ coactivator 1α (PGC1α) activate C/EBPα. (Ali *et al.*, 2013; Chen and Tong, 2013; Lo and Sun, 2013). PRDM16 acts cooperatively with C-terminal binding proteins 1 and 2 (CtBP1 and CtBP2) to inhibit white adipogenesis genes, and early B-cell factor 2 (EBF2). Further, PGC1α regulates UCP1 expression to control mitochondrial biogenesis, oxidative metabolism and

thermogenesis in both brown and beige adipocytes (Ali *et al.*, 2013; Chen and Tong, 2013; Lo and Sun, 2013). Long non-coding RNAs can regulate genes such as *Cebpa, Ucp1, Pgc1α, Cidea, Dio2, Tbx1, Tmem26* and *Cd137* (Xiong *et al.*, 2018), highlighting the importance of epigenetic factors in regulating gene expression, but this requires further investigation in the context of adipogenesis.

1.4.3. Adipose tissue expansion

WAT is extremely heterogeneous, comprising ~50% mature adipocytes, with the remainder consisting of MSCs, preadipocytes, endothelial and smooth muscle cells, and immune cells such as macrophages, innate lymphoid cells and T-cells (Vijay *et al.*, 2020; Hildreth *et al.*, 2021). Following adipogenesis, adipose tissues expand either by enlarging pre-existing adipocytes (hypertrophy) or by differentiating new preadipocytes (hyperplasia) (Stenkula and Erlanson-Albertsson, 2018; Ghaben and Scherer, 2019). This is combined with an acute pro-inflammatory response that induces hyperplasia and tissue extracellular matrix (ECM) remodelling to prevent ectopic lipid storage during healthy tissue expansion (Wernstedt Asterholm *et al.*, 2014). Indeed, hypertrophy and hyperplasia significantly increased in abdominal and gluteofemoral SAT, respectively, in humans in response to over nutrition (Figure 1.6) (Tchoukalova *et al.*, 2010).

Adipose tissue expansion has been studied in great detail, with *in vivo* transgenic models such as AdipoChaser mice allowing temporal resolution of this process in response to dietary challenge (Wang *et al.*, 2013). Both iWAT and gWAT initially expand by hypertrophy following four weeks of high-fat diet (HFD) challenge (Wang *et al.*, 2013). With prolonged HFD-feeding iWAT expanded through hypertrophy,

whilst gWAT exhibited both hypertrophy and initiation of *de novo* hyperplasia (Wang *et al.*, 2013; Jeffery *et al.*, 2015). Increased proliferation of adipocyte precursor cells in gWAT in the first week of HFD-feeding was the likely cause of this (Jeffery *et al.*, 2015).

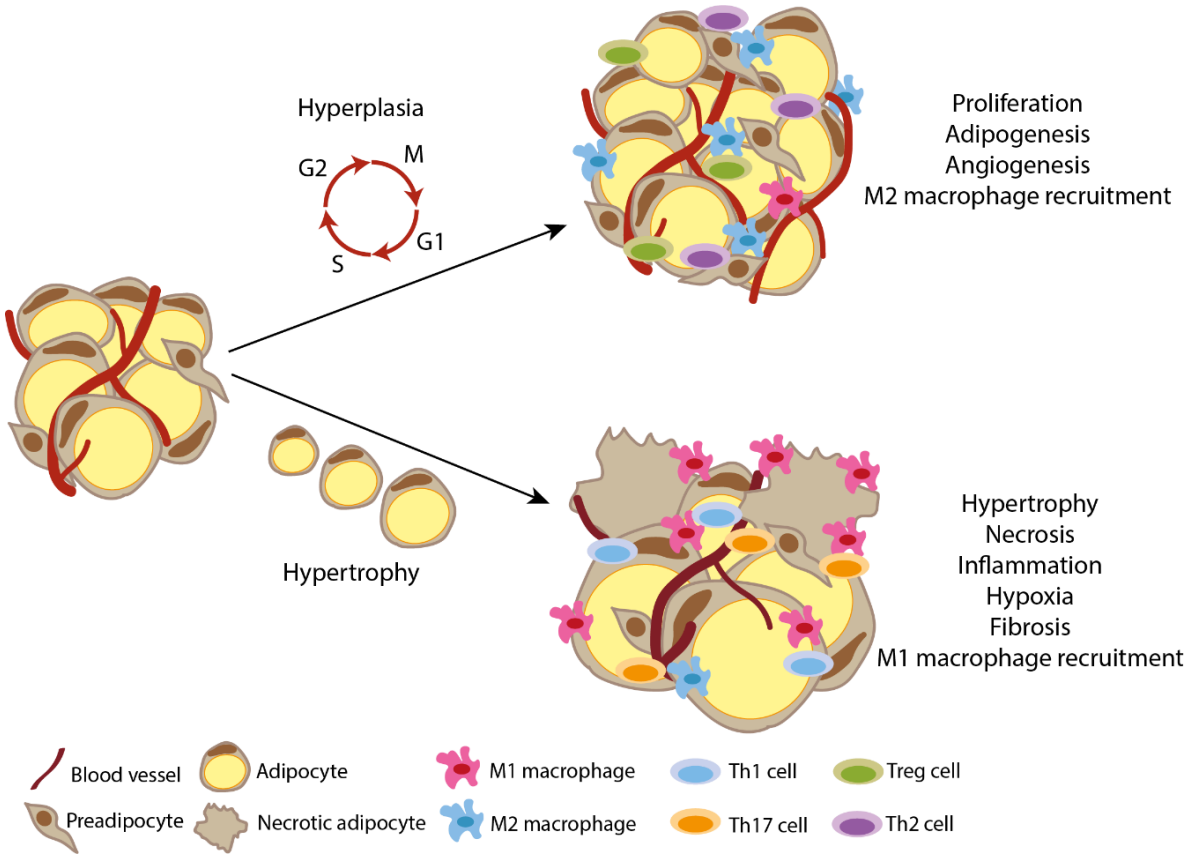

Figure 1.6. Mechanisms of adipose tissue expansion during obesity. Adipose tissues can expand by increased proliferation and differentiation of new preadipocytes (hyperplasia) or by increased size of existing adipocytes (hypertrophy). Hypertrophic expansion of adipose tissues results in necrosis and apoptosis of adipocytes and is accompanied by an increase in M1 pro-inflammatory macrophages which culminate in a chronic low-grade inflammatory state in this tissue. Adapted from (Ghaben and Scherer, 2019) with permission from Springer Nature (licence number: 5343770044752).

Similar expansion was observed in humans. For example, expansion of abdominal SAT in obese individuals resulted from adipocyte hypertrophy and hyperplasia, regardless of early- or late-onset of obesity, compared to a more hyperplastic morphology of abdominal SAT adipocytes in lean individuals (Arner *et al.*, 2022). Indeed, it is not just

VAT:SAT ratio, but intrinsic differences between VAT and SAT, that is an indicator of cardiometabolic disease. For example, in obese women, those with larger VAT had significantly increased fasting insulin, HOMA-IR (homeostatic model assessment for insulin resistance) and plasma triglyceride levels than obese women with smaller VAT, with no significant correlations observed for SAT volume in these individuals (Wajchenberg *et al.*, 2002). Further, increased visceral, but not gluteal, adipocyte size was associated with increased fasting glucose and insulin levels in a cohort of overweight children (Abbott and Foley, 1987). More recently, significantly increased proportions of larger adipocytes in both SAT and VAT, with increased numbers of pro-inflammatory macrophages in VAT, were reported in obese compared to lean individuals (Verboven *et al.*, 2018). Further, both adipocyte size and immune cell profiles were positively associated with HOMA-IR, with VAT adipocyte size accounting for ~15% of variance in insulin resistance. Thus indicating that a combination of adipocyte hypertrophy and adipose tissue inflammation contributed to insulin resistance (Verboven *et al.*, 2018). Whilst enlarged adipocytes from SAT and VAT were negatively correlated with plasma insulin and adiponectin levels, and positively correlated with triglyceride, HDL-cholesterol, glucose and haemoglobin A1c (HbA1c) levels, only visceral adipocyte size was significantly associated with CVD risk (Suárez-Cuenca *et al.*, 2021).

A hallmark of obesity is the polarisation of adipose-resident macrophages from an anti-inflammatory "M2" to a pro-inflammatory "M1" state. Subsequent expression of pro-inflammatory cytokines (e.g., tumour-necrosis factor α (TNF-α) and interleukins IL-1β, IL-18 and IL-6) induce low-grade chronic inflammation in adipose tissue. This induces adipocyte hypertrophy, leading to increased recruitment of immune cells, perpetuating the negative cycle of hypertrophic tissue expansion associated with

insulin resistance, obesity and ultimately T2DM (Zatterale *et al.*, 2020). Pro-inflammatory cytokines TNFα and IL-6 have been shown to act on wingless family member 10B (WNT10B) to promote early differentiation of 3T3-L1 preadipocytes, yet can prevent terminal differentiation by inducing an inflammatory response (Gustafson and Smith, 2006). Further, TNFα has been shown to induce WNT10B expression and a pro-inflammatory state in humans with abdominal obesity (Isakson *et al.*, 2009). Transforming growth factor beta (TGFβ) can inhibit PPARγ-C/EBPα induced adipogenesis in 3T3-L1 cells (Aykul *et al.*, 2021) suggesting inflammatory cytokines can either induce or suppress adipogenesis in response to different stimuli.

1.4.4. Adipose tissues in rodents

Mice and humans share several similarities in adipose tissues, both in composition and location of individual depots, although differences are also apparent. SAT and VAT can be further differentiated into distinct anatomical locations in both species (Figure 1.7) (Park, Kim and Bae, 2014; Chusyd *et al.*, 2016). In mice there are two main SATs, inguinal (over the hind limbs) and interscapular (between the shoulder blades). In humans, the main SATs depots are located gluteofemorally (around the buttocks and hips) and abdominally (below the skin). Human subcutaneous gluteofemoral WAT is distinctly white, whereas in mice iWAT has a browning capacity (Park, Kim and Bae, 2014; Luong, Huang and Lee, 2019). Further, VAT in mouse can be found surrounding several organs such as the heart (pericardial), kidneys (perirenal), stomach (omental) intestines (mesenteric) and gonads (gonadal) (Park, Kim and Bae, 2014; Chusyd *et al.*, 2016). These depots also exist in humans, although mouse mesenteric, rather than

gonadal, WAT is considered most similar to human VAT due to its location and venous drainage into the portal vein (Chusyd *et al.*, 2016; Miyata *et al.*, 2016).

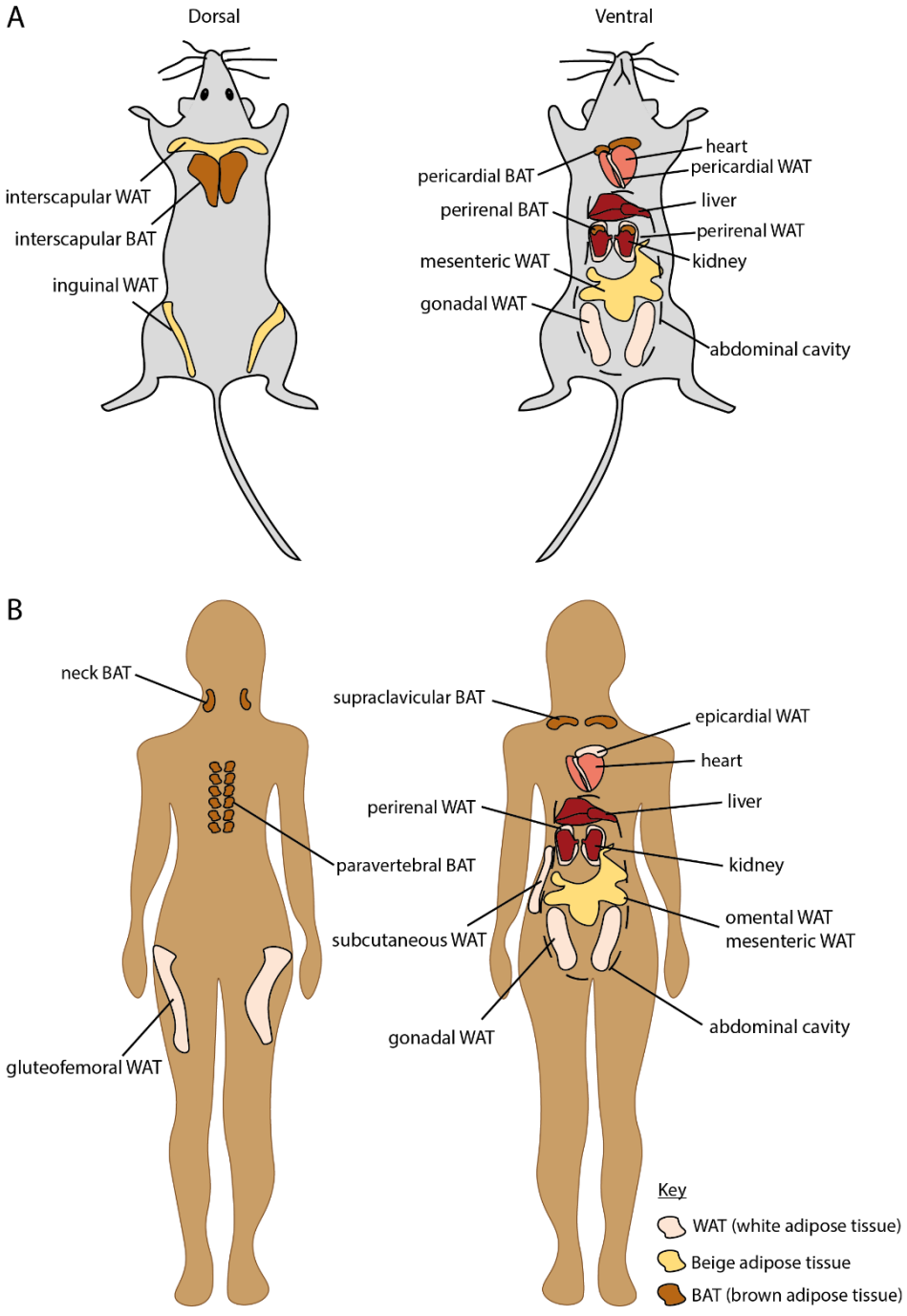

Figure 1.7. Major white, brown and beige adipose depots in mouse and human. Distribution of mouse (A) and human (B) white, brown and beige adipose tissues. Abbreviations: WAT (white adipose tissue), BAT (brown adipose tissue). Adapted from (Park, Kim and Bae, 2014) with permission from Baishideng Publishing Group Inc. (under creative commons licence: CC BY-NC 4.0).

Mice have several well-defined BATs; the major depot lies subcutaneously between the scapulae, with additional pericardial and perirenal depots (Figure 1.7) (Park, Kim and Bae, 2014). Originally thought to only exist in babies, substantial BAT depots were discovered in human adults in the neck, under the collarbones, pericardially and in the spine (Heaton, 1972; van Marken Lichtenbelt *et al.*, 2009; Giralt and Villarroya, 2013). Further, the incidence of obesity and T2DM were inversely correlated with BAT volume, although it remains to be seen if this is a causative or correlative relationship (van Marken Lichtenbelt *et al.*, 2009; Giralt and Villarroya, 2013; Leitner *et al.*, 2017).

Another considerable adipose depot is located sub-dermally. In mice, dermal WAT (dWAT) constitutes approximately half of the total adipose tissue volume (Kasza *et al.*, 2016). Murine dWAT is a distinct layer of fat separated from subcutaneous depots by the *panniculus carnosus* muscle layer, and its thickness changes in response to factors such as folliculogenesis (hair growth) (Kasza *et al.*, 2016). Whereas, in humans dermal and subcutaneous adipose are separated only by the fascia, however, in abdominal regions distinguishing these deep and superficial layers can be tricky. Based on their observations, the authors speculated dWAT thickness may be an important factor in an organism's ability to sense environmental temperature changes. In other words, a thicker dWAT layer may inhibit BAT activation in response to cold stimuli which has implications on poorer metabolic health (Kasza *et al.*, 2016).

1.5. Genome-wide association studies as a tool to identify adiposity genes

Despite the relative success in identifying genetic causes for Mendelian diseases, initial attempts to identify the underlying causal genetics of more complex traits fell short due to the inherent variability of heritability across traits (Uitterlinden, 2016). The

availability of the human genome sequence in 2001, coupled with the International HapMap project and SNP database, made it possible to map genetic associations with complex diseases such as T2DM and CVD, as well as traits such as obesity that contribute to susceptibility of these diseases (Billings and Florez, 2010; De, Bush and Moore, 2014; Uitterlinden, 2016). GWAS aimed to identify allele frequencies of SNPs in individuals affected by disease, compared to non-affected controls, to identify associations between disease and inherited DNA loci (Flint, 2013; Uitterlinden, 2016). Genotyping of 'tag' SNPs on arrays allows for identification of other nearby correlated SNPs; these short sequences are termed linkage disequilibrium (LD) blocks or haplotypes (De, Bush and Moore, 2014; Scherer and Christensen, 2016).

Initial reservations surrounding GWAS focused on the modest effect size of SNPs, suggesting their proximal genes were not important in disease phenotypes. Nonetheless, GWAS signals are replicable and have identified many novel gene loci associated with complex disease traits, made possible by this 'hypothesis-generating' approach (Scherer and Christensen, 2016; Uitterlinden, 2016). As of June 2022, the NHGRI-EBI Catalogue of GWAS had over 5800 publications with approximately 385,000 SNP associations (Buniello *et al.*, 2019). This has largely been made possible by improvements in GWAS design and analysis, such as increased sample sizes, recruitment of cases and controls, and introduction of meta-analysis and follow-up studies in secondary cohorts (McCarthy *et al.*, 2008). Finally, the recently completed telomere-to-telomere human genome sequence may provide additional information on what was previously determined 'redundant' genome (Aganezov *et al.*, 2022; Nurk *et al.*, 2022), and may identify drivers of SNP-trait associations to support polygenic risk scores (i.e. the cumulative number of SNPs that contribute to an individual's risk of developing disease) and heritability study data.

1.5.1. Type 2 diabetes mellitus

Despite reservations, GWAS have been integral in understanding complex diseases and their underlying traits. Further, meta-analyses combining GWAS increased sample sizes and genetic variation to improve detection of association signals. For example, by combining dense imputation strategies and 32 GWAS in ~ 898,000 T2DM cases and controls, over 400 independent signals across 231 loci were implicated in T2DM risk, with significant associations in 152 loci after adjustment for BMI (Mahajan *et al.*, 2018). Multiple loci contained independent signals (i.e. discrete SNPs, not in LD with one another, significantly associated with the trait), including previously associated *TCF7L2, INS1-IGF2* and *KCNQ1* loci, highlighting the complex genetic architecture of common diseases. By further employing fine-mapping and posterior probability analysis (PPA), the authors showed that the strongest associated SNP accounted for over 80% of the posterior probability at 44 loci (Mahajan *et al.*, 2018). Within these 44 loci, eight missense coding variants were identified as the leading causal association-signal, in genes such as *APOE, PAM, HNF1A, HNF4A* and *RREB1*, implicating a causal role for these genes in T2DM risk phenotypes (Mahajan *et al.*, 2018).

1.5.2. Body mass index

Traits that increase disease risk, such as BMI, have also been interrogated by GWAS. Recent meta-analyses in ~695,000 individuals identified 941 signals in 536 loci, accounting for 6.0% of variance, significantly associated with BMI (Yengo *et al.*, 2018). In fact, some of the first gene loci identified with T2DM, such as the fat mass and obesity associated gene (*FTO*), were subsequently shown to contribute to T2DM risk through

their association with obesity and BMI (Frayling *et al.*, 2007; Billings and Florez, 2010; Loos and Yeo, 2014; Mahajan *et al.*, 2018).

The *FTO* locus has been repeatedly associated with BMI, and remains the most strongly associated locus (Frayling *et al.*, 2007; Hägg *et al.*, 2015). However, modelling the *in vivo* role of *Fto* has been hindered by embryonic-lethal homozygous knock-out mice. A missense p.I367F *Fto* mutant model exhibiting an altered body composition phenotype was identified using the MRC Harwell mouse N-ethyl-N-nitrosourea (ENU) archive (Church *et al.*, 2009). Both heterozygous ($Fto^{+/I367F}$) and homozygous ($Fto^{I367F/I367F}$) mice had significantly lower bodyweights and less fat mass than wildtype ($Fto^{+/+}$) colony-mates. Further, $Fto^{+/I367F}$ and $Fto^{I367F/I367F}$ mice had dysregulated metabolic profiles, and altered expression of inflammatory and metabolic genes in several tissues, collectively suggesting *Fto* regulated adipose tissue development (Church *et al.*, 2009). A causal role for SNPs in this locus has since been established. Indeed, the most significant *FTO* GWAS signal disrupted TF binding and regulated expression of locus genes *IRX3* and *IRX5* in both brain and adipose tissues to influence obesogenic traits (Smemo *et al.*, 2014; Claussnitzer *et al.*, 2015). Further, *Fto* mouse models developed in the Cox lab to model the rs1421085 SNP exhibited altered fat mass phenotypes (Laber, 2017; Laber *et al.*, 2021). These studies highlight how mouse models can be used to elegantly study the functional impact of SNPs and their causal genes *in vivo* to improve our understanding of genetic disease drivers.

1.5.3. Waist-to-hip ratio and BMI association

Given the strong correlation between BMI, WC (r^2 ~0.9) and WHR (r^2 ~0.6) it was expected that most loci would be common between these traits. However, a GWAS

meta-analysis associated only two previously identified BMI loci, *FTO* and *MC4R,* with WHR and WC (Lindgren *et al.*, 2009). GWAS adjusted-trait models can be useful tools when trying to dissect whether a SNP is associated with a trait through a confounding covariate e.g., in the case of *FTO* influencing T2DM risk through BMI associations. Therefore, to determine whether fat distribution was regulated independently of overall obesity, traits such as WC and WHR were assessed with and without adjustment for BMI. Signals in the *MRSA* and *TFAP2B*, nominally associated with WC, did not reach significance when adjusted for BMI suggesting that these loci act through overall adiposity to influence WC and WHR (Table 1.2) (Lindgren *et al.*, 2009). Further, an intergenic SNP on chromosome 1 located between *Z3CH11B* and *LYPLAL1* was associated with increased WHR and triglyceride levels, which showed a substantially greater association when adjusted for BMI (Table 1.2) (Lindgren *et al.*, 2009). This suggested these identified loci have functional effects driven by the location of fat storage.

Subsequently, a meta-analysis of ~200,000 individuals showed novel significance for an additional 13 loci associated with WHRadjBMI, accounting for just over 1% of the WHR variance seen, despite approximately 45% heritability for this trait (Table 1.2) (Heid *et al.*, 2010). In further analysis of the relationship between WHR and BMI, only two BMI-associated loci, *FTO* and *TMEM18,* were significantly associated with WHRadjBMI. Further, a decreased BMI was associated with four WHR-increasing SNPs near *TBX15-WARS2, CPEB4, LYPLAL1* and *GRB14* (Heid *et al.*, 2010). Subsequent GWAS meta-analysis of data from the GIANT consortium identified a further 33 novel loci associated with WHRadjBMI, highlighting the complex regulatory landscape of these traits (Table 1.2) (Shungin *et al.*, 2015).

Table 1.2. Genome-wide association study meta-analyses for anthropometric body composition measurements. Abbreviations: WC (waist circumference), WHR (waist to hip ratio), WHR adjusted for BMI (WHRadjBMI), MAF (minor allele frequency).

Analysis	Reference	Sample size	Trait	Number of loci identified	Details
Meta-analysis of 16 GWAS (European ancestry)	(Lindgren *et al.*, 2009)	38,580 (follow-up 70, 689)	WC	2 (*TFAP2B, MRSA*)	N/A
			WHR	1 (*LYPLAL1*)	Female only signal
Meta-analysis of 32 GWAS (European ancestry)	(Heid *et al.*, 2010)	77,167 (follow-up 113,636)	WHRadjBMI	14 (13 novel plus *LYPLAL1*)	7 loci exhibit sexual dimorphism (female only signal)
Meta-analysis of 57 GWAS, plus Metabochip (European ancestry)	(Shungin *et al.*, 2015)	142,762 (follow-up 67,326)	WHRadjBMI	49 (33 novel plus 16 previously described)	20 loci exhibit sexual dimorphism, 19 of which are female only. Conditional analysis revealed different but correlated lead SNPs in the *HOXC* and *TBX15-WARS2* loci.
Meta-analysis (European ancestry)	(Pulit *et al.*, 2019)	694,649	WHRadjBMI	346 loci (300 novel)	266 loci associated with WHRadjBMI in women and 91 loci in men.
Meta-analysis (five ancestries)	(Justice *et al.*, 2019)	344,369 (follow-up 132,177)	WHRadjBMI	56 coding variants in 41 loci (23 novel)	Rare variants (MAF≤1%) had 3x effect size compared to common variants (MAF≥5%).

GWAS meta-analyses are becoming more sensitive through a combination of larger datasets and improved imputation strategies. The most recent meta-analysis of WHRadjBMI identified 463 signals within 346 loci explaining 3.9% of variance, further highlighting that WHR is driven by a complex axis of genes with varying functions (Table 1.2) (Pulit *et al.*, 2019). This study also examined the potential interaction between WHR and BMI associations, however, the *FTO* and *TMEM18* associations

identified by Heid *et al.* (2010) were not replicated for significant WHRadjBMI associations, despite a highly significant association ($P=4x10^{-118}$) for rs10421085 and WHR (Pulit *et al.*, 2019). Whilst the authors did not suggest a reason for this, it is possible that due to additional genetic variation in the ~3.4-fold increased sample size analysed by Pulit *et al.* (2019) these associations no longer met the significance threshold. These data indicate the majority of WHRadjBMI SNPs exert their effect independently of the positive correlation between BMI and WHR, and highlights the gaps in our current knowledge about the role of adipose tissue biology in WHR (Heid *et al.*, 2010; Pulit *et al.*, 2019).

These loci represent well replicated drivers of fat distribution in humans, identifying genetic variants that account for as much as 6% of phenotypic variation across sampled individuals. It is important to consider why despite such comprehensive GWAS meta-analyses the amount of variance accounted for remains relatively low. Some of this "missing heritability" can be accounted for with increased sample sizes, as was recently shown with a GWAS meta-analysis for height in 5.4 million individuals that showed ~12,000 SNPs accounted for 40% of the variation within sampled individuals (Yengo *et al.*, 2022). When explaining the unaccounted variance in complex traits such as obesity, genetic variants should be considered in concert with environmental factors such as diet, physical exercise, and medication. Despite the "missing heritability", these GWAS data represent a tremendous resource for functional studies to potentially identify new therapeutic pathways. Undoubtedly over time, as larger sample sets and further improvements in genomic sequencing become readily available our understanding of genetic risk factors will greatly improve. The challenge will remain to ensure robust prioritisation strategies are in place to identify the most likely causal variants for functional analyses.

1.5.4. Identifying functional variants

Whilst coding variants in GWAS have been significantly associated with a range of traits and diseases, they are often considered rare with minor allele frequencies (MAF) <5% making them difficult to study in smaller sample sizes (Mahajan *et al.*, 2018; Justice *et al.*, 2019). Over 90% of SNPs have been identified in intronic and intergenic regions, however, this also hampers attempts to identify causal associations between SNPs and diseases or phenotypic traits (Mooney, Krishnan and Evani, 2010; Tak and Farnham, 2015). A combination of computational approaches can be taken to exclude GWAS variants with weak associations. Subsequently, *in silico* and *in vitro* strategies can be utilised to predict target gene expression, TF binding and chromatin interactions (Figure 1.8) (Cooper and Shendure, 2011; Edwards *et al.*, 2013; Schaid, Chen and Larson, 2018). *In vitro* and *in vivo* gene-editing can be employed for functional analysis of target genes and their molecular mechanisms which will hopefully translate into novel therapeutic interventions (Figure 1.8) (Wu *et al.*, 2019; Cano-Gamez and Trynka, 2020; Lichou and Trynka, 2020; Park *et al.*, 2021).

An example of such variant-to-function analysis has been implemented for signals in the *RSPO3* (R-spondin 3) locus strongly associated with WHRadjBMI (Heid *et al.*, 2010; Shungin *et al.*, 2015; Pulit *et al.*, 2019). *RSPO3* locus SNPs rs72959041 and rs1936807 were significantly associated with altered fat distribution in DEXA analysis. Further, expression quantitative trait loci (eQTL) analysis revealed rs72959041 was associated with increased *RSPO3* expression in both SAT and VAT and increased adipocyte cell size in subcutaneous, but not visceral, depots (Loh *et al.*, 2020). Functional studies using stable knockdown of *RSPO3* in VAT- and SAT-derived adipocyte progenitor cells revealed *RSPO3* regulated proliferation and adipogenesis through regulation of the

WNT/β-catenin signalling pathway (Loh *et al.*, 2020). Finally, using an *in vivo* zebrafish model, the authors confirmed reduced *Rspo3* expression in mutant fish resulted in increased abdominal and peripheral adipose depots, and a significant decrease in the ratio of these fat depots, demonstrating that *RSPO3* is the likely effector gene in the locus associated with WHRadjBMI (Loh *et al.*, 2020).

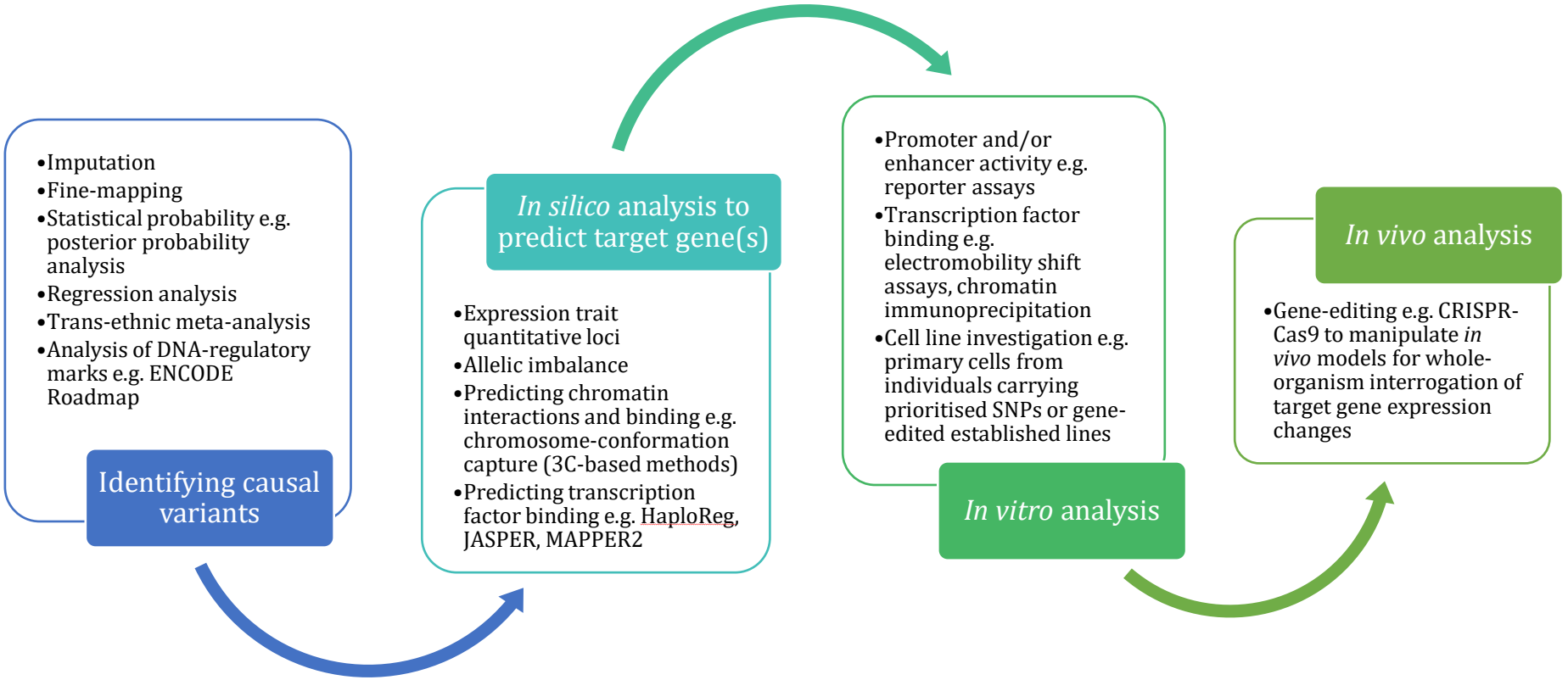

Figure 1.8 Variant-to-function analyses to investigate potentially functional SNPs. Following identification of target loci from GWAS, meta-analyses and imputation studies can be performed in follow-up cohorts to corroborate associations and narrow down lists of potentially functional SNPs. Further *in silico* analysis can be used to interrogate likely functional roles by examining known annotations for open chromatin and DNA methylation marks, as well as predicting changes to transcription factor binding motifs. Target genes can be further elucidated with the help of gene, protein and chromatin binding experiments such as RNA-sequencing and ChIP-sequencing. Functional validations can then be performed in cell lines and genetically modified in vivo models to investigate gene expression on a whole-organism level.

1.6. *TBX15-WARS2* locus

1.6.1. *TBX15-WARS2* locus associations with WHRadjBMI

Signals in the *TBX15-WARS2* locus, on human chromosome 1p12, have also been robustly replicated in GWAS meta-analyses, and are amongst some of the strongest association signals for WHRadjBMI (Heid *et al.*, 2010; Shungin *et al.*, 2015). The *TBX15-WARS2* locus contains the *TBX15* (T-box 15), *WARS2* (tryptophanyl-tRNA synthetase 2) and *SPAG17* (sperm-associated antigen-17) genes. The first SNP associated with WHRadjBMI in this locus was rs984222 (β=0.034, p=8.69x10^{-25}) located in intron 1 of *TBX15* (Heid *et al.*, 2010). This SNP was significantly associated with differential *TBX15* and *WARS2* expression in VAT and SAT. To determine whether a secondary SNP, or indeed gene expression, is independently associated with a trait conditional analysis can be performed to adjust for the effects of the first SNP. When conditioned for rs984222, the *TBX15* expression association was negated, suggesting *TBX15* may be the candidate gene driving the trait associations mediated by rs984222 and may provide evidence for underlying biological mechanisms driving fat deposition (Heid *et al.*, 2010).

The rs984222 association with increased WHRadjBMI was corroborated in a cohort of African-American individuals (Liu *et al.*, 2013). The authors then performed a trans-ethnic meta-analysis comparing the lead SNPs in their analysis with those of Heid *et al.* (2010) and showed rs984222 remained the lead SNP in the *TBX15-WARS2* locus (Liu *et al.*, 2014). Two further *TBX15* intron 1 SNPs (rs984225 and rs10923712) and an additional SNP in the promoter region of *TBX15* (rs1106529), were identified in this analysis (Liu *et al.*, 2014). rs984222, rs984225 and rs10923712 overlapped histone modification marks (H3K4me1-3, H3K9ac and H3K27ac; Roadmap ENCODE

consortium data) for a combination of adipose, bone, muscle, liver and blood tissues indicating these SNPs may regulate gene expression in a range of tissues associated with body composition (Liu *et al.*, 2014). Further, the rs984222 WHR-increasing allele was, paradoxically, associated with reduced risk of impaired fasting glucose levels in a study of obese Chinese children (Song *et al.*, 2018). This suggests TBX15 may act in a pleiotropic manner to regulate several metabolic functions associated with metabolically healthy or unhealthy obesity.

The complexity of the regulatory landscape within this locus was further highlighted by the identification of four independent association SNPs that acted in a sex-combined and sexually dimorphic manner (Figure 1.9) (Shungin *et al.*, 2015). Multiple *TBX15-WARS2* locus signals have been significantly associated with traits such as height, BMI, bio-impedance, and heel bone mineral density in the GWAS and gene atlases (Canela-Xandri, Rawlik and Tenesa, 2018; Watanabe *et al.*, 2019). More recently, Pulit *et al.* identified a coding SNP (rs10494217) in exon 3 of *TBX15* that was associated with increased WHRadjBMI (β=0.022, p=2.73x10^{-21}) (Pulit *et al.*, 2019). In a follow-up study by the same consortium, a similar association was detected for rs10494217 (β=0.018, p=1.4x10^{-10}), along with rs61730011 in exon 8 of *TBX15* (β=0.041, p=2.2x10^{-14}) (Justice *et al.*, 2019). These SNPs encode non-synonymous amino acid substitutions p.H156N and p.M566R, respectively. These data highlight the complexity of the locus and indicate a need to further investigate these signals to elucidate the causal SNPs and genes acting to drive changes in body composition.

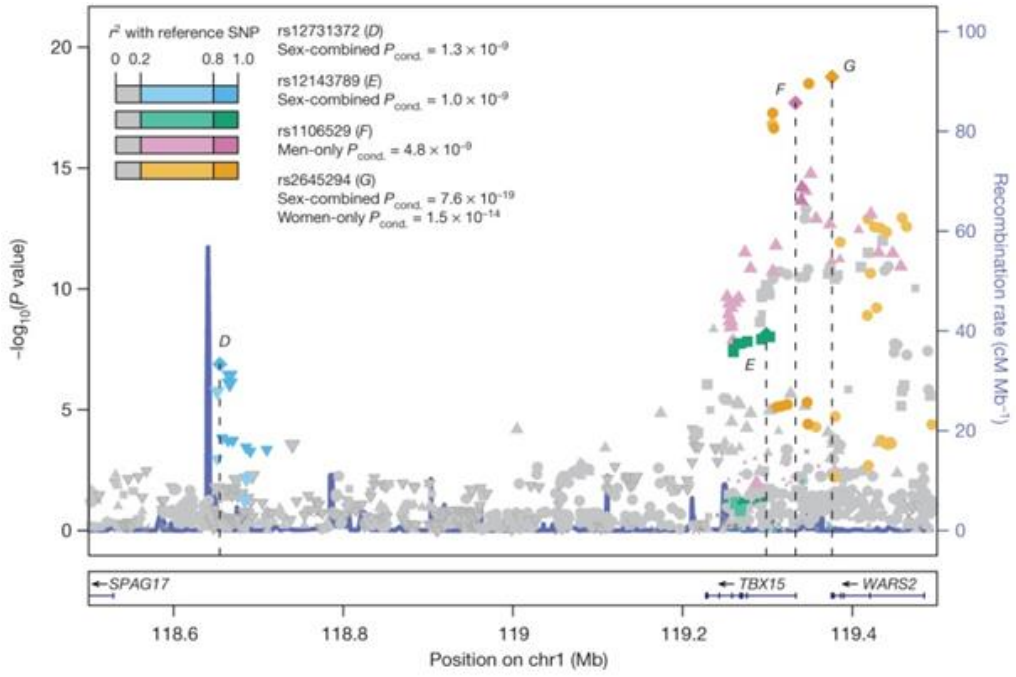

Figure 1.9. Regional association plot showing four independent association signals in the *TBX15-WARS2 locus*. D-G indicate the four independent signals; colours indicate 61 SNPs in linkage disequilibrium with each lead SNP. Reproduced from (Shungin *et al.*, 2015) with permission from Springer Nature (licence number: 5282981446424).

1.6.2. Identifying candidate genes in the *TBX15-WARS2* locus

TBX15-WARS2 locus signals have been associated with *TBX15, WARS2* and *RP11-418J17.1* (*WARS2-AS1*) expression in several tissues (Table 1.3) (Heid *et al.*, 2010; Lonsdale *et al.*, 2013; Civelek *et al.*, 2017). Additionally, *TBX15, WARS2* and *SPAG17* expression in adipose tissues were significantly associated with several cardiometabolic traits in addition to WHR (Civelek *et al.*, 2017). For example, *SPAG17* expression was negatively correlated with adiponectin, and *WARS2* was negatively associated with insulin and proinsulin levels. Further, *TBX15* expression was inversely correlated with insulin, proinsulin, WC, WHR, triglycerides, total fatty acids and diastolic blood pressure, and positively correlated with adiponectin, fat-free mass and HDL-cholesterol (Figure 1.10) (Civelek *et al.*, 2017).

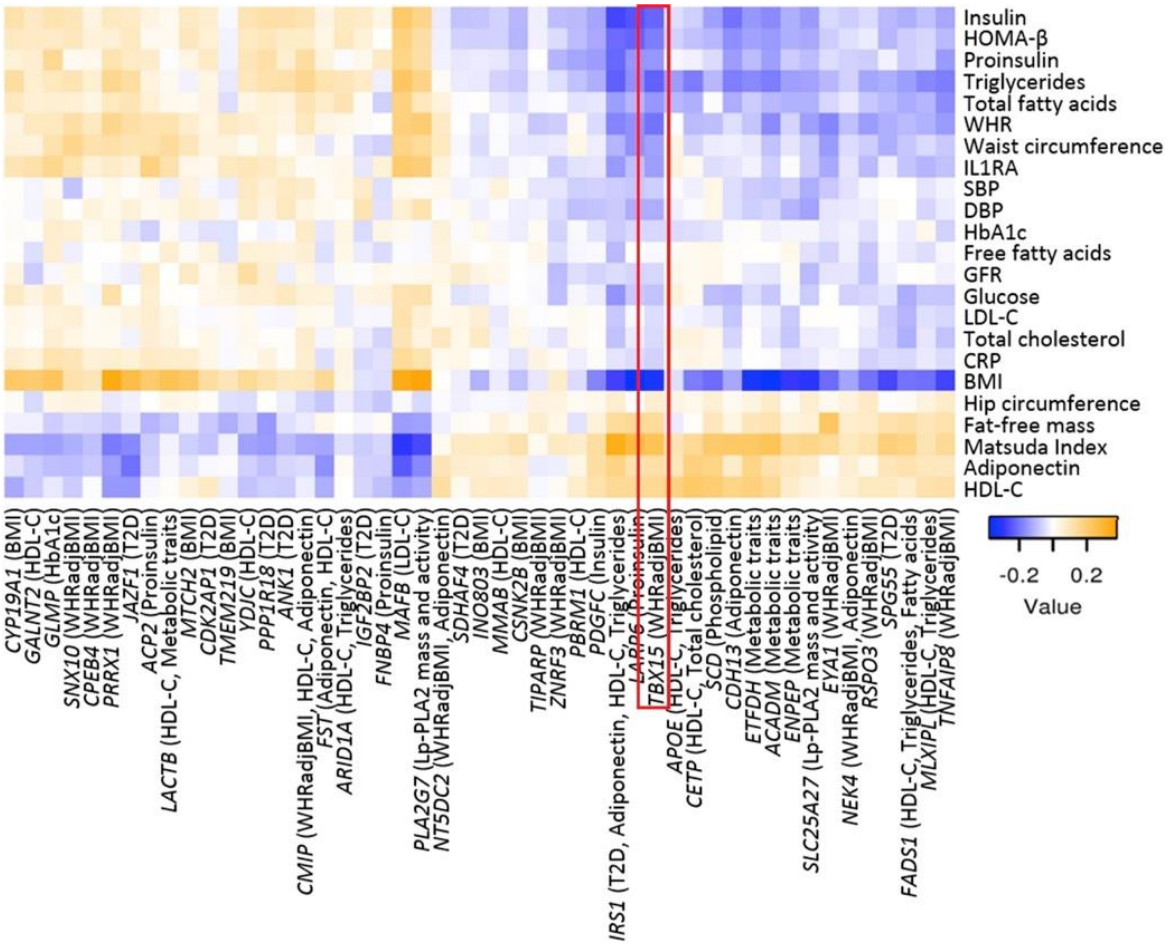

Figure 1.10. Associations between gene expression levels and cardiometabolic traits. Heat map showing positive (yellow) and negative (blue) correlations between GWAS-identified loci and 23 cardiometabolic traits. *TBX15* is highlighted in a red box. Reproduced from (Civelek *et al.*, 2017) with permission from Elsevier (licence number: 4664261172604).

Interestingly, frequencies of SNPs in *TBX15-WARS2* significantly differed between Greenland Inuit and European and Chinese Han reference populations, with decreased WHR associated with the most-frequent allele (Fumagalli *et al.*, 2015). Subsequent research showed seven SNPs within the *TBX15-WARS2* region were introgressed into modern human DNA from Denisovan ancestors, approximately 45,000 years ago (Racimo *et al.*, 2017). Many previously identified introgressed regions have been shown to have important functional roles, therefore, it was suggested the *TBX15-WARS2* locus was introgressed for its function in adaptation to cold

environments. Denisovan SNP alleles in the introgressed *TBX15-WARS2* region had a positive effect on WHR, WHRadjBMI and WC adjusted for BMI, suggesting a complex network alters this phenotype regulated by *TBX15* and *WARS2* (Racimo *et al.*, 2017). Taken together, these data implicate genes in the *TBX15-WARS2* locus in transcriptional regulation of adipocyte differentiation which regulates traits associated with fat distribution and MetS (Heid *et al.*, 2010; Civelek *et al.*, 2017; Gao *et al.*, 2018).

1.6.2.1. *SPAG17*

The first gene within the *TBX15-WARS2* locus is *SPAG17*; its protein forms central components of microtubules within motile cilia. *Spag17*-knockout mice exhibit neonatal lethality, while mutant models result in primary ciliary dyskinesia characterised by respiratory tract infections, *situs inversus* and infertility (Teves *et al.*, 2013, 2015; Kazarian *et al.*, 2018). The rs12731372 signal is not a significant eQTL, however it is predicted to alter several TF binding motifs (TFBMs) in HaploReg v4.1 (Table 1.3) (Ward and Kellis, 2012; Lonsdale *et al.*, 2013). Additional *SPAG17* signals have been associated with height in adults and children (Kim *et al.*, 2010; Zhao *et al.*, 2010). However, to date there is no evidence *SPAG17* is associated with adipogenesis suggesting it is not the causal WHRadjBMI gene in the locus.

Table 1.3. Genome-wide association data for representative set of SNPs in the *TBX15-WARS2* locus associated with WHRadjBMI. SNPs grouped in risk blocks based on high linkage disequilibrium (r^2>0.8) with the lead SNP (highlighted in bold), as identified by (Shungin *et al.*, 2015). The position of each SNP corresponds to human genome assembly GRCh38/hg38 (December 2013). Abbreviations: EA (effect allele), OA (other allele), EAF (effect allele frequency), β (effect size, positive value indicates effect allele is associated with increased WHRadjBMI or gene expression, negative value indicates effect allele is associated with decreased WHRadjBMI or gene expression), eQTL (expression quantitative locus associated with given SNP). rs61730011 was not assigned a risk block as it was not in linkage disequilibrium with any lead SNPs in this analysis.

Risk block	SNP	Position	EA	OA	EAF	β	GWAS p-value	eQTL	Reference
D	**rs12731372**	118,310,352	C	T	0.763	0.024	1.30E-09	No significant enrichment	
N/A	rs61730011 (p.M566R)	118,884,844	A	C	0.957	0.041	2.20E-14	*HAO2* (thyroid)	(*GTEx Portal*, no date; Lonsdale *et al.*, 2013)
E	**rs12143789**	118,954,531	C	G	0.206	0.026	1.00E-09	*WARS2* (adipose, β=0.749, p=6.0E-45)	(Civelek *et al.*, 2017)
								WARS2 (thyroid, subcutaneous adipose, artery, skin, cultured fibroblasts and mammary tissue) *RP11-418J17.1* (*WARS2-AS1*) (skin, oesophagus, thyroid)	(*GTEx Portal*, no date; Lonsdale *et al.*, 2013)
	rs10494217 (p.H156N)	118,926,565	T	G	0.174	0.018	1.40E-10	*WARS2* (visceral and subcutaneous adipose, skeletal muscle and pancreas tissues, β= 0.749, p=6.03E-45)	(Justice *et al.*, 2019)
								WARS2 (thyroid, subcutaneous adipose, artery, skin, cultured fibroblasts and mammary tissue) *RP11-418J17.1* (*WARS2-AS1*) (skin, oesophagus, thyroid)	(*GTEx Portal*, no date; Lonsdale *et al.*, 2013)
F	**rs1106529**	118,988,874	A	G	0.758	0.034	4.80E-09	*WARS2* (adipose β=-0.559, p= 9.1E-12)	(Civelek *et al.*, 2017)
								TBX15 (visceral adipose β=0.20, p=2.2E-06) *WARS2* (visceral adipose β=-0.31, p=2.9E-11; subcutaneous adipose β=-0.41, p=2.9E-18)	(*GTEx Portal*, no date; Lonsdale *et al.*, 2013)
								RP4-712E4.1 (subcutaneous adipose, artery and testis) *WARS2* (muscle, skin, oesophagus, subcutaneous adipose, cultured fibroblasts, skin, thyroid)	(*GTEx Portal*, no date; Lonsdale *et al.*, 2013)
G	rs984222	118,961,220	G	C	0.635	0.035	8.69 E−25	*TBX15* (visceral adipose p=7.90E−10) *WARS2* (visceral adipose p=5.11E-36; subcutaneous adipose p=1.67E-25)	(Heid *et al.*, 2010)
								TBX15 (adipose β=0.274, p= 3.5E-06) *WARS2* (adipose β=-0.644, p= 4.5E-29)	(Civelek *et al.*, 2017)
								WARS2 (muscle, skin, subcutaneous adipose, artery, thyroid, nerve, cultured fibroblasts, oesophagus and lung)	(*GTEx Portal*, no date; Lonsdale *et al.*, 2013)
	rs2645294	119,031,964	T	C	0.580	0.031	7.60E-19	*TBX15* (adipose β=0.302, p= 1.1E-07)	(Civelek *et al.*, 2017)
								WARS2 (muscle, skin, subcutaneous adipose, artery, nerve, thyroid, cultured fibroblasts, oesophagus, and lung)	(*GTEx Portal*, no date; Lonsdale *et al.*, 2013)

1.6.2.2. *WARS2*

WARS2 is a member of the essential mitochondrial aminoacyl-tRNA synthetase family that generate components of the electron transport chain for adenosine triphosphate (ATP) transport (Wortmann *et al.*, 2017; Agnew *et al.*, 2018). *WARS2* is a strong candidate gene in WHR associations as its mRNA expression was significantly reduced in SAT compared to VAT of obese individuals (Schleinitz *et al.*, 2014). Mutations in *WARS2* present a wide range of clinical phenotypes including low birth weight, altered muscle tone, cardiomyopathy, hypoglycaemia and dysregulation of oxidative phosphorylation (Wortmann *et al.*, 2017).

These phenotypes have been modelled *in vivo,* for example a mutant *Wars2* rat model carrying a loss of function (LOF) non-synonymous L53F substitution had increased bodyweight, reduced glucose oxidation, and reduced expression of several *Cyclooxygenase* genes in BAT compared to wildtype *Wars2* rats (Pravenec *et al.*, 2017). Further, homozygous LOF non-synonymous V117L mutant *Wars2* (*Wars2*$^{V117L/V117L}$) mice exhibited reduced bodyweight and a failure to gain fat mass over 6 months, with significantly smaller gWAT, iWAT and BAT, compared to wildtype littermates (Agnew *et al.*, 2018). This was driven by differential protein levels of NDUF8B, MTCO1, ATP5A UQCRC2 (mitochondrial complex I and IV proteins) across heart, liver, kidney, muscle, iWAT and BAT (Agnew *et al.*, 2018). We have since shown that these *Wars2*$^{V117L/V117L}$ mice had reduced food intake over time, with associated increases in appetite-suppressant fibroblast growth factor 21 (FGF21) and growth differentiation factor 15 (GDF15) levels in plasma, and gene expression levels of *Fgf21* and *Gdf15* in heart and BAT (Mušo *et al.*, 2022). Despite the differences between these LOF models, likely resulting from differences between rodent species or indeed the variant position within the *Wars2* gene, they highlight the importance of *WARS2* in adipose tissue biology.

1.6.2.3. *TBX15*

Of the genes in the *TBX15-WARS2* locus, *TBX15* contained the most SNPs associated with WHRadjBMI. In contrast to *WARS2* expression, *TBX15* was significantly increased in SAT versus VAT of lean, overweight and obese individuals (Schleinitz *et al.*, 2014). A member of the T-box family of TFs, TBX15 has a developmental role in skeletal limb patterning, particularly in MSC clustering for endochondral ossification and osteoclast differentiation (Candille *et al.*, 2004; Singh *et al.*, 2005; Papaioannou, 2014; Elsafadi *et al.*, 2016). Autosomal recessive mutations in *TBX15* cause Cousin Syndrome (OMIM #260660), a distinctive dwarfism characterised by hypoplasia of the scapulae and ilium, and craniofacial defects which include low-set ears (Cousin *et al.*, 1982; Lausch *et al.*, 2008; Dikoglu *et al.*, 2013). Due to the limited number of diagnosed cases, five worldwide, of Cousin Syndrome, no adipose or metabolic phenotypes were assessed in these individuals (Cousin *et al.*, 1982; Lausch *et al.*, 2008; Dikoglu *et al.*, 2013). Homozygous *Tbx15* knockout (*Tbx15*$^{-/-}$) mice, otherwise known as droopy ear, exhibit impaired skeletal development and craniofacial abnormalities including low-set ears which mirror Cousin Syndrome symptoms (Curry, 1959; Candille *et al.*, 2004; Singh *et al.*, 2005). Further, epigenetic modifications regulating *TBX15* expression have been implicated in poor prognosis, and altered lipid metabolism, proliferation, metastatic and anti-apoptotic signalling cascades in cancer (Arribas *et al.*, 2016; Gozzi *et al.*, 2016; Zheng *et al.*, 2016; Yamada *et al.*, 2018). This highlights the importance of epigenetic modifications in gene expression and disease, and points to *TBX15* as a candidate gene for regulating processes such as lipid homeostasis and apoptosis in expanding adipose tissues.

During development, *Tbx15* expression starts at E9.5 in the limb buds and continues past E12.5-13 once joints have started to develop (Singh *et al.*, 2005). Expression also occurs in the mesenchyme of craniofacial regions and dorsal skin (E10.5-12.5), vertebral bodies

(E12.5-14.5) and skeletal muscles (E13.5 onwards) (Candille *et al.*, 2004; Singh *et al.*, 2005). In developing bones, resting and proliferating chondrocytes express *Tbx15* (up to E16.5), but hypertrophic chondrocytes do not express *Tbx15* at any stages of development (Singh *et al.*, 2005). Impaired skeletal development in *Tbx15*$^{-/-}$ mice begins during cartilaginous patterning at E13.5, resulting in delayed endochondral ossification without impairing chondrocyte distribution or expression of key markers such as collagen II, collagen X, parathyroid hormone-related protein and Indian hedgehog (Singh *et al.*, 2005). This suggests that TBX15 may have a distinct role in regulating MSC determination and differentiation of committed cell types arising from these progenitors.

The smaller size of *Tbx15*$^{-/-}$ mice was suggested to result from reduced muscle mass (Singh *et al.*, 2005). In humans, an increased density of type IIB muscle fibres (produce ATP through glycolytic metabolism), compared to type I fibres (generate ATP through oxidative metabolism), was associated with insulin resistance, obesity and T2DM, and *TBX15* was almost exclusive to type II glycolytic fibres (Lee *et al.*, 2015). *Tbx15*$^{-/-}$ and heterozygous-knockout (*Tbx15*$^{+/-}$) mice had reduced muscle mass in glycolytic versus oxidative muscles, combined with a reduction in the number of glycolytic fibres and increase in oxidative fibres compared to wildtype (*Tbx15*$^{+/+}$) mice at 6 weeks of age. In contrast, at 5 months of age, *Tbx15*$^{+/-}$ mice did not exhibit significantly different bodyweight or lean mass compared to *Tbx15*$^{+/+}$ littermates but they did have more fat mass (Lee *et al.*, 2015). A similar increased fat mass and impaired glucose tolerance phenotype were observed in *Tbx15* adipocyte-knockout mice challenged with a HFD (Sun *et al.*, 2019). *In vitro* knockdown of *TBX15* downregulated expression of insulin-like growth factor 2 (*IGF2*), a myogenesis driver, resulting in poor myotubule formation (Lee *et al.*, 2015). This was reflected in lower *Igf2* expression in E14.5 muscle samples from *Tbx15*$^{+/-}$ and *Tbx15*$^{-/-}$ mice compared to *Tbx15*$^{+/+}$ littermates. It was proposed that *Tbx15*

regulated *Ampk* and *Igf2* to change the morphology and oxidative capacity of muscle fibres to differentiate into either type I or type II, which ultimately altered their function in metabolism which has implications in health and disease (Lee *et al.*, 2015).

In addition to its role in skeletal patterning, there is increasing evidence that TBX15 plays a role in adipogenesis (Table 1.4). *TBX15/Tbx15* is more highly expressed in SAT compared to VAT in humans (Lonsdale *et al.*, 2013) and in mice (Gesta *et al.*, 2006, 2011; Yamamoto *et al.*, 2010; Lee *et al.*, 2017). *TBX15* expression has been correlated with BMI and WHR in SAT (Gesta *et al.*, 2006; Ejarque *et al.*, 2019) and inversely correlated with BMI and WHR in VAT (Gesta *et al.*, 2006; Lee *et al.*, 2017). In SAT derived from obese individuals there was also a significant decrease in mitochondrial size with an associated increase in the number of mitochondria, and increased expression of mitochondrial proteins such as complex I-IV subunits NDUFA9, SDHA and COX4. This may be driven by the differential epigenetic regulation and increased expression of *TBX15* observed in adipose MSCs isolated from obese compared to lean individuals (Ejarque *et al.*, 2019).

Further, in cells both *overexpression* of TBX15 and siRNA *knockdown* of *Tbx15* resulted in similar expression patterns of adipogenic and mitochondrial gene markers (Table 1.4) (Gesta *et al.*, 2011; Gburcik *et al.*, 2012). *Overexpressing* TBX15 in the 3T3-L1 mouse preadipocyte cell line reduced *Cebpa, Pparg* and *Fabp4,* whilst *Cebpb, Cepbd* and *Klf5* levels were unchanged (Gesta *et al.*, 2011). TBX15-*overexpressing* cells had reduced lipid accumulation and lower mitochondrial mass than control cells. It was suggested that the C/EBPα-PPARγ feedback loop was therefore regulated by TBX15 with a proposed role in driving oxidative versus glycolytic metabolism in adipocytes (Gesta *et al.*, 2011). Conversely, siRNA *knockdown* of *Tbx15* significantly reduced expression levels of *Pparg* and *Fabp4* and reduced differentiation in brown and beige, but not white, adipocytes

isolated from adipose of 129/SV mice. Mitochondrial gene (*Prdm16, Pgc1a, Cox8b and Ucp1*) and protein (AP2, COX4 and UCP1) levels were reduced in *Tbx15* knockdown brown and beige cells, indicating impaired mitochondrial biogenesis (Gburcik *et al.*, 2012). The differences between the two studies (overexpression compared to knockdown both decreasing expression of key genes) likely arise from several factors such as differences in controls used between studies or intrinsic differences between cell types as 3T3-L1 cells exhibit white and brown adipocyte characteristics (Morrison and McGee, 2015). Further experimentation would be needed to clarify the mechanism of action of TBX15 in adipogenesis and browning, for example examining differentiation and gene expression patterns of adipogenic precursor cells isolated from SVF of $Tbx15^{+/-}$ and $Tbx15^{-/-}$ mice.

PRDM16 is a key regulator of early differentiation in brown and beige adipocytes, therefore, Gburcik *et al.* (2012) hypothesised that TBX15 may act upstream of this to drive adipocyte maturation of brown and beige cells (Gburcik *et al.*, 2012). This was supported by *in vitro* evidence showing TBX15 directly interacted with the promoter region of *Prdm16* to regulate its expression (Sun *et al.*, 2019). Adipocyte-specific knockout of *Tbx15* further impaired UCP1 protein expression and browning of iWAT under cold exposure, with associated decrease in brown and beige genes *Ucp1, Prdm16, Cidea, Dio2, Cox8b, Cox5b, Tbx1, Tmem26* and *Cd137*. Even within adipose tissues, *Tbx15* may play a differential role in regulating genes associated with lipid metabolism and browning. For example, ~5% of preadipocyte cells isolated from iWAT of *Tbx15*-LacZ mice expressed *Tbx15*; and were further stratified by high ($Tbx15^{Hi}$) or low ($Tbx15^{Low}$) *Tbx15* expression (Lee *et al.*, 2017). Whilst overall differentiation capacity (measured by *Fabp4, Adipoq* and *Pparg* expression) was not altered, $Tbx15^{Hi}$ cells had increased

glycolytic metabolism (*Hk2* and *Gapdh*) and decreased oxidative phosphorylation (*Pgc1α, Cox8b* and *Cox5b*) markers compared to *Tbx15*^{Low} cells (Lee *et al.*, 2017). In line with this, *TBX15* expression was positively correlated with *GAPDH* and *HK2* in human SAT (male and females) and VAT (male only) suggesting *TBX15* regulates metabolic processes in a heterogeneous manner (Lee *et al.*, 2017).

More recently, a co-expression cluster of 347 genes, enriched for adipose metabolism terms, were inversely correlated with BMI, WHR and WHRadjBMI in SAT RNA-sequencing data (Pan *et al.*, 2021). Transcription-wide association analysis identified TBX15 as one of three TFs (including iroquois homeobox 1 and x-prolyl aminopeptidase 3) within the co-expression cluster significantly associated with WHRadjBMI. Fine-mapping of these loci revealed TBX15 was the most likely to be functional and this was validated by RNA-sequencing of human primary preadipocytes following siRNA-mediated knockdown of *TBX15* (Pan *et al.*, 2021). Approximately 37% (130/347) of the co-expression network genes were significantly differentially expressed in *TBX15*-knockdown cells, including *PPARG, KLF15* and *TWIST1* (twist family BHLH transcription factor 1). Of which *KLF15* and *TWIST1* had a TBX15 motif within +2kb/-1kb of the transcription start site, implicating TBX15 as a direct regulator of key adipogenesis genes (Pan *et al.*, 2021). Together, these data indicate a pleiotropic role for TBX15 in regulating adipogenesis and fat distribution in humans and suggest *TBX15* may be causal in *TBX15-WARS2* WHRadjBMI associations.

Table 1.4. Models of *Tbx15* expression *in vitro* and *in vivo*. Abbreviations: WAT (white adipose tissue), BAT (brown adipose tissue).

Model	*Tbx15* expression	Reference
Cells	Stable overexpression of *Tbx15* in 3T3-L1 cells. Over 70% reduced expression of *Cebpa, Pparg* and *Fabp4*. Decreased expression of mitochondrial genes *Cox5b, Cox8b, Cycs, mt-ND1* and *mt-Co3*. Increased lipolysis and decreased lipogenesis. Decreased mitochondrial mass and respiration.	(Gesta *et al.*, 2011)
	siRNA knockdown of *Tbx15* in brown and beige preadipocytes extracted from 129/SV mice. (10-fold reduction in *Tbx15* expression, p<0.001). 50% reduced expression of *Pparg* and *Fabp4*. Reduced expression of *Prdm16, Pgc1α, Cox8b* and *Ucp1*.	(Gburcik *et al.*, 2012)
	Subsets of preadipocytes expressing high (*Tbx15^{HI}*) and low (*Tbx15^{LO}*) *Tbx15* from subcutaneous WAT of Tbx15-LacZ mice on a mixed genetic background. 50-80% decreased oxidative metabolism markers (*Pgc1a, Cox8b* and *Cox5a*), 60-120% increased glycolytic metabolism markers (*Hk2* and *Gapdh*) in *Tbx15^{Hi}* vs *Tbx15^{Low}* cells.	(Lee *et al.*, 2017)
129/SV mice	Brown and beige depots from 129/SV mic express higher levels of *Tbx15* than white adipose depots. Preadipocyte cells from brown and beige depots from 129/SV mic expressed higher levels of *Tbx15* than preadipocytes from white adipose	(Gburcik *et al.*, 2012)
C57BL/6N mice	Higher in adipocytes (140-fold, p=0.001) and preadipocytes (460-fold, p= 0.013) in subcutaneous compared to gonadal WAT (qPCR). 39-fold higher in subcutaneous vs gonadal tissue (p=0.005) (qPCR)	(Gesta *et al.*, 2006)
	200-fold higher in subcutaneous vs gonadal preadipocytes	(Gesta *et al.*, 2011)
	Interscapular WAT > subcutaneous WAT ~ perirenal WAT > BAT ~ gonadal WAT > mesenteric WAT. High fat diet reduced interscapular *Tbx15* expression. Overnight fasting had no effect on expression.	(Yamamoto *et al.*, 2010)
C57BL/6J mice	Adipose-specific *Tbx15* knockout (Adiponectin-Cre crossed with floxed *Tbx15*). Adipocytes in iWAT failed to undergo browning after cold challenge. Reduced expression of *Ucp1, Prdm16, Cidea, Dio2*, *Cox8b*, *Tbx1, Tmem26*, *Cd137, Hk2, Eno1* and *Pkm* in iWAT. Interaction between *Tbx15* and promoter region of *Prdm16* (required to upregulate *Ucp1* expression).	(Sun *et al.*, 2019)
129/Ola x NMRI mixed background mice	*Tbx15* global knockout (*Tbx15$^{-/-}$*). Increased oxidative and decreased glycolytic fibres in *Tbx15$^{-/-}$* compared to *Tbx15$^{+/+}$* mice	(Lee *et al.*, 2015)
Humans	In lean humans, higher *TBX15* expression in visceral compared to subcutaneous depots (male 27.1-fold p<0.05, female 38.7-fold p<0.05). Strong inverse correlation between *TBX15* and BMI and WHR in visceral depots (male and female p<0.001). Positive correlation between *TBX15* and BMI and WHR in subcutaneous depots (male and female p<0.005)	(Gesta *et al.*, 2006)
	Inverse correlation between *TBX15* and BMI in visceral and subcutaneous depots (male and female p<0.05). Positive correlation between *TBX15* and *GAPDH* and *HK2* expression in visceral and subcutaneous depots of obese individuals (p<0.05)	(Lee *et al.*, 2017)
	Increased TBX15 protein in subcutaneous adipose of obese compared to lean individuals (p<0.001). Positive correlation between TBX15 and BMI in subcutaneous depots (p=0.02)	(Ejarque *et al.*, 2019)

1.7. Prioritising functional SNPs in the *TBX15-WARS2 locus*

As the *TBX15-WARS2* locus contains several independent WHRadjBMI signals, determining the true causal SNPs required a multi-faceted approach. Our collaborators in the Lindgren (Big Data Institute, University of Oxford, UK) and Claussnitzer (Broad Institute, MIT, USA) research groups simultaneously applied bioinformatics prioritisation methods on the 61 SNPs in high LD ($r^2 \geq 0.8$) with the four lead *TBX15-WARS2* signals, to identify likely causal SNPs.

1.7.1. Epi-phylogenetic module complexity analysis

Nasa Sinnott-Armstrong (Claussnitzer group) utilised epi-phylogenetic module complexity analysis (epi-PMCA) for prioritisation (Figure 1.11). This method incorporates PMCA, previously developed by Claussnitzer *et al.* (2014), which predicts SNPs with highly conserved transcription factor binding site (TFBS) patterns are more likely to be functional. In epi-PMCA, SNPs were ranked based on the average number of TFBS in *cis*-regulatory modules (CRMs; 'TFBSinModuleRestr' column, Figure 1.11). The maximally scoring SNP, and therefore most likely to be functional, was rs10494217 . Except for rs1106529, all lead SNPs were ranked outside the top 10 in epi-PMCA, suggesting the GWAS tag SNP may not always be causal.

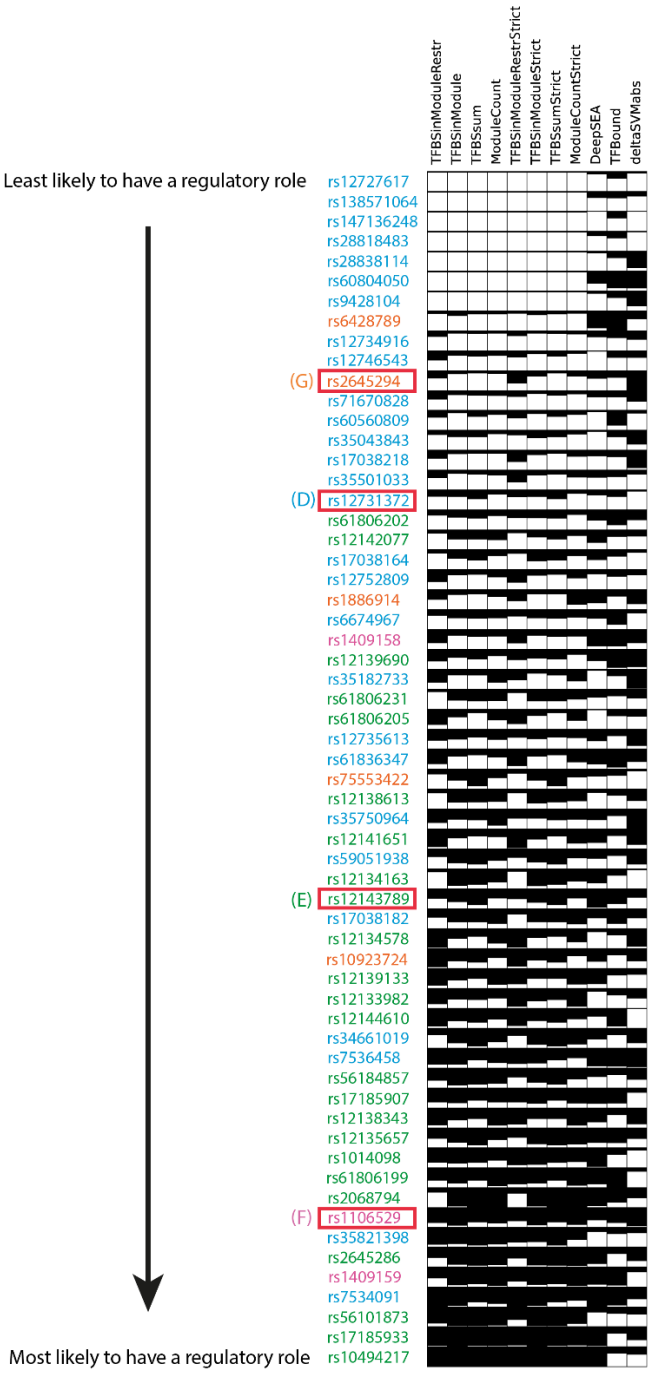

Figure 1.11. Epi-phylogenetic module complexity analysis (epi-PMCA) of *TBX15-WARS2* locus SNPs. Epi-PMCA of 61 SNPs in high linkage disequilibrium with the four index SNPs from Shungin *et al*., (2015). Columns 1-4: analysis of transcription factor binding sites (TFBS) in cis-regulatory motifs (CRM) (with loose (information content≥5.25) motif hits) 1. Number of TFBS in 50% of 15 conserved species, 2. Number of TFBS in all species, 3. Total number of TFBS and 4. Total number of cis-regulatory modules. Columns 5-8: the same analysis with strict (information content≥5.75) motif hits. Column 9: DeepSEA predictions for epigenetic state of sequence (transcription factor (TF) binding, DNAseI sensitivity and histone marks). Column 10: TF binding inferred from ChIP-sequencing data. Column 11: deltaSVM (quantifies effect size) across mesenchymal cell types plus IRM90. deltaSVM accurately predicts the impact of SNPs in DNAseI sensitivity in their native genomic context (chromatin sites sensitive to DNAseI cleavage, i.e., accessible DNA allows TF binding). Lead SNPs for each of the four risk blocks (D-G) are highlighted in red boxes. SNPs were ranked by average number of TFBS in each CRM (TFBSinModuleRestr). Adapted from unpublished data generated by Nasa Sinnott-Armstrong (Broad Institute, MIT).

1.7.2. Posterior probability analysis

Dr. Sara Pulit simultaneously performed PPA on the 61 SNPs, using UK BioBank and GIANT consortium data (Table 1.5). PPA assumes a single causal SNP drives GWAS associations, and based on this generates a score indicating the probability that the tested SNP is causal (Maller *et al.*, 2012). Scores of 1 are considered most likely to be functional, and in this analysis SNPs with a score ≥0.2 were considered potentially functional. There appears to be little correlation between epi-PMCA and PPA, with most top 10 epi-PMCA SNPs not reaching the ≥0.2 cut-off value for PPA. For example, rs10494217 had a maximal PPA score of 0.12, despite being ranked as most likely to be functional by epi-PMCA. This is likely due to differences in underlying methods and assumptions of the two analyses, highlighting the need for a multi-faceted approach when trying to determine functional SNPs from a list of potential candidate variants.

Table 1.5. Posterior probability analysis of *TBX15-WARS2* locus SNPs. The four lead SNPs in each risk block are shown in bold, with the top 10 ranked SNPs from the epi-PMCA analysis grouped with the lead SNP for which they had the highest LD score. Data generated by Dr Sara Pulit (University of Oxford, UK). Risk Block G data has previously been published by our group (Mušo *et al.*, 2020).

Risk Block	SNP	epi-PMCA Rank	PPA score					
			UKBioBank			GIANT		
			All	Female	Male	All	Female	Male
D	rs7534091	4	0	0	0	0.25	0.13	0.33
	rs35821398	7	0	0	0	N/A	N/A	N/A
	rs12731372	**44**	**0.01**	**0**	**0.01**	**0.68**	**0.56**	**0.43**
E	rs10494217	1	0	0	0	0.06	0.07	0.07
	rs12143789	**24**	**0**	**0**	**0**	**0.13**	**0.01**	**0.1**
	rs17185933	2	0	0	0	0.12	0.01	0.01
	rs56101873	3	0	0	0	N/A	N/A	N/A
	rs2645286	6	0	0	0	0.04	0.01	0.01
	rs2068794	8	N/A	N/A	N/A	N/A	N/A	N/A
	rs61806199	10	N/A	N/A	N/A	N/A	N/A	N/A
F	rs1409159	5	0	0	0	0	0	0
	rs1106529	**9**	**0**	**0**	**0**	**0.06**	**0**	**0**
G	**rs2645294**	**50**	**0.05**	**0**	**0.01**	**0.33**	**0.6**	**0.01**

1.8. Thesis aims and hypotheses

The *TBX15-WARS2* WHRadjBMI locus is complex, yet well-replicated, with four distinct association signals, and contains strong candidate genes for adipose tissue function. The challenge is to determine causal SNPs and the mechanisms through which they act to influence the associated traits. The overarching aim of my project was, therefore, to characterise potentially functional *TBX15-WARS2* locus SNPs *in vitro* and *in vivo* to understand their effect on gene expression networks leading to alterations in adipose tissue function and associated metabolic traits. The key hypotheses and aims underlying my project are addressed as follows:

Chapter 3 – *TBX15* coding SNPs rs10494217 (p.H156N) and rs61730011 (p.M566R) act at a DNA-regulatory and/or TBX15 protein-coding level to regulate gene expression. The key aims of this chapter were to:

1. Test the potential regulatory roles of rs10494217 and rs61730011 *in silico.*
2. Confirm *in vitro* any effects on protein-protein and/or protein-DNA binding.

Chapter 4 –$Tbx15^{+/-}$, $Tbx15^{H156N}$, and $Tbx15^{M566R}$ alleles alter body composition in mice. The key aims of this chapter were to:

1. Assess body composition and adipose distribution in $Tbx15^{+/-}$, $Tbx15^{H156N}$, and $Tbx15^{M566R}$ mice on high-fat and low-fat diets.
2. Assess classical T2DM phenotypes in $Tbx15^{+/-}$, $Tbx15^{H156N}$, and $Tbx15^{M566R}$ mice on high-fat and low-fat diets.
3. Assess blood plasma composition and adipocyte cell area in $Tbx15^{+/-}$, $Tbx15^{H156N}$, and $Tbx15^{M566R}$ mice on high-fat and low-fat diets.

Chapter 5 – *TBX15* is an effector gene in the *TBX15-WARS2* locus and drives an adipose transcriptional network that may differ between fat depots. The key aims of this chapter were to:

1. Identify TBX15 target DNA sites by analysing ChIP-sequencing data *in vitro* in human and mouse preadipocytes.
2. Identify the *Tbx15* gene network in iWAT and BAT from $Tbx15^{-/-}$, $Tbx15^{+/-}$ and $Tbx15^{+/+}$ mice.

Chapter 6 – The p.H156N polymorphism perturbs the TBX15 adipose transcriptional network leading to altered fat distribution and WHRadjBMI associations. The key aims of this chapter were to:

1. Identify *Tbx15* gene network perturbations in iWAT from $Tbx15^{H156N/H156N}$ and $Tbx15^{+/+}$ mice.
2. Identify *Tbx15* gene network perturbations in differentiating adipogenic precursor cells derived from stromal-vascular fraction cells isolated from iWAT in $Tbx15^{H156N/H156N}$ and $Tbx15^{+/+}$ mice.

2

Materials and Methods

2.1. Cell culture

2.1.1. General cell culture and consumables

Immortalised and primary cell lines were cultured in a class two biological safety cabinet, using aseptic techniques. Immortalised cell lines (described in 2.1.1.1 and 2.1.1.2) were maintained in T75 flasks (cat. 658170, Greiner Bio-One, Frickenhausen, Germany), and cultured in 6-well plates for transfections (cat. 657160, Greiner Bio-One), unless stated otherwise. A minimum of two independent replicates were tested on individually thawed vials of cells; cells were passaged a minimum of two times before use, and independent aliquots of DNA were used for transfections. Primary cells (described in 2.1.1.3) were maintained in 10 cm^2 dishes (cat. 664160, Greiner Bio-One) and cultured in 6-well plates for differentiation. Individual mice were considered independent replicates.

2.1.1.1. Immortalised cell line procurement

Human embryonic kidney 293 cells immortalised using SV40 T-antigen (HEK293T) were purchased from European collection of authenticated cell cultures (cat. 12022001, lot 16G020, Sigma-Aldrich, Merck Millipore, Darmstadt, Germany). Cells were used at passage 11-15 for experimental procedures.

Human white adipose tissue preadipocyte (hWAT) cells were kindly gifted by Professor Yu-Hua Tseng (Joslin Diabetes Centre, Harvard Medical School, Boston, MA, USA) (Xue *et al.*, 2015). Briefly, hWAT cells were derived from stromal vascular fraction (SVF) cells isolated from subcutaneous and subplatysmal white fat depots (Figure 2.1) from the neck of a 56-year-old female (BMI=30.8). SVF cells were immortalised by induction of stable human telomere reverse transcriptase expression and validated as described in (Xue *et al.*, 2015). Cells were used at passage 17-19 for experiments.

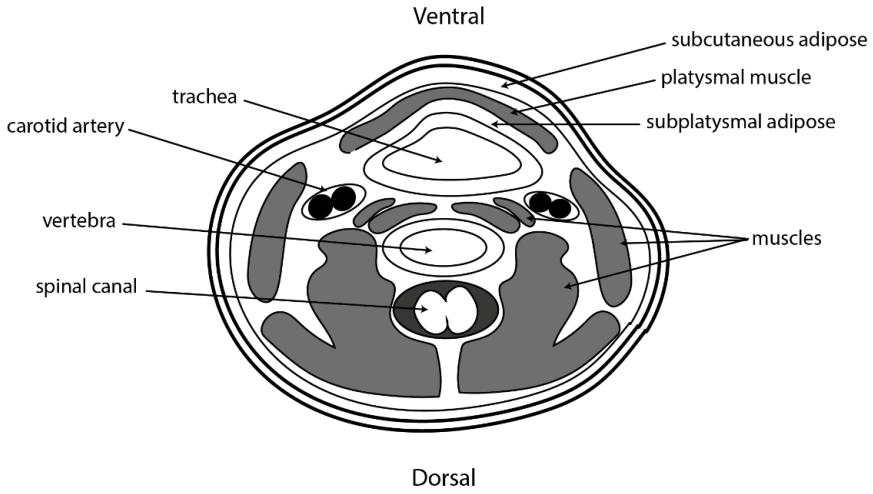

Figure 2.1. Adipose depots of the neck region. Cross-sectional schematic of cervical neck region showing subcutaneous and subplatysmal (superficial adipose depot located below the platysmal muscle) adipose depots dissected to generate hWAT cells. Figure adapted from (Cypess *et al.*, 2013) with permission from Springer Nature (licence number: 5277781370047).

Swiss-albino "3-day transfer, inoculum 3 x 10^5" (3T3) subclone L1 (3T3-L1) cells were purchased from American Type Culture Collection (cat. ATCC-CL-173, lot 61194648, ATCC, Manassas, VA, USA). Briefly, 3T3 fibroblastic cells were isolated from 17-19 day old male Swiss-albino whole embryos and cultured successively to form established lines (Todaro and Green, 1963). The L1 subclone was further isolated from pools of lipid-rich cells from confluent 3T3 cultures and was shown to have adipogenic

potential (Green & Kehinde, 1974; Green & Meuth, 1974). Cells were used at passage 11-13 for experimental procedures.

All cell lines underwent an initial 14-day quarantine upon receipt, before use in experimental procedures. After 14 days of sub-culture, cells were cultured for 5 days without antibiotics, and $1x10^6$ cells were pelleted and sent for pathogen/mycoplasma testing (IDEXX BioAnalytics, Columbia, MO, USA). Human cells (HEK293T and hWAT) were tested for human pathogens and mycoplasma (cat. h-IMPACT III) and 3T3-L1 cells were tested for mycoplasma only (cat. STAT-MYCO).

2.1.1.2. Maintenance of immortalised cell lines

Cell lines were maintained at 37°C, 5% CO_2 and 95% humidity. For passage, culture medium was removed from the flask, cells were washed with 1x Dulbecco's phospho-buffered saline (DPBS; cat.14190-094, Gibco, ThermoFisher Scientific (TFS), Waltham, MA, USA) and 1 mL trypsin-ethylenediaminetetraacetic acid (trypsin-EDTA) was added to each T75 flask. Flasks were incubated at 37°C until 90% of cells had dissociated from the surface and a minimum of three times volume of culture medium was added to neutralise trypsin-EDTA before passage into new flasks containing fresh media (Table 2.1).

2.1.1.3. Primary murine SVF isolation

Inguinal white adipose tissue (iWAT) was dissected from 6-week-old male and female C57BL/6NTac mice and washed in 1x DPBS to remove hair and blood. Left and right depots were combined and minced thoroughly in 7 mL Hank's balanced salt solution

(cat. H8264, Sigma-Aldrich) containing 0.8 mg/mL type 2 collagenase (cat. LS004174, Worthington Biochemical Corporation, Lakewood, NJ, USA) and 3% (weight/volume [w/v]) bovine serum albumin (BSA; cat. A9418, Sigma-Aldrich). Samples were digested at 37°C at 125 rpm in a shaking water bath for 45-60 minutes, with vigorous manual shaking every 10 minutes, until minimal tissue clumps remained. SVF (containing preadipocytes) were pelleted by centrifugation at 300 *x g*, and supernatant containing lipid-filled mature adipocytes was removed. The pellet was resuspended in 10 mL culture medium (Table 2.1), filtered through 40 µm mesh (cat. 431750, Corning Inc., Corning, NY, USA) and cultured in a 10 cm^2 culture dish at 37°C, 5% CO_2. Twenty-four hours post-isolation, cells were washed twice with 1x DPBS and culture medium was replenished. Cells were washed twice with 1x DPBS and culture medium was refreshed every 48 hours until cells reached 80% confluence (approximately 72-96 hours).

Table 2.1. Maintenance of immortalised and primary cell lines. Normal culture media and trypsin-EDTA used for routine culture and passage of cells. All culture reagents were purchased from Gibco. Abbreviations: DMEM (Dulbecco's modified eagle medium), EDTA (ethylenediaminetetraacetic acid), FBS (foetal bovine serum), NBCS (new-born calf serum), v/v (volume/volume).

Cell line	Normal culture medium	Trypsin-EDTA	Passage procedure
HEK293T	DMEM-GlutaMAX™ (cat. 31966-047) 10% (v/v) FBS (cat. 10082-147) 1% (v/v) penicillin/streptomycin (5000 U/mL, cat. 15070-063)	0.05% trypsin-EDTA (cat. 25300-054)	Passaged at 70-75% confluence (24-48 hours) at a ratio of 1:5
hWAT	DMEM-GlutaMAX™ 10% (v/v) FBS 1% (v/v) penicillin/streptomycin	0.25% trypsin-EDTA (cat. 25200-056)	Passaged at 85-90% confluence (48-72 hours) at a ratio of 1:3
3T3-L1	DMEM-GlutaMAX™ 10% (v/v) NBCS (cat. 26010-074) 1% (v/v) penicillin/streptomycin	TrypLE™ express enzyme (cat. 12605-010)	passaged at 75-80% confluence (48-72 hours) at a ratio of 1:5
Primary SVF	DMEM-GlutaMAX™ 10% (v/v) FBS 1% (v/v) penicillin/streptomycin	TrypLE™ express enzyme	Cultured to 80% following isolation and plated into 6-well plate for experimental procedures

2.1.1.4. Thawing cells

One vial of cells was thawed in a 37°C water bath and added to 10 mL pre-warmed culture medium. Cells were pelleted (HEK293T at 125 *x g* for 3 minutes, hWATs at 300 *x g* for 4 minutes, and 3T3-L1 at 125 *x g* for 5 minutes) in a Heraeus Megafuge 16 centrifuge (TFS) and media was discarded to remove dimethyl sulfoxide (DMSO). Cells were resuspended in culture media, plated in a T75 flask, and incubated at 37°C, 5% CO_2. Twenty-four hours later, media was replaced with culture medium and cells were cultured until required (described in 2.1.1.2).

2.1.1.5. Cell counting

Culture medium was removed from the flask and cells were washed with 1x DPBS, dissociated with trypsin-EDTA and neutralised with culture medium (described in 2.1.1.2). Cells were pelleted and resuspended in 10 mL culture medium. The cell suspension was diluted 1:1 in filtered trypan blue 0.4% solution (cat. 15250-061, Gibco). To assess viability using the live/dead dye exclusion test, 10 µL cell suspension was added to each side of a Countess™ cell counting chamber slide (cat. C10228, Invitrogen, TFS) and analysed using a Countess™ II cell counter (Invitrogen). Live cell counts from both sides of the slide were averaged to calculate seeding densities.

2.1.1.6. Freezing cells

Culture medium was removed from the flask and cells were washed with 1x DPBS, dissociated with trypsin-EDTA, neutralised with culture medium and pelleted (described in 2.1.1.2). Pellets were resuspended in 900 µL freezing medium (Table 2.2)

per T75 flask and added to 100 µL DMSO (cat. D2650, Sigma-Aldrich) in a 2 mL cryovial. Cryovials were gently frozen in an isopropanol "Mr Frosty" freezing chamber at -80°C for a minimum of 4 hours before being transferred to liquid nitrogen (LN_2) for long-term storage.

Table 2.2. Freezing media components for immortalised cell lines. Abbreviations: FBS (foetal bovine serum), DMEM (Dulbecco's modified eagle's medium), DMSO (dimethyl sulfoxide).

Cell line	Freezing medium stock	Final freezing media ratios
HEK293T	45 mL FBS	90% FBS 10% DMSO
hWAT	25 mL FBS 20 mL DMEM	50% FBS 40% DMEM 10% DMSO
3T3-L1	25 mL FBS 25 mL DMEM	45% FBS 45% DMEM 10% DMSO

2.1.2. Transfections

2.1.2.1. Poly-D-Lysine coating

Poly-D-Lysine (PDL; cat. A38904-01, Gibco) was diluted 1:1 in 1x DPBS to a 50 µg/mL solution. To coat culture wear, 1.5 mL 50 µg/mL PDL was added per well of a 6-well plate and incubated at room temperature for 60 minutes. PDL was discarded and wells were washed three times with 5 mL sterile H_2O (cat. W3500, Sigma-Aldrich). Plates were air-dried for 2 hours in a biological safety cabinet. Once dry, plates were sealed with Parafilm M (cat. 1126846, Bemis, Neenah, WI, USA) and stored at 4°C.

2.1.2.2. Seeding densities

For protein and RNA extraction, HEK293T cells were seeded in PDL-coated 6-well plates at a density of 2.5x 10^5 cells/mL and cultured for 24 hours in culture medium. hWAT cells were seeded in 6-well plates in culture medium at a density of 1x 10^5 cells/mL and cultured for 24-72 hours. 3T3-L1 cells were seeded in 6-well plates in culture medium at a density of 5x 10^4 cells/mL and cultured for 24-72 hours. Alternatively, for ChIP-sequencing hWAT and 3T3-L1 cells were sub-cultured in T175 culture flasks (cat. 660160, Greiner Bio-One) for 24-72 hours in culture media.

2.1.2.3. Lipofectamine 3000™ reagent

Cells were transfected with the Lipofectamine 3000™ kit (cat. L3000-015, Invitrogen), following manufacturer's protocols. Briefly, cells were transfected with 2.5 µg of DNA construct per well of a 6-well plate. Per well, 3.75 µL (1.5x the amount of DNA) of Lipofectamine 3000™ reagent (cat. 100022052, Invitrogen) was added to 125 µL opti-MEM™ reduced serum media (cat. 31985-062, Gibco). Then, 5 µL (2x the mass of DNA) of P3000™ reagent (cat. 100022058, Invitrogen) was added to 125 µL opti-MEM™ media along with 2.5 µg DNA. The diluted DNA-P3000™ mix was added to the Lipofectamine 3000™ solution (final volume 250 µL), mixed briefly and incubated at room temperature for 10-15 minutes. During the incubation, 1.75 mL culture medium was replenished on cells and 250 µL of the DNA-Lipofectamine complexes were added in a dropwise manner per well. Cells were incubated for 24-48 hours before harvesting. This process was scaled accordingly for ChIP-sequencing applications for transfection of 46 µg DNA per T175 flask.

2.1.3. Adipogenic differentiation

2.1.3.1. Differentiation media stocks

To differentiate preadipocytes into mature adipocytes, cells were cultured to 24 hours post-confluence in normal culture medium. Media was then exchanged for fresh differentiation cocktail medium (prepared immediately prior to use). Stock supplements (Table 2.3) were added to pre-warmed (37°C) DMEM+GlutaMAX™ containing 1% (v/v) penicillin/streptomycin and filtered through a 0.22 µM Millex-GP® filter (cat. SLGP033RB, Merck Millipore). After filtration, human insulin (10 mg/mL, cat. I9278, Sigma-Aldrich) and 10% (v/v) FBS were added to the differentiation cocktail medium before use.

Table 2.3. Adipocyte differentiation media supplement stocks. Abbreviations: ddH_2O (double distilled H_2O), KOH (potassium hydroxide), NaOH (sodium hydroxide). All reagents were purchased from Sigma-Aldrich.

Reagent	Catalogue number	Stock preparation	Stock concentration
Isobutyl methylxanthine (IBMX)	I5879	100 mg dissolved in 8.99 mL 0.1 M KOH	50 mM
Dexamethasone	D2915	100 mg dissolved in 50.9 mL 100% ethanol	5 mM
D-Pantothenic acid hemicalcium salt (Pantothenate)	P5155	20.25 mg dissolved in 10 mL ddH_2O	8.5 mM
Biotin	B4639	73.29 mg dissolved in 10 mL 0.1 M NaOH	30 mM
3,3′,5-Triiodo-L-thyronine (T3)	T6397	1.034 mg dissolved in 1 mL NaOH, then add 152.6 mL DMEM+GlutaMAX™	10 µM
Indomethacin	I7378	447.24 mg dissolved in 10 mL 100% ethanol at 75°C	125 mM

2.1.3.1. hWAT cells

hWAT cells were seeded at 1x 10^5 cells/mL in a 6-well plate, or sub-cultured at a 1:3 ratio in T75 and T175 flasks and cultured in normal growth medium for 48-72 hours until confluent. Twenty-four hours post-confluence, cells were induced to differentiate into adipocytes using a differentiation cocktail media (Table 2.4). Differentiation cocktail media was replenished every 48-72 hours for up to 20 days (to terminal differentiation).

Table 2.4. hWAT differentiation media composition. Abbreviations: IBMX (isobutyl methylxanthine), T3 (3,3′,5-Triiodo-L-thyronine). See Table 2.3 for stock reagents.

Media	Stock reagent	Dilution factor for 50 mL media	Final concentration
Differentiation cocktail media	IBMX (50 mM)	500 µL	500 µM
	Dexamethasone (5 mM)	1 µL	0.1 µM
	Human insulin (10 mg/mL)	14.5 µL	500 nM
	T3 (10 µM)	10 µL	2 nM
	Indomethacin (125 nM)	12 µL	30 µM
	Pantothenate (8.5 mM)	100 µL	17 µM
	Biotin (30 mM)	55 µL	33 µM

2.1.3.2. 3T3-L1 cells

3T3-L1 cells were seeded at 5x 10^4 cells/mL, or sub-cultured at a 1:5 ratio in a T175 flask and cultured in normal growth media for 48-72 hours until confluent. Twenty-four hours post-confluence, cells were induced to differentiate into adipocytes using a differentiation cocktail media for 4 days and were then maintained in differentiation maintenance media up to a total of 7 days (terminal differentiation)

(Table 2.5). Differentiation cocktail and maintenance media were replaced every 24-48 hours.

Table 2.5. 3T3-L1 differentiation cocktail and maintenance media composition. Abbreviations: IBMX (isobutyl methylxanthine), T3 (3,3′,5-Triiodo-L-thyronine). Human insulin was diluted to 1 mg/mL prior to addition to differentiation media. See Table 2.3 for stock reagents.

Media	Stock reagent	Dilution factor for 50 mL media	Final concentration
Differentiation cocktail media	IBMX (50 mM)	500 µL	500 µM
	Dexamethasone (5 mM)	10 µL	1 µM
	Human insulin (1 mg/mL)	6 µL	20 nM
Differentiation maintenance media	Human insulin (1 mg/mL)	6 µL	20 nM

2.1.3.3. Primary murine SVF cells

SVF cells were seeded at 8x 10^4 cells/mL in a 6-well plate and cultured in normal growth media for 48 hours until confluent. Twenty-four hours post-confluence, differentiation was induced with a "minimal" differentiation cocktail media for 4 days. Following this, cells were maintained in "minimal" differentiation maintenance media up to a total of 7 days (terminal differentiation) (Table 2.6).

Alternatively, cells were induced to differentiate with a "complete" differentiation cocktail media for 4 days. Following this, cells were maintained in "complete" differentiation maintenance media up to a total of 7 days (terminal differentiation) (Merrick *et al.*, 2019) (Table 2.6). Both "minimal" and "complete" differentiation cocktail and maintenance media were replaced every 24-48 hours.

Table 2.6. Primary murine SVF differentiation and maintenance media composition. Abbreviations: IBMX (isobutyl methylxanthine), T3 (3,3′,5-Triiodo-L-thyronine). Human insulin was diluted to 1 mg/mL prior to addition to differentiation media. See Table 2.3 for stock reagents.

Media	Stock reagent	Dilution factor for 50 mL media	Final concentration
Minimal differentiation cocktail media	IBMX (50 mM)	50 µL	0.5 µM
	Dexamethasone (5 mM)	25 µL	1 µM
	Human insulin (1 mg/mL)	60 µL	200 nM
Minimal differentiation maintenance media	Human insulin (1 mg/mL)	60 µL	200 nM
Complete differentiation cocktail media	IBMX (50 mM)	50 µL	0.5 µM
	Dexamethasone (5 mM)	25 µL	1 µM
	Human insulin (1 mg/mL)	6 µL	20 nM
	T3 (10 µM)	5 µL	1 nM
	Indomethacin (125 mM)	50 µL	125 nM
Complete differentiation maintenance media	Human insulin (1 mg/mL)	6 µL	20 nM
	T3 (10 µM)	5 µL	1 nM

2.1.3.4. OilRedO stain

To make a 0.3% (w/v) stock solution, 300 mg OilRedO powder (cat. O0625, Sigma-Aldrich) was dissolved in 100 mL 100% isopropanol (cat. 389710025, Acros Organics, TFS). The stock solution was diluted 3:2 with deionised H_2O (diH_2O; MilliQ™, Merck Millipore) to 0.18% (w/v), incubated at room temperature for 10 minutes and filtered through Whatmann filter paper prior to use. Paraformaldehyde (cat. P6148, Sigma-Aldrich) was dissolved in diH_2O with heating to make a 4% (w/v) working solution.

Differentiated cells were washed twice with 1x DPBS and fixed in 4% (w/v) paraformaldehyde on ice for 15 minutes. Fixed cells were rinsed twice in diH_2O and incubated in 60% (v/v) isopropanol for 5 minutes. Cells were stained with 0.18% OilRedO for 5 minutes at room temperature and washed in diH_2O until clear. Cells were

stored in 1x DPBS for imaging using an AxioObserver Z1 microscope (Zeiss, Oberkochen, Germany). Prior to use, IGEPAL CA-630 (cat. I8896, Sigma-Aldrich) was diluted in 100% isopropanol to make a 4% (v/v) IGEPAL CA-630/isopropanol solution. Lipid droplets were lysed with 1 mL 4% (v/v) IGEPAL CA-630/isopropanol solution for 10 minutes with gentle agitation. For quantification, 100 µL of lysate was transferred in triplicate, along with 4% (v/v) IGEPAL CA-630/isopropanol as a blank solution, to a 96-well UV transparent flat-bottom plate (cat. 3635, Corning Inc.). Absorbance was read at 500 nm on an Epoch spectrophotometer, with Gen5.200 software (BioTek, Agilent Technologies, Santa Clara, CA, USA).

2.2. Animal studies

2.2.1. Ethical statement

All animal studies were approved by the Medical Research Council Harwell (MRCH) Institute animal welfare and ethical review board. All procedures were carried out within project license permissions (PPL 30/2642, 30/3146 and PE198161E) under the UK animals (scientific procedures) act 1986 and following the ARRIVE guidelines for animal research. Mice were housed in the Mary Lyon centre (MLC) according to UK Home Office guidelines. Cohort sizes were calculated with G*Power3.1 from previous experiments using the same tests (described in 2.6). Mice were randomised by MLC staff at 3 weeks of age and all phenotyping was performed blind to genotypes.

2.2.2. Mouse husbandry

Male and female mice were maintained at 21 ± 2°C, 55 ± 10% humidity and in a 12-hour light-dark cycle (light: 7am-7pm, dark: 7pm-7am). Genotyping was performed on ear-clips at 2 weeks of age by the MRCH genotyping facility (described in 2.2.3.2). Mice for post-weaning viability assessments and RNA-sequencing cohorts were weaned randomly with *ad libitum* access to food (rat and mouse no. 3 breeding diet; RM3) and water (25 ppm chlorine) (Table 2.7). For metabolic phenotyping cohorts, mice were weaned and randomised, with *ad libitum* access to food, either low-fat diet (LFD) or high-fat diet (HFD), and water (Table 2.7).

Table 2.7. Mouse diet composition details. Diet composition for RM3, low-fat and high-fat diets. The LFD is a more appropriate control than RM3 for the HFD as fibre type and amount, source of carbohydrate, and variation in plant chemicals such as phytoestrogens are matched between these purified ingredient diets.

Diet	Catalogue number	Composition	Manufacturer
rat and mouse no. 3 breeding diet (RM3)	RM3	11% fat 27% protein 62% carbohydrate 3.6 kcal/g	Special Diet Services, Essex, UK
Low-fat diet (LFD)	D12450J	10% fat 20% protein 70% carbohydrate 7% sucrose 3.85 kcal/g	Research Diets Inc., New Brunswick, NJ, USA
High-fat diet (HFD)	D12492	60% fat 20% protein 20% carbohydrate 7% sucrose 5.24 kcal/g	Research Diets Inc.

2.2.3. Mouse lines

2.2.3.1. Stock line generation

2.2.3.1.1. TBX15-KO-B6N mouse line

A total of 35 frozen embryos (8-cell stage) were purchased from the Jackson laboratory (JAX:000551-B6EiC3 a/A-Tbx15de-H/J). Embryos were implanted into CD1 females to generate F_0 litters by MLC staff. Male and female heterozygous knockout (*Tbx15*$^{+/-}$) mice were subsequently backcrossed to C57BL/6NTac mice to generate *Tbx15*$^{+/-}$ TBX15-KO-B6N stock mice.

2.2.3.1.2. TBX15-H156N-EM2-B6N and TBX15-M566R-EM3-B6N mouse lines

All further genetic mouse models described in this thesis were generated on a C57BL/6NTac background using clustered regularly interspaced short palindromic repeats (CRISPR)/Cas9 technology by Dr. Gemma Codner and the MRCH molecular & cellular biology (MCB) facility as published in (Mianné *et al.*, 2017) (described in Appendix 9.1.1.1). Wild-type colony-mates were used as controls.

An orthologous p.H156N point mutation in exon 3 of TBX15 (*Tbx15*^{H156N}, to replicate rs10494217; designed by Dr. Rebecca Dumbell) and orthologous p.M566R point mutation in exon 8 of TBX15 (*Tbx15*^{M566R}, to replicate rs61730011) were designed in collaboration with the Harwell MCB facility to generate the TBX15-H156N-EM2-B6N and TBX15-M566R-EM3-B6N stock lines, respectively.

2.2.3.2. Genotyping

Genotyping for TBX15-KO-B6N, TBX15-H156N-EM2-B6N and TBX15-M566R-EM3-B6N mouse lines was performed by the MLC genotyping facility using an allelic discrimination real-time PCR assay (allele-specific primer and probe amplification assay (ASPPAA)) as described by (Billard *et al.*, 2012), with Dot1l as an internal control (described in Appendix 9.1.1.2).

2.2.3.3. Experimental cohorts

Table 2.8, Table 2.9 and Table 2.10 indicate the number of mice bred for TBX15-KO-B6N, TBX15-H156N-EM2-B6N and TBX15-M566R-EM3-B6N cohorts described in this thesis, respectively. Data from culled-sick mice was not included in statistical analyses.

2.2.3.3.1. TBX15-KO-B6N

Male and female *Tbx15*$^{+/-}$ mice (backcross 2) were used to generate intercross breeds for an initial viability cohort (n=35 mice, data collected by Dr. Rebecca Dumbell; one mouse culled-sick due to small size), and for tissue collection for RNA-sequencing (n=27 mice dissected by Dr. Rebecca Dumbell, RNA was isolated in collaboration with Dr. Rebecca Dumbell), wildtype littermates were used as controls. For heterozygous metabolic phenotyping cohorts, male *Tbx15*$^{+/-}$ mice (backcross 4) were mated with female C57BL/6NTac mice to generate metabolic phenotyping cohorts (all at backcross 5), with wildtype littermates used as controls. A total of 153 mice were weaned onto HFD or LFD across three cohorts (n=46, 34 and 73, respectively; one mouse-culled sick due to malocclusion).

Table 2.8. Total number of mice bred for TBX15-KO-B6N mouse line experimental cohorts. Abbreviations: RM3 (rat and mouse no. 3 diet), HFD (high-fat diet), LFD (low-fat diet).

Study (mouse line)	Diet	Sex	Genotype	Total number
Viability cohort (TBX15-KO-B6N-IC)	RM3	Female	*Tbx15*$^{+/+}$	6
			Tbx15$^{+/-}$	7
			Tbx15$^{-/-}$	1
		Male	*Tbx15*$^{+/+}$	4
			Tbx15$^{+/-}$	15
			Tbx15$^{-/-}$	1
Tissue RNA-sequencing cohort (TBX15-KO-B6N-IC)	RM3	Female	*Tbx15*$^{+/+}$	5
			Tbx15$^{+/-}$	5
			Tbx15$^{-/-}$	4
		Male	*Tbx15*$^{+/+}$	5
			Tbx15$^{+/-}$	5
			Tbx15$^{-/-}$	3
Metabolic phenotyping cohort (TBX15-KO-B6N)	HFD	Female	*Tbx15*$^{+/+}$	18
			Tbx15$^{+/-}$	22
		Male	*Tbx15*$^{+/+}$	21
			Tbx15$^{+/-}$	17
	LFD	Female	*Tbx15*$^{+/+}$	18
			Tbx15$^{+/-}$	21
		Male	*Tbx15*$^{+/+}$	21
			Tbx15$^{+/-}$	15

2.2.3.3.2. TBX15-H156N-EM2-B6N

Male and female heterozygous (*Tbx15*$^{+/H156N}$) mice were used to generate intercross litters for all experimental cohorts. For initial viability and welfare assessments, and to inform power calculations for later experimental cohorts, a total of 55 mice were weaned onto RM3 diet across two cohorts (n=17 and 33, respectively). For RNA-sequencing a total of 80 mice were weaned onto RM3 diet across two cohorts (n=24 for primary cell isolations; one mouse was culled-sick due to lack of weight gain, and n=28 for adipose tissues; one mouse was culled-sick due to hydrocephalus). For metabolic phenotyping, a total of 265 mice were weaned onto HFD or LFD across eight cohorts (n=50, 48, 24, 33, 11, 25, 54 and 20, respectively; one mouse was found dead and 10 mice were culled-sick: one due to malocclusion, one due to hydrocephalus, one

due to generally small size and missing eye, two due to fitting during intraperitoneal insulin sensitivity testing, and five due to non-healing injury/wounds).

Table 2.9. Total number of mice bred for TBX15-H156N-EM2-B6N-IC mouse line experimental cohorts. Abbreviations: RM3 (rat and mouse no. 3 diet), HFD (high-fat diet), LFD (low-fat diet).

Study (mouse line)	Diet	Sex	Genotype	Total number
Viability cohort (TBX15-H156N-EM2-B6N-IC)	RM3	Female	*Tbx15*$^{+/+}$	12
			Tbx15$^{+/H156N}$	11
			Tbx15$^{H156N/H156N}$	9
		Male	*Tbx15*$^{+/+}$	7
			Tbx15$^{+/H156N}$	13
			Tbx15$^{H156N/H156N}$	3
Tissue RNA-sequencing cohort (TBX15-H156N-EM2-B6N-IC)	RM3	Female	*Tbx15*$^{+/+}$	7
			Tbx15$^{H156N/H156N}$	5
		Male	*Tbx15*$^{+/+}$	7
			Tbx15$^{H156N/H156N}$	8
Primary cells RNA-sequencing (TBX15-H156N-EM2-B6N-IC)	RM3	Female	*Tbx15*$^{+/+}$	6
			Tbx15$^{H156N/H156N}$	6
Metabolic phenotyping cohort (TBX15-H156N-EM2-B6N-IC)	HFD	Female	*Tbx15*$^{+/+}$	24
			Tbx15$^{+/H156N}$	28
			Tbx15$^{H156N/H156N}$	17
		Male	*Tbx15*$^{+/+}$	22
			Tbx15$^{+/H156N}$	24
			Tbx15$^{H156N/H156N}$	21
	LFD	Female	*Tbx15*$^{+/+}$	24
			Tbx15$^{+/H156N}$	24
			Tbx15$^{H156N/H156N}$	16
		Male	*Tbx15*$^{+/+}$	21
			Tbx15$^{+/H156N}$	22
			Tbx15$^{H156N/H156N}$	22

2.2.3.3.3. TBX15-M566R-EM3-B6N

For initial viability and welfare assessments, a total of 22 mice were weaned onto RM3 diet in one cohort. For metabolic phenotyping, a total of 265 mice were weaned onto HFD or LFD across six cohorts (n=66, 54, 70, 35, 30 and 10, respectively; 15 mice were

culled sick: one due to hydrocephalus, one due acromegaly, one due to severe weight loss, and 12 due to non-healing injury/wounds).

Table 2.10. Total number of mice bred for TBX15-M566R-EM3-B6N-IC mouse line experimental cohorts. Abbreviations: RM3 (rat and mouse no. 3 diet), HFD (high-fat diet), LFD (low-fat diet).

Study	Diet	Sex	Genotype	Total number
Viability cohort (TBX15-M566R-EM3-B6N-IC)	RM3	Female	*Tbx15*$^{+/+}$	4
			Tbx15$^{+/M566R}$	9
			Tbx15$^{M566R/M566R}$	3
		Male	*Tbx15*$^{+/+}$	2
			Tbx15$^{+/M566R}$	4
			Tbx15$^{M566R/M566R}$	0
Metabolic phenotyping cohort (TBX15-M566R-EM3-B6N-IC)	HFD	Female	*Tbx15*$^{+/+}$	22
			Tbx15$^{+/M566R}$	22
			Tbx15$^{M566R/M566R}$	22
		Male	*Tbx15*$^{+/+}$	23
			Tbx15$^{+/M566R}$	25
			Tbx15$^{M566R/M566R}$	21
	LFD	Female	*Tbx15*$^{+/+}$	23
			Tbx15$^{+/M566R}$	22
			Tbx15$^{M566R/M566R}$	20
		Male	*Tbx15*$^{+/+}$	24
			Tbx15$^{+/M566R}$	23
			Tbx15$^{M566R/M566R}$	18

2.2.4. Metabolic phenotyping

2.2.4.1. Metabolic phenotyping pipeline

Metabolic phenotypes were assessed for mice weaned into metabolic phenotyping cohorts (Figure 2.2A). Mice were weaned onto HFD or LFD at 3 weeks of age and body composition was measured every 2 weeks by echo-MRI (described in 2.2.4.2). Intraperitoneal glucose and insulin challenge were performed at 13 and 17 weeks,

respectively (described in 2.2.4.3 and 2.2.4.4). Finally, mice underwent DEXA and dissection for tissue weights (described in 2.2.4.5 and 2.2.5.2) (Figure 2.2B).

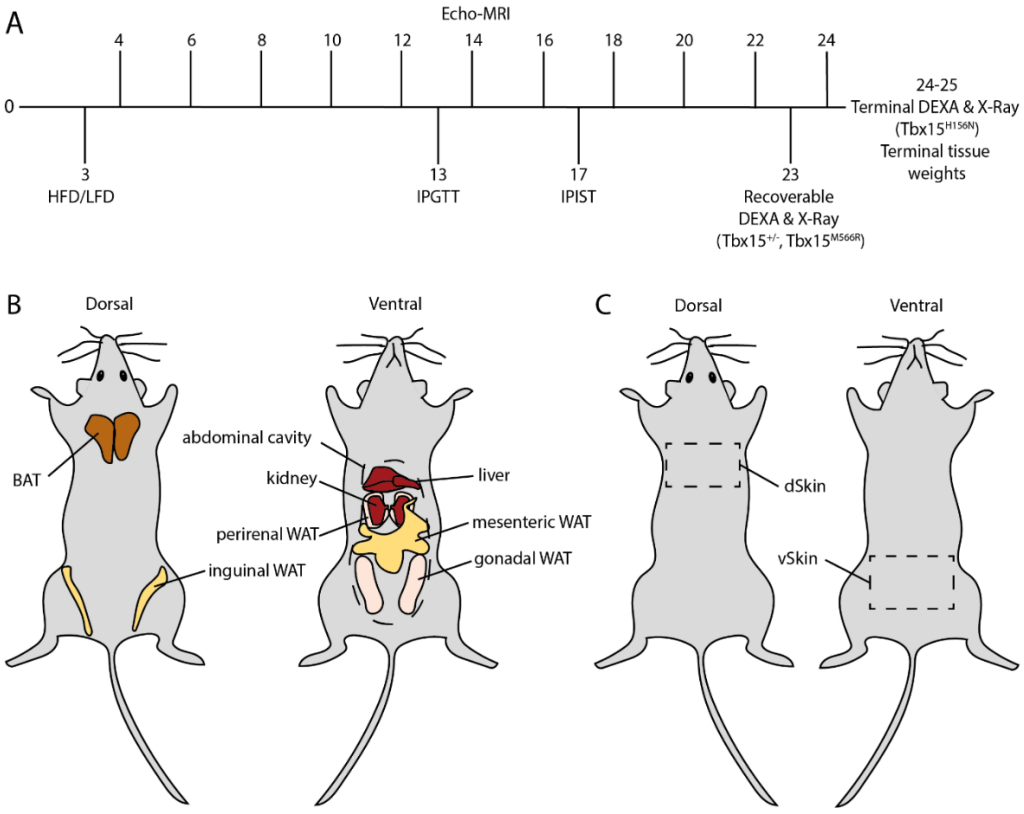

Figure 2.2. *Tbx15* metabolic phenotyping pipeline. A. Timeline of phenotyping tests from weaning onto high-fat diet (HFD) or low-fat diet (LFD) at 3 weeks of age, to early adulthood (24-25 weeks of age). B. Schematic of terminal white adipose tissues (WAT), brown adipose tissue (BAT) and liver dissections for weights and histological analysis. C. Schematic of terminal dorsal (dSkin) and ventral (vSkin) skin dissections for histological analysis.

2.2.4.2. Body composition analysis

Every two weeks, starting from 4-weeks-of-age, total body mass was measured on a scale calibrated to 0.01g. Total lean mass (g) and total fat mass (g) were measured to a 0.01g scale using an Echo-MRI body composition analysis EMR-136-M machine (Echo Medical Systems, Houston, TX, USA).

2.2.4.3. Intraperitoneal glucose tolerance test

A 20% (w/v) glucose solution was made by dissolving 20 g D-(+)-glucose (cat. G7528, Sigma-Aldrich) in 100 mL sodium chloride (NaCl) solution (cat. S8776, Sigma-Aldrich) and filtered through a 0.22 µM Millex-GP® filter.

At 12-13 weeks of age, mice were fasted for 16-18 hours. Subsequently, total body mass (g) was measured on a scale calibrated to 0.01g and EMLA™ cream (5% lidocaine/prilocaine, cat. PL39699/0088, Aspen Pharma Trading Ltd, Dublin, Ireland) was applied to tails 15 minutes prior to starting the test. A small incision was made in the tail vein and baseline blood glucose levels (0 minutes) were measured using an AlphaTrak2 with AlphaTrak2 blood glucose test strips (cat. ART2406-003 Zoetis, Parsippany-Troy Hills, NJ, USA). Following this, 20% (w/v) glucose was administered intraperitoneally (final dose 2 g/kg bodyweight). Blood glucose levels were further measured at 30, 60 and 120 minutes after glucose administration.

2.2.4.4. Intraperitoneal insulin tolerance test

At 17 weeks of age, mice were fasted for 4-5 hours. Subsequently, total body mass (g) was measured on a scale calibrated to 0.01g and EMLA™ cream was applied to tails 15 minutes prior to starting the test. A small incision was made in the tail vein and baseline blood glucose levels (0 minutes) were measured using an AlphaTrak2 with AlphaTrak2 glucose test strips. Then, 50 µL hypurin porcine insulin neutral solution (cat. FU40177, Wockhardt Ltd., Mumbai, India (100 IU/mL = 3.45 mg/mL)) was diluted in 4.95 mL NaCl solution to 1.0 IU/mL stock. The 1.0 IU/mL stock was further diluted as required (Table 2.11) and administered intraperitoneally. Blood glucose levels were further measured at 15, 30, 45, 60 and 90 minutes after insulin administration.

Table 2.11. Insulin working stock dilutions for intraperitoneal injections. Abbreviations: HFD (high-fat diet), LFD (low-fat diet), NaCl (sodium chloride solution), IU (international units).

Sex	Diet	Working stock concentration for injection	Dilution of 1.0 IU/mL stock	Dose (IU/kg)
Female	HFD	0.1 IU/mL	500 µL stock 4.5 mL NaCl	1.0 IU/kg
	LFD	0.075 IU/mL	375 µL stock 4.625 mL NaCl	0.75 IU/kg
		0.05 IU/mL	250 µL stock 4.75 mL NaCl	0.5 IU/kg
Male	HFD	0.125 IU/mL	625 µL stock 4.375 mL NaCl	1.25 IU/kg
	LFD	0.1 IU/mL	500 µL stock 4.5 mL NaCl	1.0 IU/kg

2.2.4.5. DEXA and X-Ray

Dr. Liz Bentley performed DEXAs and X-rays on terminal TBX15-H156N-EM2-B6N-IC mice at 24-25 weeks of age, using a LUNAR PIXImus™ 2 Densitometer with LUNAR PIXImus v2.10 software (GE Healthcare, Chicago, IL, USA) and Faxitron X-ray cabinet with SpecimenDR v3.0.0 software (Hologic Inc., Marlborough, MA, USA), respectively. DEXAs and X-rays were performed on 23-week-old TBX15-KO-B6N and TBX15-M566R-EM3-B6N-IC mice under recoverable inhalation isoflurane (Isofluran CP (1 mg/mL), cat. 400806.00.00, CP-Pharma Handelsgesellschaft mbH, Burgdorf, Germany) in a Faxitron Ultra Cabinet with BipoticsVisionDXA v2.2.4 software (Hologic Inc.).

2.2.5. Terminal procedures

2.2.5.1. Terminal retro-orbital bleeds

For terminal procedures, 24-25 week old mice were fasted for 4-5 hours. Mice were euthanised with either an intra-peritoneal injection of overdose anaesthetic (Euthatal (200 mg/mL pentobarbital sodium solution), Dopharma BV, Raamsdonksveer, Netherlands) (TBX15-H156N-EM2-B6N-IC bleeds performed by Dr. Liz Bentley), or inhalation overdose of isoflurane (TBX15-KO-B6N and TBX15-M566R-EM3-B6N-IC bleeds performed by MLC necropsy facility).

Once fully anaesthetised, confirmed by loss of pedal and orbital reflex, a glass capillary (cat. 1507550, Hirschmann, Belden, St. Louis, MO, USA) was used to perforate the venous retro-orbital sinus. Blood was collected into lithium-heparin microvette tubes (cat. 078028, KABE Labortechnik GmbH, Nümbrecht, Germany) and centrifuged at 2.4 *x g* for 10 minutes at 4^{o}C in a Sorvall Legend Micro 17R centrifuge (TFS). Plasma was transferred to a clean microcentrifuge tube and stored at -80^{o}C. Following exsanguination, cervical dislocation was performed to confirm euthanasia, and mice were dissected (described in 2.2.5.2).

2.2.5.2. Terminal dissections for tissue weights

Following exsanguination (described in 2.2.5.1), body length (cm) was measured from tip of the nose to the base of the tail, and cervical dislocation was performed to confirm death in line with UK Home Office regulations. A tail clip was taken to confirm genotyping (described in 2.2.3.2). Mice were dissected for multiple tissues including gonadal (gWAT), mesenteric (mWAT), perirenal (pWAT) and inguinal (iWAT) white

adipose, brown adipose tissue (BAT), liver, and abdominal (ventral) and scapular (dorsal) skin (Figure 2.2B&C). All tissues were weighed on a scale calibrated to 0.0001g, for adipose both left and right depots were weighed, and left depot (WAT) or both depots (BAT) were fixed in 10% formalin (cat. 38008010C, Leica, Wetzlar, Germany) at a minimum 20x volume to ensure complete fixation of tissues (Buesa and Peshkov, 2012). Whole livers were weighed, and the left lobe dissected for fixation in 10% formalin. For skin samples, a small cross-section was dissected and attached to a piece of filter paper and added to 10% formalin. All tissues were fixed for a minimum of 24 hours before processing.

2.2.5.3. Terminal dissections for RNA and protein isolation

For RNA isolation, 12-week-old mice were euthanised by cervical dislocation, and cessation of palpable heartbeat used as confirmation of death. Alternatively, for protein isolation tissues were dissected from pups that did not survive to weaning. A tail clip was taken post-mortem to confirm genotyping (described in 2.2.3.2). Mice were dissected for tibial muscle, gWAT, iWAT and BAT, all tissues were flash frozen in LN_2 and stored at -80°C.

2.2.6. Histology

2.2.6.1. Tissue processing and H&E staining

Fixed tissues were sent to Histologix Ltd. (Nottingham, UK) for processing and staining. Tissues were embedded in paraffin wax, sectioned (WAT = 8 µM; BAT, liver, and skin = 5 µM), and stained with haematoxylin and eosin (H&E) following standard protocols.

2.2.6.2. Adipocyte size analysis

Per mouse, 1x section per gWAT, mWAT, pWAT, iWAT, BAT, liver, dorsal skin, and ventral skin samples were scanned at 20X magnification on a NanoZoomer RS with NDP Scan v3.2 software (Hamamatsu, Hamamatsu, Japan). Up to 10 regions of interest were exported at 10x magnification for WAT and skin samples, and up to 10 regions of interest at 20x magnification were exported for BAT and liver samples using the NDP.view2 v2.9.29 Software (Hamamatsu). Cell area for WAT samples was analysed using the Adiposoft plugin in ImageJ, with the following calibration settings following initial optimisation: microns per pixel 0.920, minimum diameter 15, and maximum diameter 150 (Galarraga *et al.*, 2012; Schneider, Rasband and Eliceiri, 2012). Adiposoft analysis was run in automated batch mode and data was exported to Microsoft Excel for average cell area and cell size distribution analysis.

2.2.7. Pathology

2.2.7.1. Clinical chemistry analysis

Terminal blood plasma samples collected from metabolic phenotyping cohorts (described in 2.2.5.1) were measured by the MLC clinical pathology laboratory on a DXC 700 AU clinical chemistry analyser (Beckman Coulter, High Wycombe, UK). Samples were run in batches grouped by sex and diet (described in Appendix 9.1.1.3).

2.3. Molecular Biology

2.3.1. DNA applications

2.3.1.1. Deoxynucleoside triphosphate stocks

A 10 mM deoxynucleoside triphosphate (dNTP) stock was prepared in nuclease-free H_2O (NF-H_2O; cat. 129117, Qiagen, Hilden, Germany; Table 2.12).

Table 2.12. Preparation of 10 mM dNTP stock. Abbreviations: dATP (deoxyadenosine triphosphate), dCTP (deoxycytidine triphosphate), dGTP (deoxyguanosine triphosphate), dTTP (deoxythymidine triphosphate), NF-H_2O (nuclease-free water).

dNTP	Catalogue	Stock concentration	Volume to 1 mL	Final concentration
dATP	56172 (Invitrogen)	100 mM	100 µL	10 mM
dTTP	55085 (Invitrogen)	100 mM	100 µL	10 mM
dGTP	56174 (Invitrogen)	100 mM	100 µL	10 mM
dCTP	55083 (Invitrogen)	100 mM	100 µL	10 mM
NF-H_2O	129117 (Qiagen)		600 µL	

2.3.1.2. Oligonucleotide sequences and primers

Sub-cloning polymerase chain reaction (PCR) primers (to introduce restriction enzyme digest sites) and cDNA amplification primers (for genotyping analysis) were designed using SnapGene® v6.0.2 software (GSL Biotech LLC, San Diego, CA, USA). Sub-cloning primers were designed upstream of the endogenous Kozak sequence ((GCC)[A/G]CCATG) in the pCMV-Myc-DDK vector as this sequence was important for initiation of protein translation. Site-directed mutagenesis primers were designed using NEBaseChanger to generate single base pair substitutions. Upon receipt, oligonucleotides were resuspended in NF-H_2O to 100 µM stock concentration.

Table 2.13. PCR amplification primers for sub-cloning, site-directed mutagenesis, and template amplification. Underlined sequences refer to restriction enzyme recognition sites, lower case letters indicate desired base change edit in site-directed mutagenesis primers. Abbreviations: SDM (site-directed mutagenesis), Fw (forward primer), Rv (reverse primer), Mm (mus musculus), ex (exon). All primers were synthesised by Sigma-Aldrich (PAGE purified, scale 0.05 µmole).

Primer	Sequence	Annealing temp (°C)
H50N_SDM_Fw	CCTAGATCCAaATCAGCAGTAC	57
H50N_SDM _Rv	CCAGTGATTTTCACTCTC	57
M460R_SDM _Fw	GAGCACAGCAgGCACATGATTAG	66
M460R_SDM _Rv	CATCCCTGACGGCAGGTA	66
TBX15-1_SalI_Fw	AATGTCGACGCCGCCGCGATCGCCATGA	65
TBX15-1_KpnI_Rv	AATGGTACCAACCATGTGCACGGACATCT	65
TBX15-2_SalI_Fw	AATGTCGACGCCGCCGCGATCGCCATGT	72
TBX15-2_KpnI_Rv	AATGGTACCAACCATGTGCACGGACATCT	72
TBX18_SalI_Fw	AATGTCGACGCCGCCGCGATCGCCATGG	70
TBX18_KpnI_Rv	ATTGGTACCGACCATATGTGCAGATACTT	70
Mm_Tbx15_ex1_Fw	GGGCTGCCAGCTCAGTAG	70
Mm_Tbx15_ex1_Rv	GGGTCGTCTGTGTCTCCGA	70
Mm_Tbx15_ex8_Rv	GGTGTTGGTAGCCTGCTGAT	69

2.3.1.3. Polymerase chain reaction amplification

PCR amplification reactions using Q5 polymerase (New England Biolabs; NEB) were assembled with 10ng DNA isolated from *E. Coli* (described in 2.4.2.1), or 20ng cDNA (described in 2.3.2.4) used as template material (Table 2.14) in a T1000™ thermocycler (Bio-Rad, Hercules, CA, USA; Table 2.15).

Table 2.14. Polymerase chain reaction amplification reactions. * See Table 2.12 for dNTP stocks, $ see Table 2.13 for primers. All Q5 reagents purchased from NEB.

Reaction component	Catalogue	Volume to 50 µL	Final concentration
5x Q5® PCR buffer	B9027S	10 µL	1X
10 mM dNTPs *		1 µL	200 µM
10 µM forward primer $		2.5 µL	0.5 µM
10 µM reverse primer $		2.5 µL	0.5 µM
Template DNA		Variable	10-20ng
high fidelity Q5® polymerase	M0491	0.5 µL	
Q5® GC enhancer (optional for GC-rich templates)	B9028A	10 µL	1X
NF-H_2O		To 50 µL	

Table 2.15. Thermocycler parameters for PCR amplification. * See Table 2.13 for annealing temperatures for primer pairs

Step	Temperature	Time
Initial denaturation	98°C	30 seconds
Denaturation, annealing and elongation (25x cycles)	98°C	10 seconds
	68–72°C*	30 seconds
	72°C	20-30 seconds/kb
Final extension	72°C	2 minutes

2.3.1.4. Site-directed mutagenesis

pCMV6-TBX15-2-Myc-DDK template DNA was mutagenised using the Q5® site-directed mutagenesis kit (cat. E0552S, NEB) following manufacturer's instructions (Table 2.16,

Table ***2.17***). The PCR product was kinase, ligase & DpnI (KLD)-treated for 5 minutes at room temperature (Table 2.18). Subsequently, 5 µL reactions were transformed into DH5α chemically competent *E. Coli* cells (described in 2.4.1.4).

Table 2.16. Site-directed mutagenesis amplification reactions. $ see Table 2.13 for primers. All Q5 reagents purchased from NEB.

Reaction component	Catalogue	Volume to 25 µL	Final concentration
Q5 High-Fidelity 2X Master Mix	M0494A	12.5 µL	1X
10 µM forward primer $		1.25 µL	0.5 µM
10 µM reverse primer $		1.25 µL	0.5 µM
Plasmid DNA		Variable	10 ng
NF-H_2O	129117 (Qiagen)	To 25 µL	

Table 2.17. Thermocycler parameters for site-directed mutagenesis *see Table 2.13 for annealing temperatures for site-directed mutagenesis primer pairs

Step	Temperature	Time
Initial Denaturation	98°C	30 seconds
Denaturation, annealing and elongation (25x Cycles)	98°C	10 seconds
	50–72°C*	10–30 seconds
	72°C	3 min 30 seconds (30 seconds/kb)
Final Extension	72°C	2 minutes

Table 2.18. Kinase, Ligase & DpnI (KLD) treatment reactions. Reactions were performed following site-directed mutagenesis to remove template plasmid DNA. All KLD reagents were purchased from NEB.

Reaction component	Catalogue	Volume to 10 µL
2X KLD reaction buffer	B0554A	5 µL
KLD Enzyme Mix	M0554A	1 µL
Plasmid DNA		1 µL
NF-H_2O	129117 (Qiagen)	3 µL

2.3.1.5. Agarose gels

The MRCH laboratory services facility made a 1x TAE (tris-acetate-EDTA) solution by diluting 10x TAE buffer (cat. 20-6002-50, Severn Biotech Ltd., Kidderminster, UK) in diH_2O. For visualisation of PCR products, plasmids and restriction enzyme digest samples were separated on 0.5-2.0% agarose gels, and 0.5-2.0% ultrapure agarose gels

were used to separate samples required for downstream applications. Agarose (cat. A9539, Sigma-Aldrich) or ultrapure agarose (cat. 16500-100, Invitrogen) was dissolved in 1x TAE buffer by boiling in a microwave. Solutions were cooled to ~50°C before addition of GelRed® (cat. 41003, Biotium, Fremont, CA, USA) stain at 1:20,000 dilution. DNA samples were mixed with 6x DNA loading dye (cat. B7024S, NEB), loaded onto the gel alongside 100 bp+ DNA ladder (cat. N3231, NEB) or TrackIt™ 1kb+ DNA ladder (cat. 10488085, Invitrogen) and run at 120V for 30-60 minutes in an electrophoresis tank containing 1x TAE buffer. Gels were viewed on a GelDoc XR+ transilluminator system using the ImageLab v6.0.0 software (Bio-Rad). Alternatively, gels were visualised on a blue light block for band excision (described in 2.3.1.6).

2.3.1.6. DNA extraction from agarose gels

Ultrapure agarose gels were visualised on a blue light block and bands were excised using a clean scalpel. Excised bands were weighed, and DNA was extracted using the Monarch® DNA gel extraction kit (cat. T1020S, NEB) following manufacturer's protocol. Briefly, 4 volumes of gel dissolving buffer (cat. T1021-2, NEB) per 100 mg gel were added to gel slices and incubated at 50°C for 10 minutes, with occasional vortexing, to dissolve agarose. Samples were loaded onto a clean-up column (cat. T1034-2, NEB) and centrifuged at 16,000 *x g* for 60 seconds. Columns were washed with 200 µL DNA wash buffer (cat. T1032-2, NEB) and centrifuged at 16,000 *x g* for 60 seconds; the wash step was repeated once. DNA was eluted in 20 µL NF-H_2O into a clean microcentrifuge tube and concentration was measured (described in 2.3.1.9).

2.3.1.7. Restriction enzyme digestion

For sub-cloning, 1 µg PCR-amplified product or empty vector were digested with restriction enzymes (Table 2.19) and cutsmart buffer (cat. B7204, NEB) at 37°C for 60 minutes to ensure complete digestion, followed by heat-inactivation, if applicable. Digested samples were mixed with 6x DNA loading dye to dissociate enzymes and separated on agarose gels for DNA extraction (described in 2.3.1.6).

Table 2.19. Restriction enzymes for digestion of DNA inserts and vectors for sub-cloning applications. All restriction enzymes were purchased from NEB.

Enzyme	Catalogue	Incubation temperature (°C)	Heat inactivation
SalI_HF	R3138	37	65°C for 20 minutes
KpnI_HF	R3142	37	No

2.3.1.8. DNA ligation

For ligation of DNA insert and vectors, the NEBioCalculator was used to calculate the mass of DNA (ng) required for 1:3 molar ratio (vector:insert). Vector and insert DNA were mixed with 2 µL T4 DNA ligase buffer (cat. B0202S, NEB), 1 µL T4 DNA ligase (cat. M0292S, NEB) and NF-H_2O to 20 µL on ice. Reactions were incubated at 16°C overnight and heat inactivated at 65°C for 10 minutes in a T1000™ thermocycler. Subsequently, 5 µL reaction was transformed into *E. Coli* (described in 2.4.1.4).

2.3.1.9. DNA quantification

DNA concentration and quality were measured using a Take3 micro-volume plate on an Epoch spectrophotometer with Gen5 v2.0.0 software. The 260/280nm absorbance

ratio was used to determine sample purity; values >1.8 were deemed to be free of contamination from proteins or organic compounds and used for downstream applications including transient transfections. Duplicate values were averaged to calculate sample concentration.

2.3.1.10. Sanger Sequencing

PCR products (10 ng/µL) and plasmid DNA (100 ng/µL) were sent to Source BioScience Ltd. (Nottingham, UK) for Sanger sequencing. Custom sequencing primers were designed using SnapGene® v6.0.2 software, and synthesised by Sigma-Aldrich (desalt purified, scale 0.05 µmole). Alternatively, sequencing primers were selected from the stock primers provided by Source BioScience Ltd (Table 2.20). SnapGene® v6.0.2 was used to align sequencing results.

Table 2.20. Custom and stock sequencing primers used for Sanger Sequencing at Source Bioscience. Abbreviations: SBS (Source Bioscience). Custom sequencing primers were diluted to 3.2 pmol/µL prior to shipping with samples.

Primer name	Sequence 5'-3'
Origene Fw (VP1.5)	GGACTTTCCAAAATGTCG
Origene Rv (XL39)	ATTAGGACAAGGCTGGTGGG
SBS M13F	TGTAAAACGACGGCCAGT
SBS M13R	CAGGAAACAGCTATGACC
SBS pCMV forward	GAGCTCGTTTAGTGAACCGTC

2.3.2. RNA applications

2.3.2.1. RNA extraction

2.3.2.1.1. Primary murine cells

For RNA-sequencing analysis, primary murine SVF cells were washed twice in 1x DPBS, lysed in 500 µL 1x DPBS, pelleted at 13,000 *x g* for 3 minutes and stored at -80°C. RNA was extracted from cell pellets with the MAXwell® RSC simply RNA cells kit (cat. AS1390, Promega, Madison, WI, USA) and automated Maxwell® RSC system (Promega). Homogenisation buffer was prepared by adding 20 µL of 1-thioglycerol (cat. A208B, Promega) to 1 mL homogenisation solution (cat. Z305H, Promega) and chilled on ice prior to use. DNAseI (cat. Z358A, Promega) was reconstituted in 275 µL NF-H_2O (cat. P119C, Promega) and 5 µL blue dye (cat. C888A, Promega). To homogenise cell pellets, 200 µL 1-thioglycerol/homogenisation solution was added to cell pellets and vortexed for 30 seconds. Then, 200 µL of lysis buffer (cat. MC501C, Promega) was added to samples and mixed by vortexing for 15 seconds, and the total 400 µL sample was transferred to well 1 of the Maxwell® RSC Cartridge (cat. AS134A, Promega). Finally, 5 µL of reconstituted DNAseI was added to well 4 of the cartridges and 40 µL NF-H_2O added to elution tubes.

2.3.2.1.2. Adipose tissues

For gene expression and RNA-sequencing analysis TBX15-KO-B6N-IC (collected by Dr. Rebecca Dumbell), TBX15-H156N-EM2-B6N-IC (collected by MLC necropsy facility) and C57BL/6NTac mice were culled by cervical dislocation and tissues dissected (described in 2.2.5.3). RNA was isolated using the RNeasy lipid tissue mini kit (cat. 74804, Qiagen) following manufacturer's protocol; all centrifugation steps

were performed at 13,000 *x g*. Briefly, tissues were lysed in 1 mL QIAzol® reagent (cat. 79306) per 50 mg BAT or 100 mg WAT, with CK14 soft tissue ceramic beads (cat. P000912-LYSKO, Bertin Corp., Montigny-le-Bretonneux, France) at 5500 rpm for 60 seconds in a Precellys 24 tissue homogeniser (Bertin Corp.). Avoiding the fatty layer at the top of the sample, supernatant was transferred to a clean micro-centrifuge tube and incubated at room temperature for 5 minutes. Then, 200 µL chloroform (cat. 25668, Fluka Analytics, Buchs, Switzerland) was added to samples, mixed by vigorous shaking and incubated at room temperature for 3 minutes. Samples were centrifuged for 15 minutes at 4°C.

Avoiding the phenol layer, 600 µL of the upper aqueous phase (containing RNA) was added to a clean microcentrifuge tube and an equal volume of 70% (v/v) ethanol was added to samples and transferred to an RNEasy column. Samples were centrifuged and this step repeated until all the sample had passed through the column. Columns were then washed with 350 µL RW1 buffer (cat. 1014567, Qiagen) and centrifuged. To perform the on-column DNAseI digest (cat. 79254, Qiagen), DNAseI (cat. 1010395, Qiagen) was reconstituted in 550 µL RNAse-free H_2O and kept on ice. Just prior to use 10 µL DNAseI was diluted in 70 µL RDD buffer (cat. 1010397, Qiagen) per sample, and 80 µL was added to each column and incubated at room temperature for 15 minutes. Columns were washed with 350 µL RW1 buffer and centrifuged for 15 seconds. Columns were washed with 500 µL RPE buffer (cat. 1017974, Qiagen) and centrifuged. This wash step was repeated once, and centrifugation was performed for 2 minutes to remove all ethanol. RNA was eluted in 100 µL RNAse-free H_2O.

2.3.2.2. RNA concentration and purity analysis

RNA concentrations were measured using a NanoDrop™ 8000 spectrophotometer with ND-8000 v2.2.0 software (TFS). Purity of samples was determined using 260/280 and 260/230 ratios, where samples with a 260/280 >1.8 were considered free from DNA and protein contamination, and samples with a 260/230 ratio >1.8 were considered free from phenol/chloroform contamination. Any samples with low 260/230 ratios were ethanol precipitated (Green and Sambrook, 2020). Briefly, 10 µL (0.1x volume of sample) 3 M sodium acetate (final concentration 0.3 M; cat. 46-033-CL, Corning Inc.) was added to samples to increase salt concentrations. Then, 300 µL ice-cold 100% ethanol was added to samples, mixed well and incubated at -80°C overnight to precipitate RNA. Samples were centrifuged at 13,000 *x g* for 10 minutes at 4°C to pellet RNA and supernatant was carefully discarded. RNA pellets were washed with 500 µL ice-cold 70% (v/v) ethanol and centrifuged at 13,000 *x g* for 10 minutes at 4°C to pellet RNA and supernatant was carefully discarded. The wash step was repeated, and samples were left to air dry at room temperature until all ethanol had evaporated. The RNA pellet was then reconstituted in 100 µL RNAse-free H_2O and measured using the Nanodrop™ 8000 spectrophotometer.

2.3.2.3. RNA quality analysis

RNA quality was determined using the RNA 6000 nano kit (cat. 5067-1511, Agilent Technologies) following manufacturer's instructions. Briefly, 550 µL RNA gel matrix was centrifuged at 1,500 *x g* for 10 minutes at room temperature in a spin filter. Prior to use 65 µL of the gel matrix was aliquoted into a clean micro-centrifuge tube and 1 µL RNA dye concentrate was added, vortexed and the solution centrifuged at 13,000 *x g*

for 10 minutes at room temperature. Then, 9 µL of the filtered gel-dye mix was loaded onto an RNA nano chip. Using the chip priming station, air was gently forced through the chip for 30 seconds and an additional 9 µL gel-dye mix was added into the spare wells. The RNA ladder and all RNA samples were heat inactivated at 70°C for 2 minutes and chilled on ice. Subsequently, 5 µL RNA marker was added to each well, 1 µL RNA ladder was added to the ladder well, and 1 µL sample was added to each sample well. Chips were vortexed for 60 seconds at 2400 rpm in an IKA® MS 3 vortexer and immediately run on a Bioanalyzer 2100 with 2100 expert software (Agilent Technologies). Cell samples with RNA integrity number (RIN)≥8.5, and adipose tissues with RIN≥7.0 were considered good quality and were used for downstream analysis.

2.3.2.4. cDNA synthesis

cDNA synthesis was performed using SuperScript™ III reverse transcriptase following manufacturer's instructions, in a T1000 thermocycler (Table 2.21). Reverse transcriptase-free and RNA-free reactions were generated for use as controls in downstream gene-expression analysis procedures.

Table 2.21. cDNA synthesis reactions and thermocycler conditions. * See Table 2.12 for dNTP stocks

Step	Reaction component	Catalogue	Volume	Thermocycler conditions
1	RNA		1200 ng	65°C for 5 minutes
	random primer (200 ng/µL)	58875 (Invitrogen)	1 µL	
	10 mM dNTP *		1 µL	
	NF-H_2O	129117 (Qiagen)	Up to 14 µL	
Cool on ice 5 minutes				
2	Step 1 reaction		14 µL	25°C for 5 minutes
	5x first strand buffer	Y02321 (Invitrogen)	4 µL	50°C for 60 minutes
	0.1 M DTT	Y00147 (Invitrogen)	1 µL	70°C for 15 minutes
	Superscript™ III reverse transcriptase	18080-044 (Invitrogen)	1 µL	

2.3.2.5. Real-time quantitative PCR

2.3.2.5.1. House-keeping genes assays

Mouse GeNorm (cat. ge-DD-12-mo, Primerdesign, Novacyt, Vélizy-Villacoublay, France) analysis was performed on cDNA samples to identify housekeeping genes for real-time quantitative PCR (qPCR) experiments. Data was analysed using Qbase+ Software V3.3 (Biogazelle, Ghent, Belgium) to determine the most appropriate number and combination of house-keeping genes.

2.3.2.5.2. TaqMan® gene assays

For real-time qPCR, TaqMan® assay probes were ordered as single tube assays (cat. 4331182, TFS; Table 2.22). The delta CT ($\Delta\Delta C_T$) method was used to calculate relative gene expression, normalised to the geometric mean (n^{th} root of the product of n numbers) of a minimum of two housekeeping genes.

Table 2.22. TaqMAN® assay qPCR primers for mouse genes. Abbreviations: *Fbxo38* (F-Box Protein 38), *Csnk2a2* (Casein kinase 2 alpha 2), *Tbx15* (T-box 15), *Wars2* (Tryptophanyl tRNA synthetase 2).

Target gene	Assay number	Exon boundary (RefSeq gene)
Fbxo38	Mm00661841_m1	17-18 (NM_124136.3)
Csnk2a2	Mm01243458_m1	9-10 (NM_009974.3)
Tbx15	Mm00447443_m1	5-6 (NM_009323.2)

2.3.2.5.3. Real-time quantitative PCR reactions

For gene expression analysis, 1 µL probe was mixed with 10 µL TaqMan fast universal master mix (cat. 4352042, Applied Biosystems, TFS), 4 µL NF-H_2O and 5 µL (20 ng total) cDNA per well. For housekeeping gene assays, samples were plated in duplicate (according to manufacturer's protocol) and for experimental assays samples were plated in triplicate. Reactions were amplified using a 7500 Fast machine and accompanying 7500 v2.3 software (Applied Biosystems). The PCR reactions were performed as quantitative comparative C_T, using TaqMan® reagents and fast ramp speed, with cDNA as template material and default amplification parameters:

Table 2.23. Default thermocycler parameters for qPCR reactions using 7500 v2.3 software.

Step	Temperature	Time
1	95°C	20 seconds
2 (40x cycles)	95°C	3 seconds
	60°C	30 seconds

2.3.2.6. RNA-Sequencing

2.3.2.6.1. Sample preparation and RNA-sequencing

For RNA-sequencing, 1000 ng RNA was plated per well in a 96-well plate (cat. AB-0800, TFS), and sealed with an adhesive seal (cat. AB-0558, TFS). Samples were transported on dry ice to the Oxford Genomics Centre for pooling, library preparation and

RNA-sequencing (described in Appendix 9.1.2.1.1). Differential gene expression analysis was performed by Dr. Michelle Simon in the MRCH bioinformatics group (described in Appendix 9.1.2.1.2).

2.3.2.6.2. Functional analysis

Functional profiling of differentially expressed genes (DEGs) from RNA-sequencing experiments was performed using the g:GOST function on the g:Profiler webpage (Reimand *et al.*, 2007; Raudvere *et al.*, 2019). Queries were performed as "ordered" queries where input was ordered by importance (i.e., the most significant DEGs at the top of the list), with *mus musculus* as the organism. Default parameters were as follows: statistical domain scope (only annotated genes), significance threshold (g:SCS threshold 0.05), data sources selected (GO molecular function, GO cellular component, GO biological process, KEGG, Reactome, WikiPathways, TRANSFAC, miRTarBase, CORUM and human phenotype ontology).

2.3.3. Protein applications

2.3.3.1. Protein extraction

2.3.3.1.1. Immortalised cell lines

Cells cultured in 6-well plates were washed twice with 1x DPBS and lysed in 50 µL lysis buffer (Table 2.24). Cells were scraped from the vessel surface, transferred to a clean microcentrifuge tube and incubated on ice for 30 minutes with shaking. Samples were centrifuged at 13,000 *x g* for 30 minutes at 4°C and supernatant was transferred to a clean microcentrifuge tube. For differentiated cells containing lipids, centrifugation was repeated twice, avoiding the lipid layer during supernatant transfer.

For magnetic co-immunoprecipitation (co-IP) kits (described in 2.3.3.3.2), cells were lysed in 100 µL IP lysis buffer (Table 2.24). Cells were scraped from the vessel surface, transferred to a clean microcentrifuge tube and incubated on ice for 10 minutes with shaking. Samples were centrifuged at 13,000 *x g* for 15 minutes at 4°C and supernatant was transferred to a clean microcentrifuge tube.

Table 2.24. Protein lysis buffers. Abbreviations: EDTA (Ethylenediaminetetraacetic acid).

Buffer	Buffer components	Catalogue	To 10 mL buffer
m-PER lysis buffer	m-PER mammalian protein extraction reagent	78501 (TFS)	10 mL
	PhosSTOP tablet	04906837001 (Roche, Basel, Switzerland)	1 tablet
	cOmplete protease inhibitor	04693124001 (Roche)	1 tablet
Co-IP lysis buffer	IP lysis/wash buffer	1861603 (TFS)	10 mL
	PhosSTOP tablet	04906837001 (Roche)	1 tablet
	EDTA-free cOmplete protease inhibitor	11836170001 (Roche)	1 tablet
t-PER lysis buffer	t-PER mammalian protein extraction reagent	78510 (TFS)	10 mL
	PhosSTOP tablet	04906837001 (Roche)	1 tablet
	cOmplete protease inhibitor	04693124001 (Roche)	1 tablet

2.3.3.1.2. Mouse tissues

Approximately 100 mg of tissue (dissections described in 2.2.5.3) was lysed in 500 µL t-PER lysis buffer (Table 2.24), and homogenised with CK14 soft tissue ceramic beads at 5000 rpm for 30 seconds in a Precellys 24 tissue homogeniser. Samples were incubated on ice for 30 minutes with shaking to complete lysis. Supernatant was transferred to a clean microcentrifuge tube, centrifuged at 13,000 *x g* for 30 minutes at 4°C and transferred into a clean microcentrifuge tube. For lipid-containing tissues,

this centrifugation step was repeated twice, avoiding the lipid layer during supernatant transfer.

2.3.3.2. Protein quantification

Protein concentrations were measured by DC™ protein assay (Bio-Rad). BSA proteins (cat. P0914, Sigma-Aldrich) were diluted 1:1 in ddH_2O to generate a standard curve from 1.0 mg/mL to 0.015625 mg/mL. Cell samples were diluted 1:10 in ddH_2O, and tissues were diluted between 1:20-1:80 in ddH_2O. Lysis buffer was diluted at corresponding ratios in ddH_2O to generate blank samples. To measure samples, 5 µL of standards, blank and samples were pipetted per well, in triplicate, into a flat-bottom 96-well plate. Reagent A' was freshly prepared by adding 20 µL reagent S (cat. 500-0115, Bio-Rad) to 1 mL reagent A (cat. 500-0113, Bio-Rad), and 25 µL was added to all standard and sample wells. Finally, 200 µL reagent B (cat. 500-0114, Bio-Rad) was added to each well and the plate was gently agitated for 15 minutes to allow homogenous colour development. The plate was read at 750nm using an Epoch spectrophotometer with Gen5 v2.00 software. Total protein then was denatured in lysis buffer containing 1x NuPAGE LDS sample buffer (cat. NP0007, Invitrogen) and 1x NuPAGE sample reducing agent (cat. NP0004, Invitrogen) at 95°C for 10 minutes.

2.3.3.3. Immunoprecipitation

Figure 2.3 shows a schematic representation of co-IPs of tagged protein constructs using either sepharose G beads (Figure 2.3A, section 2.3.3.3.1) or magnetic beads (Figure 2.3B, section 2.3.3.3.2).

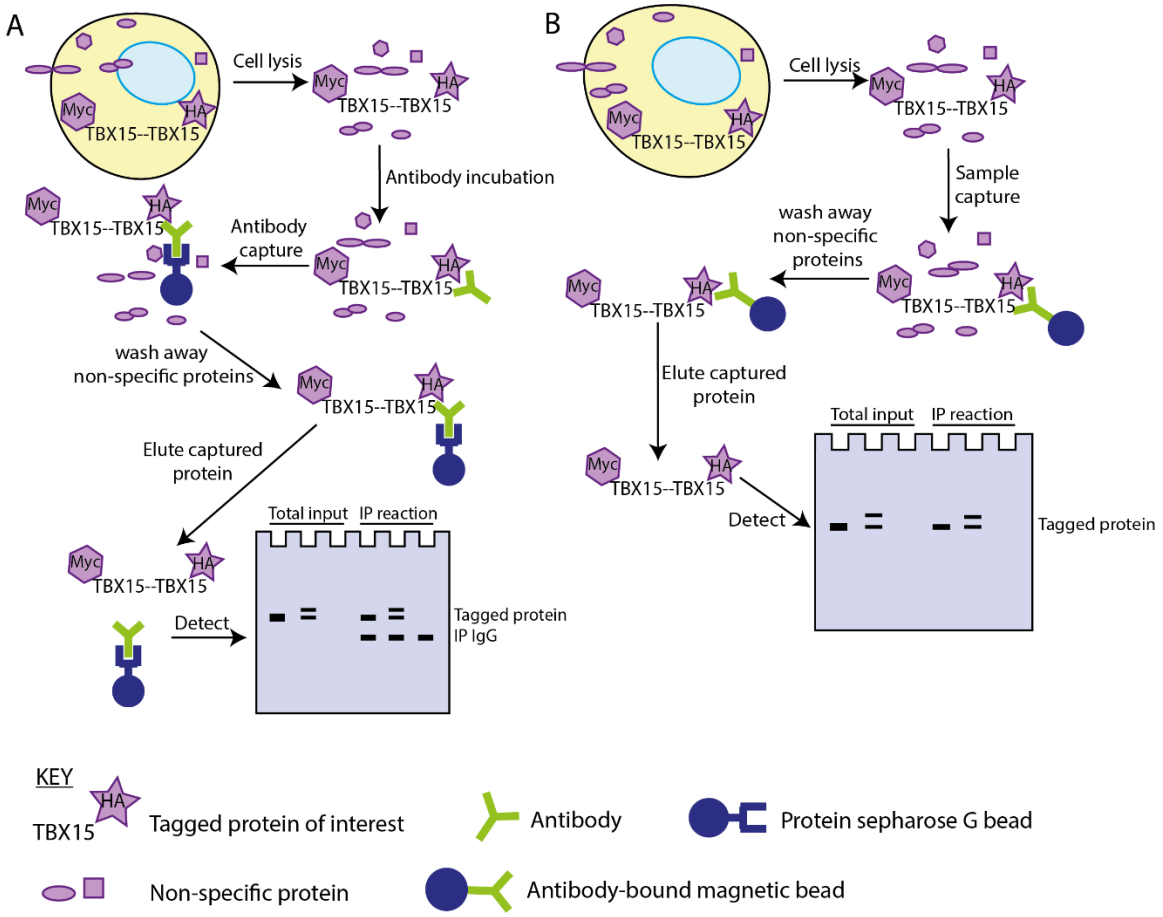

Figure 2.3. Schematic representation of protein sepharose G and magnetic bead co-IP systems. A. Protein sepharose G approach: total cell lysate was incubated with a primary antibody specific to the protein of interest (HA or Myc). Antibody-protein complexes were captured by protein sepharose G beads, washed to remove unbound protein, and eluted for SDS-PAGE and immunoblot analysis. B. Magnetic co-IP approach: total cell lysate was incubated with magnetic beads coupled to antibody of interest (HA or Myc). Beads were washed to remove non-bound protein and samples were eluted for SDS-PAGE and immunoblot analysis.

2.3.3.3.1. Sepharose G bead immunoprecipitations

To immunoprecipitate tagged TBX15 constructs using sepharose G beads, an initial 50 µL aliquot of cell protein lysate was taken for total cell input and denatured (described in section 2.3.3.2). All centrifugation steps were performed at 1,000 *x g* for 60 seconds at 4°C to pellet beads. To wash protein sepharose G beads (cat. 17-0618-01, GE Healthcare), 500 µL m-PER protein lysis buffer was added to 40 µL bead slurry, centrifuged and buffer discarded. To pre-clear the samples cell lysates were equalised

to 500 µL, incubated with beads for 1 hour at 4°C with rotation and centrifuged. Pre-cleared supernatant was transferred to a new microcentrifuge tube and incubated with 2 µg HA antibody (cat. ab9110, Abcam, Cambridge, UK), or 2 µg normal rabbit immunoglobulin G (IgG) (cat. 12-370, Merck Millipore) as a negative control, at 4°C with rotation overnight. The supernatant was then incubated with freshly washed protein sepharose G beads at 4°C with rotation for one hour to capture antibody-protein complexes.

Following antibody incubations, bead-IP complexes were centrifuged and supernatant discarded. Beads were washed with 500 µL m-PER buffer and centrifuged; this wash step was repeated twice. Antibody-protein complexes were dissociated from sepharose G beads by incubation in 20 µL 1x NuPAGE LDS sample buffer (containing 1x NuPAGE sample reducing agent) at 95°C for 10 minutes. Samples were centrifuged and supernatant was transferred to a clean microcentrifuge tube.

2.3.3.3.2. Magnetic bead immunoprecipitations

To prepare buffers for magnetic co-IP kits, 4 µL of 37% (v/v) hydrochloric acid (HCl; cat. H1758, Sigma-Aldrich) was diluted in 50 mL diH_2O (final concentration 1 mM) and stored at 4°C. Borate buffer was prepared by dissolving an entire sachet of BupH borate buffer (cat. 28384, TFS) in 500 mL diH_2O (final concentration 0.05 M sodium borate, pH 8.5) and stored at room temperature. All magnetic bead collection steps were performed using a DynaMag™-2 magnet (cat. 12321D, Invitrogen) for 60 seconds.

The Pierce™ direct magnetic co-IP kit (cat. 88828, TFS) was used to bind IgG to magnetic beads for IgG controls, following manufacturer's protocols. Briefly, 25 µL

NHS-activated magnetic beads (cat. 88826) were collected and supernatant removed. Then, 400 µL ice-cold 1 mM HCl was added to beads and vortexed; beads were collected and supernatant removed. Then, 5 µg mouse IgG control antibody (cat. 10400C, Invitrogen), 5% (w/v) BSA or no antibody was mixed with 10 µL borate buffer (final concentration 67 mM; cat. 1859833, TFS) and 90 µL diH_2O to 100 µL and incubated with beads for 60 minutes with rotation at room temperature; samples were vortexed every 15 minutes. Beads were collected and 100 µL elution buffer (cat. 1862619, TFS) was added to beads to remove non-covalently bound antibody. Beads were collected, and supernatant removed; this elution step was repeated once. Then, 500 µL quenching buffer (cat. 1856079, TFS) was added to quench free NHS-activation sites and incubated for 60 minutes with rotation; beads were collected, and supernatant removed. Subsequently, 500 µL modified borate buffer (25 µL IP lysis/wash buffer diluted in 475 µL BupH borate buffer) was added to beads and vortexed; beads were collected, and supernatant removed. The modified borate buffer was washed from the beads by addition of 500 µL IP lysis/wash buffer; beads were vortexed, collected and supernatant removed.

The anti-HA magnetic co-IP kit (cat. 88838, TFS) was used to immunoprecipitate HA-tagged proteins, following manufacturer's protocols. Briefly, 25 µL anti-HA magnetic beads (cat. 88836, TFS) were washed with 175 µL IP lysis/wash buffer, vortexed gently, collected and supernatant removed. Beads were washed with 1 mL IP lysis/wash buffer, inverted several times, collected and supernatant removed.

The anti-Myc magnetic co-IP kit (cat. 88844, TFS) was used to immunoprecipitate Myc-tagged proteins, following manufacturer's protocols. Briefly, 25 µL anti-Myc magnetic beads (cat. 88842, TFS) were washed with 175 µL c-Myc IP buffer 1

(cat. 1862827, TFS), vortexed gently, collected and supernatant removed. Beads were washed with 1 mL IP lysis/wash buffer, inverted several times, collected and supernatant removed.

To capture protein complexes in all magnetic co-IP kits, 100-500 µg protein lysate in 500 µL IP lysis buffer was added to prepared beads and incubated at room temperature for 30-60 minutes with rotation. Beads were collected and supernatant removed. For the Pierce™ direct magnetic co-IP kit, beads were washed with 500 µL IP lysis/wash buffer, vortexed gently, collected and supernatant removed; this wash step was repeated once. Beads were washed with 500 µL diH_2O, vortexed gently, collected and supernatant removed. For anti-HA and anti-Myc co-IP kits, beads were washed with 300 µL IP lysis/wash buffer (anti-HA beads) or 300 µL c-Myc IP buffer 2 (diluted 1:20 in diH_2O; cat., 1862825, TFS; anti-Myc beads). Beads were vortexed gently, collected and supernatant removed; this wash step was repeated twice. Beads were washed with 300 µL diH_2O, vortexed gently, collected and supernatant removed.

For all magnetic co-IP kits, samples were eluted from magnetic beads with 50 µL 1x non-reducing sample buffer (cat. 1959594, TFS) at 95°C for 10 minutes. Beads were collected on a magnet for 60 seconds and samples were transferred to a clean microcentrifuge tube. Following this, 5 µL NuPAGE™ reducing agent was added to samples, mixed gently and samples stored at -20°C.

2.3.3.4. Immunoblot analysis

Denatured proteins were separated by sodium dodecyl sulphate (SDS) polyacrylamide gel electrophoresis (SDS-PAGE), alongside 8 µL SeeBlue plus 2 pre-stained standard

(cat. LC5925, Invitrogen) on 1.0mm 4-12% NuPAGE Bis-Tris gels (10-well cat. NP0321, 12-well cat. NP0322, 15-well cat. NP0336, Invitrogen) in 1x MOPS-SDS buffer (cat. NP0001, Invitrogen) containing 500 µL NuPAGE antioxidant (cat. NP0005, Invitrogen) at 200 V for 50-120 minutes. Proteins were transferred to polyvinylidene difluoride (PVDF) membrane (cat. 10600023, Amersham, GE Healthcare) in 1x transfer buffer (cat. NP0006, Invitrogen) containing 10% (v/v) methanol (cat. 8.22283.2500, Merck Millipore) and 250 µL NuPAGE antioxidant at 30 V for 60 minutes.

PVDF membranes were blocked in 5% (w/v) milk (cat. LP0031, Oxoid, Basingstoke, UK) in 1x TBST buffer (1x tris-buffered saline (TBS; cat. 170-6435, Bio-Rad) containing 0.1% Tween-20 (cat. 161-0781, Bio-Rad)) for 60 minutes with shaking. Membranes were probed with primary antibodies (Table 2.25) at 4°C overnight, or 60 minutes at room temperature, and washed 5x 5 minutes with 1x TBST with shaking. Membranes were then probed with secondary antibodies (Table 2.25) for 60 minutes, and washed 5x 5 minutes with 1x TBST with shaking. HRP-conjugation of antibodies was achieved using Pierce™ enhanced chemiluminescence plus substrate (cat. 32132, TFS). Briefly, solution A (cat. 1863031, TFS) was diluted 1:40 in solution B (cat. 1863033, TFS) and incubated on membranes away from light for 5 minutes. Membranes were exposed to CL-Xposure™ X-ray films (cat. 34089 and 34090, TFS) and processed away from light. To re-probe with an alternative primary antibody, membranes were washed twice with 1x TBST for 5 minutes, stripped in restore plus western blotting stripping buffer (cat. 46430, TFS) for 5 minutes and washed twice with 1x TBST for 5 minutes. Membranes were blocked and probed as described above.

Lane densitometry was used to quantify band intensity in ImageJ. Individual lanes were marked using the analyse gel function and density of bands was quantified automatically. All bands were normalised to their respective loading controls.

Table 2.25. Primary and secondary antibodies used in immumoblotting applications. See figure legends for final antibody dilutions used in each application. All antibodies were diluted in 5% (w/v) milk/1x TBST.

Target protein	Catalogue	Dilution factor	Secondary antibody	Dilution factor
HA	ab9110 (Abcam)	1:10,000-1:1,000,000	goat anti-rabbit IgG horseradish peroxidase (HRP)-conjugate (cat. 1706-515 Bio-Rad)	1:3000
Myc	ab9106 (Abcam)	1:1000-1:5,000		
TBX15	MRCH-TBX15 (MRCH protein core)	1:250		
TBX15	NBP2-49036 (Novus)	1:400		
TBX15	abx030360 (Abbexa)	1:100		
Adiponectin	ab22554 (Abcam)	1:10,000	goat anti-mouse IgG horseradish peroxidase (HRP)-conjugate (cat. 1706-516 Bio-Rad)	1:3000
GAPDH	ab8245 (Abcam)	1:10,000-1:100,000		1:5000

2.3.3.5. DNA binding assays

DNA oligonucleotide sequences were designed based on *in vitro* binding site selection experiments performed by (Farin *et al.*, 2007). Oligonucleotides (Table 2.26) were purchased from Sigma-Aldrich and reconstituted in NF-H_2O. Complimentary oligonucleotides (Fw and Rv) were annealed at a 1:1 ratio in oligonucleotide annealing buffer (pH 8.0; Table 2.27) by gradually decreasing temperature from 95-25^{o}C (Table ***2.28***) in a thermocycler to a final concentration of either 10 ng/µL or 20 ng/µL.

A 4 µg/µL to 0.5 µg/µL serial dilution of protein lysates (described in 2.3.3.1.1 and 2.3.3.2) was generated for each sample. DNA binding assays were performed using the DNA binding colorimetric assay (cat. ab117139, Abcam) following manufacturer's protocol. Briefly, each well of a 96-well assay plate was washed twice with 150 µL freshly made 1x wash buffer. Then, 23 µL assay binding buffer, 2 µL DNA oligo (20-40 ng) and 5 µL protein (2.5-20 µg) were added to each well and incubated for 60 minutes. Wells were washed three times with 150 µL 1x wash buffer and incubated with 50 µL primary antibody (Table 2.29) diluted in antibody dilution buffer for 60 minutes with agitation. Subsequently, wells were washed four times with 150 µL 1x wash buffer and incubated with 50 µL secondary antibody diluted in 1x wash buffer for 30 minutes. Wells were washed four times with 150 µL 1x wash buffer and incubated with 100 µL developing solution away from light. When colour had developed, 50 µL stop solution was added to the wells and plates were read at 450 nm on an Epoch spectrophotometer with Gen5 v3.4 software.

Table 2.26. DNA oligonucleotide sequences for TBX15 DNA binding assay. Half-site orientations based on data from (Farin *et al.*, 2007). Abbreviations: BSp (palindromic orientation of T half-site), BSinv (inverse orientation of T half-site), BSdir (direct repeat orientation of T half-sites), Fw (forward oligonucleotide), Rv (reverse oligonucleotide).

Oligo	Sequence	Modification
BSp_Fw	GATCCGGTTTCACACCTAGGTGTGAAAGGA	3'-biotinylated
BSp_Rv	GATCTCCTTTCACACCTAGGTGTGAAACCG	
BSinv_Fw	GATCCGGAGGTGTGAAATTTCACACCTGGA	3'-biotinylated
BSinv_Rv	GATCTCCAGGTGTGAAATTTCACACCTCCG	
BSdir_Fw	GATCCGGAGGTGTGAAGGTGTGAAAGGA	3'-biotinylated
BSdir_Rv	GATCTCCTTTCACACCTTCACACCTCCG	

Table 2.27. Oligonucleotide annealing buffer stocks. Abbreviations: EDTA (Ethylenediaminetetraacetic acid), NF-H_2O (nuclease-free H_2O).

Reagent	Catalogue	Dilution	Stock concentration	Dilution to working buffer (100 mL)	Final concentration
Trizma Base	T1503 (Sigma-Aldrich)	1.2114 g in 10 mL NF-H_2O	1 M	1 mL	10 mM
EDTA	324506 (Sigma-Aldrich)	N/A	0.5 M	0.2 mL	1 mM
Sodium Chloride (NaCl)	71376 (Sigma-Aldrich)	584.4 mg in 10 mL NF-H_2O	1 M	5 mL	50 mM
NF-H_2O	129117 (Qiagen)			94 mL	

Table 2.28. Thermocycler parameters for DNA oligonucleotide annealing.

Step	Cycles	Temperature	Time
1	1	95°C	5 minutes
2	70	95°C (-1°C/cycle)	1 minute
3		4°C	hold

Table 2.29. Primary antibody dilutions for DNA binding assay. Primary antibodies were purchased from Abcam.

Antibody	Category	Dilution factor	Secondary antibody
Myc	ab9106	1:1000	Goat anti-rabbit IgG HRP-conjugate (final concentration 0.33 µg/µL)
HA	ab9110	1:2000	
		1:5000	

2.3.3.6. ChIP-sequencing

2.3.3.6.1. Sample fixation

Fixation solutions were premade according to protocols from Active Motif Inc. (Carlsbad, CA, USA; Table 2.30). To fix cells, 1/10th total culture volume of formaldehyde solution was added to cells in existing media and incubated with

agitation for 15 minutes. Fixation was halted by addition of 1/20th volume glycine solution to the culture vessels and incubated for 5 minutes. Cells were detached from the flask and transferred to a 50 mL centrifuge tube on ice for remaining steps; centrifugation was performed at 800 x *g* for 10 mins at 4^{o}C. Cells were centrifuged and supernatant discarded. Pellets were resuspended in 10 mL chilled 0.5% (v/v) IGEPAL CA-630/PBS and technical replicates were pooled, centrifuged and supernatant removed. Pellets were resuspended in 10 mL chilled 0.5% (v/v) IGEPAL CA-630/PBS containing 100 µL PMSF (final concentration 1 mM), centrifuged and supernatant removed. Cell pellets were snap frozen on dry ice and shipped to Active Motif Inc.

Table 2.30. Reagents required for cell fixation for ChIP-sequencing analysis. Abbreviations: diH_2O (deionised H_2O), DPBS (Dulbecco's phospho-buffered saline), EDTA (ethylenediaminetetraacetic acid), HEPES (4-(2-hydroxyethyl)-1-piperazineethanesulfonic acid), PMSF (Phenylmethanesulfonyl fluoride),

Solution	Stock	Catalogue	Preparation	Final concentration
Formaldehyde solution (prepared fresh just prior to use)	37% (v/v) formaldehyde	F-8775, (Sigma-Aldrich)	6 mL	11%
	5M NaCl	71376 (Sigma-Aldrich)	0.4 mL	0.1 M
	0.5 M EDTA, pH 8.0	03690 (Sigma-Aldrich)	40 µL	1 mM
	1 M HEPES, pH 7.9	H0887 (Sigma-Aldrich)	1 mL	50 mM
	diH_2O		To 20 mL	
Glycine solution (premade and stored at room temperature)	Glycine	G7403 (Sigma-Aldrich)	3.75 g	2.5 M
	diH_2O		20 mL	
IGEPAL-PBS (premade and stored at 4^{o}C)	100% IGEPAL CA-630	I8896, (Sigma-Aldrich)	2.5 mL	0.5%
	1x DPBS, pH 7.4	14190-094 (Gibco)	500 mL	
PMSF (premade and stored at -20^{o}C)	PMSF	P7626 (Sigma-Aldrich)	250 mg	100 mM
	100% ethanol	E/0650DF/17 (TFS)	14.4 mL	

2.3.3.6.2. ChIP-sequencing

Further sample preparation, library generation, antibody validation, ChIP-sequencing and basic data analysis were performed by Active Motif Inc. (described in Appendix 9.1.2.2.1, 9.1.2.2.2 and 9.1.2.2.3).

2.3.3.6.3. Functional analysis

Functional profiling of genes containing ChIP-sequencing peaks was performed using the g:GOST function on the g:Profiler webpage (Reimand *et al.*, 2007; Raudvere *et al.*, 2019). Queries were performed, with *homo sapiens* and *mus musculus* as the organism for hWAT and 3T3-L1 data, respectively. Default parameters were set as follows: statistical domain scope (only annotated genes), significance threshold (g:SCS threshold, 0.05), data sources selected (GO molecular function, GO cellular component, GO biological process, KEGG, Reactome, WikiPathways, TRANSFAC, miRTarBase, CORUM and human phenotype ontology).

2.4. Bacterial work

2.4.1. General bacterial work

All bacterial work was carried out in a sterile laminar airflow cabinet using aseptic techniques. All reagents and media were prepared in a sterile environment and autoclaved for sterilisation prior to use.

2.4.1.1. Vector construct procurement

pCMV6-entry expression plasmids containing human TBX15-2 (496 amino acid; aa, NM_152380, cat. RC218410) and TBX18 (607 aa, NM_001080508, cat. RC211838) tagged with C-terminal Myc-DDK were purchased from OriGene Technologies (Rockville, MA, USA). The 602 amino acid TBX15-1 isoform, along with TBX15-1-H156N and TBX15-1-M566R variants, were purchased as custom clones in the pCMV6-entry expression plasmid with C-terminal Myc-DDK tag from OriGene Technologies. Upon receipt, vials were centrifuged briefly, reconstituted to 10 µM in NF-H_2O, and stored at -20°C. The pCMV-HA-C vector (cat. 635690, TaKaRa Bio, Kusatsu, Japan) was centrifuged briefly, reconstituted to 5 ng/µL in NF-H_2O and stored at -20°C.

The TBX15-2-Myc, TBX15-2-H50N-Myc, TBX15-2-M460R-Myc and TBX18-Myc vectors contained the kanamycin resistance gene (Kan^R), and the TBX15-1-Myc, TBX15-1-H156N-Myc, TBX15-1-M566R-Myc and pCMV-HAC vectors contained the ampicillin resistance gene (Amp^R) for bacterial selection.

2.4.1.2. Vector construct design

SnapGene® v6.0.2 was used to visualise expression construct sequences, design primers, align sequencing results, and simulate restriction enzyme digests and ligations.

2.4.1.3. Lysogeny broth and antibiotics selection plates

Ampicillin stocks were made by dissolving 1 g ampicillin sodium salt (cat. A9518, Sigma-Aldrich) in 10 mL ddH_2O to a concentration of 100 mg/mL. The MRCH laboratory services department prepared lysogeny broth (LB; 10 g/L bactotryptone, 5 g/L bactoyeast extract and 5 g/L NaCl, pH 7.0), and boiled 40 g LB agar (cat. L3027, Sigma-Aldrich) in 1 L ddH_2O until fully dissolved.

LB agar was re-dissolved by boiling and cooled to ~50^oC before adding kanamycin (cat. KA0129, Sigma-Aldrich; final concentration 0.025 mg/mL) or ampicillin (final concentration 0.1 mg/mL). The antibiotic-containing LB agar solution was set in 10 cm^2 petri dishes (cat. 101/IRR, TFS) and stored at 4^oC for up to 4 weeks. Plates were pre-warmed at 37^oC prior to use.

2.4.1.4. Transformation of competent Escherichia coli (*E. Coli*) cells

Sub-cloning efficiency DH5α chemically competent *E. Coli* (cat. 18265-017, Invitrogen) were aliquoted into 50 µL aliquots upon receipt and stored at -80^oC. Aliquots were thawed gently on ice and up to 100 ng of plasmid DNA, 2-5 µL ligation reaction, or 5 µL pUC19 positive control DNA (500 pg total, cat. SD0061, Invitrogen) were added to *E. Coli*, mixed gently by flicking and incubated on ice for 30 minutes. *E. Coli* were heat-shocked at 42^oC in a water bath for 30 seconds, followed by 2 minutes incubation on ice. Initial colony expansion was achieved by incubation of *E. Coli* with 950 µL LB at 37^oC in an Innova®44 orbital shaker (New Brunswick Scientific, Edison, NJ, USA) at 225 rpm for 60 minutes. Subsequently, 20-200 µL cultures were plated on antibiotic selection LB agar plates (described in 2.4.1.3) and incubated at 37^oC for 16-18 hours.

Bacterial colonies were picked from LB agar plates and cultured in 5 mL LB containing kanamycin (final concentration 0.025 mg/mL), or ampicillin (final concentration 0.05 mg/mL). Cultures were incubated at 37°C in an orbital shaker at 225 rpm for 16-18 hours for DNA isolation by miniprep (described in 2.4.2.1). Alternatively, 5 mL starter cultures were incubated for 8 hours at 37°C in an orbital shaker at 225 rpm and 100-200 µL was used to inoculate 200 mL LB supplemented with kanamycin (0.0.25 mg/ mL) or ampicillin (0.05 mg/mL) in a 1000 mL conical flask and incubated at 37°C at 225 rpm for 16-18 hours for DNA isolation by maxiprep (described in 2.4.2.2).

2.4.1.5. Glycerol stocks

To make a 50% (v/v) glycerol solution, 100% glycerol (cat. 356350, Calbiochem, Sigma-Aldrich) was diluted 1:1 with ddH_2O. To make bacterial glycerol stocks, 500 µL overnight bacterial culture was added to 500 µL 50% (v/v) glycerol solution in 2 mL cryotubes, snap frozen on dry ice and stored at -80°C. To culture colonies from glycerol stocks, cryotubes were kept on dry ice and a small scraping was taken with a sterile pipette tip, streaked on an LB agar plate containing selection antibiotics (described in 2.4.1.3) and incubated at 37°C for 16-18 hours.

2.4.2. DNA isolation

2.4.2.1. Miniprep

Approximately 4 mL overnight bacterial cultures were centrifuged at 4,500 x *g* for 10 minutes in a Heraeus Megafuge 16R centrifuge fitted with a TX-400 rotor (TFS), and

supernatant discarded. DNA was isolated using the QIAprep spin miniprep kit (cat. 27106, Qiagen) following manufacturers' instructions; centrifugation was performed at 13,000 x *g* for 60 seconds and flow-through discarded each time. Briefly, bacterial pellets were resuspended in 250 µL buffer P1 (cat. 1014871, containing RNAse A (final concentration 100 µg/mL) and LyseBlue (1:1000), cat. 1072590) and transferred to a clean microcentrifuge tube. Then, 250 µL buffer P2 (cat. 1014947) was added to samples and inverted until a homogenous blue colour developed indicating bacterial lysis. To neutralise lysis, 350 µL buffer N3 (cat. 1014796) was added to tubes and mixed by inversion until cloudy. Samples were centrifuged at 13,000 x *g* for 10 minutes; lysates were transferred to a QIAprep 2.0 spin column and centrifuged. Columns were washed with 500 µL buffer PB (cat. 1015089) and centrifuged. Subsequently, columns were washed with 750 µL buffer PE (cat. 1015210) and centrifuged; centrifugation was repeated once to remove residual ethanol. DNA was eluted in 30 µL NF-H_2O in a clean microcentrifuge tube and stored at -20°C.

2.4.2.2. Maxiprep

Approximately 200 mL overnight bacterial cultures were centrifuged at 4,500 x *g* for 15 minutes at 4°C in a Beckman Allegra 6KR centrifuge (Beckman Coulter), and supernatant removed. DNA was isolated using the HiSpeed plasmid maxi kit (cat. 12663, Qiagen) following manufacturers' instructions. Briefly, pellets were resuspended in 10 mL buffer P1 (cat. 1014854, containing RNAse A and LyseBlue) by vortexing. Then, 10 mL buffer P2 (cat. 1014939) was added to tubes and mixed by inversion until a homogenous blue colour developed; samples were incubated for 5 minutes to allow lysis to occur. To neutralise lysis, 10 mL pre-chilled buffer P3

(cat. 1014955) was added to tubes and mixed by inversion until cloudy and no blue colour remained. Lysates were incubated in a QIAfilter cartridge for 10 minutes. Meanwhile, a HiSpeed tip was equilibrated with 10 mL buffer QBT (cat. 1015291). Lysates were then filtered into the equilibrated HiSpeed tip; once filtered the HiSpeed tip was washed with 60 mL buffer QC (cat. 1015371). DNA was eluted with 15 mL buffer QF (cat. 1025572) and precipitated with 10.5 mL 100% isopropanol, mixed and incubated for 5 minutes. The elute-isopropanol mixed was passed through a QIAprecipitator using a syringe using constant pressure. The QIAprecipitator was washed with 2 mL 70% (v/v) ethanol and dried by passing air through forcefully several times. DNA was eluted from the QIAprecipitator in 500 µL NF-H_2O into a clean microcentrifuge tube, the 500 µL elute was passed through the QIAprecipitator a second time to increase DNA yield; DNA was stored at -20°C.

2.5. *In silico* applications

2.5.1. ATAC-sequencing analysis

The UCSC genome browser was used to view custom tracks for previously generated assay for transposase-accessible chromatin (ATAC)-sequencing data at day 0 (post-confluence, undifferentiated), day 3 (early), day 6 (mid) and day 24 (terminal) of hWAT adipogenic differentiation (Laber, 2017). The following publicly available tracks from the Encyclopedia of DNA Elements (ENCODE) project were also visualised: H3K27Ac, DNAseI hypersensitivity clusters, TF ChIP-sequencing clusters, open chromatin using Formaldehyde-Assisted Isolation of Regulatory Elements (FAIRE)-sequencing, and chromatin state segmentation by chromatin hidden Markov model (ChromHMM).

2.5.2. Transcription factor binding motif analysis

The HaploReg v4.1 web server (Ward and Kellis, 2012) (https://pubs.broadinstitute.org/mammals/haploreg/haploreg.php) was used to examine regulatory annotations for *TBX15-WARS2* SNPs. For each rsID the following settings were applied, unless stated otherwise: LD threshold (r^2=0.8), 1000G Phase 1 population for LD calculation (EUR), Source for epigenomes ChromHMM (core 15 state model), Mammalian conservation model (SiPhy-omega), position shown relative to GENCODE genes. TFBMs were downloaded from the JASPAR database (Castro-Mondragon *et al.*, 2022) and manually aligned to the genomic DNA sequence flanking rs10494217 and rs61730011.

2.5.3. Protein sequence alignments

Protein sequences were downloaded from the Ensembl genome browser release 106 (Cunningham *et al.*, 2022) and from the national centre for biotechnology information (NCBI) (Sayers *et al.*, 2022) for individual protein transcripts (Table 2.31). T-box domain sequences for human TBX15 (amino acids 115-304; transcript Q96SF7-1) and TBX18 (amino acids 141-330; transcript O70306-1) were defined using Pfam annotations in Ensembl. EMBL-EBI multiple sequence comparison by log-expectation (MUSCLE) or Clustal Omega were used for protein sequence alignment queries (EMBL-EBI; Madeira *et al.*, 2022). FASTA sequences were aligned using default parameters and output format was set to ClustalW.

Table 2.31. T-box protein transcript sequences used for alignments. Genus given in italics.

Species	Protein	UniProt ID	Amino acid sequence length
Human (*homo sapiens*)	TBX15	Q96SF7-1	602
	TBX15	Q96SF7-2	496
	TBX18	O95935-1	607
Mouse (*mus musculus*)	TBX15	O70306-1	602
Zebrafish (*danio rerio*)	Tbx15	B0S5M8-1	620
Chicken (*gallus gallus*)	Tbx15	F1NA14-1	601
Marmoset (*callithrix jacchus*)	Tbx15	A0A2R8PB87-1	602
Dog (*canis lupus familiaris*)	Tbx15	A0A8C0SKN9-1	602
Frog (*xenopus tropicalis*)	Tbx15	A0A6I8RDF1-1	601

2.5.4. Nuclear localisation sequence analysis

Nuclear localisation sequences were analysed using the cNLS Mapper web portal (http://nls-mapper.iab.keio.ac.jp/cgi-bin/NLS_Mapper_form.cgi) (Kosugi *et al.*, 2009), with the following parameters: cut-off score 2.0, protein regions searched for bipartite NLSs with a long linker (13-20 aa) "entire region".

2.5.5. Mutation predictions

Online mutation prediction servers were used to predict the severity of non-synonymous amino acid substitutions, using default parameters. SIFT (sorting intolerant from tolerant), default parameters: database "UniProt-SwissProt 2010_09", median conservation of sequences "3.0" (Sim *et al.*, 2012). PolyPhen (polymorphism

phenotyping v2) (Adzhubei *et al.*, 2010). Condel (Consensus deleteriousness) (González-Pérez and López-Bigas, 2011).

2.5.6. Protein sequence modelling

Protein homology modelling for full-length TBX15, and T-box regions for TBX15 and TBX18 was performed in collaboration with Professor Kim Watson (School of Biological Sciences, University of Reading). Protein sequences were input into the following prediction servers, using default settings: integrated protein structure and function prediction server (IntFOLD) v5.0 and v6.0 (McGuffin *et al.*, 2018, 2019), Protein homology/analogY recognition engine v2.0 (Phyre2; intensive mode) (Kelley *et al.*, 2015), and DMPfold v1.0 on the PSIPRED workbench (Buchan and Jones, 2019). Alternatively, protein structures were downloaded directly from AlphaFold v2 (Jumper *et al.*, 2021; Varadi *et al.*, 2022). The resulting files for the homology models, in PDB format, were visualised and aligned in Pymol v2.3 software (Schrödinger Inc, New York NY, USA). Where metadata existed, molecules were coloured by B-factor [code: PyMOL>spectrum b], in IntFOLD v5.0/6.0 this was residue accuracy predictions (Angstroms), and in AlphaFold v2.0 it was the per-residue confidence score. Colour scheme - blue (high accuracy) through green, yellow and orange to red (low accuracy).

2.5.7. Dimer modelling

In silico dimer analysis was performed in collaboration with Professor Kim Watson. Crystallographic structures for T-box family proteins were downloaded from the protein data bank (Table 2.32). PDBSum was used to determine the amino acid

residues involved in protein dimerisation of these known PDB structures (Laskowski *et al.*, 2018). TBX15 and TBX18 T-box homology models (described in 2.5.6) were aligned to PDB structures, using Pymol v2.3, to compare equivalent residues. The high ambiguity driven protein-protein docking (HADDOCK) v2.4 web portal was used to predict protein-protein dimer formation (De Vries, Van Dijk and Bonvin, 2010; Van Zundert *et al.*, 2016). TBX15 and TBX18 T-box models were uploaded in .pdb format for 'Protein or Protein-Ligand' docking using default parameters. Active residues involved in interactions were manually selected based on the alignments to other T-box structures (guided docking approach). Passive residues surrounding surface residues were automatically determined by the web server using default parameters (within 6.50 angstrom radius of active residues). Default histidine protonation states, sampling and clustering parameters, and energy restraints were used for all model submissions.

Table 2.32. Crystallographic structures available in the protein data bank for T-box family members. Corresponding amino acids from PDBsum files for protein-protein interactions were used for guided docking approach.

TBX protein	Protein Data Bank ID	Reference
TBX3	1h6f	(Coll, Seidman and Müller, 2002)
TBX5	2x6v	(Stirnimann *et al.*, 2010)
T (Brachyury)	6f58	(Newman *et al.*, in preparation)
Tbet	5t1j	(Liu *et al.*, 2016)

2.6. Statistical analysis

All data was analysed using GraphPad Prism v9.0 (GraphPad Software, San Diego, CA, USA). Graphs show mean ± standard error mean (SEM), all test details are described in figure legends. $P<0.05$ (student's t-tests, one-way ANOVAs, two-way ANOVAs), $q<0.05$

(multiple unpaired t-tests), and false discovery rate (FDR)<0.05 (RNA-sequencing) were considered significant, unless stated otherwise. G*Power v3.1 (Heinrich-Heine-University, Germany) was used to calculate required sample size for mouse metabolic phenotyping studies (Table 2.33).

Table 2.33. Power calculation parameters to calculate the required sample sizes for metabolic phenotyping cohorts. Data analysed in G*Power v3.1.

Parameter	Details
test family	t-test
statistical test	means difference between two independent means
type of power analysis	*a priori* compute required sample size given α, power and effect size
input parameters	two-tails, α error probability =0.05, power =0.95

3

Prioritising the role of potentially functional coding SNPs within the *TBX15* gene

3.1. Introduction

Approximately 4% of WHRadjBMI variance can be attributed to ~460 signals in 346 loci. Further, several independent SNPs in the *TBX15-WARS2* locus have been associated with WHRadjBMI (Figure 3.1, Table 3.1) (Heid *et al.*, 2010; Liu *et al.*, 2014; Shungin *et al.*, 2015; Justice *et al.*, 2019; Pulit *et al.*, 2019), highlighting the need to identify gene targets and mechanisms driving disease risk. This complexity was further revealed by PPA and epi-PMCA prioritisation of 61 SNPs in high linkage disequilibrium (LD) with the signals identified by Shungin *et al.* (2015) which predicted different SNPs as most likely to be functional (unpublished data, Dr. Sara Pulit and Nasa Sinnott-Armstrong).

One such SNP was the *TBX15* coding SNP rs10494217 (MAF=0.174, β=0.018) (Justice *et al.*, 2019; Pulit *et al.*, 2019) which was predicted to be most likely functional in epi-PMCA. A further *TBX15* coding SNP, rs61730011 (MAF=0.047, β=0.041), was one of 13 rare variants (MAF<0.05) significantly associated with WHRadjBMI in a sample size of just 345,000 individuals (Justice *et al.*, 2019). Such rare variants may prove indispensable when trying to elucidate the functional role of association signals as their impact can be measured on the structure and function of the protein they encode.

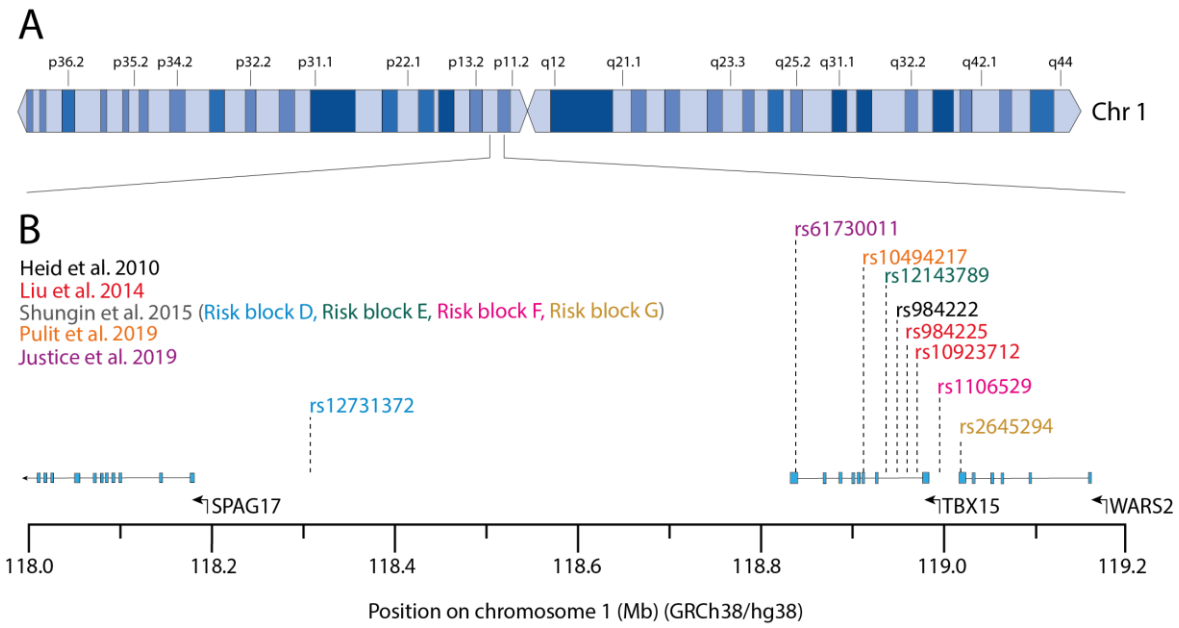

Figure 3.1. Chromosome map of the *TBX15-WARS2* locus SNPs identified by GWAS meta-analyses. A. Schematic of human chromosome 1 showing the short (p) and long (q) arms. B. A magnified schematic of the *TBX15-WARS2* locus at 1p12 indicating the location of SNPs associated with WHRadjBMI through several GWAS meta-analyses (see Heid *et al.* (2010), Liu *et al.* (2014), Shungin *et al.* (2015), Justice *et al.* (2019) and Pulit *et al.* (2019) for details of individual SNPs). This figure was generated wholly by myself and has previously been published in (Mušo *et al.*, 2020), reproduced with permission from Elsevier (licence: CC BY-NC-ND 4.0).

The *TBX15-WARS2* locus harbours several promising candidate genes for WHRadjBMI associations. For example, *TBX15* and *WARS2* regulate adipogenesis and mitochondrial browning of WAT, respectively (Gesta *et al.*, 2011; Gburcik *et al.*, 2012; Agnew *et al.*, 2018; Mušo *et al.*, 2022). Further, SAT and VAT expression of *TBX15, WARS2* and *SPAG17* were differentially associated with cardiometabolic traits such as BMI, serum plasma insulin levels, fat-free mass, adiponectin and HDL-cholesterol levels (Civelek *et al.*, 2017), suggesting genes within the locus may independently drive fat distribution.

The T-box family of transcription factors (TFs) regulate several developmental processes including embryogenesis, cardiogenesis and limb development; each T-box preferentially binds different repeat patterns of a core 5'-AGGTGTGA-3' binding

sequence (T half-site) (Papaioannou, 2014). TBX1-subfamily members TBX15 and TBX18 form heterodimers with one another, and their N- and C-terminal regions play an important role in this process (Farin *et al.*, 2007). Mutations in the highly conserved T-box region of TBX3 and TBX5 structurally altered these proteins, with TBX5 mutations further impairing DNA binding affinity of this T-box domain (Coll, Seidman and Müller, 2002; Stirnimann *et al.*, 2010). The *TBX15* coding SNPs rs10494217 and rs61730011 encode non-synonymous amino acid substitutions p.H156N (T-box domain) and p.M566R (C-terminal domain), respectively, that may impact formation of protein-protein and/or protein-DNA complexes (Figure 3.2).

Table 3.1. Haplotype blocks for the *TBX15-WARS2* locus SNPs associated with WHRadjBMI. Total number of SNPs in risk block refers to SNPs in high linkage disequilibrium (r^2>0.8) with the tag SNPs from Shungin *et al.* (2015).

SNP	Reference	Risk Block	Total number of SNPs in risk block
rs12731372	(Shungin *et al.*, 2015)	D	28
rs61730011	(Justice *et al.*, 2019)	N/A	N/A
rs12143789	(Shungin *et al.*, 2015)	E	24
rs10494217	(Justice *et al.*, 2019; Pulit *et al.*, 2019)		
rs2645294	(Shungin *et al.*, 2015)	G	5
rs1106529	(Shungin *et al.*, 2015)	F	3
rs984222	(Heid *et al.*, 2010)	N/A	N/A

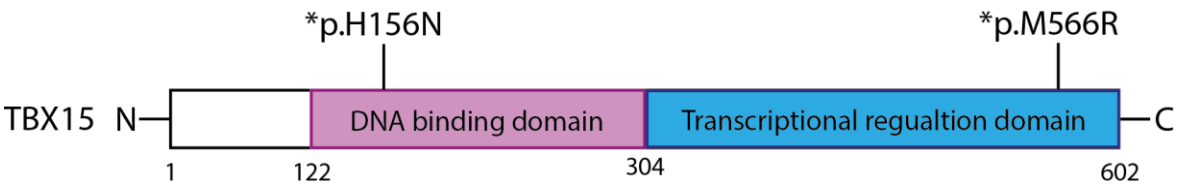

Figure 3.2. TBX15 protein domain map. Domain map of the full-length TBX15-1 protein showing amino acid positions of non-synonymous substitutions p.H156N (rs10494217) and p.M566R (rs61730011).

3.1.1. Chapter hypothesis

I hypothesised that rs10494217 (p.H156N) and rs61730011 (p.M566R) act at i) a DNA-regulatory level to alter TF binding, and/or ii) a protein-coding level to alter the structure and TF function of TBX15 itself, to regulate in *cis*- and *trans*- expression of a network of genes associated with adipogenesis and fat distribution.

3.1.2. Chapter aims

To prioritise the potential mechanisms of the *TBX15* coding SNPs rs10494217 and rs61730011, I performed *in silico* examination of:

1. Chromatin marks and TF binding motif (TFBM) alignments to determine regulatory effects of coding SNPs in comparison to non-coding SNPs in the *TBX15*-*WARS2* locus.
2. Protein homology modelling and protein-protein docking to determine alterations in TBX15 protein structure and dimer formation resulting from amino acid substitutions p.H156N (rs10494217) and p.M566R (rs61730011) (in collaboration with Professor Kim Watson, Reading University).

To validate the predicted TBX15 protein structure alterations resulting from p.H156N, I performed *in vitro* examination of:

3. TBX15 protein dimerisation affinity with TBX15 (homodimers) and TBX18 (heterodimers).
4. TBX15 binding affinity to DNA target sequences.

3.2. Results

3.2.1. *In silico* analysis of the regulatory role of *TBX15* coding SNPs

3.2.1.1. rs10494217 and rs61730011 overlapped minimal epigenetic marks in differentiating hWAT cells

Epi-PMCA prioritisation performed by Nasa Sinnott-Armstrong ranked rs10494217 as the most likely to have a functional role. Therefore, I aimed to interrogate potential regulatory roles for rs10494217 and rs61730011 using several bioinformatics tools. Firstly I visualised ATAC-sequencing data, previously generated by Dr. Samantha Laber, using human preadipocyte (hWAT) cells, derived from subcutaneous adipose depots of the neck, during adipocyte differentiation (day 0 to 24) in the UCSC browser (Laber, 2017). Publicly available tracks for DNAseI hypersensitivity, ChIP-sequencing and chromatin states were also used to visualise epigenetic marks in the locus.

Clusters of ATAC peaks in the *TBX15-WARS2* locus, indicating areas of open chromatin, were visible in intergenic regions and within *SPAG17, TBX15* and *WARS2* (Figure 3.3A). The four index SNPs (Shungin *et al.*, 2015) overlapped promoter and enhancer marks in several cell types, with rs1106529 the only SNP to overlap open chromatin marks across all time points of differentiation (ChromHMM tracks, Figure 3.3E, F and G). Conversely, rs10494217 and rs61730011 did not overlap ATAC-sequencing peaks indicating there was no open chromatin, but rs10494217 was ~600 bp downstream of a small peak (Figure 3.3C and D). Both *TBX15* coding SNPs overlapped transcriptional transition/elongation marks in skeletal muscle myoblast cells suggesting these SNPs do not have a major regulatory role in differentiating adipocytes but may act in a tissue/cell-specific manner to regulate epistasis (HSMM ChromHMM track, Figure 3.3C and D).

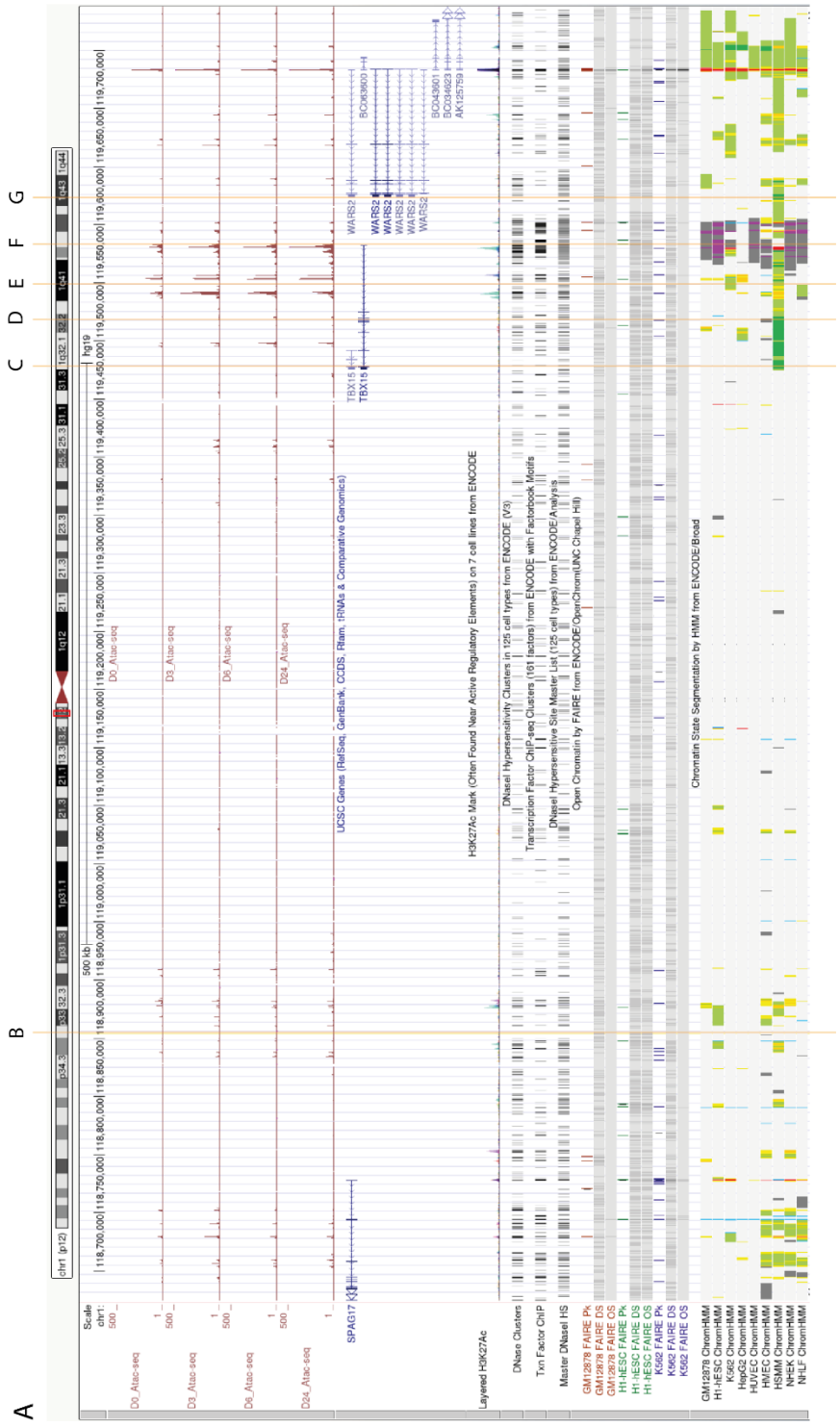

Figure 3.3 ATAC-sequencing data for hWAT cells at different adipocyte differentiation time points. A. ATAC-sequencing data produced by Dr Samantha Laber (Laber, 2017), of hWAT cells at different stages of adipogenic differentiation: pre-adipocyte (D0), early stage (D3), mid-stage (D6) and terminal differentiation (D24). Data was viewed on a custom UCSC genome browser track at the *TBX15-WARS2* locus, alongside public data for DNAseI hypersensitivity, transcription factor ChIP-sequencing and chromatin state segregation. Orange lines correspond to rs12731372 (B), rs61730011 (C), rs10494217 (D), rs12143789 (E), rs1106529 (F) and rs2645294 (G); see overleaf for zoomed-in panels. Chromatin state segregation key: bright red (active promoter), light red (weak promoter), purple (inactive/poised promoter), orange (strong enhancer), yellow (weak/poised enhancer), blue (insulator), dark green (transcriptional transition/elongation), light green (weak transcribed), grey (polycomb-repressed), light gray (heterochromatin; low signal; repetitive/copy number variation).

B - rs12731372

C - rs61730011

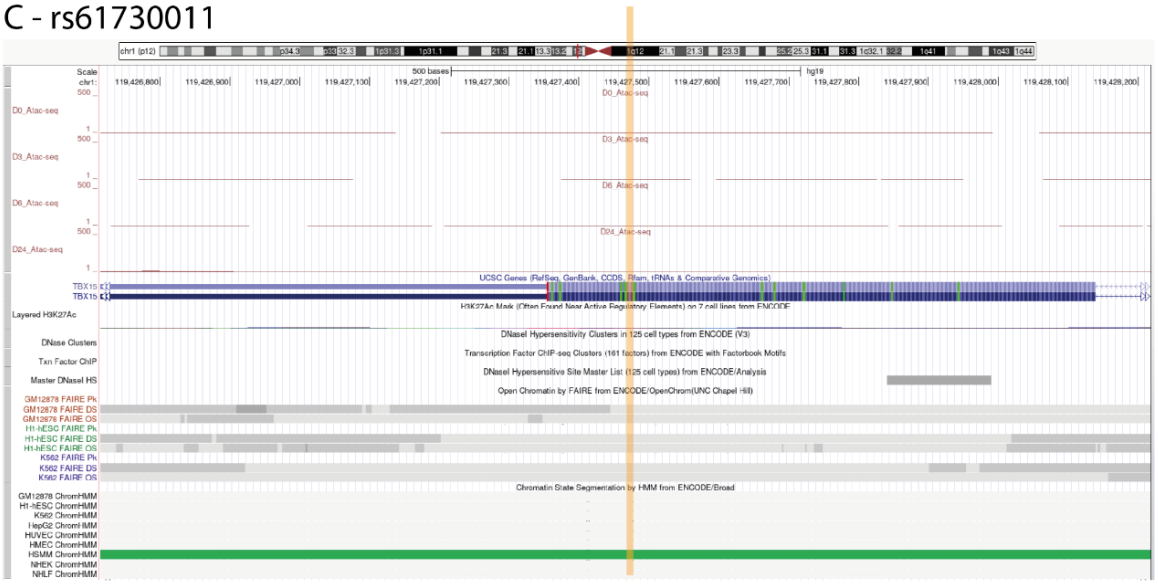

D - rs10494217

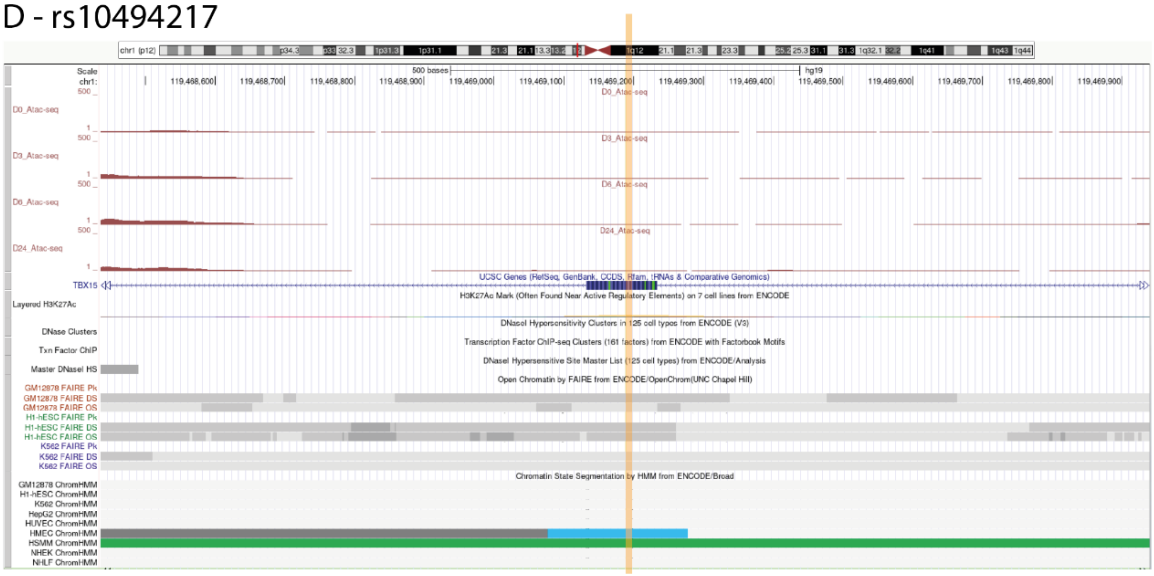

Figure 3.2 continued. B. rs12731372, C. rs61730011, D. rs10494217

E - rs12143789

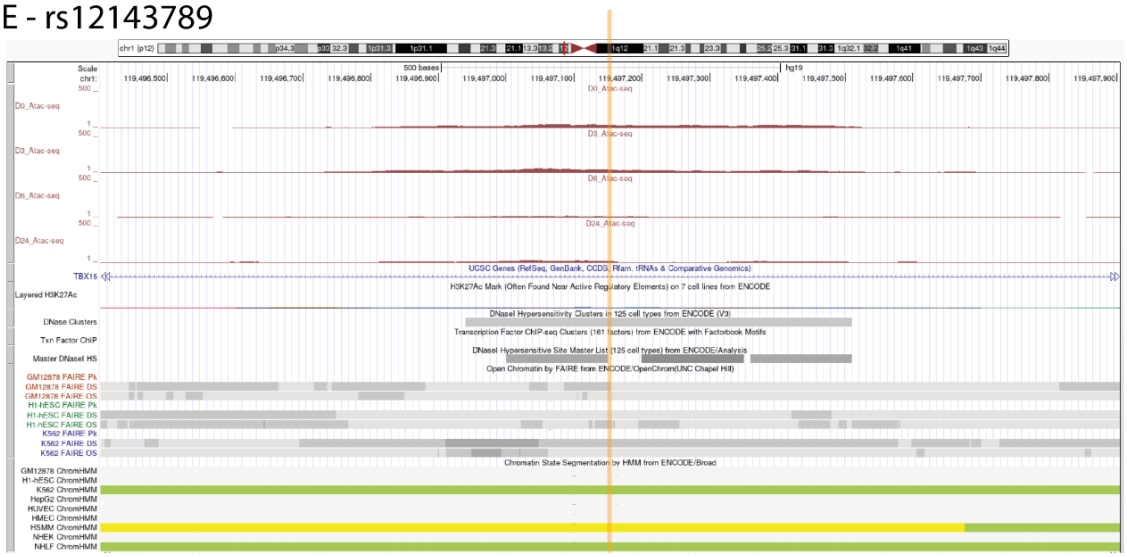

F - rs1106529

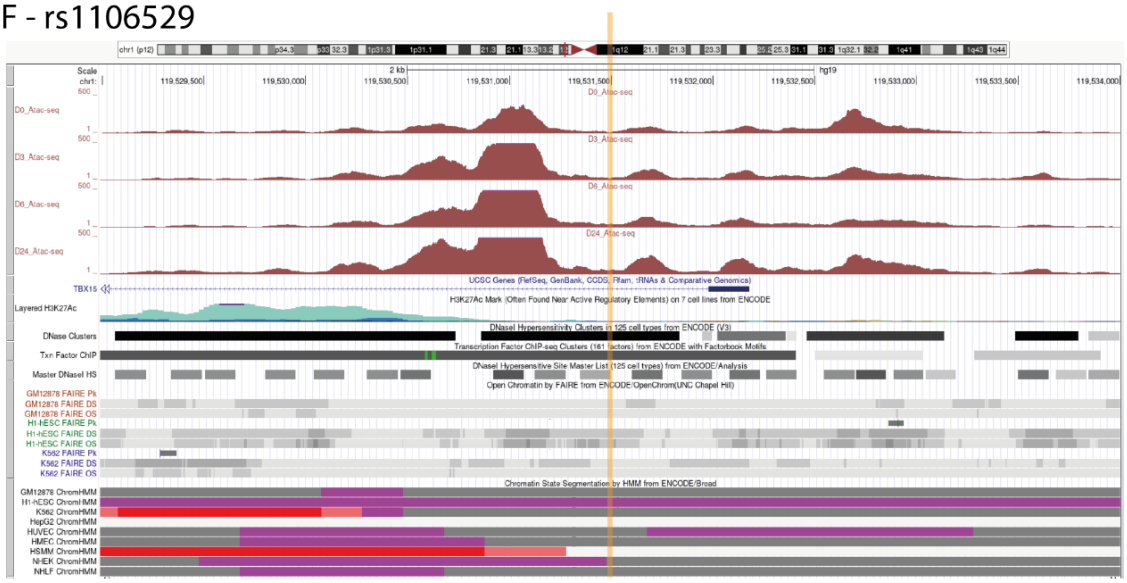

G - rs2645294

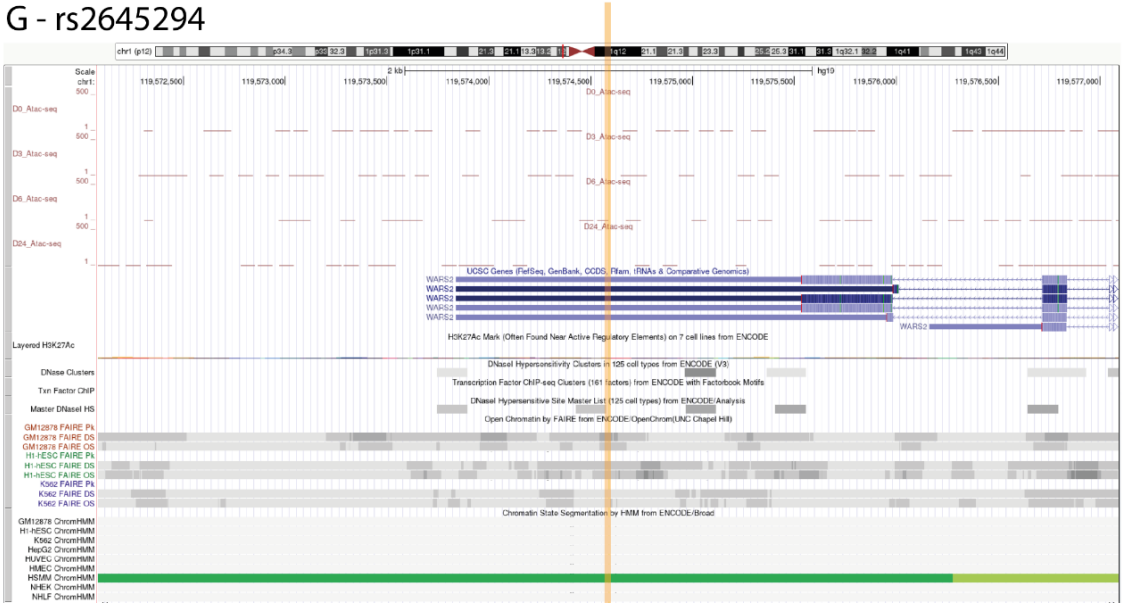

Figure 3.2 continued. E. rs12143789, F. rs1106529 and G. rs2645294

3.2.1.2. Transcription factor binding motifs altered by rs10494217 and rs61730011

I further compared the predicted cell/tissue-specific regulatory role of these six SNPs using HaploReg v4.1 (Table 3.2). *TBX15*-intronic SNPs had more DNAseI, promoter and enhancer histone marks than intergenic and coding SNPs suggesting they were more likely to be regulatory. Further, the number of altered TFBMs and eQTLs associated with *TBX15*-coding SNPs was generally lower than those in intronic and intergenic regions, with rs2645294 exhibiting the highest number of eQTLs (*WARS2* and *RP11-418J17.1* (*WARS2-AS1*) in multiple tissues).

In epi-PMCA performed by Nasa Sinnott-Armstrong, rs10494217 was the only SNP predicted to alter a TFBM, for CREB1 (cAMP responsive element binding protein 1). In addition, HaploReg v4.1 predicted rs10494217 to alter a TFBM for MAFG (Maf bZIP transcription factor G), while rs61730011 was predicted to alter TFBMs for NANOG (homeobox transcription factor), NRSF (neuron restrictive silencer factor), POU2F2 (POU class 2 transcription factor 2) and TCF12 (transcription factor 12). To validate these predictions, I manually aligned TFBMs from the JASPAR database to the genomic DNA sequence flanking each SNP (Figure 3.4). There were varying degrees of alignment of TFBMs, with CREB1 (rs10494217), POU2F2 and TCF12 (rs61730011) motifs most likely altered by alternate alleles, suggesting these SNPs may subtly alter binding affinity of TFs rather than completely introducing and/or removing TFBMs.

Table 3.2. Regulatory marks for *TBX15-WARS2* SNPs. Information compiled from HaploReg v4.1 for *TBX15* coding SNPs and four lead SNPs from Shungin *et al*. (2015). Abbreviations: SNP (single nucleotide polymorphism), EUR (European ancestry population from 1000 Genomes), LD (linkage disequilibrium), TFBM (transcription factor binding motif), GRASP QTL (genome-wide repository of associations between SNPs and phenotypes), eQTL (expression quantitative trait loci), ref/alt (reference/alternate allele).

Chr1 position (hg38)	Variant ID (SNP)	Ref/Alt	Position of SNP	EUR freq (Alt allele)	Number of Variants in LD (r^2 ≥0.8)	Promoter histone marks	Enhancer histone marks	DNAse	Number of TFBMs changed	GRASP QTL	eQTL
118310352	rs12731372	C/T	Intergenic	0.24	28	0	2	0	7	0	0
118884844	rs61730011	A/C	TBX15 Exon 8 (C-term)	0.06	0	0	0	0	4	0	0
118926565	rs10494217	G/T	TBX15 Exon 3 (T-box)	0.17	24	0	0	0	1	1	9
118958480	rs12143789	G/C	TBX15 Intronic	0.17	24	0	5	2	0	1	9
118988874	rs1106529	G/A	TBX15 Intronic	0.74	2	8	12	9	13	6	18
119031964	rs2645294	C/T	WARS2 3'-UTR	0.56	4	0	0	0	1	6	45

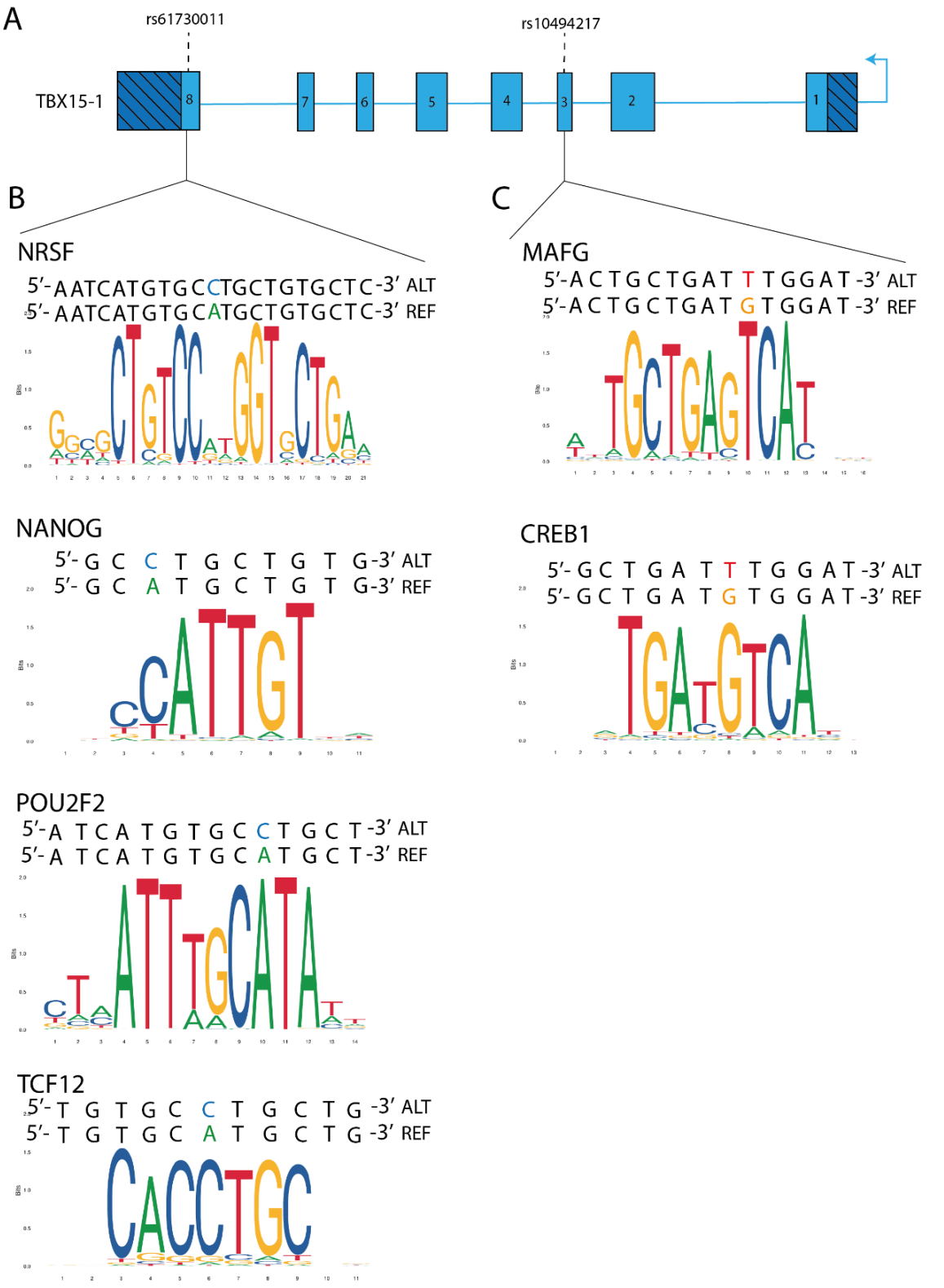

Figure 3.4. Altered transcription factor binding motifs (TFBMs) for rs10494217 and rs61730011. A. Schematic of the *TBX15-1* gene with location of rs10494217 (exon 3) and rs61730011 (exon 8). TFBMs from the JASPAR database were aligned to the sequence flanking (B) rs61730011 (reference allele 'A' green, alternate allele 'C' blue) and (C) rs10494217 (reference allele 'G' yellow, alternate allele 'T' red). Abbreviations: MAFG (Maf Bzip transcription factor G); CREB1 (CAMP-responsive element binding protein 1), NANOG (homeobox transcription factor), NRSF (neuron restrictive silencer factor), POU2F2 (POU class 2 transcription factor 2) and TCF12 (transcription factor 12).

3.2.2. *In silico* analysis of the protein-coding role of TBX15 coding SNPs

3.2.2.1. TBX15 protein sequence was conserved across vertebrate species

T-box TFs have been highly conserved throughout evolution, with paralogues of TBX15 identified in Drosophila (Dr-H15) and nematodes (ce-tbx-12) (Agulnik, Papaioannou and Silver, 1998). I first aimed to assess conservation of the TBX15 sequence across vertebrate species. TBX15 homologues were found in 205 vertebrate species ranging from birds, primates, marsupials, and fish. Large portions of sequence aligned to a minimum of 33%, particularly in the mid and C-terminal regions supporting important biological functions for these domains (Figure 3.5).

Next, I assessed sequency homology of the full-length human TBX15-1 protein sequence (602 amino acids; aa) with seven other vertebrate species (zebrafish, chicken, opossum, dog, mouse, marmoset and xenopus) using EMBL-EBI Clustal Omega. Alignments were highly conserved between these eight species, particularly in the T-box domain (95.6% between species; red box, Figure 3.6). The p.H156 and p.M566 residues were 100% conserved between these species, further highlighting a potentially functional role for these residues (blue boxes, Figure 3.6).

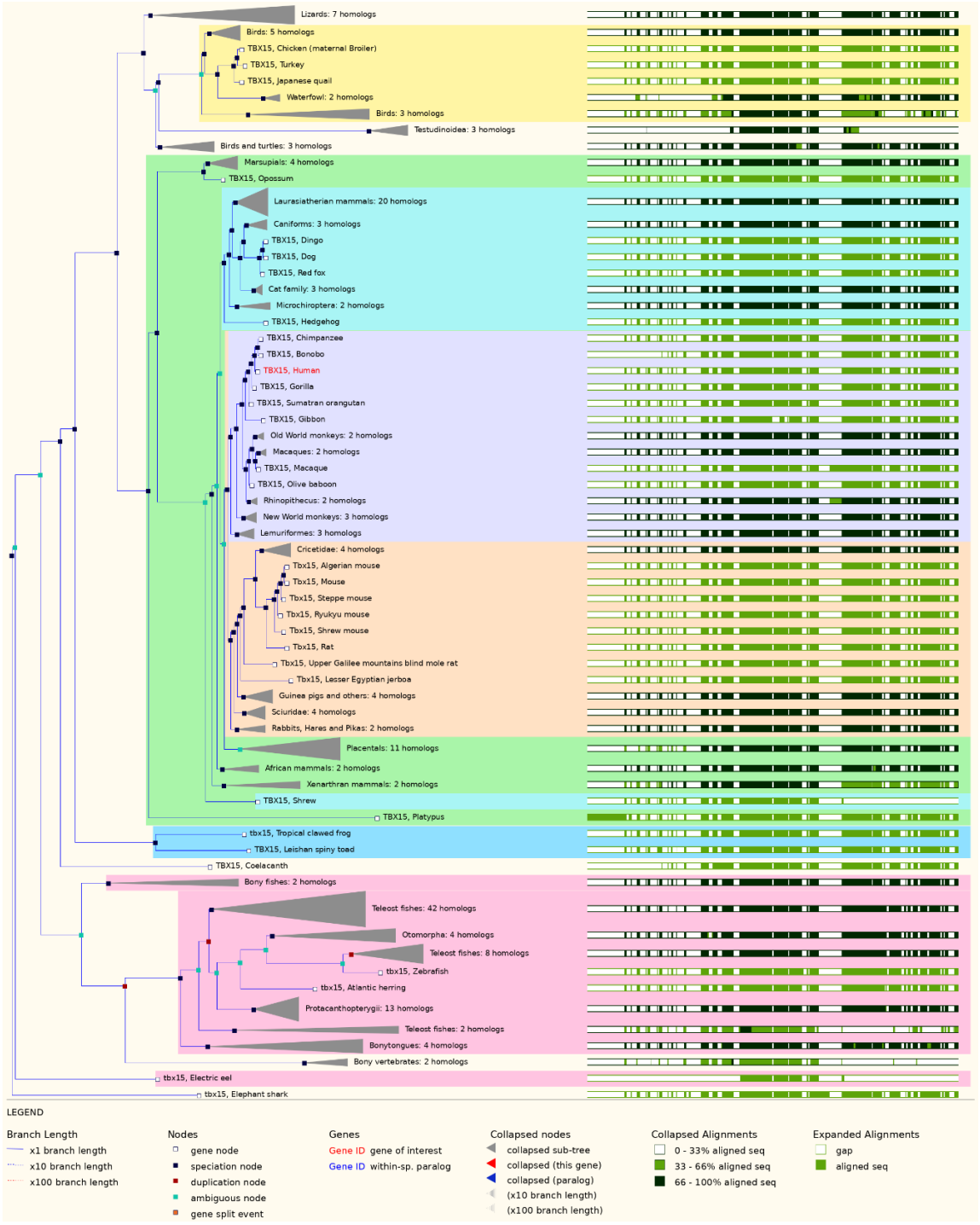

Figure 3.5. TBX15 taxonomy tree in 205 vertebrate species. Human TBX15 shown in red. Homologues were present in reptiles, birds, marsupials, monkeys, amphibians, and fish. Reproduced from Ensembl genome browser release v106 (Cunningham *et al.*, 2022).

Figure 3.6. Multiple sequence alignment of TBX15 protein between eight vertebrate species (next page). EMBL-EBI Clustal Omega sequence alignment output for human, zebrafish, chicken, opossum, dog, mouse, marmoset, and xenopus TBX15. Red box indicates T-box sequence (residues 115-304 *homo sapiens*), blue boxes denote residues H156 and M566. Alignment scores "*" fully conserved residue, ":" conservation between groups of strongly similar properties, roughly equivalent to scoring >0.5 in the Gonnet PAM 250 matrix (STA, NEQK, NHQK, NDEQ, QHRK, MILV, MILF, HY, FYW), "." conservation between groups of weakly similar properties, roughly equivalent to scoring ≤0.5>0 in the Gonnet PAM 250 matrix (CSA, ATV, SAG, STNK, STPA, SGND, SNDEQK, NDEQHK, NEQHRK, FVLIM, HFY).

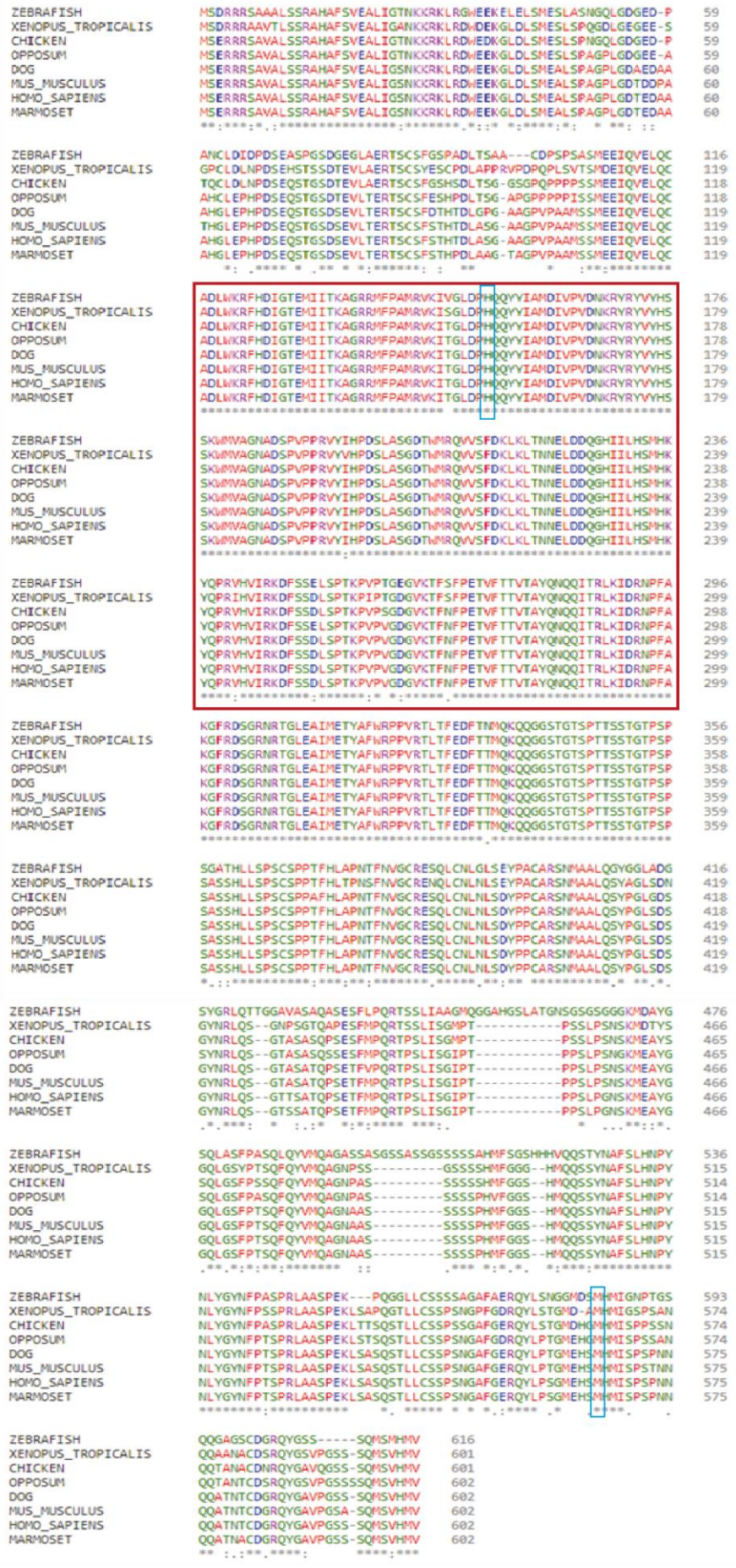
ZEBRAFISH
XENOPUS_TROPICALIS
CHICKEN
OPPOSUM
DOG
MUS_MUSCULUS
HOMO_SAPIENS
MARMOSET

3.2.2.2. Human and mouse had two full-length consensus TBX15 transcripts

I next aimed to determine a consensus TBX15 sequence for human and mouse as there were discrepancies in main transcript annotations between Ensembl and NCBI. Human TBX15 had three annotated protein-coding transcripts in the Ensembl database: TBX15-201 (496 aa), TBX15-202 (602 aa) and TBX15-203 (330 aa). Whereas four transcripts were annotated in the NCBI database: TBX15-1 (602 aa), TBX15-X1 (635 aa), TBX15-2 (496 aa) and TBX15-X2 (320 aa).

I aligned human TBX15 protein sequences using EMBL-EBI Clustal Omega. In both TBX15-1 and TBX15-202 (602 aa), and TBX15-2 and TBX15-201 (496 aa) comparisons 100% of residues aligned (Figure 3.7A, Table 3.3). Except for a 10 amino acid sequence at the 5' end of TBX15-203 (330 aa), 100% of amino acids aligned to the TBX15-X2 transcript (320 aa). The additional 10 amino acid sequence began with a glycine residue suggesting this additional sequence may have been incorrectly annotated as protein-coding. Both TBX15-203 and TBX15-X2 shared a unique 33 amino acid sequence not present in the longer (496 and 602 aa) TBX15 transcripts (Figure 3.7A, Table 3.3). Approximately 95% of residues in the TBX15-X1 (635 aa) transcript annotated in NCBI aligned to TBX15-202; this transcript also shared the 33 amino acid sequence in TBX15-X2 and TBX15-203 transcripts (Figure 3.7A, Table 3.3). As TBX15-X1 was computationally predicted as a unique transcript in NCBI, I considered TBX15-1, TBX15-2, and TBX15-X2 to be the consensus human protein sequences.

Similarly, there were differences in mouse TBX15 annotations between NCBI and Ensembl. NCBI annotated four TBX15 protein-coding transcripts (TBX15, TBX15-X1, TBX15-X2 and TBX15-X3), whereas Ensembl annotated three transcripts (TBX15-201, TBX15-202 and TBX15-203). TBX15 and TBX15-201 (602 aa) had 100% residue

alignment (Figure 3.7B, Table 3.4). TBX15-X1, TBX15-X2 and TBX15-X3 encoded identical 496 amino acid sequences; 28.43% and 10.28% of residues in TBX15-202 (141 aa) and TBX15-203 (51 aa) aligned to this 496 amino acid transcript due to sequence truncation at exon 5 and exon 3, respectively (Figure 3.7B, Table 3.4). As TBX15-X1, TBX15-X2 and TBX15-X3 produced identical protein sequences, and TBX15-202 and TBX15-203 annotations were truncated, I considered TBX15 and TBX15-X1 to be the consensus full-length mouse protein sequences.

Table 3.3. Alignment of amino acid residues in human TBX15 protein transcripts between NCBI and Ensembl annotations. Abbreviations: aa (amino acids).

NCBI transcript	Ensembl transcript	Alignment	Additional information
TBX15-2 (496 aa)	TBX15-201 (496 aa)	100% alignment	
TBX15-1 (602 aa)	TBX15-202 (602 aa)	100% alignment	
TBX15-X1 (635 aa)	TBX15-202 (602 aa)	94.64% alignment	TBX15-X1 had additional exon (33 aa)
TBX15-X2 (320 aa)	TBX15-203 (330 aa)	96.97% alignment	TBX15-203 had additional 10 aa at 5'- sequence

Table 3.4. Alignment of amino acid residues in mouse TBX15 protein transcripts between NCBI and Ensembl annotations. Abbreviations: aa (amino acids).

NCBI transcript	Ensembl transcript	Alignment	Additional information
TBX15 (602 aa)	TBX15-201 (602 aa)	100% alignment	
TBX15-X1 (496 aa)	TBX15-202 (141 aa)	28.43% alignment	TBX15-202 truncated at exon 5
TBX15-X2 (496 aa)			
TBX15-X3 (496 aa)			
TBX15-X1 (496 aa)	TBX15-203 (51 aa)	10.28% alignment	TBX15-203 truncated at exon 3
TBX15-X2 (496 aa)			
TBX15-X3 (496 aa)			

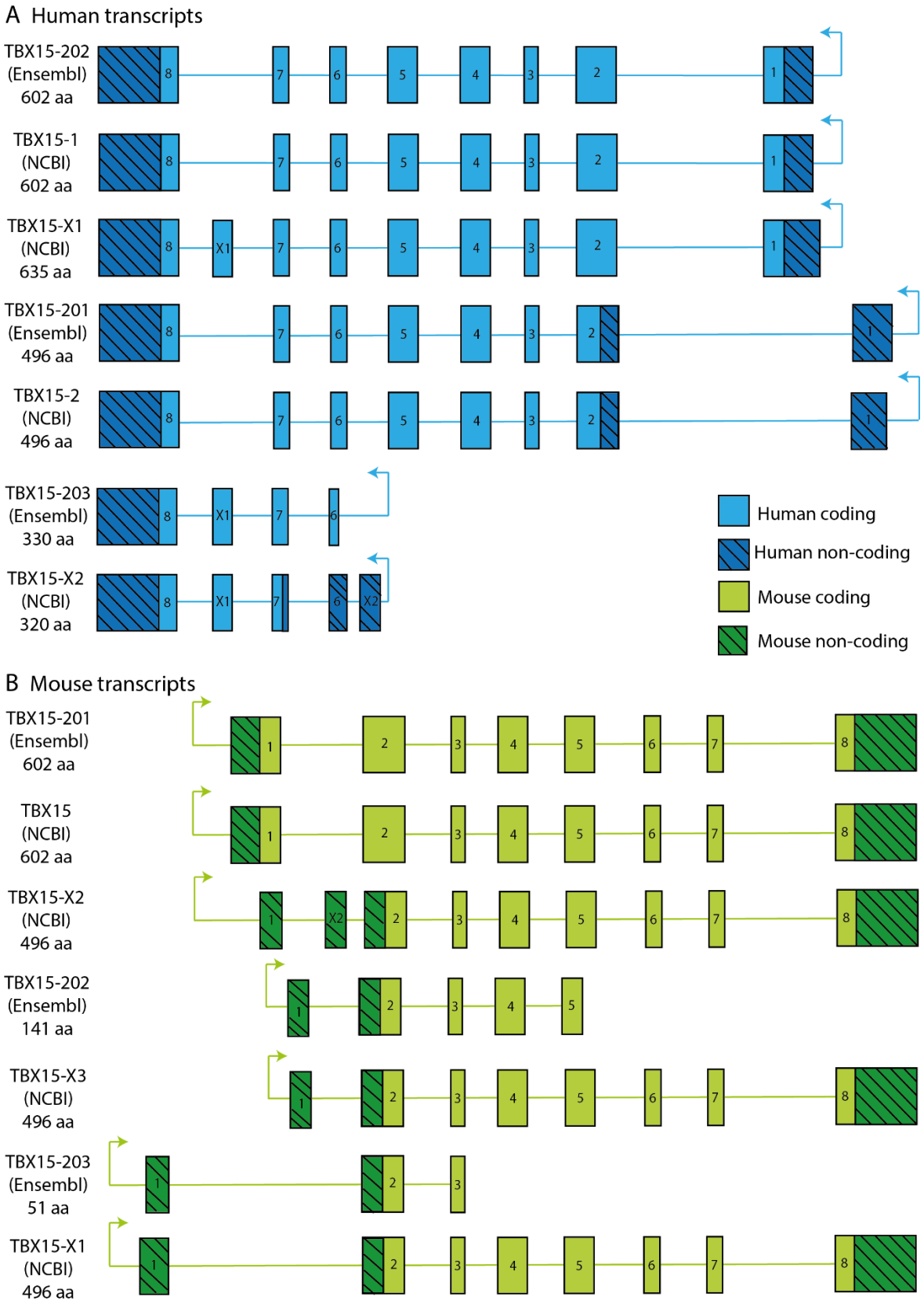

Figure 3.7. Schematic of human and mouse TBX15 protein transcripts. Schematic alignments of NCBI and Ensemble protein transcripts A. Human TBX15 protein transcripts (blue). B. Mouse TBX15 protein transcripts (green). Abbreviations: aa (amino acids).

Finally, I aimed to identify which protein transcript was predominantly expressed in human and mouse adipose tissues and adipocytes. Using EMBL-EBI MUSCLE, I aligned the protein sequences for human TBX15-1 (602 aa) and mouse TBX15 (602 aa), and human TBX15-2 (496 aa) and mouse TBX15-X1 (496 aa). TBX15-1 and TBX15 were conserved at 98.84% of residues (7 out of 602 mismatches; Figure 3.8A, Figure 3.9A), whilst TBX15-2 and TBX15-X1 were conserved at 98.99% of residues (5 out of 496 mismatches; Figure 3.8B, Figure 3.9A). In both comparisons, the mismatched residues were partially conserved based on property similarity (weak "." or strong ":").

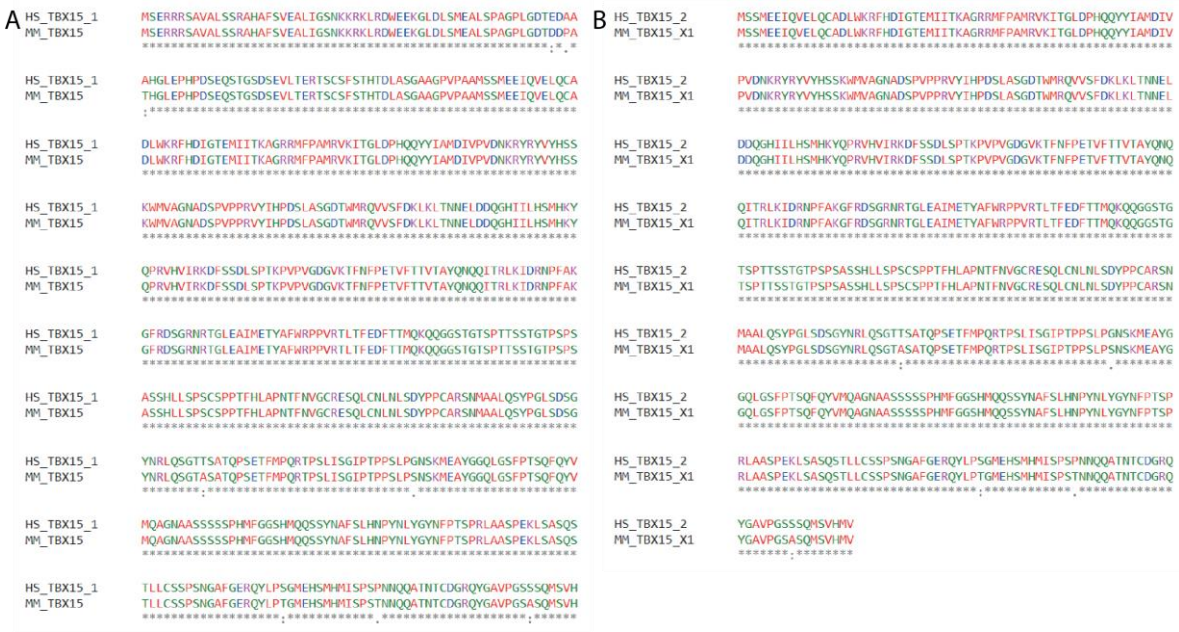

Figure 3.8. Alignment of full-length TBX15 protein transcripts between human and mouse. A-B EMBL-EBI MUSCLE sequence alignment for TBX15-1 and TBX15 (A), and TBX15-2 and TBX15-X1(B). Alignment scores for (A) and (B) "*" fully conserved residue, ":" conservation between groups of strongly similar properties, roughly equivalent to scoring >0.5 in the Gonnet PAM 250 matrix (STA, NEQK, NHQK, NDEQ, QHRK, MILV, MILF, HY, FYW), "." conservation between groups of weakly similar properties, roughly equivalent to scoring ≤0.5>0 in the Gonnet PAM 250 matrix (CSA, ATV, SAG, STNK, STPA, SGND, SNDEQK, NDEQHK, NEQHRK, FVLIM, HFY).

It was not possible to distinguish between transcripts in immunoblot analysis in either human cells or mouse muscle tissues due to the non-specificity of TBX15 antibodies (chapter 5, section 5.2.1.1.1). However, as the transcripts had unique first exons, it was possible to use read counts across these exons from RNA-sequencing experiments as a proxy for expression (data presented in chapter 5, section 5.2.2). Exon 1 of the 602 amino acid transcript had higher expression than the 496 amino acid transcript in both day 1 differentiated hWAT cells and mouse iWAT (Figure 3.9B and C, Table 3.5).

Further, I analysed nuclear localisation sequences (NLS) in the TBX15 protein transcripts using cNLS mapper. NLS were classified as either monopartite (consensus K(K/R)X(K/R) sequence) or bipartite (consensus (K/R)(K/R)X10-12(K/R)(K/R)(K/R) sequence) (Kosugi *et al.*, 2008, 2009). The TBX15-1 and TBX15 (602 aa) transcripts had an exclusively nuclear monopartite NLS in exon 1 (score 8.5), with several bipartite NLS (score 4) indicating these transcripts were exclusively nuclear (Figure 3.9B). The TBX15-2 and TBX15-X1 (496 aa) transcripts contained a monopartite NLS (score 2.5) and several bipartite NLS (score 2-4) indicating these transcripts were predominantly cytoplasmic (Figure 3.9B). I considered the human TBX15-1 and mouse TBX15 transcripts (602 aa) the most likely candidates for the main TBX15 protein transcripts, although *in vitro* work in this chapter uses both the full-length TBX15-1 (602 aa) and TBX15-2 (496 aa) human transcripts.

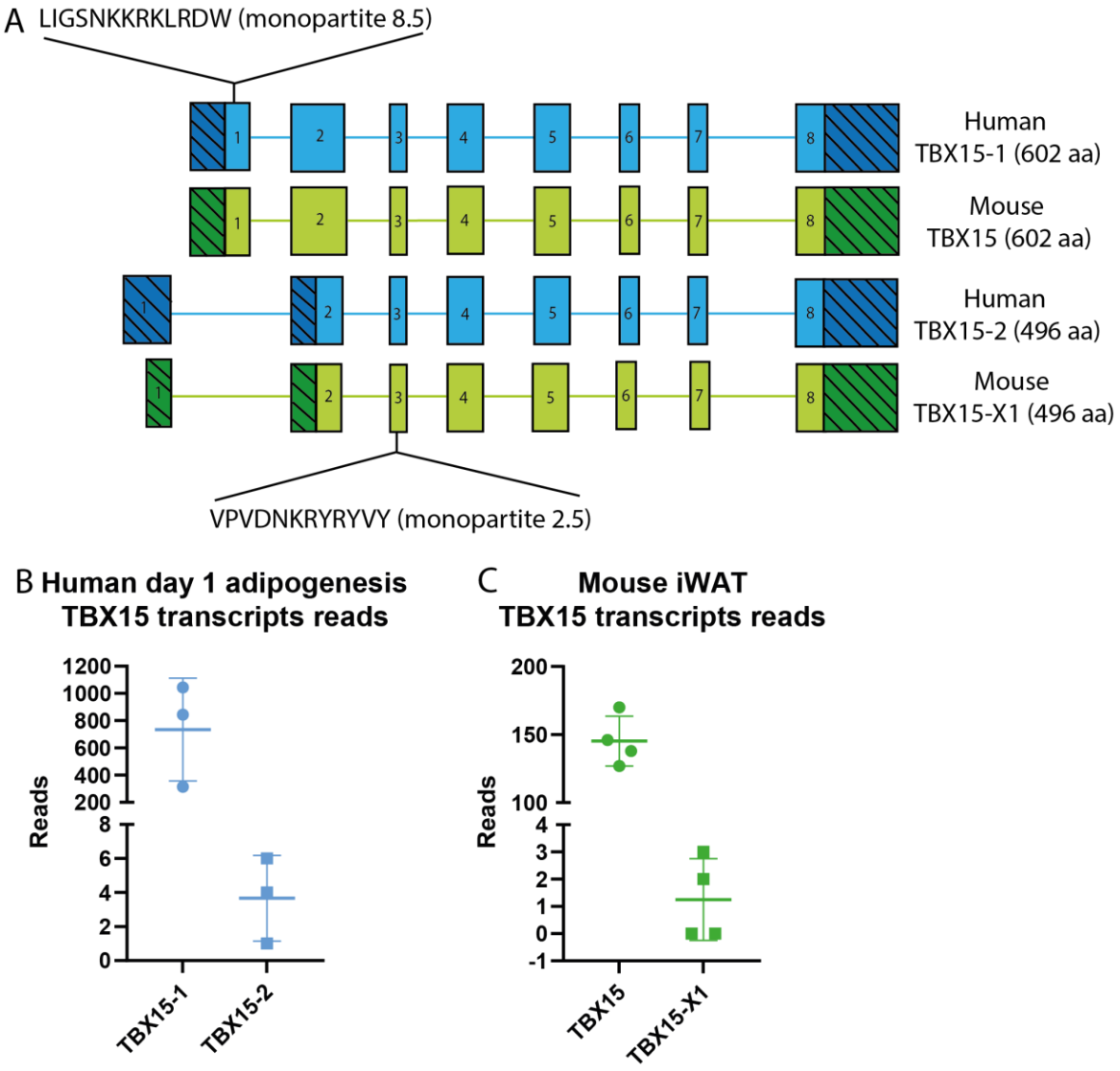

Figure 3.9. Alignment of full-length TBX15 transcripts between human and mouse. A. Schematic representation of human and mouse TBX15 protein transcript alignments with monopartite nuclear localisation sequences; scores >8 exclusively nuclear, 7-8 partially nuclear, 3-6 nuclear and cytoplasmic, and 1-2 exclusively cytoplasmic. B. Human *TBX15-1* and *TBX15-2* exon 1 transcript reads in differentiating hWAT cells at day 1 of adipogenesis (n=3). C. Mouse *Tbx15* and *Tbx15-X1* exon 1 transcript reads in iWAT (inguinal white adipose tissue) (n=4).

Table 3.5. Exon 1 read counts for human *TBX15* and mouse *Tbx15* transcripts. RNA-sequencing exon 1 reads from day 1 differentiating hWAT cells (n=3) and whole inguinal white adipose tissue from female *Tbx15*$^{+/+}$ mice (n=4) used as a proxy for individual transcript expression.

Species	Transcript	Read counts exon 1 (± standard deviation)
Human	*TBX15-1*	734.7 ± 377.1
	TBX15-2	3.667 ± 2.517
Mouse	*Tbx15*	145.3 ± 18.25
	Tbx15-X1	1.25 ± 1.5

3.2.2.3. p.M566R was predicted to have a more severe impact on TBX15 protein sequence than p.H156N

An alternative hypothesis to the *TBX15* coding SNPs altering a DNA-regulatory sequence was that rs10494217 and rs61730011 acted at a protein-coding level to alter TBX15 protein structure and its TF function. rs10494217 resides in exon 3 of TBX15-1 (p.H156N) and TBX15-2 (p.H50N), and rs61730011 lies in the terminal exon 8 of TBX15-1 (p.M566R) and TBX15-2 (p.M460R; Figure 3.10). To investigate the impact of these coding SNPs *in silico* on the TBX15 protein sequence, I used SIFT (Sim *et al.*, 2012), PolyPhen2 (Adzhubei *et al.*, 2010) and Condel (González-Pérez and López-Bigas, 2011) to predict the severity of the non-synonymous substitutions p.H156N and p.M566R.

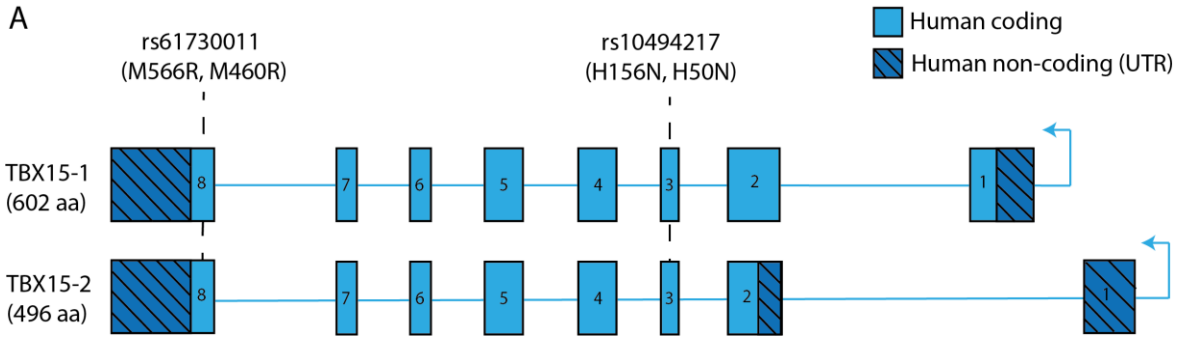

Figure 3.10. Amino acid substitutions for rs10494217 and rs61730011 in TBX15 protein-coding transcripts. TBX15-1 (602 aa, rs10494217=p.H156N, rs61730011=p.M566R) and TBX15-2 (496 aa, rs10494217=p.H50N, rs61730011=p.M460R). Abbreviations: aa (amino acids).

The p.H156N histidine to asparagine substitution was predicted to be well-tolerated in all three cases (Table 3.6). In contrast, the p.M566R methionine to arginine substitution was predicted to be deleterious by SIFT and PolyPhen2, but neutral by Condel (close to the cut-off value of 0.522; Table 3.6). Where available, prediction

scores for these substitutions in TBX15-2 were the same as for TBX15-1. These predictions suggested that p.M566R may have a more severe impact on TBX15 protein structure and TF function compared to p.H156N.

Table 3.6. Prediction scores for non-synonymous coding SNPs in TBX15 protein-coding transcripts using SIFT, PolyPhen2 and Condel. Scores: SIFT (range 0.0-1.0; 0.0-0.05=deleterious, 0.05-1.0=tolerated), PolyPhen2 (range 0.0-1.0; 0.0-0.15=benign, 0.15-1.0=possibly damaging, 0.8-1.0=probably damaging), Condel (range 0.0-1.0, 0.0-0.521=neutral, 0.522-1.0=deleterious).

Variant	SIFT		PolyPhen2		Condel	
	Prediction	**Score**	**Prediction**	**Score**	**Prediction**	**Score**
p.H156N	Tolerated	0.501	Benign	0.118	Neutral	0.475
p.M566R	Deleterious	0.019	Probably damaging	0.979	Neutral	0.509

3.2.2.4. p.H156N predicted to alter TBX15 T-box region loop structure

Whilst prediction methods such as SIFT, PolyPhen2 and Condel are widely used to predict non-synonymous amino acid substitutions, in isolation they cannot inform the structural impact of such substitutions. Therefore, a more nuanced approach, combining several prediction methods and 3D protein modelling, is required. To investigate if p.H156N and p.M566R altered TBX15 protein structure, I aimed to perform structural modelling of TBX15 *in silico.* Several crystallographic structures existed in the protein data bank (PDB) for T-box proteins, but not TBX15. Therefore, I chose to use a homology-based approach to model the TBX15 structure. I first aimed to generate a consensus 3D model for full-length TBX15-1 and TBX15-2 transcripts using: IntFOLD v5.0 and v6.0 (McGuffin *et al.*, 2019), Phyre v2.0 (Kelley *et al.*, 2015) and DMPfold v1.0 (Buchan and Jones, 2019; Greener, Kandathil and Jones, 2019).

Tertiary protein structures are represented *in silico* by coil (alpha helices) and arrow (β-sheet) structures connected by unstructured loops. For TBX15-1 and TBX15-2,

Phyre v2.0 and IntFOLD v5.0/v6.0 produced models ~200 amino acids in length containing structured alpha helices and β-sheets, surrounded by unstructured regions at both the N- and C-terminal (Appendix Figure 9.1A, C, D). DMPfold v1.0 only produced unstructured models with short alpha helices or β-sheets (~10 amino acids; Appendix Figure 9.1B). Even the TBX15-1 structure produced by the recently developed AlphaFOLD v2.0 database (Jumper *et al.*, 2021; Varadi *et al.*, 2022) was not a significant improvement on these models (Appendix Figure 9.1E). These full-length models had poor scores suggesting they were not reliable 3D models (Appendix Table 9.9).

To improve model predictions, I segregated TBX15-1 and TBX15-2 sequences into N-terminal (residues 1-306 (TBX15-1) and 1-200 (TBX15-2)) and C-terminal (residues 307-602 (TBX15-1), and 201-496 (TBX15-2)) regions. N-terminal regions containing the T-box had improved 3D models and associated scores, whilst the C-terminal regions remained poorly modelled (Appendix Figure 9.2, Table 9.10). This likely resulted from the alignment strategy of homology-based modelling which heavily relies on a template structure, which in this case was limited to the T-box domain.

The concordance of TBX15 3D models between servers was still not sufficient to generate a consensus model. Therefore, I further refined my modelling approach by using the T-box region (amino acid residues 115-304 (TBX15-1), Pfam prediction). The Phyre v2.0 server produced a well-folded T-box model, with 62% sequence ID with the TBX1 (4a04B) template, and 100% confidence (Figure 3.11A, Table 3.7). The top T-box models produced by IntFOLD v5.0 and v6.0 had global model quality scores of 0.5372 (p=3.94E-8) and 0.6431 (p=2.775E-13), respectively, suggesting high confidence in these models (Figure 3.11C and D, Table 3.7). The AlphaFold v2.0 T-box model had

very high and certain residue scores for >90% residues with no unstructured regions (Figure 3.11E, Table 3.7). When aligning all server models of the T-box sequence it was clear that there was a high degree of similarity in the predicted structures particularly for alpha helices and β-sheet structures, with only a subtle difference in an unstructured loop region between two β-sheets (white star, Figure 3.11F). This demonstrated a consensus structure across the five servers that could be reliably used for further *in silico* modelling in this chapter.

The amino acid substitution p.H156N was within the TBX15 T-box domain, therefore, I produced models with this polymorphism for comparison with wildtype structures. All servers showed p.H156N altered a loop structure within the T-box (Figure 3.12). Introduction of p.H156N into the Phyre v2.0 model did not change the % confidence or % sequence ID compared to the wildtype model (Table 3.7). The IntFold v5.0 p.H156N model had a slightly increased global model score (0.5388), and more certain p-value (p=3.5832E-8) compared to the wildtype model (Table 3.7). However, in the IntFOLD v6.0 p.H156N model there was a small reduction in both global model quality score (0.6421) and p-value (p=3.453E-13; Table 3.7). As p.M566R existed within exon 8 it was not possible to produce a useable *in silico* model of this polymorphism due to the lack of complete full-length models produced with these template-based approaches (Appendix Figure 9.1). I predicted the conformational T-box region alteration resulting from p.H156N could therefore impact TBX15 protein binding, either in forming protein-protein dimers or binding to target DNA sites.

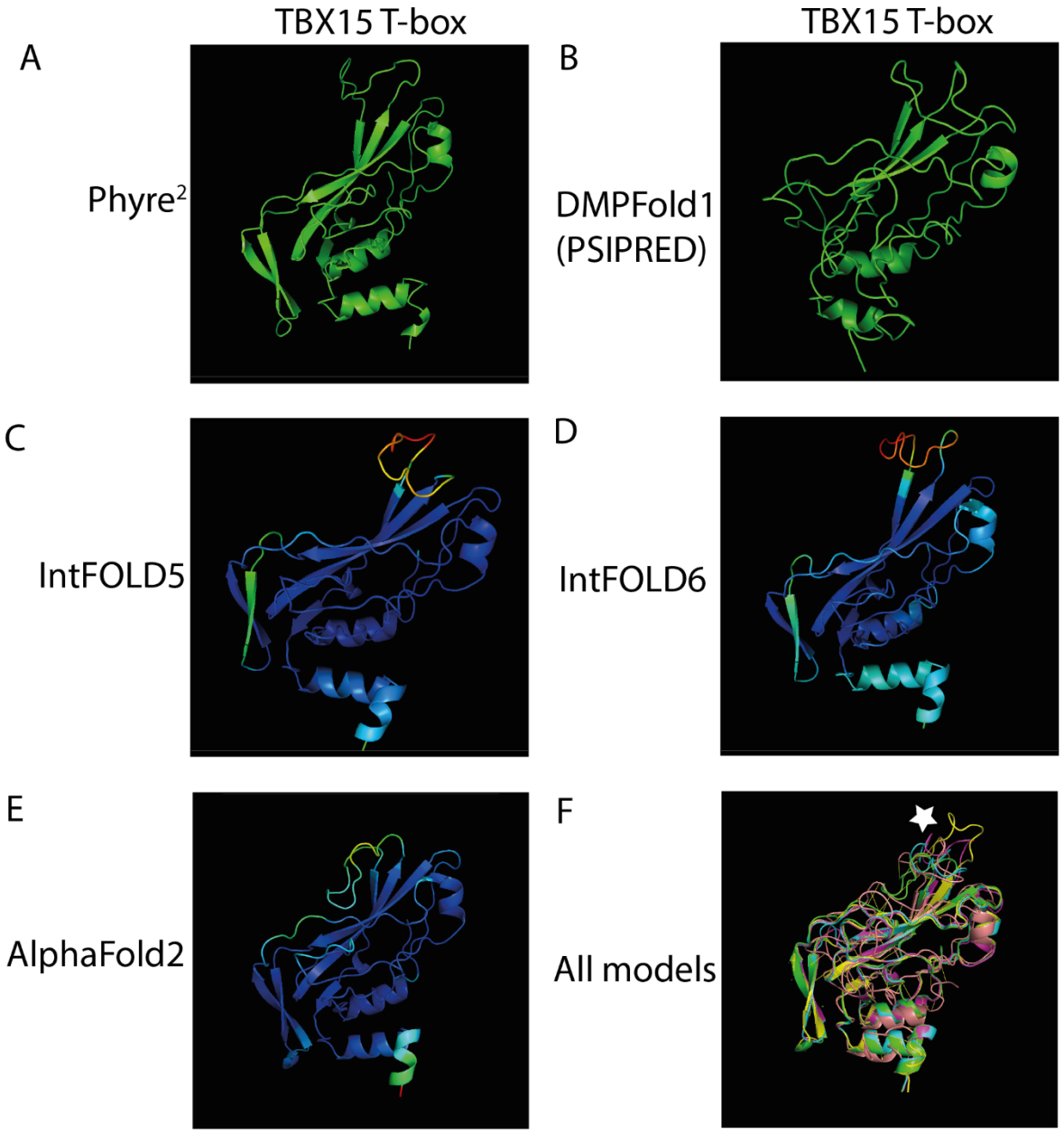

Figure 3.11. Comparison of 3D TBX15 T-box protein models between several homology modelling servers. A. Phyre v2.0, B. DMPFold v1.0 C. IntFOLD v5.0, D. IntFOLD v6.0, E. AlphaFOLD v2.0 and F. alignment of all models (green: AlphaFold v2.0, cyan: IntFOLD v5.0, magenta: IntFOLD v6.0, yellow: Phyre v2.0, and salmon: DMPFold v1.0). For C-E residues were coloured by residue accuracy predictions using reverse colour scheme - blue high accuracy, through green, yellow and orange to red low accuracy: IntFOLD v5.0/6.0 residue accuracy predictions (Angstroms), and AlphaFold v2.0 per-residue confidence score. White star indicates unstructured loop region in protein-protein binding region that exhibits subtle prediction difference between servers.

Table 3.7. Associated scores for TBX15 3D T-box protein models. IntFOLD v5.0 and v6.0 produced scores between 0-1: scores <0.2 indicate incorrectly modelled regions, scores >0.4 indicate models close to native structure of template. This is combined with a p-value that represents probability of incorrect models: p<0.001 (certain=less than 1/1000 incorrect models), p<0.01 (high=less than 1/100 incorrect models), p<0.05 (medium=less than 1/20 incorrect models), p<0.1 (low=less than 1/10 incorrect models), p≥0.1 (uncertain=more than 1/10 incorrect models). AlphaFold v2.0 produced a per-residue confidence score (pLDDT) between 0 and 100. Very high (pLDDT>90), confident (pLDDT≤90>70), low (pLDDT≤70>50), very low (pLDDT≤50). Phyre v2.0 confidence represents the probability (0-100) that the model is a true homology match to template, % sequence ID between model and template (above 30% is considered a good match, although low % ID models with high confidence can still be useful). DMPfold v1.0 does not provide "scoring" information for models.

Server	TBX15 model	PDB model used as template	Score	p-value (confidence)
Phyre v2.0	TBOX	4a04B (TBX1)	62% sequence ID	100% confidence
	TBOX-H156N	4a04B (TBX1)	62% sequence ID	100% confidence
DMPfold v1.0	TBOX	N/A (not given)	N/A (not given)	N/A (not given)
	TBOX-H156N	N/A (not given)	N/A (not given)	N/A (not given)
IntFOLD v5.0	TBOX	1h6fB (TBX3), 2x6uA (TBX5)	0.5372	3.94E-8 (certain)
	TBOX-H156N	1h6fB (TBX3), 4a04A (TBX1)	0.5388	3.582E-8 (certain)
IntFOLD v6.0	TBOX	1h6fB (TBX3), 2x6uA (TBX5)	0.6431	2.775E-13 (certain)
	TBOX-H156N	1h6fB (TBX3), 2x6uA (TBX5)	0.6421	3.453E-13 (certain)
AlphaFold v2.0	TBOX	N/A (*ab initio* modelling)	pLDDT >70	N/A

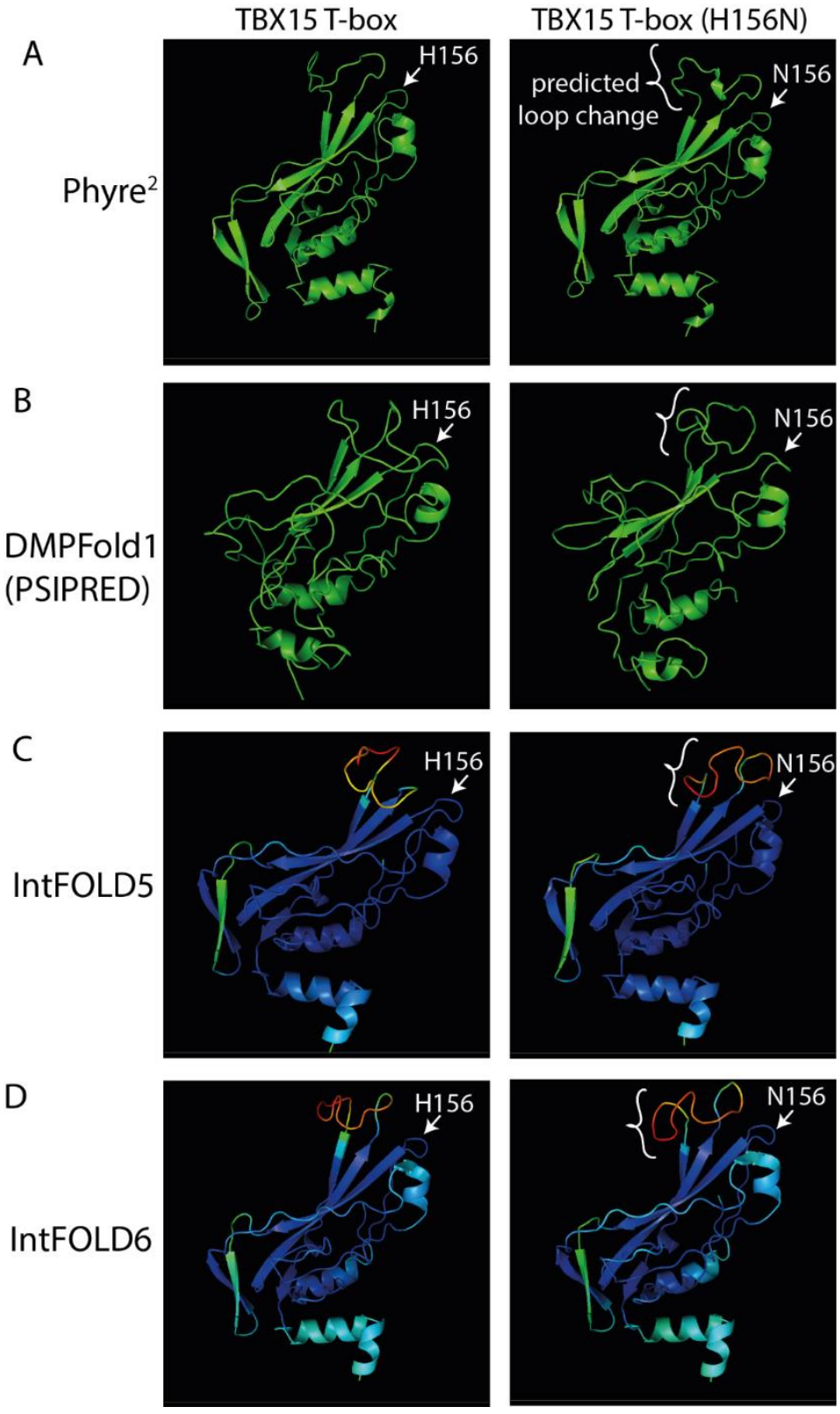

Figure 3.12. Comparative 3D protein models of TBX15 T-box structure with both alleles of rs10494217 (p.H156N). A. Phyre v2.0, B. DMPFold v1.0 C. IntFOLD v5.0, D. IntFOLD v6.0. "{" indicates the predicted loop change resulting from p.H156N. For C and D residues were coloured by residue accuracy predictions using reverse colour scheme - blue high accuracy, through green, yellow and orange to red low accuracy: IntFOLD v5.0/6.0 residue accuracy predictions (Angstroms), and AlphaFold2 per-residue confidence score.

3.2.2.5. p.H156N was predicted to alter conformation of TBX15-TBX15 and TBX15-TBX18 dimers

T-box proteins form homo- and hetero-dimers, as has been shown *in vitro* for TBX15 and TBX18 (Farin *et al.*, 2007). As p.H156N was predicted to alter T-box structure, I hypothesised that this substitution would alter TBX15 protein dimerisation, and consequently its TF function. To investigate this *in* silico, I used HADDOCK v2.4 (De Vries, Van Dijk and Bonvin, 2010; Van Zundert *et al.*, 2016) to predict TBX15 dimerisation, with itself as homodimers and with TBX18 as heterodimers.

Firstly, I aimed to select a template structure for generating dimer models. I aligned TBX15 and TBX18 T-box homology models (IntFOLD v6.0) to PDB T-box structures for human TBX3 (1h6f), Brachyury (T; 6f58), TBX5 (2x6v), and mouse Tbet (5t1j) using PyMOL v2.3. I used protein-protein interface information in PDBSum (Table 3.8) (Laskowski *et al.*, 2018) to select equivalent residues in TBX15 and TBX18 (Figure 3.13A). TBX15 and TBX18 amino acid residues were considered equivalent if they were within 5 bp of the amino acid residue in the template sequence and were the same amino acid or an amino acid with similar physio-chemical properties.

I initially produced several iterations of each TBX15-TBX15 and TBX15-TBX18 model using each template and compared dimers produced in the top clusters to determine the most favourable models based on *Z*-scores. Dimer models produced using TBX3 (1h6f) and T (6f58) as templates were orientated comparably to the template model (Figure 3.14). When comparing *Z*-scores for both TBX15-TBX15 and TBX15-TBX18 dimer models, using T (6f58) to determine the residues involved in binding produced clusters with the most negative *Z*-scores (-2.3 and -2.1, respectively; Table 3.9, Table

3.10). Therefore, I used the TBX15 dimer models produced using T (6f58) as a template for all future *in silico* modelling in this chapter.

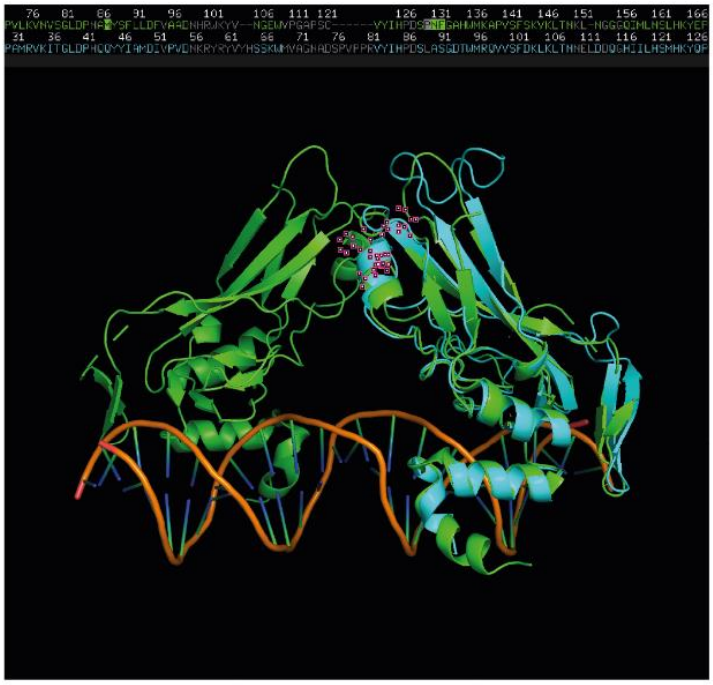

Figure 3.13. Example HADDOCK protein-protein docking strategy. A. View of PyMOL interface with Brachyury (T) T-box (6f58; green) homodimer bound to DNA, and TBX15 T-box (cyan) aligned to chain A of 6f58 to guide selection of active amino acids for protein-protein docking.

Table 3.8. Protein-protein interacting residues for T-box family proteins. Residues in chain A and B involved in protein-protein binding accessed from PDBSum (Laskowski *et al.*, 2018). Chain A and B residues correspond to the PDB structure and were used to guide equivalent residue selections in TBX15 and TBX18. Passive residues were automatically defined by HADDOCK v2.4.

PDB structure	Chain A residues involved in protein-protein binding	Chain B residues involved in protein-protein binding	Submitting authors
1h6f (TBX3)	Leu 241	Asn 238	(Coll, Seidman and Müller, 2002)
6f58 (Brachyury; T)	Met 87, Pro 130, Asn 131, Phe 132, Val 175	Met 87, Pro 130, Asn 131, Phe 132, Val 175	Newman *et. al.* (unpublished; submitted 2017)
2x6v (TBX5)	Gly 53, Ile 54, Pro 108, Asp 111, Ala 127, Pro 129, Ala 130, Met 131, Pro 132, Thr 199, Ala 200, Phe 201, Cys 202, Thr 203, His 204, Val 205	Glu 52, Asp 111, Ala 127, Pro 129, Ala 130, Met 131, Pro 132, Arg 182, Thr 199, Ala 200, Phe 201, Cys 202, Thr 203, His 204, Val 205	(Stirnimann *et al.*, 2010)
5t1j (Tbet)	His 182, Arg 184, Gln 194, Met 214, Pro 215, Asn 217, Arg 218, Leu 219, Ser 225, Pro 226, Asn 253, Val 254, Thr 255, Gln 256, Val 275, Asn 276, Asp 277, Gly 278, Glu 279, Thr 289	His 182, Tyr 183, Arg 184, Gln 194, Ser 213, Met 214, Pro 215, Gly 216, Asn 217, Arg 218, Leu 219, Tyr 220, Pro 223, Ser 225, Pro 226, Asn 253, Val 254, Thr 255, Gln 256, Gln 267, Val 275, Asn 276, Asp 277, Ala 286, Thr 289	(Liu *et al.*, 2016)

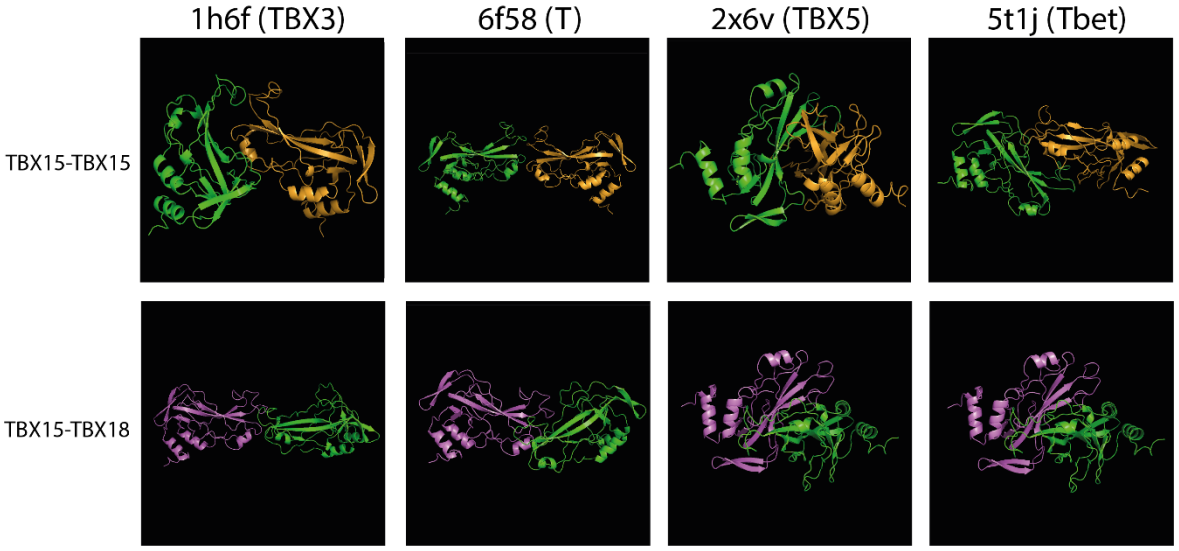

Figure 3.14. Optimisation of *in silico* protein-protein docking TBX15 and TBX18 T-box dimerisation models. PDB crystallographic structures for TBX3 (1h6f), T (6f58), TBX5 (2x6v) and Tbet (5t1j) were used as templates to determine amino acid residues in TBX15 and TBX18 involved in dimer formation. Key: TBX15 chain A (green), TBX15 chain B (orange), TBX18 (violet).

Table 3.9. Optimised TBX15-TBX15 T-box homodimer models *in silico*. The top cluster from each PDB structure used to optimise docking protocol. Active residues in TBX15 chains based on information in PDBSum for each crystallographic structure used as a template. Clusters represent a 3D energy landscape of how molecules come together in space and defines the energetically most favourable combination of structures. The HADDOCK scores were made up of RMSD (root-mean-square deviation of the distance between atoms), Van der Waals, electrostatic, desolvation, and restraints violation energies. Clusters were ranked by HADDOCK score, with more negative values being considered the most accurate models. *Z*-scores represent the standard deviation of the HADDOCK score for a cluster from the mean of all clusters, with more negative *Z*-scores considered more favourable (De Vries, Van Dijk and Bonvin, 2010; Van Zundert *et al.*, 2016).

	TBX family PDB model used as template for amino acid residues involved in protein-protein docking			
	1h6f (TBX3)	**6f58 (Brachyury; T))**	**2x6v (TBX5)**	**5t1j (mouse Tbet)**
Active residues chain 1 (TBX15)	L141	Q44, P86, D87, K135	P53, D55, S76, P77, P79, G152, V153, K154, T155, F156, N157	Q44, Y46, N56, P79, R81, V82, L89, G116, H117, K135, D136, F137, S138, S139, V149
Active residues chain 2 (TBX15)	S139	Q44, P86, D87, K135	D55, S76, P77, P79, R129, G152, V153, K154, T155, F156, N157	Q44, Y45, Y46, N56, P77, P79, P80, R81, V82, Y83, P86, L89, G116, H117, Q127, K135, D136, F137, P146, V149
Total number of structures (total clusters)	149 (12)	107 (12)	187 (8)	173 (15)
HADDOCK score	-66.3 +/- 13.6	-80.3 +/- 4.2	-148.6 +/- 10.7	-91.7 +/- 10.3
Cluster size	5	7	13	19
RMSD from the overall lowest-energy structure	1.2 +/- 0.7	2.1 +/- 1.4	0.6 +/- 0.3	8.9 +/- 0.2
Van der Waals energy	-32.5 +/- 9.1	-26.3 +/- 3.3	-114.6 +/- 15.6	64.0 +/- 6.1
Electrostatic energy	-149.3 +/- 71.6	-242.4 +/- 40.3	-161.5 +/- 35.3	-114.7 +/- 31.2
Desolvation energy	-4.6 +/- 2.8	-5.4 +/- 8.2	-4.5 +/- 1.4	-20.3 +/- 2.3
Restraints violation energy	7.2 +/- 9.4	0.0 +/- 0.0	27.9 +/- 15.2	155.4 +/- 35.2
Buried Surface Area	1332.4 +/- 159.3	1088.0 +/- 28.1	3171.7 +/- 133.1	1816.8 +/- 179.9
***Z*-Score**	-1.8	-2.3	-1.7	-1.5

Table 3.10. Optimised TBX15-TBX18 T-box heterodimer models *in silico*. The top cluster from each PDB structure used to optimise protocol. Active residues in TBX15 and TBX18 chains based on information in PDBSum for each crystallographic structure used as a template. Clusters represent a 3D energy landscape of how molecules come together in space and defines the energetically most favourable combination of structures. The HADDOCK scores were made up of RMSD (root-mean-square deviation of the distance between atoms), Van der Waals, electrostatic, desolvation, and restraints violation energies. Clusters were ranked by HADDOCK score, with more negative values being considered the most accurate models. *Z*-scores represent the standard deviation of the HADDOCK score for a cluster from the mean of all clusters, with more negative *Z*-scores considered more favourable (De Vries, Van Dijk and Bonvin, 2010; Van Zundert *et al.*, 2016).

	TBX family PDB model used as template for amino acid residues involved in protein-protein docking			
	1h6f (TBX3)	**6f58 (Brachyury; T))**	**2x6v (TBX5)**	**5t1j (mouse Tbet)**
Active residues chain 1 (TBX15)	L141	Q44, P86, D87, S88, V132	P53, D55, A74, S76, P77, V78, P79, D151, G152, V153, K154, T155, F156, N157	Q44, Y45, Y46, N56, P77, V78, P79, P80, R81, V82, Y83, P86, S88, L89, G116, H117, Q127, K135, D136, F137, P146, V149
Active residues chain 2 (TBX18)	S142	Q44, P86, D87, S88, V132	D55, A74, S76, P77, V78, P79, R129, E151, G152, V153, K154, A155, F156, S157	H42, Y46, N56, P77, V78, P80, R81, V82, S88, P89, D114, Q115, G116, H117, K135, D136, C137, G138, D139, G152
Total number of structures (total clusters)	133 (7)	103 (13)	168 (9)	145 (6)
HADDOCK score	-82.3 +/- 1.3	-78.5 +/- 6.3	-124.3 +/- 5.6	-114.6 +/- 0.9
Cluster size	89	16	36	9
RMSD from the overall lowest-energy structure	1.1 +/- 0.7	7.9 +/- 0.7	0.6 +/- 0.4	19.0 +/- 0.2
Van der Waals energy	-24.3 +/- 2.2	-40.5 +/- 5.1	-71.0 +/- 4.6	-64.1 +/- 5.3
Electrostatic energy	-286.3 +/- 16.3	-215.3 +/- 17.3	-322.1 +/- 42.9	-338.8 +/- 58.5
Desolvation energy	-0.8 +/- 1.3	3.8 +/- 2.1	6.5 +/- 4.9	4.9 +/- 5.2
Restraints violation energy	0.0 +/- 0.0	12.6 +/- 21.0	46.8 +/- 13.9	123.1 +/- 41.2
Buried Surface Area	910.5 +/- 7.4	1331.0 +/- 32.6	2413.3 +/- 88.7	2774.3 +/- 86.4
***Z*-Score**	-2.1	-2.1	-1.8	-1.7

Next, I aimed to model the impact of p.H156N on TBX15 dimerisation, using T (6f58) as a template. Introduction of p.H156N in one chain of TBX15 resulted in a more negative *Z*-score than two wildtype chains in both TBX15-TBX15 and TBX15-TBX18 models (Figure 3.15, Table 3.11). Conversely, two p.H156N chains in TBX15-TBX15 homodimers resulted in a less negative *Z*-score than wildtype models (Figure 3.15, Table 3.11). Further, p.H156N affected the orientation, but did not prevent binding, of the two interacting chains in all dimer models (Figure 3.15). Comparing all *in silico* investigations, the most plausible mechanism-of-action for the rs10494217 (p.H156N) variant was through altering the structure of the encoded TBX15 protein. The resulting changes in protein-protein docking model suggested a heterozygous gain-of-function mechanism-of-action that may further impact the TF function of TBX15 potentially through altering recognition of, or binding-affinity to, target DNA sequences.

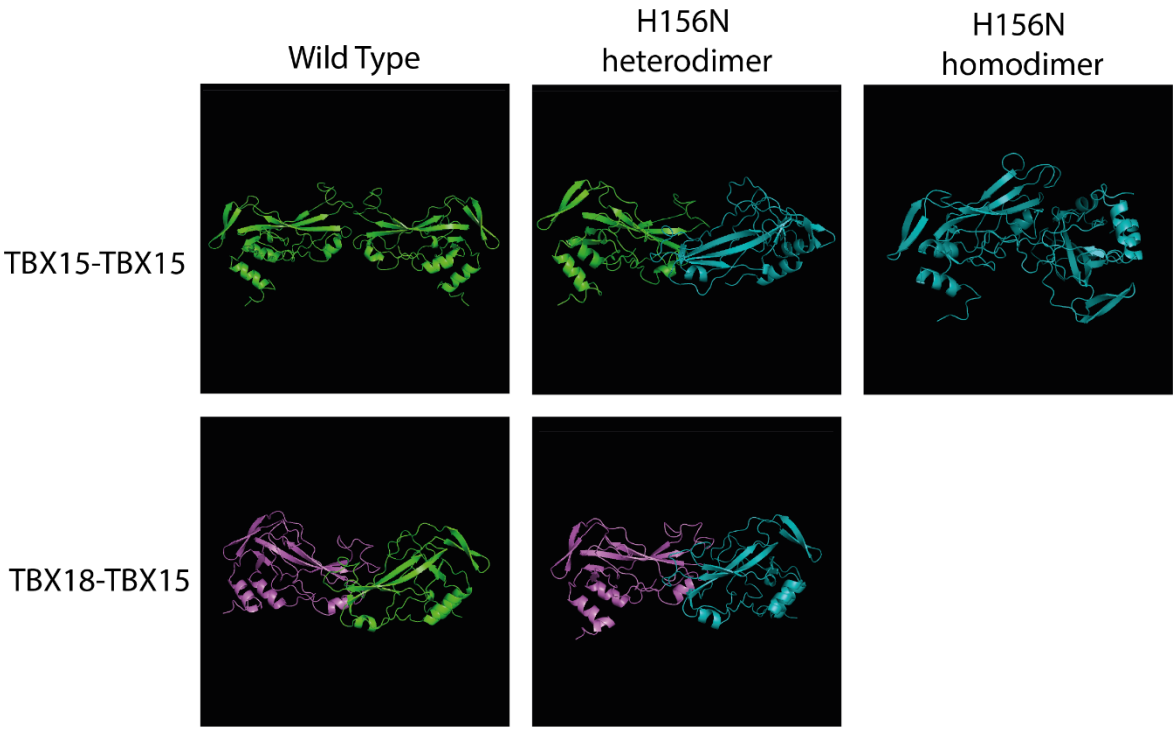

Figure 3.15. Impact of p.H156N on TBX15-TBX15 and TBX15-TBX18 dimers *in silico*. T (6f58) was used as the template to select amino acid residues involved in dimer formation. Key: TBX15 (green), TBX15-H156N (blue), TBX18 (violet).

Table 3.11. Impact of p.H156N on TBX15-TBX15 and TBX15-TBX18 dimers *in silico*. T (6f58) was used as a template to select amino acid residues involved in dimer formation. Top cluster scores from each model. Clusters represent a 3D energy landscape of how molecules come together in space and defines the energetically most favourable combination of structures. The HADDOCK scores were made up of RMSD (root-mean-square deviation of the distance between atoms), Van der Waals, electrostatic, desolvation, and restraints violation energies. Clusters were ranked by HADDOCK score, with more negative values being considered the most accurate models. *Z*-scores represent the standard deviation of the HADDOCK score for a cluster from the mean of all clusters, with more negative *Z*-scores considered more favourable (De Vries, Van Dijk and Bonvin, 2010; Van Zundert *et al.*, 2016).

	TBX15 protein-protein dimer model				
	TBX15-TBX15	**TBX15-TBX15-H156N**	**TBX15-H156N-TBX15-H156N**	**TBX18-TBX15**	**TBX18-TBX15-H156N**
Active residues chain 1	Q44, P86, D87, K135	Q44, P86, D87, S88, K135	Q44, P86, D87, S88	Q44, P86, D87, S88, V132	Q44, P86, D87, S88, V132
Active residues chain 2	Q44, P86, D87, K135	Q44, P86, D87, S88	Q44, P86, D87, S88	Q44, P86, D87, S88, V132	Q44, P86, D87, S88, V132
Total number of structures (total clusters)	107 (12)	144 (11)	136 (13)	103 (13)	90 (9)
HADDOCK score	-80.3 +/- 4.2	-96.3 +/- 1.1	-82.6 +/- 5.4	-78.5 +/- 6.3	-87.8 +/- 3.8
Cluster size	7	61	7	16	22
RMSD from the overall lowest-energy structure	2.1 +/- 1.4	0.8 +/- 0.5	0.9 +/- 0.5	7.9 +/- 0.7	2.1 +/- 0.6
Van der Waals energy	-26.3 +/- 3.3	-51.6 +/- 2.3	-39.8 +/- 6.7	-40.5 +/- 5.1	-46.2 +/- 5.5
Electrostatic energy	-242.4 +/- 40.3	-263.4 +/- 8.6	-279.3 +/- 42.9	-215.3 +/- 17.3	-250.6 +/- 34.8
Desolvation energy	-5.4 +/- 8.2	8.0 +/- 2.5	11.1 +/- 4.0	3.8 +/- 2.1	5.9 +/- 3.1
Restraints violation energy	0.0 +/- 0.0	0.3 +/- 0.3	20.0 +/- 9.2	12.6 +/- 21.0	25.2 +/- 23.2
Buried Surface Area	1088.0 +/- 28.1	1653.6 +/- 75.9	1750.5 +/- 101.5	1331.0 +/- 32.6	1652.3 +/- 91.8
Z-Score	-2.3	-2.5	-1.2	-2.1	-1.9

3.2.3. *In vitro* validation of the impact of p.H156N and p.M566R on TBX15 transcription factor function

3.2.3.1. Generation and validation of HA- and Myc-tagged TBX15 and TBX18 cDNA constructs in HEK293T cells

Based on *in silico* prioritisation, I showed that the coding SNP rs10494217 (p.H156N/p.H50N) may alter TBX15 T-box protein structure by altering loop structures in protein-protein-interacting regions, resulting in altered dimer affinity. I hypothesised that this would impact its TF function and regulation of downstream target genes associated with adipogenesis and body composition. Although *in silico* modelling of rs61730011 (p.M566R/p.M460R) in the C-terminal region was not possible using homology template modelling, this domain is regarded as functionally important (Farin *et al.*, 2007; Lausch *et al.*, 2008). Therefore, I hypothesised that p.M566R may also act to alter TBX15 protein structure and TF function, although potentially through alternate mechanisms such as regulating protein stability.

To test this *in vitro*, I first aimed to generate cDNA expression constructs for TBX15 and TBX18 with different expression tags. Commercially available human TBX15-2 (496 aa isoform) and TBX18 cDNA constructs with a C-terminal Myc-DDK tag were purchased, and either p.H50N or p.M460R were further introduced into separate TBX15-2 constructs by site-directed mutagenesis (Figure 3.16A). Sanger sequencing was performed to confirm only the desired base edit had been introduced into the cDNA constructs (Figure 3.16B). All constructs were then sub-cloned into a C-terminal HA-tag expression vector by PCR amplification, restriction enzyme digestion and ligation (Figure 3.16C).

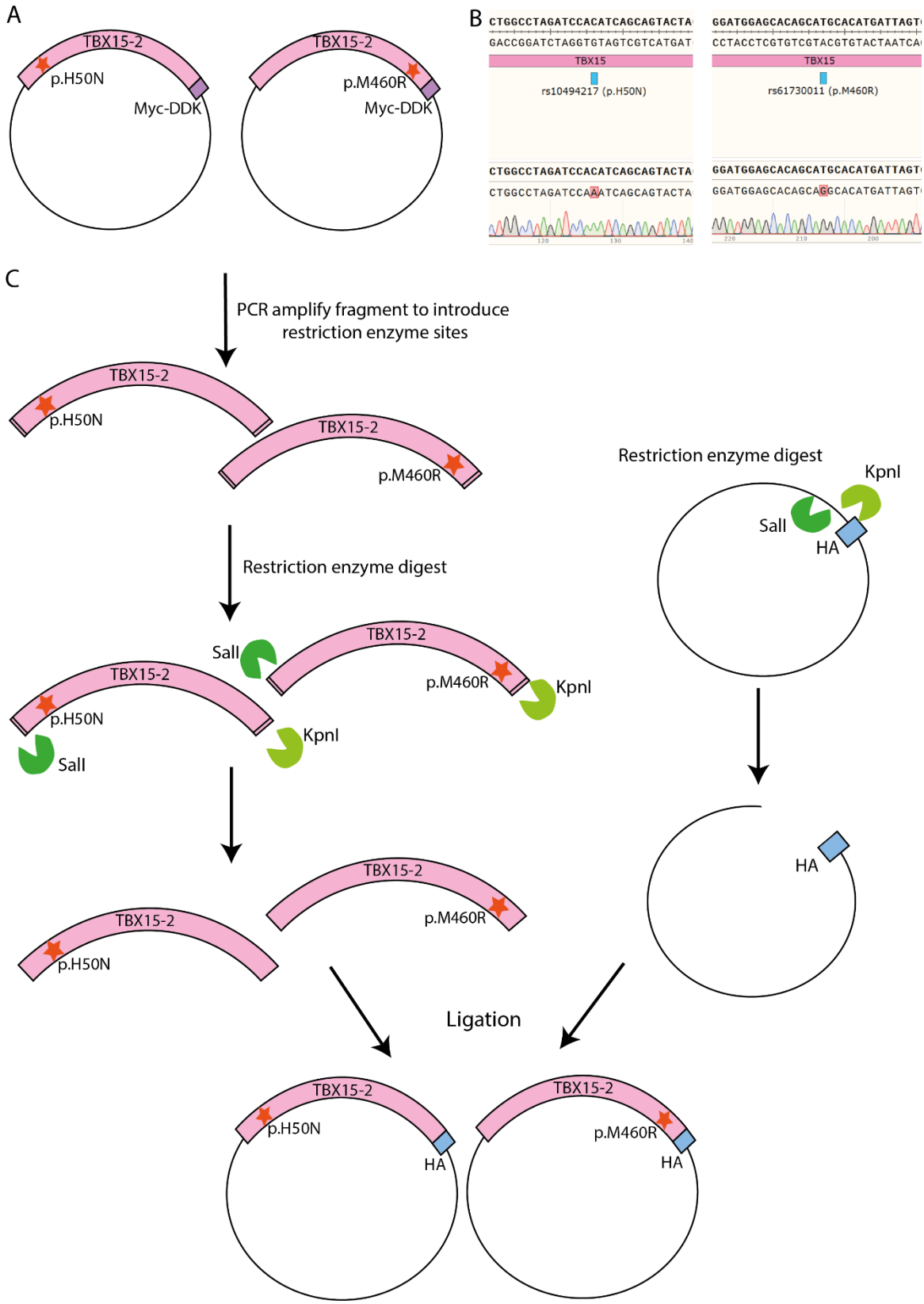

Figure 3.16. Schematic representation of cloning strategies for TBX15-2. A. Schematic of TBX15-2-Myc vector with location of p.H50N or p.M460R (star) introduced into the cDNA sequence by site-directed mutagenesis. B. Sanger sequencing alignments for p.H50N and p.M460R to confirm desired base edits. C. Representative sub-cloning of TBX15-2 sequence, amplified by PCR to introduce SalI and KpnI restriction sites, restriction enzyme digestion and ligation into the pCMV-HAC vector.

To validate expression of Myc- and HA-tagged TBX15-2 and TBX18 constructs for downstream experiments, expression vectors were transiently transfected in HEK293T cells for 24 hours and lysed for total protein. Protein samples were separated by SDS-PAGE, and immunoblotting was performed against the HA and Myc tags. All HA-tagged TBX15-2 and TBX18 expression constructs were clearly detected by immunoblot with no HA detected in the untransfected control lane (Figure 3.17A). All Myc-tagged TBX15-2 and TBX18 constructs were also clearly detected. However, endogenous Myc was additionally detected in these samples as evidenced by the ~98 kDa band present in the untransfected control lane (Figure 3.17B). As there was a clear difference in separation of this band on the gel compared to the TBX15-2 and TBX18 bands, it was deemed unlikely to interfere with further quantitative experiments.

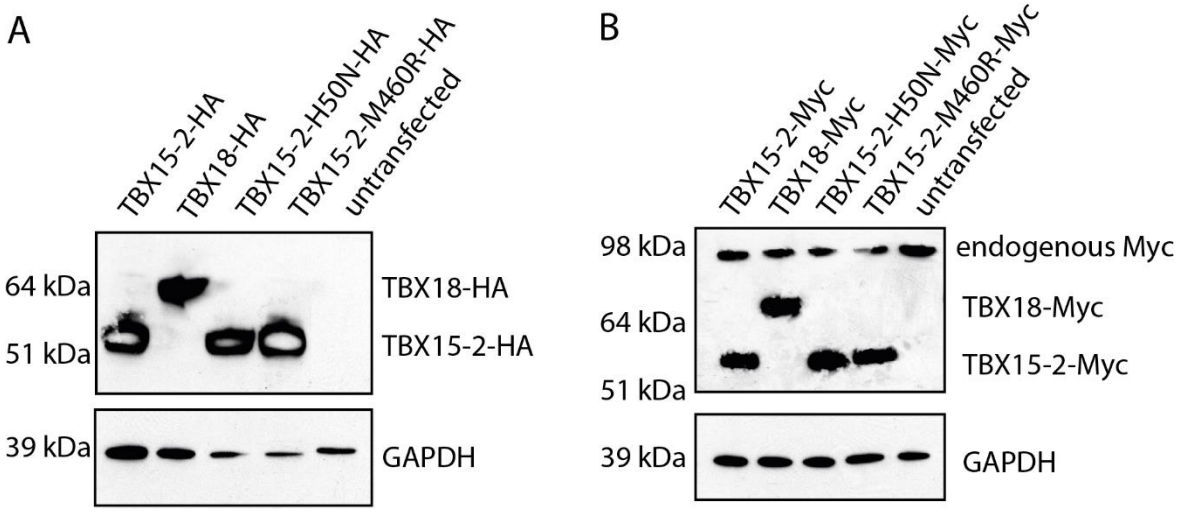

Figure 3.17. Validation of TBX15-2 and TBX18 target expression in HEK293T cells by immunoblotting. A. Western blot against HA (1:5000). B. Western blot against Myc (1:1000). In both cases GAPDH (1:10,000) was used as a loading control.

3.2.3.2. TBX15 immunoprecipitations using sepharose G beads showed non-specific binding in IgG control

TBX15 forms heterodimer complexes with its T-box sub-family member TBX18 in the absence of DNA *in vitro* (Farin *et al.*, 2007). To investigate the effect of p.H50N and p.M460R on dimer formation, I performed co-immunoprecipitation experiments for the tagged TBX15-2 and TBX18 constructs. I initially optimised transfection of HEK293T cells using different concentrations of Lipofectamine™ 3000 reagent and determined the optimal amount of protein lysate for immunoprecipitation. Following this, I immunoprecipitated protein lysates containing HA- and Myc-tagged TBX15-2 and TBX18 constructs with either non-specific protein sepharose G beads with a HA antibody or rabbit IgG antibody, or with anti-Myc protein sepharose G beads. I determined that optimal immunoprecipitations were achieved with 500 µg protein lysate precipitated with the HA antibody.

To quantify the effect of p.H50N and p.M460R on protein dimerisation, I co-expressed Myc-tagged TBX15-2, TBX15-2-H50N and TBX15-2-M460R constructs with either HA-tagged TBX15-2 or TBX18 constructs in HEK293T cells and lysed cells for total protein. A total of 500 µg cell lysate was immunoprecipitated with either HA or rabbit IgG primary antibody. Samples were separated by SDS-PAGE and the HA and Myc tags were simultaneously probed for by immunoblot. TBX15-2-H50N-Myc and TBX15-2-M460R-Myc were immunoprecipitated in complex with both TBX15-2-HA and TBX18-HA (right hand portion of blot, Figure 3.18A and B, respectively). However, the TBX15-2-HA signal was very strong, and saturation of the TBX15-2-HA band was visible (Figure 3.18A). Further, TBX15-2-HA and TBX18-HA bands were also both detected in the IgG control sample (IgG control lane, Figure 3.18A and B, respectively). This indicated non-specific binding of these overexpression constructs to the

sepharose G beads themselves, which may have been partly exacerbated by overloading of HA-tagged protein. Further investigation showed this non-specific binding was also seen in IgG control immunoprecipitations for co-transfected TBX15-2-Myc and TBX15-2-HA, and TBX15-2-Myc and TBX18-HA samples.

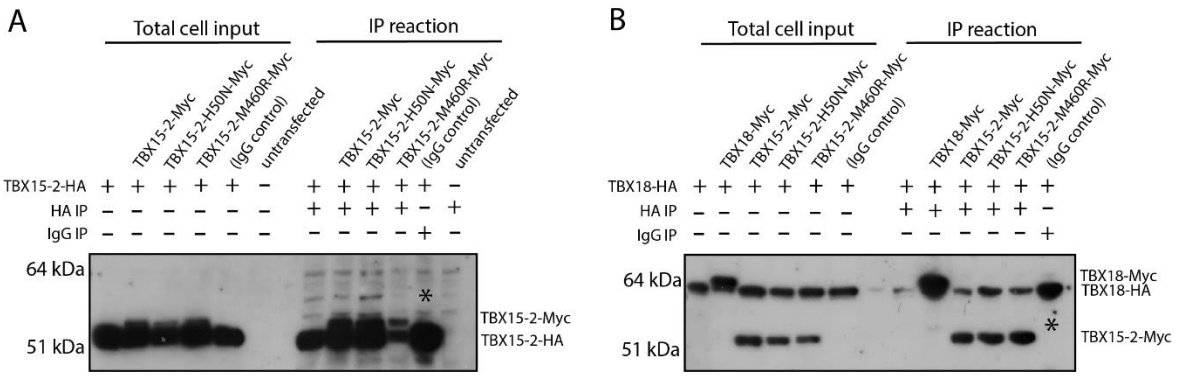

Figure 3.18. Representative immunoblot for sepharose G bead immunoprecipitation. A. TBX15-2-HA and TBX15-2-Myc co-immunoprecipitation, * non-specific binding of TBX15-2-HA to sepharose G beads in IgG control immunoprecipitation (primary antibody dilutions HA 1:100,000 and Myc 1:1000). B. TBX15-2-Myc and TBX18-HA co-immunoprecipitation, * non-specific binding of TBX18-HA to sepharose G beads in IgG control immunoprecipitation (primary antibody dilutions HA 1:50,000 and Myc 1:1000). Abbreviations: IP (immunoprecipitation).

3.2.3.3. Optimisation of magnetic co-immunoprecipitation systems for quantification of TBX15 protein dimers

I next sought to overcome the issues of non-specific binding by using a magnetic immunoprecipitation system where magnetic beads were coupled to HA, Myc or control IgG antibodies. Using magnetic immunoprecipitation bead kits offered several advantages, for example as the antibodies were covalently bound to the beads, they enabled higher yield and specificity for target capture. Additionally, sample elution was performed under low pH and non-reducing conditions which prevented antibody leaching. Finally, as the antibodies used for the beads were raised in mouse, I used primary antibodies raised in rabbit for immunoblotting to reduce cross-reactivity.

To compare the sepharose G and magnetic immunoprecipitation systems, I immunoprecipitated 500 μg cell lysate with magnetic beads and separated samples by SDS-PAGE for simultaneous HA and Myc immunoblot detection. TBX15-2-HA and TBX15-2-Myc were clearly immunoprecipitated in a complex (homodimerisation) in both HA and Myc immunoprecipitations (Figure 3.19A). TBX15-2-HA was also immunoprecipitated in a complex with TBX18-Myc (heterodimerisation) in both HA and Myc immunoprecipitations (Figure 3.19B), but TBX15-2-Myc was not detected in complex with TBX18-HA in either HA or Myc immunoprecipitations (Figure 3.19C). There was some non-specific binding of HA constructs detected in both IgG and bead-only controls. However, this appeared to be absent in some samples, or minimal and much less than the specific immunoprecipitation signal. The untransfected HEK293T samples showed no HA or Myc expression in any of the immunoprecipitation reaction lanes indicating this method reduced the detection of background expression from endogenous Myc in these cells (Figure 3.19D).

Next, I aimed to optimise the magnetic immunoprecipitation system to reduce overloading and non-specific binding in the negative control reactions. To achieve this, I immunoprecipitated 250 μg and 100 μg total cell lysate and detected HA and Myc simultaneously by immunoblot (Figure 3.20). For TBX15-2-HA complexed with TBX15-2-Myc, both HA and Myc constructs were detected in the 250 μg input HA, but not Myc, immunoprecipitation. In the 100 μg input immunoprecipitations only TBX15-2-HA was detected in the HA immunoprecipitation and TBX15-2-Myc was detected in the Myc immunoprecipitation (Figure 3.20A). This was also true for TBX18-HA complexed with TBX15-2-Myc (Figure 3.20B). For TBX18-Myc complexed with TBX15-2-HA, both constructs were detected in the 250 μg and 100 μg HA immunoprecipitation samples, but only TBX18-Myc was detected in the Myc

immunoprecipitation (Figure 3.20C). For all reaction complexes there was a complete absence of non-specific bands detected in the control IgG and bead samples (Figure 3.20A-C). The untransfected HEK293T samples showed no HA or Myc expression in any of the immunoprecipitation reactions, as seen previously (Figure 3.20D).

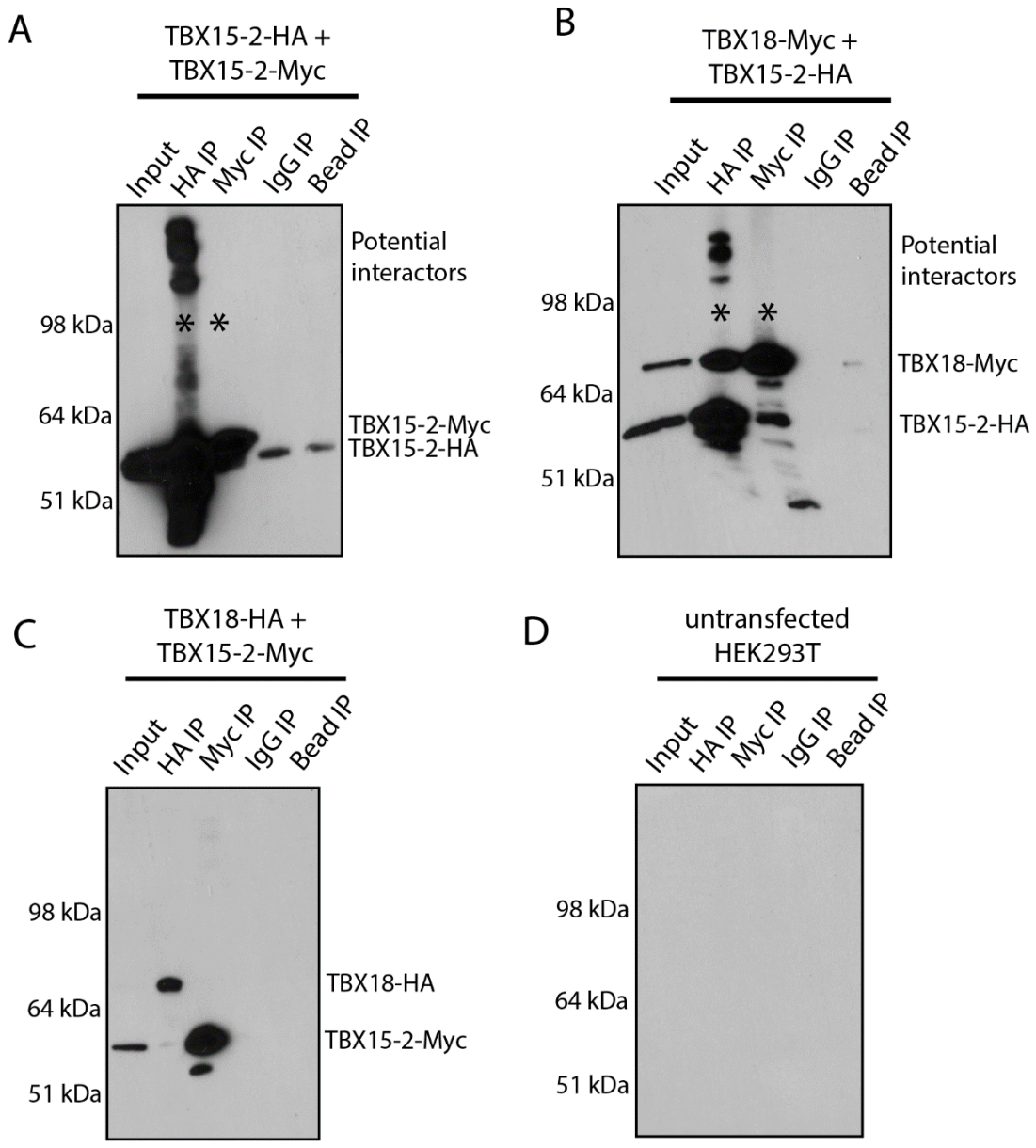

Figure 3.19. Initial magnetic co-immunoprecipitation optimisation. A-D. Western blots showing HA, Myc, mouse-IgG and bead immunoprecipitations using 500 µg input of protein lysate. A. TBX15-2-HA and TBX15-2-Myc. B. TBX15-2-HA and TBX18-Myc. C. TBX15-2-Myc and TBX18-HA. D. Untransfected HEK293T (primary antibody dilutions HA 1:100,000 and Myc 1:1000) for blots A-D. * indicates lanes with successful co-immunoprecipitation of both HA- and Myc-tagged constructs. Abbreviations: IP (immunoprecipitation).

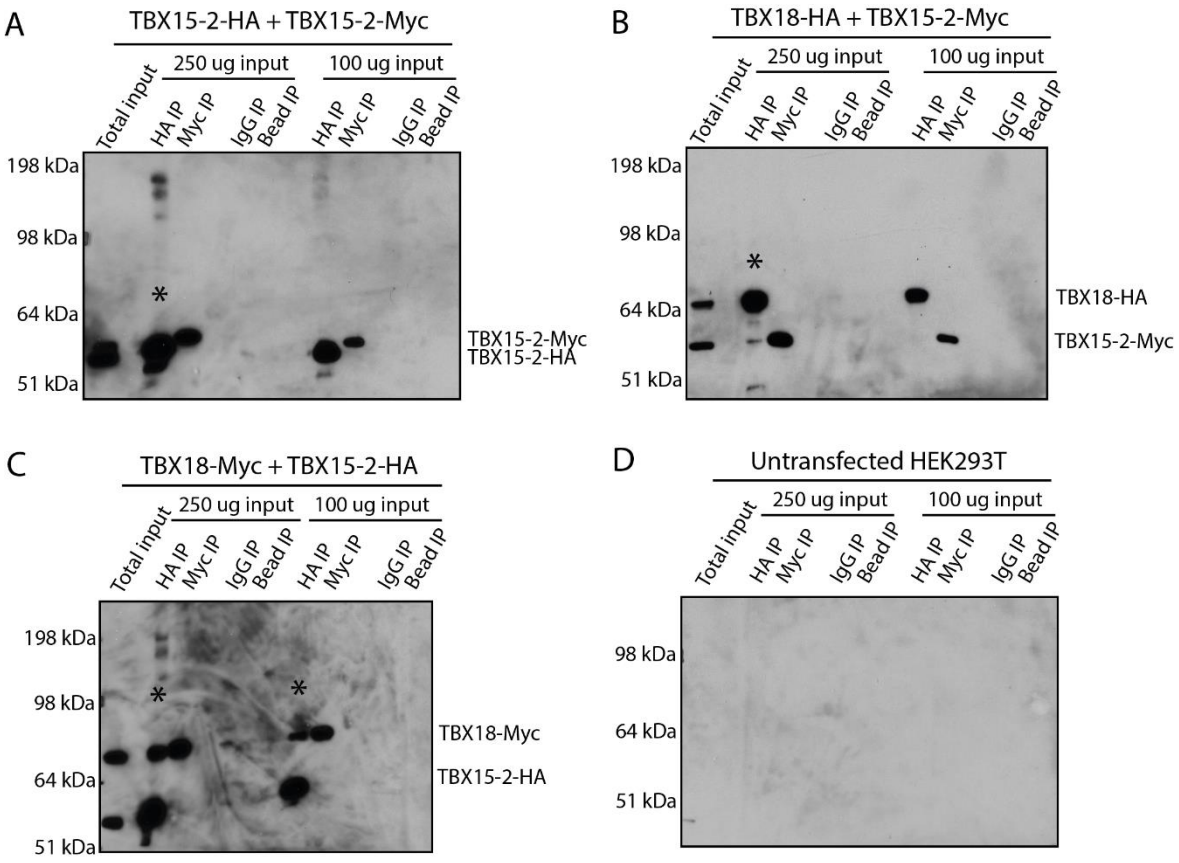

Figure 3.20. Magnetic co-immunoprecipitation optimisation for protein lysate input. A-D. Western blots for HA, Myc, mouse IgG and bead 250 µg or 100 µg input protein immunoprecipitations. A. TBX15-2-HA and TBX15-2-Myc (primary antibody dilutions HA 1:100,000 and Myc 1:1000). B. TBX15-2-Myc and TBX18-HA (primary antibody dilutions HA 1:50,000 and Myc 1:1000). C. TBX15-2-HA and TBX18-Myc (primary antibody dilutions HA 1:100,000 and Myc 1:1000). D. Untransfected HEK293T (primary antibody dilutions HA 1:100,000 and Myc 1:1000). * Indicates lanes with successful co-immunoprecipitation of both HA- and Myc-tagged constructs. Abbreviations: IP (immunoprecipitation).

Due to the weak detection of some complexes, I aimed to improve immunoblot detection of samples through two approaches. Firstly, by utilising the longer TBX15-1 protein transcript, and secondly, by optimising primary antibody concentrations for immunoblot detection. I sub-cloned a custom-made TBX15-1-Myc-DDK construct into the C-terminal HA vector, with the expectation that the increased size of this protein (~64 kDa compared to ~51 kDa for TBX15-2) would improve separation issues from using HA- and Myc-tagged TBX15-2 (~2kDa size difference) during SDS-PAGE.

Using these HA- and Myc-tagged TBX15-1 constructs, in addition to TBX15-2 and TBX18 constructs, I co-transfected HEK293T cells and immunoprecipitated 250 µg protein lysates. From this I separated 10 µL, 5 µL and 2.5 µL of immunoprecipitation elute samples by SDS-PAGE for immunoblotting. Replacing one TBX15-2 transcript with TBX15-1 in the TBX15-TBX15 immunoprecipitations improved SDS-PAGE separation of bands (Figure 3.21A and B). However, immunoprecipitation of both TBX15 proteins was only confirmed for TBX15-1-Myc complexed with TBX15-2-HA in the Myc immunoprecipitation (10 µL elute; Figure 3.21B). Reducing the amount of protein loaded to 5 µL or 2.5 µL was no longer sufficient to detect both TBX15 proteins. Similarly, for TBX15-TBX18 complexes, the only successful detection for both proteins was in the HA immunoprecipitation of TBX18-Myc and TBX15-2-HA (10 µL elute); again, reducing the amount of protein was no longer sufficient to detect both proteins (Figure 3.21D).

For TBX15-1-HA immunoprecipitated with TBX15-2-Myc, TBX15-1-HA was only detected in the HA immunoprecipitation and TBX15-2-Myc was only detected in the Myc immunoprecipitation (Figure 3.21A). Further, for TBX18-HA immunoprecipitated with TBX15-2-Myc, TBX18-HA was only detected in the HA immunoprecipitation and TBX15-2-Myc was only detected in the Myc immunoprecipitation (Figure 3.21C). Taken together, these data highlighted that detection of TBX15 dimers using immunoprecipitation was not consistent, possibly due to the low affinity nature of these interactions with co-precipitation more apparent when the overexpressed protein concentrations were highest.

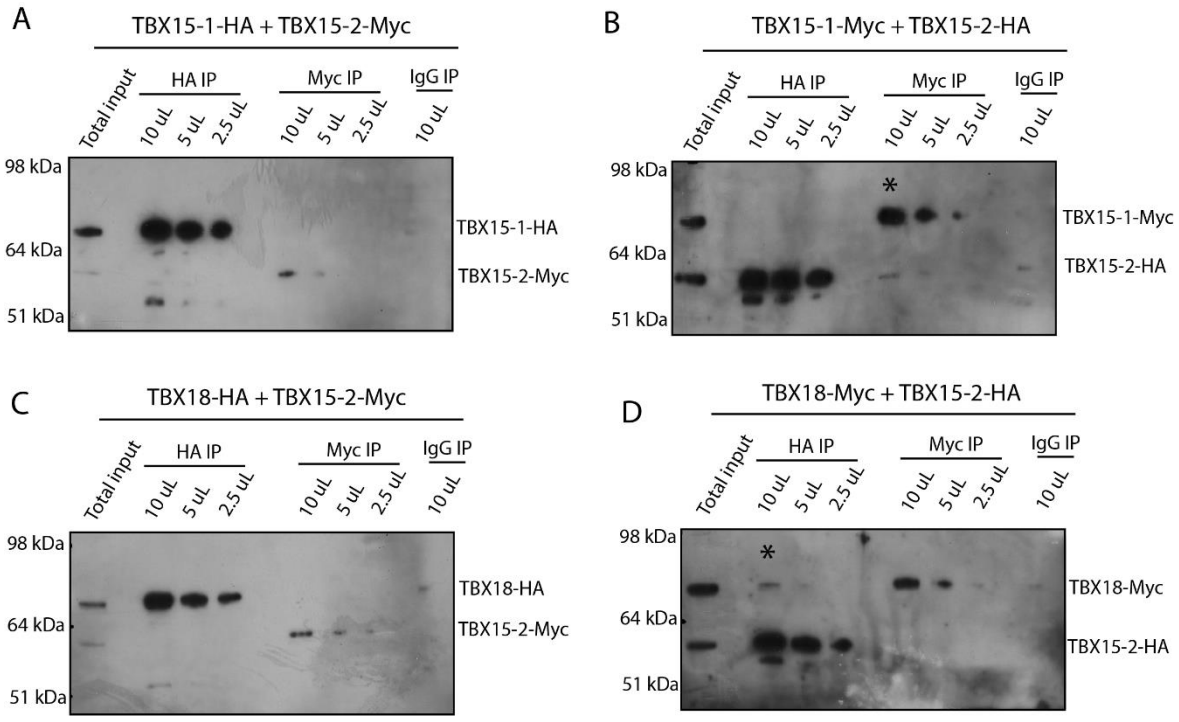

Figure 3.21. Magnetic co-immunoprecipitation optimisation for SDS-PAGE. A-D. 10 µL, 5 µL or 2.5 µL immunoprecipitation elute were separated by SDS-PAGE. A. TBX15-1-HA and TBX15-2-Myc (primary antibody dilutions HA 1:50,000 and Myc 1:1000). B. TBX15-1-Myc and TBX15-2-HA (primary antibody dilutions HA 1:100,000 and Myc 1:1000). C. TBX18-HA and TBX15-2-Myc (primary antibody dilutions HA 1:50,000 and Myc 1:1000). D. TBX18-Myc and TBX15-2-HA (primary antibody dilutions HA 1:100,000 and Myc 1:1000). * indicates lanes with successful co-immunoprecipitation of both HA- and Myc-tagged constructs. Abbreviations: IP (immunoprecipitation).

The second approach to improve immunoblot detection of bands was to alter the ratios of primary antibody concentrations for HA and Myc detection. For HA immunoprecipitations I decreased HA and increased Myc antibody concentrations, while for Myc immunoprecipitations I decreased Myc and increased HA antibody concentrations. Increasing the Myc antibody concentration improved detection of TBX15-2-Myc when immunoprecipitated with TBX15-1-HA but not TBX18-HA (Figure 3.22A and B, respectively). In both cases, there was an increased detection of non-specific bands in the total input lanes (notably endogenous Myc from HEK293T cells at 98 kDa), although this was not carried over into immunoprecipitation lanes. Increasing the HA antibody concentration also improved detection of TBX15-2-HA in

both TBX15-1-Myc and TBX18-Myc immunoprecipitations (Figure 3.22C and D, respectively), but there was also a marked increase in non-specific binding of TBX15-2-HA in the IgG control (Figure 3.22C).

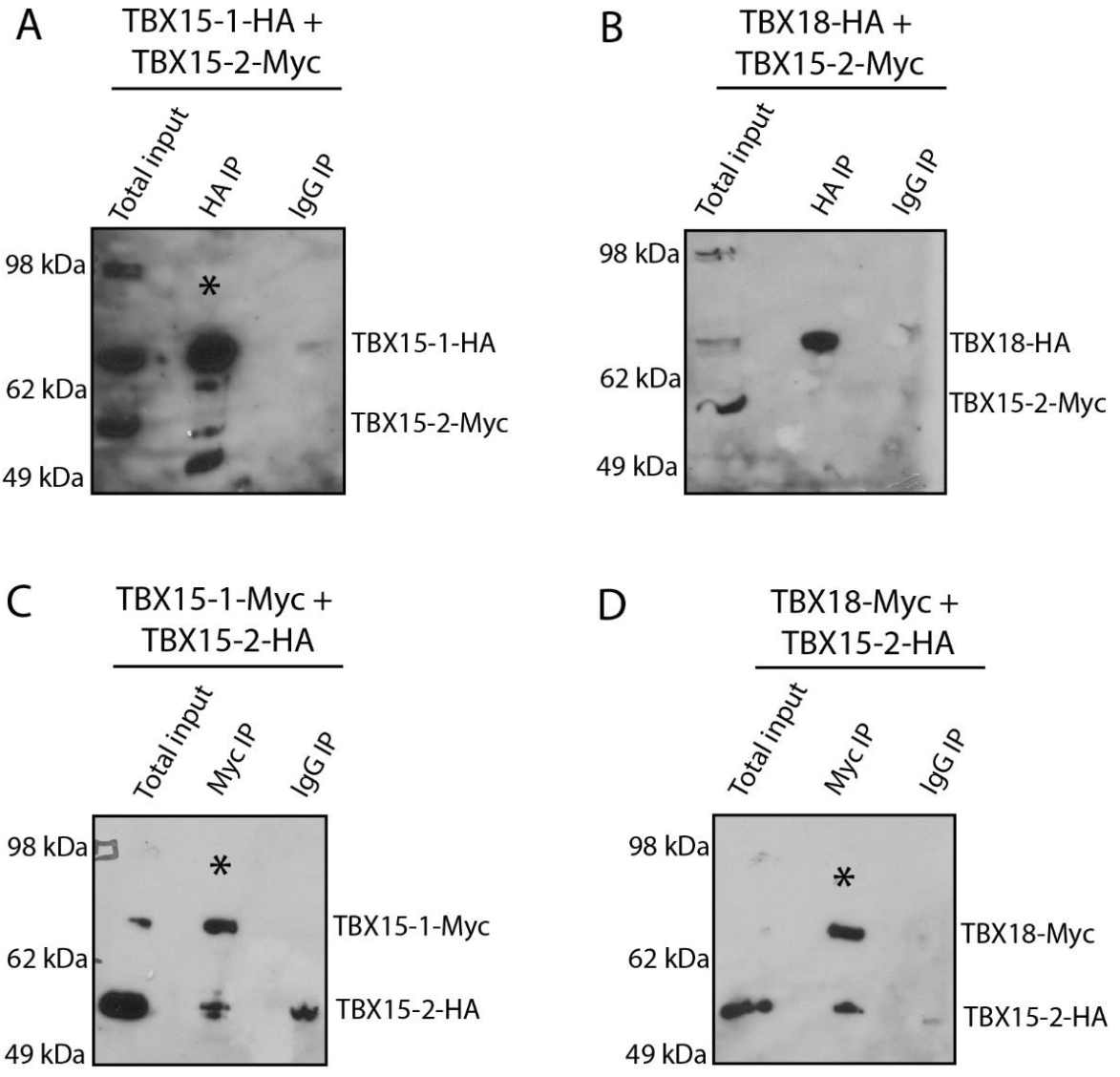

Figure 3.22. TBX15 magnetic co-immunoprecipitation primary antibody detection optimisation. A. TBX15-1-HA+TBX15-2-Myc (primary antibody dilutions HA 1:100,000, Myc 1:250). B. TBX18-HA and TBX15-2-Myc (primary antibody dilutions HA 1:100,000, Myc 1:250). C. TBX15-1-Myc and TBX15-2-HA (primary antibody dilutions HA 1:25,000, Myc 1:1000). D. TBX18-Myc and TBX15-2-HA (primary antibody dilutions HA 1:25,000, Myc 1: 1000). * indicates lanes with successful co-immunoprecipitation of both HA- and Myc-tagged constructs. Abbreviations: IP (immunoprecipitation).

3.2.3.4. Protein dimerisation was not significantly altered by p.H50N or p.M460R substitutions in the TBX15-2 protein

Based on these optimisations, I aimed to quantify the effect of p.H50N and p.M460R on TBX15 protein dimer formation *in vitro* to validate *in silico* predictions. TBX15-1-Myc and TBX18-Myc were co-transfected with either TBX15-2-HA, TBX15-2-H50N-HA or TBX15-2-M460R-HA constructs for 24 hours in HEK293T cells. A total of 250 µg protein was immunoprecipitated with Myc- or mouse IgG-coupled magnetic beads. Subsequently, 10 µL of the immunoprecipitation reaction was separated by SDS-PAGE and HA and Myc were probed simultaneously by immunoblot. TBX15-2-H50N and TBX15-2-M460R did not ablate TBX15-2 dimer formation with either TBX15-1 or TBX18, in line with *in silico* models (Figure 3.23A and C, respectively).

To quantify affinity differences resulting from these variants, the intensity of TBX15-2-HA, TBX15-2-H50N-HA and TBX15-2-M460R-HA bands were measured and normalised to the intensity of their respective TBX15-1-Myc or TBX18-Myc co-immunoprecipitation bands. The ratio was then calculated between TBX15-2-HA, TBX15-2-H50N-HA and TBX15-2-M460R-HA samples for TBX15-1 and TBX18 dimers (Figure 3.23B and D, respectively). There was no significant difference in dimer formation with TBX15-2-H50N-HA or TBX15-2-M460R-HA compared to TBX15-2-HA in TBX15-1-Myc complexes when using this quantification method (overall SNP effect p=0.2369, one-way ANOVA). Similarly, there was no significant difference in dimer formation resulting from TBX15-2-H50N or TBX15-2-M460R compared to TBX15-2-HA in TBX18-Myc complexes (overall SNP effect p=0.3368, one-way ANOVA). In summary, I have shown the amino acid substitutions p.H50N and p.M566R did not ablate or alter (within the detection limits of the assay) binding affinity of TBX15 protein dimers *in vitro*.

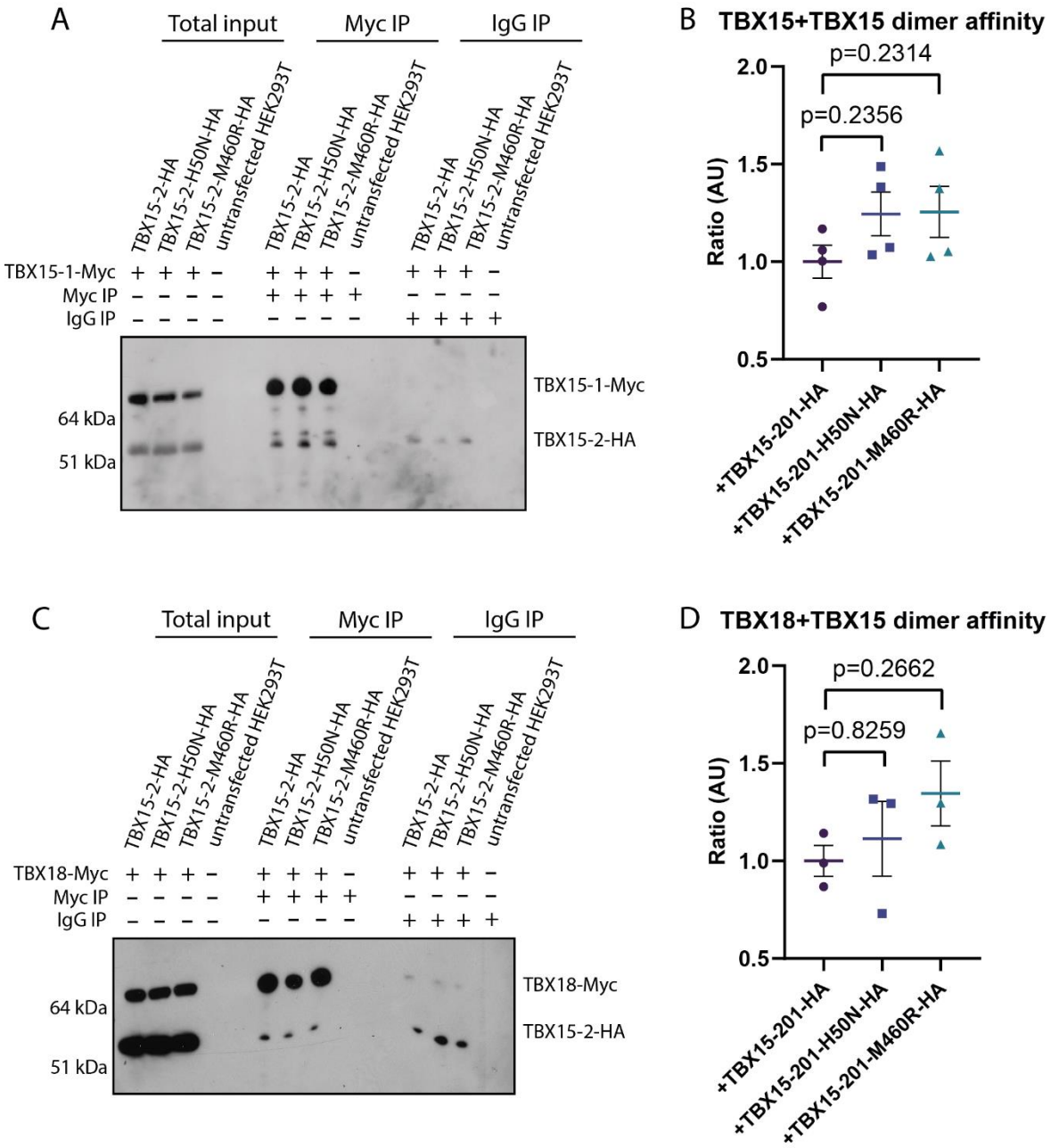

Figure 3.23. Non-synonymous amino acid substitutions p.H50N and p.M460R do not affect TBX15 protein dimerisation *in vitro*. A. Representative western blot for TBX15-1-Myc and TBX15-2-HA immunoprecipitation (n=4 biological replicates) (primary antibody dilutions HA 1:50,000 and Myc 1:5000). B. Quantification of n=4 biological replicates of co-IP from (A). C. Representative western blot for TBX18-Myc+TBX15-2-HA immunoprecipitation (n=4 biological replicates) (primary antibody dilutions HA 1:50,000 and Myc 1:5000). D. Quantification of n=3 biological replicates of co-IP from (C) (for n=1 replicate, no TBX15-2-HA bands were detected). Data analysed by one-way ANOVA with post-hoc Dunnett's multiple comparisons. Graphs represent mean ± SEM of n=3 and n=4 independent biological replicates. Abbreviations: IP (immunoprecipitation).

3.2.3.5. DNA binding was not significantly altered by p.H156N or p.M566R substitutions in the TBX15-1 protein

T-box proteins bind repeats of a conserved 'T half-site' 5′-AGGTGTGA-3′ DNA consensus sequence (Kispert and Herrmann, 1993). TBX15 preferentially bound inverse (BSinv) and direct (BSdir) half-site repeats, compared to palindromic orientations of repeats (BSp) (Farin *et al.*, 2007). Therefore, I aimed to quantify the effects of p.H156N and p.M566R on TBX15-1 DNA binding activity via spectrophotometric detection. I initially optimised DNA binding assays to determine optimal DNA oligonucleotide concentrations (20 ng or 40 ng) and tag detection (Myc- and HA-tagged constructs).

Based on this optimisation, I incubated 20 ng DNA oligonucleotides (BSp, BSinv or BSdir) with a 2.5-20 µg serial dilution of TBX15-1-HA, TBX15-1-H156N-HA, TBX15-1-M566R-HA or untransfected HEK293T protein lysate to generate protein-DNA binding curves (Figure 3.24B-D). There were no significant differences in AUC between TBX15-1, TBX15-1-H156N or TBX15-1-M566R for BSp, BSinv or BSdir ($p=0.9701$, $p=0.9818$, and $p=0.9473$, respectively, one-way ANOVA; Figure 3.24E). To conclude, I have shown the amino acid substitutions resulting from rs10494217 and rs61730011 did not ablate TBX15 protein-protein or protein-DNA binding. However, due to sensitivity limits of the *in vitro* assays used it was not possible to detect differences in mutant protein behaviours. Repeating these experiments with alternative and more sensitive assays would allow detection of potentially subtle changes in protein function *in vitro*.

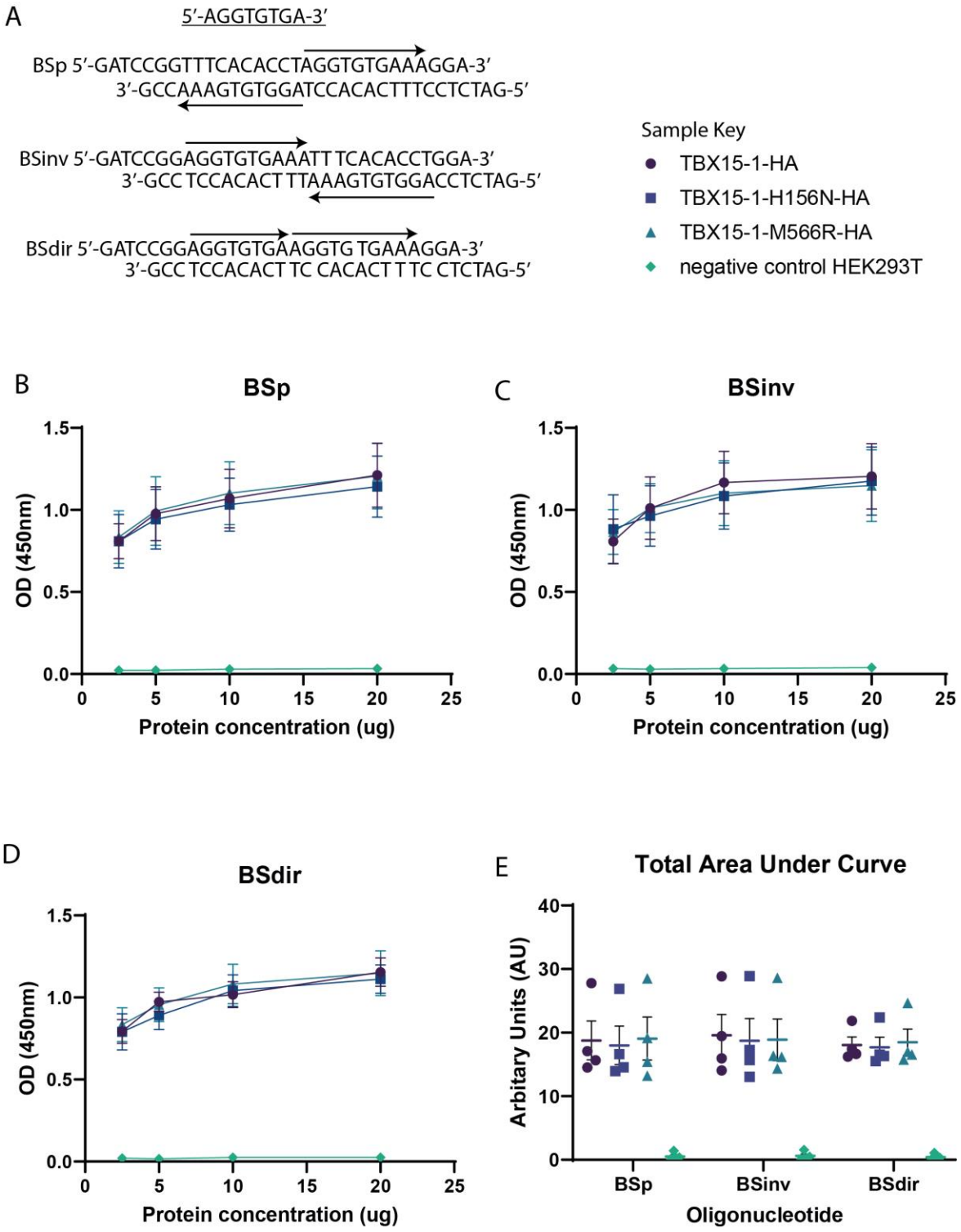

Figure 3.24. Non-synonymous amino acid substitutions p.H156N and p.M566R do not alter TBX15 protein-DNA binding *in vitro*. A. Binding site (BS) orientation of T-half site 5′-AGGTGTGA-3′ for BSp (palindromic repeat), BSinv (inverse repeat) and BSdir (direct repeat) DNA oligonucleotides. Adapted from (Farin *et al.*, 2007), reproduced under creative commons licence (CC-BY). B-D Binding curves for TBX15-1-HA, TBX15-1-H156N-HA, TBX15-1-M566R-HA and untransfected HEK293T incubated with BSp (B), BSinv (C) and BSdir (D) (primary antibody concentrations HA 1:5000). Total area under the curve for binding curves from (B-D). Total area under the curve data was analysed by one-way ANOVA with post-hoc Dunnett's multiple comparisons per individual binding oligonucleotide.

3.3. Discussion

In this chapter I have shown that the TBX15 protein sequence was highly conserved across ~200 vertebrate species, particularly in the T-box domain involved in protein dimerisation and DNA binding. I confirmed consensus protein transcripts for full-length TBX15 in both human (TBX15-1 and TBX15-2) and mouse (TBX15 and TBX15-X1) and showed that there was 98% homology between these species, specifically at the p.H156 and p.M566 residues. I further used several *in silico* methods to prioritise potential mechanisms of action of the coding SNPs, rs10494217 and rs61730011, associated with WHRadjBMI. These SNPs marked regions of minimal epigenetic marks, whereas there was strong evidence to suggest the resulting amino acid substitutions impacted TBX15 protein sequence and structure *in silico*. Finally, I validated these predictions *in vitro* and showed that p.H156N and p.M566R did not ablate protein-protein dimerisation or DNA-binding. I did not, however, detect a significant difference in activity compared to wildtype proteins based upon the assays employed to test the hypothesis *in vitro*.

3.3.1. *In silico* analysis of the regulatory role of *TBX15* coding SNPs

The *TBX15-WARS2* locus contains an array of independent and correlated signals associated with WHRadjBMI (Heid *et al.*, 2010; Shungin *et al.*, 2015; Justice *et al.*, 2019; Pulit *et al.*, 2019). Our collaborators (Lindgren and Claussnitzer research groups) have previously taken a comprehensive, unbiased approach to prioritise 61 potentially regulatory SNPs in the *TBX15-WARS2* locus in high LD ($r^2 \geq 0.8$) with the four lead SNPs identified by Shungin *et al.* (2015). However, predicted functionality for SNPs varied greatly between these two methods, likely due to different assumptions made in their

underlying methodologies. Further, rs61730011 (p.M566R, MAF=0.043, β=0.041), which had an effect size 2.3x greater than that of rs10494217 (p.H156N, MAF=0.174, β=0.018) (Justice et al., 2019) was not included in either prioritisation analysis. Therefore, I chose to prioritise a potentially functional role for both variants at either a DNA-regulatory or protein-coding level using several *in silico* techniques. This was the first known attempt to determine whether these coding SNPs were functional and identify their mechanism of action in the *TBX15-WARS2* locus, which may inform our understanding of the genetic associations of metabolic traits that increase MetS risk.

Initially, I aimed to investigate a potential DNA-regulatory role of rs10494217 and rs61730011. Neither rs10494217 nor rs61730011 overlapped regions of open chromatin in hWAT cells undergoing adipogenic differentiation in ATAC-sequencing data (Laber, 2017). However, epigenetic marks were evident in the ChromHMM skeletal muscle myoblast cells track for these coding SNPs, suggesting a potential cell-type specific regulatory mechanism, for example through MSC lineage determination. Further, TFBM alignments positioned these SNPs within binding motifs for MAFG and CREB1 (rs10494217), and NANOG, NRSF, POU2F2, and TCF12 (rs61730011) suggesting these SNPs potentially altered the binding affinity of these TFs. Several of these TF families have been implicated in adipogenesis. For example, CREB is considered a vital TF in the initiation of adipogenesis, directly regulating expression of PPARγ, CEBPα and FABP in differentiating 3T3-L1 cells (Reusch, Colton and Klemm, 2000). Maf family protein MAFA also induced expression of *Pparg* and *Cebpa* in 3T3-L1 cells, with other Maf proteins implicated in energy homeostasis (Tsuchiya *et al.*, 2009, 2015). Further, NANOG acts in combination with OCT4 (octamer-binding transcription factor 4) and SOX2 (SRY-box transcription factor 2) to regulate MSC self-renewal and lineage commitment; recently confirmed in

human-derived adipose MSCs (Pitrone *et al.*, 2019). This suggests these SNPs may act, in part, by regulating a network of *trans*-genes associated with adipogenesis or lineage determination. However, when considered with the minimal epigenetic marks identified in ATAC-sequencing data, it is suggestive that these coding SNPs do not act predominantly at a DNA-regulatory level. Although they may act in cell/tissue-specific manners, not captured in the methods used in this chapter, to impact WHR phenotypes.

3.3.2. *In silico* analysis of the protein-coding role of *TBX15* coding SNPs

I next took an *in silico* approach to investigate the alternative hypothesis that rs10494217 (p.H156N) and rs61730011 (p.M566R) may affect TBX15 protein structure and function. Initially, I aimed to determine consensus sequences for human and mouse TBX15 protein-coding transcripts as discrepancies in transcript annotations existed between NCBI and Ensembl. These discrepancies were likely due to differences in the RefSeq and GENCODE methods used, respectively (Long, Reeves and Simon, 2022). However, it was still possible to determine two consensus full-length transcripts which had greater than 98% homology between species, including conservation of the p.H156 and p.M566 amino acid residues indicating their potential biological importance.

The p.H156N and p.M566R amino acid substitutions were predicted to be neutral and damaging, respectively, by prediction servers SIFT, Condel and PolyPhen2. These predictions were generated based on sequence homology data, combined with comparisons of physio-chemical properties of the alternate amino acids. Histidine (H) and asparagine (N) are both polar in nature, and whilst asparagine has no charge, histidine is capable of switching between neutral and positive charges (Betts and

Russell, 2003). Despite the relative resistance of histidine for amino acid exchange, asparagine is considered one of the well-tolerated substitutions for this amino acid (Betts and Russell, 2003), which likely explains the benign/well tolerated predictions for p.H156N. In contrast, methionine is hydrophobic and often considered aliphatic, whilst arginine is both polar and positively charged (Betts and Russell, 2003). These amino acids are not favourably interchangeable, likely indicating the more deleterious predictions for p.M566R compared to p.H156N.

However, in isolation, these predictions offered no insight into how these substitutions may alter the 3D structure of TBX15. Therefore, I next modelled full-length, N- and C-terminal TBX15 sequences which resulted in poor model quality. This could indicate intrinsically disordered regions in TBX15, which are known to assist in post-translational modifications, scaffolding or recruitment of binding partners (Van Der Lee *et al.*, 2014). The more likely possibility resulted from limitations of homology-based modelling approaches. Given the T-box protein structures available in the PDB were solely for the T-box region, it follows that the web servers used for modelling TBX15 could only model this region of the full-length proteins with any confidence. This was further evidenced by the increased resolution of models produced solely for the T-box region of TBX15.

The T-box region is highly conserved between family members, and is critical for protein-protein dimerisation and DNA-binding of these TFs (Farin *et al.*, 2007; Papaioannou, 2014). In all servers, introduction of p.H156N within the T-box domain of TBX15 was predicted to alter a loop region in this structure. Histidine is commonly located in binding sites of proteins, often interacting with serine or cysteine amino acids, and can be either buried in an active site or exposed to aqueous solution.

Asparagine, on the other hand, is a surface protein but can also interact with cysteine amino acids (Betts and Russell, 2003). The altered loop structure in p.H156N predictions was in the region of amino acids 250-266; near the start of this loop are two serine amino acids at residues 253 and 254. I therefore hypothesised that p.N156 orientated in a different manner to p.H156, thus preventing histidine interaction with the serine amino acids in the loop structure, which could impact recognition of other T-box proteins or target DNA T-half sites.

Using the HADDOCK v2.4 server, I showed p.H156N impaired conformation of both TBX15-TBX15 and TBX15-TBX18 protein dimers in the absence of DNA *in silico.* Whilst T-box proteins have been shown to form dimers in the absence of DNA both in crystallographic structures and *in vitro* (Farin *et al.*, 2007; Pradhan *et al.*, 2016), the absence of DNA in my models would certainly have impacted the orientation of the protein dimers. In fact, the DNA-free form of TBX5 T-box dimers contained a disordered structure in the C-terminal region of the crystal structures, which in the presence of DNA assembled an ordered helix (Pradhan *et al.*, 2016). Further, the authors indicated the N-terminal amino acids (residues 1-50) of TBX5 were predicted to be intrinsically disordered using the IUPred webserver, and were indeed disordered in the crystallographic dimers (Pradhan *et al.*, 2016). Finally, the authors identified multiple TBX5 binding sites within 100-1000bp of each other in the transcription start site of its regulatory targets ANF and Connexin 40, and suggested TBX5 protein dimers could initiate DNA loop formation (Pradhan *et al.*, 2016).

The high degree of conservation across the T-box family suggests that T-box proteins require i) contact with DNA for certain regions to become structurally ordered, and ii) DNA loops to form protein dimers. However, this also presents a chicken-and-egg

dilemma as it remains to be determined whether these contacts are required for, or occur in response to, T-box dimer conformation. It is also plausible that the N- and C-terminal regions are intrinsically disordered, therefore, future investigations into the structure of TBX15, and other T-box proteins, should focus on crystallising full-length proteins with longer DNA target sequences to determine whether this induces ordered formation of the N- and C-terminal. Further investigation of *in vitro* dimer formation is needed, for example through crystallography of TBX15 and TBX15-H156N proteins.

Poor full-length TBX15 models meant it was not possible to model p.M566R with confidence using template-based approaches. Methionine is usually buried within a hydrophobic core with limited function, whereas arginine is partially exposed to the outer surface of a protein and functions to stabilise proteins through formation of salt-bridges in hydrogen bonds (Betts and Russell, 2003). This suggests the p.M566R substitution might force a change in structure in the C-terminal region of TBX15 that alters stability of the protein when binding DNA targets or other T-box proteins. With more time, it would be beneficial to take an *ab initio* protein modelling approach to determine any potential structural impact of this variant, for example using the AlphaFOLD v2.0 source code (Jumper *et al.*, 2021; Varadi *et al.*, 2022).

The C-terminal region of several T-box proteins contains activator and/or repressor domains (Kispert, 1995; Zaragoza *et al.*, 2004; Stennard *et al.*, 2005). Additionally, documented Cousin Syndrome cases resulted from premature stop codons in the C-terminal region of TBX15 which induced proteasomal degradation (Lausch *et al.*, 2008; Dikoglu *et al.*, 2013). I therefore hypothesised that the C-terminal region could play a functional role in stabilising protein expression, and protein-protein or

protein-DNA complexes. Given p.M566R lies in the terminal exon of TBX15 it is possible that this variant impacts such functions, leading to altered WHR phenotypes seen in human GWAS. Further *in vitro* assays would be needed to fully decipher how p.M566R, and p.H156N, might alter other important cellular functions. For example, immunofluorescence examination of cellular localisation or inhibition of proteasomes to examine relative expression levels which might elucidate the mechanisms underpinning the associations for these SNPs with cell/tissue-specific expression of TBX15. Considering all *in silico* regulatory and structural predictions for these coding SNPs, there was stronger evidence to suggest these non-synonymous variants acted predominantly to alter TBX15 protein structure and TF function.

3.3.3. *In vitro* validation of protein-protein and protein-DNA binding effects of *TBX15* coding SNPs

Having established structural and protein dimer conformational changes in TBX15 resulting from p.H156N, I aimed to validate these results *in vitro*. It stood to reason that the predicted conformational changes, resulting from p.H156N, might alter TBX15 binding affinity in both protein-protein dimers and protein-DNA complexes. Indeed, several substitutions in the DNA binding interface of TBX5 (p.M74V, p.G80R, p.W121G, p.G169R, p.T223M and p.R237W/Q) altered its DNA binding affinity (Stirnimann *et al.*, 2010). The equivalent amino acid to p.H156 of TBX15 is p.K94 in TBX5. Whilst p.M74V and p.G80R (TBX5) are sequentially within 20 amino acids of p.K94, structurally these amino acids lie in different interfaces, with p.K94 (TBX5) and p.H156 (TBX15) closer to the protein-interacting region than p.M74 and p.G80. This further supported *in silico* predictions that showed p.H156N altered TBX15 protein dimer formation.

Subtle changes in dimerisation or DNA binding affinity may still cause disruptions in the TBX15 transcriptional network leading to small but significant changes in fat distribution, which would be reflective of the small effect sizes of the coding SNPs associated with WHRadjBMI. I showed for the first time that TBX15 formed homodimers, and confirmed previous TBX15-TBX18 heterodimer formation *in vitro* (Farin *et al.*, 2007). I further showed that p.H50N and p.M460R did not ablate protein dimer formation, however, I was not able to quantify a significant difference within assay sensitivity limits. Similarly, there was no significant difference in DNA binding affinity resulting from p.H156N or p.M566R constructs. Given rs10494217 and rs61730011 had small effect sizes for WHRadjBMI associations, I hypothesised that there would be a subtle difference in binding affinity as a result of p.H50N and p.M460R. It is likely that the detection methods developed in this chapter were not sensitive enough to detect any significant differences in binding affinity. Further, structural changes could alter the interaction with other proteins forming part of the TBX15 transcriptional complex, which was not evaluated.

With more time, it would have been beneficial to explore alternative methods for investigating TBX15 protein dimerisation and DNA binding. For example, pulldown assays are similar in approach to immunoprecipitation assays but are based on the principal of a specific bait protein, in this instance wildtype TBX15 or TBX18, being conjugated to a bead. The major benefit of this approach is that any captured prey proteins can be eluted whilst the bait protein remains covalently bound to the beads, thus removing potential interference with downstream quantification analysis. Such a method has been developed for generating binding curves as a simple alternative to dissociation constant experiments (Lapetina and Gil-Henn, 2017) and could provide a useful tool for assessing altered binding affinity resulting from p.H156N and p.M566R.

Similarly, when assessing the DNA binding potential of p.H156N and p.M566R, I aimed to generate binding curves to assess differences in binding affinities. However, the resulting curves were fairly linear indicating saturation was not achieved. Therefore, it would be beneficial, in the first instance, to improve this assay by generating a broader range of protein concentrations for analysis.

Another limitation of the co-immunoprecipitation experiments was the difference in band intensity using immunoblotting. Despite attempts to optimise primary antibody concentrations to improve this detection, the HA-tagged protein bands were relatively weak in comparison to the Myc-tagged bands. This could indicate that in this system dimer interactions are relatively weak, which could be influenced by several factors including overly stringent co-immunoprecipitation buffers, or a lack of other TFs required for complex formation/stabilisation. Methodologies such as genetic code expansion could be utilised to overcome some of these issues. This approach replaces canonical amino acids with non-canonical amino acids (i.e. analogue derivatives), of which the unique properties can then be leveraged for a range of applications (e.g. introduction of photo-cross-linkers to stabilise bonds between interacting proteins) (Chung, Amikura and Söll, 2020; Tang, Zhang and Luo, 2022). This could prove beneficial for improving TBX15 protein dimer stability and ultimately quantification of co-immunoprecipitation studies performed in this thesis.

Finally, alternative *in vitro* approaches could be employed to assess the impact of p.H156N and p.M566R on the transcriptional activity of TBX15. For example, luciferase reporter assays could be used to generate vectors containing known TBX15 binding sites that are co-transfected with wildtype-, p.H156N- or p.M566R-TBX15 constructs and assessed for luciferase activity. Significant differences in luciferase activity with

either p.H156N or p.M566R would indicate that these polymorphisms directly altered transcriptional regulation of TBX15 target gene. This could be combined with ChIP-sequencing to evaluate whether these polymorphisms alter TBX15 recognition of transcriptional targets in the genome. Alternatively, developing more sensitive detection methods that circumvent the need for antibody-based approaches for protein dimerisation and DNA-binding kinetics (e.g. mass-spectrometry or circular dichroism spectroscopy and isothermal titration calorimetry based techniques) (Heck and Van Den Heuvel, 2004; Stirnimann *et al.*, 2010) would provide insights into the mechanism of action of these protein-coding SNPs.

In conclusion, *in silico* prioritisation of the potential role of coding SNPs rs10494217 (p.H156N) and rs61730011 (p.M566R) in *TBX15* indicated the most likely mode of function was through alteration of TBX15 protein structure, with identifiable structural changes that may be functional. *In vitro* validation confirmed that protein binding was not completely ablated with either SNP. However, the methods used were not sensitive enough to detect significant quantitative affinity differences compared to reference alleles. These data do not rule out the possibility that p.H156N and p.M566R act in a cell/tissue-specific manner to regulate WHRadjBMI in humans. Therefore, using *in vivo* models to assess the physiological effects of these SNPs in whole organisms may still prove a useful tool to uncover the functional effects of these SNPs.

4

Characterising the function of *Tbx15 in vivo*

4.1. Introduction

TBX15/WARS2 locus variants were strongly associated with WHRadjBMI in human GWAS (Heid *et al.*, 2010; Liu *et al.*, 2014; Shungin *et al.*, 2015; Justice *et al.*, 2019; Pulit *et al.*, 2019). However, determining the causal variant(s) in the locus remains challenging, and to date, no functional studies have addressed this. In chapter 3, I showed that p.H156N (rs10494217) was predicted to alter i) a loop structure in the T-box region of TBX15, and ii) protein-protein dimer orientation *in silico*. Subsequent *in vitro* validation of these findings did not identify significant differences in binding affinity, within sensitivity limits of the assays, resulting from p.H156N, or the alternative coding SNP rs61730011 (p.M566R). Therefore, generating mouse models of these variants within their correct cellular context was necessary to analyse their functional role in relation to human WHR phenotypes.

Global disruption of *Tbx15* was associated with poor viability of homozygous-null pups (*Tbx15*$^{-/-}$), with severe craniofacial and skeletal defects observed in those pups that survived to weaning (Curry, 1959; Candille *et al.*, 2004; Singh *et al.*, 2005). Initial observations suggested heterozygous-null (*Tbx15*$^{+/-}$) mice were phenotypically identical to wildtype (*Tbx15*$^{+/+}$) littermates (Curry, 1959; Candille *et al.*, 2004).

However, more recent studies showed a significant increase in fat mass, but not lean mass, in *Tbx15*$^{+/-}$ mice compared to *Tbx15*$^{+/+}$ littermates at 20 weeks of age (Lee *et al.*, 2015). Further, adipose-specific *Tbx15*-knockout inhibited browning of inguinal white adipose tissues (iWAT) of homozygous mice, following cold stimulation, compared to wildtype littermates (Sun *et al.*, 2019). These studies indicate TBX15 plays a key role in regulating adipose tissues and body composition that warrants further investigation to understand its mechanisms of action.

High conservation of the TBX15 amino acid sequence between human and mouse species meant it was possible to generate two orthologous mouse lines using CRISPR/Cas9 technology for both p.H156N (*Tbx15*^{H156N}) and p.M566R (*Tbx15*^{M566R}). These models could therefore be used to simultaneously interrogate a range of associated phenotypes that might drive the WHR phenotype seen in humans. Whilst subtle differences exist in adipose depots between mice and humans, mice have distinct subcutaneous and visceral WAT like humans. In particular, they share common visceral depots such as pericardial, perirenal and mesenteric WAT (Park, Kim and Bae, 2014). Whilst WHR cannot be measured directly in mice, a common proxy is the ratio of gonadal to inguinal WAT (gWAT:iWAT) which has been successfully used in mouse models of impaired adiposity (Gray *et al.*, 2006; Mušo *et al.*, 2022).

4.1.1. Chapter hypothesis

Whilst TBX15 has been implicated in regulation of body composition and adipogenesis, underlying mechanisms remain unclear. I hypothesised that global heterozygous knockout *Tbx15*$^{+/-}$ would alter body composition in mice. Further, given p.H156N and p.M566R were predicted to mildly or more severely alter TBX15 protein structure and

function, respectively, I hypothesised that orthologous substitutions would alter body composition in allelic series compared to *Tbx15*$^{+/-}$ mice.

4.1.2. Chapter aims

I therefore aimed to investigate these *in vivo* alterations to reveal potential mechanistic links between the *Tbx15* gene and the human WHR trait by assessing:

1. Global body composition of *Tbx15*$^{+/-}$, *Tbx15*^{H156N} and *Tbx15*^{M566R} mice fed high-fat and control low-fat diets from weaning, over 4-24 weeks of age by echo-MRI, and at early adulthood (23-24 weeks of age) by DEXA.
2. Adipose depot weight distribution at 24 weeks of age in *Tbx15*$^{+/-}$, *Tbx15*^{H156N} and *Tbx15*^{M566R} mice, and adipocyte size in *Tbx15*$^{+/-}$ mice.
3. T2DM phenotypes in *Tbx15*$^{+/-}$, *Tbx15*^{H156N} and *Tbx15*^{M566R} mice.
4. Terminal clinical chemistry profiles of *Tbx15*$^{+/-}$, *Tbx15*^{H156N} and *Tbx15*^{M566R} mice.

4.2. Results

4.2.1. Initial viability assessment

To model different *Tbx15* alleles *in vivo*, I first assessed the viability of three *Tbx15* mouse lines: *Tbx15* knockout (*Tbx15*$^{-/-}$), and homologous p.H156N (*Tbx15*^{H156N}) and p.M566R (*Tbx15*^{M566R}). To generate intercross litters, heterozygous (*Tbx15*$^{+/-}$, *Tbx15*$^{+/H156N}$, or *Tbx15*$^{+/M566R}$) male and female mice were mated to generate litters of pups at an expected wildtype:heterozygous:homozygous ratio of 1:2:1. Initial viability assessments confirmed that pups of all genotypes were born, indicating the *Tbx15*$^{-/-}$,

Tbx15^{H156N} and *Tbx15*^{M566R} alleles were not homozygous lethal. However, χ^2 analysis of observed versus expected genotype ratios indicated significant differences in *Tbx15*$^{-/-}$ (p=0.0350), but not *Tbx15*^{H156N} (p=0.2628) or *Tbx15*^{M566R} (p=0.4618), alleles (Figure 4.1, B and C, respectively). Given the poor survival rates of *Tbx15*$^{-/-}$ mice, and welfare concerns consistent with licence permissions, these mice could not be bred for metabolic phenotyping studies, instead we chose to proceed with *Tbx15*$^{+/-}$ mice only.

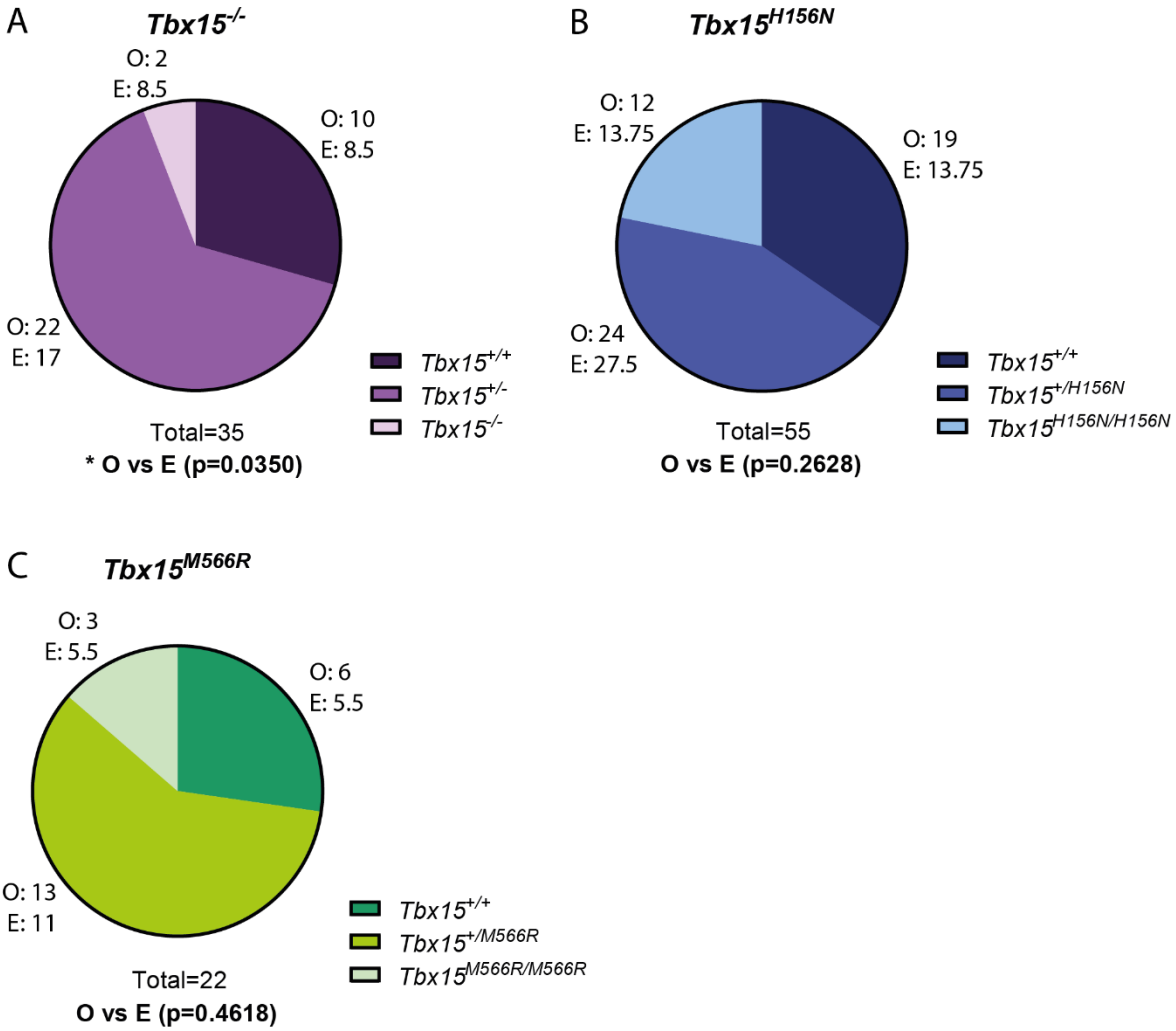

Figure 4.1. χ^2 analysis of observed versus expected genotype ratios in *Tbx15* mouse line viability cohorts. A. *Tbx15*$^{-/-}$ *line; Tbx15*$^{+/+}$ (dark purple), *Tbx15*$^{+/-}$ (purple), *Tbx15*$^{-/-}$ (light purple). B. *Tbx15*^{H156N} line; *Tbx15*$^{+/+}$ (dark blue), *Tbx15*$^{+/H156N}$ (blue), *Tbx15*$^{H156N/H156N}$ (light blue). C. *Tbx15*^{M566R} line; *Tbx15*$^{+/+}$ (dark green), *Tbx15*$^{+/M566R}$ (green), *Tbx15*$^{M566R/M566R}$ (light green). Observed (O) and expected (E) values given for each genotype. Data analysed by χ^2 analysis: *p<0.05.

4.2.2. Metabolic phenotyping pipeline and sample size calculations

To investigate the functional effects of *Tbx15* on fat distribution and metabolic phenotype *in vivo*, $Tbx15^{+/-}$, and heterozygous and homozygous $Tbx15^{H156N}$ and $Tbx15^{M566R}$ mice were challenged with a HFD or LFD from weaning (3 weeks of age) to early adulthood at 24-25 weeks of age (Figure 4.2). To determine cohort sizes with appropriate statistical power to detect differences in subtle effects in these metabolic cohort studies, I performed power calculations using G*Power v3.1 software; required sample sizes ranged from n=9 (male fat mass) to n=145 (female bodyweight; Table ***4.1***). Based on the suggested sample sizes, combined with previous power calculations performed in the Cox group (unpublished data), I determined that n=20 was sufficient to detect an effect between groups for key metabolic traits.

Table 4.1. Calculated sample sizes using *a priori* power analysis to detect an effect with α=0.95 power and p<0.05 significance (two-sided). Total bodyweight, fat mass, lean mass, and adipose depot weights were measured in male and female $Tbx15^{+/+}$ and $Tbx15^{+/-}$ mice at 19 weeks of age on RM3 diet by Dr. Rebecca Dumbell. Female $Tbx15^{+/+}$ (n=6), $Tbx15^{+/-}$ (n=7), male $Tbx15^{+/+}$ (n=4), $Tbx15^{+/-}$ (n=15).

Sex	Bodyweight	Fat mass	gWAT	mWAT	pWAT	BAT	iWAT
Female	145	26	23	83	49	71	16
Male	57	9	10	10	46	22	13

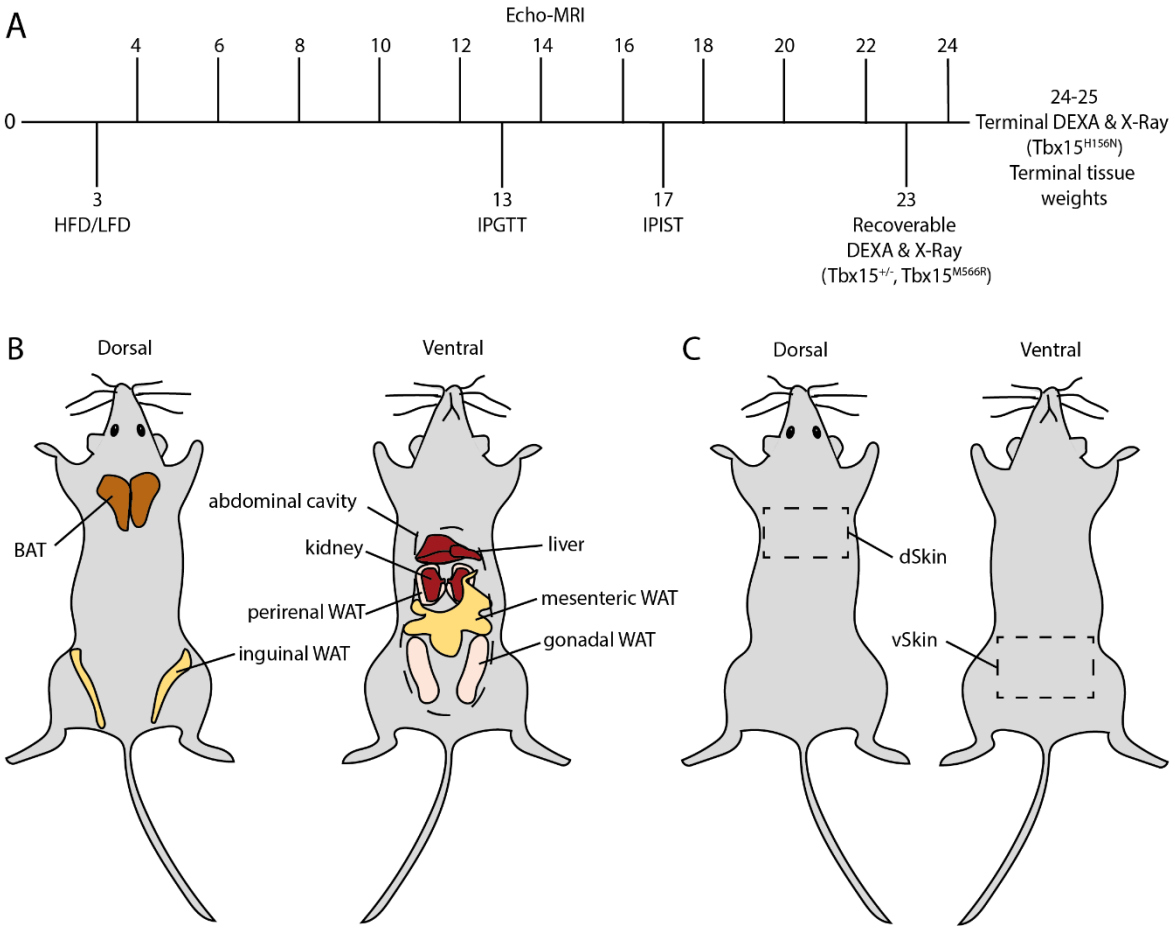

Figure 4.2. *Tbx15* metabolic phenotyping cohort experimental pipeline. A. Pipeline showing weaning onto a high-fat diet (HFD) or low-fat diet (LFD) at 3 weeks of age. Mice underwent echo-MRI every 2 weeks, glucose and insulin tolerance testing, DEXA and X-Ray, and terminal dissection for tissue weights. B. Schematic representation of white (WAT) and brown (BAT) adipose tissues for dissection. C. Schematic representation of skin from dorsal (dSkin) and ventral (vSkin) regions dissected for histological analysis.

4.2.3. *Tbx15*$^{+/-}$ and *Tbx15*^{H156N} lines exhibit sexually dimorphic sub-viability post-weaning

Initial viability assessments were performed on small cohorts of mice, therefore, I next aimed to determine if the *Tbx15*$^{+/-}$, *Tbx15*^{H156N} or *Tbx15*^{M566R} alleles were associated with sub-viability. Observed versus expected genotype ratios for a total of 165, 426 and 361 mice were analysed by χ^2 for pups that survived post-weaning in all experimental cohorts, respectively. For *Tbx15*$^{+/-}$ mice, a 1:1 ratio of *Tbx15*$^{+/+}$ to *Tbx15*$^{+/-}$

was expected as mice were bred by back-crossing male *Tbx15*$^{+/-}$ to wildtype female C57BL/6NTac mice. Of 165 mice born, overall genotype ratios did not differ significantly from the expected 1:1 ratio (p=0.1379; Figure 4.3A). However, there was a significant difference between ratios in male mice (p=0.0295) resulting from an increase of *Tbx15*$^{+/+}$, and decrease of *Tbx15*$^{+/-}$, mice (Figure 4.3B and C).

For *Tbx15*^{H156N} and *Tbx15*^{M566R} mice, a 1:2:1 ratio of wildtype:heterozygous:homozygous mice was expected as mice were bred by inter-crossing heterozygous mice. In a total of 426 mice born in the *Tbx15*^{H156N} cohorts, there was a significant difference in genotype ratios (p=0.0420; Figure 4.3D). When separated by sex, this was attributed to female mice (p=0.0463) and appeared to result from an imbalance between *Tbx15*$^{+/+}$ and *Tbx15*$^{H156N/H156N}$ mice (Figure 4.3E and F).

In the *Tbx15*^{M566R} line, a total of 361 mice were born and no significant differences were detected between genotype ratios in sex-combined and within-sex analyses (p=0.2635; Figure 4.3G-I). A total of n=40 mice per sex and genotype were required to achieve the calculated n=20 per HFD and LFD. Due to COVID-19 limitations and UK Home Office breeding regulations, it was not possible to breed sufficient male *Tbx15*$^{+/-}$, female *Tbx15*$^{H156N/H156N}$ or male *Tbx15*$^{M566R/M566R}$ mice (Table 4.2).

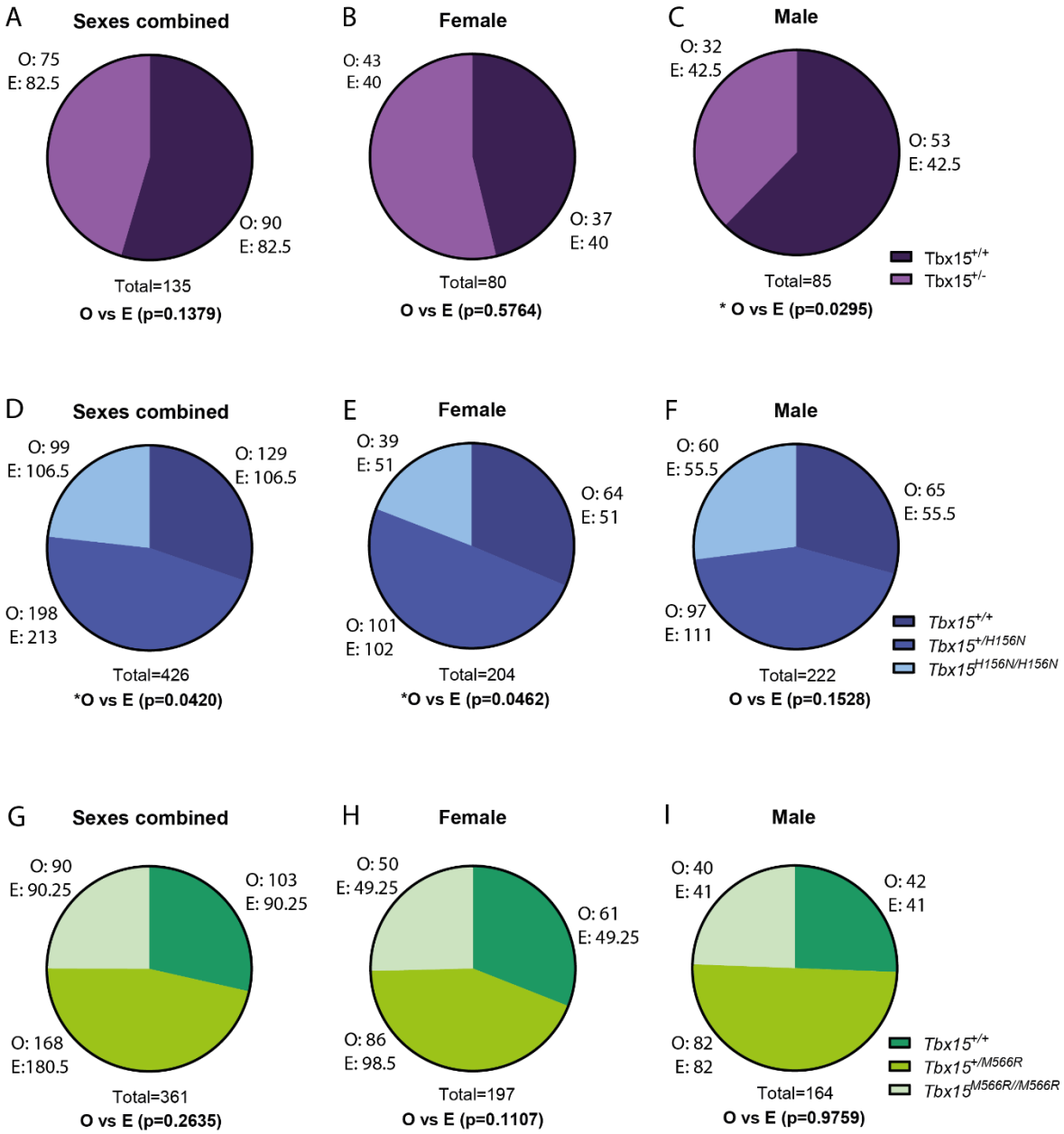

Figure 4.3. χ^2 analysis of observed versus expected genotype ratios for *Tbx15*$^{+/-}$, *Tbx15*^{H156N} and *Tbx15*^{M566R} mice post-weaning. (A-C) *Tbx15*$^{+/-}$ line; A. Sexes combined, B. Female, C. Male. *Tbx15*$^{+/+}$ (dark purple), *Tbx15*$^{+/-}$ (purple). (D-F) *Tbx15*^{H156N} line; D. Sexes combined, E. Female, F. Male. *Tbx15*$^{+/+}$ (dark blue), *Tbx15*$^{+/H156N}$ (blue), *Tbx15*$^{H156N/H156N}$ (light blue). (G-I). *Tbx15*^{M566R} line; G. Sexes combined, H. Female, I. Male. *Tbx15*$^{+/+}$ (dark green), *Tbx15*$^{+/M566R}$ (green), *Tbx15*$^{M566R/M566R}$ (light green). Observed (O) and expected (E) values given for each genotype. Data analysed by χ^2 analysis: *p<0.05.

Table 4.2. Total numbers of mice weaned per sex and diet group for *Tbx15* metabolic phenotyping cohorts. *The following mice were culled sick during phenotyping and were excluded from statistical analysis: one *Tbx15*$^{+/-}$ low-fat diet (LFD) male; two *Tbx15*$^{+/+}$, two *Tbx15*$^{+/H156N}$ and one *Tbx15*$^{H156N/H156N}$ high-fat diet (HFD) females, one *Tbx15*$^{+/+}$, one *Tbx15*$^{+/H156N}$ and one *Tbx15*$^{H156N/H156N}$ LFD females, one *Tbx15*$^{+/H156N}$ HFD male, two *Tbx15*$^{+/H156N}$ and two *Tbx15*$^{H156N/H156N}$ LFD males; one *Tbx15*$^{M566R/M566R}$ HFD female, and one *Tbx15*$^{+/M566R}$ and one *Tbx15*$^{M566R/M566R}$ LFD females, one *Tbx15*$^{+/+}$, three *Tbx15*$^{+/M566R}$ and two *Tbx15*$^{M566R/M566R}$ HFD males, two *Tbx15*$^{+/+}$, one *Tbx15*$^{+/M566R}$ and one *Tbx15*$^{M566R/M566R}$ LFD males.

Mouse line	Genotype	Female		Male	
		HFD	LFD	HFD	LFD
***Tbx15*$^{+/-}$**	*Tbx15*$^{+/+}$	18	18	21	21
	Tbx15$^{+/-}$	22	21	17	15*
***Tbx15*^{H156N}**	*Tbx15*$^{+/+}$	24*	24*	22	21
	Tbx15$^{+/H156N}$	28*	24*	24*	22*
	Tbx15$^{H156N/H156N}$	17*	16*	21	22*
***Tbx15*^{M566R}**	*Tbx15*$^{+/+}$	22	23	23*	24*
	Tbx15$^{+/M566R}$	22	22*	25*	23*
	Tbx15$^{M566R/M566R}$	22*	20*	21*	18*

4.2.4. Echo-MRI body composition analysis over time

To assess the effects of the *Tbx15* alleles on body composition, total bodyweight (g), fat mass (g) and lean mass (g) were estimated using echo-MRI every two weeks from 4 to 24 weeks of age, in mice challenged with a HFD or LFD. As diet and sex are known to influence body composition, echo-MRI data was analysed by repeated measures two-way ANOVA (time and genotype as factors, with post-hoc multiple comparisons) within each sex and diet separately.

4.2.4.1. *Tbx15*$^{+/-}$ mice fed a low-fat-diet had lower bodyweight and less fat mass

In LFD-fed female *Tbx15*$^{+/-}$ mice there was a significant genotype effect for bodyweight and fat mass (p=0.0326 and p=0.0329, respectively), however, Šidak's post-hoc multiple comparisons did not reveal significant differences at any individual time points (Figure 4.4A and B, Appendix Table 9.11). There was no significant difference

between *Tbx15*$^{+/-}$ and *Tbx15*$^{+/+}$ female mice for bodyweight or fat mass on a HFD (Figure 4.4A and B, Appendix Table 9.11). In HFD- and LFD-fed mice there was a significant interaction effect for lean mass (p=0.0162 and p=0.0281, respectively; Figure 4.4C, Appendix Table 9.11).

A similar trend was seen in male mice; a significant genotype effect was detected in bodyweight between *Tbx15*$^{+/+}$ and *Tbx15*$^{+/-}$ mice on LFD (p=0.0226; Figure 4.4D, Appendix Table 9.12). This was likely driven by a significant interaction effects in fat mass (p=0.0014; Figure 4.4E, Appendix Table 9.12). No significant bodyweight or fat mass differences were detected between genotypes in males fed HFD (Figure 4.4D and E, Appendix Table 9.11). Further, no significant genotype differences were detected in lean mass in male HFD- or LFD-fed mice (Figure 4.4F, Appendix Table 9.11). To summarise, a significant genotype effect was detected for bodyweights in LFD-fed male and female *Tbx15*$^{+/-}$ mice which appeared to be largely driven by total fat mass differences in these mice.

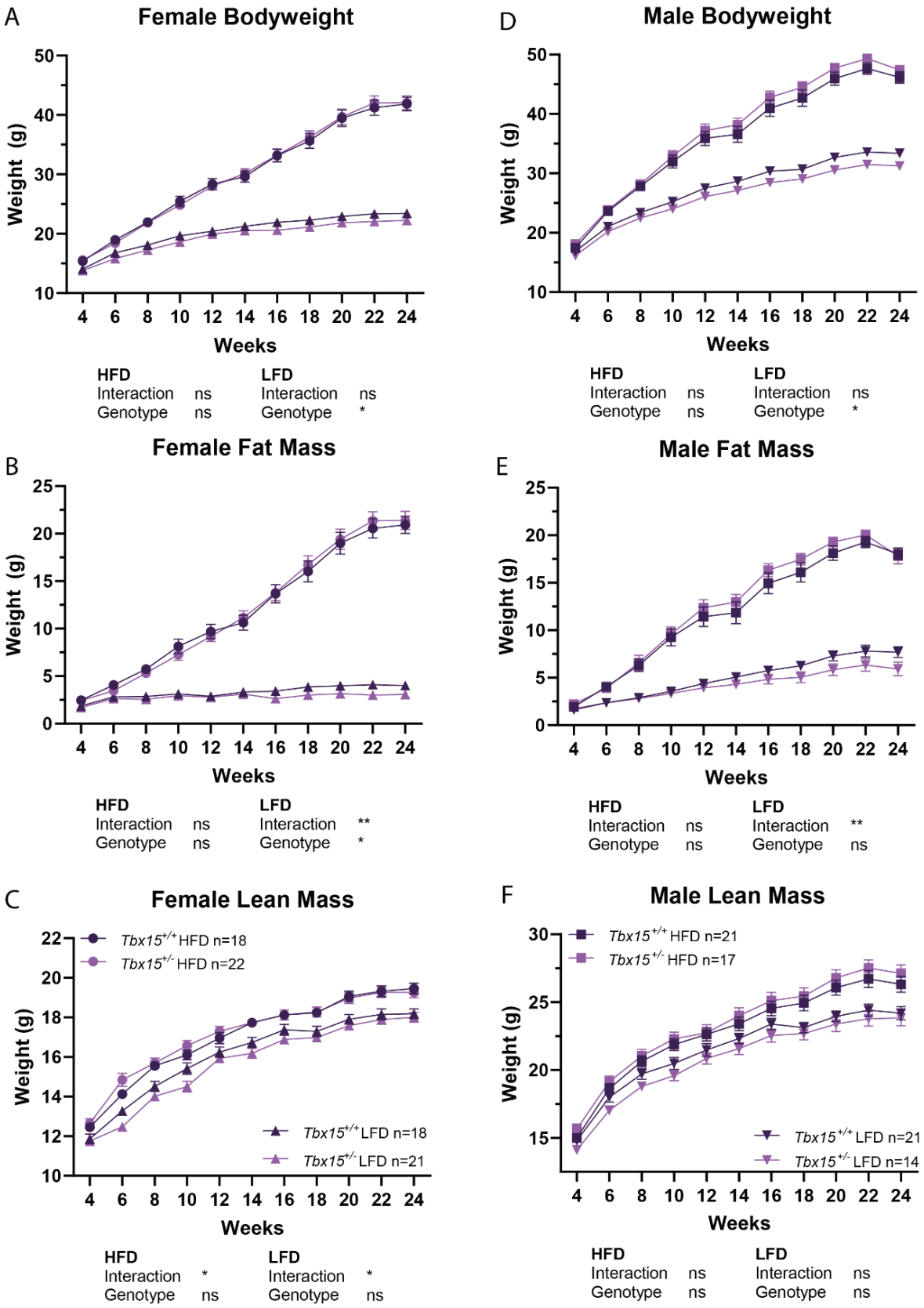

Figure 4.4. *Tbx15*$^{+/-}$ echo-MRI body composition over 4 to 24 weeks. Female (A-C), male (D-F). A, D. Body weight. B, E. Fat mass. C, F. Lean mass. *Tbx15*$^{+/+}$ (dark purple), *Tbx15*$^{+/-}$ (purple), female high-fat diet (HFD; circle), female low-fat diet (LFD; upwards triangle), male HFD (square), male LFD (downwards triangle). Data was analysed by two-way ANOVA with post-hoc Šídák's multiple comparisons: *p<0.05, **p<0.01 (*Tbx15*$^{+/+}$ *vs Tbx15*$^{+/-}$). Interaction effect (time x genotype).

4.2.4.2. *Tbx15*$^{+/H156N}$ mice had increased lean mass on high-fat diet

In comparison to *Tbx15*$^{+/-}$ mice, there was no significant genotype effect for bodyweight or fat mass between *Tbx15*^{H156N} female mice on either HFD or LFD (Figure 4.5A, Appendix Table 9.13). However, significantly more fat mass was detected in *Tbx15*$^{H156N/H156N}$ mice compared to *Tbx15*$^{+/+}$ littermates at 6, 8 and 10 weeks on LFD (p=0.0420, p=0.0429 and p=0.0267, respectively; Figure 4.5B). Strikingly, there was a strong genotype effect for lean mass in HFD-fed mice (p=0.0190; Figure 4.5C, Appendix Table 9.13). This was driven by more lean mass in *Tbx15*$^{+/H156N}$, but not *Tbx15*$^{H156N/H156N}$, mice compared to *Tbx15*$^{+/+}$ littermates at 10 and 14-24 weeks of age (p≤0.0444; Figure 4.5C, Appendix Table 9.13).

Similarly, there were no significant differences in bodyweight or fat mass between *Tbx15*^{H156N} male mice fed HFD or LFD (Figure 4.5D and E, Appendix Table 9.14). However, fat mass was significantly lower in *Tbx15*$^{H156N/H156N}$ mice compared to *Tbx15*$^{+/H156N}$ (8 weeks) and *Tbx15*$^{+/+}$ (24 weeks) mice fed a HFD (p=0.0229 and p=0.0333, respectively; Figure 4.5E, Appendix Table 9.14). The significant fat mass interaction effect in LFD-fed mice was not significantly driven by any individual time points (p=0.0093; Figure 4.5E, Appendix Table 9.14). Further, there was a significant genotype effect for lean mass in male mice on HFD (p=0.0131) but not LFD (Figure 4.5F, Appendix Table 9.14). This was driven by higher lean mass values in *Tbx15*$^{+/H156N}$ male mice compared to *Tbx15*$^{+/+}$ littermates from 6 weeks of age (p≤0.0117; Figure 4.5F, Appendix Table 9.13, Appendix Table 9.14). Overall, there was a significant lean mass phenotype in male and female *Tbx15*$^{+/H156N}$ mice compared to *Tbx15*$^{+/+}$ littermates fed a HFD, with *Tbx15*$^{H156N/H156N}$ male mice exhibiting a fat mass phenotype somewhat reflective of that seen in *Tbx15*$^{+/-}$ mice.

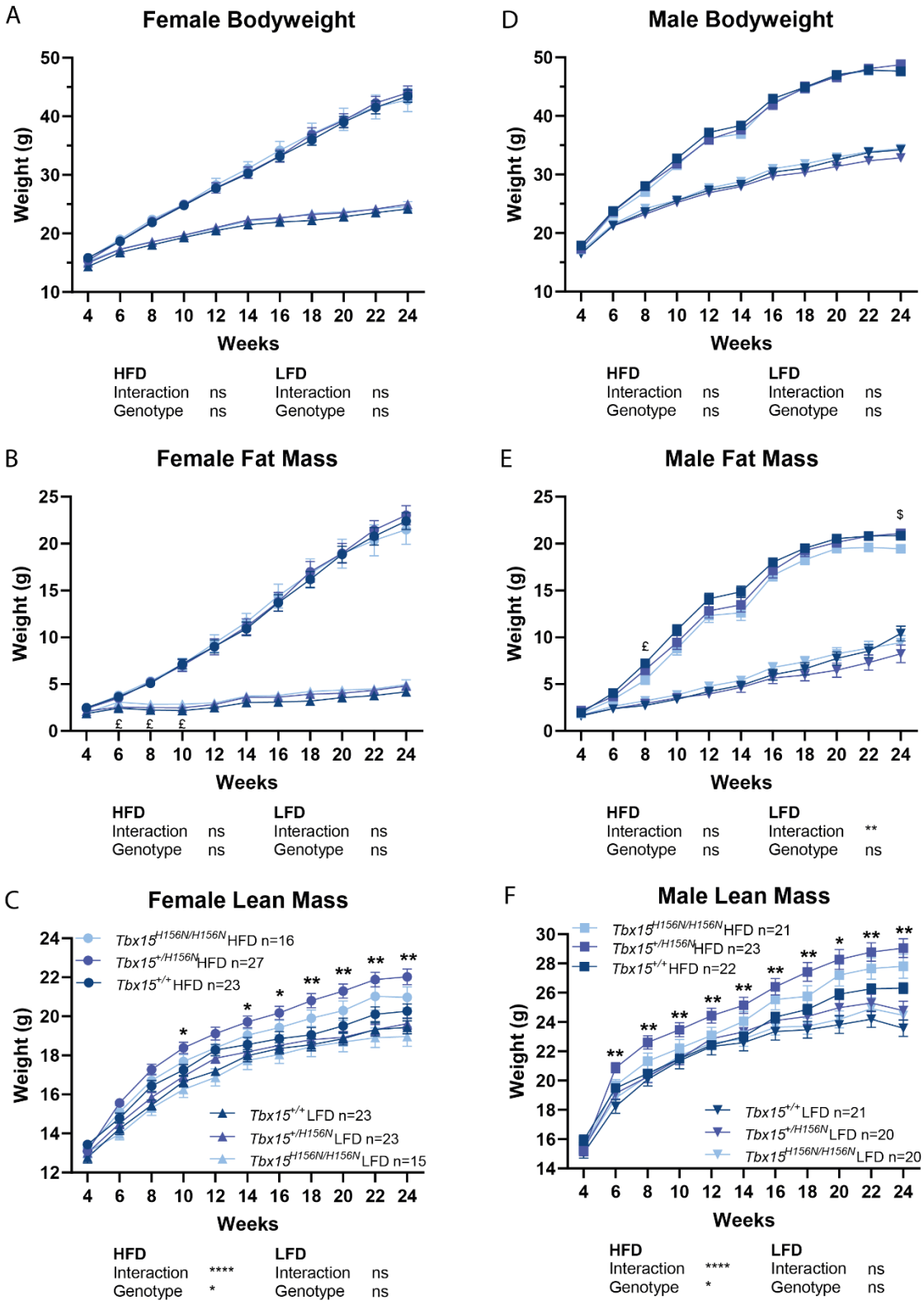

Figure 4.5. *Tbx15*^{H156N} echo-MRI body composition over 4 to 24 weeks. Female (A-C), male (D-F). A, D. Bodyweight. B, E. Fat mass. C, F. Lean mass. *Tbx15*$^{+/+}$ (dark blue), *Tbx15*$^{+/H156N}$ (blue), *Tbx15*$^{H156N/H156N}$ (light blue), female high-fat diet (HFD; circle), female low-fat diet (LFD; upwards triangle), male HFD (square), male LFD (downwards triangle). Data was analysed by two-way ANOVA with post-hoc Šídák's multiple comparisons: *p<0.05, **p<0.01, ****p<0.0001. Post-hoc Šídák's multiple comparisons: *p<0.05, **p<0.01 (*Tbx15*$^{+/+}$ *vs Tbx15*$^{+/H156N}$), £ p<0.05 (*Tbx15*$^{+/+}$ *vs Tbx15*$^{H156N/H156N}$) and $ p<0.05 (*Tbx15*$^{+/H156N}$ *vs Tbx15*$^{H156N/H156N}$). Interaction effect (time x genotype).

4.2.4.3. *Tbx15*^{M556R} did not exhibit body composition differences over time

There were very few significant body composition differences detected in *Tbx15*^{M566R} mice. In female mice fed HFD and LFD there were no significant genotype effects for bodyweight, fat mass or lean mass (Figure 4.6A-C, Appendix Table 9.15). In female mice fed a LFD there was a significant interaction (p=0.0245) effect for fat mass with a single significant difference detected between *Tbx15*$^{+/+}$ and *Tbx15*$^{M566R/M566R}$ mice at 16 weeks (p=0.0241; Figure 4.6B, Appendix Table 9.15).

In male mice on HFD and LFD, there were also no significant genotype effects for bodyweight, fat mass or lean mass (Figure 4.6D-F, Appendix Table 9.16). For male mice fed a LFD, there was a significant interaction effect for bodyweight (p=0.0082), however, no individual time points appeared to drive this (Figure 4.6D, Appendix Table 9.16). Despite *in silico* predictions suggesting the p.M566R substitution was damaging, this did not translate to a whole organism level with no obvious whole body phenotype detected in *Tbx15*^{M566R} mice in either sex or diet which contrasts the phenotypes observed in both *Tbx15*$^{+/-}$ and *Tbx15*^{H156N} mice.

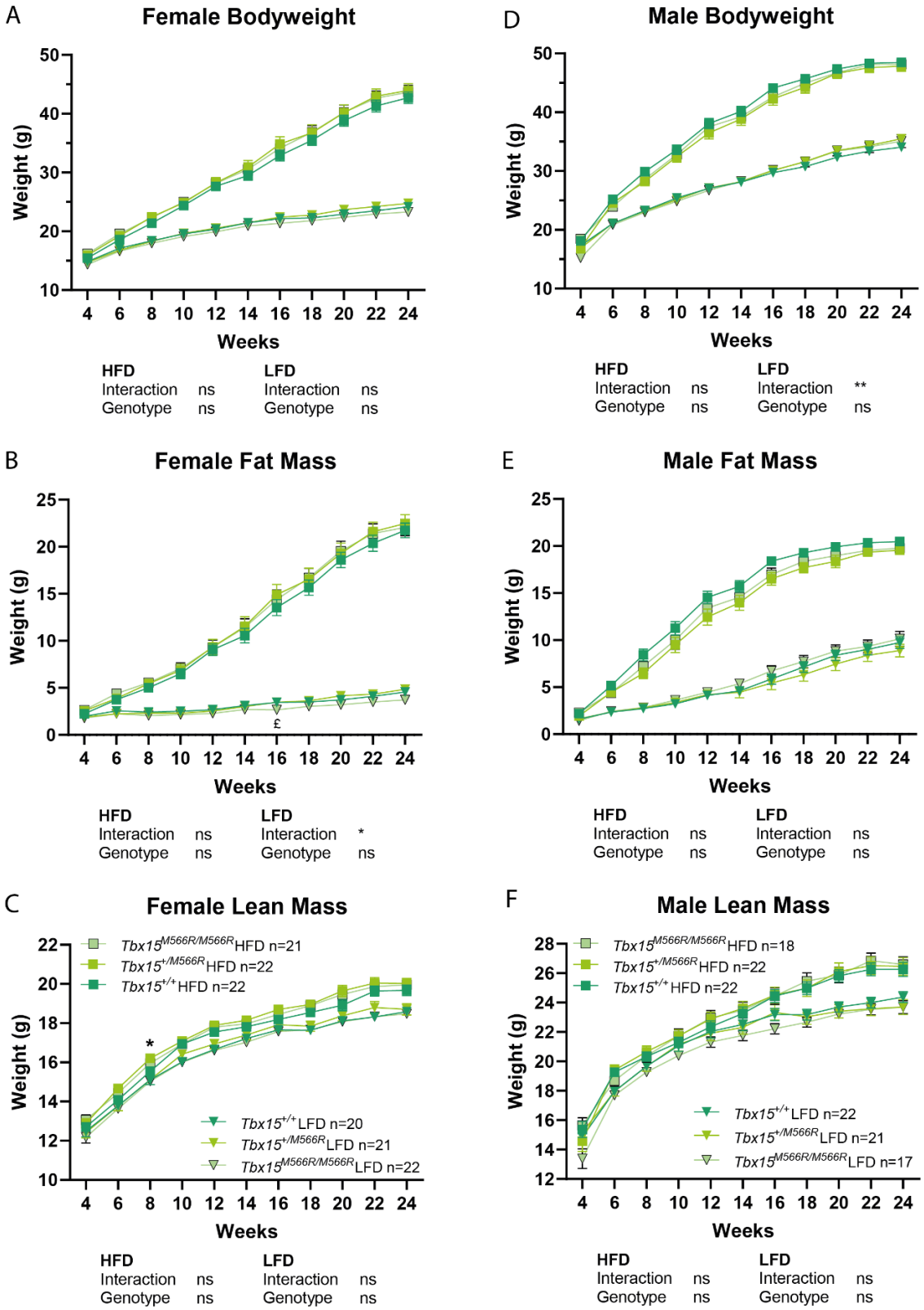

Figure 4.6. *Tbx15*^{M566R} echo-MRI body composition over 4 to 24 weeks. Female (A-C), male (D-F). A, D. Bodyweight. B, E. Fat mass. C, F. Lean mass. *Tbx15*$^{+/+}$ (dark green), *Tbx15*$^{+/H156N}$ (green), *Tbx15*$^{M566R/M566R}$ (light green), female high-fat diet (HFD; circle), female low-fat diet (LFD; upwards triangle), male HFD (square), male LFD (downwards triangle). Data was analysed by two-way ANOVA with post-hoc Šídák's multiple comparisons: *p<0.05, **p<0.01. Šídák's post-hoc comparisons: *p<0.05 (*Tbx15*$^{+/+}$ *vs Tbx15*$^{+/M566R}$), £ p<0.05 (*Tbx15*$^{+/+}$ *vs Tbx15*$^{M566R/M566R}$). Interaction effect (time x genotype).

4.2.5. Glucose response

As body composition was altered by *Tbx15* alleles, I sought to determine if these alleles affected T2DM phenotypes such as blood glucose response to glucose or insulin challenge. IPGTTs and IPISTs were performed under overnight fasted conditions at 13 weeks of age, and at 17 weeks of age following a 4-5 hour fast, respectively.

4.2.5.1. Female *Tbx15*$^{+/-}$ mice fed LFD had impaired glucose tolerance

Female *Tbx15*$^{+/-}$ mice on LFD had increased blood glucose levels in response to glucose challenge (p=0.0403, two-way ANOVA), however no individual time points drive this difference (Figure 4.7A, Appendix Table 9.17). Although a HFD reduced glucose tolerance, there was no significant difference in blood glucose response between genotypes (two-way ANOVA; Figure 4.7A, Appendix Table 9.17). No significant genotype differences were detected in either HFD- or LFD-fed mice for either AUC or fasted blood glucose levels (unpaired t-tests; Figure 4.7B-C, Appendix Table 9.18).

There was no significant difference in overall blood glucose response, AUC or fasted blood glucose levels between *Tbx15*$^{+/+}$ and *Tbx15*$^{+/-}$ male mice on either HFD or LFD, although similar to female mice a HFD reduced glucose tolerance generally (Figure 4.7D, E and F, respectively, Appendix Table 9.17, Appendix Table 9.18). Further, *Tbx15*$^{+/-}$ mice did not present an altered insulin response phenotype irrespective of diet or sex (Figure 4.8, Appendix Table 9.19, Appendix Table 9.20). In conclusion, *Tbx15*$^{+/-}$ female mice fed an LFD exhibited a significantly impaired glucose tolerance compared to *Tbx15*$^{+/+}$ littermates, although no underlying differences in response to glucose challenge were identified.

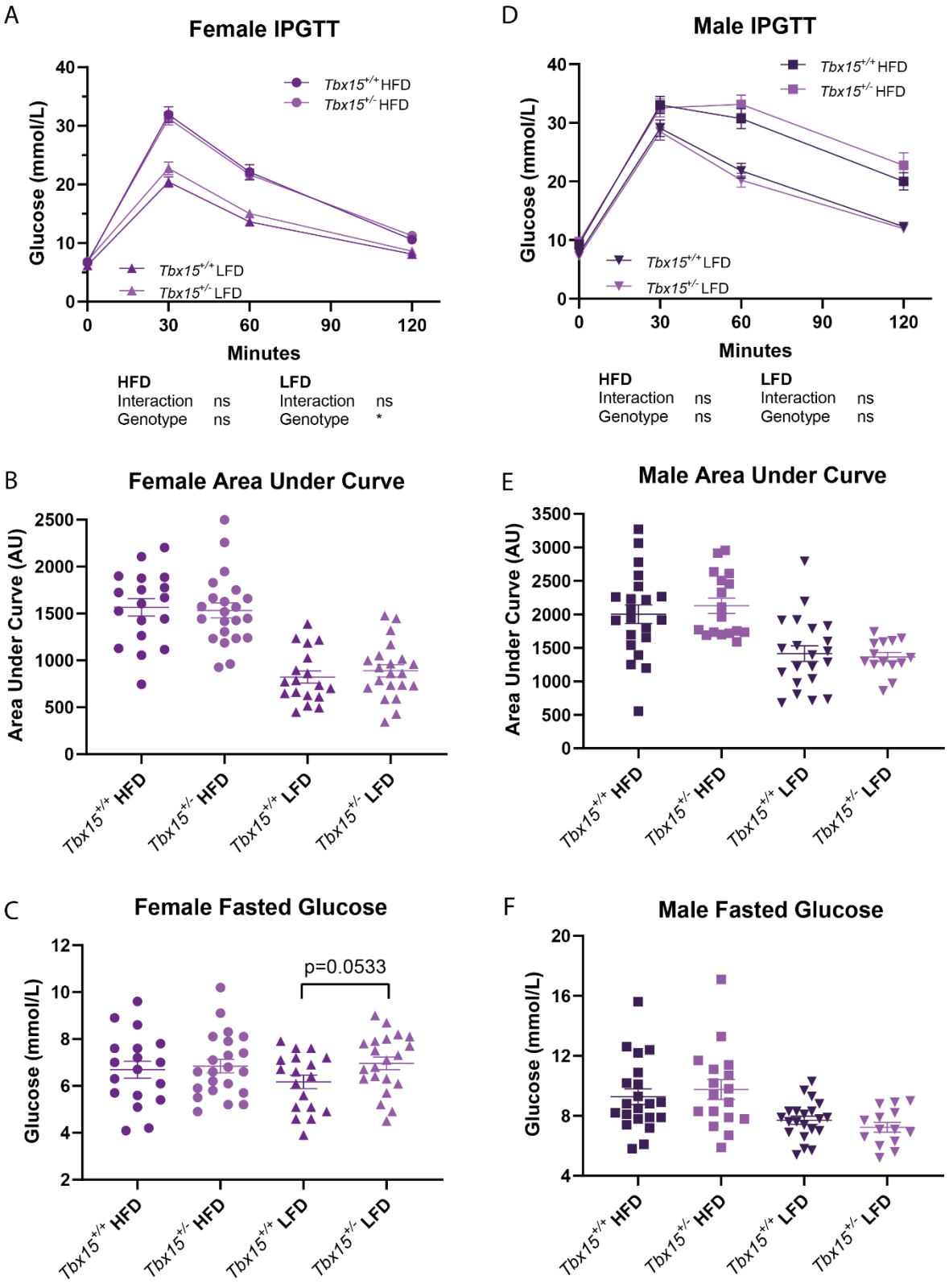

Figure 4.7. *Tbx15*$^{+/-}$ intraperitoneal glucose tolerance tests (IPGTT) at 13 weeks. Female (A-C), male (D-F). A, D. IPGTT. B, E. Area under curve. C, F. Fasted blood glucose. *Tbx15*$^{+/+}$ (dark purple), *Tbx15*$^{+/-}$ (purple), female high-fat diet (HFD; circle), female low-fat diet (LFD; upwards triangle), male HFD (square), male LFD (downwards triangle). IPGTT data was analysed by two-way ANOVA with pos_thoc Šídák's multiple comparisons: *p<0.05. Interaction effect (time x genotype). Area under curve and fasted glucose data was analysed by unpaired t-tests.

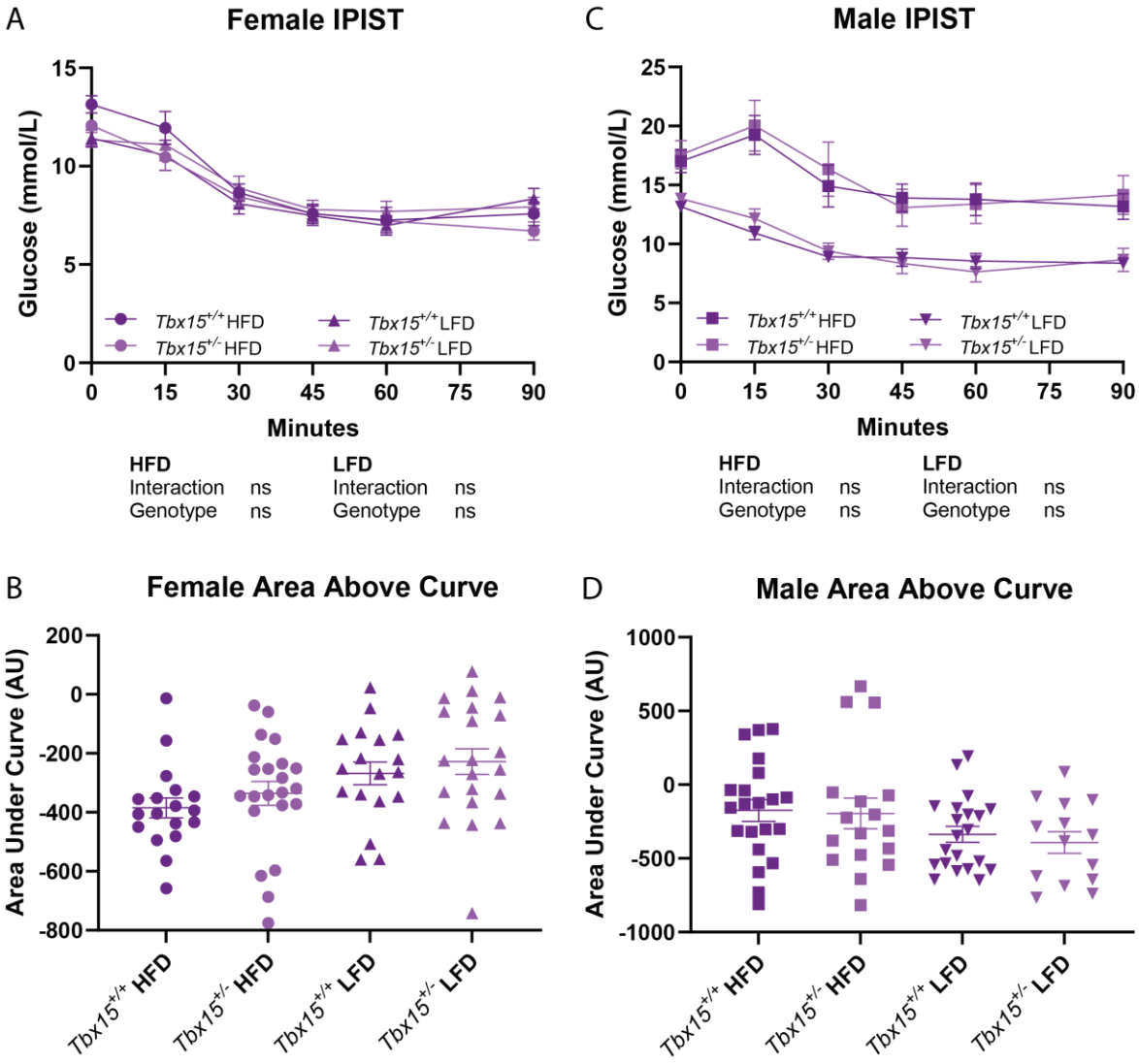

Figure 4.8. *Tbx15*$^{+/-}$ intraperitoneal insulin sensitivity tests (IPIST) at 17 weeks. Female (A-B), male (C-D). A, C. IPIST. B, D. Area under curve (AUC). *Tbx15*$^{+/+}$ (dark purple), *Tbx15*$^{+/-}$ (purple), female high-fat diet (HFD, circle), female low-fat diet (LFD, upwards triangle), male HFD (square), male LFD (downwards triangle). IPIST data analysed by two-way ANOVA with post-hoc Šídák's multiple comparisons per sex and diet. Interaction (time x genotype). Area above the curve data was analysed by unpaired t-tests per sex and diet.

4.2.5.2. *Tbx15*^{H156N} mice did not exhibit a differential glucose response

In comparison, there was no significant genotype effect for overall glucose response, AUC or fasted blood glucose levels in *Tbx15*^{H156N} female or male mice on HFD or LFD (two-way ANOVA; Figure 4.9, Appendix Table 9.21, Appendix Table 9.22). Further, *Tbx15*^{H156N} mice did not present an altered insulin response phenotype irrespective of

diet or sex, with the exception of an interaction effect in male mice on LFD (p=0.0436, two-way ANOVA; Figure 4.10, Appendix Table 9.23, Appendix Table 9.24). In summary, the p.H156N variant did not significantly alter glucose or insulin tolerance in these mice.

4.2.5.3. *Tbx15*$^{+/M566R}$ male mice fed a HFD had improved glucose clearance

Similar to *Tbx15*^{H156N} mice, there was no significant genotype effect in glucose response, AUC or fasted blood glucose levels in female *Tbx15*^{M566R} mice on either a HFD or LFD (two-way ANOVA; Figure 4.11A, Appendix Table 9.25, Appendix Table 9.26). Male mice on HFD and LFD also showed no significant genotype effect for glucose tolerance or AUC (Figure 4.11D and E, respectively, Appendix Table 9.25, Appendix Table 9.26). However, significantly lower blood glucose levels were detected in HFD-fed *Tbx15*$^{+/M566R}$ mice at both T0 and T30 compared to *Tbx15*$^{+/+}$ littermates (p=0.0497 and p=0.0198, respectively, two-way ANOVA; Figure 4.11D, Appendix Table 9.25). This was reflected in a significant genotype effect for fasted blood glucose levels in male mice on HFD (p=0.0318, one-way ANOVA; Figure 4.11F, Appendix Table 9.26). No significant differences in fasted blood glucose levels were detected in male mice on LFD (one-way ANOVA; Figure 4.11F, Appendix Table 9.26). Due to the minimal/no response seen in IPISTs in *Tbx15*$^{+/-}$ and *Tbx15*^{H156N} mice, IPISTs were not performed on *Tbx15*^{M566R} mice. In summary, *Tbx15*$^{+/M566R}$ male mice fed a HFD exhibited reduced fasted blood glucose and short-term (30 minutes post-injection) improved glucose tolerance compared to *Tbx15*$^{+/+}$ littermates which contrasted with both *Tbx15*$^{+/-}$ and *Tbx15*^{H156N} alleles.

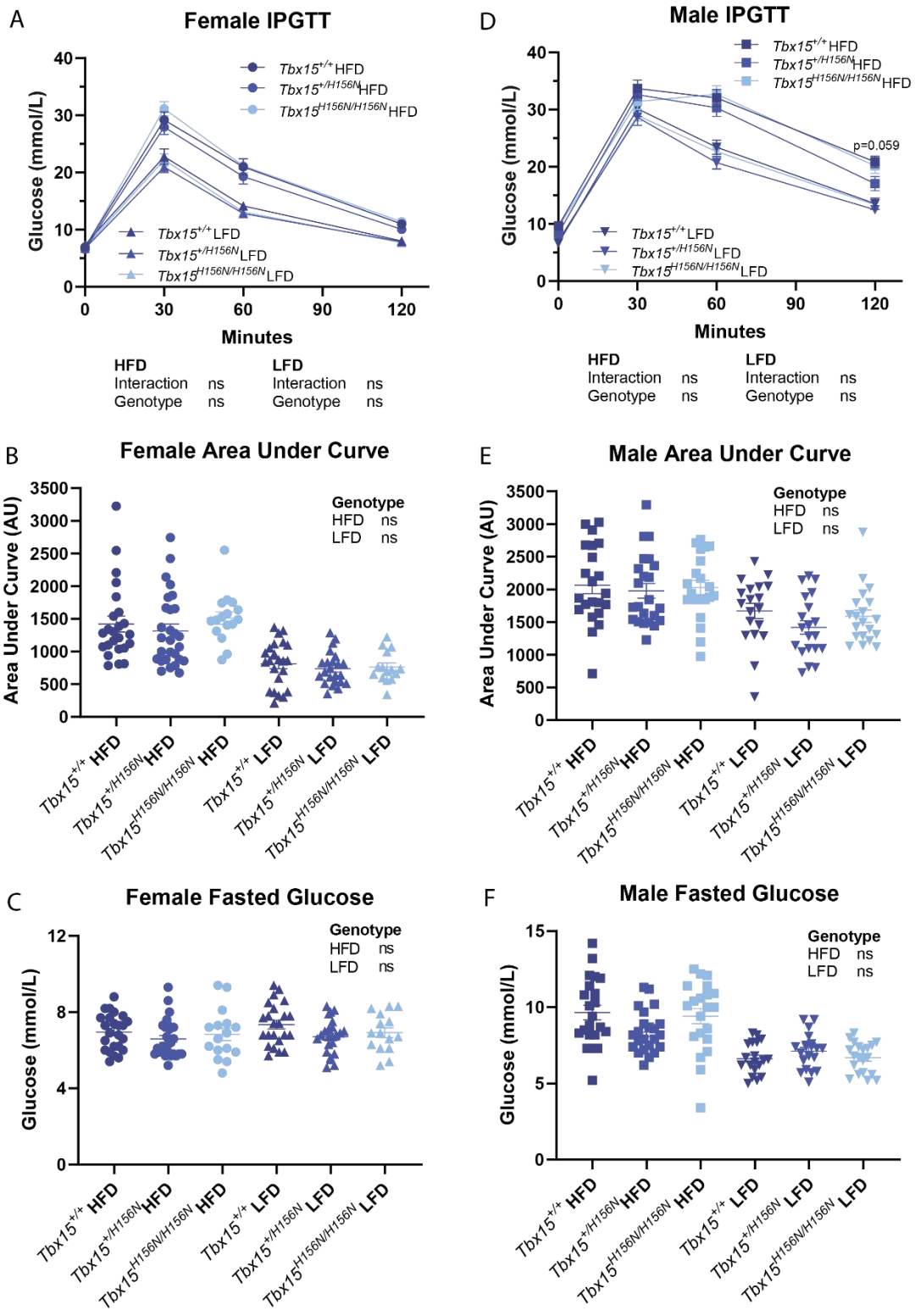

Figure 4.9. *Tbx15*^{H156N} intraperitoneal glucose tolerance tests (IPGTT) at 13 weeks. Female (A-C), male (D-F). A, D. IPGTT. B, E. Area under curve. C, F. Fasted blood glucose (T0). *Tbx15*$^{+/+}$ (dark blue), *Tbx15*$^{+/H156N}$ (blue), *Tbx15*$^{H156N/H156N}$ (light blue) female high-fat diet (HFD; circle), female low-fat diet (LFD; upwards triangle), male HFD (square), male LFD (downwards triangle). IPGTT data was analysed by two-way ANOVA with post-hoc Šídák's multiple comparisons, interaction (time x genotype). Area under curve and T0 glucose data was analysed by one-way ANOVA with post-hoc Tukey's multiple comparisons. Two *Tbx15*$^{+/+}$ and one *Tbx15*$^{+/H156N}$ LFD males were not included in IPGTT testing due to fighting-induced wounds (identified after overnight fast).

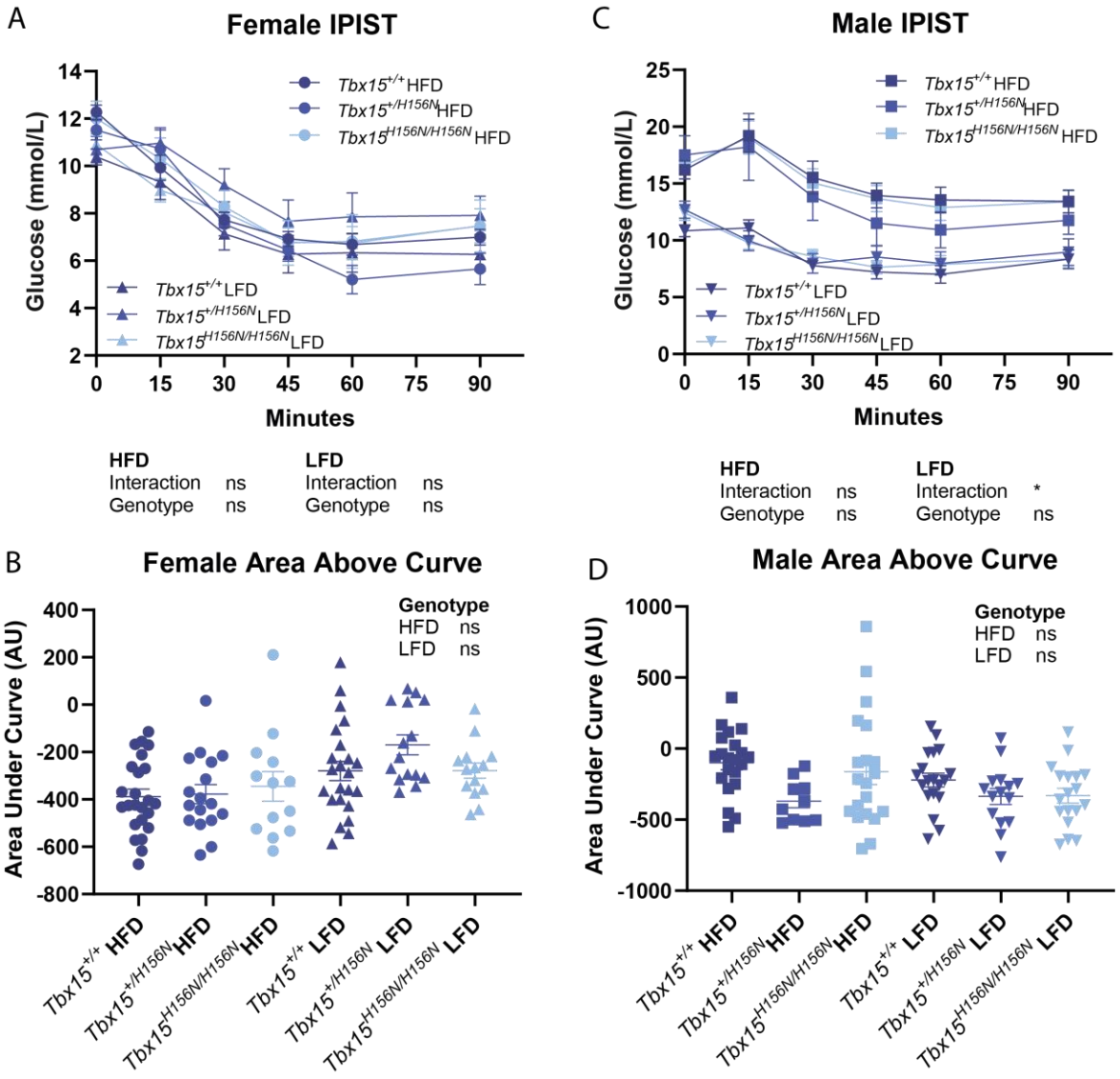

Figure 4.10. *Tbx15*^{H156N} intraperitoneal insulin sensitivity test (IPIST) at 17 weeks. Female (A-B), male (C-D). A, C. IPIST. B, D. Area under curve (AUC). *Tbx15*$^{+/+}$ (dark blue), *Tbx15*$^{+/H156N}$ (blue), *Tbx15*$^{H156N/H156N}$ (light blue), female high-fat diet (HFD, circle), female low-fat diet (LFD, upwards triangle), male HFD (square), male LFD (downwards triangle). IPIST data analysed by two-way ANOVA with post-hoc Šídák's multiple comparisons per sex and diet. Interaction (time x genotype). Area above the curve data was analysed by one-way ANOVA with post-hoc Tukey's multiple comparisons. *p<0.05.

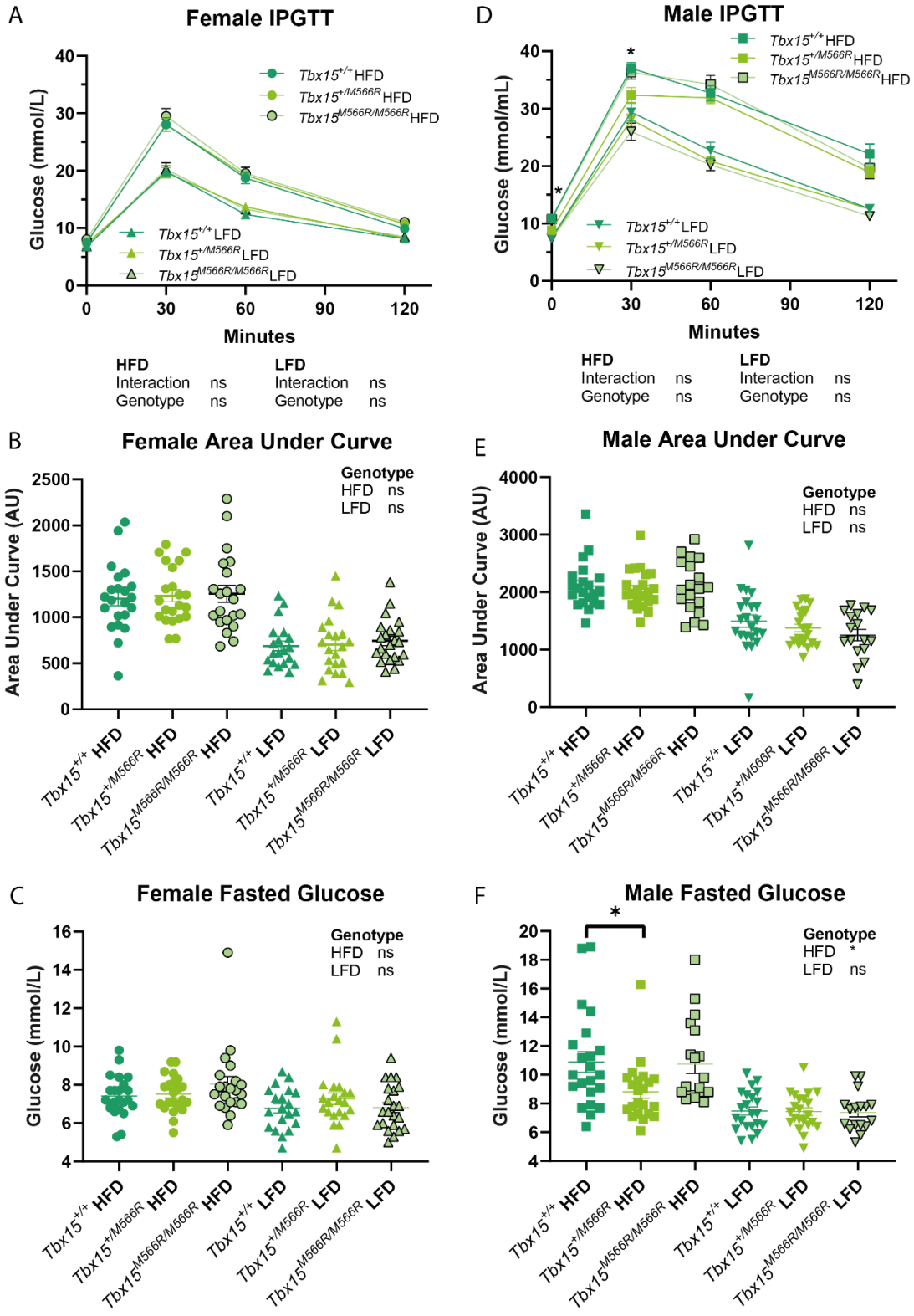

Figure 4.11. *Tbx15*^{M566R} intraperitoneal glucose tolerance tests (IPGTT) at 13 weeks. Female (A-C), male (D-F). A, D. IPGTT. B, E. Area under curve. C, F. Fasted blood glucose (T0). *Tbx15*$^{+/+}$ (dark green), *Tbx15*$^{+/M566R}$ (green), *Tbx15*$^{M566R/M566R}$ (light green) female high-fat diet (HFD; circle), female low-fat diet (LFD; upwards triangle), male HFD (square), male LFD (downwards triangle). IPGTT data was analysed by two-way ANOVA with post-hoc Šídák's multiple comparisons, interaction (time x genotype). Šídák's post-hoc comparisons: *p<0.05 (*Tbx15*$^{+/+}$ *vs Tbx15*$^{+/M566R}$). Area under curve and T0 glucose data was analysed by one-way ANOVA with post-hoc Tukey's multiple comparisons, genotype: *p<0.05. Tukey's post-hoc comparisons: *p<0.05 (*Tbx15*$^{+/+}$ *vs Tbx15*$^{+/M566R}$).

4.2.6. DEXA body composition at early adulthood

While echo-MRI provides total fat mass (g) and lean mass (g) values, it does not distinguish other body parts that make up the lean mass value. DEXA provides more detailed information on body composition, such as bone mineral content and density (BMC and BMD, respectively), than echo-MRI procedures. As *Tbx15*$^{-/-}$ mice exhibited skeletal abnormalities (Curry, 1959; Candille *et al.*, 2004; Singh *et al.*, 2005), I aimed to determine if the *Tbx15* alleles affected bone mineral composition.

4.2.6.1. *Tbx15*$^{+/-}$ mice on LFD exhibit sexually dimorphic body composition

Tbx15$^{+/-}$ mice underwent DEXA at 23 weeks of age under recoverable anaesthesia. In line with echo-MRI data, there was no significant difference in body composition or bone mineral composition in female and male mice on HFD (unpaired t-tests; Figure 4.12, Appendix Table 9.27). In mice fed a LFD, there was no significant difference in bodyweight in female mice, but *Tbx15*$^{+/-}$ mice had less total fat mass than *Tbx15*$^{+/+}$ littermates (p=0.0413, unpaired t-tests; Figure 4.12A-C, Appendix Table 9.27). Conversely, *Tbx15*$^{+/-}$ male mice on LFD had significantly less bodyweight than *Tbx15*$^{+/+}$ littermates (p=0.0340), with no significant differences in fat mass or lean mass driving this (unpaired t-tests, Figure 4.12G-J, Appendix Table 9.27). BMD and BMC were not significantly different between genotypes in either female or male mice on LFD (unpaired t-tests; Figure 4.12D-F, and J-L, respectively, Appendix Table 9.27). These DEXA data were reflective of the overall body composition data from echo-MRI for mice fed a LFD, with reduced bodyweight (male) and fat mass (female) in *Tbx15*$^{+/-}$ mice compared to *Tbx15*$^{+/+}$ littermates.

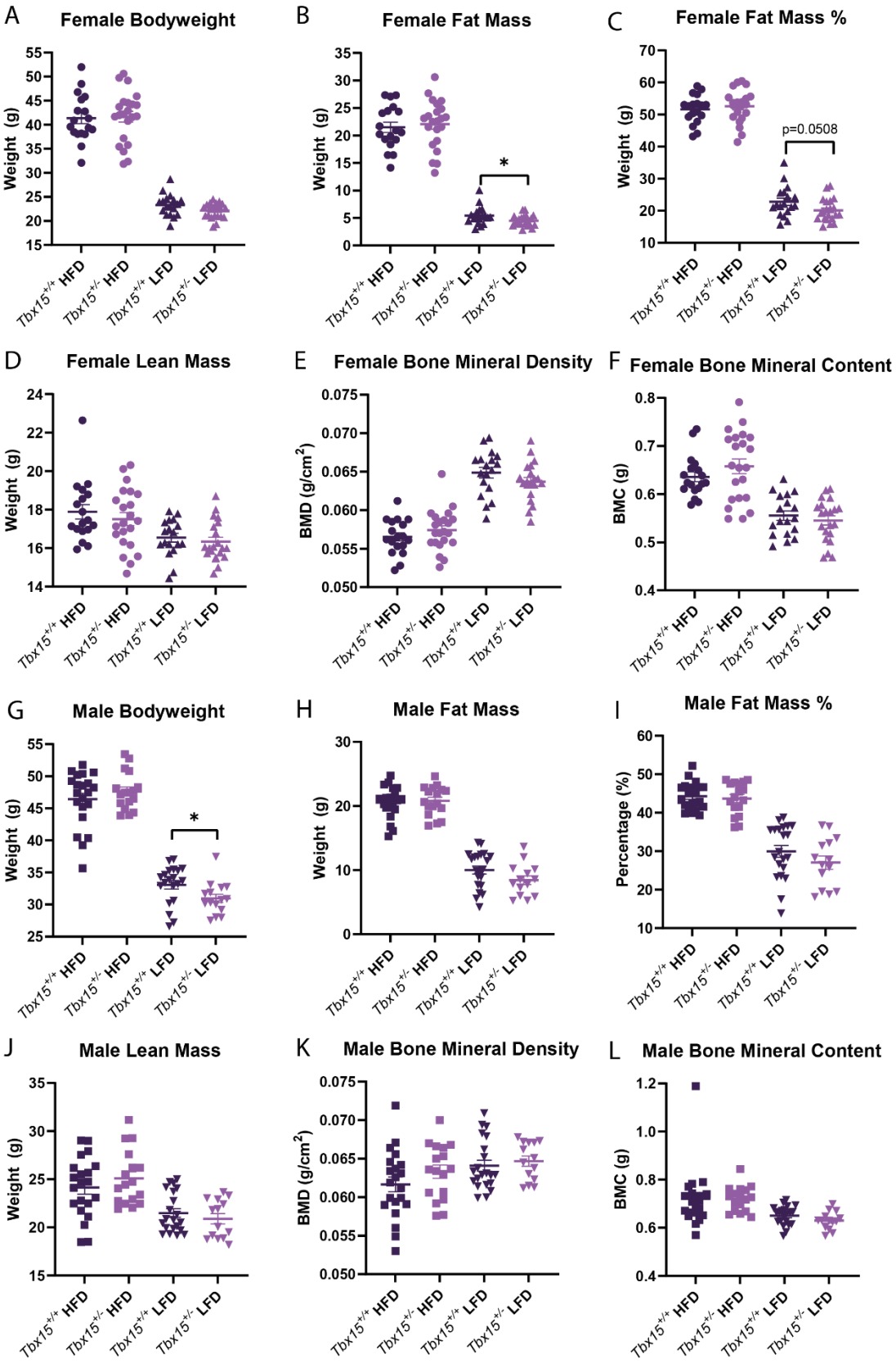

Figure 4.12. *Tbx15*$^{+/-}$ DEXA at 23 weeks under recoverable anaesthesia. Female (A-F), male (G-L). A, G. Bodyweight. B, H. Fat mass. C, I. Fat mass %. D, J. Lean mass. E, K. Bone mineral density (BMD). F, L. Bone mineral content (BMC). *Tbx15*$^{+/+}$ (dark purple), *Tbx15*$^{+/-}$ (purple), female high-fat diet (HFD; circle), female low-fat diet (LFD; upwards triangle), male HFD (square), male LFD (downwards triangle). All data was analysed by unpaired t-tests per sex and diet: *p<0.05.

4.2.6.2. *Tbx15*$^{H156N/H156N}$ male mice fed a HFD exhibited less fat mass

Tbx15^{H156N} mice underwent DEXA at 24 weeks of age under terminal anaesthesia (performed by Dr. Liz Bentley). There was no significant difference in body composition in female mice on either HFD or LFD (one-way ANOVA; Figure 4.13A-F, Appendix Table 9.28). Further, despite the strong genotype effects for lean mass in HFD-fed female and male mice using echo-MRI (Figure 4.4C and F, respectively), this was not detected in DEXA (one-way ANOVA; Figure 4.13D and J, respectively, Appendix Table 9.28, Appendix Table 9.29). However, in male mice on HFD, fat mass and fat mass percentage were significantly different (p=0.0364, and p=0.0231, respectively) driven by lower fat mass and fat mass percentage in *Tbx15*$^{H156N/H156N}$ mice compared to *Tbx15*$^{+/+}$ littermates (p=0.0346 and p=0.0355, respectively, one-way ANOVA; Figure 4.13H and I, Appendix Table 9.29). *Tbx15*$^{+/H156N}$ mice showed an intermediate, albeit not significant, phenotype for fat mass and fat mass percentage (Figure 4.13H and I, Appendix Table 9.29). These DEXA data reflected the significant decrease in fat mass in *Tbx15*$^{H156N/H156N}$ male mice fed a HFD detected in echo-MRI data. However, the lack of significant differences detected in lean mass in *Tbx15*$^{+/H156N}$ mice suggested there may be differences in measurement techniques between the methods.

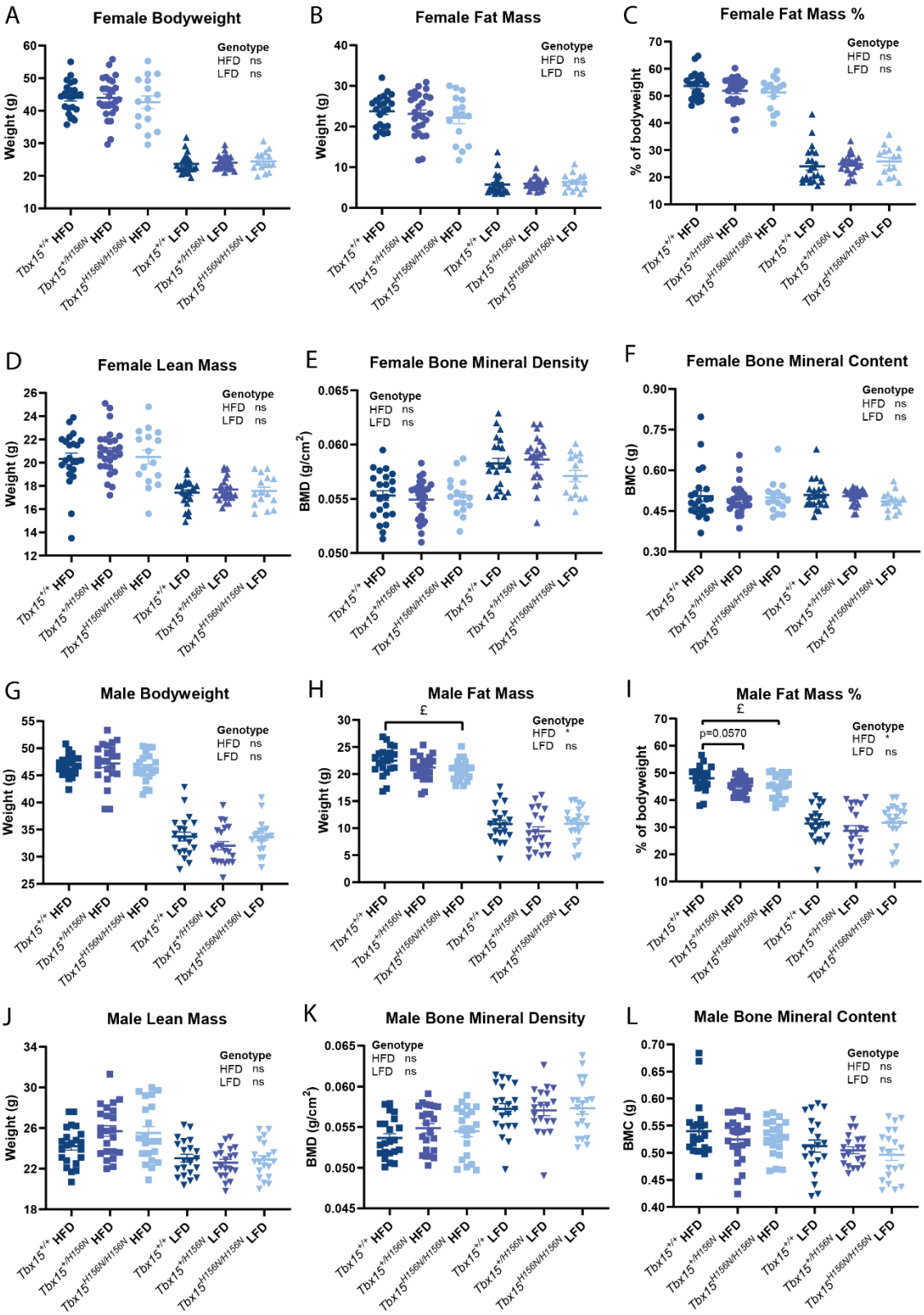

Figure 4.13. *Tbx15*^{H156N} DEXA at 24 weeks under terminal anaesthesia. Female (A-F), male (G-L). A, G. Bodyweight. B, H. Fat mass. C, I. Fat mass %. D, J. Lean mass. E, K. Bone mineral density (BMD). F, L. Bone mineral content (BMC). *Tbx15*$^{+/+}$ (dark blue), *Tbx15*$^{+/H156N}$ (blue), *Tbx15*$^{H156N/H156N}$ (light blue), female high-fat diet (HFD; circle), female low-fat diet (LFD; upwards triangle), male HFD (square), male LFD (downwards triangle). All data analysed by one-way ANOVA with post-hoc Tukey's multiple comparisons per sex and diet, genotype: *p<0.05. Tukey's post-hoc comparisons: £ p<0.05 (*Tbx15*$^{+/+}$ vs *Tbx15*$^{H156N/H156N}$).

4.2.6.3. *Tbx15*$^{M566R/M566R}$ female mice fed a LFD had less fat mass

Tbx15^{M566R} mice underwent DEXA with recoverable anaesthesia at 23 weeks of age. Similar to echo-MRI, DEXA analysis indicated there was no significant difference in body composition between genotypes for female mice fed a HFD (one-way ANOVA; Figure 4.14A-C, Appendix Table 9.30). There was, however, a significant genotype effect in fat mass (p=0.0427) in female mice fed a LFD, driven by less fat mass in *Tbx15*$^{M566R/M566R}$ mice compared to *Tbx15*$^{+/M566R}$ littermates, with fat mass percentage also significantly lower in *Tbx15*$^{M566R/M566R}$ mice (p=0.0329 and p=0.04030, respectively, one-way ANOVA; Figure 4.14B and C, Appendix Table 9.30).

There were no significant differences in body composition phenotypes measured in male mice on HFD or LFD (Figure 4.14G-L, Appendix Table 9.31). These data were largely indicative of the minimal significant differences detected in echo-MRI data for *Tbx15*^{M566R} mice. The significantly less fat mass and fat mass percentage between LFD-fed female *Tbx15*$^{M566R/M566R}$ and *Tbx15*$^{+/M566R}$ littermates may explain the interaction effect detected for fat mass in echo-MRI. All three *Tbx15* alleles exhibited reduced fat mass phenotypes, albeit to varying degrees, in a sex- and diet-specific manner.

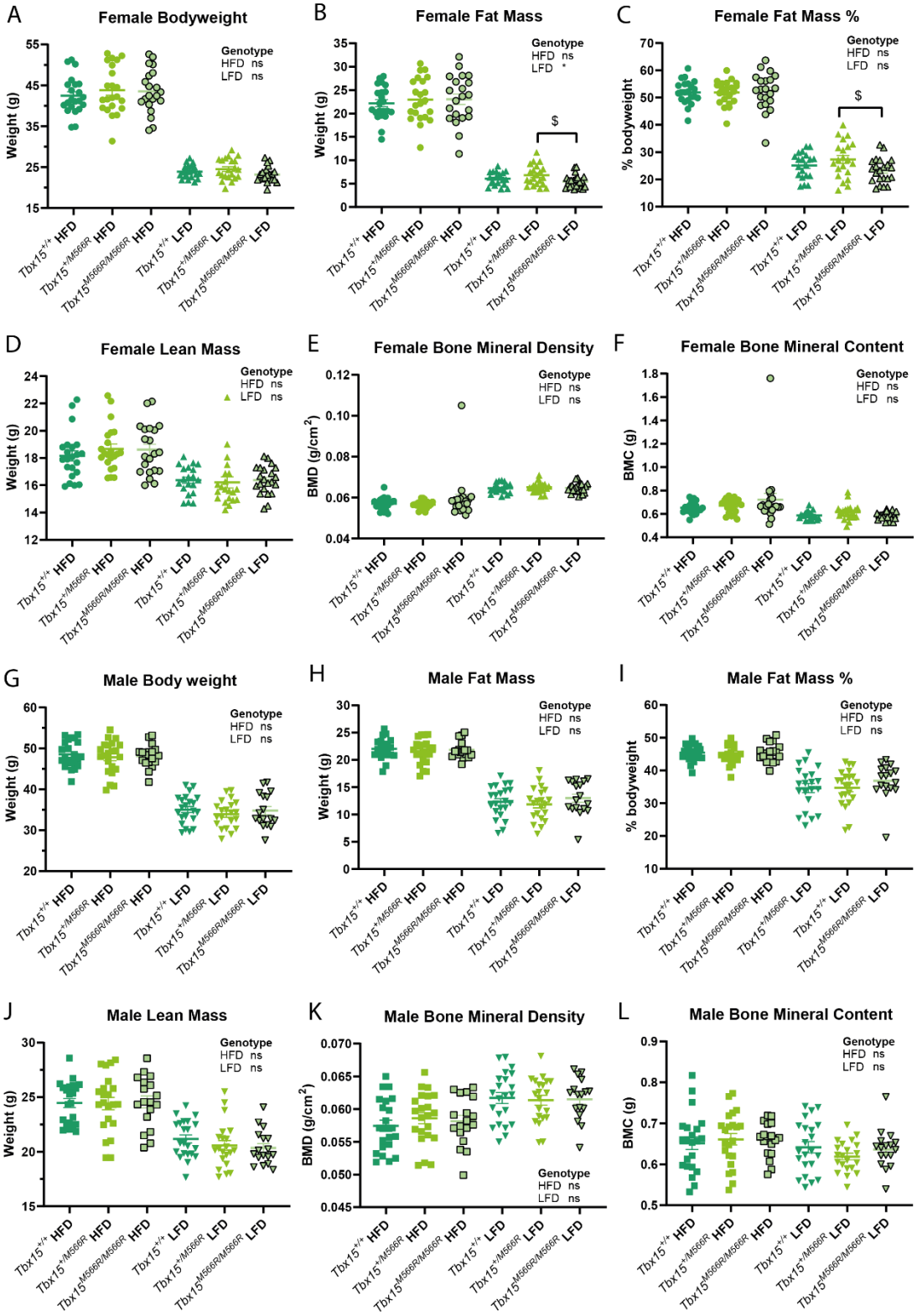

Figure 4.14. *Tbx15*^{M566R} DEXA at 23 weeks under recoverable anaesthesia. Female (A-F), male (G-L). A, G. Bodyweight. B, H. Fat mass. C, I. Fat mass %. D, J. Lean mass. E, K. Bone mineral density. F, L. Bone mineral content. *Tbx15*$^{+/+}$ (dark green), *Tbx15*$^{+/M566R}$ (green), *Tbx15*$^{M566R/M566R}$ (light green), female high-fat diet (HFD; circle), female low-fat diet (LFD; upwards triangle), male HFD (square), male LFD (downwards triangle). All data was analysed by one-way ANOVA with post-hoc Tukey's multiple comparisons per sex and diet, genotype *p<0.05. Tukey's post-hoc comparisons: $ p<0.05 (*Tbx15*$^{+/M566R}$ vs *Tbx15*$^{M566R/M566R}$). In panel E and F, the "outlier" sample was retained for analysis as there was no biological reason to exclude it.

4.2.7. Adipose depot distribution

I next aimed to determine if fat mass differences could be attributed to altered adipose depot distribution. At 24-25 weeks of age mice were fasted for 4-5 hours, humanely euthanised by anaesthetic overdose and blood plasma samples were collected (*Tbx15*^{H156N} by Dr. Liz Bentley, and *Tbx15*$^{+/-}$ and *Tbx15*^{M566R} by the MLC necropsy facility). Following this, body length was measured from tip-of-the-nose to base-of-the-tail, and tissues were dissected and weighed.

4.2.7.1. *Tbx15*$^{+/-}$ mice on LFD had smaller adipose tissues

LFD-fed *Tbx15*$^{+/-}$ female mice had significantly lower bodyweights than *Tbx15*$^{+/+}$ littermates (p=0.0351, unpaired t-test; Figure 4.15A, Appendix Table 9.32). Further, gWAT (q=0.0448), mWAT (q=0.0448), BAT (q=0.0448) and iWAT (q=0.0448) depots were smaller in *Tbx15*$^{+/-}$ mice, of which gWAT (p=0.0182) and mWAT (p=0.0353) remained nominally significant when adjusted for bodyweight (multiple unpaired t-tests; Figure 4.15A-O, Appendix Table 9.33). On HFD, *Tbx15*$^{+/-}$ mice had shorter nose-to-base-of-tail length than *Tbx15*$^{+/+}$ littermates (p=0.0013, unpaired t-test) and significantly larger gWAT after adjustment for bodyweight (q=0.0246, multiple unpaired t-tests; Figure 4.15B and I, respectively, Appendix Table 9.32, Appendix Table 9.33). There was no significant difference in gWAT:iWAT ratio, a proxy measure for WHR, between genotypes on either HFD or LFD (unpaired t-tests; Figure 4.15O, Appendix Table 9.32).

LFD-fed *Tbx15*$^{+/-}$ male mice also had lower bodyweights than *Tbx15*$^{+/+}$ littermates (p=0.0421, unpaired t-test; Figure 4.16A, Appendix Table 9.32). Lower gWAT weights

were nominally significant (p=0.0186) in *Tbx15*$^{+/-}$ LFD mice, remaining so after adjustment for bodyweight (p=0.0269, multiple unpaired t-tests; Figure 4.16C and I, respectively, Appendix Table 9.33). No significant genotype effects were detected for any terminal measurements in male mice fed a HFD (Figure 4.16A-O, Appendix Table 9.32, Appendix Table 9.33). This data suggested the overall lower bodyweights and fat mass in *Tbx15*$^{+/-}$ mice fed a LFD may be driven by smaller visceral and subcutaneous depots in females, whilst in males this was seemingly driven only by smaller gWAT depots.

4.2.7.2. *Tbx15*^{H156N} male mice had decreased WAT weights

In female *Tbx15*^{H156N} mice, no significant terminal measurement differences were detected in either HFD or LFD-challenged mice (Figure 4.17, Appendix Table 9.34, Appendix Table 9.36). In HFD-fed male mice, there were no significant differences in bodyweight, length or gWAT:iWAT ratio (one-way ANOVA; Figure 4.18A, B and O, Appendix Table 9.35). HFD-fed *Tbx15*$^{H156N/H156N}$ male mice had significantly smaller iWAT than *Tbx15*$^{+/H156N}$ littermates, which remained significant when adjusted for bodyweight (p=0.0087 and p=0.0071, respectively, two-way ANOVA; Figure 4.18H and N, Appendix Table 9.36). After adjustment for bodyweight, *Tbx15*$^{+/H156N}$ mice also had significantly smaller pWAT than *Tbx15*$^{+/+}$ littermates when challenged with a HFD (p=0.0375, two-way ANOVA; Figure 4.18L, Appendix Table 9.36).

In male mice fed a LFD, there were no significant differences in bodyweight or gWAT:iWAT ratio measurements (one-way ANOVA; Figure 4.18A and O, Appendix Table 9.35). However, a significant genotype effect for body length (p=0.0162) was driven by a shorter nose-to-base-of-tail length in *Tbx15*$^{+/H156N}$ mice compared to

Tbx15$^{+/+}$ littermates (p=0.0123, one-way ANOVA; Figure 4.18B, Appendix Table 9.35). Similar to HFD male mice, LFD-fed *Tbx15*$^{+/H156N}$ mice had significantly smaller pWAT than *Tbx15*$^{+/+}$ littermates, which remained significant after adjustment for bodyweight (p=0.0048 and p=0.0054, respectively, two-way ANOVA; Figure 4.18F and L, Appendix Table 9.36). Most notably, male *Tbx15*$^{H156N/H156N}$ mice fed a HFD had significantly smaller iWAT depots than *Tbx15*$^{+/H156N}$ littermates which may explain the subtle reduction in overall fat mass seen in echo-MRI and DEXA data. However, overall differences in *Tbx15*^{H156N} mice were fewer than in *Tbx15*$^{+/-}$ mice.

4.2.7.3. *Tbx15*^{M566R} mice did not have altered tissue distribution

In contrast to both *Tbx15*$^{+/-}$ and *Tbx15*^{H156N} mouse lines, the *Tbx15*^{M566R} line exhibited no significant genotype differences for any terminal body measurements or depot weights, irrespective of sex or diet (Figure 4.19, Figure 4.20, Appendix Table 9.37, Appendix Table 9.38, Appendix Table 9.39). Whilst this data largely supported the lack of significant differences identified in echo-MRI and DEXA data, it did not reveal any potential underlying causes for the lower fat mass and fat mass percentage detected in *Tbx15*$^{M566R/M566R}$ female mice fed a LFD. These data suggest the p.H156N and p.M566R alleles may alter fat distribution independently of the *Tbx15*$^{+/-}$ allele.

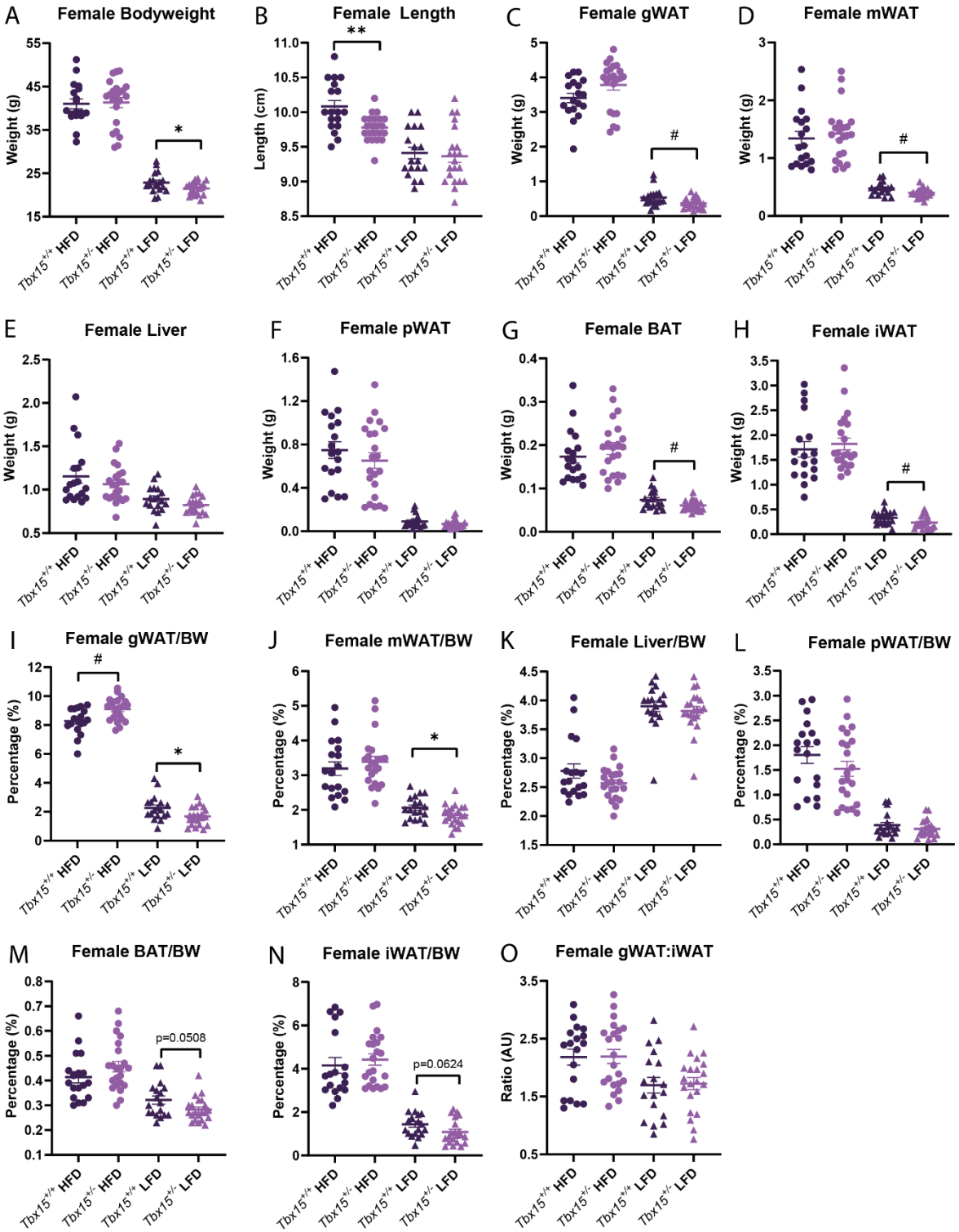

Figure 4.15. Female *Tbx15*$^{+/-}$ terminal adipose depot measurements and distribution. A. Bodyweight, B. Length, C. gWAT, D. mWAT, E. Liver, F. pWAT, G. BAT, H. iWAT, I. gWAT/BW (bodyweight), J. mWAT/BW, K. Liver/BW, L. pWAT/BW, M. BAT/BW, N. iWAT/BW, O. gWAT:iWAT ratio. *Tbx15*$^{+/+}$ (dark purple), *Tbx15*$^{+/-}$ (purple), female high-fat diet (HFD; circle), female low-fat diet (LFD; upwards triangle). Bodyweight, length and gWAT:iWAT ratio analysed by unpaired t-test, *p<0.05, **p<0.01. Depots and depots/BW analysed by multiple unpaired t-test (Two-stage step-up (Benjamini, Krieger, and Yekutieli) (false discovery rate 5%)). *p<0.05, **p<0.01, #q<0.05.

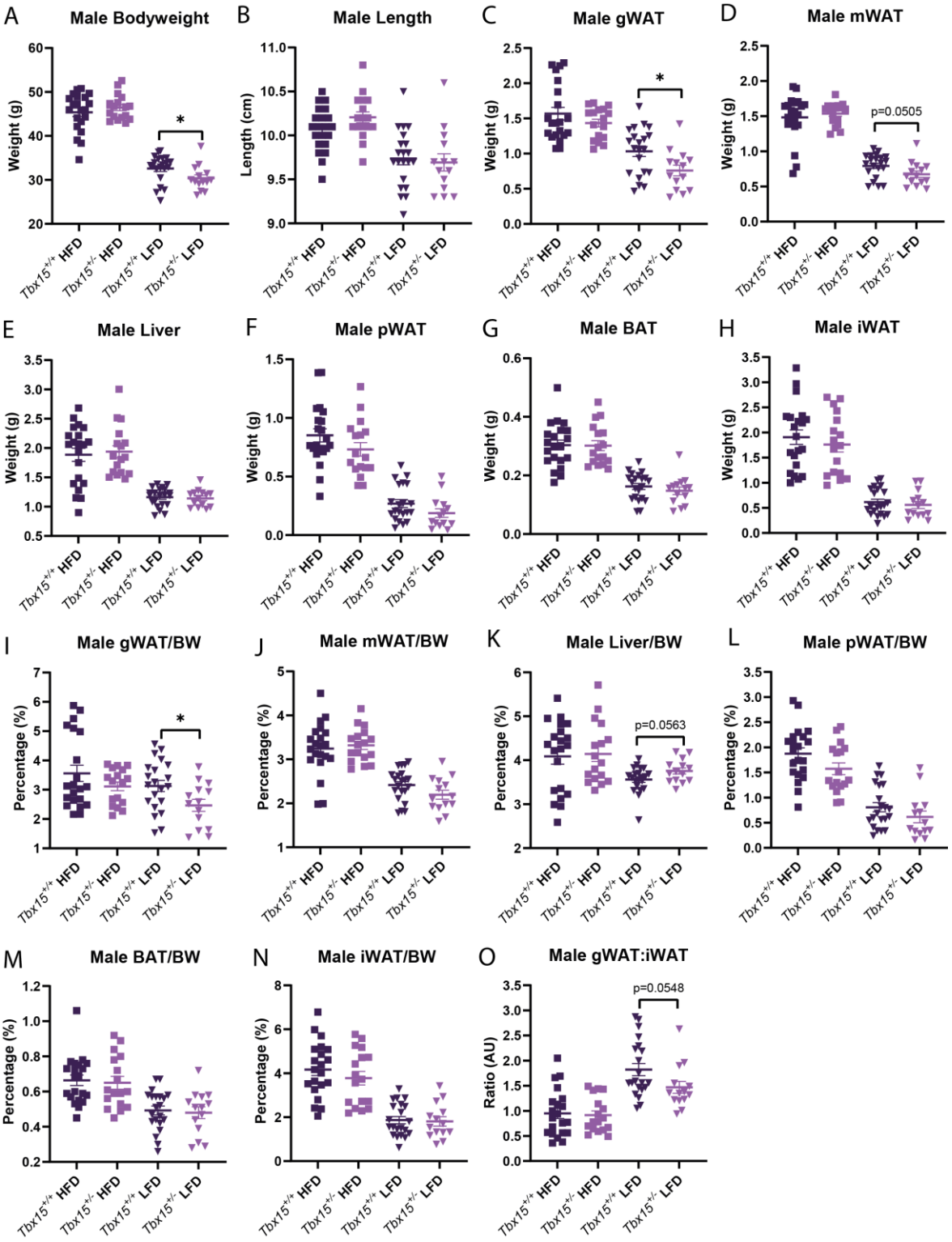

Figure 4.16. Male *Tbx15*$^{+/-}$ terminal adipose depot measurements and distribution. A. Bodyweight, B. Length, C. gWAT, D. mWAT, E. Liver, F. pWAT, G. BAT, H. iWAT, I. gWAT/BW (bodyweight), J. mWAT/BW, K. Liver/BW, L. pWAT/BW, M. BAT/BW, N. iWAT/BW, O. gWAT:iWAT ratio. *Tbx15*$^{+/+}$ (dark purple), *Tbx15*$^{+/-}$ (purple), male high-fat diet (HFD; square), male low-fat diet (LFD; downwards triangle). Bodyweight, length and gWAT:iWAT ratio analysed by unpaired t-test, *P<0.05. Depots and depots/BW analysed by multiple unpaired t-test (Two-stage step-up (Benjamini, Krieger, and Yekutieli) (false discovery rate 5%)). *p<0.05.

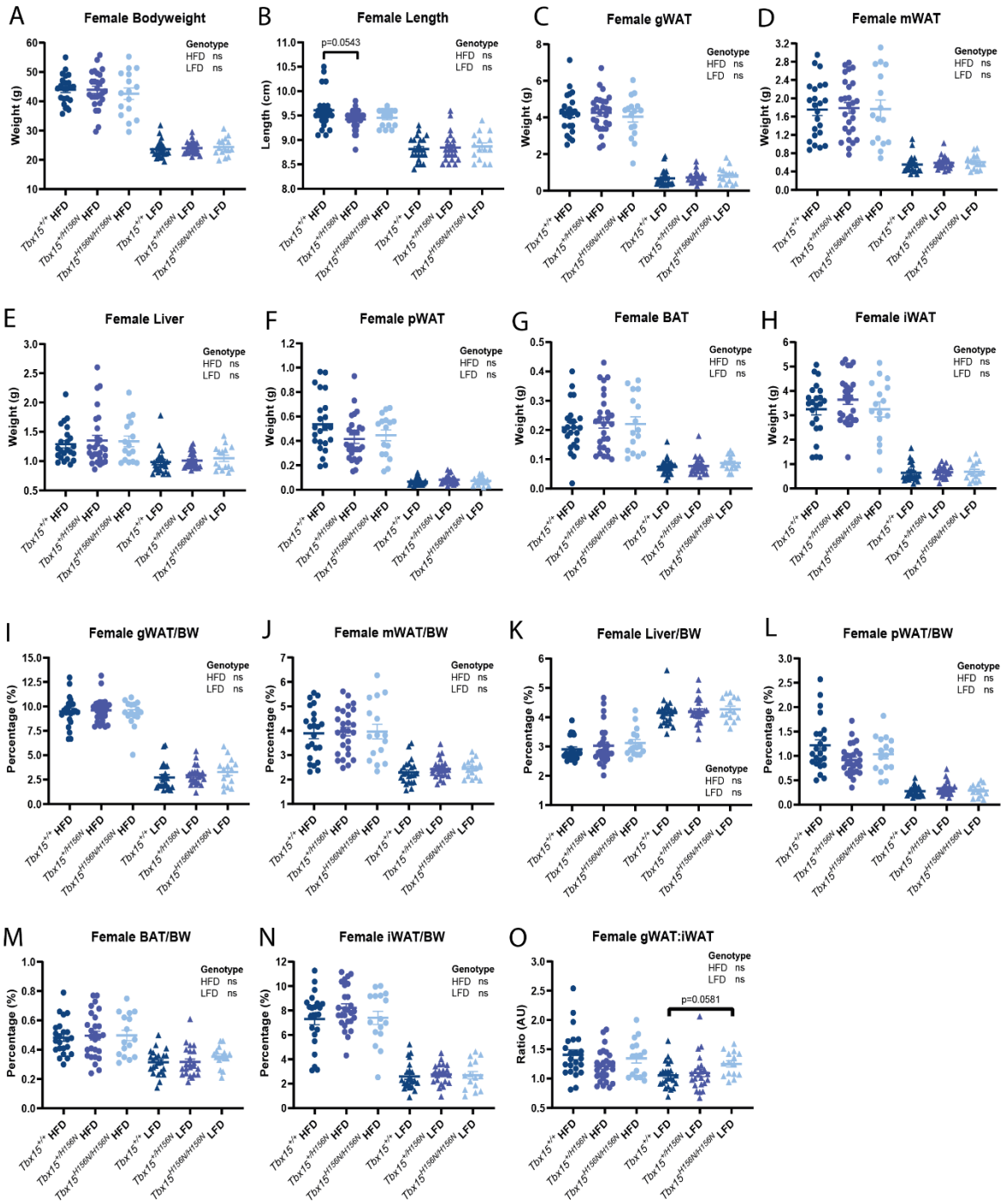

Figure 4.17. Female *Tbx15*^{H156N} terminal adipose depot measurements and distribution. A. Bodyweight, B. Length, C. gWAT, D. mWAT, E. Liver, F. pWAT, G. BAT, H. iWAT, I. gWAT/BW (bodyweight), J. mWAT/BW, K. Liver/BW, L. pWAT/BW, M. BAT/BW, N. iWAT/BW, O. gWAT:iWAT ratio. *Tbx15*$^{+/+}$ (dark blue), *Tbx15*$^{+/H156N}$ (blue), *Tbx15*$^{H156N/H156N}$ (light blue), female high-fat diet (HFD; circle), female low-fat diet (LFD; upwards triangle). Bodyweight, length and gWAT:iWAT ratio were analysed by one-way ANOVA with post-hoc Tukey's multiple comparisons, per diet. Depots and depots/BW were analysed by repeated measures two-way ANOVA with post-hoc Šídák's multiple comparisons, per diet.

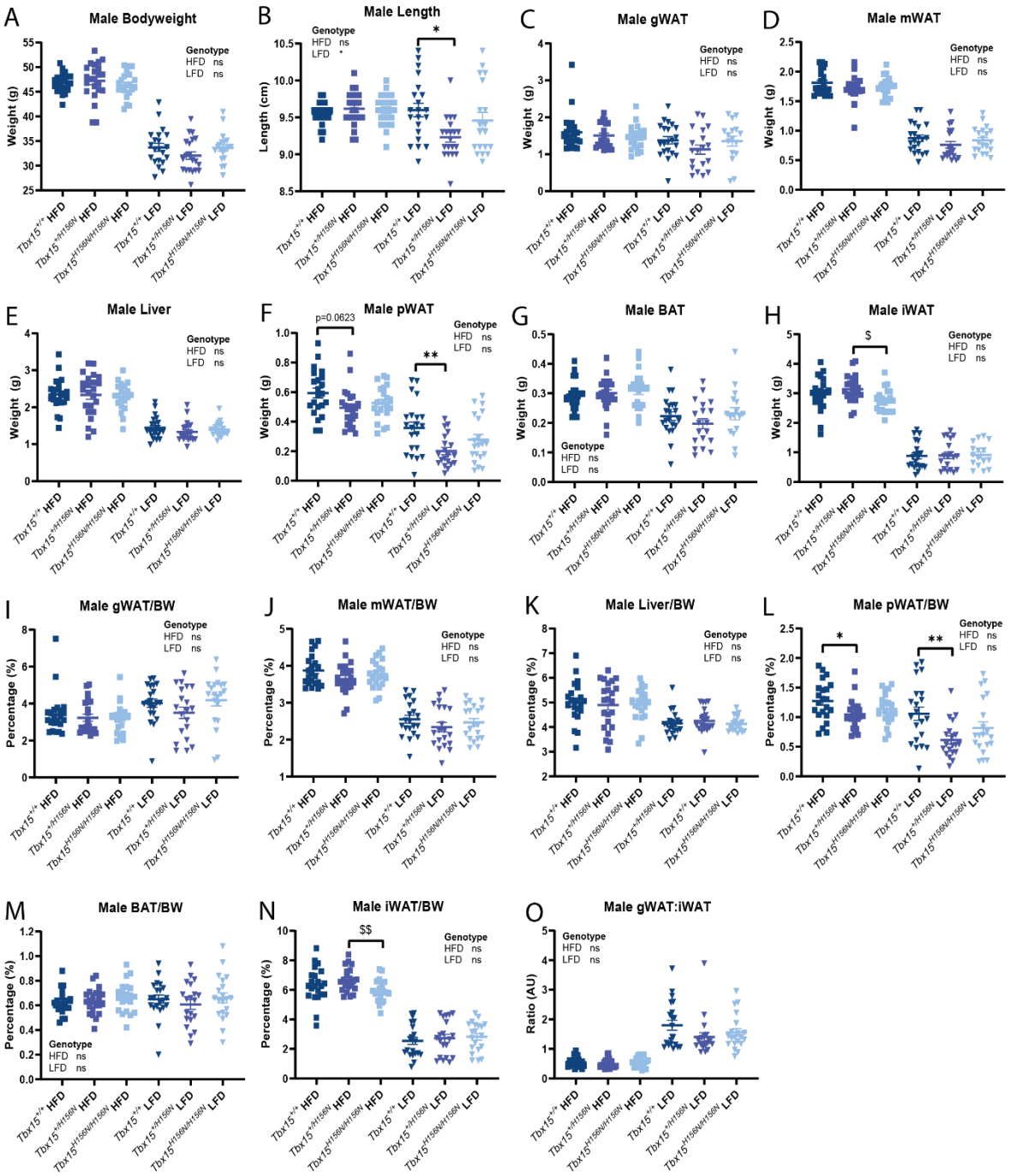

Figure 4.18. Male *Tbx15*^{H156N} terminal adipose depot measurements and distribution. A. Bodyweight, B. Length, C. gWAT, D. mWAT, E. Liver, F. pWAT, G. BAT, H. iWAT, I. gWAT/BW (bodyweight), J. mWAT/BW, K. Liver/BW, L. pWAT/Bodyweight, M. BAT/BW, N. iWAT/BW, O. gWAT:iWAT ratio. *Tbx15*$^{+/+}$ (dark blue), *Tbx15*$^{+/H156N}$ (blue), *Tbx15*$^{H156N/H156N}$ (light blue), male high-fat diet (HFD; square), male low-fat diet (LFD; downwards triangle). Bodyweight, length and gWAT:iWAT ratio were analysed by one-way ANOVA with post-hoc Tukey's multiple comparisons, per diet, genotype: *p<0.05. Tukey's multiple comparisons: *p<0.05 (*Tbx15*$^{+/+}$ vs *Tbx15*$^{+/H156N}$). Depots and depots/BW were analysed by repeated measures two-way ANOVA with post-hoc Šídák's multiple comparisons, per diet. Šídák's multiple comparisons: *p<0.05, **p<0.01 (*Tbx15*$^{+/+}$ vs *Tbx15*$^{+/H156N}$), $ p<0.05, $$ p<0.01 (*Tbx15*$^{+/H156N}$ vs *Tbx15*$^{H156N/H156N}$).

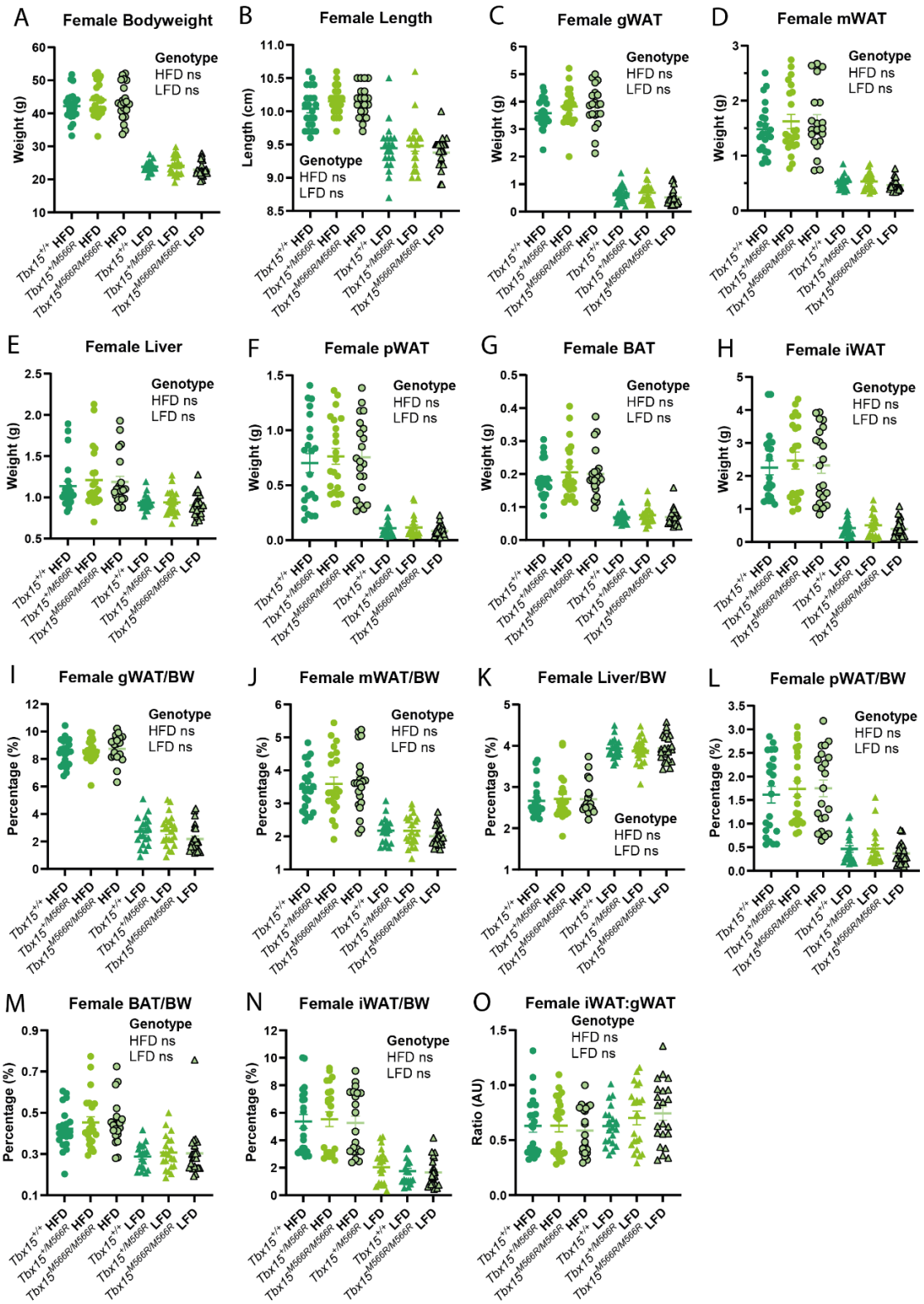

Figure 4.19. Female *Tbx15*^{M566R} terminal adipose depot measurements and distribution. A. Bodyweight, B. Length, C. gWAT, D. mWAT, E. Liver, F. pWAT, G. BAT, H. iWAT, I. gWAT/BW (bodyweight), J. mWAT/BW, K. Liver/BW, L. pWAT/BW, M. BAT/BW, N. iWAT/BW, O. gWAT:iWAT ratio. *Tbx15*$^{+/+}$ (dark green), *Tbx15*$^{+/M566R}$ (green), *Tbx15*$^{M566R/M566R}$ (light green), female high-fat diet (HFD; circle), female low-fat diet (LFD; upwards triangle). Bodyweight, length and gWAT:iWAT ratio were analysed by one-way ANOVA with post-hoc Tukey's multiple comparisons, per diet. Depots and depots/bodyweight were analysed by repeated measures two-way ANOVA with post-hoc Šídák's multiple comparisons, per diet.

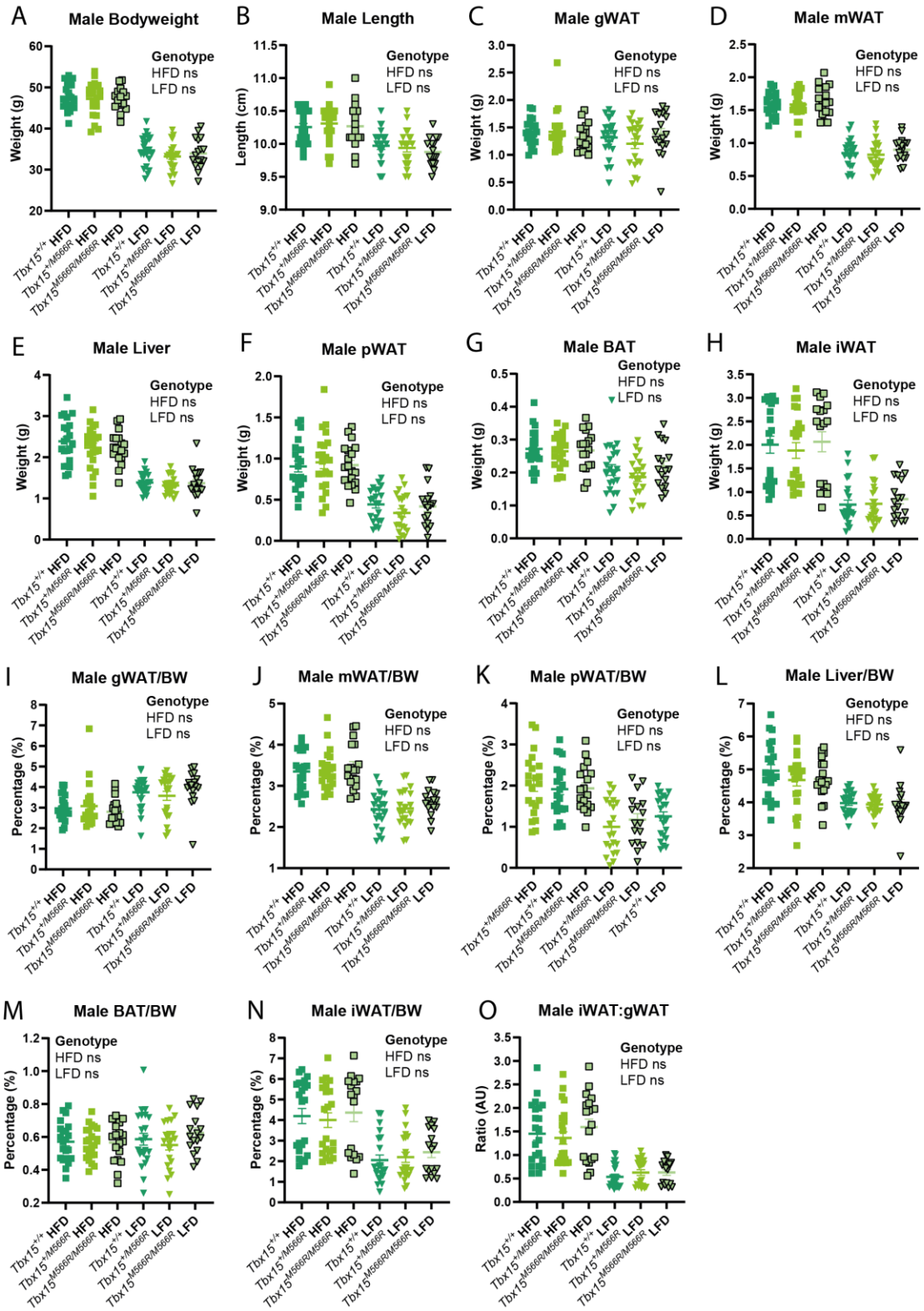

Figure 4.20. Male *Tbx15*^{M566R} terminal adipose depot measurements and distribution. A. Bodyweight, B. Length, C. gWAT, D. mWAT, E. Liver, F. pWAT, G. BAT, H. iWAT, I. gWAT/BW (bodyweight), J. mWAT/BW, K. Liver/BW, L. pWAT/BW, M. BAT/BW, N. iWAT/BW, O. gWAT:iWAT ratio. *Tbx15*$^{+/+}$ (dark green), *Tbx15*$^{+/M566R}$ (green), *Tbx15*$^{M566R/M566R}$ (light green), male high-fat diet (HFD; square), male low-fat diet (LFD; downwards triangle). Bodyweight, length and gWAT:iWAT ratio were analysed by one-way ANOVA with post-hoc Tukey's multiple comparisons, per diet. Depots and depots/bodyweight were analysed by repeated measures two-way ANOVA with post-hoc Šídák's multiple comparisons, per diet.

4.2.8. Terminal blood plasma clinical chemistry

TBX15 expression was previously associated with cardiometabolic traits such as insulin, triglycerides, FFAs and adiponectin levels, in addition to WHRadjBMI (Civelek *et al.*, 2017). Therefore, blood plasma was collected for analysis of a panel of analytes to determine if the *Tbx15* alleles influenced other traits associated with MetS risk.

4.2.8.1. *Tbx15*$^{+/-}$ mice had decreased LDH and glycerol levels

Across 27 analytes measured, significant decreases in uric acid and glycerol were detected in female *Tbx15*$^{+/-}$ mice fed a HFD ($q<0.00001$ and $q=0.00526$, respectively, multiple unpaired t-tests; Figure 4.21A and C, respectively, Appendix Table 9.40). Further, a nominally significant increase in lactate dehydrogenase (LDH) was detected in female *Tbx15*$^{+/-}$ mice fed a LFD ($p=0.0026$, multiple unpaired t-tests; Figure 4.21B, Appendix Table 9.40).

In male mice, a significant decrease in LDH levels was also detected in *Tbx15*$^{+/-}$ compared to *Tbx15*$^{+/+}$ mice on LFD ($q=0.002950$), with creatine kinase (CK), amylase and glycerol levels also nominally significantly different ($p=0.01474$, $p=0.02822$ and $p=0.03862$, respectively, multiple unpaired t-tests; Figure 4.21D-G, respectively, Appendix Table 9.40). No significant differences were detected in any analytes for male mice on HFD (multiple unpaired t-tests; Appendix Table 9.40). Significant differences in blood plasma analytes between *Tbx15*$^{+/-}$ and *Tbx15*$^{+/+}$ mice on both diets indicated *Tbx15* may be associated with altered systemic signalling. For example, the decreased glycerol levels, in the absence of altered triglyceride or fatty acid levels, could indicate impaired lipolysis in response to fasting.

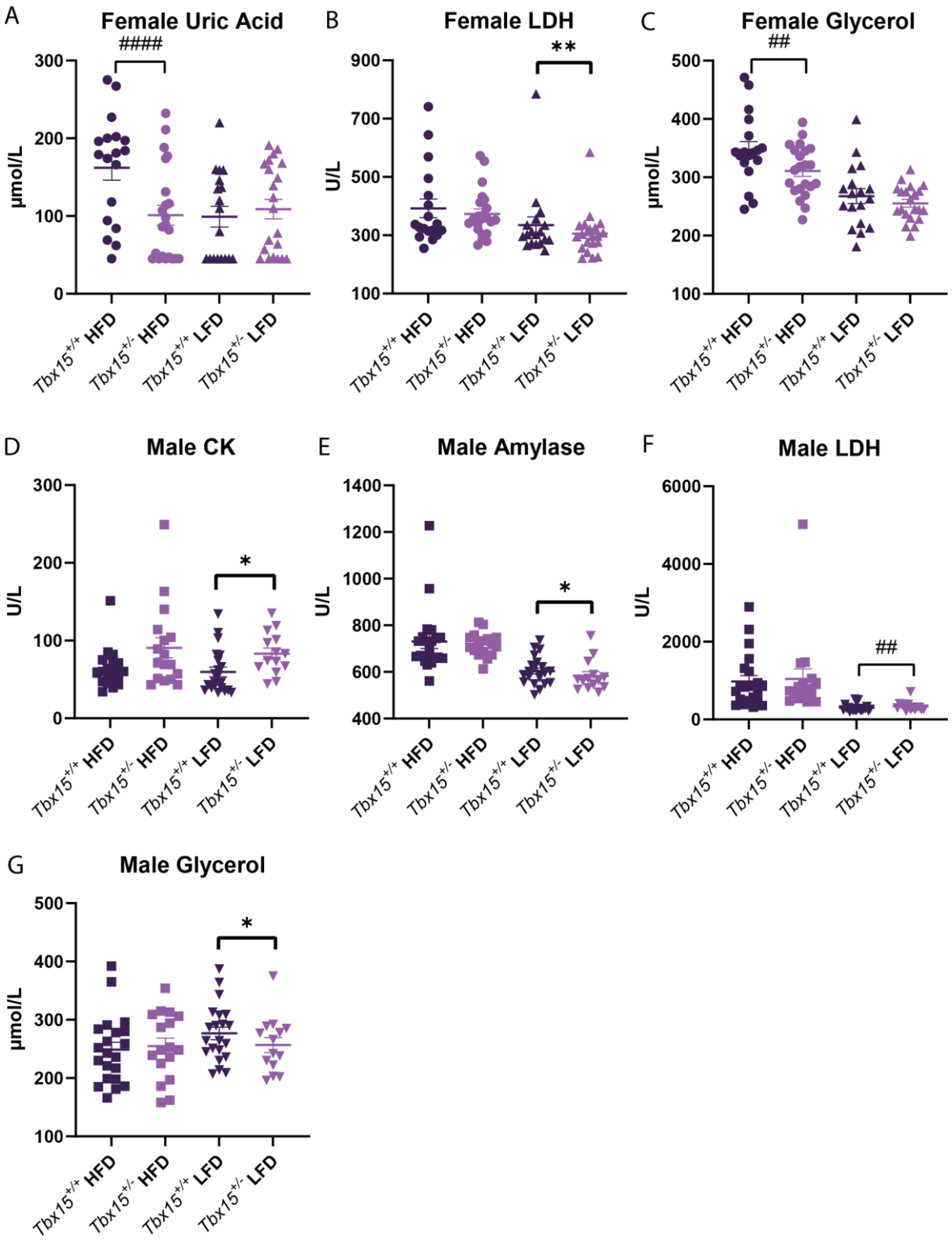

Figure 4.21. *Tbx15*$^{+/-}$ mice had decreased LDH and glycerol levels. A-G. Significantly different analytes for female (A-C) and male (D-G) mice. A. Uric acid, B. Lactate dehydrogenase (LDH), C. Glycerol, D. Creatine kinase (CK), E. Amylase, F. LDH, G. Glycerol. *Tbx15*$^{+/+}$ (dark purple), *Tbx15*$^{+/-}$ (purple), female high-fat diet (HFD; circle), female low-fat diet (LFD; upwards triangle), male HFD (square), male LFD (downwards triangle). All data was analysed by multiple unpaired t-tests per sex and diet:*p<0.05, **p<0.01, ##q<0.01, ####q<0.0001. The baseline detection limit for uric acid was 45 µmol/L, all values detected as <45 µmol/L in the assay were reported as 45 µmol/L.

4.2.8.2. *Tbx15*$^{+/H156N}$ mice had increased blood plasma analytes

In female *Tbx15*^{H156N} mice, there were significant genotype effects for both HFD- and LFD-fed mice (p=0.0223 and p=0.0051, respectively, two-way ANOVA; Appendix Table 9.41). Potassium, inorganic phosphorous, total bilirubin, alanine aminotransferase (ALT), aspartate aminotransferase (AST), and LDH were significantly higher in HFD-fed *Tbx15*$^{+/H156N}$ compared to *Tbx15*$^{+/+}$ mice (p≤0.0439, two-way ANOVA; Figure 4.22A, C, D, E, G and I, respectively, Appendix Table 9.41). *Tbx15*$^{+/H156N}$ mice also had significantly higher inorganic phosphorous, total bilirubin, ALT, AST and LDH levels than *Tbx15*$^{H156N/H156N}$ littermates (p≤0.0421, two-way ANOVA; Figure 4.22C, D, E, F, and I, respectively, Appendix Table 9.41).

In LFD-fed females, *Tbx15*$^{H156N/H156N}$ mice had higher blood glucose levels than both *Tbx15*$^{+/+}$ and *Tbx15*$^{+/H156N}$ mice (p=0.0098, and p=0.0168, respectively), and increased albumin compared to *Tbx15*$^{+/H156N}$ littermates (p=0.0025, two-way ANOVA; Figure 4.22B and F, respectively, Appendix Table 9.41). Further, Tbx15+/H156N mice had higher ALT, AST and amylase levels compared to Tbx15+/+ littermates, and higher ALT, AST and LDH levels compared to Tbx15H156N/H156N mice (p≤0.0405, two-way ANOVA; Figure 4.22E, G, H, and I, Appendix Table 9.41).

In male mice there was a significant genotype effect in HFD (p=0.0333), but not LFD mice (two-way ANOVA; Appendix Table 9.41). Potassium, total bilirubin, AST, amylase, and LDH were significantly higher in *Tbx15*$^{+/H156N}$ compared to *Tbx15*$^{H156N/H156N}$ mice (p≤0.0360, two-way ANOVA; Figure 4.22J, L, M, N and O, respectively). Inorganic phosphorous was higher in *Tbx15*$^{+/H156N}$ than *Tbx15*$^{+/+}$ mice (p=0.0232, two-way ANOVA; Figure 4.22K, Appendix Table 9.41). Significant differences in several analytes were detected between *Tbx15*$^{+/H156N}$ and their *Tbx15*$^{+/+}$ or *Tbx15*$^{H156N/H156N}$ littermates

on HFD and LFD in females, and HFD in males. Therefore, these differences may be driven by increased lean mass metabolism in in *Tbx15*$^{+/H156N}$ HFD-fed mice.

4.2.8.3. *Tbx15*$^{+/M566R}$ and *Tbx15*$^{M566R/M566R}$ mice had altered blood plasma analytes

HFD-fed female *Tbx15*$^{M566R/M566R}$ and *Tbx15*$^{+/M566R}$ mice had significantly higher blood glucose levels than *Tbx15*$^{+/+}$ littermates (p=0.0210 and p=0.0488, respectively, two-way ANOVA; Figure 4.23A, Appendix Table 9.42). Further, *Tbx15*$^{M566R/M566R}$ mice had decreased CK levels compared to *Tbx15*$^{+/+}$ littermates (p=0.0177, two-way ANOVA), with *Tbx15*$^{+/M566R}$ mice showing an intermediate, albeit not significant, phenotype (Figure 4.23B, Appendix Table 9.42).

Whereas, HFD-fed male *Tbx15*$^{+/M566R}$ and *Tbx15*$^{M566R/M566R}$ mice had higher sodium levels than *Tbx15*$^{+/+}$ littermates (p=0.0465 and p=0.0004, respectively, two-way ANOVA; Figure 4.23C, Appendix Table 9.42). *Tbx15*$^{M566R/M566R}$ mice also had higher chloride levels compared to *Tbx15*$^{+/+}$ littermates (p=0.0228) and lower potassium levels than *Tbx15*$^{+/M566R}$ and *Tbx15*$^{+/+}$ littermates (p=0.0471 and p=0.0015, respectively, two-way ANOVA; Figure 4.23D and E, Appendix Table 9.42). Glucose levels in *Tbx15*$^{M566R/M566R}$ mice (p=0.00127) and total protein, total cholesterol and LDL in *Tbx15*$^{+/M566R}$ mice (p=0.0145, p=0.0275 and p=0.0228, respectively) were significantly lower than *Tbx15*$^{+/+}$ littermates (two-way ANOVA; Figure 4.23F-I, Appendix Table 9.42). Overall, challenging *Tbx15*^{M566R} mice with a high-fat, but not low-fat, diet resulted in detectable differences in blood plasma analytes. This suggests the *Tbx15*^{M566R} allele may regulate changes in systemic metabolic traits other than body composition, and acts as a tag SNP, for other undetected SNPs in the haplotype that may be causal for WHRadjBMI associations.

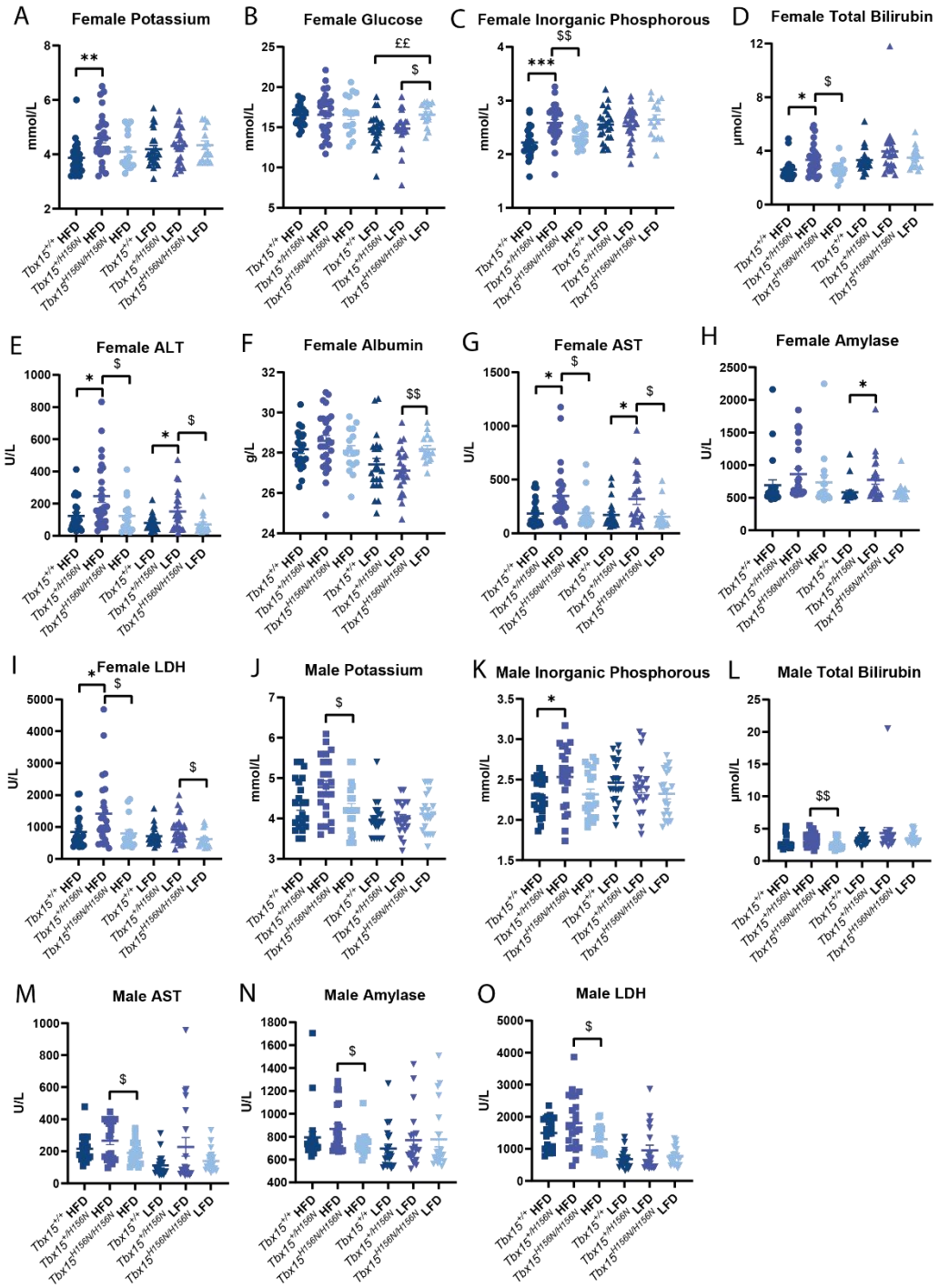

Figure 4.22. *Tbx15*$^{+/H156N}$ mice had increased blood plasma analytes. A-O. Significantly different analytes for female (A-I) and male (J-O) mice. A. Potassium, B. Glucose, C. Inorganic phosphorous, D. Total bilirubin, E. Alanine aminotransferase (ALT), F. Albumin, G. Aspartate aminotransferase (AST), H. Amylase, I. Lactate dehydrogenase (LDH), J. Potassium, K. Inorganic phosphorous, L. Total bilirubin, M. AST, N. Amylase, O. LDH. *Tbx15*$^{+/+}$ (dark blue), *Tbx15*$^{+/H156N}$ (blue), *Tbx15*$^{H156N/H156N}$ (light blue), female high-fat diet (HFD; circle), female low-fat diet (LFD; upwards triangle), male HFD (square), male LFD (downwards triangle). Female high-fat diet and low-fat diet, and male high-fat diet data was analysed by two-way ANOVA with Tukeys's multiple corrections. Two male LFD samples did not have sufficient volume to run a full analyte panel: one *Tbx15*$^{+/H156N}$ (no ALT, Free Fatty Acids, Glycerol, Ketones or Magnesium) and one *Tbx15*$^{H156N/H156N}$ (no Free Fatty Acids, Glycerol or Ketones); male LFD data was analysed by mixed-effect model (REML) with Tukey's multiple comparisons. Tukey's post-hoc multiple comparisons: *p<0.05, **p<0.01, ***p<0.001 (*Tbx15*$^{+/+}$ vs *Tbx15*$^{+/H156N}$), ££ p<0.01 (*Tbx15*$^{+/+}$ vs *Tbx15*$^{H156N/H156N}$) and $ p<0.05, $$ p<0.01 (*Tbx15*$^{+/H156N}$ vs *Tbx15*$^{H156N/H156N}$).

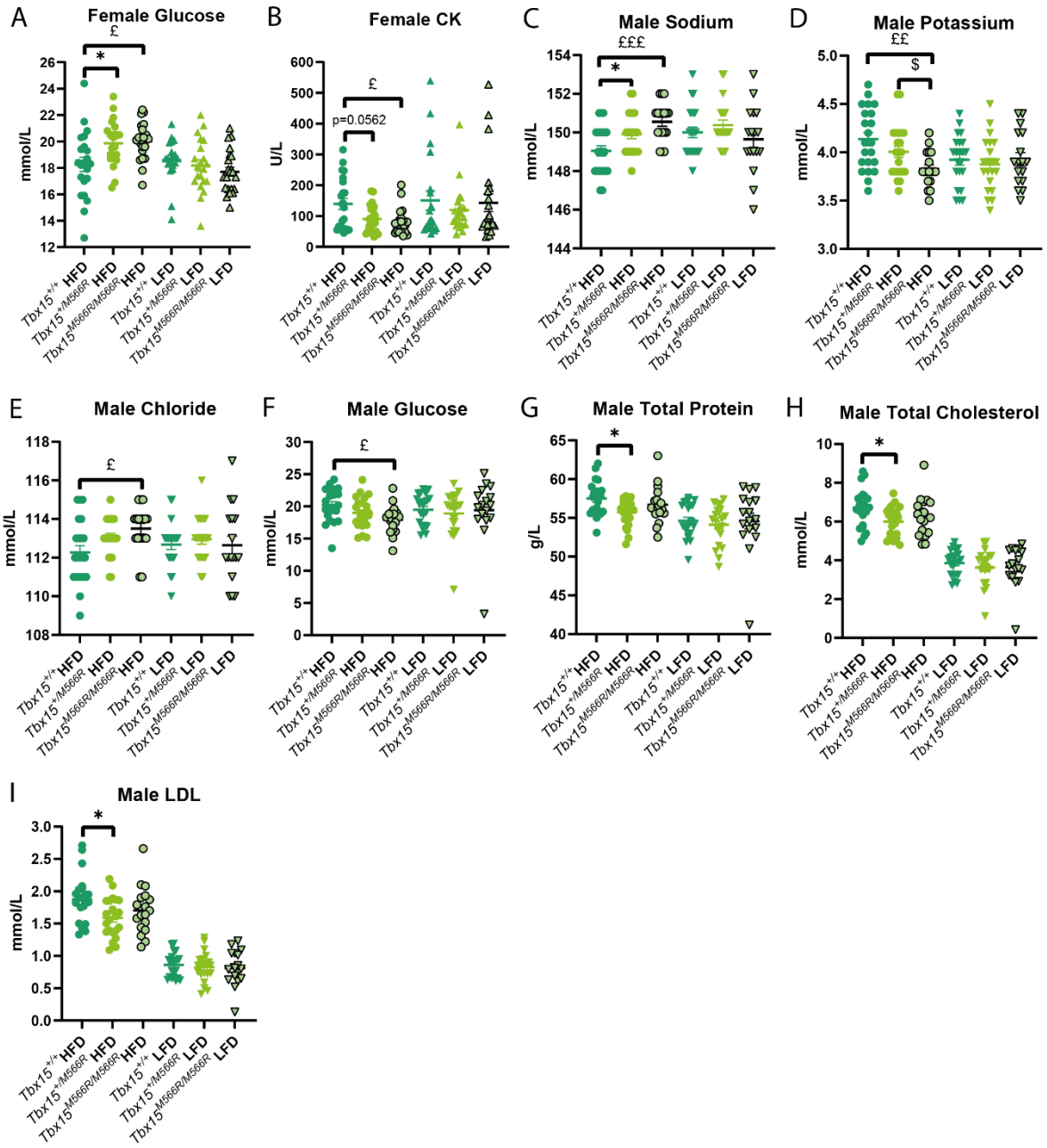

Figure 4.23. *Tbx15*$^{+/M566R}$ and *Tbx15*$^{M566R/M566R}$ mice had altered blood plasma analytes. A-I. Significantly different analytes for female (A-B) and male (C-I) mice. A. Glucose, B. Creatine kinase (CK), C. Sodium, D. Potassium, E. Chloride, F. Glucose, G. Total protein, H. Total cholesterol, I. Low density lipoprotein (LDL). *Tbx15*$^{+/+}$ (dark green), *Tbx15*$^{+/M566R}$ (green), *Tbx15*$^{M566R/M566R}$ (light green), female high-fat diet (HFD; circle), female low-fat diet (LFD; upwards triangle), male HFD (square), male LFD (downwards triangle). Female LFD, and male HFD and LFD data was analysed by two-way ANOVA with Tukey's multiple corrections. One female HFD *Tbx15*$^{+/+}$ sample did not have sufficient volume to run a full analyte panel (no total protein or uric acid); female HFD data was analysed by mixed-effect model (REML) with Tukey's multiple comparisons. Tukey's post-hoc multiple comparisons: *p<0.05 (*Tbx15*$^{+/+}$ vs *Tbx15*$^{+/M566R}$), $ p<0.05 (*Tbx15*$^{+/M566R}$ vs *Tbx15*$^{M566R/M566R}$), £ p<0.05, ££ p<0.01, £££ p<0.001 (*Tbx15*$^{+/+}$ vs *Tbx15*$^{M566R/M566R}$).

4.2.9. Terminal adipose tissue cell analysis

Finally, I analysed adipocyte cell sizes from H&E stained tissue sections, using Adiposoft, to investigate whether this contributed to adipose depot weight differences.

4.2.9.1. *Tbx15*$^{+/-}$ mice on HFD had altered cell size distribution in WAT

In *Tbx15*$^{+/-}$ mice, there were no significant genotype effects for average adipocyte cell area for female or male mice on HFD or LFD (two-way ANOVA; Figure 4.24, Figure 4.26, Appendix Table 9.43). However, nominally significant differences ($p<0.05$) in cell area distribution were detected in HFD-fed mice. For example, female *Tbx15*$^{+/-}$ mice had significantly more adipocytes with an area of 500-999 μm^2 and 1500-1999 μm^2 ($p=0.0491$, and $p=0.0284$, respectively), and fewer adipocytes in almost all area ranges above 3500 μm^2 in pWAT ($p\leq0.0327$, multiple unpaired t-tests; Figure 4.25C, Appendix Table 9.44). Further, HFD-fed male *Tbx15*$^{+/-}$ mice had significantly fewer adipocytes in almost all area ranges above 7500 μm^2 compared to *Tbx15*$^{+/+}$ littermates in mWAT ($p\leq0.0422$, multiple unpaired t-tests; Figure 4.27B, Appendix Table 9.46). No significant differences were detected in adipocyte area distribution in any depots in LFD-fed female or male mice (Figure 4.25E-H, Figure 4.27E-H, Appendix Table 9.45, Appendix Table 9.47).

There were no obvious differences in lipid accumulation in either BAT or liver depots in female or male *Tbx15*$^{+/-}$ mice (Figure 4.24, Figure 4.26). Further work is underway to assess the thickness of superficial dWAT layers in dorsal and ventral skin samples from these mice. Additionally, adipocyte area and dWAT thickness will be analysed in samples from *Tbx15*^{H156N} and *Tbx15*^{M566R} mice.

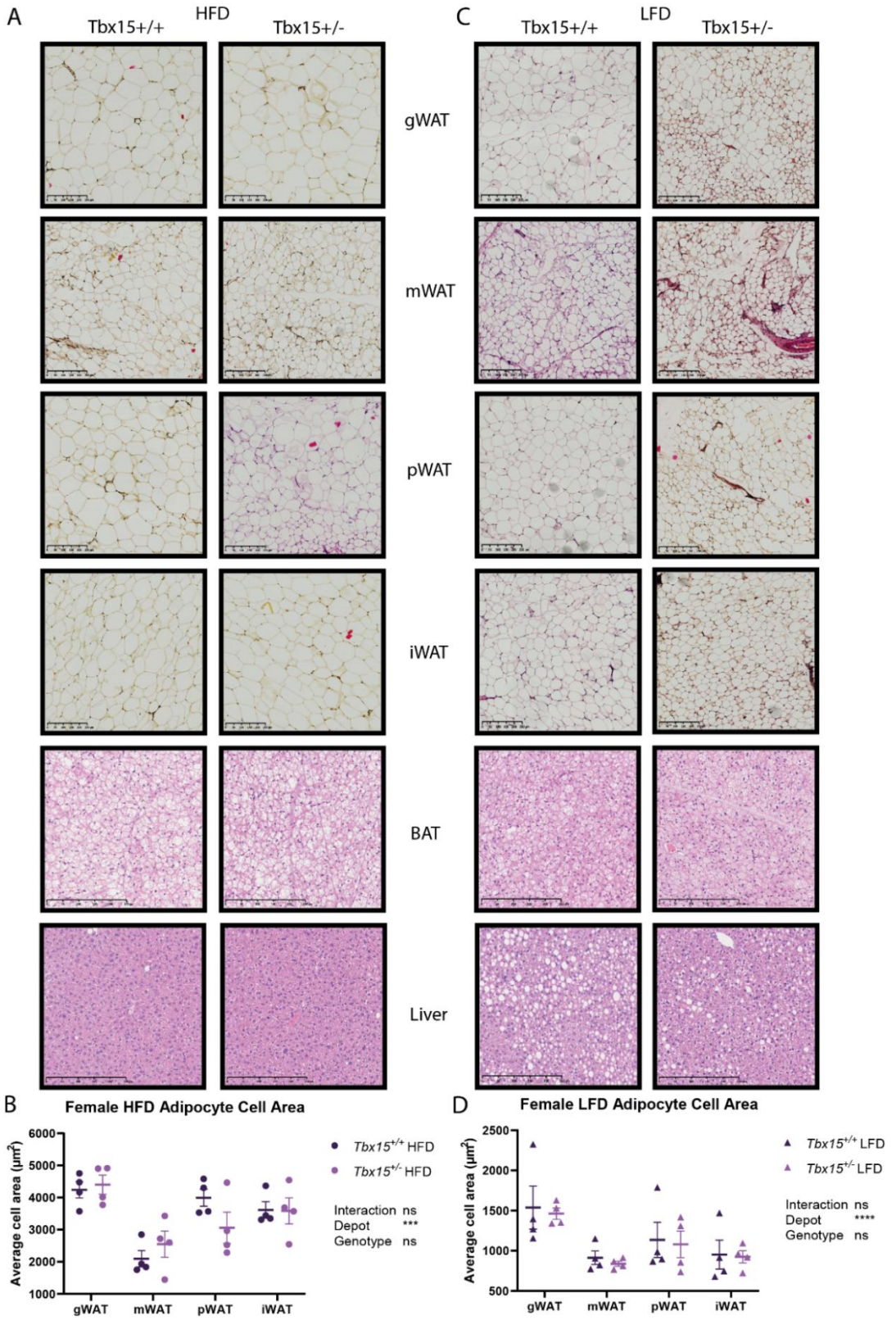

Figure 4.24. Female *Tbx15*$^{+/-}$ terminal adipocyte cell area. A. Representative images of high-fat diet (HFD) *Tbx15*$^{+/+}$ and *Tbx15*$^{+/-}$ of haematoxylin and eosin (H&E) stained white adipose tissues (WAT), brown adipose tissue (BAT) and liver. B. Average WAT cell area per depot for HFD mice. C. Representative images of low-fat diet (LFD) *Tbx15*$^{+/+}$ and *Tbx15*$^{+/-}$ of H&E stained WAT, BAT and liver. D. Average WAT cell area per depot for LFD mice. *Tbx15*$^{+/+}$ (dark purple), *Tbx15*$^{+/-}$ (purple), female HFD (circle), female LFD (upwards triangle). All data analysed by two-way ANOVA with Tukey's multiple corrections: ***p<0.001, ****p<0.0001. Graphs representative of mean±SEM of n=4 samples per group.

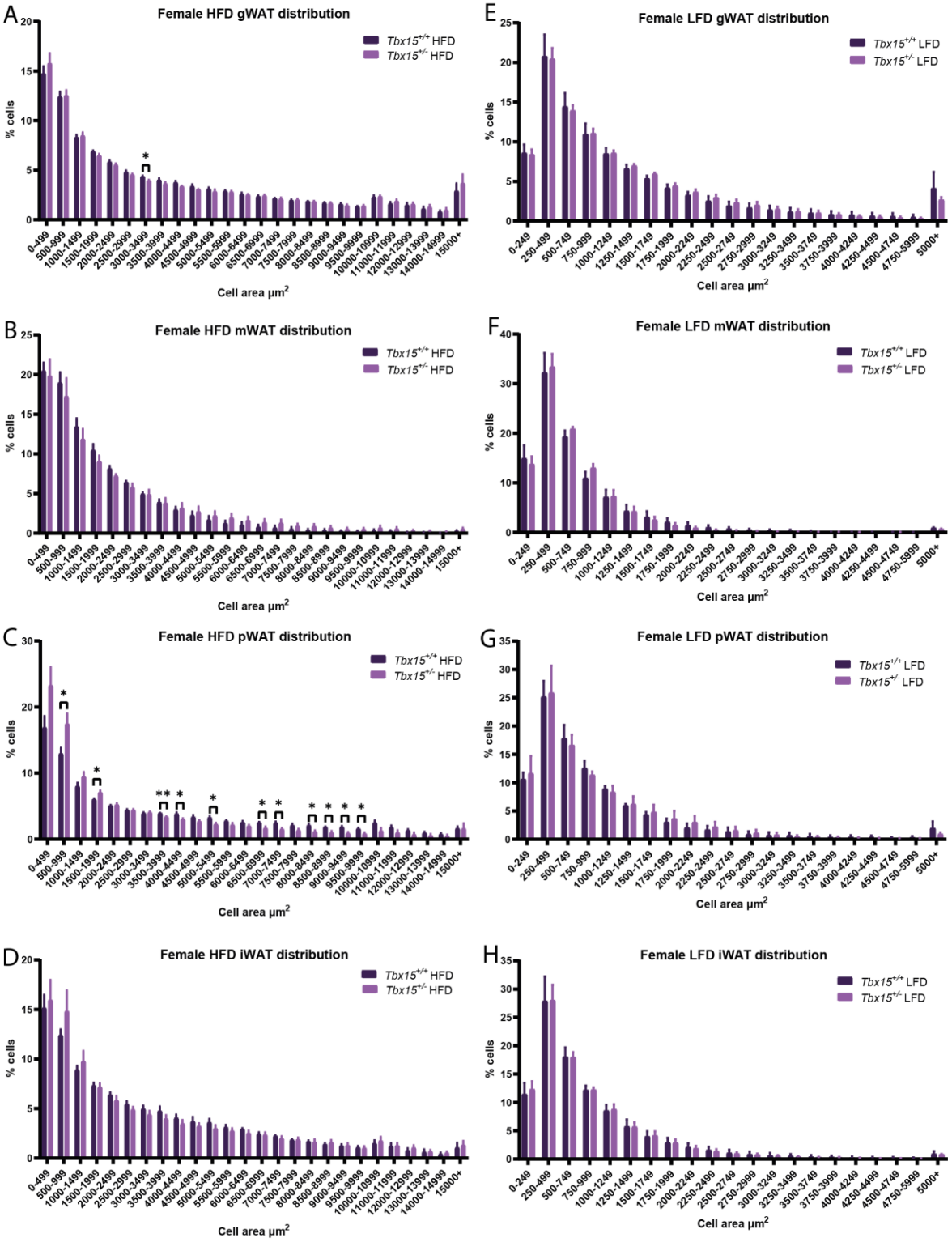

Figure 4.25. Female *Tbx15*$^{+/-}$ adipocyte cell area distribution for white adipose tissues (WAT). (A-D) high-fat diet (HFD) and (E-H) low-fat diet (LFD) mice. A, E. gonadal WAT (gWAT), B, F. mesenteric WAT (mWAT), C, G. perirenal WAT (pWAT), D, H. inguinal WAT (iWAT). *Tbx15*$^{+/+}$ (dark purple), *Tbx15*$^{+/-}$ (purple), female HFD (circle), female LFD (upwards triangle). Graphs representative of mean±SEM of n=4 samples per group. All data analysed by multiple unpaired t-tests (two-stage step-up (Benjamini, Krieger, and Yekutieli) (false discovery rate 5%)) per diet and depot: *p<0.05, **p<0.01.

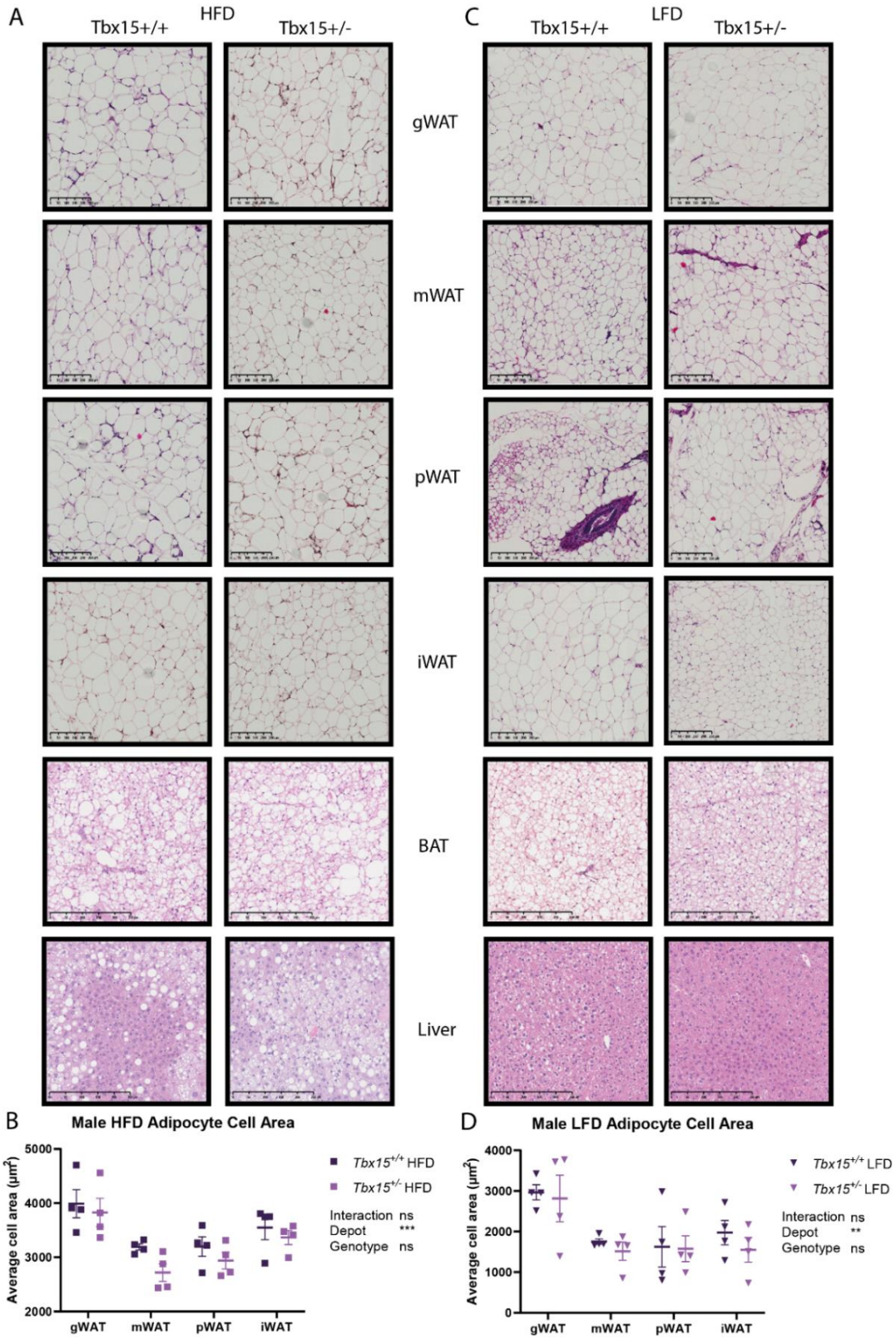

Figure 4.26. Male *Tbx15*$^{+/-}$ terminal adipocyte cell area. A. Representative images of high-fat diet (HFD) *Tbx15*$^{+/+}$ and *Tbx15*$^{+/-}$ of haematoxylin and eosin (H&E) stained white adipose tissues (WAT), brown adipose tissue (BAT) and liver. B. Average WAT cell area per depot for HFD mice. C. Representative images of low-fat diet (LFD) *Tbx15*$^{+/+}$ and *Tbx15*$^{+/-}$ of H&E stained WAT, BAT and liver. D. Average WAT cell area per depot for LFD mice. *Tbx15*$^{+/+}$ (dark purple), *Tbx15*$^{+/-}$ (purple), male HFD (square), male LFD (downwards triangle). All data analysed by two-way ANOVA with Tukey's multiple corrections: **p<0.01, ***p<0.001. Graphs representative of mean±SEM of n=4 samples per group.

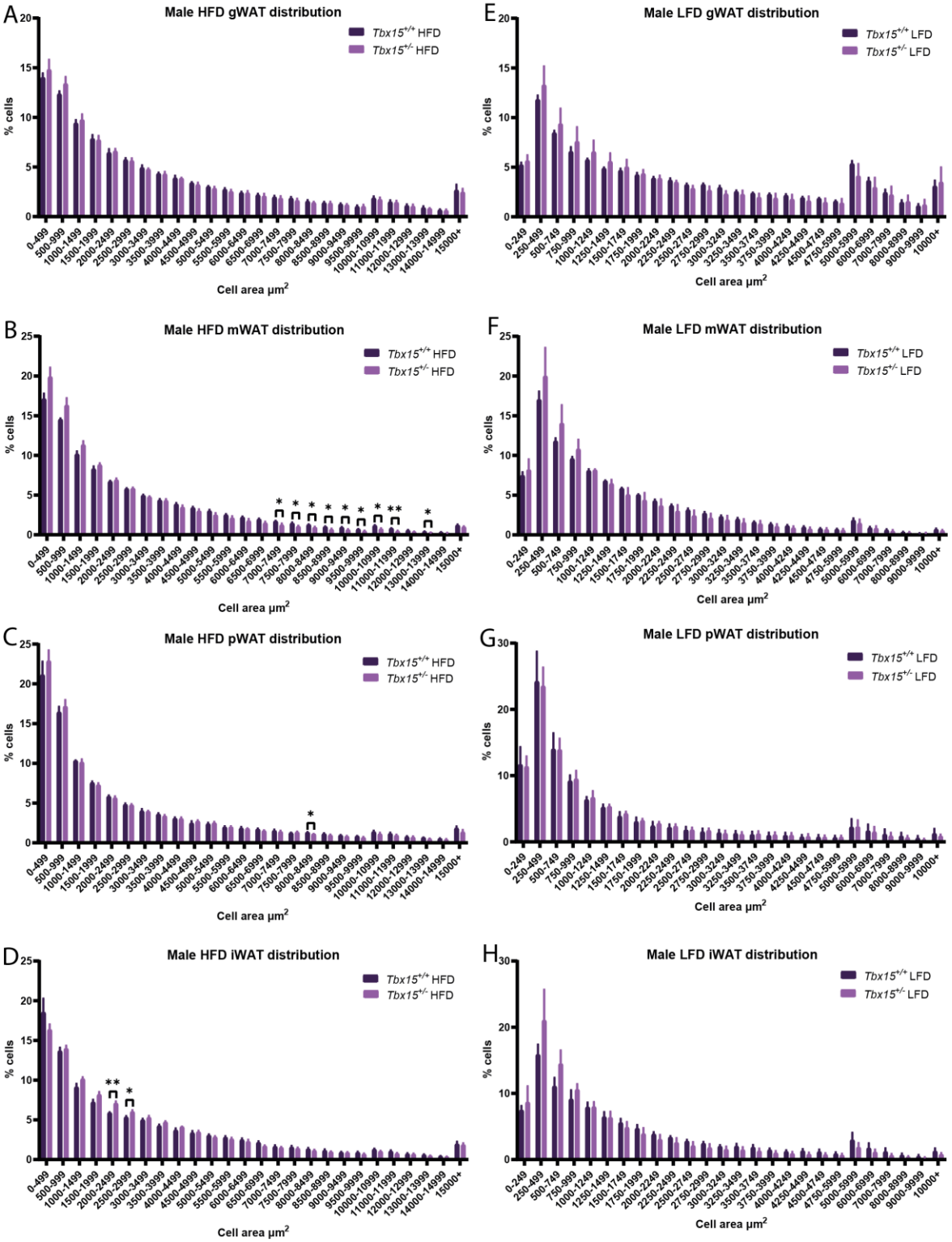

Figure 4.27. Male *Tbx15*$^{+/-}$ adipocyte cell area distribution for white adipose tissues (WAT). (A-D) high-fat diet (HFD) and (E-H) low-fat diet (LFD) mice. A, E. gonadal WAT (gWAT), B, F. mesenteric WAT (mWAT), C, G. perirenal WAT (pWAT), D, H. inguinal WAT (iWAT). Graphs representative of mean±SEM of n=4 samples per group. *Tbx15*$^{+/+}$ (dark purple), *Tbx15*$^{+/-}$ (purple), male HFD (square), male LFD (downwards triangle). All data was analysed by multiple unpaired t-tests (two-stage step-up (Benjamini, Krieger, and Yekutieli) (false discovery rate 5%)) per diet and depot: *p<0.05, **p<0.01.

4.3. Discussion

In this chapter, I have shown significant effects on metabolic phenotypes in all three *Tbx15* mouse lines characterised (Figure 4.28, Table 4.3). *Tbx15*$^{+/-}$, *Tbx15*$^{H156N/H156N}$ and *Tbx15*$^{M566R/M566R}$ mice all exhibited fat mass phenotypes, albeit to varying degrees in a sex- and diet-specific manner (Figure 4.28, Table 4.3). The most striking phenotype was a higher lean mass detect in HFD-challenged *Tbx15*$^{+/H156N}$, but not *Tbx15*$^{H156N/H156N}$, mice compared to *Tbx15*$^{+/+}$ (Figure 4.28, Table 4.3). Further, all *Tbx15* alleles resulted in dysregulated blood plasma analytes, such as decreased plasma lipids suggesting *Tbx15* may regulate systemic metabolic effects independently of WHR (Table 4.3).

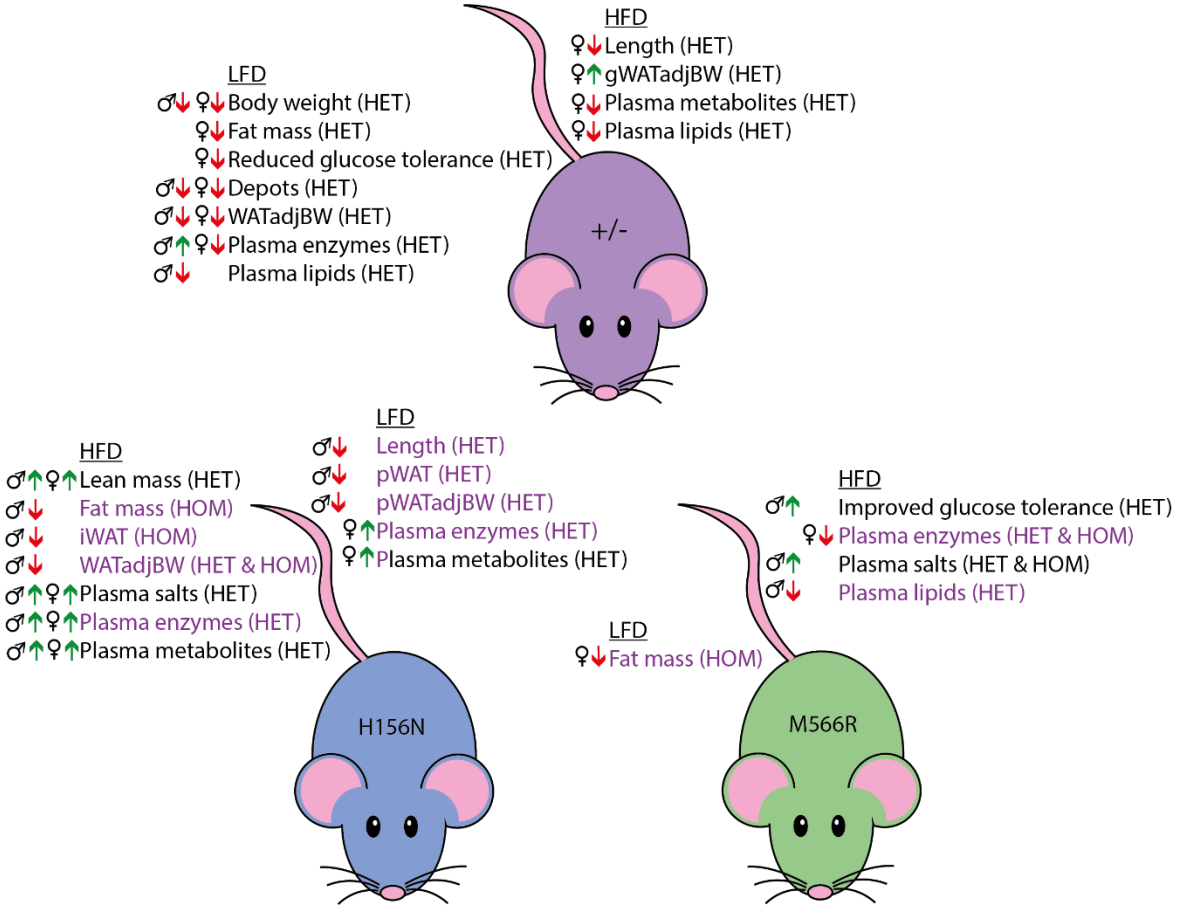

Figure 4.28. Summary of metabolic phenotypes in *Tbx15* mouse lines. *Tbx15*$^{+/-}$ (purple), *Tbx15*^{H156N} (blue) and *Tbx15*^{M566R} (green) metabolic phenotyping cohorts. Purple text indicates similar phenotype trend compared to *Tbx15*$^{+/-}$ line, irrespective of sex or diet.

Table 4.3. Summary of metabolic phenotypes in *Tbx15* mouse lines. *Tbx15*$^{+/-}$, *Tbx15*^{H156N} and *Tbx15*^{M566R} metabolic phenotyping cohorts. Abbreviations: HFD (high-fat diet), LFD (low-fat diet), NSD (no significant differences), N/A (not applicable – test was not performed). Purple text indicates similar phenotype trend compared to *Tbx15*$^{+/-}$ line, irrespective of sex or diet.

		***Tbx15*$^{+/-}$**		***Tbx15*^{H156N}**		***Tbx15*^{M566R}**	
		HFD	**LFD**	**HFD**	**LFD**	**HFD**	**LFD**
Echo-MRI	Bodyweight	NSD	Female: *Tbx15*$^{+/-}$ smaller Male: *Tbx15*$^{+/-}$ smaller	NSD	NSD	NSD	Male: time x genotype effect (no clear driving effect)
	Fat Mass	NSD	Female: *Tbx15*$^{+/-}$ less fat mass Male: time x genotype effect (*Tbx15*$^{+/-}$ less fat mass)	NSD	Male: time x genotype effect (*Tbx15*$^{+/H156N}$ less fat mass vs *Tbx15*$^{+/+}$ and *Tbx15*$^{H156N/H156N}$)	NSD	Female: time x genotype effect (*Tbx15*$^{M566R/M566R}$ less fat mass vs *Tbx15*$^{+/+}$ and *Tbx15*$^{+/M566R}$)
	Lean Mass	Female: time x genotype effect (-*Tbx15*$^{+/-}$ more lean mass at early time points)	Female: time x genotype effect (*Tbx15*$^{+/-}$ less lean mass at early time points)	Female: *Tbx15*$^{+/H156N}$ more lean mass vs *Tbx15*$^{+/+}$ Male: *Tbx15*$^{+/H156N}$ have more lean mass vs *Tbx15*$^{+/+}$	NSD	NSD	NSD
IPGTT	Fasted glucose	NSD	NSD	NSD	NSD	Male: *Tbx15*$^{+/M566R}$ have decreased fasted glucose vs *Tbx15*$^{+/+}$ mice	NSD
	Glucose response	NSD	Female: *Tbx15*$^{+/-}$ impaired glucose tolerance	NSD	NSD	Male: *Tbx15*$^{+/M566R}$ have increased tolerance at T30 vs *Tbx15*$^{+/+}$ mice	NSD
IPIST		NSD	NSD	NSD	NSD	N/A	N/A
DEXA	Bodyweight	NSD	Male: *Tbx15*$^{+/-}$ are smaller	NSD	NSD	NSD	NSD
	Fat mass	NSD	Female: *Tbx15*$^{+/-}$ less fat mass and fat mass %	Male: *Tbx15*$^{H156N/H156N}$ less fat mass and fat mass % vs *Tbx15*$^{+/+}$	NSD	NSD	Female: *Tbx15*$^{M566R/M566R}$ (less fat mass and fat mass % vs *Tbx15*$^{+/M566R}$
	Lean mass	NSD	NSD	NSD	NSD	NSD	NSD
	BMC	NSD	NSD	NSD	NSD	NSD	NSD
	BMD	NSD	NSD	NSD	NSD	NSD	NSD

		***Tbx15*$^{+/-}$**		***Tbx15*^{H156N}**		***Tbx15*^{M566R}**	
		HFD	**LFD**	**HFD**	**LFD**	**HFD**	**LFD**
Depots	Bodyweight	NSD	Female: *Tbx15*$^{+/-}$ smaller Male: *Tbx15*$^{+/-}$ smaller	NSD	NSD	NSD	NSD
	Length	Female: *Tbx15*$^{+/-}$ are shorter	NSD	NSD	Male: *Tbx15*$^{+/H156N}$ shorter vs *Tbx15*$^{+/+}$	NSD	NSD
	Depots	NSD	Female: *Tbx15*$^{+/-}$ gWAT, mWAT, BAT and iWAT smaller Male: *Tbx15*$^{+/-}$ gWAT smaller	Male: *Tbx15*$^{H156N/H156N}$ have smaller iWAT than *Tbx15*$^{+/H156N}$	Male: *Tbx15*$^{+/H156N}$ pWAT smaller vs *Tbx15*$^{+/+}$	NSD	NSD
	Depots adjBW	Female: *Tbx15*$^{+/-}$ increased gWATadjBW	Female: *Tbx15*$^{+/-}$ smaller gWAT and mWAT adjBW Male: *Tbx15*$^{+/-}$ smaller gWATadjBW	Male: *Tbx15*$^{H156N/H156N}$ smaller iWATadjBW vs *Tbx15*$^{+/H156N}$; *Tbx15*$^{+/H156N}$ pWATadjBW smaller vs *Tbx15*$^{+/+}$	Male: *Tbx15*$^{+/H156N}$ pWATadjBW smaller vs *Tbx15*$^{+/+}$	NSD	NSD
Plasma	Differential analytes	Female: 1 Male: 0	Female:2 Male: 4	Female: 6 Male: 6	Female: 6 Male: 0	Female: 2 Male: 7	Female: 0 Male: 0
	Analytes changed	Female: *Tbx15*$^{+/-}$ decreased uric acid	Female: *Tbx15*$^{+/-}$ increased LDH and decreased glycerol Male: *Tbx15*$^{+/-}$ increased CK, and decreased amylase, LDH and glycerol	Female: potassium increased in *Tbx15*$^{+/H156N}$ vs *Tbx15*$^{+/+}$, and inorganic phosphorous, total bilirubin, ALT, AST and LDH increased in *Tbx15*$^{+/H156N}$ vs *Tbx15*$^{+/+}$ and *Tbx15*$^{H156N/H156N}$ Male: inorganic phosphorous increased in *Tbx15*$^{+/H156N}$ vs *Tbx15*$^{+/+}$; potassium, total bilirubin, AST, amylase and LDH increased in *Tbx15*$^{+/H156N}$ vs *Tbx15*$^{H156N/H156N}$	Female: glucose increased in *Tbx15*$^{+/H156N}$ and *Tbx15*$^{H156N/H156N}$ vs *Tbx15*$^{+/+}$, ALT and AST increased in *Tbx15*$^{+/H156N}$ vs *Tbx15*$^{+/+}$ and *Tbx15*$^{H156N/H156N}$, amylase increased in *Tbx15*$^{+/H156N}$ vs *Tbx15*$^{+/+}$, and albumin increased and LDH decreased in *Tbx15*$^{H156N/H156N}$ vs *Tbx15*$^{+/H156N}$	Female: glucose increased in *Tbx15*$^{+/M566R}$ and *Tbx15*$^{M566R/M566R}$ vs *Tbx15*$^{+/+}$, and CK decreased in *Tbx15*$^{M566R/M566R}$ vs *Tbx15*$^{+/+}$ Male: sodium increased, and potassium decreased in *Tbx15*$^{+/M566R}$ and *Tbx15*$^{M566R/M566R}$ vs *Tbx15*$^{+/+}$, chloride increased and glucose decreased in *Tbx15*$^{M566R/M566R}$ vs *Tbx15*$^{+/+}$, and total protein, total cholesterol and LDL decreased in *Tbx15*$^{+/M566R}$ vs *Tbx15*$^{+/+}$	NSD

4.3.1. *Tbx15*$^{+/-}$ mice

Chow-fed global heterozygous-knockout (*Tbx15*$^{+/-}$) and HFD-fed adipocyte-specific *Tbx15*-knockout mice were previously shown to have significantly more fat mass than their respective wildtype littermates (Lee *et al.*, 2015; Sun *et al.*, 2019). Further, adipocyte-specific *Tbx15*-knockout mice had heavier iWAT and gWAT compared to wildtype littermates (Sun *et al.*, 2019). This directly contradicted data collected from our *Tbx15*$^{-/-}$ viability (chow diet; unpublished data, Dr. Rebecca Dumbell) and metabolic phenotyping (HFD and LFD; presented in this chapter) cohorts. Chow-fed *Tbx15*$^{+/-}$ mice had significantly less fat mass between 13-19 weeks of age, with no difference in bodyweight or lean mass (unpublished data, Dr. Rebecca Dumbell). Similarly, I showed LFD-fed *Tbx15*$^{+/-}$ mice had decreased bodyweight and fat mass, with smaller subcutaneous and visceral WAT.

Intrinsic genetic differences between the *Tbx15*-knockout models were the most likely cause for the different direction of effect for body composition between these studies; both in terms of the genetic architecture of background strains and differences in the specific interruption of *Tbx15* within the locus. For example, Lee *et al.* (2015) and Sun *et al.* (2019) used *neo*-cassette targeted *Tbx15* deletions in a mixed 129/Ola x NMRI background (F2 offspring), or C57BL/6J mice, respectively. Whereas studies presented in this chapter used C56BL/6J mice, carrying a spontaneous 216 kb deletion of all but exon 1 of *Tbx15,* back-crossed to a C57BL/6NTac background (back-cross 5). Such differences have been observed in other mouse models of obesity. For example *Irx3*-knockout mice (C57BL/6NTac) did not present a metabolic phenotype (Laber, 2017), in contrast to the significant phenotypes observed in 129/SV x C57BL/6 mixed-background *Irx3*-knockout mice (Smemo *et al.*, 2014). Even sub-strains derived

from the same background can exhibit significantly different metabolic phenotypes, as reported for C57BL6/J and C57BL6/NTac mice (Harley *et al.*, 2013; Montgomery *et al.*, 2013; Simon *et al.*, 2013; Doran *et al.*, 2016; Hull *et al.*, 2017). Additionally, it has been reported that *neo*-cassettes can exert *cis*- and *trans*- off-target effects (Pham *et al.*, 1996; Scacheri *et al.*, 2001; Meier *et al.*, 2010; West *et al.*, 2016). This could explain the differential knockout phenotypes observed, however, further investigation would be required to confirm any off-target effects in these models.

Further, given obesity traits are influenced by environmental factors, differences in diet composition, and age at dietary challenge, could have influenced the different outcomes. For example, the chow diet used by Lee *et al.* (2015) was composed of twice as much fat as the RM3 chow diet used at Harwell (Table 4.4). Whilst Sun *et al.* (2019) used the same HFD (D12492) used in the studies presented here, HFD-feeding commenced at 8 weeks of age for a total of 12 weeks and a control diet was not assessed (Table 4.4). It is likely that interaction between several factors caused the different directional effects seen in these studies, however, together they support the hypothesis that *Tbx15* has a role in adipose tissue biology.

Table 4.4. Diet composition between *Tbx15* mouse studies. Abbreviations: HFD (high-fat diet), LFD (low-fat diet), N/A (not applicable i.e. not used in the study).

Diet	MRC Harwell	Lee *et al.* (2015)	Sun *et al.* (2019)
Chow	RM3 diet (Special Diet Services) 11% fat, 27% protein and 62% carbohydrate	mouse diet 9F 5020 (PharmaServ) 22% fat, 23% protein and 55% carbohydrate	N/A
HFD	D12492 (Research Diets Inc) 60% fat, 20% protein, 20% carbohydrate, 7% sucrose	N/A	D12492 (Research Diets Inc) 60% fat, 20% protein, 20% carbohydrate, 7% sucrose
LFD	D12450J (Research Diets Inc) 10% fat, 20% protein, 70% carbohydrate, 7% sucrose	N/A	N/A

Tbx15 is differentially expressed between adipose tissues in mice, with the highest expression levels detected in iWAT and BAT, and minimal expression detected in gWAT (Yamamoto *et al.*, 2010; Gburcik *et al.*, 2012). Despite this, male and female *Tbx15*$^{+/-}$ mice had significantly smaller gWAT than *Tbx15*$^{+/+}$ littermates, suggesting adipose depot weight may not be solely regulated by intrinsic mechanisms. As *Tbx15*$^{+/-}$ mice also had lower terminal bodyweights, it suggests TBX15 may regulate systemic metabolic processes such as energy expenditure and/or thermogenesis that would influence adipose deposition. Therefore, it would be beneficial to asses energy metabolism, such as food intake and energy expenditure, in these mice using direct or indirect calorimetry approaches to determine whether TBX15 alters adipose deposition through these mechanisms (Speakman, 2013; Moir, Bentley and Cox, 2016).

Increased VAT accumulation and increased adipocyte size have been positively correlated with metabolic parameters such as insulin resistance, pro-inflammatory macrophage infiltration, hepatic lipid accumulation and decreased expression of adipogenesis genes (e.g. *PPARG*, *GLUT4, SREBP1* and *ADIPOQ*) (McLaughlin *et al.*, 2007, 2014, 2016; Rydén *et al.*, 2014; Kranendonk *et al.*, 2015; Verboven *et al.*, 2018). Whilst WAT depot weights in HFD-fed mice were not significantly different, histological analysis revealed a shift in distribution towards smaller adipocytes in *Tbx15*$^{+/-}$ mice indicating a higher degree of adipose expansion through hyperplasia rather than hypertrophy. Conversely, despite significant differences in WAT depot weights in LFD mice, no significant differences in adipocyte area distribution were detected suggesting an alternative mechanism is driving this phenotype. Together, this suggests that *Tbx15* regulates overall fat mass deposition, and in an obesogenic environment the shift towards smaller adipocytes in *Tbx15*$^{+/-}$ mice may confer a protective metabolic effect, although further investigation of underlying mechanisms is required.

Despite the significant body composition differences seen in *Tbx15*$^{+/-}$ mice, there were few significantly different blood plasma analytes, for example uric acid, glycerol, LDH and CK. Uric acid is a by-product of apoptotic purine metabolism of nucleic acids (Shi, Evans and Rock, 2003), while glycerol and fatty acids are by-products of triacylglycerol lipolysis in response to nutrient deficiency (Mahendran *et al.*, 2013). Both hyperuricemia (increased uric acid) and increased glycerol levels have been associated with increased risk for CVD and MetS, and hyperglycaemia and T2DM incidence, respectively (De Oliveira and Burini, 2012; Wang *et al.*, 2012; Mahendran *et al.*, 2013; Borghi *et al.*, 2014). Further, hyperuricemia was correlated with increased VAT, but not SAT, lipid storage when adjusted for BMI (Rospleszcz *et al.*, 2020). Therefore, it was expected that the hypouricemia and decreased glycerol levels in *Tbx15*$^{+/-}$ HFD mice would correlate with decreased gWATadjBW indicating a protective cardiometabolic effect in these mice, rather than the observed increased gWATadjBW.

In contrast, serum CK and LDH plasma levels were significantly differential in *Tbx15*$^{+/-}$ mice. Whilst CK is usually used as a measure of muscle injury, studies have shown a correlation between plasma CK levels and adipose tissue browning and overall fat mass (Bekkelund and Jorde, 2017; Wallimann *et al.*, 2020). The LDH enzyme, expressed in most tissue, is involved in converting pyruvate to lactate during glycolysis and is used as a marker of tissue damage (Farhana and Lappin, 2022). Elevated lactate levels in WAT have been strongly correlated with increased LDH plasma levels *in vivo* in rats suggesting LDH can be used as a proxy measure for lactate production during glycolysis (Arriarán *et al.*, 2015). Indeed, increased lactate levels were associated with reduced glucose tolerance in both lean and obese individuals (Berhane *et al.*, 2015), and LDH-*knockdown* targeted in *drosophila* fat bodies improved glucose clearance (Krycer *et al.*, 2020). Therefore, it could be inferred that increased LDH levels in female

Tbx15$^{+/-}$ mice may be correlated with the impaired glucose clearance seen in IPGTTs at 13 weeks of age, however, the lack of significant difference in glucose response in male *Tbx15*$^{+/-}$ mice suggests LDH is not sufficient to drive this response.

Global *Tbx15*$^{+/-}$ influenced overall fat mass in a largely diet- but not sex-specific manner. In response to HFD-feeding, *Tbx15* played a role in regulating adipocyte cell size distribution, particularly in visceral depots. These changes were further correlated with altered serum plasma levels for factors which are largely indicative of tissue damage and increased MetS risk. Further work is needed to investigate the underlying mechanisms driving altered body composition and systemic plasma differences in these mice.

4.3.2. *Tbx15*^{H156N} mice

In contrast, the most striking phenotype in *Tbx15*^{H156N} mice was the significantly higher lean mass detected in *Tbx15*$^{+/H156N}$ mice compared to *Tbx15*$^{+/+}$ littermates in echo-MRI. Based on *in silico* modelling of TBX15 T-box protein-protein dimers (discussed in chapter 3), I hypothesised that p.H156N may act in a gain-of-function manner in heterozygous mice at a physiological level *in vivo.*

BMI and WHR measures over-classify individuals with increased muscle mass as obese, and cannot accurately depict lean versus fat mass distribution (Heinrich *et al.*, 2008; Alasagheirin *et al.*, 2011; Zhu *et al.*, 2020). It is therefore possible that some WHRadjBMI SNP-associations were driven by lean, rather than fat, mass. Using techniques such as MRI, CT, DEXA and bio-impedance (Mattsson and Thomas, 2006) or indeed a fat-to-lean ratio (Lee *et al.*, 2018; Gamboa-Gómez *et al.*, 2019) would help to accurately distinguish body composition, and the tissue(s) driving SNP-associations,

in individuals with increased WHRadjBMI that would provide more accurate predictions for cardiometabolic disease risk. Given the lean mass phenotype in *Tbx15*$^{+/H156N}$ mice, it would be worthwhile assessing whether this, and other variants, are associated with WHRadjBMI through lean mass or additional adiposity traits using DEXA data from Biobank cohorts (Zillikens *et al.*, 2017; Agrawal *et al.*, 2022).

Despite strong genotype associations for increased lean mass in HFD-fed *Tbx15*$^{+/H156N}$ compared to *Tbx15*$^{+/+}$ mice using echo-MRI data, this was not recapitulated in DEXA. Whilst both of these techniques were designed to analyse body composition, studies have shown that nuclear magnetic resonance-based techniques such as echo-MRI outperform DEXA with regard to accuracy (Taicher *et al.*, 2003; Tinsley, Taicher and Heiman, 2004; Halldorsdottir *et al.*, 2009). It was shown that DEXA overestimated lean mass by approximately 8% compared to an underestimation of just 0.2% in nuclear magnetic resonance techniques (Halldorsdottir *et al.*, 2009) which may explain why lean mass difference were not statistically significant using DEXA. Further, DEXA revealed male *Tbx15*$^{H156N/H156N}$ mice had less fat mass and fat mass percentage compared to *Tbx15*$^{+/+}$ littermates. This may have been driven, in part, by significantly smaller iWAT (*Tbx15*$^{H156N/H156N}$ compared to *Tbx15*$^{+/H156N}$) and pWAT (*Tbx15*$^{+/H156N}$ compared to *Tbx15*$^{+/+}$) suggesting p.H156N may drive altered fat distribution, although exact mechanisms remain unknown.

No fat mass phenotypes were detected in female *Tbx15*^{H156N} mice, however, meta-analyses indicated rs10494217 was significantly associated with increased WHRadjBMI in both males and females (Justice *et al.*, 2019; Pulit *et al.*, 2019). Therefore, I considered other factors that could explain the lack of significant differences detected in female mice. Firstly, due to sub-viability issues with breeding

female *Tbx15*$^{H156N/H156N}$ mice, it was possible that the female cohorts were underpowered to detect more subtle fat mass phenotype effects. Secondly, in HFD-challenged mice, I observed greater variability in bodyweight and fat mass-gain in female mice which potentially confounded detection of more subtle phenotypes. Therefore, it would be beneficial to further investigate the role of p.H156N in different genetic backgrounds and in response to sex-specific hormones in mice.

Skeletal muscle is the primary site for glucose clearance, and has been negatively correlated with plasma glucose levels in lean individuals (Thiebaud *et al.*, 1982; DeFronzo and Tripathy, 2009; Rattarasarn, Leelawattana and Soonthornpun, 2010). However, in obese individuals increased VAT, not lean mass, was associated with impaired glucose tolerance (Brochu *et al.*, 2000, 2008; Kuk *et al.*, 2008), which may explain the lack of glucose tolerance phenotype in HFD-fed *Tbx15*^{H156N} mice. In line with the higher lean mass seen in *Tbx15*$^{+/H156N}$ mice, most differential plasma analytes were detected between these mice and *Tbx15*$^{+/+}$ or *Tbx15*$^{H156N/H156N}$ littermates. However, it was unclear whether these changes directly influenced, or were a consequence of, differential body composition. For example, skeletal muscle is the major potassium store and increased plasma potassium concentrations occur in response to exercise under normal conditions (McDonough, Thompson and Youn, 2002; Lindinger and Sjøgaard, 2012). Further, serum potassium levels have been negatively correlated with MetS, central obesity, dyslipidaemia and insulin resistance (Sun *et al.*, 2014). It would therefore appear that the increased plasma potassium levels in *Tbx15*$^{+/H156N}$ mice indicate a correlative rather than causative association, given fat distribution and insulin sensitivity were not significantly different in these mice.

Further, bilirubin, ALT, AST and LDH were significantly altered in *Tbx15*$^{+/H156N}$ mice; such analytes are often used as clinical markers of liver function. Bilirubin is a product

of heme catabolism in red blood cells, ALT and AST are transaminase enzymes involved in amino acid metabolism, and LDH is integral in glycolysis. Serum levels of these factors are elevated in response to exercise (Pettersson *et al.*, 2008; Banfi *et al.*, 2012), and bilirubin plasma levels have been negatively correlated with hepatic lipid accumulation in NAFLD (Jang, 2012; Kwak *et al.*, 2012) and atherosclerosis risk in men (Novotný and Vítek, 2003). It is likely, therefore, that the increased plasma levels of these factors were correlated with the higher lean mass in *Tbx15*$^{+/H156N}$ mice. However, further interrogation of general activity levels of these mice (e.g., indirect calorimetry) and ectopic fat deposition (e.g., histological liver sections) may explain any causative effects for these differences. The significantly higher lean mass in *Tbx15*$^{+/H156N}$ mice may be more representative of the increased WHRadjBMI associations for rs10494217, than differences in fat distribution. Further, metabolic traits associated with this SNP may in fact be driven by increased muscle metabolism and be correlated with, rather than driving, metabolic phenotypes associated with MetS risk.

4.3.3. *Tbx15*^{M566R} mice

The final allele assessed in this chapter, *Tbx15*^{M566R}, is representative of the human rs61730011 variant (A>C) which had a larger effect size (β=0.041) than rs10494217 (β=0.018; p.H156N) (Justice *et al.*, 2019). The deleterious prediction for the p.M566R substitution (discussed in chapter 3) suggested *Tbx15*^{M566R} mice would have a more severe phenotype than carriers of the *Tbx15*^{H156N} allele. However, this was not the case, with no significant genotype effects detected in *Tbx15*^{M566R} mice in echo-MRI, irrespective of sex or diet. Conversely, DEXA revealed LFD-fed female *Tbx15*$^{M566R/M566R}$ mice had significantly less fat mass and fat mass percentage compared to *Tbx15*$^{+/M566R}$

littermates. However, this was not recapitulated in individual adipose depot weights, suggesting another depot may account for this overall fat mass difference. Dermal WAT (dWAT), constituting ~50% of overall fat mass, increases relative to overall weight gain in mice and is proposed to be an important metabolic tissue (Kasza *et al.*, 2016). dWAT remains relatively unexplored in models of obesity, therefore, future work will examine relative thickness of dorsal and ventral dWAT samples, to determine whether p.M566R alters fat distribution within this depot that may also be associated with altered metabolic plasma profiles in these mice.

Despite no significant body composition differences in HFD-fed mice, analytes such as glucose, and electrolytes (potassium, chloride, sodium) were differentially expressed between genotypes in terminal blood plasma. Glucose levels were sexually dimorphic between male and female *Tbx15*$^{M566R/M566R}$ mice compared to *Tbx15*$^{+/+}$ littermates at 25 weeks of age. Significantly lower fasting blood glucose levels, and increased glucose clearance 30 minutes after glucose challenge, were further detected in male *Tbx15*$^{+/M566R}$ mice compared to *Tbx15*$^{+/+}$ mice during IPGTTs. In cross-trait association analysis using previously published ExomeChip datasets no significant associations were detected for rs61730011 and fasting glucose (β=-0008, *P*=0.975), fasting insulin (β=0.0041, *P*=0.399), two-hour glucose (β=0.000, *P*=0.964) or T2DM (β=-0.0205, *P*=0.510) (Justice *et al.*, 2019). Given these data were from several sources and were sex-combined results, it is possible that the associations for rs61730011 did not reach significance in humans due to confounding effects in sample populations such as sexual dimorphism for effect direction, or insufficient sample sizes to detect rarer effects.

Electrolytes such a sodium, potassium and chloride are critical for nerve conduction, muscle contraction and osmotic homeostasis in cells. Electrolyte abnormalities can be indicative of renal dysfunction in T2DM (Liamis *et al.*, 2014). Hyperglycaemia in

diabetic patients was further associated with increased serum potassium (hyperkalaemia), and decreased serum sodium (hyponatremia) and chloride (hypochloraemia) levels (Khan *et al.*, 2019). This suggests the hypoglycaemia, hypokalaemia, hypernatremia and hyperchloremia in *Tbx15*$^{M566R/M566R}$ and *Tbx15*$^{+/M566R}$ mice inferred a protective effect, in males at least, against hyperglycaemia and T2DM in obesogenic environments.

Two questions have arisen from the minimal phenotype observed in *Tbx15*^{M566R} mice. Firstly, what is driving the larger effect size for rs61730011 (β=0.041) compared to that of rs10494217 (β=0.018), and secondly, given the deleterious predictions for p.M566R why was a stronger phenotype not observed? The meta-analysis performed by Justice *et al.* (2019) combined individuals from five ancestries and conditional analyses indicated that rs61730011 was not independent of the four lead locus SNPs identified by Shungin *et al.* (2015) (Justice *et al.*, 2019), suggesting that ancestry-specific regulatory mechanisms and/or inherited haplotypes may be driving the WHRadjBMI association of this SNP. In European and American populations rs61730011 was only moderately (r^2≥0.4) or weakly associated (r^2≥0.2) with other variants, however in African and Asian populations it was in perfect LD (r^2=1) with one and four SNPs, respectively, spanning a ~2kb region (Table 4.5). Whilst r^2 is commonly used to define LD, MAF with rare variants result in lower r^2 values irrespective of true disequilibrium. Therefore, other statistical representations of LD (such as D' which does not account for MAF) may be more informative predictors of variant independence (Turkmen and Lin, 2017; Kang and Rosenberg, 2019; Good, 2020). In this respect, variants in low and moderate LD with rs61730011 had D' scores of ≥0.5 and 1, respectively, in HaploReg v4.1 suggesting rs61730011 may be tagging an unidentified causal SNP in the co-inherited haplotype.

Several of the SNPs in LD with rs61730011 marked enhancer histone marks for a range of tissues and were predicted to alter TFBMs for homeobox B9 (HOXB9), NFκB, and NK homeobox 2 and 3 (NKX2 and NKX3; rs1779432), and oestrogen receptor alpha (ERα) and forkhead box M1 (FOXM1; rs1886915; Table 4.5). Several of these genes have been implicated in regulating adipogenesis and adipose tissue biology (Gesta *et al.*, 2006; Ijichi *et al.*, 2007; Yamamoto *et al.*, 2010; Davis *et al.*, 2013; Chen *et al.*, 2019) further suggesting rs61730011 may be tagging, or acting in concert with, another functional variant in the locus. Further deep genome sequencing analysis may uncover other rare SNPs in the haplotype that could be driving WHRadjBMI associations. Given the differences in human haplotypes for rs61730011 in different genetic populations, C57BL/6NTac mice may not be the most appropriate model for this SNP due to potential divergence of regulatory landscapes in the *TBX15-WARS2* locus between humans and mice, or indeed between mouse strains (Simon *et al.*, 2013; Perlman, 2016; Powell *et al.*, 2022). Therefore, modelling this variant in alternative mouse backgrounds may reveal body composition phenotypes driven by this variant.

Finally, I considered why p.M566R was predicted to be deleterious and more damaging than p.H156N yet resulted in a minimal *in vivo* body composition phenotype. *In silico* prediction servers such as Polyphen2, SIFT and Condel fail to account for i) the biological function of proteins, and ii) the potential for any intrinsically disordered regions in the protein when assembled *in vivo.* Intrinsically disordered regions in proteins are widely expressed *in vivo* (~50% of all TFs) and play a crucial functional role in protein-protein and protein-nucleic acid interactions (Wright and Dyson, 1999; Liu *et al.*, 2006; Minezaki *et al.*, 2006; Nishikawa, 2009). Indeed, X-ray crystallographic structures exist only for the T-box region of TBX proteins, indicating that the C-terminal region of TBX15 (containing p.M566) could be intrinsically disordered

whilst still being functionally important. Further, human Cousin Syndrome-causing mutations in TBX15 reside in the C-terminal region and result in truncation of the protein, highlighting the critical role for this region in TBX15 TF function (Lausch *et al.*, 2008; Dikoglu *et al.*, 2013). It is therefore plausible that if the region is disordered the non-synonymous p.M566R substitution may not significantly alter the structure of this domain *in vivo* resulting in the minimal body composition phenotype.

In conclusion, I have shown the *Tbx15*$^{+/-}$, *Tbx15*^{H156N} and *Tbx15*^{M566R} alleles alter body composition, glucose response and serum plasma levels *in vivo.* All *Tbx15* alleles resulted in decreased fat mass phenotypes, albeit in a sex- and diet-specific manner, highlighting a regulatory role for *Tbx15* in adipose tissue expansion and body composition. Further, plasma analyte differences were detected across the alleles, further implicating *Tbx15* in cell-intrinsic metabolic processes that may be associated with MetS risk. TBX15 is a known TF involved in MSC condensation, suggesting it may play a role in determining MSC lineage determination and differentiation into osteoblasts, adipocytes, or myoblasts. Perhaps the most striking phenotype observed was the higher lean mass in *Tbx15*$^{+/H156N}$ mice, suggesting the p.H156N polymorphism may perturb the normal function of TBX15 to increase the proportion of myoblast cells, and ultimately muscle fibres, generated from MSCs *in vivo.* More mechanistic investigations are required to dissect what is driving the phenotypic differences between the *Tbx15* alleles. For example, assessing the differentiation potential of SVF cells isolated from iWAT into osteoblast, adipocyte and myocyte lineages may provide evidence for a potential dominant-negative mechanism of action of the pH156N allele.

Table 4.5. HaploReg v4.1 regulatory associations for SNPs in high LD ($r^2 \geq 0.8$) with rs61730011. Abbreviations: ESC (embryonic stem cell), iPSC (induced pluripotent stem cells), ESDR (embryonic stem cell-derived cell), MUS (muscle).

Ancestry	pos (hg38)	LD (r^2)	variant	Ref	Alt	Enhancer histone marks	Motifs changed	GENCODE genes	dbSNP functional annotation
European	1:118884844		rs61730011	A	C		NRSF, NANOG, POU2F2, TCF12	*TBX15*	missense
African	1:118952473	1	rs78395856	C	A	adipose nuclei, muscle tissues, skeletal muscle myoblast cells and osteoblast primary cells		*TBX15*	intronic
Asian	1:118919954	1	rs1779432	A	C	ESC, iPSC	HOXB9, NKX2, NKX3	*TBX15*	intronic
	1:118999069	1	rs1886915	A	G	ESC, ESDR	ERα, FOXM1	1.3kb 3' of *RP4-712E4.1*	
	1:119013987	1	rs1590543	T	C			13kb 5' of *RP4-712E4.2*	
	1:119097464	1	rs6428791	A	C	ESCs, iPSCs, adipose nuclei, adipose-derived MSCs, skeletal muscle myoblast cells, osteoblast primary cells and skeletal muscle tissues		*WARS2*	intronic

5

Identifying the TBX15 transcriptional network

5.1. Introduction

The TBX15 transcription factor (TF) regulates a network of genes in adipose and other tissues; these genes and their products exert a quantitative effect on cellular and ultimately organismal physiology. *TBX15/Tbx15* is differentially expression in adipose depots in both humans and mice (Figure 5.1) (Gesta *et al.*, 2006; Yamamoto *et al.*, 2010; Gburcik *et al.*, 2012; Lonsdale *et al.*, 2013). Further, using RNA-sequencing we showed the 602 amino acid isoform was the main transcript in both species.

Conflicting roles for TBX15 in regulating adipogenesis were apparent *in vivo* and *in vitro.* For example, I showed *Tbx15*$^{+/-}$ mice were resistant to fat mass gain, in contrast to published *Tbx15*$^{+/-}$ and *Tbx15* adipose-specific knockout mouse models that showed increased fat mass phenotypes (Lee *et al.*, 2015; Sun *et al.*, 2019). *In vitro*, both TBX15-*overexpression* in 3T3-L1 cells, and *Tbx15-silencing* in SVF cells impaired key adipogenesis genes such as *Cebpa, Pparg* and *Fabp4,* (Gesta *et al.*, 2011; Gburcik *et al.*, 2012). Mitochondrial (*Cox5b, Cox8b, Pgc1a* and *Tfam*) and browning (*Prdm16, Pgc1a, Cox8b* and *Ucp1*) markers were also downregulated in these TBX15-*overexpression* and *Tbx15-silencing* cell models, respectively, implicating TBX15 in regulating browning of adipocytes (Gesta *et al.*, 2011; Gburcik *et al.*, 2012). Further, brown (*Prdm16, Cidea, Dio2, Cox8b* and *Ucp1*) and beige (*Tbx1, Tmem26* and *Cd137*) markers were

downregulated in iWAT from *Tbx15* adipose-specific knockout mice, with TBX15 implicated in the direct regulation of *Prdm16* (Sun *et al.*, 2019). These studies highlight a key regulatory role for TBX15 in adipogenesis and browning of adipocytes, which appears heavily influenced by stimuli such as cell type or nutrient availability.

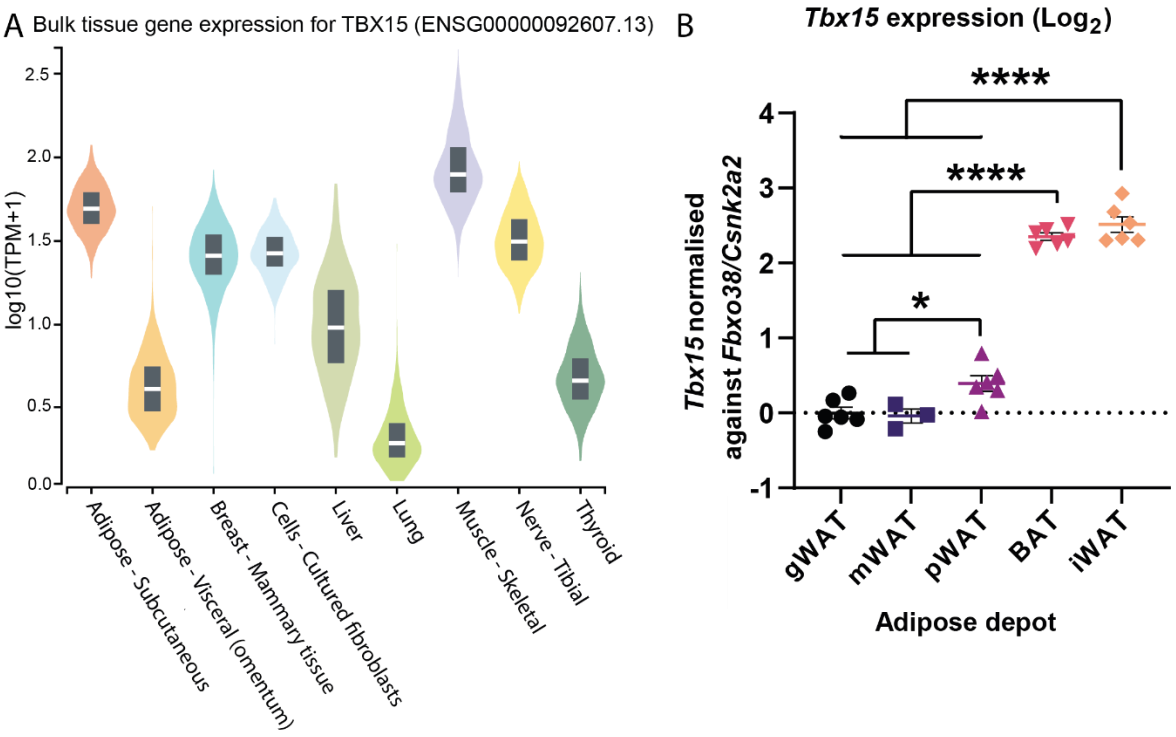

Figure 5.1. *TBX15* adipose tissue expression in human and mouse. A. Subcutaneous (orange) and visceral (yellow) *TBX15* gene expression in human GTEx samples on a $\log_{10}$ expression scale (data accessed from the GTEx portal on 16th August 2022) (Lonsdale *et al.*, 2013). B. *Tbx15* expression in white adipose tissues (WAT) and brown adipose tissue (BAT): gonadal WAT (gWAT; black circle), mesenteric WAT (mWAT; dark purple square), perirenal WAT (pWAT; light purple upwards triangle), BAT (pink downwards triangle) and inguinal WAT (iWAT; orange diamond) from male C57BL/6NTac mice (n=6). *Tbx15* expression was normalised to the geometric mean of *Fbxo38* and *Csnk2a2* housekeeping genes, data analysed by one-way ANOVA with post-hoc Tukey's multiple comparisons: *p<0.05, ****p<0.0001.

Even though evidence of *Tbx15* function was conflicting in mouse, more recently in humans there have been investigations into *TBX15* function using GWAS. For example integrative genomic approaches were leveraged to compare WHRadjBMI GWAS variants and RNA-sequencing data to generate TF co-expression networks (Pan *et al.*,

2021). *TBX15* was predicted as a key regulator of its network, and siRNA-mediated knockdown of *TBX15* in human white preadipocyte cells confirmed differential expression of over one-third of co-expression network genes, including *PPARG, KLF15* and *TWIST1* (Pan *et al.*, 2021). The above studies have all taken a targeted approach to investigate the TBX15 expression network in limited models, therefore, future investigations of the network require a focus on understanding the complex communication between cell types in a tissue. Further, identifying cross-species similarities may help with future *in vivo* modelling of *TBX15-WARS2* variants association with WHRadjBMI.

5.1.1. Chapter hypothesis

Several targeted studies have implicated TBX15 in regulating a network of adipogenesis-related genes *in vitro* and *in vivo.* However, to date, an untargeted and comprehensive analysis of the TBX15 regulatory network in adipose tissues, and adipocytes themselves, remains elusive. I hypothesised that the decreased fat mass in *Tbx15*$^{+/-}$ mice was driven by decreased expression of adipogenesis genes *in vivo*.

5.1.2. Chapter aims

I aimed to elucidate the TBX15 regulatory network in adipocytes and adipose tissues by:

1. Identifying TBX15 binding sites in human (hWAT) and mouse (3T3-L1) immortalised preadipocytes overexpressing HA-tagged TBX15 *in vitro* using ChIP-sequencing (in collaboration with Active Motif Inc., Carlsbad, USA).

2. Assessing differentially expressed genes (DEGs) in whole adipose tissues from *Tbx15*$^{+/+}$, *Tbx15*$^{+/-}$ and *Tbx15*$^{-/-}$ mice to determine a *Tbx15* regulatory network (in collaboration with Dr. Michelle Simon, Biocomputing group, MRC Harwell).

5.2. Results

5.2.1. Determining TBX15 target genes in 3T3-L1 and hWAT cells using ChIP-sequencing

5.2.1.1. Quality control and method optimisation

5.2.1.1.1. TBX15 antibodies exhibited cross-reactivity in muscle tissues and hWAT cell samples

As TBX15 has been implicated in the regulation of several key adipogenesis markers, I aimed to determine a comprehensive target network of genes using chromatin immunoprecipitation with whole genome sequencing (ChIP-sequencing). Gold standard ChIP-sequencing experiments are performed on cells or tissues expressing endogenous levels of the protein of interest, requiring an antibody that is not only specific to the protein but also suitable for ChIP protocols. Therefore, I initially aimed to validate specificity of three TBX15 antibodies using protein isolated from muscle tissues of *Tbx15*$^{+/+}$, *Tbx15*$^{+/-}$ and *Tbx15*$^{-/-}$ mice and differentiated hWAT cells during adipogenic differentiation.

The 602 and 496 amino acid TBX15 protein transcripts were predicted to resolve at ~65 kDa and 55 kDa by SDS-PAGE, respectively. With all antibodies, there was no complete ablation of bands around 65 or 55 kDa in the *Tbx15*$^{-/-}$ samples, and additional non-specific bands were present on immunoblots (Figure 5.2B). In differentiating hWAT cells, all three antibodies showed cross-reactivity, likely with other TBX family

proteins (Figure 5.2C). I concluded these antibodies were not suitable for endogenous TBX15 ChIP-sequencing and I sought a different experimental approach.

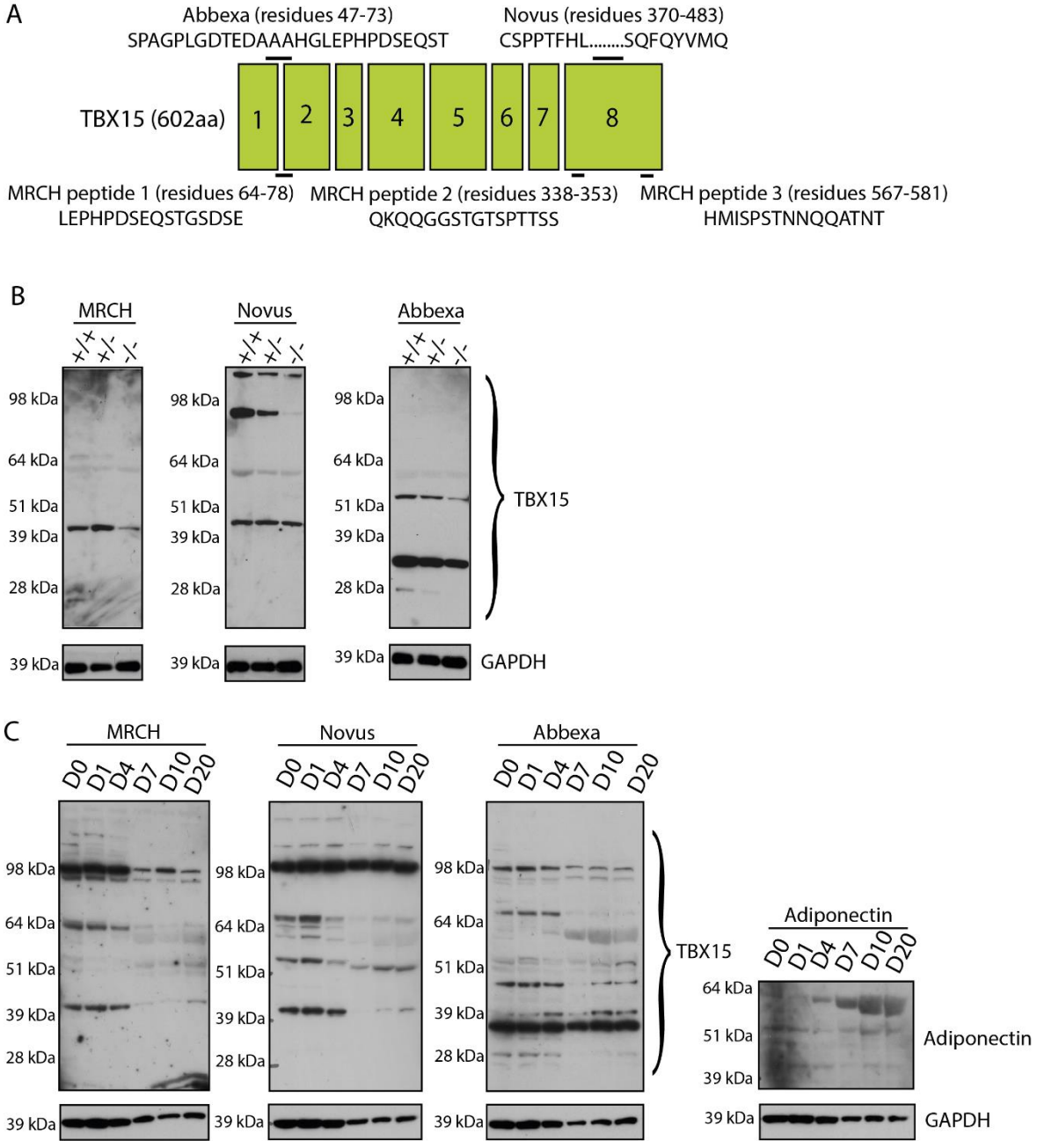

Figure 5.2. TBX15 antibody validation. A. Schematic representation of the mouse TBX15 protein with TBX15 antibody peptide alignments for Abbexa, Novus and MRC Harwell TBX15 antibodies. B. Western blot for TBX15 using muscle protein samples from *Tbx15*$^{+/+}$, *Tbx15*$^{+/-}$, and *Tbx15*$^{-/-}$ mice. Primary antibody concentrations (TBX15-MRCH 1:250, TBX15-Novus 1:400, TBX15-Abbexa 1:100, Adiponectin 1:10,000, GAPDH 1:100,000). C. Western blot for TBX15, and adiponectin, using differentiated hWAT cells from day 0 (D0) to day 20 (D20) post-differentiation. Primary antibody concentrations (TBX15-MRCH 1:250, TBX15-Novus 1:400, TBX15-Abbexa 1:100, Adiponectin 1:10,000, GAPDH 1:100,000). Adiponectin was used to confirm hWAT differentiation was successful.

5.2.1.1.2. Optimisation of sample collection for accessibility of target binding sites

I next aimed to develop an alternative approach for TBX15 ChIP-sequencing using tagged overexpression constructs *in vitro*. In this thesis I considered the 602 amino acid TBX15-1 (human) and TBX15 (mouse) protein transcripts, conserved at 98.8% between species, to be the main transcripts in adipocytes and adipose tissues. Based on this, I chose to use the human HA-tagged TBX15-1 cDNA construct under a pCMV6 promoter for ChIP-sequencing analysis in 3T3-L1 and hWAT cells, given TBX15-1 protein expression was not detected in these cells when using a synthetic AM-tagged TBX15-1 construct under an ACTB promoter (data not shown).

Further, endogenous *TBX15/Tbx15* expression was highest 24 hours after induction of adipogenesis (day 1) in hWAT cells and mouse SVF derived from iWAT in RNA-sequencing experiments (Figure 5.3A-B). Based on these expression levels, we inferred that endogenous TBX15 expression would be highest, and as a result target binding sites would be most accessible, around day 0 to day 1 of adipogenesis. Therefore, I aimed to optimise sample collection to recapitulate this by transfecting 3T3-L1 and hWAT cells with pCMV6-TBX15-1-HA or empty pcMV6-HA cDNA constructs and collected protein at post-confluence (day 0) and 24 hours post-induction of differentiation (day 1). In both 3T3-L1 and hWAT cells, HA-tagged TBX15-1 was detected in day 0 and day 1 lysates, with no HA expression detected in the lysates from cells transfected with an empty HA vector (Figure 5.3C). In hWAT cells, TBX15-1 expression appeared slightly stronger at day 0, therefore I chose to proceed with this time point for sample collection for ChIP-sequencing (Figure 5.3C).

In both ChIP-sequencing biological replicates for 3T3-L1 and hWAT cells, expression of TBX15-1-HA was detected in the transfected samples; one hWAT replicate had

reduced TBX15-1-HA expression which was likely due to a poorer transfection efficiency (Figure 5.3D). As this expression was detectable, all samples were sent to Active Motif Inc. for ChIP-sequencing which included HA antibody qualification, ChIP-sequencing and descriptive bioinformatics analysis of data.

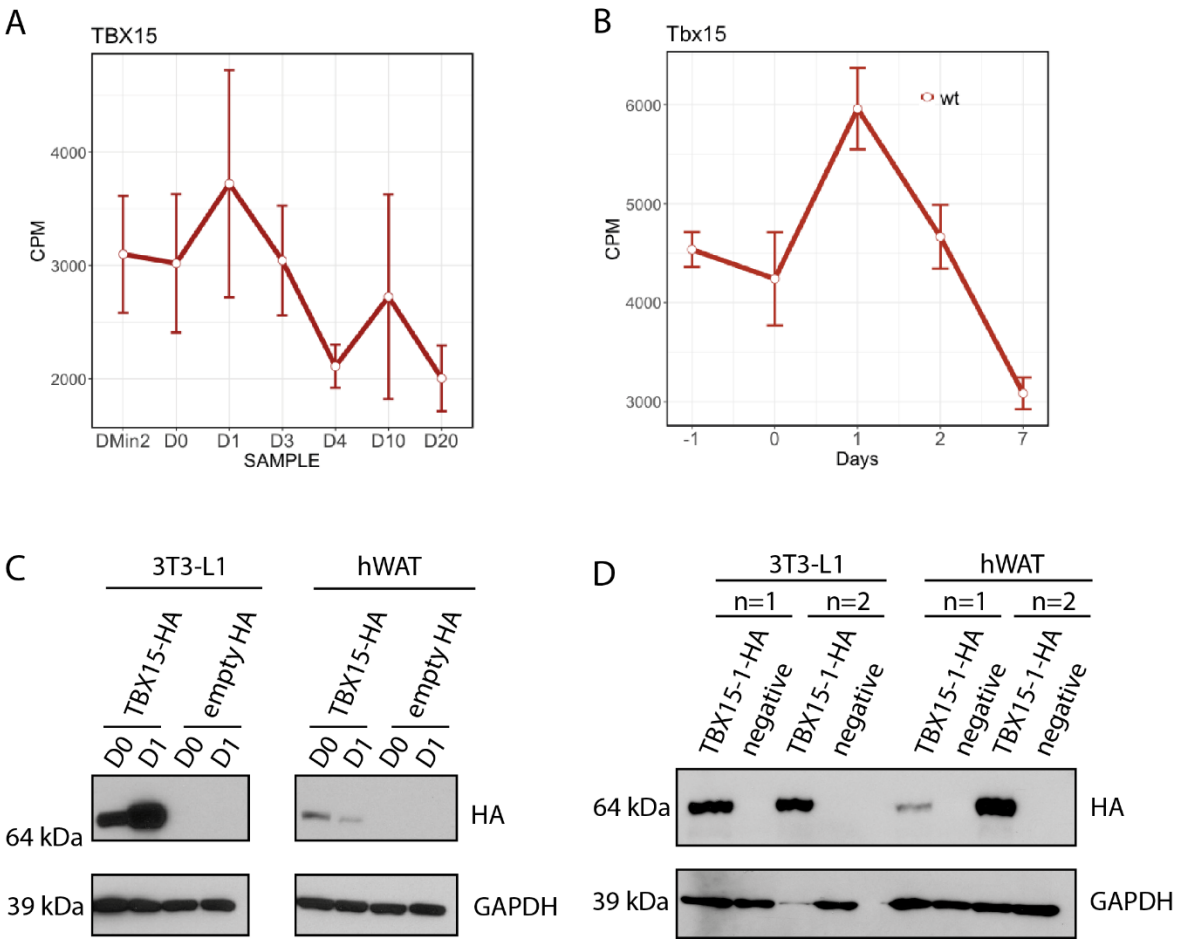

Figure 5.3. Optimisation of transfection for TBX15 for ChIP-sequencing. A-B. RNA-sequencing analysis of (A) *TBX15* expression in differentiating hWAT cells and (B) *Tbx15* in differentiating primary SVF cells isolated from iWAT (data produced by Dr. Michelle Simon) C. Optimisation of protein collection time point for HA-tagged TBX15-1 (primary antibody concentrations HA 1:50,000, GAPDH 1:100,000). D. Western blot analysis of TBX15-1-HA expression in 3T3-L1 and hWAT cells (n=2 biological replicates) (primary antibody concentrations HA 1:50,000, GAPDH 1:100,000).

5.2.1.1.3. Sample quality control and validation for ChIP-sequencing

Initial HA antibody qualification was performed by Active Motif Inc. using TBX15-1-HA expressing 3T3-L1 and hWAT cells (n=1 each). Fragment densities (blue tracks) and significant peaks (default cut-off $p<1x10^{-7}$; red tracks) along the genome were generated and visualized in the integrated genome browser by Active Motif (Appendix Figure 9.3). A total of 12154 and 9199 peaks were identified for 3T3-L1 and hWAT samples, respectively, confirming successful HA antibody validation for ChIP. Further ChIP quality control was performed by qPCR amplification of samples; strong signals were detected in cells overexpressing TBX15 with considerable enrichment over background signal for both species (~16-fold in mouse, and ~22-fold in human; Appendix Figure 9.4A and B, respectively). There was very little amplification in the negative control cells suggesting that the immunoprecipitations were specific. The data indicated that the chromatin was of good quality and the ChIP reactions worked well, therefore, Active Motif Inc. considered these samples sufficient quality to continue with ChIP-sequencing.

ChIP-sequencing data produced by Active Motif Inc. showed that considerably more peaks were found in the TBX15-1-HA-expressing samples compared to the negative controls in mouse 3T3-L1 samples (Figure 5.4A and B, Table 5.1). For human hWAT samples, one biological sample for TBX15-1-HA expressing cells (TBX15-HA n1) showed less peak enrichment than the second sample, but this was still ~5-fold higher than the two negative control samples (Figure 5.5A and B, Table 5.1). In both 3T3-L1 and hWAT samples overexpressing TBX15, a large proportion of peaks were detected over intronic regions (Figure 5.4C and Figure 5.5C, respectively). In 3T3-L1 samples overexpressing TBX15, there was also a large fraction of peaks detected at distal

intergenic, promoter and 5'-UTR regions (Figure 5.4C). In TBX15-overexpressing hWAT samples, notable proportions of binding peaks were detected at promoter, 5'-UTR and exonic regions (Figure 5.5C). Previous ChIP-sequencing of 3T3-L1 cells showed ~50% of peaks were detected in intronic regions and the number of detected peaks was highly dependent on protein expression (Nielsen *et al.*, 2008). Given I used a TBX15-overexpression system, this likely correlated with primed chromatin states surrounding the target genes and supported the high number of binding sites detected in my data.

In comparison, negative control samples for both 3T3-L1 and hWAT cells showed the highest proportion of peaks at proximal promoters, 5'-UTR and 3'-UTR regions (Figure ***5.4***D and Figure 5.5D, respectively). Promoter regions are known to show more false-positive peaks in ChIP-sequencing assays (Jain *et al.*, 2015), therefore, given the overall fewer peaks in the negative control samples, it was concluded that the TBX15-overexpressing samples would provide an insight into the target binding network of TBX15. Active Motif Inc. did not provide raw data for the relative size or number of peaks overlapping the individual genomic features assessed, nor which peaks contained the TBX15 motif. Based on this data alone, it was difficult to infer whether TBX15 was directly binding to these regions or co-binding with other TFs. However, due to the high proportion of peaks in intronic regions in TBX15-HA-overexpressing samples, it suggests TBX15 may preferentially bind enhancer elements over gene promoters. Further work is underway, in collaboration with Dr. Michelle Simon, to assess this hypothesis and to determine which peaks contain the TBX15 motif which would be indicative of direct target binding.

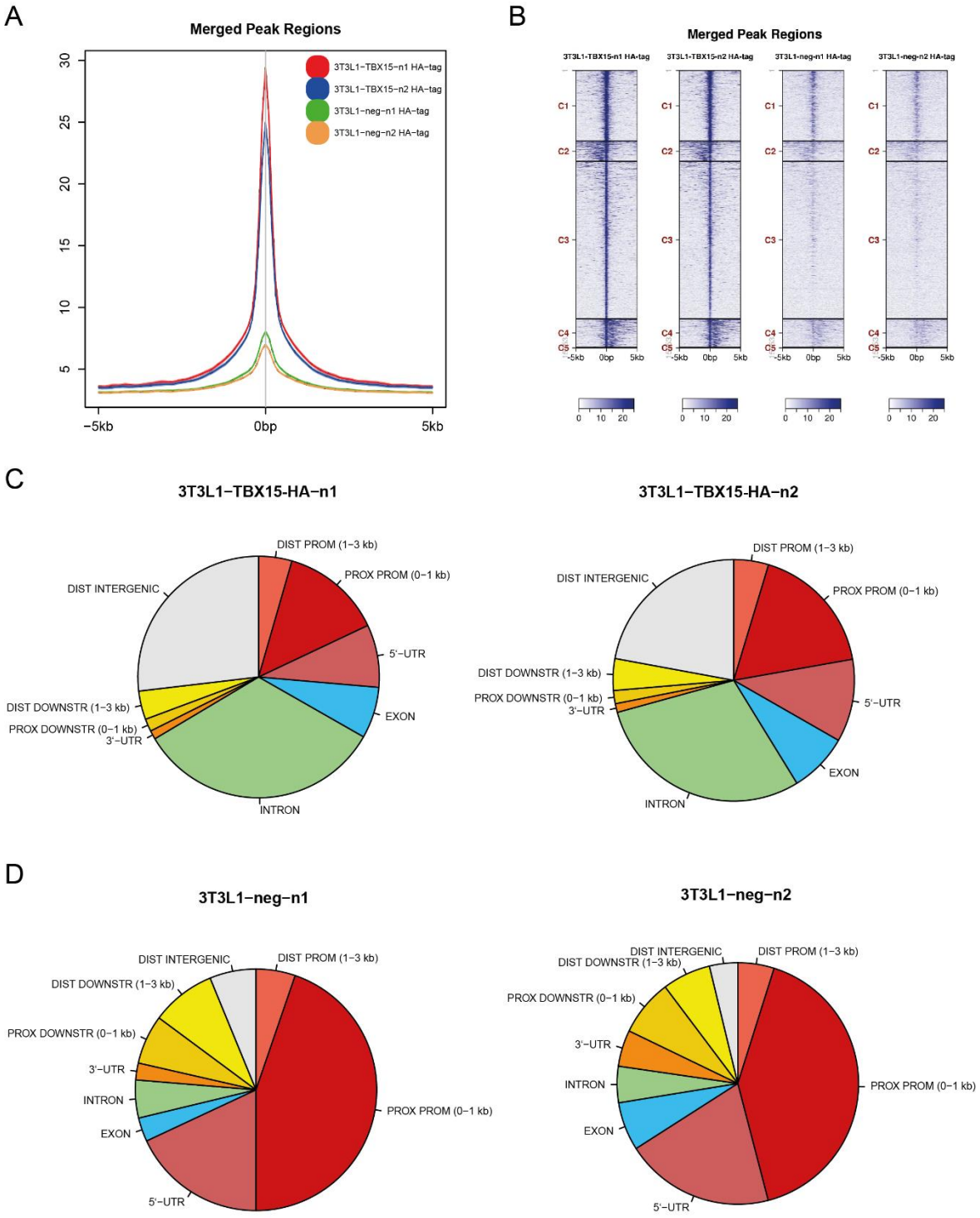

Figure 5.4. Example ChIP-sequencing infographics for 3T3-L1 cells. A-B Merged peak regions for all 3T3-L1 samples presented as an average plot (A) and heat map (B). C-D. Pie chart representation of distribution of peaks for TBX15-HA (C) and negative control (D) samples. For the pie charts, Active Motif counted the overlap between the peak summits and a database of genomic features but did not list the peaks/summits that were overlapping with each feature; all peak/summits were used (no cut-off). Experiments and data visualisation produced by Active Motif Inc.

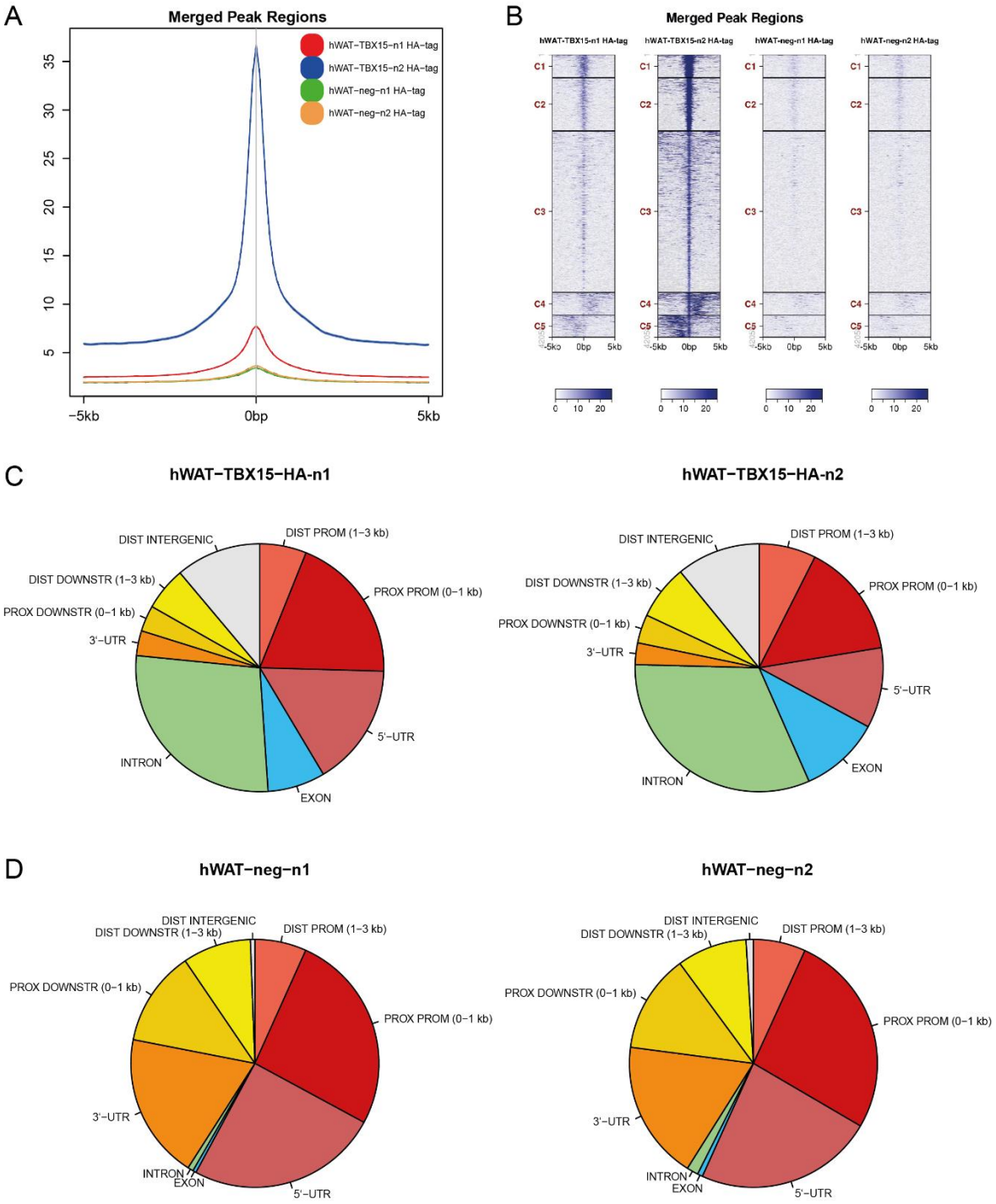

Figure 5.5. Example ChIP-sequencing infographics for hWAT cells. A-B Merged peak regions for all hWAT samples presented as an average plot (A) and heat map (B). C-D. Pie chart representation of distribution of peaks for TBX15-HA (C) and negative control (D) samples. For the pie charts, Active Motif counted the overlap between the peak summits and a database of genomic features but did not list the peaks/summits that were overlapping with each feature. All peak/summits were used (no cut-off). Experiments and data visualisation produced by Active Motif Inc.

Table 5.1. Total number of peaks detected in ChIP-sequencing samples. Peak threshold was set at $p<1x10^{-7}$ by Active Motif Inc.

	3T3-L1 TBX15-HA n1	3T3-L1 TBX15-HA n2	3T3-L1 negative n1	3T3-L1 negative n2	hWAT TBX15-HA n1	hWAT TBX15-HA n2	hWAT negative n1	hWAT negative n2
Number of peaks	13,619	9,690	434	148	5,932	40,110	336	376

5.2.1.2. TBX15 binding network *in vitro*

After discussion with Active Motif Inc., I continued with analysis on all four TBX15-HA samples and used shared peaks (indicating target binding sites) between biological replicates to determine targets of TBX15. A total of 6497 (3T3-L1) and 6595 (hWAT) shared peaks were detected in the TBX15-1-HA-overexpressing sample replicates (n=2 per 3T3-L1 and hWAT cell line), with no overlap with negative controls (using peak threshold $p<1x10^{-7}$ set by Active Motif Inc.). This was in line with previously reported ChIP-sequencing data. For example, 11078, 6880 and 2117 target genes were identified for PPARγ, CEBPα and liver-X receptor, respectively, in Simpson-Golabi-Behmel syndrome cells (Galhardo *et al.*, 2014). Further, 6592 (PPARγ) and 8228 (retinoid-X receptor) peaks were detected in differentiating 3T3-L1 cells (Nielsen *et al.*, 2008), suggesting the TBX15-HA-overexpression did not result in overly-promiscuous binding of TBX15. In order to elucidate potential mechanisms regulated by TBX15, I performed functional enrichment analysis using g:Profiler which revealed EGF/EGFR signalling, Wnt signalling, androgen receptor signalling and adipogenesis terms were enriched in both 3T3-L1 and hWAT samples (Table 5.2).

Table 5.2. Enriched WikiPathways terms for TBX15 target binding sites in 3T3-L1 and hWAT cells. Functional enrichment analysis for 6497 and 6595 shared peaks in TBX15-HA-overexpressing samples in 3T3-L1 and hWAT cells, respectively. Terms ranked based on adjusted p-value in 3T3-L1 samples.

Term name	Term ID	Adjusted p-value (3T3-L1)	Adjusted p-value (hWAT)
TGF-beta signalling pathway	WP:WP366	7.95E-07	Not enriched
EGF/EGFR signalling pathway	WP:WP437	2.97E-06	0.026317875
VEGFA-VEGFR2 signalling pathway	WP:WP3888	2.29E-05	Not enriched
Wnt signalling pathway	WP:WP363	0.002357	0.040807387
Androgen receptor signalling pathway	WP:WP138	0.004963	0.04196357
Insulin signalling	WP:WP481	0.00556	Not enriched
DNA damage response (only ATM dependent)	WP:WP710	0.005575	0.018412284
Cell cycle	WP:WP179	0.007333	Not enriched
DYRK1A	WP:WP5180	0.00784	Not enriched
Physiological and pathological hypertrophy of the heart	WP:WP1528	0.010701	0.010461292
Neuroinflammation and glutamatergic signalling	WP:WP5083	0.011107	Not enriched
Apoptosis-related network due to altered Notch3 in ovarian cancer	WP:WP2864	0.024714	Not enriched
Primary focal segmental glomerulosclerosis (FSGS)	WP:WP2572	0.030843	Not enriched
Malignant pleural mesothelioma	WP:WP5087	0.034363	Not enriched
Gastrin signalling pathway	WP:WP4659	0.048525	0.002697269
Adipogenesis	WP:WP236	0.049027	0.009722197
Thyroid stimulating hormone (TSH) signalling pathway	WP:WP2032	Not enriched	0.003179353
Cell migration and invasion through p75NTR	WP:WP4561	Not enriched	0.027069361
Splicing factor NOVA regulated synaptic proteins	WP:WP4148	Not enriched	0.02972455
EGFR tyrosine kinase inhibitor resistance	WP:WP4806	Not enriched	0.03801006

Further, 2083 genes (approximately one-third of peaks) were common between the TBX15-HA-overexpressing 3T3-L1 and hWAT samples. Functional enrichment

analysis using g:Profiler revealed EGF/EGFR signalling and androgen receptor signalling terms remained significantly enriched among these common target sites (Table 5.3). Interestingly, TGF-beta signalling and VEGFA-VEGFR2 signalling terms, previously only enriched in 3T3-L1 samples, were enriched for these common terms (Table 5.3). Conversely, Wnt signalling and adipogenesis terms, previously enriched in both 3T3-L1 and hWAT samples, were not significantly enriched among the common target binding sites. Taken together, these data indicate that TBX15 binds a network of target genes in adipocyte precursor cells involved in cell growth and differentiation particularly EGF, Wnt and adipogenesis signalling, although unsurprisingly there was some species specificity in the direct targets identified.

Table 5.3. Enriched WikiPathways terms for common TBX15 target binding sites in 3T3-L1 and hWAT cells. Functional enrichment analysis for shared peaks of 2083 common genes in TBX15-HA-overexpressing samples in 3T3-L1 and hWAT cells. Terms ranked based on adjusted p-value.

Term name	Term ID	Adjusted p-value
Physiological and pathological hypertrophy of the heart	WP:WP1528	0.000219
TGF-beta signalling pathway	WP:WP366	0.000315
Thyroid stimulating hormone (TSH) signalling pathway	WP:WP2032	0.00042
Gastrin signalling pathway	WP:WP4659	0.000692
Apoptosis-related network due to altered Notch3 in ovarian cancer	WP:WP2864	0.001478
Androgen receptor signalling pathway	WP:WP138	0.002368
VEGFA-VEGFR2 signalling pathway	WP:WP3888	0.003033
DNA damage response (only ATM dependent)	WP:WP710	0.003842
EGF/EGFR signalling pathway	WP:WP437	0.008463
Clear cell renal cell carcinoma pathways	WP:WP4018	0.014273
Myometrial relaxation and contraction pathways	WP:WP289	0.028326
Pathways affected in adenoid cystic carcinoma	WP:WP3651	0.031157
CAMKK2 pathway	WP:WP4874	0.034782
Neuroinflammation and glutamatergic signalling	WP:WP5083	0.041121
Corticotrophin-releasing hormone signalling pathway	WP:WP2355	0.049261

5.2.2. Determining the *Tbx15* regulatory network in adipose tissues using RNA-sequencing

Whilst TBX15 has a known role in regulating adipogenesis and browning of white adipocytes *in vitro* and *in vivo* (Gesta *et al.*, 2011; Gburcik *et al.*, 2012; Sun *et al.*, 2019), a complete regulatory network in adipose tissues is lacking. We hypothesised that TBX15 regulated adipogenesis in different adipose depots to drive the reduced fat mass phenotype seen in *Tbx15*$^{+/-}$ mice (discussed in chapter 4). To elucidate a comprehensive, unbiased TBX15 regulatory network among adipose tissues gWAT, iWAT and BAT were isolated from *Tbx15*$^{+/+}$, *Tbx15*$^{+/-}$ and *Tbx15*$^{-/-}$ mice for bulk RNA-sequencing. In line with previously reported data *Tbx15* was not expressed in gWAT (Yamamoto *et al.*, 2010; Gburcik *et al.*, 2012), therefore, this tissue was excluded from further analysis and analysis in this chapter focussed on iWAT and BAT gene expression networks.

5.2.2.1. Sample quality control for *Tbx15*$^{-/-}$ tissues

The first aim of this experiment was to interrogate the TBX15 regulatory network in the context of adipose tissue gene regulation. Adipose tissues were dissected by Dr. Rebecca Dumbell, and high-quality RNA samples were submitted for RNA-sequencing analysis (Figure 5.6A-D). There was a significant sex ($p<0.0001$) and genotype ($p<0.0001$), but not interaction, effect for bodyweight in these mice (Figure ***5.6***C, Table 5.4). In both females and males, *Tbx15*$^{-/-}$ mice were significantly smaller than both *Tbx15*$^{+/+}$ and *Tbx15*$^{+/-}$ littermates ($p\leq0.0097$), with no significant difference in bodyweight detected between *Tbx15*$^{+/+}$ and *Tbx15*$^{+/-}$ littermates (Figure ***5.6***C, Table

5.4). For the purposes of this thesis, I have described analysis from female data only as analysis of male data sets is ongoing.

Principal component analysis, performed as part of initial QC by Dr. Michelle Simon, of female *Tbx15*$^{+/+}$ (n=5), *Tbx15*$^{+/-}$ (n=5) and *Tbx15*$^{-/-}$ (n=4) iWAT samples indicated a sample assigned *Tbx15*$^{+/+}$ genotype at weaning (sample ID: TBX15-KO-B6N-IC/10.1d) clustered with *Tbx15*$^{-/-}$ samples (Appendix Figure 9.5). I therefore performed confirmatory genotyping of cDNA from iWAT samples amplified with primers specific to exon 1 of *Tbx15* (42bp product), the full-length *Tbx15* transcript (exon 1-8, 1253bp product) or a duplex of both primer pairs. At least one full-length *Tbx15* transcript is expressed by *Tbx15*$^{+/+}$ and *Tbx15*$^{+/-}$ mice therefore, bands at both 42bp and 1253bp were required to confirm genotyping. *Tbx15*$^{-/-}$ mice only express exon 1 of *Tbx15* (confirmed by initial RNA-sequencing read alignments; data not shown). Therefore, the presence of only the 42bp product band was required to confirm *Tbx15-knockout* genotypes (Figure 5.6E and F). As expected *Tbx15*$^{+/+}$ and *Tbx15*$^{+/-}$, but not *Tbx15*$^{-/-}$, samples expressed both 42bp and 1253bp products indicating the presence of the full-length transcript in these samples (Figure 5.6F). However, in sample TBX15-KO-B6N-IC/10.d only the 42bp product was detected indicating absence of the full-length transcript in this sample, therefore, this sample was excluded from gene expression analysis (red asterisks, Figure 5.6F).

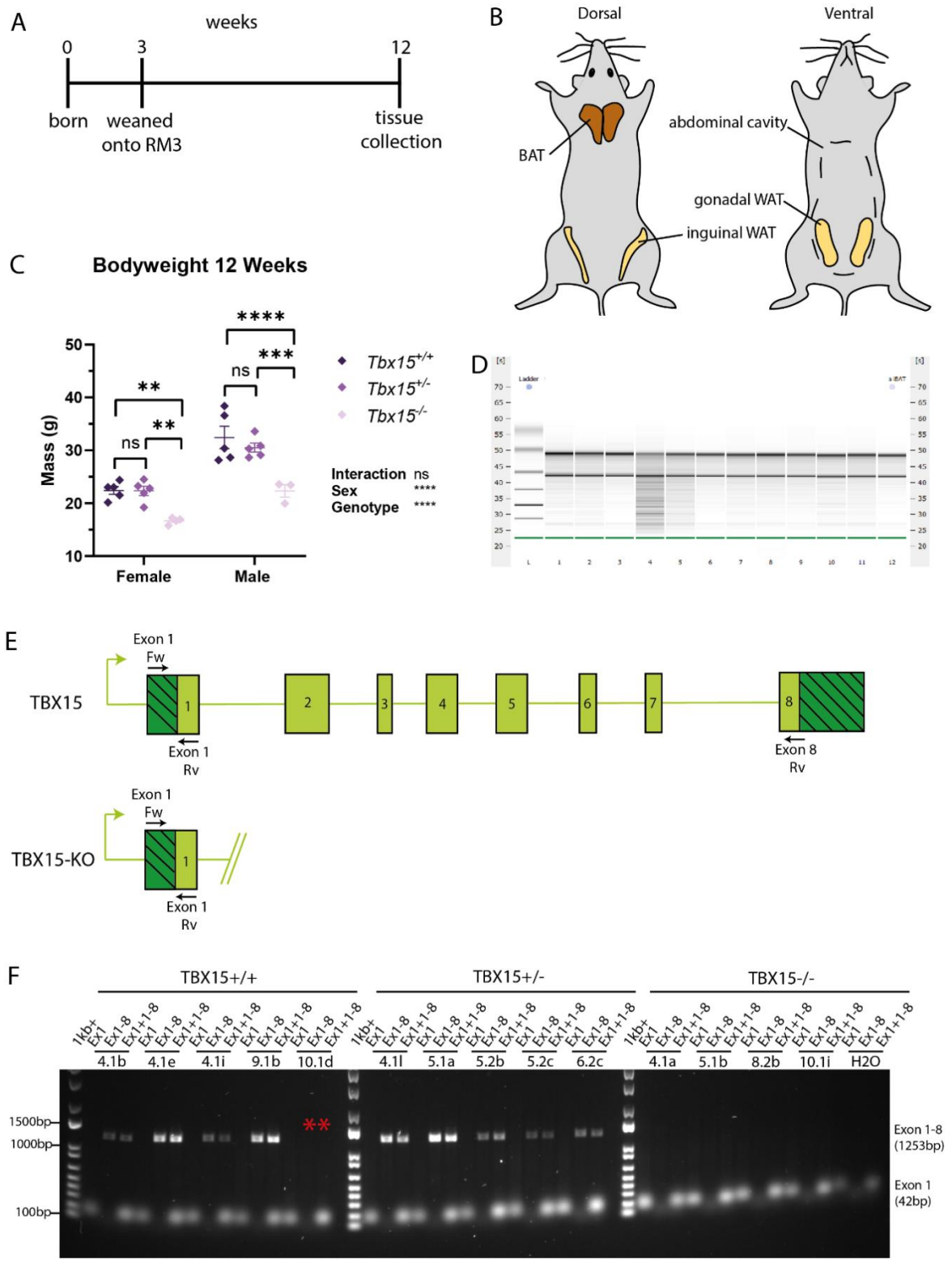

Figure 5.6. *Tbx15*$^{-/-}$ RNA-sequencing cohort experimental pipeline and sample collection. A. Schematic pipeline for RNA-sequencing cohort. B. Location of adipose depots in mice dissected for RNA. C. Bodyweight at 12 weeks of age for *Tbx15*$^{+/+}$ (dark purple), *Tbx15*$^{+/-}$ (purple) and *Tbx15*$^{-/-}$ (light purple) mice. All data analysed by two-way ANOVA with post-hoc Tukey's multiple comparisons: **p<0.01, ***p<0.001 and ****p<0.0001. D. Example of RNA quality analysis using the BioAnalyzer 2100 series. E. Schematic representation of primers used for PCR genotyping of *Tbx15*$^{+/+}$ and *Tbx15*$^{-/-}$ samples. F. Gel electrophoresis of PCR products from *Tbx15*$^{+/+}$, *Tbx15*$^{+/-}$ and *Tbx15*$^{-/-}$ samples used for genotyping (red asterisks indicate lack of full length transcript in sample TBX15-KO-B6N-IC/10.1d).

Table 5.4. Female and male *Tbx15*$^{-/-}$ bodyweights at 12 weeks of age. All data analysed by two-way ANOVA with post-hoc Tukey's multiple comparisons; significant values (p<0.05) highlighted in bold.

	Female	Male
Interaction	0.2575	
Sex	**<0.0001**	
Genotype	**<0.0001**	
Post-hoc analysis (adjusted p-value)		
	Female	**Male**
***Tbx15*$^{+/+}$ vs *Tbx15*$^{+/-}$**	0.9990	0.4786
***Tbx15*$^{+/+}$ vs *Tbx15*$^{-/-}$**	**0.0088**	**<0.0001**
***Tbx15*$^{+/-}$ vs *Tbx15*$^{-/-}$**	**0.0097**	**0.0008**

5.2.2.2. *Tbx15*$^{-/-}$ RNA regulatory network in adipose tissues

Following sample QC, I aimed to determine a TBX15 regulatory network in iWAT and BAT using DEGs between *Tbx15*$^{+/+}$ and *Tbx15*$^{-/-}$ mice that might elucidate mechanisms regulating fat mass phenotypes seen in *Tbx15*$^{+/-}$ mice in metabolic phenotyping cohorts. Due to multiple statistical testing in DEG analysis, a false discovery rate (FDR)<0.05 signified significant results, while a more relaxed cut-off (nominal significance; p<0.05) allowed inclusion of more DEGs in downstream analysis.

DEGs were detected in both iWAT and BAT between *Tbx15*$^{+/+}$ and *Tbx15*$^{+/-}$, and *Tbx15*$^{+/+}$ and *Tbx15*$^{-/-}$ mice. A total of 3325 DEGs (FDR<0.05) were detected between *Tbx15*$^{+/+}$ and *Tbx15*$^{-/-}$ mice in iWAT, of which 897 were upregulated and 2328 were downregulated in *Tbx15*$^{-/-}$ mice (Figure 5.7A). In contrast, only three DEGs (FDR<0.05) were detected in iWAT between *Tbx15*$^{+/+}$ and *Tbx15*$^{+/-}$ mice, all of which were upregulated in *Tbx15*$^{+/-}$ mice (Figure 5.7A). A further 790 genes reached nominal significance (p<0.05) for differential expression between *Tbx15*$^{+/+}$ and *Tbx15*$^{+/-}$ mice in iWAT. Given the high number of significant DEGs (FDR<0.05) in *Tbx15*$^{-/-}$ iWAT samples, I applied a more stringent cut-off for FDR (FDR<0.01) and a minimum log fold-change (logFC±1.5) to perform functional analyses. In this case, 1613 genes

(153 upregulated, 1478 downregulated) met the cut-off values in *Tbx15*$^{-/-}$ iWAT, with the three genes upregulated in *Tbx15*$^{+/-}$ mice also significant with these criteria (Figure ***5.7***B). Of the 793 nominally significant (p<0.05) genes in iWAT between *Tbx15*$^{+/-}$ and *Tbx15*$^{+/+}$ mice, 153 were significant (FDR<0.01, logFC±1.5) in *Tbx15*$^{-/-}$ mice (~9.5%) indicating a subtle dose-dependent response of the *Tbx15* gene knockout (Table 5.5).

Far fewer significant DEGs (FDR<0.05) were detected in BAT than iWAT. In BAT, 104 genes (36 upregulated, 68 downregulated) were differentially expressed between *Tbx15*$^{+/+}$ and *Tbx15*$^{-/-}$ mice, and 28 genes (6 upregulated, 22 downregulated) were significantly different between *Tbx15*$^{+/+}$ and *Tbx15*$^{+/-}$ mice (Figure 5.7A). A further 1291 and 742 genes, respectively, reached nominal significance (p<0.05) in these tissues. Approximately 20% of genes were common between *Tbx15*$^{-/-}$ and *Tbx15*$^{+/-}$ DEGs in BAT (FDR<0.05; Table 5.6). When comparing the gene expression networks between *Tbx15*$^{-/-}$ adipose tissues, a total of 21 significant DEGs (FDR<0.05) were common between iWAT and BAT networks, this accounted for <1% of genes and suggests *Tbx15* regulated distinct gene profiles in the different adipose tissues. Despite relatively high expression of *Tbx15* in BAT, and previous reports indicating it regulated expression of browning genes, I have shown *Tbx15* primarily regulated gene expression in subcutaneous iWAT. Further, the majority of DEGs were downregulated in both *Tbx15*$^{+/-}$ and *Tbx15*$^{-/-}$ compared to *Tbx15*$^{+/+}$ samples, suggesting TBX15 functions mainly as a transcriptional activator in adipose tissues.

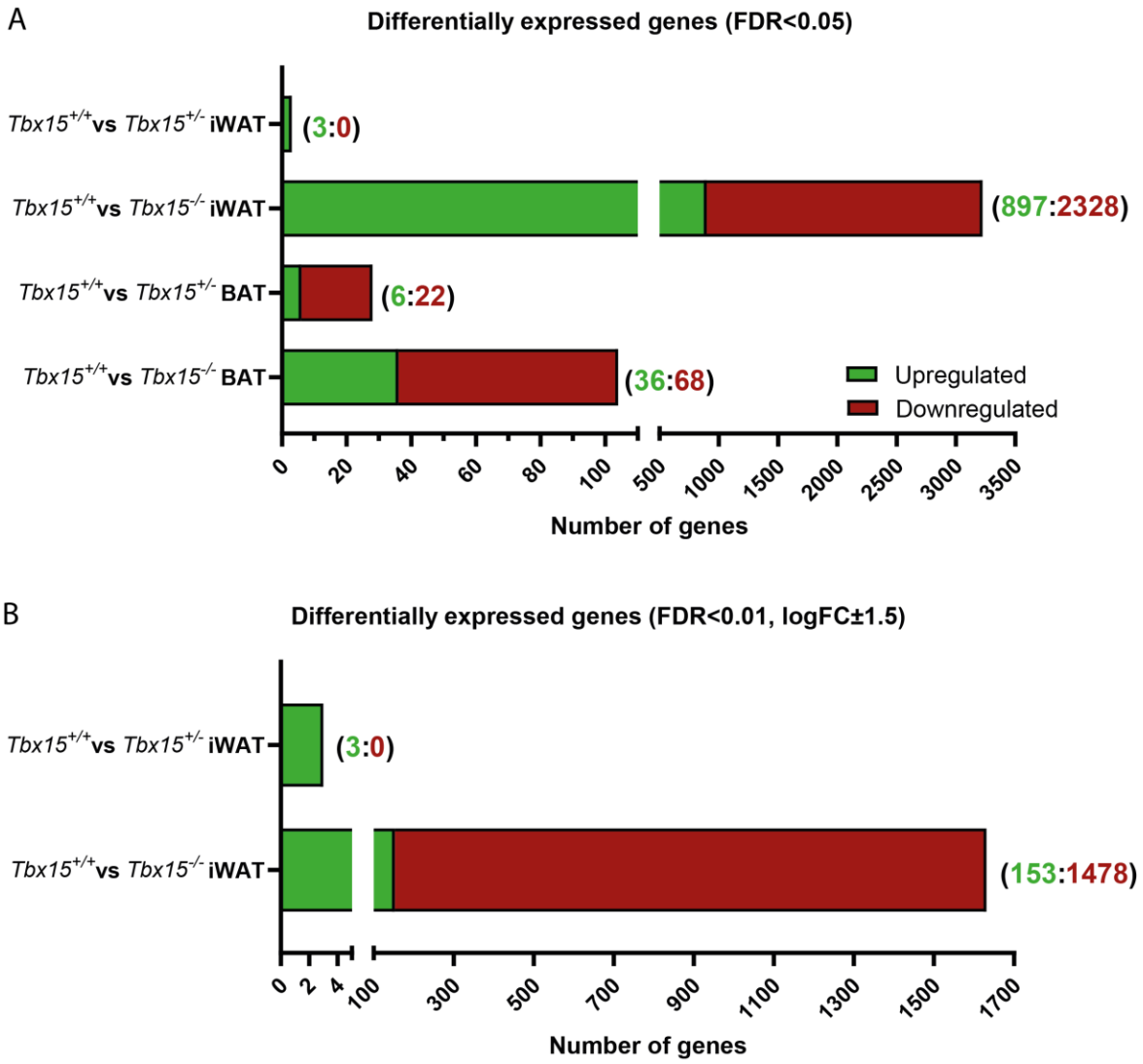

Figure 5.7. Total number of significantly differentially expressed genes in adipose tissues. A-B. Total number of differentially expressed genes in inguinal white adipose tissue (iWAT) and brown adipose tissue (BAT) from 12-week old female *Tbx15*$^{+/+}$ (n=4), *Tbx15*$^{+/-}$ (n=5) and *Tbx15*$^{-/-}$ (n=4) mice fed RM3 diet. A. Differentially expressed genes (FDR<0.05) for iWAT and BAT. B. Differentially expressed genes (FDR<0.01, logFC±1.5) in iWAT. Number of upregulated (green) and downregulated (red) genes are given in brackets.

Table 5.5. Top common upregulated and downregulated genes in *Tbx15*$^{-/-}$ and *Tbx15*$^{+/-}$ inguinal white adipose tissue. Differentially expressed genes from *Tbx15*$^{+/+}$ versus *Tbx15*$^{-/-}$ (logFC±1.5, FDR<0.01) and *Tbx15*$^{+/+}$ versus *Tbx15*$^{+/-}$ (p<0.05) compared for common genes. Top genes ranked on FDR in *Tbx15*$^{-/-}$ mice (upregulated/downregulated in homozygous *Tbx15*$^{-/-}$ and heterozygous *Tbx15*$^{+/-}$ compared to wild-type *Tbx15*$^{+/+}$ mice).

	***Tbx15*$^{-/-}$**			***Tbx15*$^{+/-}$**		
Gene	**LogFC**	**p-value**	**FDR**	**LogFC**	**p-value**	**FDR**
Upregulated						
Hist1h2al	11.3647	2.84E-46	4.72E-43	10.14686	1.13E-47	4.88E-43
Gm3608	4.5791	2.14E-31	9.22E-29	4.211064	1.33E-11	1.92E-07
Mpz	2.7232	2.63E-17	3.18E-15	0.879919	0.003302	1
Ugt8a	2.6338	8.73E-10	4.84E-08	1.007125	0.002072	1
Hist2h2bb	3.3233	1.35E-09	7.34E-08	3.285876	3.28E-12	7.07E-08
D430041D05Rik	2.8484	7.61E-09	3.74E-07	1.230142	0.010103	1
Dusp15	1.9525	1.49E-07	6.23E-06	0.751957	0.036505	1
Ppbp	2.6468	9.24E-06	0.000291	2.016074	0.00043	0.741615
Phkg1	2.1495	1.19E-05	0.000369	0.897262	0.037879	1
Tmod4	3.5158	1.22E-05	0.000379	2.455446	2.59E-05	0.185886
Gjb1	2.8854	1.70E-05	0.000516	1.699732	0.010726	1
Rbpsuh-rs3	4.0058	2.21E-05	0.00065	3.084868	0.004244	1
Thbs4	3.4154	3.34E-05	0.000948	0.86637	0.015659	1
Serpina3k	3.0650	3.69E-05	0.00103	2.619847	0.00341	1
Bcl2l15	1.8152	4.67E-05	0.001278	0.941919	0.014763	1
Gm24505	2.0788	5.36E-05	0.00144	1.65751	0.017658	1
Sh3bgr	4.5514	8.17E-05	0.002106	2.626195	0.004675	1
Mlip	3.2448	8.91E-05	0.002277	1.22043	0.047204	1
Ldb3	4.5846	0.00012	0.002953	2.291447	0.019141	1
Pfkm	2.7580	0.000124	0.003032	1.152542	0.022421	1
Downregulated						
Trbv31	-7.5326	1.60E-28	5.08E-26	-0.53294	0.035772	1
Gzmc	-4.3966	2.21E-15	2.23E-13	-1.30336	6.84E-05	0.294985
Capza1	-1.8669	2.95E-12	2.16E-10	-0.40442	0.012846	1
Ighv5-16	-9.1492	1.78E-11	1.20E-09	-2.59046	6.62E-05	0.294985
Traj17	-5.9559	2.63E-10	1.54E-08	-0.86789	0.03497	1
4930469K13Rik	-3.1976	7.62E-09	3.75E-07	-0.79569	0.013177	1
Zfp697	-2.0634	1.87E-08	8.76E-07	-0.78019	0.002633	1
Rps3a1	-1.7249	1.38E-07	5.81E-06	-0.48513	0.003996	1
RP24-146B4.3	-3.2057	1.14E-06	4.17E-05	-1.07889	0.002819	1
Erich5	-6.1372	2.30E-06	8.07E-05	-2.12627	0.00199	1
Gm16071	-2.4680	3.28E-06	0.000112	-0.67235	0.043509	1
Phldb3	-3.9005	9.57E-06	0.0003	-2.8434	8.00E-05	0.313596
Lrch4	-2.8976	6.78E-05	0.001779	-0.97066	0.037388	1
Mst1	-2.0915	8.59E-05	0.002201	-0.79167	0.018833	1
Celf3	-1.7387	0.000116	0.002867	-0.61777	0.022934	1
RP23-291L24.4	-5.3810	0.000143	0.003437	-1.38225	0.043795	1
Gm15008	-2.4970	0.000147	0.003515	-1.17512	0.023731	1
Krt25	-8.5702	0.000337	0.007176	-8.59202	2.09E-05	0.180272

Table 5.6. Top common upregulated and downregulated genes in *Tbx15*$^{-/-}$ and *Tbx15*$^{+/-}$ brown adipose tissue. Differentially expressed genes from *Tbx15*$^{+/+}$ versus *Tbx15*$^{-/-}$ (FDR<0.05) and *Tbx15*$^{+/+}$ versus *Tbx15*$^{+/-}$ (FDR<0.05) compared for common genes. Top genes ranked on FDR in *Tbx15*$^{-/-}$ mice (upregulated/downregulated in homozygous *Tbx15*$^{-/-}$ and heterozygous *Tbx15*$^{+/-}$ compared to wild-type *Tbx15*$^{+/+}$ mice).

	***Tbx15*$^{-/-}$**			***Tbx15*$^{+/-}$**		
Gene	**LogFC**	**p-value**	**FDR**	**LogFC**	**p-value**	**FDR**
Upregulated						
Hist1h2al	8.899794	8.67E-50	3.74E-45	7.8134936	7.50E-52	3.23E-47
Gm3608	5.205827	4.67E-46	1.01E-41	4.3177511	1.31E-11	1.88E-07
Hist2h2bb	6.866817	1.70E-21	1.84E-17	5.6254096	4.38E-11	4.73E-07
Selenbp2	7.288973	4.23E-14	1.66E-10	6.051501	3.92E-08	0.000176
Downregulated						
Krt19	-5.55917	1.04E-16	7.44E-13	-2.84265	5.94E-07	0.002329
Areg	-6.58688	9.44E-16	5.09E-12	-5.43361	1.40E-17	3.02E-13
Krt17	-7.45035	1.82E-11	6.05E-08	-3.27103	1.30E-06	0.004013
Wfdc2	-7.86303	3.88E-11	1.03E-07	-3.69079	2.17E-06	0.005838
Atp6v1b1	-6.76124	4.06E-11	1.03E-07	-4.33608	4.07E-08	0.000176
Csn3	-7.00333	1.68E-10	4.02E-07	-4.57313	3.09E-08	0.000167
Slc5a5	-2.81413	4.68E-10	1.05E-06	-2.28073	8.01E-06	0.016447
Ly6d	-2.80535	6.43E-09	9.91E-06	-1.87311	3.30E-06	0.007918
Ccdc129	-6.80766	1.37E-07	0.00018	-3.68856	5.01E-06	0.010798
Esrp1	-5.29416	1.98E-07	0.000224	-3.77978	9.21E-07	0.003056
Ltf	-4.77476	6.30E-07	0.000618	-4.83179	2.99E-08	0.000167
Aqp5	-4.69245	6.66E-07	0.000639	-3.68799	6.10E-09	5.26E-05
Pgr	-5.62691	7.26E-07	0.000681	-5.68237	1.88E-08	0.000135
Serpinb5	-6.01961	3.08E-06	0.002558	-3.72794	1.69E-05	0.029159
Lcn2	-2.30692	5.78E-06	0.004455	-1.91676	1.02E-05	0.0191
Defb1	-6.21001	9.05E-06	0.006621	-6.08654	8.70E-07	0.003056
Phldb3	-5.0316	2.56E-05	0.014543	-4.54989	9.29E-06	0.018216

Given the largely distinct DEGs across adipose tissues, I next utilised gProfiler to perform functional enrichment analysis for DEGs in iWAT (FDR<0.01, logFC±1.5) and BAT (FDR<0.05) between *Tbx15*$^{+/+}$ and *Tbx15*$^{-/-}$ samples. In iWAT, the 153 upregulated genes in *Tbx15*$^{-/-}$ samples were enriched for actin and cytoskeletal protein binding (gene ontology: molecular functions (GO:MF); Table 5.7). These genes were further enriched for biological processes (GO:BP) terms such as muscle contraction and muscle structure development (Table 5.7). In contrast, the 1478 downregulated genes in *Tbx15*$^{-/-}$ iWAT were enriched for cytokine receptor activity (GO:MF) and immune

response terms (GO:BP; Table 5.7). The 36 upregulated DEGs in *Tbx15*$^{-/-}$ BAT were enriched for troponin T and tropomyosin binding (GO:MF) and were further enriched for muscle structural development and muscle system process terms (GO:BP; Table 5.8). In comparison, the 68 downregulated genes in *Tbx15*$^{-/-}$ BAT were enriched for scaffold protein binding and cell adhesion terms (GO:MF) and GO:BP terms including gland and tissue development (Table 5.8). Whilst upregulated *Tbx15*$^{-/-}$ iWAT and BAT genes were enriched for some common terms, this data highlighted the largely unique functional processes regulated by TBX15 between adipose tissues. There was a striking enrichment for immune response terms in downregulated genes in *Tbx15*$^{-/-}$ iWAT, suggesting a potential role for TBX15 in regulating immune processes in WAT. However, given the strong phenotype in *Tbx15*$^{-/-}$ mice, further experiments are required to determine whether TBX15 directly regulates these immune process genes.

Table 5.7. Top enriched terms in *Tbx15*$^{-/-}$ inguinal white adipose tissue. Enriched gene ontology (GO) molecular function (MF) and biological processes (BP) terms for upregulated and downregulated genes (logFC±1.5, FDR<0.01) in inguinal white adipose tissue from 12-week old female *Tbx15*$^{+/+}$ and *Tbx15*$^{-/-}$ mice fed RM3 diet. Upregulated and downregulated in homozygous *Tbx15*$^{-/-}$ mice. Queries were run as ordered query (most significant genes listed at the top of the list).

Source	Term name	Term ID	Adjusted p-value
Upregulated			
GO:MF	actin binding	GO:0003779	0.005947
	cytoskeletal protein binding	GO:0008092	0.021706
GO:BP	muscle system process	GO:0003012	2.30E-08
	muscle contraction	GO:0006936	4.74E-06
	anatomical structure development	GO:0048856	7.23E-05
	muscle structure development	GO:0061061	0.000153
	transmission of nerve impulse	GO:0019226	0.00019
Downregulated			
GO:MF	immunoglobulin receptor binding	GO:0034987	3.12E-47
	antigen binding	GO:0003823	3.47E-43
	cytokine receptor activity	GO:0004896	5.26E-10
	immune receptor activity	GO:0140375	3.54E-09
	signalling receptor binding	GO:0005102	1.43E-07
GO:BP	immune response	GO:0006955	2.83E-114
	immune system process	GO:0002376	2.90E-105
	leukocyte activation	GO:0045321	9.04E-93
	lymphocyte activation	GO:0046649	1.40E-92
	cell activation	GO:0001775	1.38E-85

5.2.3. The core TBX15 regulatory network consists of 236 genes

I finally aimed to determine a core set of TBX15 target genes by identifying common genes with TBX15 peaks in 3T3-L1 ChIP-sequencing and DEGs (FDR<0.01, logFC±1.5) in *Tbx15*$^{-/-}$ iWAT. A total of 236 common genes were identified, suggesting these genes may be direct targets of TBX15 within preadipocyte cells. Functional analysis revealed these genes were enriched for ATP binding, serine/threonine kinase activity (GO:MF), regulation of immune system process (GO:BP), cytokine-cytokine receptor interaction and NF-kappa B signalling (KEGG; Figure 5.8, Table 5.9). When considered together, the ChIP-sequencing and RNA-sequencing data presented in this chapter indicated

TBX15 acts on a network of genes in a cell- and tissue-specific manner to regulate cell proliferation, differentiation and immune response processes.

Table 5.8. Top enriched terms in *Tbx15*$^{-/-}$ brown adipose tissue. Enriched gene ontology (GO) molecular function (MF) and biological processes (BP) terms for upregulated and downregulated genes (FDR<0.05) in brown adipose tissue from 12-week old female *Tbx15*$^{+/+}$ and *Tbx15*$^{-/-}$ mice fed RM3 diet. Upregulated and downregulated in homozygous *Tbx15*$^{-/-}$ mice. Queries were run as ordered query (most significant genes listed at the top of the list).

Source	Term name	Term ID	Adjusted p-value
Upregulated			
GO:MF	troponin T binding	GO:0031014	0.000658
	tropomyosin binding	GO:0005523	0.010114
	heparin binding	GO:0008201	0.021257
GO:BP	sarcoplasmic reticulum calcium ion transport	GO:0070296	0.000427
	muscle structure development	GO:0061061	0.001558
	skeletal muscle adaptation	GO:0043501	0.001761
	muscle system process	GO:0003012	0.002015
	myofibril assembly	GO:0030239	0.010904
Downregulated			
GO:MF	scaffold protein binding	GO:0097110	0.000439
	cell-cell adhesion mediator activity	GO:0098632	0.008413
	cell adhesion mediator activity	GO:0098631	0.014099
	cell adhesion molecule binding	GO:0050839	0.01824
	inorganic molecular entity transmembrane transporter activity	GO:0015318	0.036532
GO:BP	gland development	GO:0048732	6.33E-07
	gland morphogenesis	GO:0022612	9.87E-07
	tissue development	GO:0009888	1.26E-06
	epithelium development	GO:0060429	1.47E-06
	animal organ development	GO:0048513	1.17E-05

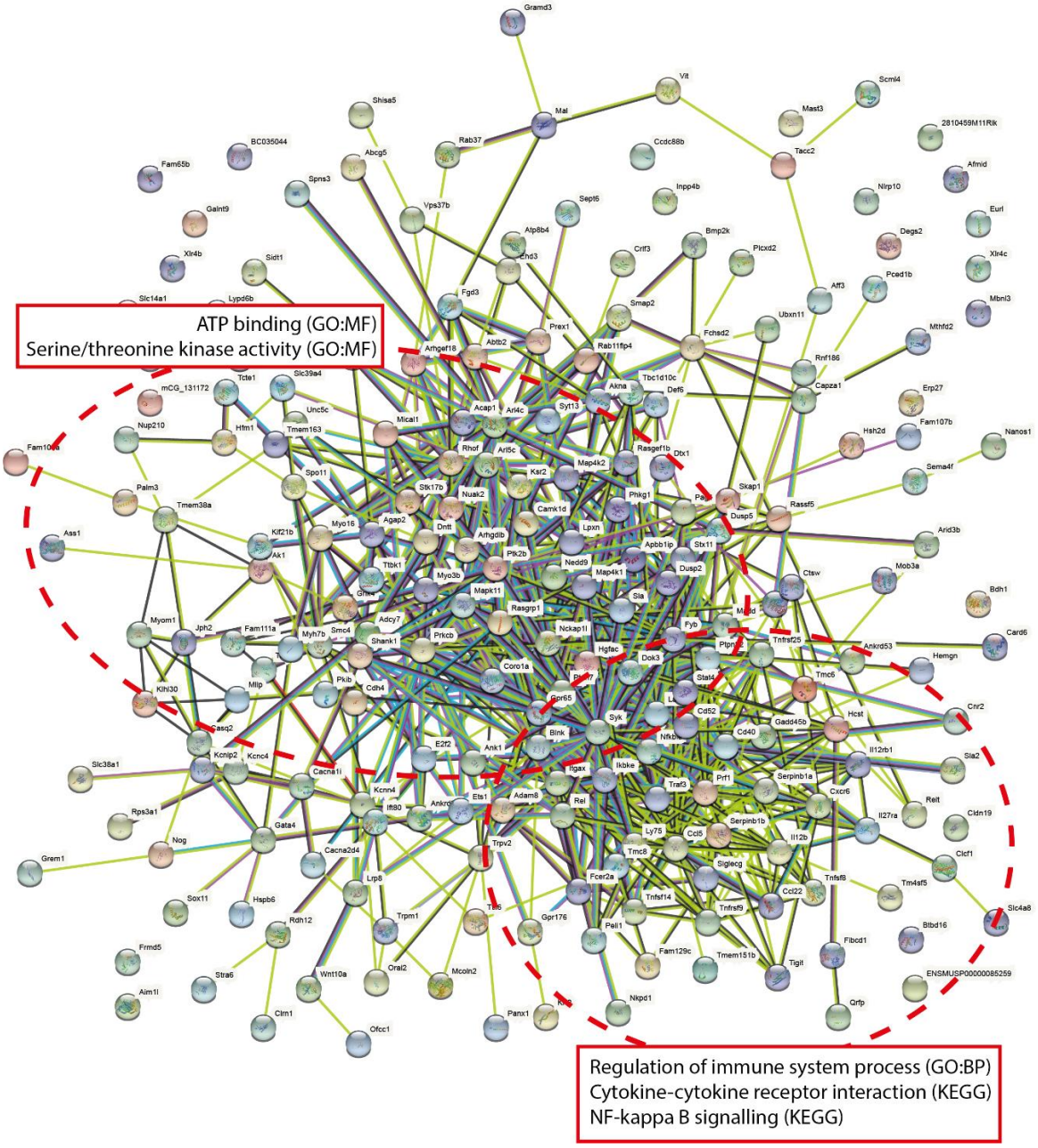

Figure 5.8. STRING network of TBX15 common network genes. STRING network map of 236 common genes between TBX15-HA ChIP-sequencing in 3T3-L1 cells and RNA-sequencing in iWAT from 12-week old female *Tbx15*$^{-/-}$ mice fed RM3 diet (FDR<0.01, logFC±1.5). Red circles show two main clusters of genes enriched for ATP binding and serine/threonine kinase activity (gene ontology: molecular function (GO:MF)), and regulation of immune system (gene ontology: biological process (GO:BP)), cytokine-cytokine receptor interaction and NF-kappa B signalling (Kyoto encyclopaedia of genes and genomes (KEGG)). The network map was produced using STRING v11 (https://string-db.org/) (Szklarczyk *et al.*, 2019, 2021).

Table 5.9. Top enriched terms in TBX15 common network genes. Gene ontology (GO) molecular function (MF) and biological processes (BP), and Kyoto encyclopaedia of genes and genomes (KEGG) pathways for 236 common genes between TBX15-HA ChIP-sequencing in 3T3-L1 cells and RNA-sequencing in iWAT from 12-week old female *Tbx15*$^{-/-}$ mice fed RM3 diet (FDR<0.01, logFC±1.5).

Source	Term name	Term ID	Adjusted p-value
GO:MF	protein binding	GO:0005515	1.94E-06
	binding	GO:0005488	0.000925
	ATP binding	GO:0005524	0.001406
	metal ion transmembrane transporter activity	GO:0046873	0.001645
	passive transmembrane transporter activity	GO:0022803	0.002056
	channel activity	GO:0015267	0.002056
	purine ribonucleoside triphosphate binding	GO:0035639	0.002256
	carbohydrate derivative binding	GO:0097367	0.002889
	protein serine/threonine kinase activity	GO:0004674	0.002989
	cation channel activity	GO:0005261	0.003082
GO:BP	regulation of immune system process	GO:0002682	7.37E-12
	biological regulation	GO:0065007	2.63E-11
	intracellular signal transduction	GO:0035556	3.29E-11
	localization	GO:0051179	1.46E-10
	positive regulation of biological process	GO:0048518	1.75E-10
	regulation of biological process	GO:0050789	2.31E-10
	signalling	GO:0023052	4.17E-10
	response to stimulus	GO:0050896	4.18E-10
	lymphocyte activation	GO:0046649	5.42E-10
	regulation of cellular process	GO:0050794	5.53E-10
KEGG	NF-kappa B signalling pathway	KEGG:04064	0.010367
	Cytokine-cytokine receptor interaction	KEGG:04060	0.023011
	Epstein-Barr virus infection	KEGG:05169	0.049555

5.3. Discussion

Whilst there is evidence of an adipocyte-intrinsic role for TBX15 in regulating adipogenesis and adipocyte browning, a detailed regulatory network remains to be determined. More recent studies using RNA-sequencing used directed approaches to examine expression of pre-determined target genes, therefore, a key aim of this work was to generate a comprehensive and unbiased TBX15 regulatory network in adipose tissues. Using ChIP-sequencing of HA-tagged TBX15-overexpressing 3T3-L1 and hWAT preadipocyte cells at post-confluence, I showed TBX15 binding at target genes

that were enriched for processes involved in cell cycle, proliferation and adipogenesis signalling. Further, using RNA-sequencing of WAT and BAT from *Tbx15*$^{+/+}$, *Tbx15*$^{+/-}$ and *Tbx15*$^{-/-}$ mice, I produced a comprehensive and unbiased TBX15 regulatory network in these tissues. I showed an upregulation of genes enriched for muscle processes in both iWAT and BAT, and a pronounced downregulation of genes in iWAT enriched for immune response processes. Finally, I identified a core set of 236 genes that had both TBX15 binding in 3T3-L1 cells and were significantly differentially expressed in iWAT of *Tbx15*$^{-/-}$ suggesting these genes were targets of TBX15.

5.3.1. Possible novel regulatory roles for TBX15

Based on the data presented in this chapter, we proposed three potential mechanisms of action for TBX15 to regulate i) lineage determination of mesenchymal precursor cells, ii) adipogenic differentiation of committed preadipocytes, and iii) immune receptor signalling in adipocyte-immune cell crosstalk in iWAT.

5.3.1.1. Lineage determination

Given *Tbx15*$^{+/H156N}$ mice had such a striking lean mass phenotype in comparison to the adipose phenotype of *Tbx15*$^{+/-}$ mice, it is plausible that TBX15 regulated precursor cell lineage determination. Adipocytes arise from MSCs which also produce osteoblasts, chondrocytes, brown adipocytes and myocytes. Determination of cells into these lineages is tightly regulated by a network of TFs, with WNT10β, RUNX2 and PPARγ at the core of this process (Figure 5.9). Further, TGF-β, FGF, SOX, BMP and WNT family members are involved in regulating lineage determination, particularly at the

transition from progenitors to committed precursor cells. Indeed, Wnt, EGF/EGFR and TGF-beta signalling pathways were enriched in TBX15 target genes in 3T3-L1 and hWAT ChIP-sequencing. Interestingly, *TBX15* expression was significantly increased in human bone marrow-derived MSCs induced to differentiate into osteoblast cells (Elsafadi *et al.*, 2016). Therefore, I hypothesised that TBX15 regulated expression of several of these genes to regulate lineage determination.

I identified genes that had TBX15 binding peaks in preadipocytes and were differentially expressed in *Tbx15*$^{-/-}$ iWAT. Several key regulators in lineage differentiation, particularly *WNT10B, RUNX2* and *PPARG* had mouse and/or human ChIP-sequencing peaks, although only *Pparg* was significantly upregulated in *Tbx15*$^{-/-}$ iWAT (Figure 5.9, Table 5.10). Further, TBX15 peaks were detected for *TWISTs, TGFB, IGFs, FGFs, BMPs* and *SOXs*, with *Tgfb1* downregulated, and *Twist1, Sox6, Igf1, Nog* upregulated in *Tbx15*$^{-/-}$ iWAT. This suggests TBX15 both directly and indirectly regulates genes associated with MSC differentiation into different cell lineages (Figure 5.9, Table 5.10). In contrast, siRNA mediated *Tbx15* knockdown in human preadipocytes resulted in downregulation of both *PPARG* and *TWIST1* (Pan *et al.*, 2021). Therefore, it is possible that in response to different genetic/environmental stimuli the TBX15-driven regulation of these processes may be altered to impact body composition.

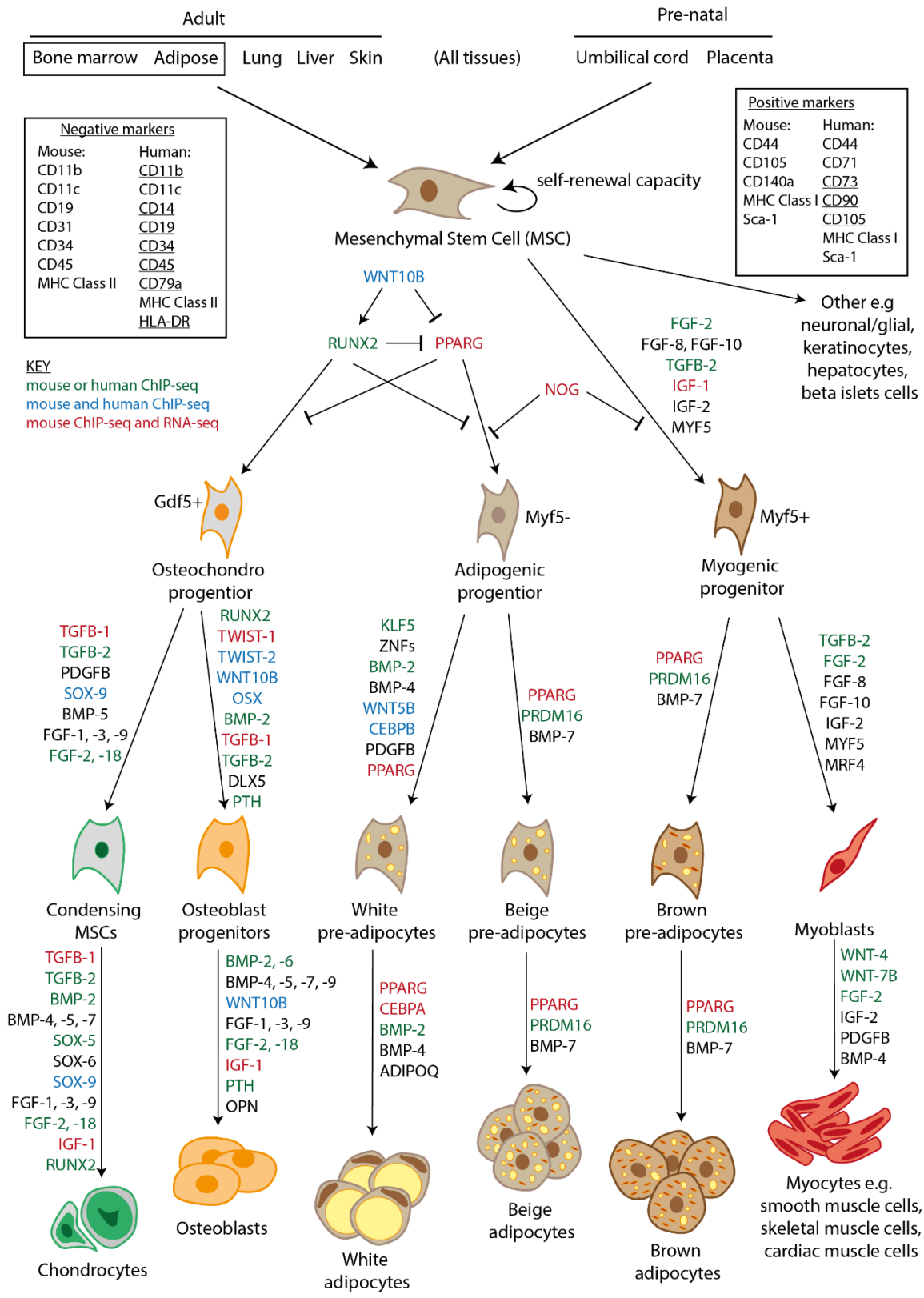

Figure 5.9. TBX15 regulation of mesenchymal stem cell differentiation. Genes identified as TBX15 binding and regulatory targets from ChIP-sequencing analysis in 3T3-L1 and hWAT cells, and *Tbx15*$^{-/-}$ iWAT RNA-sequencing. Gene colours denote TBX15-HA binding site in either 3T3-L1 or hWAT cells (green); TBX15-HA binding site in both 3T3-L1 and hWAT cells (blue); and TBX15-HA binding site in 3T3-L1 cells and differential gene expression in *Tbx15*$^{-/-}$ iWAT RNA-sequencing (red). Figure adapted from (Chen *et al.*, 2016) (under creative commons licence: CC BY-NC-SA 4.0).

Table 5.10. TBX15 regulation of mesenchymal stem cell lineage determination genes. Genes identified as TBX15 binding and regulatory targets from ChIP-sequencing analysis in 3T3-L1 and hWAT cells, and *Tbx15*$^{-/-}$ iWAT RNA-sequencing. Upregulated/downregulated genes in homozygous *Tbx15*$^{-/-}$ samples. Abbreviations: NSD (not significantly different).

Gene Human/mouse	hWAT ChIP-sequencing peak	3T3-L1 ChIP-sequencing peak	*Tbx15*$^{-/-}$ iWAT RNA-sequencing expression (LogFC)
CTNNB1/Ctnnb1	Yes	Yes	NSD
DVL1/Dvl1	Yes	Yes	NSD
DVL2/Dvl2	No	Yes	NSD
FGF1/Fgf1	No	No	NSD
FGF2/Fgf2	No	Yes	NSD
IGF1/Igf1	No	Yes	NSD
LRP5/Lrp5	No	Yes	NSD
LRP6/Lrp6	Yes	Yes	NSD
NOG/Nog	No	Yes	Upregulated (3.6424)
PPARG/Pparg	No	Yes	Upregulated (1.0474)
RUNX2/Runx2	Yes	No	NSD
SOX5/Sox5	No	Yes	NSD
SOX6/Sox6	No	No	Upregulated (1.3039)
SOX9/Sox9	Yes	Yes	NSD
TGFB1/Tgfb1	No	Yes	Downregulated (-0.9676)
TGFB2/Tgfb2	Yes	No	NSD
TWIST1/Twist1	Yes	Yes	Upregulated (0.9196)
TWIST2/Twist2	Yes	Yes	NSD
WNT4/Wnt4	Yes	No	NSD
WNT5A/Wnt5a	No	Yes	NSD
WNT5B/Wnt5b	Yes	Yes	NSD
WNT7B/Wnt7b	Yes	No	NSD
WNT10A/Wnt10a	Yes	Yes	Downregulated (-1.9495)
WNT10B/Wnt10b	Yes	Yes	NSD

Further, Wnt, EGF/EGFR and TGF-beta signalling pathways have been implicated in regulating cell proliferation and differentiation. For example, Wnt signalling acts through canonical and non-canonical pathways. In the canonical pathway, Wnt binds the Frizzled and low-density lipoprotein receptor-related protein 5 and 6 co-receptors to recruit dishevelled to activate β-catenin mediated transcription of downstream target genes associated with stem cell maintenance and proliferation (Christodoulides *et al.*, 2009; de Winter and Nusse, 2021). Conversely, an Axin-APC-CK1-GSK3 complex

degrades β-catenin in the absence of Wnt binding which leads to an upregulation of genes associated with lineage determination and differentiation, for example *PPARG* and *CEBPA* in adipogenesis (Christodoulides *et al.*, 2009; de Winter and Nusse, 2021). WNT10β and WNT5α/WNT5β are the main regulators of the canonical and non-canonical pathways, with anti- and pro-adipogenic properties, respectively, with other WNTs implicated in stem cell maintenance and differentiation (Christodoulides *et al.*, 2009; de Winter and Nusse, 2021). Whilst the main role for Wnt signalling has been shown in early stages of MSC proliferation and differentiation, there is growing evidence to support a role for Wnt/β-catenin in regulating lipogenesis in mature adipocytes (Bagchi *et al.*, 2020).

Alternatively, EGF/FGF signalling pathways act through ERK to regulate CREB-mediated proliferation and differentiation of cells (Bost *et al.*, 2005). By contrast, TNF, IL-1 and TGF-β regulate JNK-mediated activation of cell cycle and apoptosis genes, and also signal through NLK-mediated regulation of the Wnt signalling pathway (Johnson and Lapadat, 2002). Further evidence supports a dose-dependent role for EGF to regulate both proliferation and differentiation of 3T3-L1 cells, where proliferation was induced under low EGF concentrations, and adipogenesis was preferentially induced under high EGF concentrations (Harrington, Pond-Tor and Boney, 2007).

TFs act at the core of regulatory complexes to interact with gene promoters and enhancers to enhance and/or repress gene expression (Simicevic and Deplancke, 2010). Based on these results I therefore hypothesise that TBX15 may act as a master regulator of these signalling pathways, potentially acting at several points in a pathway to stimulate/repress MSC lineage determination in response to environmental stimuli. However, DNA binding does not always equate to regulation of the most proximal gene,

as has been extensively shown prokaryotes and eukaryotes (Sun, Nawaz and Slingerland, 2007; Makkonen *et al.*, 2009; Myers *et al.*, 2013). Other factors, such as incompatible stimulatory conditions, and lack of available co-factors may explain why target gene expression is not always directly regulated by the bound TF. This suggests that TBX15 may bind MSC pathway genes in complex with other TFs and is therefore not sufficient to drive changes in gene expression in isolation. Alternatively, TBX15 may only regulate expression of these pathway genes at the earlier stages of MSC fate determination, in which case, gene expression differences may not be sufficiently differential to be detected in mature *Tbx15*$^{-/-}$ adipose tissue.

5.3.1.2. Adipocyte Differentiation

All three *Tbx15* mouse lines exhibited altered fat mass phenotypes and functional enrichment analysis of TBX15 ChIP-sequencing targets revealed enrichment for adipogenesis in both 3T3-L1 and hWAT cells. Further, TBX15 has been implicated in altered expression of key adipogenesis genes in several *in vitro* models (Gesta *et al.*, 2011; Gburcik *et al.*, 2012). Therefore, I hypothesised that TBX15 also regulated adipogenesis of committed preadipocytes to drive the altered fat mass phenotypes seen in *Tbx15* mice.

TBX15 bound several adipogenesis genes in both hWAT and 3T3-L1 preadipocytes, and there was a corresponding upregulation of the majority of these genes in *Tbx15*$^{-/-}$ iWAT, for example *Pparg, Cebpa, Adipoq* and *Fabp4* (Table 5.11). This suggested TBX15 acted to negatively regulate adipogenesis under normal growth conditions by directly binding and regulating expression of central adipogenesis TFs *Pparg* and *Cebpa,* which would have subsequent effect on downstream targets such as *Adipoq* and *Fabp4*

(Figure 5.10). Both Gesta *et al.* (2011) and Gburcik *et al.* (2012) showed downregulation of *Pparg* and *Fabp4* in response to stable overexpression of TBX15 or silencing knockdown of *Tbx15*, respectively. My data showed for the first time, direct binding of TBX15 within several key adipogenesis genes and further supported the data of Gesta *et al.* (2011) by suggesting TBX15 acts as a transcriptional repressor of adipogenesis. Further work is needed to validate these findings *in vitro,* particularly over the course of differentiation.

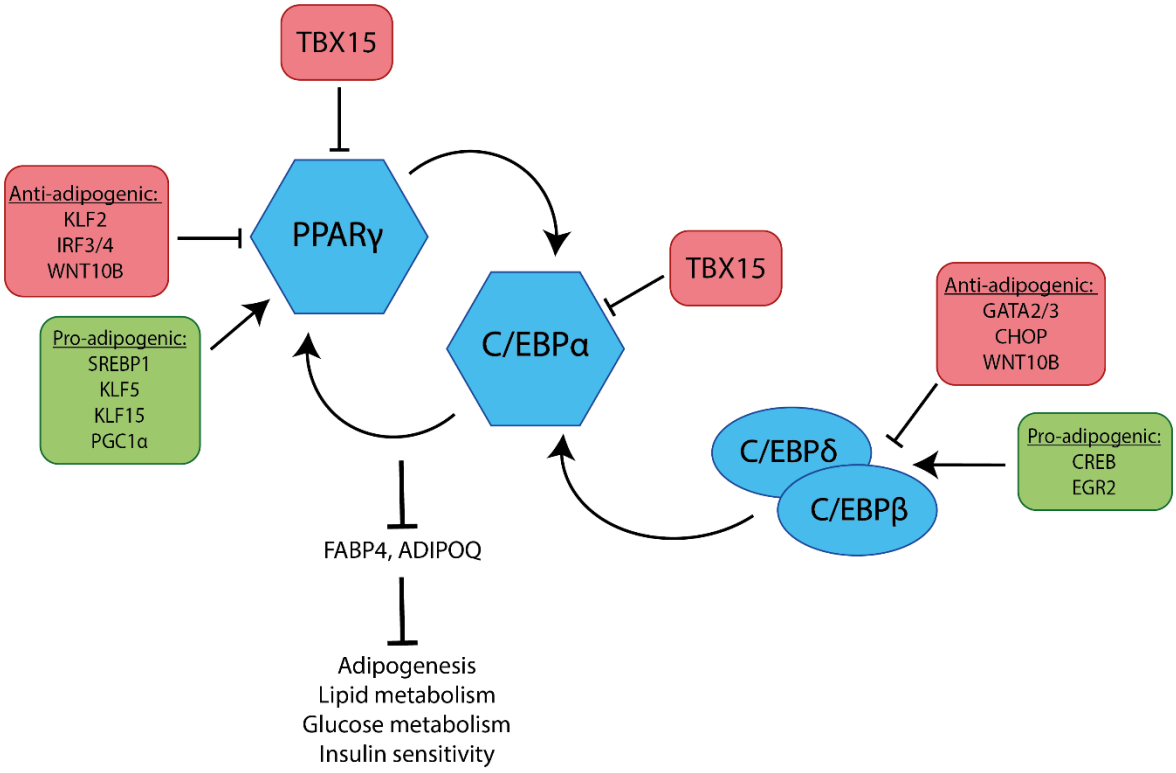

Figure 5.10. The role of TBX15 in regulating the PPARγ-CEBPα adipogenesis feedback loop. Under normal growth conditions it is proposed that TBX15 binds to and directly inhibits the core adipogenesis transcription factors peroxisome proliferator-activated receptor gamma (PPARγ) and CCAAT/enhancer-binding protein alpha (C/EBPα) to downregulate expression of late-stage adipogenesis and lipolysis genes such as adiponectin (ADIPOQ) and fatty acid binding protein 4 (FABP4). Abbreviations: sterol regulatory element-binding protein 1 (SREBP1), Krüppel-like factors 5 and 15 (KLF5, KLF15), PPARγ coactivator 1 alpha (PGC1α), interferon regulatory factors 3 and 4 (IRF3, IRF4) and wingless family member 10B (WNT10B, cAMP-response element binding protein (CREB), early growth response protein 2 (EGR2), GATA-binding factors 2 and 3 (GATA2, GATA3), C/EBP homologous protein (CHOP). Adapted from (Ali *et al.*, 2013) with permission from Elsevier (licence number: 4664301278198).

Table 5.11. TBX15 regulation of key adipogenesis genes. Adipogenesis genes identified as TBX15 binding and regulatory targets from ChIP-sequencing analysis in 3T3-L1 and hWAT cells, and *Tbx15*$^{-/-}$ iWAT RNA-sequencing. Upregulated/downregulated genes in *Tbx15*$^{-/-}$ samples. Abbreviations: NSD (not significantly different).

Gene	hWAT ChIP-sequencing peak	3T3-L1 ChIP-sequencing peak	*Tbx15*$^{-/-}$ iWAT RNA-sequencing expression (LogFC)
ADIPOQ/Adipoq	No	Yes	Upregulated (0.9148)
CEBPA/Cebpa	No	Yes	Upregulated (0.8799)
CEBPB/Cebpb	Yes	Yes	NSD
CEBPD/Cebpd	No	Yes	NSD
CEBPG/Cebpg	No	No	NSD
FABP4/Fabp4	No	No	Upregulated (1.0892)
IGF1/Igf1	No	Yes	Upregulated (0.7707)
LIPE/Lipe	No	Yes	Upregulated (1.0477)
PPARG/Pparg	No	Yes	Upregulated (1.0474)
WNT5B/Wnt5b	Yes	Yes	NSD
WNT10B/Wnt10b	Yes	Yes	NSD

5.3.1.3. Immune regulation/inflammation

Finally, and perhaps most intriguingly, network analysis revealed a novel role for TBX15 in regulating immune-response pathways. After applying stringent cut-off criteria (logFC±1.5 and FDR<0.01), a total of 1613 genes were differentially expressed in iWAT from *Tbx15*$^{-/-}$ compared to *Tbx15*$^{+/+}$ female mice. Over 90% of these genes were downregulated in *Tbx15*$^{-/-}$ iWAT indicating TBX15 normally acts as a transcriptional activator rather than repressor in mature adipose tissues. Further, these downregulated genes were enriched for immune- and cytokine-receptor activity in both ChIP-sequencing and RNA-sequencing. Therefore, I hypothesised that TBX15 may directly regulate the expression of immune receptor genes in adipocytes themselves to modulate adipocyte-immune cell crosstalk to influence fat mass phenotypes in *Tbx15* mice.

Cytokines and chemokines are often expressed in similar patterns, and can bind common receptors, activating signalling pathways to recruit immune cells into the tissue niche (Legler and Thelen, 2018; Morris, Kershaw and Babon, 2018). Adipocytes secrete pro- and anti-inflammatory cytokines and chemokines such as interleukins, TNFs and interferon gamma (IFNγ) to recruit, differentiate and stimulate immune cells within adipose tissues which has implication for inflammation and insulin resistance in obesity and MetS (Song and Deng, 2020; Man, Kallies and Vasanthakumar, 2021; Al-Mansoori *et al.*, 2022).

Indeed, several cytokine, chemokine, interleukin and TNF receptors were all downregulated in *Tbx15*$^{-/-}$ iWAT (Table 5.12). Evidence shows expression of chemokine and cytokine receptors not only in immune cells of adipose tissues, but in adipocytes themselves. For example, expression of chemokine and cytokine receptors (e.g. *Ccr1, Ccr3, Ccr10, Cxcr1, Cxcr2, Cxcr4, Cxcr5,* and *Cx3cr1*) were markedly increased in differentiated compared to undifferentiated 3T3-L1 adipocytes (Kusuyama *et al.*, 2016). Specifically, CXCR2 regulated CXCL3-mediated induction of *Cebpb* and *Cebpd* adipogenesis genes through phosphorylation of ERK/JNK (Kusuyama *et al.*, 2016). *Cxcr2* expression was further confirmed in adipocytes from WAT, and was shown to regulate expression of adipogenesis genes, and ultimately adipocyte size in global *cxcr2*-knockout mice (Dyer *et al.*, 2019). Further, *Cxcr2*-knockout mice had smaller iWAT and gWAT, driven by smaller adipocyte size in these tissues; iWAT also exhibited reduced expression of *Fabp4* and *Pparg,* which the authors speculated was driving the smaller adipocytes and adipose tissue sizes (Dyer *et al.*, 2019).

Table 5.12. TBX15 regulation of immune response genes. Cytokine, chemokine and immune receptor genes identified as TBX15 binding and regulatory targets from ChIP-sequencing analysis in 3T3-L1 and hWAT cells, and *Tbx15*$^{-/-}$ iWAT RNA-sequencing. Upregulated/downregulated genes in *Tbx15*$^{-/-}$ samples. Abbreviations: NSD (not significantly different).

Gene	hWAT ChIP-sequencing peak	3T3-L1 ChIP-sequencing peak	*Tbx15*$^{-/-}$ iWAT RNA-sequencing expression (LogFC)
CCR1/Ccr1	No	No	NSD
CCR2/Ccr2	No	No	NSD
CCR3/Ccr3	No	No	NSD
CCR4/Ccr4	No	No	Downregulated (-3.3097)
CCR6/Ccr6	No	No	Downregulated (-6.9164)
CCR7/Ccr7	Yes	No	Downregulated (-6.5508)
CCR8/Ccr8	No	No	Downregulated (-3.4883)
CCR9/Ccr9	No	No	Downregulated (-6.4270)
CXCR1/Cxcr1	No	No	NSD
CXCR2/Cxcr2	No	No	Downregulated (-6.2303)
CXCR3/Cxcr3	No	No	Downregulated (-1.5650)
CXCR4/Cxcr4	No	No	Downregulated (-2.5307)
CXCR5/Cxcr5	No	No	Downregulated (-3.1139)
CXCR6/Cxcr6	No	Yes	Downregulated (-2.7912)
IL1R/Il1r	Yes	Yes	NSD
IL2R/Il2r	No	No	Downregulated (-3.2114)
IL6R/Il6r	Yes	Yes	Downregulated (-1.0288)
IL7R/Il7r	No	No	Downregulated (-6.2983)
IL9R/Il9r	No	No	Downregulated (-4.8298)
IL10RA/Il10ra	No	No	Downregulated (-1.9463)
IL21R/Il21r	No	No	Downregulated (-5.2060)
IL27RA/Il27ra	No	Yes	Downregulated (-4.2861)
TNFRSF1A/Tnfrsf1a	Yes	No	NSD
TNFRSF1B/Tnfrsf1b	Yes	No	Downregulated (-1.2964)
TNFRSF4/Tnfrsf4	No	No	Downregulated (-2.7159)
TNFRSF9/Tnfrsf9	Yes	Yes	Downregulated (-2.40460
TNFRSF14/Tnfrsf14	Yes	No	Downregulated (-1.9673)
TNFRSF25/Tnfrsf25	Yes	Yes	Downregulated (-1.5707)

Several other chemokine and cytokine receptors have been implicated in adipose tissue biology. For example, both CCR2 and CXC3CR1 induced macrophage recruitment into adipose tissue and subsequent inflammatory signalling profiles (Weisberg *et al.*, 2006; Polyák *et al.*, 2014). Ablation of *Ccr2 in vivo* resulted in

resistance to obesity on HFD, and reduced macrophage infiltration and inflammatory markers (*Tnfa, Cd68, Emr1* and *Serpine1*) in WAT of *Ccr2*-knockout mice compared to wildtype littermates (Weisberg *et al.*, 2006). Similarly, *Cx3cr1*-deficient mice were resistant to HFD-induced weight gain, and had significantly smaller WAT with reduced pro-inflammatory *Mcp1, Il1a* and *Tnfa* expression (Polyák *et al.*, 2014). Adipocyte-specific expression of CXCRs has further been shown to regulate thermogenesis, with UCP1 expression inhibited in response to cold exposure in adipocyte-specific *Cxcr4*-knockout mice (Yao *et al.*, 2014). Immune cells such as macrophages, T-regulatory and invariant natural killer T cells are suggested to induce browning of adipocytes, although many of these mechanisms remain unclear (Man, Kallies and Vasanthakumar, 2021). Several chemokine receptors were downregulated in *Tbx15*$^{-/-}$ iWAT, suggesting TBX15 may act through such receptors to mediate macrophage recruitment and browning resulting in the resistance to fat mass gain observed in *Tbx15*$^{+/-}$ mice.

Further, interleukins have been implicated in adipogenesis and a significant downregulation of several interleukin receptor genes was detected in *Tbx15*$^{-/-}$ iWAT (Table 5.12). For example, siRNA knockdown of *IL21R* resulted in a reduced proportion of cells undergoing lipid-accumulation in primary human adipose MSCs (Falavinha *et al.*, 2022). Expression levels of *PPARG* were not significantly altered as a result of this *IL21R*-kockdown, with the authors speculating that *IL21R* may regulate commitment to the adipogenic lineage through JAK/STAT signalling (Falavinha *et al.*, 2022). Similarly, IL-12 family member receptors *Il27r, Il12r* and *Il23r* were detected in undifferentiated and differentiated 3T3-L1 cells (Nam *et al.*, 2016). IL-27Rα was further detected in differentiating preadipocytes and mature adipocyte fractions from WAT, and mediated the IL-27 signalling pathway to regulate UCP1, PPARα and PGC-1α

expression (Wang *et al.*, 2021). Additionally, *Il10*-knockout mice had significantly reduced bodyweight, total fat mass and adipose depots on both chow and HFD (Rajbhandari *et al.*, 2018). *Il10*-knockout mice also had significantly increased browning of iWAT, driven by increased expression of browning genes such as *Ucp1, Cidea, Cox8b* and *Prdm16*. Further, adipocyte-specific expression of *Il10ra* increased during adipogenesis, with high expression in mature adipocytes in response to obesity (Rajbhandari *et al.*, 2018). The authors further confirmed that knockdown of *Il10ra* both *in vitro* and *in vivo*, resulted in increased thermogenic gene expression and decreased total fat mass and WAT weights, highlighting a key role for the IL10-IL10R axis in adipose tissue function and body composition (Rajbhandari *et al.*, 2018).

These data highlight a secondary role for inflammatory cytokines in adipogenesis, browning and thermogenesis, and collectively with my data suggest a novel role for TBX15 in regulating these processes through regulation of immune receptor signalling pathways in adipose tissues. The downregulation of several core adipokine receptors (e.g., *Cxcr2, Cxcr6, Il10ra, Il21r, Il27ra, Tnfrsf9* and *Tnfrsf25*) in *Tbx15*$^{-/-}$ iWAT suggests TBX15 may act as a master TF to modulate cytokine- and chemokine-signalling axes in adipose tissues to regulate recruitment of immune cells associated with adipose tissue expansion and obesity resulting in the reduced fat mass phenotype in *Tbx15*$^{+/-}$ mice.

I have shown a potential binding and regulatory network for TBX15 using ChIP-sequencing and RNA-sequencing *in vitro* and *in vivo.* This implicates TBX15 as a novel regulator of pathways associated with adipogenesis and mature adipose tissue biology, for example MSC lineage commitment and recruitment of immune cells that may be associated with body composition and metabolic health over an organism's lifetime.

Current analysis is underway, in collaboration with Dr Michelle Simon, to further analyse these data using computational approaches to compare the ChIP-sequencing and RNA-sequencing networks. An initial focus is to prioritise candidate genes for functional experiments to determine key pathways regulated by TBX15 during adipogenesis. This will include identification of targets with a TBX15 motif in promoter and/or enhancers to determine whether TBX15 acts directly, or as part of a TF complex, to regulate target gene expression.

Further *in vitro* validation would then be utilised to confirm regulatory mechanisms of TBX15, for example gene and protein expression analysis of differentiating preadipocytes with both overexpression and knockdown approaches. Given RNA-sequencing analysis was performed on whole tissues, it would be informative to further elucidate which cell types were driving differential expression of immune response genes. We are leveraging methodologies such as bulk RNA-sequencing deconvolution in an attempt to achieve this (Wang *et al.*, 2019). However, with more time single-cell RNA-sequencing, culture of adipose-resident immune cell types, or even induced pluripotent stem cell (iPSC)-based approaches may also elucidate underlying cell types driving differential gene expression. Further, quantifying expression of the corresponding chemokines and cytokines in blood plasma samples from *Tbx15*$^{-/-}$ mice would inform whether TBX15 regulates a systemic inflammatory profile, or a more targeted response profile in cells within adipose tissues.

6

Identifying p.H156N perturbations of the TBX15 transcriptional network

6.1. Introduction

The TF role of TBX15 in adipogenesis and adipose tissue biology has been well established, particularly with the advent of GWAS that have implicated several *TBX15-WARS* locus variants in altered body fat distribution, measured as WHRadjBMI (Gesta *et al.*, 2006, 2011; Heid *et al.*, 2010; Gburcik *et al.*, 2012; Lee *et al.*, 2015, 2017; Shungin *et al.*, 2015; Sun *et al.*, 2019; Justice *et al.*, 2019; Pulit *et al.*, 2019; Pan *et al.*, 2021). Whilst the consensus is that TBX15 is an important regulator of adipogenesis and adipocyte browning, there is conflicting evidence for the direction of this regulation, most likely due to differences in cell and *in vivo* models used between studies.

Using a combination of ChIP-sequencing and RNA-sequencing I identified a TBX15-regulatory network in preadipocytes and adipose tissues suggesting TBX15 as a novel regulator of immune receptor signalling that may explain the altered body composition phenotype of *Tbx15*$^{+/-}$ mice. However, comparing the networks remains challenging given the cellular heterogeneity of whole adipose tissues hindering identification of the cell origin of these transcriptional signals. I further showed that p.H156N altered body composition phenotypes *in vivo* indicating a need to investigate

the underlying mechanisms of action of this polymorphism on the TBX15 gene expression network.

6.1.1. Chapter hypothesis

Having proposed a role for TBX15 in regulating MSC lineage determination, adipogenesis and immune response processes, I hypothesised that p.H156N would perturb this network to drive the increased lean mass and decreased fat mass phenotypes detected in *Tbx15*$^{+/H156N}$ and *Tbx15*$^{H156N/H156N}$ mice, respectively.

6.1.2. Chapter aims

I aimed to investigate the p.H156N regulatory network in adipocytes and adipose tissues by:

1. Assessing DEGs in whole adipose tissues (*in vivo*) and in differentiating primary adipocytes (*in vitro*) from *Tbx15*$^{+/+}$ and *Tbx15*$^{H156N/H156N}$ mice to determine how p.H156N alters the TF function of TBX15 (in collaboration with Dr. Michelle Simon, Biocomputing group, MRC Harwell).
2. Comparing DEGs between *Tbx15*$^{H156N/H156N}$ and *Tbx15*$^{-/-}$ mice to understand the mechanistic action of p.H156N.

6.2. Results

6.2.1. Determining the *Tbx15^{H156N}* regulatory network using RNA-sequencing

In chapter 5 I proposed a potential regulatory role for TBX15 in MSC lineage determination, differentiation of committed preadipocytes, and immune receptor signalling that may drive the altered body composition phenotypes seen in *Tbx15$^{+/-}$* mice. We therefore hypothesised that p.H156N would perturb the TBX15 network to drive alterations in body composition to mirror human WHR-phenotypes. This hypothesis was formed prior to collecting and analysing all *Tbx15^{H156N}* phenotyping data, therefore iWAT and BAT were isolated from *Tbx15$^{+/+}$* and *Tbx15$^{H156N/H156N}$* mice for RNA-sequencing. Further, to elucidate the impact of p.H156N on the function of *Tbx15* during adipogenic differentiation, I isolated SVF cells from iWAT of *Tbx15$^{+/+}$* and *Tbx15$^{H156N/H156N}$* mice for differentiation *in vitro,* and RNA-sequencing.

6.2.1.1. *Tbx15^{H156N}* regulatory network in adipose tissue

Firstly, I aimed to determine how p.H156N altered the TBX15 regulatory network in adipose tissues using RNA-sequencing. There was a significant sex effect ($p<0.0001$), but not interaction or genotype effect for bodyweight in female and male *Tbx15$^{+/+}$* and *Tbx15$^{H156N/H156N}$* mice (Figure 6.1C, Table 6.1). iWAT and BAT samples from female *Tbx15$^{+/+}$* (n=6) and *Tbx15$^{H156N/H156N}$* (n=5), and male *Tbx15$^{+/+}$* (n=6) and *Tbx15$^{H156N/H156N}$* (n=6) mice were sent to the Oxford Genomics Centre for bulk RNA-sequencing. Principle component analysis during initial QC indicated a high level of biological variability in these samples (Appendix Figure 9.6).

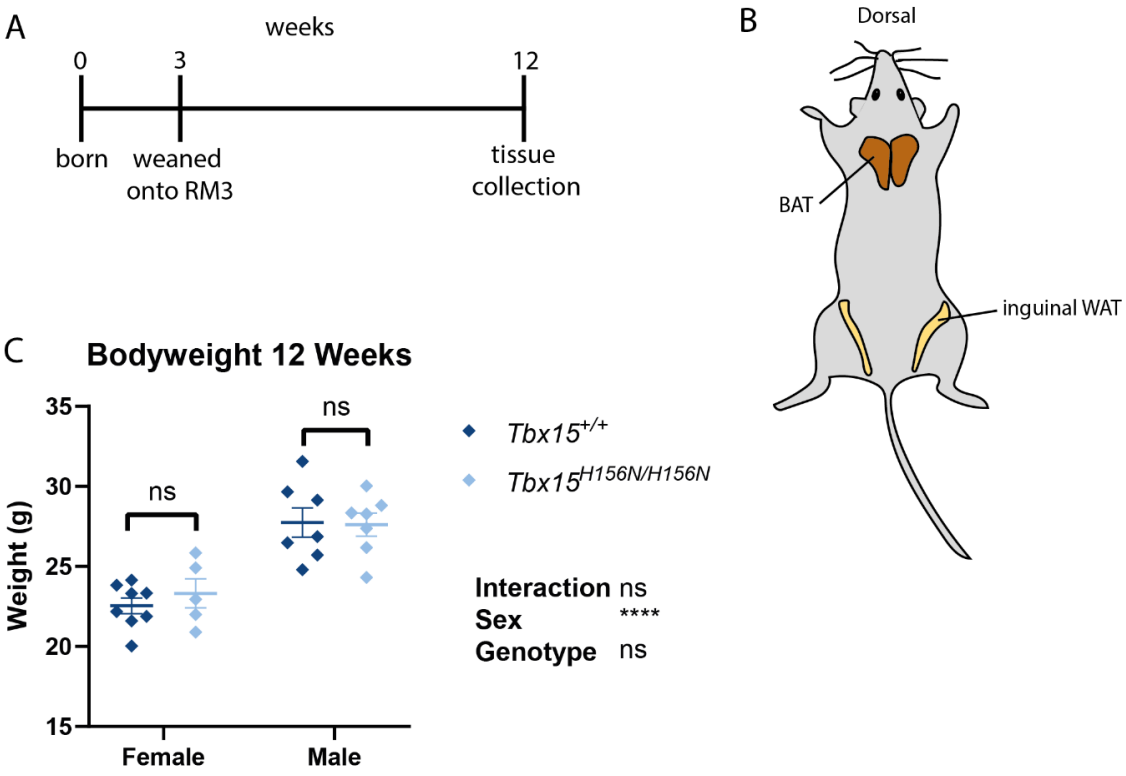

Figure 6.1. *Tbx15*^{H156N} RNA-sequencing cohort. A. pipeline for tissue collection at 12 weeks. B. Location of adipose depots in mice. C. Bodyweight at 12 weeks of age. All data analysed by two-way ANOVA with post-hoc Tukey's multiple comparisons (within each sex); ****p<0.0001, ns (not significant).

Table 6.1. Female and male *Tbx15*^{H156N} bodyweight at 12 weeks of age. All data analysed by two-way ANOVA with post-hoc Tukey's multiple comparisons (within each sex); significant values (p<0.05) highlighted in bold.

	Female	**Male**
Interaction	0.5545	
Sex	**<0.0001**	
Genotype	0.6723	
Post-hoc analysis (adjusted p-value)		
	Female	**Male**
***Tbx15*$^{+/+}$ vs *Tbx15*$^{H156N/H156N}$**	0.7378	0.9903

Data analysis is ongoing; therefore, I have focussed on female iWAT data in this chapter. Similar to *Tbx15*$^{-/-}$, DEGs (FDR<0.05) were detected in iWAT of female *Tbx15*$^{H156N/H156N}$ mice; 337 significant DEGs were detected between *Tbx15*$^{+/+}$ and *Tbx15*$^{H156N/H156N}$ mice (305 downregulated, 32 upregulated; Figure 6.2). A total of 150 genes (FDR<0.05) were common between *Tbx15*$^{H156N/H156N}$ and *Tbx15*$^{-/-}$ iWAT. All

downregulated genes in *Tbx15*$^{H156N/H156N}$ samples were upregulated in *Tbx15*$^{-/-}$ tissues, and vice versa with upregulated genes in *Tbx15*$^{H156N/H156N}$ downregulated in *Tbx15*$^{-/-}$ samples (Table 6.2). Overall, fewer DEGs were significant in *Tbx15*$^{H156N/H156N}$ than in *Tbx15*$^{-/-}$ which was in line with the predicted subtle effect of this coding SNP.

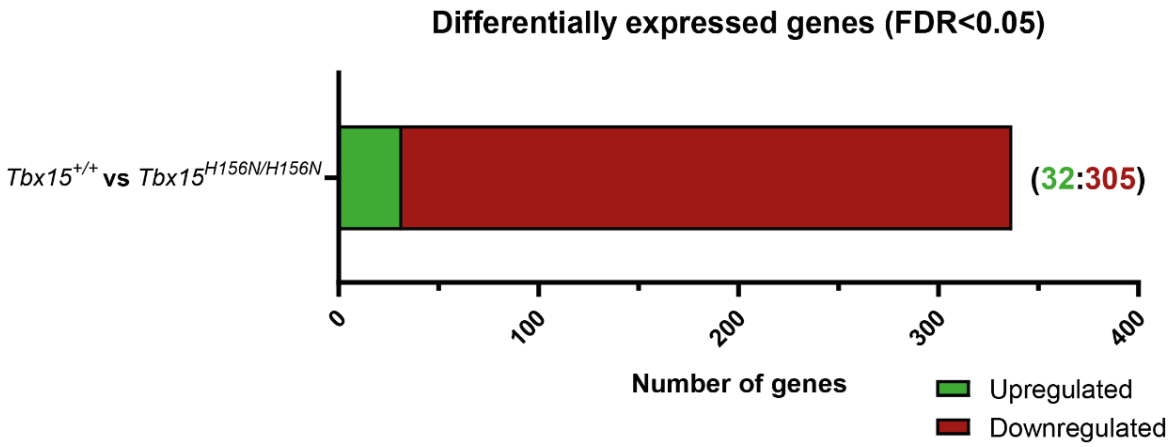

Figure 6.2. Total number of significantly differentially expressed genes in *Tbx15*^{H156N} adipose tissues. Total number of differentially expressed genes (FDR<0.05) in inguinal white adipose tissue (iWAT) from 12-week old female *Tbx15*$^{+/+}$ (n=6) and *Tbx15*$^{H156N/H156N}$ (n=5) mice. Number of upregulated (green) and downregulated (red) genes are given in brackets.

Next, I compared the enriched terms for DEGs in *Tbx15*$^{H156N/H156N}$ and *Tbx15*$^{-/-}$ tissues. Functional enrichment analysis of DEGs (FDR<0.05) in *Tbx15*$^{H156N/H156N}$ iWAT returned enriched terms for downregulated genes only, which were enriched for cytoskeletal protein binding, actin binding and structural constituents of muscle (GO:MF), and muscle structure development, contraction and development (GO:BP) (Table 6.3). Interestingly, several of these terms were also enriched in *Tbx15*$^{-/-}$ iWAT within *upregulated* genes (Table 6.3), suggesting that p.H156N may directly perturb the TBX15 regulatory network in a gain-of-function manner to drive a change in direction of expression of these genes.

Table 6.2. Top common upregulated and downregulated genes in *Tbx15^{H156N}* and *Tbx15$^{-/-}$* inguinal white adipose tissue. Differentially expressed genes (FDR<0.05) in *Tbx15$^{+/+}$* versus *Tbx15$^{H156N/H156N}$* and *Tbx15$^{+/+}$* versus *Tbx15$^{-/-}$* mice, compared for common genes. Top genes ranked on FDR in *Tbx15$^{H156N/H156N}$* mice (upregulated/downregulated in homozygous *Tbx15$^{H156N/H156N}$* and homozygous *Tbx15$^{-/-}$* compared to their respective wildtype *Tbx15$^{+/+}$* littermates).

	Tbx15$^{H156N/H156N}$			***Tbx15$^{-/-}$***		
Gene	**LogFC**	**p-value**	**FDR**	**LogFC**	**p-value**	**FDR**
Upregulated in *Tbx15$^{H156N/H156N}$*						
Spata31d1b	6.946265	7.00E-07	0.000186	-8.6808	6.19E-18	7.95E-16
Ighv1-19	6.372601	2.28E-06	0.000555	-5.9858	4.84E-12	3.47E-10
Ighv14-3	6.126683	3.70E-06	0.000853	-7.0960	2.70E-09	1.41E-07
Gm26583	2.741739	2.32E-05	0.004497	-2.5843	1.43E-06	5.16E-05
Cacnb3	1.470481	2.40E-05	0.00463	-2.4923	2.26E-19	3.35E-17
Nudt17	2.017078	2.85E-05	0.005396	-2.7763	2.36E-14	2.16E-12
Trbv26	4.042699	4.92E-05	0.008808	-5.8577	4.11E-08	1.84E-06
Gzmc	3.301869	6.57E-05	0.011292	-4.3966	2.21E-15	2.23E-13
Tm4sf5	2.322105	8.87E-05	0.014715	-4.1936	8.52E-10	4.73E-08
Ccl17	2.822454	9.79E-05	0.015997	-2.3685	0.001873	0.029149
Stx11	1.532901	0.000105	0.016945	-1.9969	4.00E-09	2.03E-07
Fasl	2.201269	0.00013	0.020274	-2.2407	8.57E-05	0.002198
Bach2os	3.366369	0.000153	0.023121	-2.3571	8.29E-05	0.002135
Klra17	3.555238	0.000159	0.023849	-3.2812	2.52E-05	0.000732
B4galnt1	1.50311	0.000169	0.0253	-2.7029	6.35E-20	9.85E-18
Cytip	1.510444	0.000179	0.026325	-3.1785	4.21E-28	1.29E-25
Pglyrp1	1.985716	0.000185	0.026986	-3.0050	4.54E-11	2.92E-09
Cxcr4	1.637615	0.000195	0.028121	-2.5307	2.00E-13	1.64E-11
Rasal1	1.385498	0.00024	0.033801	-2.3341	2.76E-12	2.03E-10
Mab21l3	2.99816	0.000256	0.035287	-3.4603	4.40E-09	2.23E-07
Downregulated *Tbx15$^{H156N/H156N}$*						
Casq1	-9.55144	1.72E-15	1.23E-11	5.1126	0.001197	0.020485
Actn3	-11.1958	3.00E-15	1.85E-11	6.4489	0.001688	0.026813
Mybpc2	-8.79801	8.78E-14	2.23E-10	5.9486	0.001375	0.022786
Pygm	-8.30492	1.48E-13	3.36E-10	5.0117	0.000891	0.01605
Mylpf	-8.16889	4.79E-13	8.98E-10	4.7748	0.003	0.04229
Hrc	-8.01066	6.80E-13	1.09E-09	5.2118	0.001339	0.022336
Rpl3l	-9.16851	6.55E-13	1.09E-09	4.9676	0.003493	0.047465
Ppp1r27	-10.1309	2.18E-12	2.69E-09	5.7805	0.00259	0.037874
Pgam2	-6.96502	3.17E-12	3.60E-09	4.1752	0.001736	0.027406
Ryr1	-7.43304	4.97E-12	4.90E-09	4.4750	0.00265	0.038543
Neb	-7.94365	5.11E-12	4.90E-09	4.6268	0.001079	0.01879
Cmya5	-7.40098	7.56E-12	6.66E-09	4.0192	0.00264	0.038453
Asb11	-8.51096	2.10E-11	1.78E-08	5.6254	0.001391	0.023026
Vgll2	-11.1042	2.14E-11	1.78E-08	7.8617	0.00104	0.018255
Sypl2	-8.99755	3.28E-11	2.53E-08	5.8873	0.001469	0.024072
Mybpc1	-8.26501	4.20E-11	3.07E-08	5.6148	0.003521	0.047739
Txlnb	-6.74802	6.67E-11	4.56E-08	4.4702	0.000602	0.011669
Rbfox1	-8.04678	6.77E-11	4.56E-08	4.4337	0.002928	0.041525
Jsrp1	-7.16783	8.63E-11	5.64E-08	4.4998	0.001553	0.025096
Trim72	-6.59846	1.15E-10	7.42E-08	5.0877	0.000178	0.004145

Table 6.3. Top common enriched terms between *Tbx15*$^{H156N/H156N}$ and *Tbx15*$^{-/-}$ inguinal white adipose tissue. Common enriched gene ontology (GO) molecular function (MF) and biological processes (BP) terms for downregulated genes (FDR<0.05) in inguinal white adipose tissue from 12-week old female *Tbx15*$^{H156N/H156N}$ and *Tbx15*$^{-/-}$ mice. Downregulated genes in *Tbx15*$^{H156N/H156N}$ mice and upregulated in *Tbx15*$^{-/-}$ mice compared to their respective *Tbx15*$^{+/+}$ colony-mates.

Source	Term name	Term ID	*Tbx15*$^{H156N/H156N}$ p-value	*Tbx15*$^{-/-}$ p-value
Downregulated genes in *Tbx15*$^{H156N/H156N}$ and upregulated in *Tbx15*$^{-/-}$ mice				
GO:MF	cytoskeletal protein binding	GO:0008092	2.29E-27	0.021706
	actin binding	GO:0003779	1.22E-22	0.005947
	structural constituent of muscle	GO:0008307	1.05E-14	Not enriched
	protein binding	GO:0005515	1.06E-14	Not enriched
	actin filament binding	GO:0051015	2.88E-13	Not enriched
GO:BP	muscle system process	GO:0003012	4.11E-48	2.30E-08
	muscle structure development	GO:0061061	8.07E-46	0.000153
	striated muscle cell differentiation	GO:0051146	1.04E-39	Not enriched
	muscle cell development	GO:0055001	7.27E-39	Not enriched
	muscle cell differentiation	GO:0042692	2.79E-37	Not enriched

6.2.1.2. *Tbx15*^{H156N} regulatory network in differentiating primary adipocytes

6.2.1.2.1. Optimisation of primary SVF isolation and differentiation

Subsequently, I aimed to determine whether the p.H156N polymorphism impacted adipogenesis *in vitro.* Inguinal and visceral WAT-derived SVF cells have different adipogenic potential *in vitro* (Macotela *et al.*, 2012), and differentiation cocktails containing IBMX, dexamethasone and insulin resulted in less than 50% lipid accumulation in cultured preadipocytes after seven days of adipogenic induction (unpublished data, Cox group). The mixture of preadipocytes and mature adipocytes in a sample can confound downstream expression analysis. Therefore, I aimed to determine if a complete adipogenic cocktail containing IBMX, dexamethasone, indomethacin, T3 and insulin (Merrick *et al.*, 2019) increased differentiation efficiency of cultured SVF cells isolated from iWAT.

I isolated SVF from iWAT from two female and two male wildtype C57BL/6NTac mice and seeded three technical replicates per mouse for each differentiation media

cocktail. Cells were cultured to post-confluence and differentiated with either a minimal adipogenic cocktail or complete adipogenic cocktail for a total of four days, followed by three days of culture in their respective maintenance media. Seven days post-differentiation, cells were fixed and stained for quantification of lipid accumulation with OilRedO. There was a significant ~3.5-fold increase in lipid accumulation in SVF cells cultured with a complete adipogenic cocktail media compared to minimal cocktail media (p=0.0107, paired t-test; Figure 6.3). Therefore, I used the complete adipogenic cocktail media to differentiate SVF cells for RNA-sequencing.

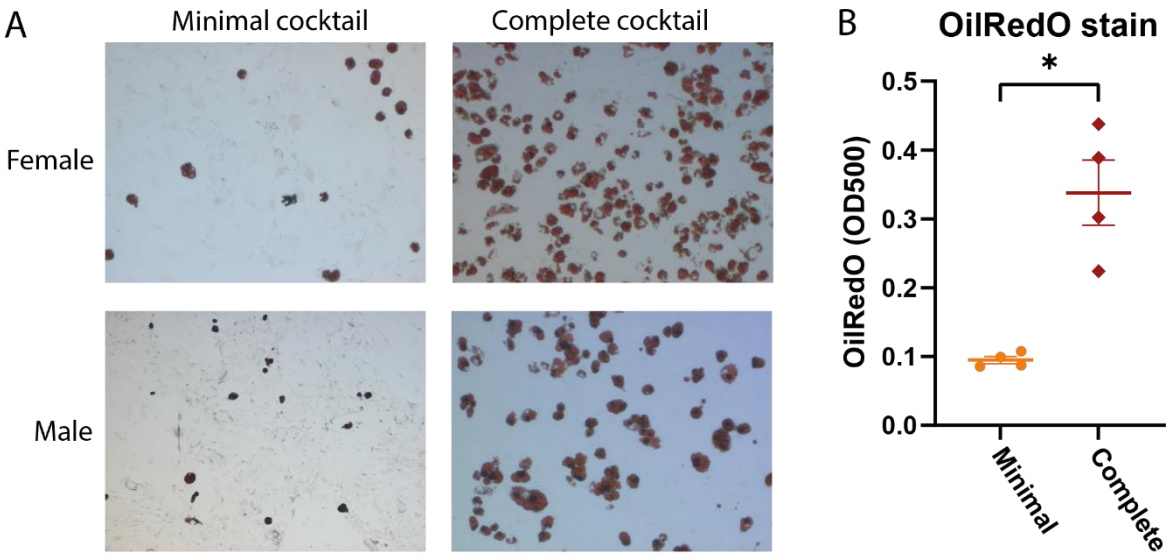

Figure 6.3. Optimisation of differentiation protocol for stromal-vascular fraction (SVF) cells derived from inguinal white adipose tissue (iWAT). SVF cells were cultured in a minimal or complete adipogenic cocktail media for seven days and lipid accumulation inspected by OilRedO staining. A. Representative brightfield images of OilRedO stain (red) of female (n=2) and male (n=2) SVF cells differentiated with either a minimal or complete adipogenic media. B. Quantification of OilRedO stain for SVF cells differentiated with either a minimal (orange circles) or complete (red diamond) adipogenic cocktail media. Three technical replicates per mouse were pooled and data was analysed by paired t-test: *p<0.05. Graph representative of mean ± standard error mean of n=4 independent biological replicates.

6.2.1.2.2. *TBX15*$^{H156N/H156N}$ did not have altered total lipid accumulation in differentiated iWAT-derived SVF cells

TBX15 overexpression inhibited lipid accumulation in 3T3-L1 cells (Gesta *et al.*, 2011), therefore, I aimed to determine if p.H156N affected lipid accumulation in differentiated SVF cells. I differentiated iWAT-derived SVF cells from female *Tbx15*$^{+/+}$ and *Tbx15*$^{H156N/H156N}$ mice for seven days using a complete adipogenic cocktail media and assessed lipid accumulation. SVF cells isolated from *Tbx15*$^{H156N/H156N}$ mice did not have significantly different lipid accumulation compared to SVF of *Tbx15*$^{+/+}$ mice at seven days post-differentiation (p=0.6485, unpaired t-test; Figure 6.4).

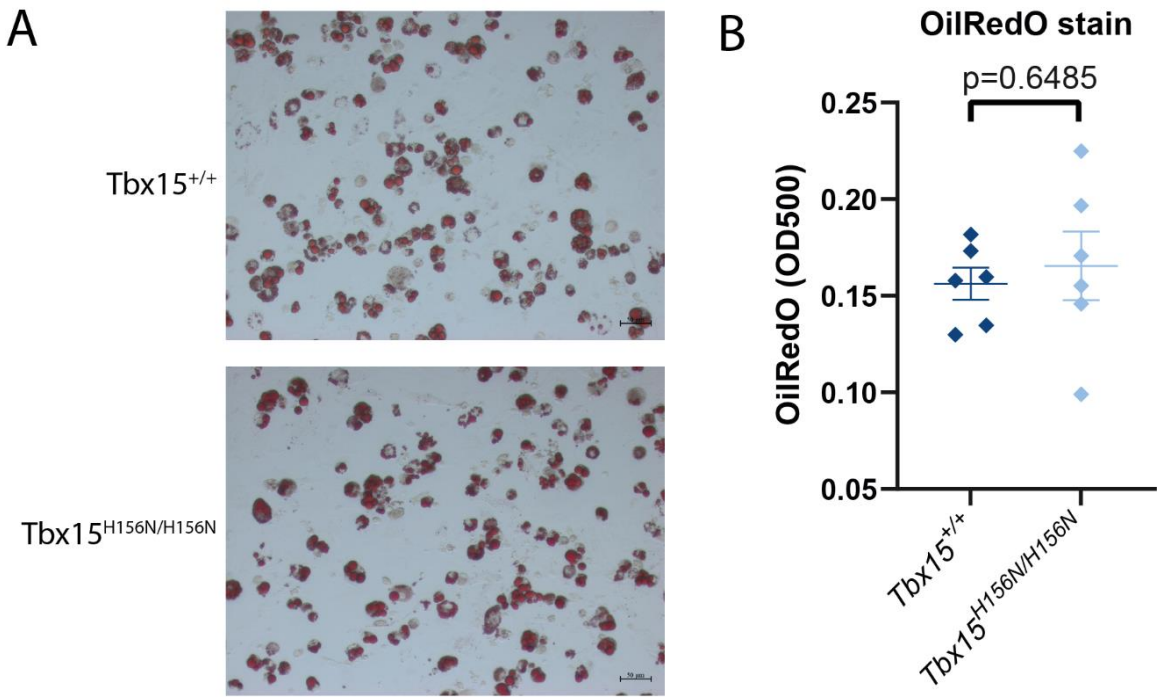

Figure 6.4. Differentiation of stromal-vascular fraction (SVF) cells derived from inguinal white adipose tissue from female *Tbx15*$^{+/+}$ and *Tbx15*$^{H156N/H156N}$ mice. SVF cells were cultured in a complete adipogenic cocktail media for 7 days and lipid accumulation quantified by OilRedO stain. A. Representative brightfield images of OilRedO stain (red) of female SVF cells differentiated with a complete adipogenic cocktail media. B. Quantification of OilRedO stain for *Tbx15*$^{+/+}$ (dark blue diamond) and *Tbx15*$^{H156N/H156N}$ (light blue diamond) differentiated SVF cells. One technical replicated per mouse was analysed by unpaired t-test. Graph representative of mean ± standard error mean of n=11 independent biological replicates.

6.2.1.2.3. *Tbx15*$^{H156N/H156N}$ regulatory network

I then aimed to investigate the impact of p.H165N on gene expression in differentiating SVF cells *in vitro*. RNA was isolated from undifferentiated (confluent (day -1) and post-confluent (day 0)), early differentiating (day 1 and day 2) and terminally differentiated (day 7) cells for RNA-sequencing. Across five time points analysed, two genes were significant at FDR<0.05: *Siglec1* at day -1 (q=0.044564) and *Kcnk12* at day 1 (q=0.001017). Therefore, I examined the nominally significant genes (p<0.05) at each time point. A total of 1272 (day -1), 1309 (day 0), 1092 (day 1), 900 (day 2) and 670 (day 7) genes were differentially expressed, several of which were common across at least two time points (Figure 6.5, Table 6.4, Table 6.5). Upregulated genes represented a larger proportion of DEGs at each time point, ~3-fold more at day -1, suggesting p.H156N may decrease TBX15-mediated repression of adipogenesis genes.

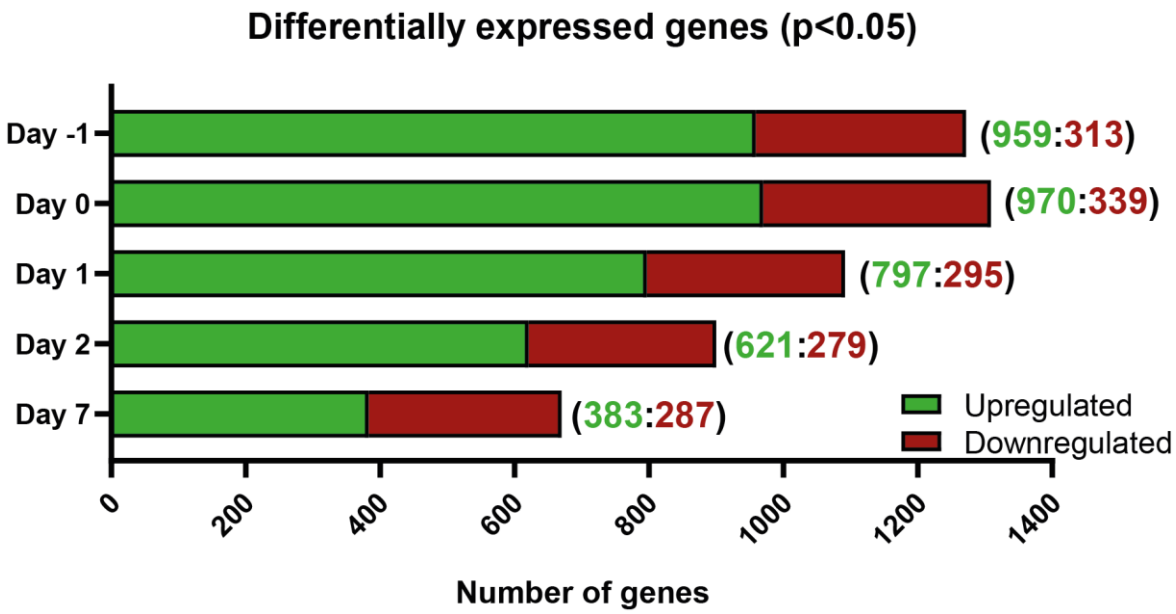

Figure 6.5. Total number of significantly differentially expressed genes in *Tbx15*^{H156N} stroma-vascular fraction cells. Total number of differentially expressed genes (p<0.05) in differentiating stromal-vascular fraction cells derived from inguinal white adipose tissue from female *Tbx15*$^{+/+}$ and *Tbx15*$^{H156N/H156N}$ mice.

Table 6.4. Top common upregulated genes in *Tbx15^{H156N}* differentiating stromal-vascular fraction cells. Common genes in at least two time points of differentiating stromal-vascular fraction cells isolated from inguinal white adipose tissue from 6-week old female *Tbx15$^{+/+}$* and *Tbx15$^{H156N/H156N}$* mice. Upregulated genes in homozygous *Tbx15$^{H156N/H156N}$* cells. Ranked based on p-value from D0 genes. Abbreviations: NSD (not significantly different).

	Day -1		Day 0		Day 1		Day 2		Day 7	
Gene	LogFC	p-value	LogFC	p-value	LogFC	p-value	LogFC	p-value	LogFC	p-value
Upregulated										
Trim30a	0.522376	0.007195	0.808245	1.39E-05	0.417813	0.006349	NSD	NSD	NSD	NSD
Ifit1	0.675812	0.017816	1.050565	1.55E-05	NSD	NSD	NSD	NSD	NSD	NSD
Gm4951	0.888612	0.000799	1.223268	1.61E-05	0.501596	0.029925	NSD	NSD	NSD	NSD
Pik3ap1	0.756931	0.000495	1.012263	1.72E-05	0.812936	0.001094	0.337143	0.021735	NSD	NSD
Itgam	0.718101	0.000312	1.186689	1.72E-05	0.656306	0.000561	0.525604	0.002262	0.412391	0.044356
Adam8	0.739395	5.94E-05	0.783608	2.43E-05	0.422653	0.000887	NSD	NSD	NSD	NSD
Bhlhe22	0.488329	0.015299	0.692878	2.57E-05	NSD	NSD	NSD	NSD	NSD	NSD
Ccr5	1.24825	1.39E-05	1.62808	3.12E-05	1.522629	0.005626	0.998608	0.009415	1.189321	0.007471
Itgb2	0.703555	0.000344	0.98738	3.83E-05	0.521193	0.001113	0.425632	0.003508	NSD	NSD
Cybb	0.822539	9.69E-05	1.040414	3.84E-05	0.493875	0.003762	NSD	NSD	NSD	NSD
Slc15a3	0.47189	0.026777	0.67988	4.48E-05	NSD	NSD	NSD	NSD	NSD	NSD
Kcnab2	0.668493	0.001111	0.908621	4.62E-05	0.315469	0.040397	0.432069	0.004352	NSD	NSD
Il10ra	0.783357	0.00186	1.11287	4.66E-05	0.888615	0.004579	0.572536	0.003094	NSD	NSD
Mpeg1	0.826845	0.000294	1.090342	5.27E-05	0.640285	0.001057	0.526432	0.000935	NSD	NSD
Gm12250	1.116627	9.43E-06	1.385398	5.32E-05	NSD	NSD	NSD	NSD	NSD	NSD
Lyz2	0.683536	0.006307	0.995455	5.51E-05	0.610658	0.000316	0.507279	0.000659	NSD	NSD
Gm5431	1.025732	0.000746	1.164304	6.82E-05	0.945119	0.001121	0.711176	0.005274	NSD	NSD
Sp110	0.445257	0.020093	0.74142	7.32E-05	0.563939	0.033249	NSD	NSD	NSD	NSD
Coro2a	0.667027	0.010114	1.023034	7.88E-05	NSD	NSD	NSD	NSD	NSD	NSD
Plek	0.691551	0.00043	0.988615	8.45E-05	0.601495	0.001286	0.37602	0.008245	NSD	NSD

Table 6.5. Top common downregulated genes in *Tbx15*^{H156N} differentiating stromal-vascular fraction cells. Common genes in at least two time points of differentiating stromal-vascular fraction cells isolated from inguinal white adipose tissue from 6-week old female *Tbx15*$^{+/+}$ and *Tbx15*$^{H156N/H156N}$ mice. Downregulated genes in homozygous *Tbx15*$^{H156N/H156N}$ cells. Ranked based on p-value from D0 genes. Abbreviations: NSD (not significantly different).

	Day -1		Day 0		Day 1		Day 2		Day 7	
Gene	LogFC	p-value	LogFC	p-value	LogFC	p-value	LogFC	p-value	LogFC	p-value
Downregulated										
Angptl7	NSD	NSD	-1.96951	8.54E-05	-1.10588	0.00197	NSD	NSD	-0.94194	0.019257
Sp9	NSD	NSD	-2.14393	0.000536	-1.69539	0.00072	NSD	NSD	NSD	NSD
Apoh	-1.75574	0.03247	-1.72793	0.001445	NSD	NSD	-1.27126	0.015811	NSD	NSD
Ldb3	-0.53374	0.027178	-0.60985	0.002076	NSD	NSD	NSD	NSD	NSD	NSD
Unc13c	NSD	NSD	-1.00961	0.002743	NSD	NSD	-2.84467	0.014128	-1.85777	0.021714
Pitx2	-0.75717	0.037827	-0.84295	0.002755	NSD	NSD	-1.06367	0.040273	NSD	NSD
Adamts13	NSD	NSD	-3.56487	0.003292	-2.62789	0.013411	NSD	NSD	NSD	NSD
Cck	-0.7624	0.02668	-1.0928	0.003519	-1.01167	0.012612	-0.88647	0.040227	NSD	NSD
Sncg	-0.58386	0.003874	-0.65611	0.005233	NSD	NSD	NSD	NSD	NSD	NSD
Lingo2	-1.19451	0.005604	-1.15021	0.006119	NSD	NSD	NSD	NSD	NSD	NSD
Pitx1	-0.89332	0.012434	-0.82575	0.007924	-0.87584	0.007267	-0.89574	0.004697	-0.8498	0.021131
Tspan13	NSD	NSD	-0.72735	0.008916	-0.82107	0.023455	-0.71266	0.013888	-0.88423	0.008665
Mlip	NSD	NSD	-0.97896	0.010769	-1.13183	0.026745	NSD	NSD	NSD	NSD
Grem1	NSD	NSD	-0.5336	0.010944	NSD	NSD	-0.59703	0.03207	NSD	NSD
Gm11842	NSD	NSD	-4.11575	0.011442	NSD	NSD	NSD	NSD	-4.613	0.002498
4930426L09Rik	NSD	NSD	-0.39911	0.011997	-0.68066	0.049632	NSD	NSD	NSD	NSD
Gm10800	NSD	NSD	-1.3344	0.012554	NSD	NSD	-0.75761	0.026408	NSD	NSD
Fstl4	NSD	NSD	-0.70783	0.013688	NSD	NSD	NSD	NSD	-0.83205	0.036211
Gm13521	-2.55904	0.030659	-3.02115	0.013885	NSD	NSD	NSD	NSD	NSD	NSD
Wnt10b	-0.87898	0.035846	-0.82918	0.01397	NSD	NSD	NSD	NSD	NSD	NSD

Finally, I performed functional enrichment analysis on the DEGs ($p<0.05$) at each of the differentiation time points. For upregulated genes, immune response and defence response terms (GO:BP) were enriched in all five time points, with immune system process, response to other organism and response to external biotic stimulus enriched across day -1 to day 2 (Table 6.6). Further, KEGG terms for osteoclast differentiation and B cell receptor signalling were enriched in upregulated genes across day -1 to day 2 (Table 6.6). Far fewer terms were enriched for downregulated genes. Indeed, enriched terms were only generated for day -1 and day 0 genes by g:Profiler (Table 6.6). Overall, these pathways were different to the cytoskeletal/muscle pathways enriched in downregulated genes from iWAT of female *Tbx15*$^{H156N/H156N}$ but were comparable to the enriched immune/cytokine pathways in downregulated genes from iWAT of female *Tbx15*$^{-/-}$ mice. This suggests p.H156N may regulate gene expression in a cell-specific manner within a tissue to directly perturb the TBX15 transcriptional network. Further analysis is underway, in collaboration with Dr. Michelle Simon, to investigate the functionality of these genes in the context of adipogenesis.

Table 6.6. Top common enriched terms in *Tbx15^{H156N}* differentiating stromal-vascular fraction cells. Enriched gene ontology biological processes (GO:BP) and Kyoto encyclopaedia of genes and genomes (KEGG) terms for upregulated and downregulated genes (p<0.05) in differentiating stromal-vascular fraction cells isolated from inguinal white adipose tissue from 6-week old female *Tbx15$^{+/+}$* and *Tbx15$^{H156N/H156N}$* mice. Upregulated/downregulated in homozygous *Tbx15$^{H156N/H156N}$* mice. Queries were run as ordered query (most significant genes listed at the top of the list).

Source	Term name	Term ID	Day -1 p-value	Day 0 p-value	Day 1 p-value	Day 2 p-value	Day 7 p-value
Upregulated							
GO:BP	Immune system process	GO:0002376	1.38E-51	1.64E-82	1.20E-29	9.13E-22	Not enriched
	Immune response	GO:0006955	3.32E-48	1.46E-69	1.33E-22	7.02E-19	0.009494
	Defence response	GO:0006952	1.38E-43	3.77E-63	8.93E-23	7.93E-23	0.007559
	Response to other organism	GO:0051707	2.74E-38	5.21E-56	1.81E-15	9.44E-11	Not enriched
	Response to external biotic stimulus	GO:0043207	9.88E-36	6.98E-56	7.11E-16	1.05E-10	Not enriched
KEGG	Osteoclast differentiation	KEGG:04380	2.64E-06	5.97E-07	0.002511	0.002398	Not enriched
	B cell receptor signalling pathway	KEGG:04662	3.71E-06	3.52E-06	8.03E-05	0.002189	Not enriched
	Chemokine signalling pathway	KEGG:04062	2.1E-05	5E-05	Not enriched	Not enriched	Not enriched
	Staphylococcus aureus infection	KEGG:05150	0.000115	8.9E-05	0.000248	0.014716	Not enriched
	Natural killer cell mediated cytotoxicity	KEGG:04650	0.002231	0.000139	0.003761	Not enriched	Not enriched
Downregulated							
GO:BP	Neuron projection extension	GO:1990138	Not enriched	0.014704	Not enriched	Not enriched	Not enriched
	DNA replication-dependent nucleosome assembly	GO:0006335	Not enriched	0.031107	Not enriched	Not enriched	Not enriched
	DNA replication-dependent nucleosome organization	GO:0034723	Not enriched	0.031107	Not enriched	Not enriched	Not enriched
	Developmental growth involved in morphogenesis	GO:0060560	Not enriched	0.04414	Not enriched	Not enriched	Not enriched
	Nose development	GO:0043584	0.008836	Not enriched	Not enriched	Not enriched	Not enriched

6.3. Discussion

Having identified a TBX15 regulatory network in iWAT and BAT in *Tbx15*$^{-/-}$ mice, I subsequently sought to investigate the mechanisms of the p.H156N polymorphism in adipose tissues and differentiating SVF cells that might explain WHRadjBMI associations in humans and altered body composition in *Tbx15*^{H156N} mice. I showed homozygous *Tbx15*$^{H156N/H156N}$ mice had decreased expression of genes enriched for cytoskeletal binding and muscle processes in iWAT. Further, differentiating adipose progenitor cells isolated from iWAT of these mice exhibited increased expression of genes enriched for immune response and osteoclast differentiation terms. Several of these terms were enriched in *Tbx15*$^{-/-}$ tissues, albeit in genes expressed in the opposite direction to *Tbx15*$^{H156N/H156N}$ mice. This suggested the p.H156N polymorphism directly perturbed the TBX15 network within whole adipose tissues and differentiating adipose progenitor cells.

6.3.1. p.H156N directly perturbed the TBX15 regulatory network

Fewer significant DEGs (FDR<0.05), approximately 10%, were detected in iWAT of *Tbx15*$^{H156N/H156N}$ compared to *Tbx15*$^{-/-}$ mice. This was also reflected in differentiating adipose progenitor cells, with only two genes reaching FDR<0.05 significance, and up to ~1300 DEGs reaching nominal significance (p<0.05), across all time points measured. This more subtle difference in DEGs was not surprising given the relatively small effect size (β=0.018) for rs10494217 in GWAS (Justice *et al.*, 2019; Pulit *et al.*, 2019). In iWAT of *Tbx15*$^{H156N/H156N}$ mice 90% of genes were downregulated, while in differentiating adipose-progenitor cells ~70% of genes were upregulated indicating

p.H156N acts in a cell-, tissue- and developmental timepoint-specific manner to drive gene expression.

I found an overrepresentation of cytoskeletal protein binding, actin binding, muscle system process and muscle structure development terms for genes *downregulated* in *Tbx15*$^{H156N/H156N}$ iWAT that were *upregulated* in *Tbx15*$^{-/-}$ iWAT, for example *Actc1, Actn3, Myl1, Myl2, Myl3 and Myh2.* Several of these genes, amongst others, have previously been implicated in spontaneous development of beating myocyte-like cells in SVF cells isolated from iWAT (Takashima *et al.*, 2021). Further, *Actn3* is a key components of skeletal muscle fibres and several *Actn3*-knockout mouse models exhibited less lean mass, specifically decreased muscle tissue weights, than their wildtype littermates (Macarthur *et al.*, 2008; Houweling *et al.*, 2017).

Additionally, tropomyosin-1α, tropomyosin-β, myosin light chain (MYL)-2, MYL-3, and parvalbumin-α were negatively regulated by PPARα in BAT (Tong *et al.*, 2005). These proteins had previously been implicated in cytoskeletal structure, microtubule formation and cell adhesion which are known to impact adipogenesis, therefore, the authors hypothesised that PPARα may play an important role in tissue integrity through mediation of these cytoskeletal and muscle proteins (Tong *et al.*, 2005). Indeed, cytoskeletal remodelling of components such as α-tubulin spindles required to enable lipid droplet accumulation of triacylglycerides during differentiation into mature adipocytes (Yang *et al.*, 2013; Hansson *et al.*, 2019). Whilst it was not possible to investigate direct underlying mechanisms for these gene expression changes in *Tbx15*$^{H156N/H156N}$ tissues, it would be beneficial to analyse adipocyte cell size in *Tbx15*^{H156N} metabolic phenotyping cohorts to confirm whether p.H156N altered adipocyte structure leading to decreased fat mass in *Tbx15*$^{H156N/H156N}$ mice.

In contrast to *Tbx15*$^{H156N/H156N}$ tissues, the majority of genes were *upregulated* in differentiating adipose progenitor cells, and these were enriched for immune and cytokine receptor signalling, which was more in line with enriched terms from *downregulated* genes in *Tbx15*$^{-/-}$ iWAT. One question that arises from these comparisons was why were there differences in DEGs and enriched terms between the *Tbx15*$^{H156N/H156N}$ iWAT and differentiating adipose progenitor cells? The most likely explanation is that mature adipose tissues consist of a heterogeneous mixture of cell types including adipocytes, precursor cells, immune cells, smooth muscle and vasculature cells. In contrast, SVF-derived adipose progenitor cells are a more homogenous population of cells induced to differentiate along the adipocyte lineage. Another explanation could be the influence of extracellular stimuli resulting from *in vitro* culture on plastic cultureware which could have altered ECM remodelling and induced stress in adipocytes resulting in dysregulated gene expression and lipid accumulation. Therefore, it would be beneficial to utilise 3D models of adipocyte cell cultures to assess gene expression in an environment more similar to *in vivo* adipose tissues (Graham *et al.*, 2019).

An alternative explanation is that p.H156N acts in a cell-specific manner to perturb the TBX15 network, and given the more subtle gene expression differences, it is possible that detection of more common genes between tissues and differentiating adipose progenitor cells was confounded by biological or experimental variation in RNA-sequencing, resulting in significance values that did not meet the required threshold to be classified as significant. Therefore, further work is underway to assess gene expression trends and directions between the *Tbx15* alleles that may consolidate these findings. In this regard, adipose progenitor cell models from *Tbx15*$^{-/-}$ mice may

prove a more accurate comparison for the differentiating adipose progenitor cells from *Tbx15*$^{H156N/H156N}$ mice.

As we did not assess gene expression in muscle tissues or in *Tbx15*$^{+/H156N}$ mice, it is difficult to draw conclusions from this data that might explain the higher lean mass phenotype seen in *Tbx15*$^{+/H156N}$ mice. However, it is interesting to speculate that heterozygous p.H156N TF complexes act in a gain-of-function fashion to alter recognition of, or affinity to, target genes resulting in dysregulated cytoskeletal and muscle gene expression in alternative tissues such as skeletal muscle. This could occur through alterations in the probability of MSCs differentiating into adipose and muscle lineages, although further experiments would be required to assess gene expression in across several developmental time points and tissues.

In conclusion, I have shown the p.H156N polymorphism perturbed the TBX15 regulatory network in adipose tissues to downregulate expression of genes enriched for cytoskeletal and muscle system processes. Primary cell culture work also supported a role for TBX15 in regulating immune signals from differentiating adipose progenitor cells. Overall, these data suggest *Tbx15* may have distinct regulatory roles during adipogenesis and in mature adipose tissues, although further work is needed to clarify this. Further prioritisation analysis is ongoing, in collaboration with Dr. Michelle Simon, to identify potential mechanisms of action for the p.H156N polymorphism in relation to altered WHRadjBMI and body composition phenotypes. This will then be used to inform functional validation experiments such as assessing the differentiation capacity of SVF-derived progenitor cells isolated from iWAT of *Tbx15*$^{-/-}$ and *Tbx15*$^{H156N/H156N}$ mice into osteoblast, adipocyte and myocyte lineages to determine whether TBX15 regulates this process. Finally, these data demonstrate opposite

patterns of transcriptional regulation by the two alleles of TBX15 examined in this and the preceding chapter, supporting functional consequences for the p.H156N polymorphism that may act to result in organismal body composition changes over a lifetime.

7

General discussion and future perspectives

7.1. Summary

One of the main aims of this thesis was to characterise potential mechanisms of action of two *TBX15*-coding SNPs associated with WHRadjBMI, rs10494217 and rs61730011, encoding non-synonymous amino acid substitutions p.H156N and p.M566R, respectively. This work focused on the role of these SNPs in modulating adipose tissue biology associated with altered fat distribution. Using a combination of *in silico, in vitro* and *in vivo* models, I demonstrated a functional protein-coding role for p.H156N and showed the $Tbx15^{+/-}$, $Tbx15^{H156N}$ and $Tbx15^{M566R}$ alleles altered body composition.

In a second major aim, I investigated the TBX15 regulatory network using *in vitro* and *in vivo* models. I generated a comprehensive and unbiased regulatory network for TBX15 and showed that p.H156N perturbed this network. Together, this work provides an insight into potential regulatory mechanisms of TBX15 in adipose tissues and provides the basis for further work to elucidate a mechanism of action for TBX15.

7.2. Dissecting the functional role of polymorphisms within complex WHRadjBMI loci

GWAS have highlighted the complexity of genetic associations with a range of disease risk traits. For example, 463 independent SNPs associated with WHRadjBMI accounted for less than 4% of body fat distribution variation (Pulit *et al.*, 2019). This was substantially lower than the ~60% heritability estimated from twin studies for WHRadjBMI (Zillikens *et al.*, 2008; Schleinitz *et al.*, 2014). This *missing heritability* could result from several factors such as small effect sizes of individual SNPs, epigenetic interactions, or GWAS methodology limitations. For example, SNPs are thought to act collectively to influence trait associations. However, co-occurrence of SNPs, or indeed haplotypes, could act agonistically or antagonistically between individuals (depending on heritability patterns) to regulate epistasis and gene regulatory networks which may confound more subtle trait associations (Sandoval-Motta *et al.*, 2017).

Further, GWAS-arrays and imputation methods may fail to capture all SNPs within the genome, particularly rare variants with larger effect sizes (Yang *et al.*, 2010, 2015, 2017; Wray *et al.*, 2013). The recently completed telomere-to-telomere human genome (Aganezov *et al.*, 2022; Nurk *et al.*, 2022), combined with increased sample sizes, will likely improve the detection of causal variants associated with complex traits. Finally, environmental influences such as diet and disease status are heterogeneous between individuals, with our microbiomes suggested to play a key role in regulating SNP-trait associations (Sandoval-Motta *et al.*, 2017). Despite this, some GWAS have proved more successful in explaining the underlying variance of disease-variant associations, for example 18% of variance in T2DM risk was explained using polygenic risk scoring

(Mahajan *et al.*, 2018). This highlights the value of identifying loci associated with body fat distribution that can aid our understanding of pathways associated with adipose biology and provide potential options for therapeutic targeting.

Additionally, individual loci can have added levels of complexity. For example, the *TBX15-WARS2* and *HOXC* loci harboured four and three independent WHRadjBMI SNPs, respectively, suggesting they may act through different mechanisms to drive WHR-associated phenotypes (Shungin *et al.*, 2015). Given the relatively modest effect size of many of these variants, is it clear that that they do not act in isolation, rather having an additive effect to influence genetic predisposition for cardiometabolic diseases. In fact, even in seemingly simple loci associated with given traits, it is becoming clear that additional variants within a locus may be associated with the trait either acting independently or in concert (Cano-Gamez and Trynka, 2020).

Multiple factors must be considered when attempting to interpret SNP-trait associations, including identifying causal variants, gene targets and true pathophysiological cells and/or tissues. For example, fine-mapping performed in the *TBX15-WARS2* locus for the association region identified by Heid *et al.* (2010) predicted rs984222 as the most likely to be functional (Liu *et al.*, 2014). Epigenetics data, such as the NIH Roadmap epigenomics mapping consortium, can also be leveraged to examine enrichment of these SNPs in a range of samples to identify disease-relevant tissues for further investigation, e.g., rs984222 located within an adipocyte enhancer (Liu *et al.*, 2014; Roadmap Epigenomics Consortium *et al.*, 2015). Further, co-localisation and eQTL analysis can be used to determine candidate target genes regulated by these identified SNPs; with web portals such as GTEx providing this data in an easily accessible format (Lonsdale *et al.*, 2013). For example, several SNPs

in the *TBX15-WARS2* locus are eQTLs for differential expression of *TBX15* and *WARS2* in several tissues including subcutaneous and visceral adipose tissues (Figure 7.1, Table 7.1). Collectively, this work highlights the need for, and the difficulty of, variant-to-function analyses to dissect the regulatory roles and direct targets of these signals.

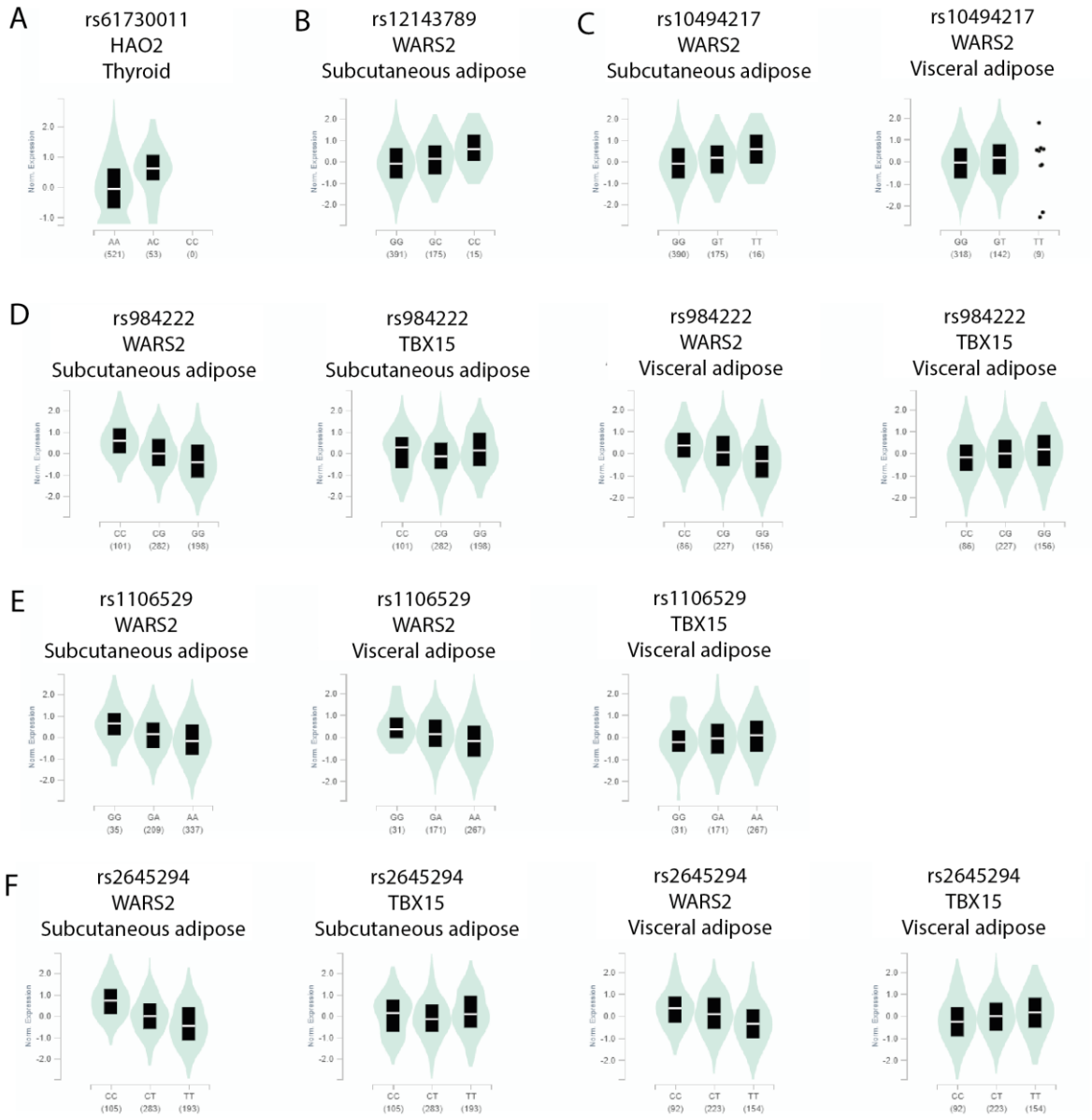

Figure 7.1. *TBX15-WARS2* locus expression quantitative trait loci plots. Representative expression quantitative trait loci plots for WHRadjBMI SNPs in subcutaneous and visceral adipose tissues for *HAO2* (hydroxyacid oxidase 2), *TBX15* (T-box 15) and *WARS2* (tryptophanyl t-RNA synthetase 2) expression. A. rs61730011, B. rs12143789, C. rs10494217, D. rs984222, E. rs1106529 and F. rs2645294. Plots generated from GTEx Portal (Lonsdale *et al.*, 2013).

Table 7.1. *TBX15-WARS2* locus expression quantitative trait loci. Expression quantitative trait loci for WHRadjBMI SNPs in the *TBX15-WARS2* locus. Abbreviations: *HAO2* (hydroxyacid oxidase 2), *TBX15* (T-box 15) and *WARS2* (tryptophanyl t-RNA synthetase 2), SAT (subcutaneous white adipose tissue), VAT (visceral white adipose tissue).

SNP	eQTL	Reference
rs61730011 (p.M566R)	*HAO2* (thyroid)	(Lonsdale *et al.*, 2013)
rs12143789	*WARS2* (adipose, β=0.749, p=6.0E-45)	(Civelek *et al.*, 2017)
	WARS2 (thyroid, SAT, artery, skin, cultured fibroblasts, and mammary tissue) *RP11-418J17.1* (*WARS2-AS1*) (skin, oesophagus, thyroid)	(Lonsdale *et al.*, 2013)
rs10494217 (p.H156N)	*WARS2* (VAT, SAT, skeletal muscle and pancreas tissues, β= 0.749, p=6.03E-45)	(Justice *et al.*, 2019)
	WARS2 (thyroid, SAT, artery, skin, cultured fibroblasts, and mammary tissue) *RP11-418J17.1* (*WARS2-AS1*) (skin, oesophagus, thyroid)	(Lonsdale *et al.*, 2013)
rs1106529	*WARS2* (adipose β=-0.559, p= 9.1E-12)	(Civelek *et al.*, 2017)
	TBX15 (VAT β=0.20, p=2.2E-06) *WARS2* (VAT β=-0.31, p=2.9E-11; SAT β=-0.41, p=2.9E-18)	(Lonsdale *et al.*, 2013)
	RP4-712E4.1 (SAT, artery, and testis) *WARS2* (muscle, skin, oesophagus, SAT, cultured fibroblasts, skin, thyroid)	(Lonsdale *et al.*, 2013)
rs984222	*TBX15* (VAT p=7.90E−10) *WARS2* (VAT p=5.11E-36; SAT p=1.67E-25)	(Heid *et al.*, 2010)
	TBX15 (adipose β=0.274, p= 3.5E-06) *WARS2* (adipose β=-0.644, p= 4.5E-29)	(Civelek *et al.*, 2017)
	WARS2 (muscle, skin, SAT, artery, thyroid, nerve, cultured fibroblasts, oesophagus, and lung)	(Lonsdale *et al.*, 2013)
rs2645294	*TBX15* (adipose β=0.302, p= 1.1E-07)	(Civelek *et al.*, 2017)
	WARS2 (muscle, skin, SAT, artery, nerve, thyroid, cultured fibroblasts, oesophagus, and lung)	(Lonsdale *et al.*, 2013)

7.3. *In silico* prioritisation of DNA-regulatory or protein-coding mechanisms of potential effector SNPs in the *TBX15-WARS2* locus

Prior work in the Cox lab has focused on variant-to-function analyses in loci associated with BMI (*FTO* (Laber, 2017; Laber *et al.*, 2021)), T2DM (*ARL15* (Bai, 2019)) and WHRadjBMI (*VEGFA, C5orf67, EMILIN2* and *TBX15-WARS2* (Mušo, 2019; Mušo *et al.*, 2020)). These studies provided novel insights into potential regulatory mechanisms, and causal pathways, of these association signals.

No prioritisation method is without significant limitations, highlighting a need for a multifaceted approach to prioritise regulatory variants, particularly in complex loci such as *TBX15-WARS2*. Using PPA and epi-PMCA, performed by our collaborators Dr. Sara Pulit and Nasa Sinnott-Armstrong, was fundamental in prioritising the 61 *TBX15-WARS2* locus SNPs for functional analyses. The coding SNP rs10494217 in *TBX15* was ranked as the highest potentially functional variant in epi-PMCA. Further, electromobility shift assay (EMSA) screens indicated altered TF binding patterns with reference and alternate alleles for several *TBX15-WARS2* locus SNPs, including rs10494217 (unpublished data, Dr. Rebecca Dumbell and Dr. Milan Mušo). Further, work in the Cox group identified that rs984222 is within a strong enhancer cluster specifically in mesenchymal cells, and we have validated its altered enhancer activity using *in vitro* reporter assays (Dumbell *et al.,* in preparation). Together, this work suggested that several causal variants may be conferring different effects that contribute to the association, potentially also acting in cell lineages derived from MSCs such as adipocytes and myocytes, to drive WHRadjBMI phenotypes in the population.

Whilst Bayesian methods are generally powerful tools, PPA has an underlying assumption that a single signal in a locus is causative of the associated phenotype (Maller *et al.*, 2012). For example, in loci such as *VEGFA, C5orf67* and *EMILIN2,* a single signal accounted for over 95% of WHRadjBMI association (Shungin *et al.*, 2015); these SNPs scored ≥0.95, close to the maximum score of 1, using PPA (unpublished data, Dr. Sara Pulit). Conversely, the highest score in the *TBX15-WARS2* locus was 0.68 (rs12731372; GIANT dataset) with many SNPs scoring ≤0.1. It is likely that the complex nature of the locus, with four independent index SNPs, limited the prediction ability of this approach. Further, the main analysis component of epi-PMCA assessed the level of conservation between species for cis-regulatory motifs (CRMs), i.e. clusters of TF

binding sites (TFBS) (Claussnitzer *et al.*, 2014). The *TBX15-WARS2* locus SNPs were ranked for predicted functionality based on the average number of conserved TFBS in CRMs. The protein-coding region of TBX15 was highly conserved between species, particularly in the T-box region surrounding rs10494217, which may have artificially inflated the ranking of this SNP despite minimal scores for other regulatory effects such as TF binding and accessibility.

Based on these analyses, an initial aim of my thesis was to prioritise the most likely mechanistic action of rs10494217 and rs61730011 that would explain the WHRadjBMI associations. As rs61730011 was not included in either bioinformatics prioritisation or EMSA screens and given the higher effect size for this variant compared to rs10494217, I hypothesised that the coding SNPs acted in an allelic series of severity at i) a DNA-regulatory level to alter binding of TFs associated with adipogenesis, and/or ii) a protein-coding level to alter TBX15 TF function and regulation of genes associated with adipogenesis. Using a combination of *in silico* approaches I predicted the most likely functional role for the p.H156N substitution, encoded by rs10494217, was through alteration of a loop structure within the T-box of TBX15 and further implicated this in altered protein dimerisation. However, these findings were not recapitulated in either protein-dimer or DNA binding experiments *in vitro*. Given the relatively small effect sizes of these coding SNPs, it is reasonable to assume that if binding affinity of protein dimers is affected by these SNPs that this difference will also be at a relatively subtle magnitude, therefore methodological limitations may have hampered detection of these subtle differences (described in detail in chapter 3). It is also apt to consider that alternative aspects of protein-binding may have been impacted by coding SNP substitutions, such as dimer conformation or DNA sequence recognition which would require further validation *in vitro.*

For coding variants, it remains to be seen how well predictive tools can identify functionality. It would be beneficial to prioritise the functionality of all variants associated with WHRadjBMI in the *TBX15-WARS2* locus, in promoter/enhancer assays to aid selection of variants for follow-up analysis. For example, massively-parallel luciferase reporter assays (combined with high-throughput sequencing) allow for simultaneous screening of thousands of variants *in vitro* (Kircher *et al.*, 2019). Further, these methods have been developed for *in vivo* analysis using Cre-drivers for cell-type specific interrogation of non-coding variants, for example in cortical neurons (Lagunas *et al.*, 2021). Indeed, induced pluripotent stem cell (iPSC) models may also prove useful to dissect cell-specific regulatory mechanisms of these variants, which could be edited using CRISPR technologies. In future, a similar approach could be developed for adipocyte-specific expression regulated by variants associated with WHRadjBMI to determine the regulatory effects on target genes of these SNPs.

Given the relatively small effect sizes for the *TBX15*-coding SNPs, there is a need to further assess the potential interacting regulatory and protein-coding effects of SNPs within the *TBX15-WARS2* locus and quantify expression of *cis*- and *trans*- target genes that drive the WHRadjBMI associations. Integrating several SNPs into a model to investigate their additive effects will likely produce better predictions of SNP functionality with a focus on risk haplotypes. Further, implementing a robust prioritisation and validation strategy to determine likely causal SNPs and potential mechanisms of action *in vitro,* such as those undertaken in our *TBX15-WARS2* locus work, will ensure the correct variants are translated into *in vivo* models (Figure 7.2).

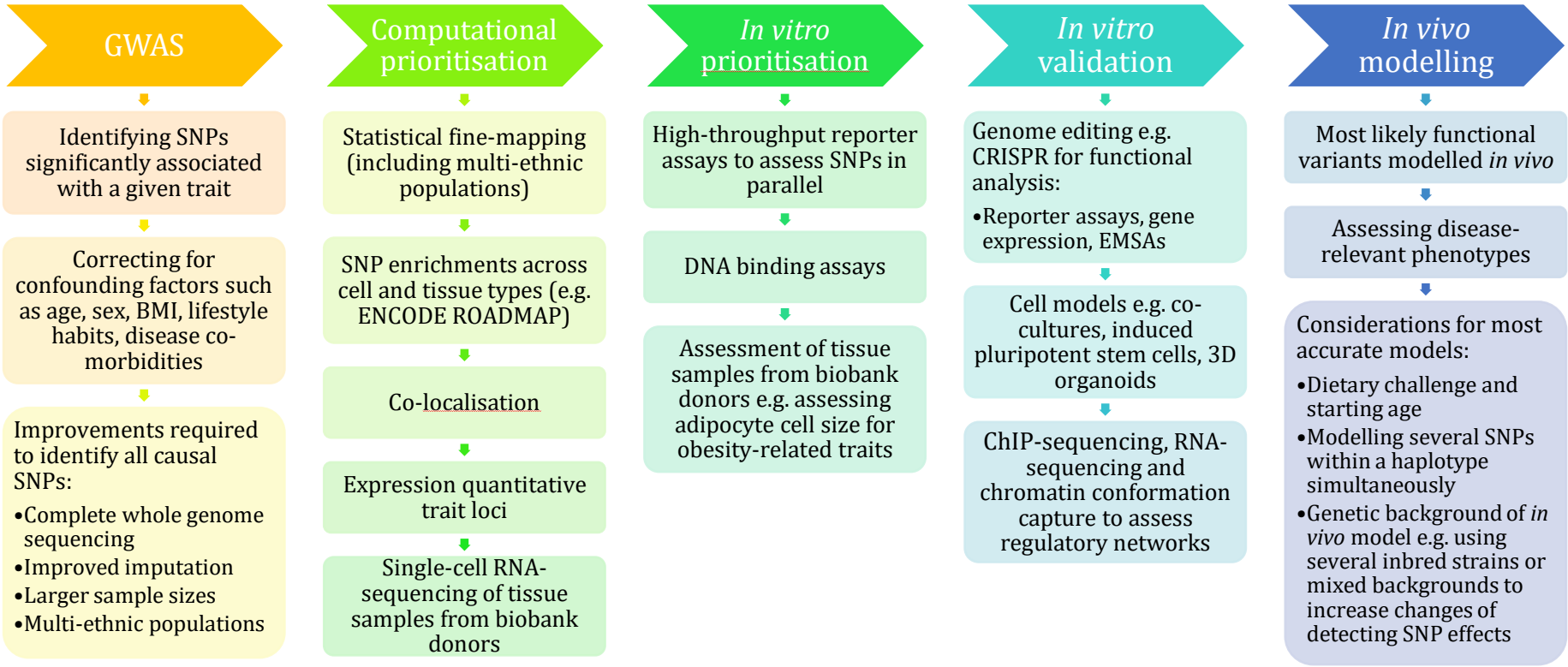

Figure 7.2. Proposed variant to function approach to prioritise multiple SNPs associated with complex traits.

7.4. Modelling WHR and metabolic phenotypes associated with *Tbx15* alleles *in vivo*

The human Cousin Syndrome results from homozygous *TBX15* mutations that cause truncation of the C-terminal domain (Lausch *et al.*, 2008; Dikoglu *et al.*, 2013). Given only five cases have been recorded worldwide, it suggests these mutations are largely incompatible with life. This was reflected in poor viability of $Tbx15^{-/-}$ mice in my work and others (Curry, 1959; Candille *et al.*, 2004). As expected, $Tbx15^{+/-}$, $Tbx15^{H156N}$ and $Tbx15^{M566R}$ were all viable post-weaning, indicative of the subtle associations at the population level detected for rs10494217 and rs61730011 in human GWAS studies.

Tbx15 has been implicated in regulating body composition *in vivo*, both in global $Tbx15^{+/-}$ (increased total fat mass on chow diet) (Lee *et al.*, 2015), and adipocyte-specific knockout (increased bodyweight and total fat mass on HFD) mice (Sun *et al.*, 2019). Therefore, we hypothesised that mouse models of p.H156N and p.M566R would exhibit body composition phenotypes in line with WHRadjBMI associations, and in an allelic series of severity compared to $Tbx15^{+/-}$ mice. I showed that $Tbx15^{+/-}$, $Tbx15^{H156N/H156N}$ and $Tbx15^{M566R/M566R}$ had significantly less fat mass than their respective littermates, albeit to varying degrees, with $Tbx15^{+/H156N}$ mice further showing a strikingly higher lean mass compared to $Tbx15^{+/+}$ littermates.

Several factors, including differences in genetic background and diet composition, may have influenced the differences in phenotypes observed in my studies and those performed by Lee *et al.* (2015) and Sun *et al.* (2019) (discussed in detail in chapter 4). These factors, and others, must be considered when using mice to model human phenotypes. Firstly, genetic architecture plays an important role in gene regulation, in the case of the *TBX15-WARS2* locus there appears to be a high degree of conservation

in topologically associated domian architecture between human and mouse (Figure 7.3). Despite this, non-coding regions of the regulatory genome are poorly conserved, with ≤25% of CRMs being bound by the same TF between species (Denas *et al.*, 2015; Powell *et al.*, 2022).

However, as rs10494217 and rs61730011 may not be the primary effector SNPs in the locus this should not detract from using mice to model human phenotypes. Rather, it is pertinent to consider the overall parallels between species when modelling WHR-related traits as there is strong evidence to support a role for both *TBX15* and *WARS2* expression in differential body composition and adipose tissue browning. As such, parallels can be drawn from the *Tbx15* models assessed in this thesis which all exhibited adipose tissue phenotypes relevant to human WHRadjBMI GWAS associations. Further, it is important to consider the relative scale of any metabolic differences resulting from variants modelled in mice, rather than the direction of change, particularly when trying to assess whether SNPs with small effect sizes are functional in the context of human traits and/or diseases.

It is also necessary to appreciate the differences in adipose depots between humans and mice. Whilst gWAT and iWAT in mice are commonly regarded as equivalent to human VAT and SAT, cited for ease of dissection and comparable roles in metabolism, their anatomical locations differ between species. Further, combined gWAT and iWAT mass accounts for ~20-25% of total fat mass in female and male wildtype C57BL/6 mice at six months of age (calculated from *Tbx15*$^{+/+}$ data) which is comparably less than dermal WAT (dWAT) which accounted for almost half of the total fat mass in C57BL/6 mice (Kasza *et al.*, 2016).

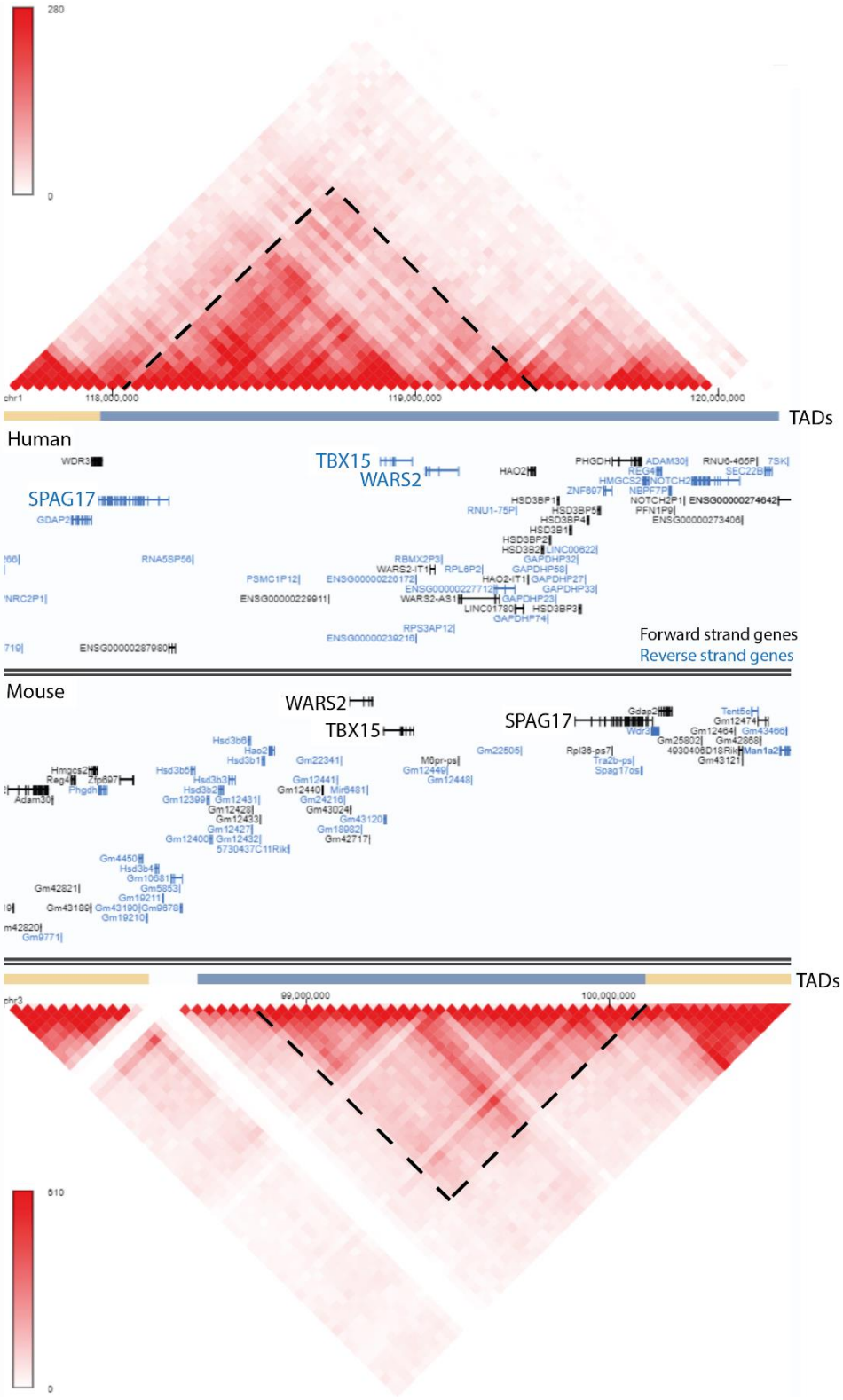

Figure 7.3. Topologically associated domain (TAD) architecture for human and mouse *TBX15-WARS2* locus. The 3D genome browser (http://3dgenome.fsm.northwestern.edu/index.html) was used to visualise Hi-C data showing TADs in the human and mouse genomes (Wang *et al.*, 2018). For compare Hi-C, human (Dataset type: Hi-C; Species: human, assembly: hg38; tissue: H1-MSC (Dixon_2015-raw); resolution: 40kb (Dixon *et al.*, 2015)) and mouse (Dataset type: Hi-C; Species: mouse, assembly: mm10; tissue: mESC (Bonev_2017-raw); resolution: 40kb (Bonev *et al.*, 2017)) publicly available datasets were used to view regions around the *TBX15-WARS2* locus. The black dashed line denotes sub-TADs, black genes (forward strand) and blue genes (reverse strand).

Further, a common proxy for WHR in mice is gWAT:iWAT ratio which was decreased in lipodystrophy mouse models harbouring *Pparg* mutations (Gray *et al.*, 2006) and increased in *Wars2*$^{V117L/V117L}$ mice resistant to fat mass gain (Mušo *et al.*, 2022). It has been reported that reduced visceral fat (specifically omental and mesenteric, rather than gonadal WAT) (Foster *et al.*, 2011), and transplantation of iWAT into visceral regions (Tran *et al.*, 2008) improved fat accumulation, glucose sensitivity and adipokine expression in mice, supporting conservation of adverse metabolic effects through VAT expansion. Therefore, it may be useful to additionally assess mWAT:iWAT ratios as a WHR-equivalent, as mWAT is more physiologically comparable to human VAT (Tchoukalova *et al.*, 2010; Tchkonia *et al.*, 2013).

Finally, BAT is an important metabolic tissue, with *Tbx15* implicated in browning of adipocytes, through direct regulation of the key browning factor *Prdm16* (Gburcik *et al.*, 2012; Sun *et al.*, 2019). PET scanning has identified distinct supraclavicular, neck and paravertebral BAT depots in humans. The main interscapular BAT isolated from mice housed under thermoneutral conditions and fed "humanised" high-fat high-sugar diets closely resembled morphological and gene expression signatures of human supraclavicular BAT (de Jong *et al.*, 2019). Further, several reports have indicated an inverse correlation between BAT and obesity, WHR and T2DM (Cypess *et al.*, 2009; Giralt and Villarroya, 2013; Wibmer *et al.*, 2021), suggesting adipose tissues have distinct properties that influence metabolism at a physiological level. Therefore, future studies in both human and rodent models should focus on characterising a broader selection of adipose depots to truly understand their regulatory effects on whole-body metabolism and fat distribution phenotypes. Further, this highlights BAT as a promising therapeutic target for obesity that can be easily modelled *in vivo.*

Data presented in chapter 4, together with previous work in the Cox group (Agnew *et al.*, 2018; Mušo *et al.*, 2022), suggest the *TBX15-WARS2* locus contains genes that are functionally important for adipose tissue biology. However, one major question that remains to be answered is why the *Tbx15*$^{+/H156N}$, but not the *Tbx15*$^{H156N/H156N}$, mice exhibited a lean mass phenotype? Based on my *in silico* dimer modelling, I hypothesised that p.H156N may act through different mechanisms in heterozygous or homozygous dimers. In other words, in a heterodimer a p.H156N subunit titrates a wildtype TBX15 subunit, and/or accessory TFs, altering its function to drive a gene expression pattern that leads to the lean mass phenotype. Whilst a p.H156N homodimer is unable to recognise and/or bind to its target DNA sequences, therefore an alternative TF complex binds these regulatory sequences and attempts to compensate the regulatory network.

Indeed, such non-functional dimers have been reported previously. For example, a heterozygous paired-like homeodomain 2 (PITX2) p.K88E substitution bound wild-type PITX2 subunits five times more strongly than two wildtype PITX2 subunits, resulting in impaired DNA binding in p.K88E heterodimers *in vitro* (Saadi *et al.*, 2003). Further, mice harbouring a heterozygous growth differentiation factor 5 (GDF5) p.W408R substitution (*Gdf5*$^{+/W408R}$) had a similar loss-of-function phenotype to homozygous knock-out mice (*Gdf5*$^{-/-}$), while homozygous p.W408R (*Gdf5*$^{W408R/W408R}$) mice had a more severe joint abnormality phenotype (Masuya *et al.*, 2007). The authors speculated that p.W408R acted in a dominant-negative mechanism in heterozygote dimers to inhibit wildtype GDF5 action, but that homozygous p.W408R acted through alternative mechanisms (Masuya *et al.*, 2007). This would support my hypothesis, partly based on *in silico* structural modelling and dimerisation results, that p.H156N acts via alternate mechanisms in heterozygous and homozygous TBX15

protein complexes to regulate TF function. In fact, dominant-negative and gain-of-function mutations were predicted to result in more subtle structural changes than loss-of-function mutations which can result in more stable protein complexes (Witham *et al.*, 2011; Gerasimavicius, Livesey and Marsh, 2022). Therefore, it is conceivable that a single p.H156N results in more stable TBX15 homodimers and TBX18 heterodimers that act in a gain-of-function manner to increase lean mass in *Tbx15*$^{+/H156N}$ mice, whilst acting through an alternative mechanism in *Tbx15*$^{H156N/H156N}$ mice to drive the reduced fat mass.

I have shown the *Tbx15*$^{+/-}$, *Tbx15*^{H156N} and *Tbx15*^{M566R} alleles were all functional and generally showed resistance to fat mass-gain in contrast to previously published data for *Tbx15*-knockout models. These observed discrepancies could be explained by, in part, the predicted gain-of-function activity of the p.H156N polymorphism. Further, the minor allele of both rs10494217 (p.H156N) and rs61730011 (p.M566R) exhibit directionally opposite associations with WHRadjBMI, suggesting the p.M566R variant could act through loss-of-function mechanisms. This brings into focus the need for more robust testing and reporting of mouse phenotyping studies. For example, careful consideration of when to start diet challenge (at weaning or later in life), which background strain to use, use of appropriate controls, and which tissues and developmental time points to assess will ensure greater accuracy and reproducibility of data when using mice to model human variants in metabolic research.

7.4.1. TBX15 regulatory network

At the outset of my DPhil, there was limited information on the TBX15 regulatory network. Data suggested TBX15 regulated adipogenesis and browning of adipocytes,

myotube formation, and oxidative/glycolytic signalling (Gesta *et al.*, 2011; Gburcik *et al.*, 2012; Lee *et al.*, 2015, 2017; Sun *et al.*, 2019). However, adipogenesis studies were contradictory, with both TBX15-overexpression and *Tbx15*-knockdown inhibiting key adipogenesis genes such as *Pparg, Cebpb* and *Fabp4.* More recently, TBX15 was implicated as a master TF regulating a co-expression network of GWAS obesity genes such as *PPARG, ADIPOQ* and *KLF15* (Pan *et al.*, 2021).

Considering these targeted approaches, I aimed to provide an unbiased TBX15 target-binding and gene-regulatory network in preadipocytes, WAT and BAT using ChIP-sequencing and RNA-sequencing. I hypothesised that TBX15 regulated genes associated with adipogenesis to alter adipose tissue expansion, and that p.H156N perturbed this to cause changes in fat distribution and WHRadjBMI associations. Collectively, my data highlighted a potential pleiotropic role for TBX15 in regulating adipogenesis, lineage determination and immune regulation, and further provided insights into the implications of the p.H156N polymorphism in a comprehensive and unbiased approach (Figure 7.4).

We faced two major challenges in analysing these large amounts of data, across two ChIP-sequencing and three RNA-sequencing experiments. Firstly, choosing the most appropriate comparisons to make between datasets, and secondly, how to interpret these comparisons whilst considering the caveats from using different model systems in each approach. For example, different models were used for ChIP-sequencing (TBX15-overexpression in undifferentiated 3T3-L1 and hWAT cells) and RNA-sequencing (whole iWAT and BAT, and differentiating iWAT-derived SVF cells), hindering direct comparisons between data sets.

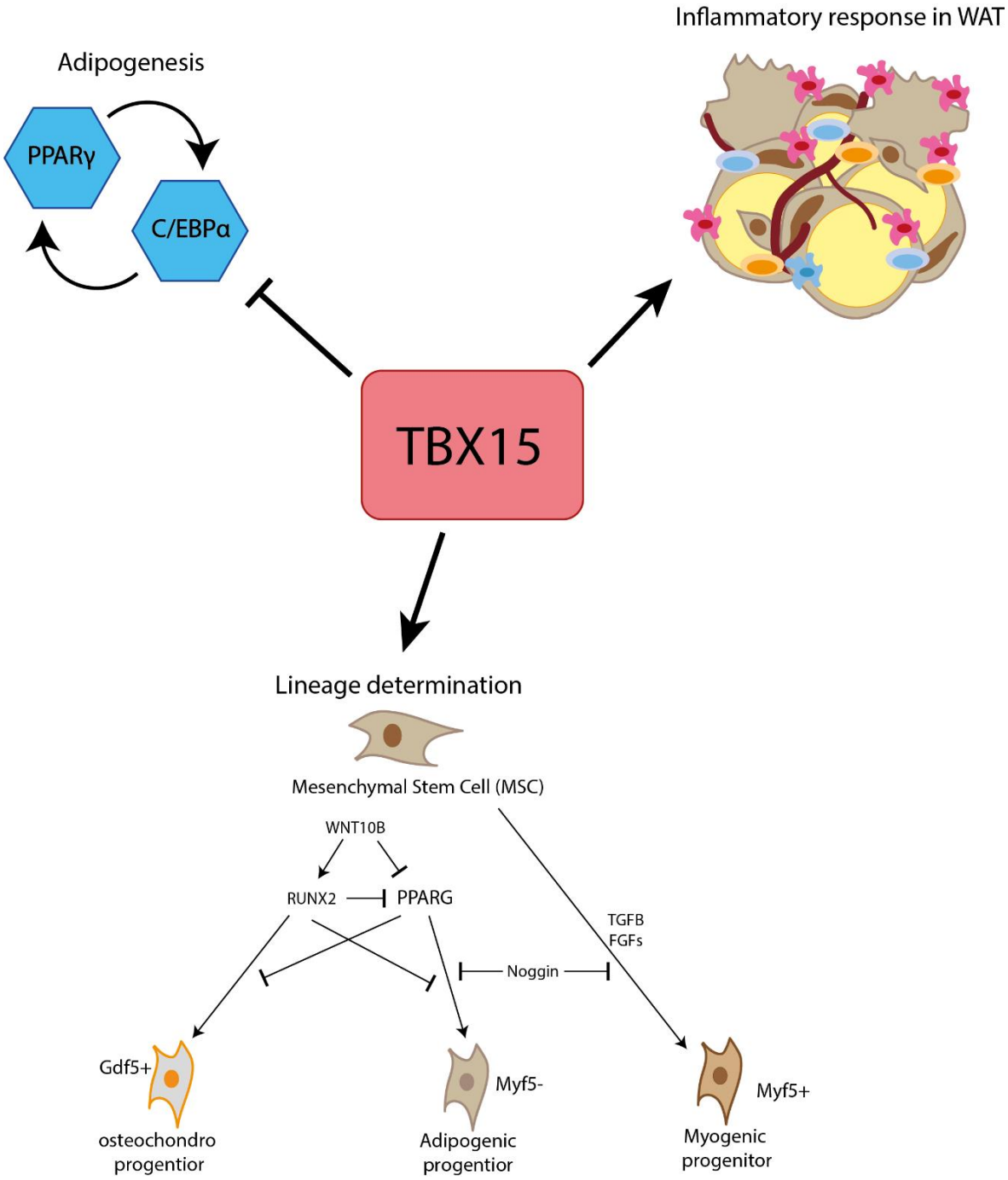

Figure 7.4. Potential transcription factor role for TBX15 in adipose tissues. Based on ChIP-sequencing and RNA-sequencing data analysis, TBX15 bound to and directly regulated expression of several key transcription factors involved in mesenchymal stem cell differentiation, and further was implicated in negative regulation of adipogenesis both *in vitro* and *in vivo*. In white adipose tissues, TBX15 regulated immune response signalling, suggesting this could drive inflammatory profiles associated with obesity and altered metabolic profiles.

A further caveat of these comparisons was the comparison between ChIP-sequencing binding peaks detected in human and mouse preadipocyte cells as differential epigenetic regulation may result in different in downstream targets of TBX15 between species. Utilising humanised models, such as (iPSCs) programmed to differentiate into white or brown adipocytes, may provide a more comparable dataset for the hWAT ChIP-sequencing data in the context of human phenotypes (Mohsen-Kanson *et al.*, 2014). Such an approach was elegantly applied to characterise the effects of *CELSR2*-rs12740374 (G>T) in iPSCs differentiated into either adipocytes or hepatocytes from a cohort of 34 donors carrying either SNP allele (Warren *et al.*, 2017). In GWAS, the minor allele of rs12740374 was associated with increased hepatic *SORT1, PSRC1* and *CELSR2* expression, and reduced risk of myocardial infarction. The authors confirmed increased expression of *SORT1, PSRC1* and *CELSR2,* and further identified novel *trans*-eQTLs, in iPSCs differentiated into hepatocytes, but not adipocytes, from minor allele-carrying donors (Warren *et al.*, 2017). This suggests statistically significant effects can be detected with enough power, even in small cohort sizes from GWAS participants, and thus provides a useful tool for future variant-to-function analyses.

In my initial *in silico* prioritisation work, both coding SNPs overlapped a strong transcriptional transition/elongation region in skeletal muscle myoblast cells. When considered with the pleiotropic effects seen in the different cell and tissue models used to evaluate the TBX15 regulatory network, this suggested that TBX15 may act in a tissue/cell-specific manner, and that coding SNPs may perturb this regulatory network to drive the WHRadjBMI associations detected in GWAS. This also brings into focus the need to further investigate the TBX15 regulatory network in alternate tissues, and time

points of differentiation of different cell lineages, to truly understand the role of this TF in regulating body composition phenotypes.

7.5. Future perspectives

Further investigations are required to unravel the exact mechanisms of TBX15, and the p.H156N and p.M566R coding polymorphisms, on adipogenesis and overall body composition in relation to WHRadjBMI. Firstly, improved detection methods are required to assess TBX15 protein-protein and protein-DNA binding *in vitro.* Further, it would prove beneficial to assess other metabolic phenotypes in *Tbx15* mouse models for example, browning and thermogenesis, lipogenesis and brain-signalling pathways that would be relevant to understanding human body composition, and may highlight potential therapeutic targets. Finally, completing adipocyte cell size analysis in different tissues, including BAT and liver, could be improved with a recently-developed quantification method for small, multilocular lipid droplets using ImageJ (Tero *et al.*, 2022). This could be compared to adipocyte size in human carriers of the rs10494217 and rs61730011 WHRadjBMI alleles that could inform adipocyte-intrinsic mechanisms regulated by TBX15 related to metabolic health, irrespective of overall adiposity, that may reflect metabolically healthy and unhealthy obesity in humans.

Finally, functional analyses are required to confirm direct mechanisms of action for TBX15 in the proposed regulatory network in adipose tissues. Investigating the lineage determination potential of SVF cells from *Tbx15* mice and iPSCs from human GWAS participants would provide evidence to explain a potential role for TBX15 in regulating lineage determination. Utilisation of single-cell sequencing approaches would also provide insights into specific cell types driving differential gene expression in adipose

tissues. Further, overexpression, silencing-RNA and knockout cell models would allow for quantification of direct gene targets of TBX15 identified in ChIP-sequencing and RNA-sequencing experiments.

7.6. Final impact and conclusions

Obesity is a global health pandemic, and fat distribution, independent of overall adiposity, has long been associated with disease risk. In particular, increased WHR (more visceral adipose accumulation) is associated with an increased risk of T2DM, CVD, osteoarthritis and several forms of cancer (Søgaard *et al.*, 2015; Emdin *et al.*, 2017; Morris, 2017; Tang *et al.*, 2017). A plethora of research has shown that within obese BMI classifications, there are individuals that are considered metabolically healthy obese and metabolically unhealthy obese (Blüher, 2020). This is largely associated with the concept of "safe" lipid storage in which adipose tissue expands through hyperplasia (increased adipocyte numbers), rather than hypertrophy (increased adipocyte cell size) (Ghaben and Scherer, 2019).

GWAS meta-analyses revealed robust replication of signals in the *TBX15-WARS2* locus associated with WHRadjBMI (Heid *et al.*, 2010; Shungin *et al.*, 2015; Justice *et al.*, 2019). Further, both *TBX15* and *WARS2* expression drive WHR-associated gene expression associated with cardiometabolic traits in humans, and have been shown to regulate adipogenesis and thermogenesis, respectively (Gesta *et al.*, 2011; Gburcik *et al.*, 2012; Civelek *et al.*, 2017; Agnew *et al.*, 2018; Mušo *et al.*, 2022). Additionally, a 100 kb haplotype region containing the *TBX15-WARS2* locus was shown to have been introgressed into modern human DNA from archaic populations through natural

positive-selection, suggesting this locus was important for cold-dwelling populations as they migrated out of central Africa (Racimo *et al.*, 2017).

To conclude, I have implicated TBX15 in regulating gene networks relevant to the development and metabolic function of adipose tissue. Functional enrichment analysis indicated TBX15 both binds to and regulates expression of genes integral to lineage determination of MSCs into osteoclasts, adipocytes and myocytes, differentiation of committed preadipocytes into mature adipocytes, and immune response genes associated with adipocyte-immune cell crosstalk. I propose that a combination of these mechanisms drive the altered fat mass phenotypes seen in *Tbx15* allele manipulated mice. Further, I showed the p.H156N polymorphism is functional, affecting both lean mass and fat mass phenotypes *in vivo.* This was predicted to result from altered TBX15 protein structure and protein-protein dimer formation.

Indeed, I showed both rs10494217 and rs61730011 were unlikely to be functional at a DNA-regulatory level. Further, there was a degree of LD between the risk blocks identified by Shungin *et al.* (2015), for example risk block F and G were moderately correlated (r^2=0.43) suggesting these haplotypes may be co-inherited due to biological importance. Together, this highlights the complex architecture of the *TBX15-WARS2* locus driving WHR-associations and suggests these effects are the sum of different signals acting through *TBX15* and *WARS2* as synergistic co-effector genes in a cell-, tissue- and developmental-specific manner to influence adipose tissue biology. Dissecting this locus with further *in vitro* studies will validate these findings and give insights into the complexity of other genome-wide association loci and identify promising targets for obesity treatments in the future.

8

References

Abbott, W.G.H. and Foley, J.E. (1987) 'Comparison of body composition, adipocyte size, and glucose and insulin concentrations in Pima Indian and Caucasian children', *Metabolism: clinical and experimental*, 36(6), pp. 576–579. doi:10.1016/0026-0495(87)90170-3.

Adzhubei, I.A. *et al.* (2010) 'A method and server for predicting damaging missense mutations', *Nature methods*, 7(4), p. 248. doi:10.1038/NMETH0410-248.

Aganezov, S. *et al.* (2022) 'A complete reference genome improves analysis of human genetic variation', *Science*, 376(6588). doi:10.1126/SCIENCE.ABL3533/SUPPL_FILE/SCIENCE.ABL3533_MDAR_REPRODUCIBILITY_CHECKLIST.PDF.

Agha, M. and Agha, R. (2017) 'The rising prevalence of obesity: part A: impact on public health', *International Journal of Surgery. Oncology*, 2(7), p. e17. doi:10.1097/IJ9.0000000000000017.

Agnew, T. *et al.* (2018) 'A Wars2 Mutant Mouse Model Displays OXPHOS Deficiencies and Activation of Tissue-Specific Stress Response Pathways', *Cell Reports*, 25(12), pp. 3315-3328.e6. doi:10.1016/J.CELREP.2018.11.080.

Agrawal, S. *et al.* (2022) 'Inherited basis of visceral, abdominal subcutaneous and gluteofemoral fat depots', *Nature Communications 2022 13:1*, 13(1), pp. 1–17. doi:10.1038/s41467-022-30931-2.

Agulnik, S.I., Papaioannou, V.E. and Silver, L.M. (1998) 'Cloning, mapping, and expression analysis of TBX15, a new member of the T-box gene family', *Genomics*, 51(1), pp. 68–75. doi:10.1006/GENO.1998.5278.

Al-Mansoori, L. *et al.* (2022) 'Role of Inflammatory Cytokines, Growth Factors and Adipokines in Adipogenesis and Insulin Resistance', *Inflammation*, 45(1), p. 31. doi:10.1007/S10753-021-01559-Z.

Alasagheirin, M.H. *et al.* (2011) 'Body mass index misclassification of obesity among community police officers', *AAOHN journal : official journal of the American Association of Occupational Health Nurses*, 59(11), pp. 469–475. doi:10.3928/08910162-20111017-01.

Ali, A.T. *et al.* (2013) 'Adipocyte and adipogenesis', *European Journal of Cell Biology*, 92(6–7), pp. 229–236. doi:10.1016/J.EJCB.2013.06.001.

Anders, S., Pyl, P.T. and Huber, W. (2015) 'HTSeq—a Python framework to work with

high-throughput sequencing data', *Bioinformatics*, 31(2), pp. 166–169. doi:10.1093/BIOINFORMATICS/BTU638.

Andreasson, A. *et al.* (2017) 'Waist/Hip Ratio Better Predicts Development of Severe Liver Disease Within 20 Years Than Body Mass Index: A Population-based Cohort Study', *Clinical Gastroenterology and Hepatology*, 15(8), pp. 1294-1301.e2. doi:10.1016/j.cgh.2017.02.040.

Arner, P. *et al.* (2022) 'Subcutaneous adipose tissue expansion mechanisms are similar in early and late onset overweight/obesity', *International Journal of Obesity 2022 46:6*, 46(6), pp. 1196–1203. doi:10.1038/s41366-022-01102-6.

Arriarán, S. *et al.* (2015) 'Evidences of Basal Lactate Production in the Main White Adipose Tissue Sites of Rats. Effects of Sex and a Cafeteria Diet', *PLoS ONE*, 10(3). doi:10.1371/JOURNAL.PONE.0119572.

Arribas, J. *et al.* (2016) 'NF-κB Mediates the Expression of TBX15 in Cancer Cells', *PLOS ONE*. Edited by J.S. Castresana, 11(6), p. e0157761. doi:10.1371/journal.pone.0157761.

Aschard, H. *et al.* (2015) 'Adjusting for heritable covariates can bias effect estimates in genome-wide association studies', *American journal of human genetics*, 96(2), pp. 329–339. doi:10.1016/J.AJHG.2014.12.021.

Aykul, S. *et al.* (2021) 'Smad2/3 Activation Regulates Smad1/5/8 Signaling via a Negative Feedback Loop to Inhibit 3T3-L1 Adipogenesis', *International journal of molecular sciences*, 22(16). doi:10.3390/IJMS22168472.

Bagchi, D.P. *et al.* (2020) 'Wnt/β-catenin signaling regulates adipose tissue lipogenesis and adipocyte-specific loss is rigorously defended by neighboring stromal-vascular cells', *Molecular metabolism*, 42. doi:10.1016/J.MOLMET.2020.101078.

Bai, Y. (2019) *Characterizing the function of the Arl15 gene and its role in the development of metabolic traits*. University of Oxford.

Banfi, G. *et al.* (2012) 'Metabolic markers in sports medicine', *Advances in clinical chemistry*, 56, pp. 1–54. doi:10.1016/B978-0-12-394317-0.00015-7.

Bekkelund, S.I. and Jorde, R. (2017) 'Creatine kinase in relation to body fat in a Caucasian overweight and obese population', *https://doi.org/10.1080/00365513.2017.1408140*, 78(1–2), pp. 43–48. doi:10.1080/00365513.2017.1408140.

Bentley, D.R. *et al.* (2008) 'Accurate whole human genome sequencing using reversible terminator chemistry', *Nature*, 456(7218), pp. 53–59. doi:10.1038/NATURE07517.

Berhane, F. *et al.* (2015) 'Plasma Lactate Levels Increase during Hyperinsulinemic Euglycemic Clamp and Oral Glucose Tolerance Test', *Journal of Diabetes Research*, 2015. doi:10.1155/2015/102054.

Berndt, S.I. *et al.* (2013) 'Genome-wide meta-analysis identifies 11 new loci for anthropometric traits and provides insights into genetic architecture', *Nature Genetics*, 45(5), pp. 501–512. doi:10.1038/ng.2606.

Betts, M.J. and Russell, R.B. (2003) 'Amino Acid Properties and Consequences of

Substitutions', *Bioinformatics for Geneticists*, pp. 289–316. doi:10.1002/0470867302.CH14.

Billard, A. *et al.* (2012) 'The Allele-Specific Probe and Primer Amplification Assay, a New Real-Time PCR Method for Fine Quantification of Single-Nucleotide Polymorphisms in Pooled DNA', *Applied and Environmental Microbiology*, 78(4), p. 1063. doi:10.1128/AEM.06957-11.

Billings, L.K. and Florez, J.C. (2010) 'The genetics of type 2 diabetes: what have we learned from GWAS?', *Annals of the New York Academy of Sciences*, 1212, pp. 59–77. doi:10.1111/j.1749-6632.2010.05838.x.

Blasco, B.V. *et al.* (2020) 'Obesity and Depression: Its Prevalence and Influence as a Prognostic Factor: A Systematic Review', *Psychiatry Investigation*, 17(8), p. 715. doi:10.30773/PI.2020.0099.

Blüher, M. (2020) 'Metabolically Healthy Obesity', *Endocrine Reviews*, 41(3), pp. 405–420. doi:10.1210/ENDREV/BNAA004.

Bonev, B. *et al.* (2017) 'Multiscale 3D Genome Rewiring during Mouse Neural Development', *Cell*, 171(3), pp. 557-572.e24. doi:10.1016/J.CELL.2017.09.043.

Borghi, C. *et al.* (2014) 'Hyperuricemia and cardiovascular disease risk', *Expert review of cardiovascular therapy*, 12(10), pp. 1219–1225. doi:10.1586/14779072.2014.957675.

Bost, F. *et al.* (2005) 'The role of MAPKs in adipocyte differentiation and obesity', *Biochimie*, 87(1), pp. 51–56. doi:10.1016/J.BIOCHI.2004.10.018.

Brochu, M. *et al.* (2000) 'Visceral adipose tissue is an independent correlate of glucose disposal in older obese postmenopausal women', *The Journal of clinical endocrinology and metabolism*, 85(7), pp. 2378–2384. doi:10.1210/JCEM.85.7.6685.

Brochu, M. *et al.* (2008) 'Contribution of the lean body mass to insulin resistance in postmenopausal women with visceral obesity: a Monet study', *Obesity (Silver Spring, Md.)*, 16(5), pp. 1085–1093. doi:10.1038/OBY.2008.23.

Buchan, D.W.A. and Jones, D.T. (2019) 'The PSIPRED Protein Analysis Workbench: 20 years on', *Nucleic acids research*, 47(W1), pp. W402–W407. doi:10.1093/NAR/GKZ297.

Buesa, R.J. and Peshkov, M. V. (2012) 'How much formalin is enough to fix tissues?', *Annals of diagnostic pathology*, 16(3), pp. 202–209. doi:10.1016/J.ANNDIAGPATH.2011.12.003.

Buniello, A. *et al.* (2019) 'The NHGRI-EBI GWAS Catalog of published genome-wide association studies, targeted arrays and summary statistics 2019', *Nucleic acids research*, 47(D1), pp. D1005–D1012. doi:10.1093/NAR/GKY1120.

Bunnell, K.M. *et al.* (2021) 'Body composition predictors of outcome in patients with COVID-19', *International journal of obesity (2005)*, 45(10), pp. 2238–2243. doi:10.1038/S41366-021-00907-1.

Cameron, A.J. *et al.* (2012) 'The influence of hip circumference on the relationship between abdominal obesity and mortality', *International Journal of Epidemiology*,

41(2), p. 484. doi:10.1093/IJE/DYR198.

Candille, S.I. *et al.* (2004) 'Dorsoventral Patterning of the Mouse Coat by Tbx15', *PLoS Biology*. Edited by Brigid L. M. Hogan, 2(1), p. e3. doi:10.1371/journal.pbio.0020003.

Canela-Xandri, O., Rawlik, K. and Tenesa, A. (2018) 'An atlas of genetic associations in UK Biobank', *Nature Genetics 2018 50:11*, 50(11), pp. 1593–1599. doi:10.1038/s41588-018-0248-z.

Cano-Gamez, E. and Trynka, G. (2020) 'From GWAS to Function: Using Functional Genomics to Identify the Mechanisms Underlying Complex Diseases', *Frontiers in Genetics*, 11, p. 424. doi:10.3389/FGENE.2020.00424/BIBTEX.

Castro-Mondragon, J.A. *et al.* (2022) 'JASPAR 2022: the 9th release of the open-access database of transcription factor binding profiles', *Nucleic Acids Research*, 50(D1), pp. D165–D173. doi:10.1093/NAR/GKAB1113.

Chen, M.-H. and Tong, Q. (2013) 'An update on the regulation of adipogenesis', *Drug Discovery Today: Disease Mechanisms*, 10(1–2), pp. e15–e19. doi:10.1016/J.DDMEC.2013.04.002.

Chen, N. *et al.* (2019) 'The transcription factor NKX1-2 promotes adipogenesis and may contribute to a balance between adipocyte and osteoblast differentiation', *Journal of Biological Chemistry*, 294(48), pp. 18408–18420. doi:10.1074/JBC.RA119.007967.

Chen, Q. *et al.* (2016) 'Fate decision of mesenchymal stem cells: adipocytes or osteoblasts?', *Cell Death & Differentiation 2016 23:7*, 23(7), pp. 1128–1139. doi:10.1038/cdd.2015.168.

Cheng, C.-H. *et al.* (2010) 'Waist-to-hip ratio is a better anthropometric index than body mass index for predicting the risk of type 2 diabetes in Taiwanese population.', *Nutrition research (New York, N.Y.)*, 30(9), pp. 585–93. doi:10.1016/j.nutres.2010.08.007.

Chooi, Y.C., Ding, C. and Magkos, F. (2019) 'The epidemiology of obesity', *Metabolism: Clinical and Experimental*, 92, pp. 6–10. doi:10.1016/J.METABOL.2018.09.005.

Christodoulides, C. *et al.* (2009) 'Adipogenesis and WNT signalling', *Trends in endocrinology and metabolism: TEM*, 20(1), p. 16. doi:10.1016/J.TEM.2008.09.002.

Chung, C.Z., Amikura, K. and Söll, D. (2020) 'Using Genetic Code Expansion for Protein Biochemical Studies', *Frontiers in Bioengineering and Biotechnology*, 8, p. 598577. doi:10.3389/FBIOE.2020.598577.

Church, C. *et al.* (2009) 'A Mouse Model for the Metabolic Effects of the Human Fat Mass and Obesity Associated FTO Gene', *PLoS Genetics*, 5(8), p. 1000599. doi:10.1371/JOURNAL.PGEN.1000599.

Chusyd, D.E. *et al.* (2016) 'Relationships between Rodent White Adipose Fat Pads and Human White Adipose Fat Depots', *Frontiers in Nutrition*, 3, p. 10. doi:10.3389/FNUT.2016.00010/BIBTEX.

Civelek, M. *et al.* (2017) 'Genetic Regulation of Adipose Gene Expression and Cardio-Metabolic Traits', *The American Journal of Human Genetics*, 100(3), pp. 428–443. doi:10.1016/j.ajhg.2017.01.027.

Claussnitzer, M. *et al.* (2014) 'Leveraging cross-species transcription factor binding site patterns: From diabetes risk loci to disease mechanisms', *Cell* [Preprint]. doi:10.1016/j.cell.2013.10.058.

Claussnitzer, M. *et al.* (2015) 'FTO Obesity Variant Circuitry and Adipocyte Browning in Humans', *The New England journal of medicine*, 373(10), pp. 895–907. doi:10.1056/NEJMOA1502214.

Coll, M., Seidman, J.G. and Müller, C.W. (2002) 'Structure of the DNA-bound T-box domain of human TBX3, a transcription factor responsible for ulnar-mammary syndrome', *Structure*, 10(3), pp. 343–356. doi:10.1016/S0969-2126(02)00722-0.

Cooper, G.M. and Shendure, J. (2011) 'Needles in stacks of needles: finding disease-causal variants in a wealth of genomic data', *Nature Reviews Genetics*, 12(9), pp. 628–640. doi:10.1038/nrg3046.

Cousin, J. *et al.* (1982) 'DYSPLASIE PELVI-SCAPULAIRE FAMILIALE AVEC ANOMALIES EPIPHYSAIRES, NANISME ET DYSMORPHIES: UN NOUVEAU SYNDROME?', *Archives Francaises de Pediatrie*, 39(3), pp. 173–178.

Cunningham, F. *et al.* (2022) 'Ensembl 2022', *Nucleic Acids Research*, 50(D1), pp. D988–D995. doi:10.1093/NAR/GKAB1049.

Curry, G.A. (1959) 'Genetical and Developmental Studies on Droopy-eared Mice', *Development*, 7(1).

Cypess, A.M. *et al.* (2009) 'Identification and importance of brown adipose tissue in adult humans', *The New England journal of medicine*, 360(15), pp. 1509–1517. doi:10.1056/NEJMOA0810780.

Cypess, A.M. *et al.* (2013) 'Anatomical localization, gene expression profiling and functional characterization of adult human neck brown fat', *Nature Medicine 2013 19:5*, 19(5), pp. 635–639. doi:10.1038/nm.3112.

Czernichow, S. *et al.* (2011) 'Comparison of waist-to-hip ratio and other obesity indices as predictors of cardiovascular disease risk in people with type-2 diabetes: A prospective cohort study from ADVANCE', *European Journal of Preventive Cardiology*, 18(2), pp. 312–319. doi:10.1097/HJR.0b013e32833c1aa3.

Davis, K.E. *et al.* (2013) 'The sexually dimorphic role of adipose and adipocyte estrogen receptors in modulating adipose tissue expansion, inflammation, and fibrosis', *Molecular Metabolism*, 2(3), pp. 227–242. doi:10.1016/J.MOLMET.2013.05.006.

De, R., Bush, W.S. and Moore, J.H. (2014) 'Bioinformatics Challenges in Genome-Wide Association Studies (GWAS)', in, pp. 63–81. doi:10.1007/978-1-4939-0847-9_5.

DeFronzo, R.A. and Tripathy, D. (2009) 'Skeletal Muscle Insulin Resistance Is the Primary Defect in Type 2 Diabetes', *Diabetes Care*, 32(suppl_2), pp. S157–S163. doi:10.2337/DC09-S302.

Denas, O. *et al.* (2015) 'Genome-wide comparative analysis reveals human-mouse regulatory landscape and evolution', *BMC genomics*, 16(1). doi:10.1186/S12864-015-1245-6.

Dikoglu, E. *et al.* (2013) 'Homozygosity for a novel truncating mutation confirms *TBX15*

deficiency as the cause of Cousin syndrome', *American Journal of Medical Genetics Part A*, 161(12), pp. 3161–3165. doi:10.1002/ajmg.a.36173.

Dixon, J.R. *et al.* (2015) 'Chromatin architecture reorganization during stem cell differentiation', *Nature*, 518(7539), pp. 331–336. doi:10.1038/NATURE14222.

Dommermuth, R. and Ewing, K. (2018) 'Metabolic Syndrome: Systems Thinking in Heart Disease', *Primary Care: Clinics in Office Practice*, 45(1), pp. 109–129. doi:10.1016/J.POP.2017.10.003.

Doran, A.G. *et al.* (2016) 'Deep genome sequencing and variation analysis of 13 inbred mouse strains defines candidate phenotypic alleles, private variation and homozygous truncating mutations', *Genome Biology*, 17(1), pp. 1–16. doi:10.1186/S13059-016-1024-Y/TABLES/4.

Dyer, D.P. *et al.* (2019) 'The chemokine receptor CXCR2 contributes to murine adipocyte development', *Journal of Leukocyte Biology*, 105(3), p. 497. doi:10.1002/JLB.1A0618-216RR.

Edwards, S.L. *et al.* (2013) 'Beyond GWASs: Illuminating the Dark Road from Association to Function', *The American Journal of Human Genetics*, 93(5), pp. 779–797. doi:10.1016/j.ajhg.2013.10.012.

Ejarque, M. *et al.* (2019) 'Adipose tissue mitochondrial dysfunction in human obesity is linked to a specific DNA methylation signature in adipose-derived stem cells', *International journal of obesity (2005)*, 43(6), pp. 1256–1268. doi:10.1038/S41366-018-0219-6.

Elffers, T.W. *et al.* (2017) 'Body fat distribution, in particular visceral fat, is associated with cardiometabolic risk factors in obese women', *PloS one*, 12(9). doi:10.1371/JOURNAL.PONE.0185403.

Elsafadi, M. *et al.* (2016) 'Characterization of Cellular and Molecular Heterogeneity of Bone Marrow Stromal Cells', *Stem Cells International*, 2016. doi:10.1155/2016/9378081.

EMBL-EBI (no date) *MUSCLE < Multiple Sequence Alignment < EMBL-EBI*. Available at: https://www.ebi.ac.uk/Tools/msa/muscle/ (Accessed: 8 May 2022).

Emdin, C.A. *et al.* (2017) 'Genetic association of waist-to-hip ratio with cardiometabolic traits, type 2 diabetes, and coronary heart disease', *JAMA - Journal of the American Medical Association*, 317(6), pp. 626–634. doi:10.1001/jama.2016.21042.

Falavinha, B.C. *et al.* (2022) 'Interleukin 21 Receptor Affects Adipogenesis of Human Adipose-Derived Stem/Stromal Cells', *Stem Cells International*, 2022. doi:10.1155/2022/4930932.

Farhana, A. and Lappin, S.L. (2022) *Biochemistry, Lactate Dehydrogenase*, *StatPearls*. StatPearls Publishing. Available at: https://www.ncbi.nlm.nih.gov/books/NBK557536/ (Accessed: 19 July 2022).

Farin, H.F. *et al.* (2007) 'Transcriptional Repression by the T-box Proteins Tbx18 and Tbx15 Depends on Groucho Corepressors', *Journal of Biological Chemistry*, 282(35), pp. 25748–25759. doi:10.1074/jbc.M703724200.

Flint, J. (2013) 'GWAS', *Current Biology*, 23(7), pp. R265–R266. doi:10.1016/J.CUB.2013.01.040.

Foster, M.T. *et al.* (2011) 'Removal of intra-abdominal visceral adipose tissue improves glucose tolerance in rats: Role of hepatic triglyceride storage', *Physiology & Behavior*, 104(5), pp. 845–854. doi:10.1016/J.PHYSBEH.2011.04.064.

Frayling, T.M. *et al.* (2007) 'A Common Variant in the FTO Gene Is Associated with Body Mass Index and Predisposes to Childhood and Adult Obesity', *Science*, 316(5826), pp. 889–894. doi:10.1126/science.1141634.

Fumagalli, M. *et al.* (2015) 'Greenlandic Inuit show genetic signatures of diet and climate adaptation.', *Science*, 349(6254), pp. 1343–7. doi:10.1126/science.aab2319.

Galarraga, M. *et al.* (2012) 'Adiposoft: automated software for the analysis of white adipose tissue cellularity in histological sections', *Journal of Lipid Research*, 53(12), pp. 2791–2796. doi:10.1194/JLR.D023788.

Galhardo, M. *et al.* (2014) 'Integrated analysis of transcript-level regulation of metabolism reveals disease-relevant nodes of the human metabolic network', *Nucleic acids research*, 42(3), pp. 1474–1496. doi:10.1093/NAR/GKT989.

Gallagher, D. *et al.* (1996) 'How Useful Is Body Mass Index for Comparison of Body Fatness across Age, Sex, and Ethnic Groups?', *American Journal of Epidemiology*, 143(3), pp. 228–239. doi:10.1093/OXFORDJOURNALS.AJE.A008733.

Gamboa-Gómez, C.I. *et al.* (2019) 'The fat-to-lean mass ratio, a novel anthropometric index, is associated to glucose metabolic disorders', *European journal of internal medicine*, 63, pp. 74–78. doi:10.1016/J.EJIM.2019.03.017.

Gao, C. *et al.* (2018) 'Genome-wide study of subcutaneous and visceral adipose tissue reveals novel sex-specific adiposity loci in Mexican Americans: The Insulin Resistance Atherosclerosis Family Study', *Obesity*, 26(1), pp. 202–212. doi:10.1002/oby.22074.

Gardiner, W.J.K. and Teboul, L. (2009) 'Overexpression Transgenesis in Mouse: Pronuclear Injection', *Methods in Molecular Biology*, 561, pp. 111–126. doi:10.1007/978-1-60327-019-9_8.

Gburcik, V. *et al.* (2012) 'An essential role for Tbx15 in the differentiation of brown and "brite" but not white adipocytes', *American Journal of Physiology-Endocrinology and Metabolism*, 303(8), pp. E1053–E1060. doi:10.1152/ajpendo.00104.2012.

Gerasimavicius, L., Livesey, B.J. and Marsh, J.A. (2022) 'Loss-of-function, gain-of-function and dominant-negative mutations have profoundly different effects on protein structure', *Nature Communications 2022 13:1*, 13(1), pp. 1–15. doi:10.1038/s41467-022-31686-6.

Gesta, S. *et al.* (2006) 'Evidence for a role of developmental genes in the origin of obesity and body fat distribution.', *Proceedings of the National Academy of Sciences of the United States of America*, 103(17), pp. 6676–81. doi:10.1073/pnas.0601752103.

Gesta, S. *et al.* (2011) 'Mesodermal developmental gene Tbx15 impairs adipocyte differentiation and mitochondrial respiration.', *Proceedings of the National Academy of Sciences of the United States of America*, 108(7), pp. 2771–6. doi:10.1073/pnas.1019704108.

Ghaben, A.L. and Scherer, P.E. (2019) 'Adipogenesis and metabolic health', *Nature Reviews Molecular Cell Biology 2018 20:4*, 20(4), pp. 242–258. doi:10.1038/s41580-018-0093-z.

Giralt, M. and Villarroya, F. (2013) 'White, Brown, Beige/Brite: Different Adipose Cells for Different Functions?', *Endocrinology*, 154(9), pp. 2992–3000. doi:10.1210/EN.2013-1403.

González-Pérez, A. and López-Bigas, N. (2011) 'Improving the Assessment of the Outcome of Nonsynonymous SNVs with a Consensus Deleteriousness Score, Condel', *American Journal of Human Genetics*, 88(4), p. 440. doi:10.1016/J.AJHG.2011.03.004.

Good, B.H. (2020) 'Linkage disequilibrium between rare mutations', *bioRxiv*, p. 2020.12.10.420042. doi:10.1101/2020.12.10.420042.

Gozzi, G. *et al.* (2016) 'Promoter methylation and downregulated expression of the TBX15 gene in ovarian carcinoma.', *Oncology letters*, 12(4), pp. 2811–2819. doi:10.3892/ol.2016.5019.

Graham, A.D. *et al.* (2019) 'The development of a high throughput drug-responsive model of white adipose tissue comprising adipogenic 3T3-L1 cells in a 3D matrix', *Biofabrication*, 12(1). doi:10.1088/1758-5090/AB56FE.

Gray, S.L. *et al.* (2006) 'Leptin Deficiency Unmasks the Deleterious Effects of Impaired Peroxisome Proliferator–Activated Receptor γ Function (P465L PPARγ) in Mice', *Diabetes*, 55(10), pp. 2669–2677. doi:10.2337/DB06-0389.

Green, H. and Kehinde, O. (1974) 'Sublines of mouse 3T3 cells that accumulate lipid', *Cell*, 1(3), pp. 113–116. doi:10.1016/0092-8674(74)90126-3.

Green, H. and Meuth, M. (1974) 'An established pre-adipose cell line and its differentiation in culture', *Cell*, 3(2), pp. 127–133. doi:10.1016/0092-8674(74)90116-0.

Green, M.R. and Sambrook, J. (2020) 'Precipitation of RNA with Ethanol', *Cold Spring Harbor Protocols*, 2020(3), p. pdb.prot101717. doi:10.1101/PDB.PROT101717.

Greener, J.G., Kandathil, S.M. and Jones, D.T. (2019) 'Deep learning extends de novo protein modelling coverage of genomes using iteratively predicted structural constraints', *Nature Communications 2019 10:1*, 10(1), pp. 1–13. doi:10.1038/s41467-019-11994-0.

GTEx Portal (no date). Available at: https://gtexportal.org/home/ (Accessed: 14 November 2019).

Gustafson, B. and Smith, U. (2006) 'Cytokines promote Wnt signaling and inflammation and impair the normal differentiation and lipid accumulation in 3T3-L1 preadipocytes', *The Journal of biological chemistry*, 281(14), pp. 9507–9516. doi:10.1074/JBC.M512077200.

Hägg, S. *et al.* (2015) 'Gene-based meta-analysis of genome-wide association studies implicates new loci involved in obesity', *Human molecular genetics*, 24(23), pp. 6849–6860. doi:10.1093/HMG/DDV379.

Halldorsdottir, S. *et al.* (2009) 'Reproducibility and accuracy of body composition

assessments in mice by dual energy x-ray absorptiometry and time domain nuclear magnetic resonance', *International journal of body composition research*, 7(4), p. 147.

Hansson, B. *et al.* (2019) 'Adipose cell size changes are associated with a drastic actin remodeling', *Scientific Reports 2019 9:1*, 9(1), pp. 1–14. doi:10.1038/s41598-019-49418-0.

Harley, I.T.W. *et al.* (2013) 'Differential colonization with segmented filamentous bacteria and Lactobacillus murinus do not drive divergent development of diet-induced obesity in C57BL/6 mice', *Molecular Metabolism*, 2(3), pp. 171–183. doi:10.1016/J.MOLMET.2013.04.004.

Harrington, M., Pond-Tor, S. and Boney, C.M. (2007) 'Role of epidermal growth factor and ErbB2 receptors in 3T3-L1 adipogenesis', *Obesity (Silver Spring, Md.)*, 15(3), pp. 563–571. doi:10.1038/OBY.2007.562.

Heaton, J.M. (1972) 'The distribution of brown adipose tissue in the human.', *Journal of Anatomy*, 112(Pt 1), p. 35.

Heck, A.J.R. and Van Den Heuvel, R.H.H. (2004) 'Investigation of intact protein complexes by mass spectrometry', *Mass spectrometry reviews*, 23(5), pp. 368–389. doi:10.1002/MAS.10081.

Heid, I.M. *et al.* (2010) 'Meta-analysis identifies 13 new loci associated with waist-hip ratio and reveals sexual dimorphism in the genetic basis of fat distribution', *Nature Genetics*, 42(11), pp. 949–960. doi:10.1038/ng.685.

Heinrich, K.M. *et al.* (2008) 'Obesity classification in military personnel: a comparison of body fat, waist circumference, and body mass index measurements', *Military medicine*, 173(1), pp. 67–73. doi:10.7205/MILMED.173.1.67.

Heitmann, B.L. and Lissner, L. (2011) 'Hip Hip Hurrah! Hip size inversely related to heart disease and total mortality', *Obesity Reviews*, 12(6), pp. 478–481. doi:10.1111/j.1467-789X.2010.00794.x.

Hildreth, A.D. *et al.* (2021) 'Single-cell sequencing of human white adipose tissue identifies new cell states in health and obesity', *Nature Immunology 2021 22:5*, 22(5), pp. 639–653. doi:10.1038/s41590-021-00922-4.

Houweling, P.J. *et al.* (2017) 'Exploring the relationship between α-actinin-3 deficiency and obesity in mice and humans', *International Journal of Obesity (2005)*, 41(7), p. 1154. doi:10.1038/IJO.2017.72.

Hull, R.L. *et al.* (2017) 'High fat feeding unmasks variable insulin responses in male C57BL/6 mouse substrains', *Journal of Endocrinology*, 233(1), pp. 53–64. doi:10.1530/JOE-16-0377.

Ijichi, N. *et al.* (2007) 'Estrogen-related receptor α modulates the expression of adipogenesis-related genes during adipocyte differentiation', *Biochemical and Biophysical Research Communications*, 358(3), pp. 813–818. doi:10.1016/J.BBRC.2007.04.209.

Isakson, P. *et al.* (2009) 'Impaired preadipocyte differentiation in human abdominal obesity: role of Wnt, tumor necrosis factor-alpha, and inflammation', *Diabetes*, 58(7), pp. 1550–1557. doi:10.2337/DB08-1770.

Jafari-Koshki, T. *et al.* (2016) 'Association of waist and hip circumference and waist-hip ratio with type 2 diabetes risk in first-degree relatives', *Journal of Diabetes and its Complications*, 30(6), pp. 1050–1055. doi:10.1016/j.jdiacomp.2016.05.003.

Jain, D. *et al.* (2015) 'Active promoters give rise to false positive "Phantom Peaks" in ChIP-seq experiments', *Nucleic Acids Research*, 43(14), pp. 6959–6968. doi:10.1093/NAR/GKV637.

Jang, B.K. (2012) 'Elevated serum bilirubin levels are inversely associated with nonalcoholic fatty liver disease', *Clinical and molecular hepatology*, 18(4), pp. 357–359. doi:10.3350/CMH.2012.18.4.357.

Jeffery, E. *et al.* (2015) 'Rapid Depot-Specific Activation of Adipocyte Precursor Cells at the Onset of Obesity', *Nature cell biology*, 17(4), p. 376. doi:10.1038/NCB3122.

Johnson, G.L. and Lapadat, R. (2002) 'Mitogen-activated protein kinase pathways mediated by ERK, JNK, and p38 protein kinases', *Science (New York, N.Y.)*, 298(5600), pp. 1911–1912. doi:10.1126/SCIENCE.1072682.

de Jong, J.M.A. *et al.* (2019) 'Human brown adipose tissue is phenocopied by classical brown adipose tissue in physiologically humanized mice', *Nature Metabolism 2019 1:8*, 1(8), pp. 830–843. doi:10.1038/s42255-019-0101-4.

Jumper, J. *et al.* (2021) 'Highly accurate protein structure prediction with AlphaFold', *Nature 2021 596:7873*, 596(7873), pp. 583–589. doi:10.1038/s41586-021-03819-2.

Justice, A.E. *et al.* (2019) 'Protein-coding variants implicate novel genes related to lipid homeostasis contributing to body-fat distribution', *Nature Genetics*, 51(3), pp. 452–469. doi:10.1038/s41588-018-0334-2.

Kaess, B.M. *et al.* (2012) 'The ratio of visceral to subcutaneous fat, a metric of body fat distribution, is a unique correlate of cardiometabolic risk', *Diabetologia*, 55(10), pp. 2622–2630. doi:10.1007/S00125-012-2639-5/FIGURES/1.

Kang, J.T.L. and Rosenberg, N.A. (2019) 'Mathematical Properties of Linkage Disequilibrium Statistics Defined by Normalization of the Coefficient D = pAB – pApB', *Human Heredity*, 84(3), pp. 127–143. doi:10.1159/000504171.

Kasza, I. *et al.* (2016) 'Thermogenic profiling using magnetic resonance imaging of dermal and other adipose tissues', *JCI Insight*, 1(13), p. 87146. doi:10.1172/JCI.INSIGHT.87146.

Katsiki, N. *et al.* (2014) 'Metabolic Syndrome and Non-Cardiac Vascular Diseases: An Update from Human Studies', *Current Pharmaceutical Design*, 20(31), pp. 4944–4952. doi:10.2174/1381612819666131206100750.

Katsuyama, H., Kawaguchi, A. and Yanai, H. (2015) 'Not visceral fat area but the ratio of visceral to subcutaneous fat area is significantly correlated with the marker for atherosclerosis in obese subjects', *International Journal of Cardiology*, 179, pp. 112–113. doi:10.1016/J.IJCARD.2014.10.112.

Kazarian, E. *et al.* (2018) 'SPAG17 Is Required for Male Germ Cell Differentiation and Fertility.', *International journal of molecular sciences*, 19(4). doi:10.3390/ijms19041252.

Kelley, L.A. *et al.* (2015) 'The Phyre2 web portal for protein modeling, prediction and analysis', *Nature Protocols 2015 10:6*, 10(6), pp. 845–858. doi:10.1038/nprot.2015.053.

Khan, R.N. *et al.* (2019) 'Pattern of electrolyte imbalance in Type 2 diabetes patients: Experience from a tertiary care hospital', *Pakistan Journal of Medical Sciences*, 35(3), p. 797. doi:10.12669/PJMS.35.3.844.

Kim, J.-J. *et al.* (2010) 'Identification of 15 loci influencing height in a Korean population', *Journal of Human Genetics*, 55(1), pp. 27–31. doi:10.1038/jhg.2009.116.

Kircher, M. *et al.* (2019) 'Saturation mutagenesis of twenty disease-associated regulatory elements at single base-pair resolution', *Nature Communications 2019 10:1*, 10(1), pp. 1–15. doi:10.1038/s41467-019-11526-w.

Kispert, A. (1995) 'The Brachyury protein: A T-domain transcription factor', *Seminars in Developmental Biology*, 6(6), pp. 395–403. doi:10.1016/S1044-5781(06)80003-4.

Kispert, A. and Herrmann, B.G. (1993) 'The Brachyury gene encodes a novel DNA binding protein.', *The EMBO Journal*, 12(8), pp. 3211–3220. doi:10.1002/J.1460-2075.1993.TB05990.X.

Kosugi, S. *et al.* (2008) 'Design of peptide inhibitors for the importin alpha/beta nuclear import pathway by activity-based profiling', *Chemistry & biology*, 15(9), pp. 940–949. doi:10.1016/J.CHEMBIOL.2008.07.019.

Kosugi, S. *et al.* (2009) 'Systematic identification of cell cycle-dependent yeast nucleocytoplasmic shuttling proteins by prediction of composite motifs', *Proceedings of the National Academy of Sciences of the United States of America*, 106(25), pp. 10171–10176. doi:10.1073/PNAS.0900604106/SUPPL_FILE/0900604106SI.PDF.

Kranendonk, M.E.G. *et al.* (2015) 'Inflammatory characteristics of distinct abdominal adipose tissue depots relate differently to metabolic risk factors for cardiovascular disease: distinct fat depots and vascular risk factors', *Atherosclerosis*, 239(2), pp. 419–427. doi:10.1016/J.ATHEROSCLEROSIS.2015.01.035.

Krycer, J.R. *et al.* (2020) 'Lactate production is a prioritized feature of adipocyte metabolism', *Journal of Biological Chemistry*, 295(1), pp. 83–98. doi:10.1074/JBC.RA119.011178/ATTACHMENT/9F857325-6660-4DFA-A59C-D20968142EF5/MMC1.PDF.

Kuk, J.L. *et al.* (2008) 'Whole-body skeletal muscle mass is not related to glucose tolerance or insulin sensitivity in overweight and obese men and women', *Applied physiology, nutrition, and metabolism = Physiologie appliquee, nutrition et metabolisme*, 33(4), pp. 769–774. doi:10.1139/H08-060.

Kullberg, J. *et al.* (2009) 'Whole-body adipose tissue analysis: comparison of MRI, CT and dual energy X-ray absorptiometry', *The British journal of radiology*, 82(974), pp. 123–130. doi:10.1259/BJR/80083156.

Kusuyama, J. *et al.* (2016) 'CXCL3 positively regulates adipogenic differentiation', *Journal of Lipid Research*, 57(10), pp. 1806–1820. doi:10.1194/JLR.M067207.

Kwak, M.S. *et al.* (2012) 'Serum bilirubin levels are inversely associated with nonalcoholic fatty liver disease', *Clinical and molecular hepatology*, 18(4), pp. 383–390.

doi:10.3350/CMH.2012.18.4.383.

Laber, S. (2017) *Deciphering the Function of Obesity-associated Regulatory Elements within FTO*. University of Oxford.

Laber, S. *et al.* (2021) 'Linking the FTO obesity rs1421085 variant circuitry to cellular, metabolic, and organismal phenotypes in vivo', *Science advances*, 7(30). doi:10.1126/SCIADV.ABG0108.

Lagunas, T. *et al.* (2021) 'A Cre-dependent massively parallel reporter assay allows for cell-type specific assessment of the functional effects of genetic variants in vivo', *bioRxiv*, p. 2021.05.17.444514. doi:10.1101/2021.05.17.444514.

Lamble, S. *et al.* (2013) 'Improved workflows for high throughput library preparation using the transposome-based nextera system', *BMC Biotechnology*, 13(1), pp. 1–10. doi:10.1186/1472-6750-13-104/FIGURES/4.

Lane, J.T. *et al.* (2005) 'Comparison of CT and dual-energy DEXA using a modified trunk compartment in the measurement of abdominal fat', *Endocrine*, 27(3), pp. 295–299. doi:10.1385/ENDO:27:3:295.

Lapetina, S. and Gil-Henn, H. (2017) 'A guide to simple, direct, and quantitative in vitro binding assays', *Journal of Biological Methods*, 4(1), p. e62. doi:10.14440/JBM.2017.161.

Laskowski, R.A. *et al.* (2018) 'PDBsum: Structural summaries of PDB entries', *Protein Science : A Publication of the Protein Society*, 27(1), p. 129. doi:10.1002/PRO.3289.

Lausch, E. *et al.* (2008) 'TBX15 mutations cause craniofacial dysmorphism, hypoplasia of scapula and pelvis, and short stature in Cousin syndrome.', *American journal of human genetics*, 83(5), pp. 649–55. doi:10.1016/j.ajhg.2008.10.011.

Lee, H.S. *et al.* (2018) 'Fat-to-Lean Mass Ratio Can Predict Cardiac Events and All-Cause Mortality in Patients Undergoing Hemodialysis', *Annals of nutrition & metabolism*, 73(3), pp. 241–249. doi:10.1159/000492939.

Lee, K.Y. *et al.* (2015) 'Tbx15 controls skeletal muscle fibre-type determination and muscle metabolism.', *Nature communications*, 6, p. 8054. doi:10.1038/ncomms9054.

Lee, K.Y. *et al.* (2017) 'Tbx15 Defines a Glycolytic Subpopulation and White Adipocyte Heterogeneity', *Diabetes*, 66, p. 2822. doi:10.2337/db17-0218.

Van Der Lee, R. *et al.* (2014) 'Classification of intrinsically disordered regions and proteins', *Chemical Reviews*, 114(13), pp. 6589–6631. doi:10.1021/CR400525M/ASSET/IMAGES/CR400525M.SOCIAL.JPEG_V03.

Legler, D.F. and Thelen, M. (2018) 'New insights in chemokine signaling', *F1000Research*, 7. doi:10.12688/F1000RESEARCH.13130.1.

Leitner, B.P. *et al.* (2017) 'Mapping of human brown adipose tissue in lean and obese young men', *Proceedings of the National Academy of Sciences of the United States of America*, 114(32), pp. 8649–8654. doi:10.1073/PNAS.1705287114/SUPPL_FILE/PNAS.201705287SI.PDF.

Lemos, T. and Gallagher, D. (2017) 'Current body composition measurement techniques', *Current Opinion in Endocrinology, Diabetes and Obesity*, 24(5), pp. 310–

314. doi:10.1097/MED.0000000000000360.

Li, H. and Durbin, R. (2009) 'Fast and accurate short read alignment with Burrows-Wheeler transform', *Bioinformatics (Oxford, England)*, 25(14), pp. 1754–1760. doi:10.1093/BIOINFORMATICS/BTP324.

Liamis, G. *et al.* (2014) 'Diabetes mellitus and electrolyte disorders', *World Journal of Clinical Cases : WJCC*, 2(10), p. 488. doi:10.12998/WJCC.V2.I10.488.

Liao, Y., Smyth, G.K. and Shi, W. (2019) 'The R package Rsubread is easier, faster, cheaper and better for alignment and quantification of RNA sequencing reads', *Nucleic Acids Research*, 47(8), pp. e47–e47. doi:10.1093/NAR/GKZ114.

Lichou, F. and Trynka, G. (2020) 'Functional studies of GWAS variants are gaining momentum', *Nature Communications 2020 11:1*, 11(1), pp. 1–4. doi:10.1038/s41467-020-20188-y.

Lindgren, C.M. *et al.* (2009) 'Genome-wide association scan meta-analysis identifies three Loci influencing adiposity and fat distribution.', *PLoS genetics*, 5(6), p. e1000508. doi:10.1371/journal.pgen.1000508.

Lindinger, M.I. and Sjøgaard, G. (2012) 'Potassium Regulation during Exercise and Recovery', *Sports Medicine 1991 11:6*, 11(6), pp. 382–401. doi:10.2165/00007256-199111060-00004.

Liu, C.F. *et al.* (2016) 'Crystal structure of the DNA binding domain of the transcription factor T-bet suggests simultaneous recognition of distant genome sites', *Proceedings of the National Academy of Sciences of the United States of America*, 113(43), pp. E6572–E6581. doi:10.1073/PNAS.1613914113.

Liu, C.T. *et al.* (2013) 'Genome-Wide Association of Body Fat Distribution in African Ancestry Populations Suggests New Loci', *PLOS Genetics*, 9(8), p. e1003681. doi:10.1371/JOURNAL.PGEN.1003681.

Liu, C.T. *et al.* (2014) 'Multi-ethnic fine-mapping of 14 central adiposity loci', *Human Molecular Genetics*, 23(17), pp. 4738–4744. doi:10.1093/hmg/ddu183.

Liu, J. *et al.* (2006) 'Intrinsic disorder in transcription factors', *Biochemistry*, 45(22), pp. 6873–6888. doi:10.1021/BI0602718.

Lo, K.A. and Sun, L. (2013) 'Turning WAT into BAT: a review on regulators controlling the browning of white adipocytes.', *Bioscience reports*, 33(5). doi:10.1042/BSR20130046.

Loh, N.Y. *et al.* (2020) 'RSPO3 impacts body fat distribution and regulates adipose cell biology in vitro', *Nature Communications*, 11(1). doi:10.1038/S41467-020-16592-Z.

Long, H., Reeves, R. and Simon, M.M. (2022) 'Mouse genomic and cellular annotations', *Mammalian Genome*, 33(1), pp. 19–30. doi:10.1007/S00335-021-09936-7/TABLES/4.

Lonsdale, J. *et al.* (2013) 'The Genotype-Tissue Expression (GTEx) project', *Nature Genetics*, pp. 580–585. doi:10.1038/ng.2653.

Loos, R.J.F. and Yeo, G.S.H. (2014) 'The bigger picture of FTO: the first GWAS-identified obesity gene.', *Nature reviews. Endocrinology*, 10(1), pp. 51–61. doi:10.1038/nrendo.2013.227.

Luong, Q., Huang, J. and Lee, K.Y. (2019) 'Deciphering White Adipose Tissue Heterogeneity', *Biology*, 8(2). doi:10.3390/BIOLOGY8020023.

Macarthur, D.G. *et al.* (2008) 'An Actn3 knockout mouse provides mechanistic insights into the association between α-actinin-3 deficiency and human athletic performance', *Human Molecular Genetics*, 17(8), pp. 1076–1086. doi:10.1093/HMG/DDM380.

Macotela, Y. *et al.* (2012) 'Intrinsic differences in adipocyte precursor cells from different white fat depots', *Diabetes*, 61(7), pp. 1691–1699. doi:10.2337/DB11-1753.

Madeira, F. *et al.* (2022) 'Search and sequence analysis tools services from EMBL-EBI in 2022.', *Nucleic Acids Research* [Preprint]. doi:10.1093/NAR/GKAC240.

Mahajan, A. *et al.* (2018) 'Fine-mapping type 2 diabetes loci to single-variant resolution using high-density imputation and islet-specific epigenome maps', *Nature Genetics 2018 50:11*, 50(11), pp. 1505–1513. doi:10.1038/s41588-018-0241-6.

Mahendran, Y. *et al.* (2013) 'Glycerol and fatty acids in serum predict the development of hyperglycemia and type 2 diabetes in Finnish men', *Diabetes Care*, 36(11), pp. 3732–3738. doi:10.2337/DC13-0800/-/DC1.

Makkonen, H. *et al.* (2009) 'Long-range activation of FKBP51 transcription by the androgen receptor via distal intronic enhancers', *Nucleic acids research*, 37(12), pp. 4135–4148. doi:10.1093/NAR/GKP352.

Maller, J.B. *et al.* (2012) 'Bayesian refinement of association signals for 14 loci in 3 common diseases', *Nature Genetics 2012 44:12*, 44(12), pp. 1294–1301. doi:10.1038/ng.2435.

Man, K., Kallies, A. and Vasanthakumar, A. (2021) 'Resident and migratory adipose immune cells control systemic metabolism and thermogenesis', *Cellular & Molecular Immunology 2021 19:3*, 19(3), pp. 421–431. doi:10.1038/s41423-021-00804-7.

van Marken Lichtenbelt, W.D. *et al.* (2009) 'Cold-activated brown adipose tissue in healthy men', *The New England journal of medicine*, 360(15), pp. 1500–1508. doi:10.1056/NEJMOA0808718.

Masuya, H. *et al.* (2007) 'A novel dominant-negative mutation in Gdf5 generated by ENU mutagenesis impairs joint formation and causes osteoarthritis in mice', *Human Molecular Genetics*, 16(19), pp. 2366–2375. doi:10.1093/HMG/DDM195.

Mattsson, S. and Thomas, B.J. (2006) 'Development of methods for body composition studies', *Physics in medicine and biology*, 51(13). doi:10.1088/0031-9155/51/13/R13.

McCarthy, M.I. *et al.* (2008) 'Genome-wide association studies for complex traits: consensus, uncertainty and challenges', *Nature Reviews Genetics 2008 9:5*, 9(5), pp. 356–369. doi:10.1038/nrg2344.

McDonough, A.A., Thompson, C.B. and Youn, J.H. (2002) 'Skeletal muscle regulates extracellular potassium', *American journal of physiology. Renal physiology*, 282(6). doi:10.1152/AJPRENAL.00360.2001.

McGuffin, L.J. *et al.* (2018) 'Accurate template-based modeling in CASP12 using the IntFOLD4-TS, ModFOLD6, and ReFOLD methods', *Proteins: Structure, Function and Bioinformatics*, 86, pp. 335–344. doi:10.1002/prot.25360.

McGuffin, L.J. *et al.* (2019) 'IntFOLD: An integrated web resource for high performance protein structure and function prediction', *Nucleic Acids Research*, 47(W1), pp. W408–W413. doi:10.1093/nar/gkz322.

McLaughlin, T. *et al.* (2007) 'Enhanced proportion of small adipose cells in insulin-resistant vs insulin-sensitive obese individuals implicates impaired adipogenesis', *Diabetologia*, 50(8), pp. 1707–1715. doi:10.1007/S00125-007-0708-Y.

McLaughlin, T. *et al.* (2014) 'Subcutaneous adipose cell size and distribution: relationship to insulin resistance and body fat', *Obesity (Silver Spring, Md.)*, 22(3), pp. 673–680. doi:10.1002/OBY.20209.

McLaughlin, T. *et al.* (2016) 'Adipose Cell Size and Regional Fat Deposition as Predictors of Metabolic Response to Overfeeding in Insulin-Resistant and Insulin-Sensitive Humans', *Diabetes*, 65(5), pp. 1245–1254. doi:10.2337/DB15-1213.

McPherson, K., Marsh, T. and Brown, M. (2007) *Tackling Obesities: Future Choices–Modelling Future Trends in Obesity & Their Impact on Health 2nd Edition*.

Meier, I.D. *et al.* (2010) 'Short DNA sequences inserted for gene targeting can accidentally interfere with off-target gene expression', *The FASEB Journal*, 24(6), pp. 1714–1724. doi:10.1096/FJ.09-140749.

Merrick, D. *et al.* (2019) 'Identification of a mesenchymal progenitor cell hierarchy in adipose tissue', *Science*, 364(6438), p. eaav2501. doi:10.1126/SCIENCE.AAV2501.

Mianné, J. *et al.* (2017) 'Analysing the outcome of CRISPR-aided genome editing in embryos: Screening, genotyping and quality control', *Methods (San Diego, Calif.)*, 121–122, pp. 68–76. doi:10.1016/J.YMETH.2017.03.016.

Minezaki, Y. *et al.* (2006) 'Human transcription factors contain a high fraction of intrinsically disordered regions essential for transcriptional regulation', *Journal of molecular biology*, 359(4), pp. 1137–1149. doi:10.1016/J.JMB.2006.04.016.

Miyata, Y. *et al.* (2016) 'Identification of Mouse Mesenteric and Subcutaneous in vitro Adipogenic Cells', *Scientific Reports 2016 6:1*, 6(1), pp. 1–14. doi:10.1038/srep21041.

Mohsen-Kanson, T. *et al.* (2014) 'Differentiation of human induced pluripotent stem cells into brown and white adipocytes: role of Pax3', *Stem cells (Dayton, Ohio)*, 32(6), pp. 1459–1467. doi:10.1002/STEM.1607.

Moir, L., Bentley, L. and Cox, R.D. (2016) 'Comprehensive Energy Balance Measurements in Mice', *Current Protocols in Mouse Biology*, 6(3), pp. 211–222. doi:10.1002/CPMO.13.

Montgomery, M.K. *et al.* (2013) 'Mouse strain-dependent variation in obesity and glucose homeostasis in response to high-fat feeding', *Diabetologia*, 56(5), pp. 1129–1139. doi:10.1007/S00125-013-2846-8/FIGURES/6.

Mooney, S.D., Krishnan, V.G. and Evani, U.S. (2010) 'Bioinformatic tools for identifying disease gene and SNP candidates.', *Methods in molecular biology (Clifton, N.J.)*, 628, pp. 307–19. doi:10.1007/978-1-60327-367-1_17.

Morris, A. (2017) 'Apple or pear — waist-to-hip ratio and the risk of CHD and T2DM', *Nature Reviews Endocrinology*, 13(4), pp. 187–187. doi:10.1038/nrendo.2017.26.

Morris, R., Kershaw, N.J. and Babon, J.J. (2018) 'The molecular details of cytokine signaling via the JAK/STAT pathway', *Protein Science : A Publication of the Protein Society*, 27(12), p. 1984. doi:10.1002/PRO.3519.

Morrison, S. and McGee, S.L. (2015) '3T3-L1 adipocytes display phenotypic characteristics of multiple adipocyte lineages', *Adipocyte*, 4(4), pp. 295–302. doi:10.1080/21623945.2015.1040612.

Mušo, M. (2019) *Functional study of waist-hip ratio associated loci and the WARS2 gene as modulators of fat distribution.* University of Oxford.

Mušo, M. *et al.* (2020) 'A lead candidate functional single nucleotide polymorphism within the WARS2 gene associated with waist-hip-ratio does not alter RNA stability', *Biochimica et biophysica acta. Gene regulatory mechanisms*, 1863(11). doi:10.1016/J.BBAGRM.2020.194640.

Mušo, M. *et al.* (2022) 'A Wars2 mutant mouse shows a sex and diet specific change in fat distribution, reduced food intake and depot-specific upregulation of WAT browning', *Frontiers in Physiology*, 0, p. 1637. doi:10.3389/FPHYS.2022.953199.

Myers, K.S. *et al.* (2013) 'Genome-scale Analysis of Escherichia coli FNR Reveals Complex Features of Transcription Factor Binding', *PLoS Genetics*, 9(6), p. 1003565. doi:10.1371/JOURNAL.PGEN.1003565.

Myint, P.K. *et al.* (2014) 'Body fat percentage, body mass index and waist-to-hip ratio as predictors of mortality and cardiovascular disease', *Heart*, 100(20), pp. 1613–1619. doi:10.1136/HEARTJNL-2014-305816.

Nam, H. *et al.* (2016) 'Modulation of IL-27 in adipocytes during inflammatory stress', *Obesity*, 24(1), pp. 157–166. doi:10.1002/OBY.21351.

Newman, O. *et al.* (no date) 'Crystal structure of human Brachyury (T) in complex with DNA'.

Nielsen, R. *et al.* (2008) 'Genome-wide profiling of PPARγ:RXR and RNA polymerase II occupancy reveals temporal activation of distinct metabolic pathways and changes in RXR dimer composition during adipogenesis', *Genes & Development*, 22(21), p. 2953. doi:10.1101/GAD.501108.

Nishikawa, K. (2009) 'Natively unfolded proteins: An overview', *Biophysics*, 5, p. 53. doi:10.2142/BIOPHYSICS.5.53.

Novotný, L. and Vítek, L. (2003) 'Inverse relationship between serum bilirubin and atherosclerosis in men: a meta-analysis of published studies', *Experimental biology and medicine (Maywood, N.J.)*, 228(5), pp. 568–571. doi:10.1177/15353702-0322805-29.

Nurk, S. *et al.* (2022) 'The complete sequence of a human genome', *Science*, 376(6588), pp. 44–53. doi:10.1126/SCIENCE.ABJ6987/SUPPL_FILE/SCIENCE.ABJ6987_MDAR_REPRODUCIBILITY_CHECKLIST.PDF.

De Oliveira, E.P. and Burini, R.C. (2012) 'High plasma uric acid concentration: causes and consequences', *Diabetology & metabolic syndrome*, 4(1). doi:10.1186/1758-5996-4-12.

Pan, D.Z. *et al.* (2021) 'Identification of TBX15 as an adipose master trans regulator of abdominal obesity genes', *Genome medicine*, 13(1). doi:10.1186/S13073-021-00939-2.

Papaioannou, V.E. (2014) 'The T-box gene family: emerging roles in development, stem cells and cancer.', *Development (Cambridge, England)*, 141(20), pp. 3819–33. doi:10.1242/dev.104471.

Park, A., Kim, W.K. and Bae, K.-H. (2014) 'Distinction of white, beige and brown adipocytes derived from mesenchymal stem cells', *World Journal of Stem Cells*, 6(1), p. 33. doi:10.4252/wjsc.v6.i1.33.

Park, Y.J. *et al.* (2021) 'Emerging roles of epigenetic regulation in obesity and metabolic disease', *The Journal of biological chemistry*, 297(5). doi:10.1016/J.JBC.2021.101296.

De Pergola, G. and Silvestris, F. (2013) 'Obesity as a Major Risk Factor for Cancer', *Journal of Obesity*, 2013. doi:10.1155/2013/291546.

Perlman, R.L. (2016) 'Mouse models of human disease: An evolutionary perspective', *Evolution, Medicine, and Public Health*, 2016(1), p. 170. doi:10.1093/EMPH/EOW014.

Pettersson, J. *et al.* (2008) 'Muscular exercise can cause highly pathological liver function tests in healthy men', *British Journal of Clinical Pharmacology*, 65(2), p. 253. doi:10.1111/J.1365-2125.2007.03001.X.

Pham, C.T.N. *et al.* (1996) 'Long-range disruption of gene expression by a selectable marker cassette', *Proceedings of the National Academy of Sciences of the United States of America*, 93(23), pp. 13090–13095. doi:10.1073/PNAS.93.23.13090/ASSET/2358E180-0CE7-4A0F-8B8E-49EC427375E8/ASSETS/GRAPHIC/PQ2262496005.JPEG.

Pilkington, A.C., Paz, H.A. and Wankhade, U.D. (2021) 'Beige Adipose Tissue Identification and Marker Specificity—Overview', *Frontiers in Endocrinology*, 12, p. 8. doi:10.3389/FENDO.2021.599134/BIBTEX.

Pitrone, M. *et al.* (2019) 'Knockdown of NANOG Reduces Cell Proliferation and Induces G0/G1 Cell Cycle Arrest in Human Adipose Stem Cells', *International Journal of Molecular Sciences 2019, Vol. 20, Page 2580*, 20(10), p. 2580. doi:10.3390/IJMS20102580.

Polyák, Á. *et al.* (2014) 'The fractalkine/Cx3CR1 system is implicated in the development of metabolic visceral adipose tissue inflammation in obesity', *Brain, behavior, and immunity*, 38, pp. 25–35. doi:10.1016/J.BBI.2014.01.010.

Powell, G. *et al.* (2022) 'Modelling the genetic aetiology of complex disease: human–mouse conservation of noncoding features and disease-associated loci', *Biology Letters*, 18(3). doi:10.1098/RSBL.2021.0630.

Pradhan, L. *et al.* (2016) 'Intermolecular Interactions of Cardiac Transcription Factors NKX2.5 and TBX5', *Biochemistry*, 55(12), pp. 1702–1710. doi:10.1021/ACS.BIOCHEM.6B00171/ASSET/IMAGES/LARGE/BI-2016-00171W_0005.JPEG.

Pravenec, M. *et al.* (2017) 'Mutant Wars2 Gene in Spontaneously Hypertensive Rats Impairs Brown Adipose Tissue Function and Predisposes to Visceral Obesity', *Physiol.*

Res, 66, pp. 917–924.

Pulit, S.L. *et al.* (2019) 'Meta-analysis of genome-wide association studies for body fat distribution in 694 649 individuals of European ancestry.', *Human molecular genetics*, 28(1), pp. 166–174. doi:10.1093/hmg/ddy327.

Qin, W. *et al.* (2015) 'Efficient CRISPR/Cas9-Mediated Genome Editing in Mice by Zygote Electroporation of Nuclease', *Genetics*, 200(2), pp. 423–430. doi:10.1534/GENETICS.115.176594.

Racimo, F. *et al.* (2017) 'Archaic Adaptive Introgression in TBX15/WARS2.', *Molecular biology and evolution*, 34(3), pp. 509–524. doi:10.1093/molbev/msw283.

Rajbhandari, P. *et al.* (2018) 'IL-10 Signaling Remodels Adipose Chromatin Architecture to Limit Thermogenesis and Energy Expenditure In Brief Article IL-10 Signaling Remodels Adipose Chromatin Architecture to Limit Thermogenesis and Energy Expenditure', *Cell*, 172, pp. 218–233. doi:10.1016/j.cell.2017.11.019.

Rashiti, P. *et al.* (2016) 'Relationship of Plasma Adiponectin and Waist-hip Ratio with Coronary Artery Disease', *Medical Archives*, 70(6), p. 413. doi:10.5455/medarh.2016.70.413-418.

Rattarasarn, C., Leelawattana, R. and Soonthornpun, S. (2010) 'Contribution of skeletal muscle mass on sex differences in 2-hour plasma glucose levels after oral glucose load in Thai subjects with normal glucose tolerance', *Metabolism*, 59(2), pp. 172–176. doi:10.1016/J.METABOL.2009.06.029.

Raudvere, U. *et al.* (2019) 'g:Profiler: a web server for functional enrichment analysis and conversions of gene lists (2019 update)', *Nucleic Acids Research*, 47(W1), pp. W191–W198. doi:10.1093/NAR/GKZ369.

Reimand, J. *et al.* (2007) 'g:Profiler—a web-based toolset for functional profiling of gene lists from large-scale experiments', *Nucleic Acids Research*, 35(Web Server issue), p. W193. doi:10.1093/NAR/GKM226.

Reusch, J., Colton, L. and Klemm, D. (2000) 'CREB Activation Induces Adipogenesis in 3T3-L1 Cells', *Molecular and Cellular Biology*, 20(3), p. 1008. doi:10.1128/MCB.20.3.1008-1020.2000.

Ritchie, H. and Roser, M. (2017) *Obesity - Our World in Data*. Available at: https://ourworldindata.org/obesity#citation (Accessed: 21 June 2022).

Roadmap Epigenomics Consortium *et al.* (2015) 'Integrative analysis of 111 reference human epigenomes', *Nature 2015 518:7539*, 518(7539), pp. 317–330. doi:10.1038/nature14248.

Robinson, M.D., McCarthy, D.J. and Smyth, G.K. (2010) 'edgeR: a Bioconductor package for differential expression analysis of digital gene expression data', *Bioinformatics*, 26(1), pp. 139–140. doi:10.1093/BIOINFORMATICS/BTP616.

Rospleszcz, S. *et al.* (2020) 'Association of serum uric acid with visceral, subcutaneous and hepatic fat quantified by magnetic resonance imaging', *Scientific Reports 2020 10:1*, 10(1), pp. 1–9. doi:10.1038/s41598-020-57459-z.

Rydén, M. *et al.* (2014) 'Adipose tissue and metabolic alterations: regional differences

in fat cell size and number matter, but differently: a cross-sectional study', *The Journal of clinical endocrinology and metabolism*, 99(10), pp. E1870–E1876. doi:10.1210/JC.2014-1526.

Saadi, I. *et al.* (2003) 'Dominant Negative Dimerization of a Mutant Homeodomain Protein in Axenfeld-Rieger Syndrome', *Molecular and Cellular Biology*, 23(6), pp. 1968–1982. doi:10.1128/MCB.23.6.1968-1982.2003/ASSET/B4A3A56B-D56C-431D-8A74-B31907A6CA94/ASSETS/GRAPHIC/MB0630727010.JPEG.

Sandoval-Motta, S. *et al.* (2017) 'The Human Microbiome and the Missing Heritability Problem', *Frontiers in Genetics*, 8(JUN), p. 80. doi:10.3389/FGENE.2017.00080.

Sayers, E.W. *et al.* (2022) 'Database resources of the national center for biotechnology information', *Nucleic acids research*, 50(D1), pp. D20–D26. doi:10.1093/NAR/GKAB1112.

Scacheri, P.C. *et al.* (2001) 'Bidirectional transcriptional activity of PGK-neomycin and unexpected embryonic lethality in heterozygote chimeric knockout mice', *genesis*, 30(4), pp. 259–263. doi:10.1002/GENE.1072.

Schaid, D.J., Chen, W. and Larson, N.B. (2018) 'From genome-wide associations to candidate causal variants by statistical fine-mapping', *Nature Reviews Genetics*, 19(8), pp. 491–504. doi:10.1038/s41576-018-0016-z.

Scherer, A. and Christensen, G.B. (2016) 'Concepts and Relevance of Genome-Wide Association Studies', *Science Progress*, 99(1), pp. 59–67. doi:10.3184/003685016X14558068452913.

Schleinitz, D. *et al.* (2014) 'Fat depot-specific mRNA expression of novel loci associated with waist–hip ratio', *International Journal of Obesity*, 38(1), pp. 120–125. doi:10.1038/ijo.2013.56.

Schneider, C.A., Rasband, W.S. and Eliceiri, K.W. (2012) 'NIH Image to ImageJ: 25 years of image analysis', *Nature Methods 2012 9:7*, 9(7), pp. 671–675. doi:10.1038/nmeth.2089.

Shi, Y., Evans, J.E. and Rock, K.L. (2003) 'Molecular identification of a danger signal that alerts the immune system to dying cells', *Nature*, 425(6957), pp. 516–521. doi:10.1038/NATURE01991.

Shungin, D. *et al.* (2015) 'New genetic loci link adipose and insulin biology to body fat distribution.', *Nature*, 518(7538), pp. 187–196. doi:10.1038/nature14132.

Sim, N.L. *et al.* (2012) 'SIFT web server: predicting effects of amino acid substitutions on proteins', *Nucleic Acids Research*, 40(Web Server issue), p. W452. doi:10.1093/NAR/GKS539.

Simicevic, J. and Deplancke, B. (2010) 'DNA-centered approaches to characterize regulatory protein–DNA interaction complexes', *Molecular BioSystems*, 6(3), pp. 462–468. doi:10.1039/B916137F.

Simon, M.M. *et al.* (2013) 'A comparative phenotypic and genomic analysis of C57BL/6J and C57BL/6N mouse strains', *Genome Biology*, 14(7), pp. 1–22. doi:10.1186/GB-2013-14-7-R82/TABLES/3.

Singh, M.K. *et al.* (2005) 'The T-box transcription factor Tbx15 is required for skeletal development', *Mechanisms of Development*, 122(2), pp. 131–144. doi:10.1016/J.MOD.2004.10.011.

Smemo, S. *et al.* (2014) 'Obesity-associated variants within FTO form long-range functional connections with IRX3', *Nature*, 507(7492), pp. 371–375. doi:10.1038/nature13138.

Søgaard, A.J. *et al.* (2015) 'Abdominal obesity increases the risk of hip fracture. A population-based study of 43 000 women and men aged 60-79 years followed for 8 years. Cohort of Norway', *Journal of Internal Medicine*, 277(3), pp. 306–317. doi:10.1111/joim.12230.

Song, J. and Deng, T. (2020) 'The Adipocyte and Adaptive Immunity', *Frontiers in Immunology*, 11. doi:10.3389/FIMMU.2020.593058.

Song, Q.Y. *et al.* (2018) 'Waist-hip ratio related genetic loci are associated with risk of impaired fasting glucose in Chinese children: A case control study', *Nutrition and Metabolism*, 15(1). doi:10.1186/s12986-018-0270-2.

Spalding, K.L. *et al.* (2008) 'Dynamics of fat cell turnover in humans', *Nature*, 453(7196), pp. 783–787. doi:10.1038/NATURE06902.

Speakman, J.R. (2013) 'Measuring energy metabolism in the mouse - theoretical, practical, and analytical considerations', *Frontiers in Physiology*, 4 MAR, p. 34. doi:10.3389/FPHYS.2013.00034/BIBTEX.

Speliotes, E.K. *et al.* (2010) 'Association analyses of 249,796 individuals reveal 18 new loci associated with body mass index', *Nature Genetics*, 42(11), pp. 937–948. doi:10.1038/ng.686.

Srivastava, A.K. (2012) 'Challenges in the treatment of cardiometabolic syndrome.', *Indian journal of pharmacology*, 44(2), pp. 155–6. doi:10.4103/0253-7613.93579.

Stenkula, K.G. and Erlanson-Albertsson, C. (2018) 'Adipose cell size: Importance in health and disease', *American Journal of Physiology - Regulatory Integrative and Comparative Physiology*, 315(2), pp. R284–R295. doi:10.1152/AJPREGU.00257.2017/ASSET/IMAGES/LARGE/ZH60061894830002.JPEG.

Stennard, F.A. *et al.* (2005) 'Murine T-box transcription factor Tbx20 acts as a repressor during heart development, and is essential for adult heart integrity, function and adaptation', *Development (Cambridge, England)*, 132(10), pp. 2451–2462. doi:10.1242/DEV.01799.

Stirnimann, C.U. *et al.* (2010) 'Structural Basis of TBX5–DNA Recognition: The T-Box Domain in Its DNA-Bound and -Unbound Form', *Journal of Molecular Biology*, 400(1), pp. 71–81. doi:10.1016/J.JMB.2010.04.052.

Storz, C. *et al.* (2018) 'The role of visceral and subcutaneous adipose tissue measurements and their ratio by magnetic resonance imaging in subjects with prediabetes, diabetes and healthy controls from a general population without cardiovascular disease', *The British journal of radiology*, 91(1089). doi:10.1259/BJR.20170808.

Sturm, R. (2007) 'Increases in morbid obesity in the USA: 2000–2005', *Public health*, 121(7), p. 492. doi:10.1016/J.PUHE.2007.01.006.

Suárez-Cuenca, J.A. *et al.* (2021) 'Enlarged adipocytes from subcutaneous vs. visceral adipose tissue differentially contribute to metabolic dysfunction and atherogenic risk of patients with obesity', *Scientific Reports 2021 11:1*, 11(1), pp. 1–11. doi:10.1038/s41598-021-81289-2.

Sun, J., Nawaz, Z. and Slingerland, J.M. (2007) 'Long-range activation of GREB1 by estrogen receptor via three distal consensus estrogen-responsive elements in breast cancer cells', *Molecular endocrinology (Baltimore, Md.)*, 21(11), pp. 2651–2662. doi:10.1210/ME.2007-0082.

Sun, K. *et al.* (2014) 'Serum potassium level is associated with metabolic syndrome: A population-based study', *Clinical Nutrition*, 33(3), pp. 521–527. doi:10.1016/J.CLNU.2013.07.010.

Sun, W. *et al.* (2019) 'Tbx15 is required for adipocyte browning induced by adrenergic signaling pathway', *Molecular Metabolism* [Preprint]. doi:10.1016/J.MOLMET.2019.07.004.

Symonds, M.E. *et al.* (2012) 'Adipose tissue and fetal programming', *Diabetologia*, 55(6), pp. 1597–1606. doi:10.1007/S00125-012-2505-5/FIGURES/4.

Szklarczyk, D. *et al.* (2019) 'STRING v11: protein-protein association networks with increased coverage, supporting functional discovery in genome-wide experimental datasets', *Nucleic acids research*, 47(D1), pp. D607–D613. doi:10.1093/NAR/GKY1131.

Szklarczyk, D. *et al.* (2021) 'The STRING database in 2021: customizable protein-protein networks, and functional characterization of user-uploaded gene/measurement sets', *Nucleic acids research*, 49(D1), pp. D605–D612. doi:10.1093/NAR/GKAA1074.

Taicher, G.Z. *et al.* (2003) 'Quantitative magnetic resonance (QMR) method for bone and whole-body-composition analysis', *Analytical and bioanalytical chemistry*, 377(6), pp. 990–1002. doi:10.1007/S00216-003-2224-3.

Tak, Y.G. and Farnham, P.J. (2015) 'Making sense of GWAS: using epigenomics and genome engineering to understand the functional relevance of SNPs in non-coding regions of the human genome', *Epigenetics & chromatin*, 8(1). doi:10.1186/S13072-015-0050-4.

Takashima, S. *et al.* (2021) 'Myocyte-specific enhancer factor 2c triggers transdifferentiation of adipose tissue-derived stromal cells into spontaneously beating cardiomyocyte-like cells', *Scientific Reports*, 11(1), p. 1520. doi:10.1038/S41598-020-80848-3.

Tang, B. *et al.* (2017) 'Waist-hip Ratio (WHR), a Better Predictor for Prostate Cancer than Body Mass Index (BMI): Results from a Chinese Hospital-based Biopsy Cohort', *Scientific Reports*, 7(1), p. 43551. doi:10.1038/srep43551.

Tang, H., Zhang, P. and Luo, X. (2022) 'Recent Technologies for Genetic Code Expansion and their Implications on Synthetic Biology Applications', *Journal of Molecular Biology*, 434(8), p. 167382. doi:10.1016/J.JMB.2021.167382.

Tchkonia, T. *et al.* (2013) 'Mechanisms and Metabolic Implications of Regional Differences among Fat Depots', *Cell metabolism*, 17(5), p. 644. doi:10.1016/J.CMET.2013.03.008.

Tchoukalova, Y.D. *et al.* (2010) 'Regional differences in cellular mechanisms of adipose tissue gain with overfeeding', *Proceedings of the National Academy of Sciences of the United States of America*, 107(42), pp. 18226–18231. doi:10.1073/PNAS.1005259107.

Tero, B.W. *et al.* (2022) 'Quantification of Lipid Area within Thermogenic Mouse Perivascular Adipose Tissue Using Standardized Image Analysis in FIJI', *Journal of vascular research*, 59(1), pp. 43–49. doi:10.1159/000517178.

Teves, M.E. *et al.* (2013) 'Sperm-associated antigen-17 gene is essential for motile cilia function and neonatal survival.', *American journal of respiratory cell and molecular biology*, 48(6), pp. 765–72. doi:10.1165/rcmb.2012-0362OC.

Teves, M.E. *et al.* (2015) 'Spag17 Deficiency Results in Skeletal Malformations and Bone Abnormalities', *PLOS ONE*. Edited by L. Malaval, 10(5), p. e0125936. doi:10.1371/journal.pone.0125936.

Thiebaud, D. *et al.* (1982) 'The Effect of Graded Doses of Insulin on Total Glucose Uptake, Glucose Oxidation, and Glucose Storage in Man', *Diabetes*, 31(11), pp. 957–963. doi:10.2337/DIACARE.31.11.957.

Tinsley, F.C., Taicher, G.Z. and Heiman, M.L. (2004) 'Evaluation of a quantitative magnetic resonance method for mouse whole body composition analysis', *Obesity research*, 12(1), pp. 150–160. doi:10.1038/OBY.2004.20.

Todaro, G.J. and Green, H. (1963) 'Quantitative studies of the growth of mouse embryo cells in culture and their development into established lines', *Journal of Cell Biology*, 17(2), pp. 299–313. doi:10.1083/JCB.17.2.299.

Tong, Y. *et al.* (2005) 'Suppression of expression of muscle-associated proteins by PPARα in brown adipose tissue', *Biochemical and Biophysical Research Communications*, 336(1), pp. 76–83. doi:10.1016/J.BBRC.2005.08.041.

Tran, T.T. *et al.* (2008) 'Beneficial effects of subcutaneous fat transplantation on metabolism', *Cell metabolism*, 7(5), pp. 410–420. doi:10.1016/J.CMET.2008.04.004.

Trapnell, C. *et al.* (2012) 'Differential gene and transcript expression analysis of RNA-seq experiments with TopHat and Cufflinks', *Nature Protocols 2012 7:3*, 7(3), pp. 562–578. doi:10.1038/nprot.2012.016.

Tsuchiya, M. *et al.* (2009) 'Suppression of MafA mRNA with siRNA prevents adipose cell differentiation in 3T3-L1 cells', *International journal of molecular medicine*, 23(6), pp. 725–732. doi:10.3892/IJMM_00000186.

Tsuchiya, M. *et al.* (2015) 'Transcriptional factors, Mafs and their biological roles', *World Journal of Diabetes*, 6(1), p. 175. doi:10.4239/WJD.V6.I1.175.

Turkmen, A. and Lin, S. (2017) 'Are rare variants really independent?', *Genetic Epidemiology*, 41(4), pp. 363–371. doi:10.1002/GEPI.22039.

Uitterlinden, A. (2016) 'An Introduction to Genome-Wide Association Studies: GWAS for Dummies', *Seminars in Reproductive Medicine*, 34(04), pp. 196–204. doi:10.1055/s-

0036-1585406.

Unger, R.H. and Scherer, P.E. (2010) 'Gluttony, sloth and the metabolic syndrome: a roadmap to lipotoxicity', *Trends in Endocrinology & Metabolism*, 21(6), pp. 345–352. doi:10.1016/J.TEM.2010.01.009.

Vague, J. (1956) 'The Degree of Masculine Differentiation of ObesitiesA FACTOR DETERMINING PREDISPOSITION TO DIABETES, ATHEROSCLEROSIS, GOUT, AND URIC CALCULOUS DISEASE', *The American Journal of Clinical Nutrition*, 4(1), pp. 20–34. doi:10.1093/AJCN/4.1.20.

Varadi, M. *et al.* (2022) 'AlphaFold Protein Structure Database: massively expanding the structural coverage of protein-sequence space with high-accuracy models', *Nucleic Acids Research*, 50(D1), pp. D439–D444. doi:10.1093/NAR/GKAB1061.

Vazquez, G. *et al.* (2007) 'Comparison of body mass index, waist circumference, and waist/hip ratio in predicting incident diabetes: A meta-analysis', *Epidemiologic Reviews*, pp. 115–128. doi:10.1093/epirev/mxm008.

Vegiopoulos, A., Rohm, M. and Herzig, S. (2017) 'Adipose tissue: between the extremes', *The EMBO Journal*, 36(14), pp. 1999–2017. doi:10.15252/EMBJ.201696206.

Verboven, K. *et al.* (2018) 'Abdominal subcutaneous and visceral adipocyte size, lipolysis and inflammation relate to insulin resistance in male obese humans', *Scientific reports*, 8(1). doi:10.1038/S41598-018-22962-X.

Vijay, J. *et al.* (2020) 'Single-cell analysis of human adipose tissue identifies depot and disease specific cell types', *Nature metabolism*, 2(1), pp. 97–109. doi:10.1038/S42255-019-0152-6.

Virtue, S. and Vidal-Puig, A. (2008) 'It's Not How Fat You Are, It's What You Do with It That Counts', *PLOS Biology*, 6(9), p. e237. doi:10.1371/JOURNAL.PBIO.0060237.

De Vries, S.J., Van Dijk, M. and Bonvin, A.M.J.J. (2010) 'The HADDOCK web server for data-driven biomolecular docking', *Nature Protocols 2010 5:5*, 5(5), pp. 883–897. doi:10.1038/nprot.2010.32.

Wajchenberg, B.L. *et al.* (2002) 'Depot-specific hormonal characteristics of subcutaneous and visceral adipose tissue and their relation to the metabolic syndrome', *Hormone and metabolic research = Hormon- und Stoffwechselforschung = Hormones et metabolisme*, 34(11–12), pp. 616–621. doi:10.1055/S-2002-38256.

Wallimann, T. *et al.* (2020) 'Role of creatine and creatine kinase in UCP1-independent adipocyte thermogenesis', *American Journal of Physiology - Endocrinology and Metabolism*, 319(5), pp. E944–E946. doi:10.1152/AJPENDO.00367.2020/ASSET/IMAGES/LARGE/AJ-AEND200042F001.JPEG.

Wang, J.Y. *et al.* (2012) 'Predictive value of serum uric acid levels for the diagnosis of metabolic syndrome in adolescents', *The Journal of pediatrics*, 161(4). doi:10.1016/J.JPEDS.2012.03.036.

Wang, Q. *et al.* (2021) 'IL-27 signalling promotes adipocyte thermogenesis and energy expenditure', *Nature 2021 600:7888*, 600(7888), pp. 314–318. doi:10.1038/s41586-021-04127-5.

Wang, Q.A. *et al.* (2013) 'Tracking adipogenesis during white adipose tissue development, expansion and regeneration', *Nature medicine*, 19(10), pp. 1338–1344. doi:10.1038/NM.3324.

Wang, X. *et al.* (2019) 'Bulk tissue cell type deconvolution with multi-subject single-cell expression reference', *Nature Communications 2019 10:1*, 10(1), pp. 1–9. doi:10.1038/s41467-018-08023-x.

Wang, Y. *et al.* (2018) 'The 3D Genome Browser: A web-based browser for visualizing 3D genome organization and long-range chromatin interactions', *Genome Biology*, 19(1), pp. 1–12. doi:10.1186/S13059-018-1519-9/FIGURES/5.

Ward, L.D. and Kellis, M. (2012) 'HaploReg: A resource for exploring chromatin states, conservation, and regulatory motif alterations within sets of genetically linked variants', *Nucleic Acids Research*, 40(D1), pp. D930–D934. doi:10.1093/nar/gkr917.

Warren, C.R. *et al.* (2017) 'Induced Pluripotent Stem Cell Differentiation Enables Functional Validation of GWAS Variants in Metabolic Disease', *Cell stem cell*, 20(4), pp. 547-557.e7. doi:10.1016/J.STEM.2017.01.010.

Watanabe, K. *et al.* (2019) 'A global overview of pleiotropy and genetic architecture in complex traits', *Nature genetics*, 51(9), pp. 1339–1348. doi:10.1038/S41588-019-0481-0.

Weisberg, S.P. *et al.* (2006) 'CCR2 modulates inflammatory and metabolic effects of high-fat feeding', *The Journal of clinical investigation*, 116(1), pp. 115–124. doi:10.1172/JCI24335.

Wernstedt Asterholm, I. *et al.* (2014) 'Adipocyte inflammation is essential for healthy adipose tissue expansion and remodeling', *Cell Metabolism*, 20(1), pp. 103–118. doi:10.1016/j.cmet.2014.05.005.

West, D.B. *et al.* (2016) 'Transcriptome Analysis of Targeted Mouse Mutations Reveals the Topography of Local Changes in Gene Expression', *PLOS Genetics*, 12(2), p. e1005691. doi:10.1371/JOURNAL.PGEN.1005691.

WHO (2011) *Waist circumference and waist-hip ratio: report of a WHO expert consultation*.

WHO (2016) *GLOBAL REPORT ON DIABETES*, *ISBN*. doi:10.5944/EDUCXX1.16026.

WHO (2021) *Obesity and overweight*. Available at: https://www.who.int/news-room/fact-sheets/detail/obesity-and-overweight (Accessed: 20 June 2022).

Wibmer, A.G. *et al.* (2021) 'Brown adipose tissue is associated with healthier body fat distribution and metabolic benefits independent of regional adiposity', *Cell Reports Medicine*, 2(7), p. 100332. doi:10.1016/J.XCRM.2021.100332.

Wickham, H. (2016) *ggplot2: Elegant Graphics for Data Analysis*. 2nd edn. Springer-Verlag New York. doi:https://doi.org/10.1007/978-3-319-24277-4.

Winkler, T.W. *et al.* (2018) 'A joint view on genetic variants for adiposity differentiates subtypes with distinct metabolic implications', *Nature communications*, 9(1). doi:10.1038/S41467-018-04124-9.

de Winter, T.J.J. and Nusse, R. (2021) 'Running Against the Wnt: How Wnt/β-Catenin

Suppresses Adipogenesis', *Frontiers in Cell and Developmental Biology*, 9, p. 140. doi:10.3389/FCELL.2021.627429/XML/NLM.

Witham, S. *et al.* (2011) 'A missense mutation in CLIC2 associated with intellectual disability is predicted by in silico modeling to affect protein stability and dynamics', *Proteins: Structure, Function, and Bioinformatics*, 79(8), pp. 2444–2454. doi:10.1002/PROT.23065.

Wortmann, S.B. *et al.* (2017) 'Biallelic variants in *WARS2* encoding mitochondrial tryptophanyl-tRNA synthase in six individuals with mitochondrial encephalopathy', *Human Mutation*, 38(12), pp. 1786–1795. doi:10.1002/humu.23340.

Wray, N.R. *et al.* (2013) 'Pitfalls of predicting complex traits from SNPs', *Nature reviews. Genetics*, 14(7), pp. 507–515. doi:10.1038/NRG3457.

Wright, P.E. and Dyson, H.J. (1999) 'Intrinsically unstructured proteins: re-assessing the protein structure-function paradigm', *Journal of molecular biology*, 293(2), pp. 321–331. doi:10.1006/JMBI.1999.3110.

Wu, Y. *et al.* (2019) 'Colocalization of GWAS and eQTL signals at loci with multiple signals identifies additional candidate genes for body fat distribution', *Human molecular genetics*, 28(24), pp. 4161–4172. doi:10.1093/HMG/DDZ263.

Xiong, Y. *et al.* (2018) 'A novel brown adipocyte-enriched long non-coding RNA that is required for brown adipocyte differentiation and sufficient to drive thermogenic gene program in white adipocytes.', *Biochimica et biophysica acta. Molecular and cell biology of lipids*, 1863(4), pp. 409–419. doi:10.1016/j.bbalip.2018.01.008.

Xue, R. *et al.* (2015) 'Clonal analyses and gene profiling identify genetic biomarkers of the thermogenic potential of human brown and white preadipocytes', *Nature Medicine*, 21(7), pp. 760–768. doi:10.1038/nm.3881.

Yamada, Y. *et al.* (2018) 'Impact of novel oncogenic pathways regulated by antitumor miR-451a in renal cell carcinoma'. doi:10.1111/cas.13526.

Yamamoto, Y. *et al.* (2010) 'Adipose depots possess unique developmental gene signatures', *Obesity*, 18(5), pp. 872–878. doi:10.1038/oby.2009.512.

Yang, J. *et al.* (2010) 'Common SNPs explain a large proportion of the heritability for human height', *Nature genetics*, 42(7), pp. 565–569. doi:10.1038/NG.608.

Yang, J. *et al.* (2015) 'Genetic variance estimation with imputed variants finds negligible missing heritability for human height and body mass index', *Nature genetics*, 47(10), pp. 1114–1120. doi:10.1038/NG.3390.

Yang, J. *et al.* (2017) 'Concepts, estimation and interpretation of SNP-based heritability', *Nature genetics*, 49(9), pp. 1304–1310. doi:10.1038/NG.3941.

Yang, W. *et al.* (2013) 'Regulation of adipogenesis by cytoskeleton remodelling is facilitated by acetyltransferase MEC-17-dependent acetylation of α-tubulin', *The Biochemical journal*, 449(3), p. 605. doi:10.1042/BJ20121121.

Yao, L. *et al.* (2014) 'Deficiency in adipocyte chemokine receptor CXCR4 exacerbates obesity and compromises thermoregulatory responses of brown adipose tissue in a mouse model of diet-induced obesity', *The FASEB Journal*, 28(10), pp. 4534–4550.

doi:10.1096/FJ.14-249797.

Yengo, L. *et al.* (2018) 'Meta-analysis of genome-wide association studies for height and body mass index in ~700000 individuals of European ancestry', *Human molecular genetics*, 27(20), pp. 3641–3649. doi:10.1093/HMG/DDY271.

Yengo, L. *et al.* (2022) 'A saturated map of common genetic variants associated with human height', *Nature 2022 610:7933*, 610(7933), pp. 704–712. doi:10.1038/s41586-022-05275-y.

Zaragoza, M. V. *et al.* (2004) 'Identification of the TBX5 transactivating domain and the nuclear localization signal', *Gene*, 330(1–2), pp. 9–18. doi:10.1016/J.GENE.2004.01.017.

Zatterale, F. *et al.* (2020) 'Chronic Adipose Tissue Inflammation Linking Obesity to Insulin Resistance and Type 2 Diabetes', *Frontiers in Physiology*, 10, p. 1607. doi:10.3389/FPHYS.2019.01607/BIBTEX.

Zhang, Y. *et al.* (2008) 'Model-based analysis of ChIP-Seq (MACS)', *Genome Biology*, 9(9), pp. 1–9. doi:10.1186/GB-2008-9-9-R137/FIGURES/3.

Zhao, J. *et al.* (2010) 'The role of height-associated loci identified in genome wide association studies in the determination of pediatric stature.', *BMC medical genetics*, 11, p. 96. doi:10.1186/1471-2350-11-96.

Zheng, Y. *et al.* (2016) 'Genome-wide DNA methylation analysis identifies candidate epigenetic markers and drivers of hepatocellular carcinoma', *Briefings in Bioinformatics*, 19(1), p. bbw094. doi:10.1093/bib/bbw094.

Zhu, Q. *et al.* (2020) 'Body mass index and waist-to-hip ratio misclassification of overweight and obesity in Chinese military personnel', *Journal of Physiological Anthropology*, 39(1). doi:10.1186/S40101-020-00236-8.

Zillikens, M.C. *et al.* (2008) 'Sex-specific genetic effects influence variation in body composition', *diabetologia*, 50(12), pp. 2233–2241. doi:10.1007/s00125-008-1163-0.

Zillikens, M.C. *et al.* (2017) 'Large meta-analysis of genome-wide association studies identifies five loci for lean body mass', *Nature Communications 2017 8:1*, 8(1), pp. 1–13. doi:10.1038/s41467-017-00031-7.

Van Zundert, G.C.P. *et al.* (2016) 'The HADDOCK2.2 Web Server: User-Friendly Integrative Modeling of Biomolecular Complexes', *Journal of Molecular Biology*, 428(4), pp. 720–725. doi:10.1016/J.JMB.2015.09.014.

9

Appendix

9.1. Methods

9.1.1. Animal Studies

9.1.1.1. TBX15-H156N-EM2-B6N and TBX15-M566R-EM3-B6N stock line generation using CRISPR/Cas9

Single guide RNA (sgRNA) sequences were designed by the MRCH MCB facility for the sequence flanking intended point mutations and were screened for cutting efficiency *in vitro* using the Guide-it™ sgRNA screening kit (cat. 632639, TaKaRa Bio; Table 9.1). Donor homology directed repair sequence templates (ssODNs) are show in Table 9.2.

Table 9.1. sgRNA sequence used for TBX15-H156N and TBX15-M566R CRISPR/Cas9 repair to generate mouse models. sgRNAs were initially selected based on minimal predicted off-target effects, sgRNA with best cutting efficiency used to generate the mouse lines are shown in the table.

sgRNA	5'-3' Sequence [PAM]
Tbx15_H156N #3	GCCATGAGAGTGAAAATCAC[TGG]
Tbx15_M566R #1	ATGCTATGCTCCATCCCTGT[AGG]

For TBX15-H156N-EM2-B6N mice, pronuclear microinjection of CRISPR/Cas9 reagents into C57BL/6NTac embryos was performed by the MCB facility as described by (Gardiner and Teboul, 2009). Cas9 mRNA, sgRNAs and ssODNs were diluted and mixed in microinjection buffer (10 mM Tris–HCl, 0.1 mM EDTA, 100 mM NaCl, pH7.5) to 50 ng/µL, 6.5 ng/µL and 100 ng/µL, respectively. The ssODNs contain

phosphothiocyate bonds to protect from degradation in the embryo. Injected embryos were re-implanted in CD1 pseudo-pregnant females. Host females were allowed to litter and rear F_0 progeny.

Table 9.2. Homology directed repair donor sequence for TBX15-H156N and TBX15-M566R CRISPR/Cas9 repair compared to wildtype sequence. Donor homology-directed repair sequence templates (ssODNs) were designed to introduce intended point mutations (either p.H156N or p.M566R substitution), and additional silent point mutations to remove the seed and PAM sequences for the sgRNA to prevent re-processing/re-cutting of the modified allele by Cas9. Point mutations indicated in red, point mutations for amino acid substitution are further underlined.

Mouse line	Donor Sequence	5'-3' Sequence
TBX15-H156N	Wild type sequence	AATGAGAAGACACTCTAAGCTCCTACTCGAGTTTACTTTC CTCCTCTCTGTGCTCATGATCTTATTCATCTTCACAGGAG GATGTTTCCTGCCATGAGAGTGAAAATCACTGGCCTGGA TCCACATCAGCAATACTATATAGCAATGGACATTGTTCCT GTGGACAATAAAAGATACAGGTAAGGACACTGGAATCTG GAGC
	TBX15-H156N	AATGAGAAGACACTCTAAGCTCCTACTCGAGTTTACTTTC CTCCTCTCTGTGCTCATGATCTTATTCATCTTCACAGGAG GATGTTTCCTGCCATGAGAGTGAAAAT**T**AC**A**GGCCTGGA TCCA**A**ATCAGCAATACTATATAGCAATGGACATTGTTCC TGTGGACAATAAAAGATACAGGTAAGGACACTGGAATCT GGAGC
TBX15-M566R	Wild type sequence	AGCGCGTCTCAAAGCACTTTACTCTGTTCTTCTCCTTCTA ATGGGGCCTTTGGAGAGAGGCAGTACCTGCCTACAGGGA TGGAGCATAGCATGCACATGATCAGCCCTTCAACTAATA ATCAGCAGGCTACCAACACCTGTGATGGCCGACAGTATGG GGCAGTCCCAGGCTCTGCCTCTCAGATGTCCGTACACATG GTTT
	TBX15-M566R	AGCGCGTCTCAAAGCACTTTACTCTGTTCTTCTCCTTCTA ATGGGGCCTTTGGAGAGAGGCAGTACCTGCCTAC**T**GG**A**A TGGAGCATAGCA**G**GCACATGATCAGCCCTTCAACTAATA ATCAGCAGGCTACCAACACCTGTGATGGCCGACAGTATGG GGCAGTCCCAGGCTCTGCCTCTCAGATGTCCGTACACATG GTTT

For TBX15-M566R-EM3-B6N mice, electroporation of 1-cell embryos was performed by the MCB team as described in (Qin *et al.*, 2015). Briefly, Cas9 protein, sgRNAs and ssODNs were diluted and mixed in Opti-MEM reduced serum media (Gibco) to 650 ng/µl, 130 ng/µl and 400 ng/µl, respectively. Embryos were electroporated using

the following conditions: 30 V, 3 ms pulse length, 100 ms pulse interval, 12 pulses. Electroporated embryos were re-implanted in CD1 pseudo-pregnant females. Host females were allowed to litter and rear F_0 progeny.

9.1.1.2. Genotyping

All primer design and genotyping were carried out by the MRCH genotyping facility. For ASPPAA, an allele-specific primer and an allele-specific probe were designed specific to each of the Tbx15 alleles (Table 9.3, Table 9.4). The primers were designed in such a way that 3' ends ended with a base specific to the targeted allele. The probes were also designed specific to the allele at 3' ends giving a primer-probe overlap (maximum 3 nucleotides). Dot1l was used as an internal control for all reactions (Table 9.4, Table 9.5).

Table 9.3. qPCR reaction mixes for Tbx15 allele specific FAM assays. *See Table 9.4 for primers and probe for specific assays.

Reagent	Volume
ABI GTX TaqMan master mix	5 µL
FAM Assay (5 µM probe, 15 µM primer 1 and 15 µM primer 2)*	0.3 µL
DNA (1/10 dilution of ABI Sample-to-SNP prep)	2.5 µL
ddH_2O	1.55 µL

Table 9.4. *Tbx15* mouse line genotyping assay details. Primer sequences highlighted in blue, probe sequences highlighted in red and any overlap between primer and probe highlighted in yellow.

Assay	Assay details (DNA sequence)	Primer/probe
Tbx15 -WT1 assay (FAM labelled probe)	CTTCACAGGAGGATGTTTCCTGCCATGAGA GTGAAAATCACTGGCCTGGATCCACATCAG CAATACTATATAGCAATGGACATTGTTCCT GTGGACAATAAAAGATACAGGTAAGGACA CTGGAATCTGGAGC	Primer 1 = GCTCCAGATTCCAGTGTCCTTAC Primer 2 = TTCCTGCCATGAGAGTGAAAATC Probe = ATGTGGATCCAGGCCAGTGAT
Tbx15-KO-MUT1 assay (FAM labelled probe)	AAATATGTTTTATTTAAGAGGCAGATAAC CTTTTAAAAGGAAGAGGCTTAAGTATATT AAGAAGTTCAAGATGGAAGGAGGT[215,502bp DELETION] TGCACTTTTCTCACAGATCTGTAGTTTGGC TTTTTATACTTTCCCCAATCTTAAAGGAAG GGAATGGAAGCAGAA	Primer 1 = GAGGCAGATAACCTTTTAAAAGG AAGAGG Primer 2 = GCTTCCATTCCCTTCCTTTAAGAT TG Probe = TCAAGATGGAAGGAGGTTGCACT TTTC
Tbx15-H156N-WT1 assay (FAM labelled probe)	CTTCACAGGAGGATGTTTCCTGCCATGAGA GTGAAAATCACTGGCCTGGATCCACATCAG CAATACTATATAGCAATGGACATTGTTCCT GTGGACAATAAAAGATACAGGTAAGGACA CTGGAATCTGGAGC	Primer 1 = GCTCCAGATTCCAGTGTCCTTAC Primer 2 = TTCCTGCCATGAGAGTGAAAAT**C** Probe = AT**G**TGGATCCAGGCC**A**GT**G**AT
TBX15-H156N-MUT1 assay (FAM labelled probe)	CTTCACAGGAGGATGTTTCCTGCCATGAGA GT**G**AAAAT**T**AC**A**GGCCTGGATCCA**A**ATCA GCAATACTATATAGCAATGGACATTGTTCC TGTGGACAATAAAAGATACAGGTAAGGAC ACTGGAATCTGGAGC	Primer 1 = GAAAAT**T**AC**A**GGCCTGGATCCA**A** Primer 2 = GCTCCAGATTCCAGTGTCCTTAC Probe = ATAGCAATGGACATTGTTCCTGT GGACA
TBX15-M566R-WT1 assay (FAM labelled probe)	AGCGCGTCTCAAAGCACTTTACTCTGTTCT TCTCCTTCTAATGGGGCCTTTGGAGAGAGG CAGTACCTGCCTACA**GGGATGGAGCATAG CAT**GCACATGATCAGCCCTTCAACTAAT**AA TCAGCAGGCTACCAACACCTG**TGATGGCC GACAGTATGGGGCAGTCCCAGGCTCTGC**CT CTCAGATGTCCGTACAC**ATGGTTTAAAGA GCAGTGCACACACTATCGAGGTGATGGCGG CCAAGACTCCAGAATCTCTGTGGGTGGATC	Primer 1 = GGGATGGAGCATAGCAT Primer 2 = GTGTACGGACATCTGAGAG Probe = AATCAGCAGGCTACCAACACCTG
TBX15-M566R-MUT1 assay (FAM labelled probe)	AGCGCGTCTCAAAGCACTTTACTCTGTTCT TCTCCTTCTAATGGGGCCTTTGGAGAGAGG CAGTACCTGCCTA**CTGGAATGGAGCATAG CAG**GCACATGATCAGCCCTTCAACTAAT**AA TCAGCAGGCTACCAACACCTGT**GATGGCC GACAGTATGGGGCAGTCCCAGGC**TCTGCCT CTCAGATGTCC**GTACACATGGTTTAAAGA GCAGTGCACACACTATCGAGGTGATGGCGG CCAAGACTCCAGAATCTCTGTGGGTGGATC	Primer 1 = CTGGAATGGAGCATAGCAG Primer 2 = GGACATCTGAGAGGCAGA Probe = AATCAGCAGGCTACCAACACCTGT
Dot1l internal control (VIC labelled probe)	CTGTTAGTAGTTGGCATCCTTATGCTTCAT CTTACAGTCGACTTGAGAGCTGGCCCTGAA TGGTCGTGCTGGGGC	Primer 1 = GCCCCAGCACGACCATT Primer 2 = TAGTTGGCATCCTTATGCTTCATC Probe = CCAGCTCTCAAGTCG

Table 9.5. qPCR reaction mixes for Dot1l VIC internal control assay. *See Table 9.4 for primers and probe for Dot1l assay.

Reagent	Volume
ABI GTX TaqMan master mix	5 µL
Dot1L Fw (20 µM)*	0.225 µL
Dot1L Rv (20 µM) *	0.225 µL
Dot1L probe (5 µM) *	0.2 µL
DNA (1/10 dilution of ABI Sample-to-SNP prep)	2.5 µL
ddH_2O	1.55 µL

9.1.1.3. Clinical chemistry analysis

Blood plasma analysis was performed by the MLC clinical chemistry facility. The DXC 700 AU analyser was maintained following strict periodical maintenance plans. Subsequently, assay performance was tested by running a reagent blank (diH_2O) and the appropriate calibrator for the reagent, if required (Table 9.6). QC using the appropriate material was performed before every run (Table 9.8). Following optimal reagent calibration and QC performance, lithium-heparinised plasma samples were analysed using reagents and settings recommended by the manufacturer (Table 9.7).

Table 9.6 Beckman Coulter calibration material information.

Calibration material	Name	Product ID	Manufacturer
1	System Calibrator	066300	Beckman Coulter
2	HDL-Cholesterol Calibrator	ODC0011	Beckman Coulter
3	LDL-Cholesterol Calibrator	ODC0012	Beckman Coulter
6	Ketone Calibrator (human assayed serum L3)	CAL2351	Randox
9	NEFA standard Solution	270-7700	Fujufilm Wako
10	Glycerol Reagent & Calibrator	GY105	Randox

Table 9.7. Beckman Coulter Assay information. *Test not QC controlled or calibrated. Reagents manufactured by Beckman Coulter, unless stated otherwise)

Assay		Reagent	QC material	Calibrator material
Electrolytes	Sodium Potassium Chloride	ISE Reference Solution (066318) ISE MID standard (066319) ISE Buffer (066320)	1 & 2	ISE Serum high (066316) ISE Serum low (066317)
Full metabolic panel	Albumin	OSR6202	1 & 2	1
	ALP	OSR6104	1 & 2	1
	ALT	OSR6107	1 & 2	1
	Amylase	OSR6106	1 & 2	1
	AST	OSR6009	1 & 2	1
	Bilirubin Total	OSR6112	1 & 2	1
	Calcium (Arsenazo III)	OSR61117	1 & 2	1
	Total Cholesterol	OSR6216	1 & 2	1
	CK (NAC)	OSR6179	1 & 2	1
	Creatinine (Enzymatic method)	OSR61204	1 & 2	1
	Glucose	OSR6121	1 & 2	1
	HDL-Cholesterol	OSR6287	7 & 8	2
	Inorganic Phosphorous	OSR6122	1 & 2	1
	Iron	OSR6186	1 & 2	1
	LDH	OSR6126	1 & 2	1
	LDL-Cholesterol	OSR6183	7 & 8	3
	LIH	OSR62166	N/A *	N/A *
	Magnesium	OSR6189	1 & 2	1
	Total Protein	OSR6132	1 & 2	1
	Triglycerides	OSR61118	1 & 2	1
	Urea	OSR6234	1 & 2	1
	Uric Acid	OSR6198	1 & 2	1
	Glycerol Reagent & Calibrator	GY105 (Randox)	5	10
	Ketone bodies (D-3-Hydroxybutyrate)	RB 1007 (Randox)	11 & 12	6
	Free fatty acids (NEFA-HR(2) reagent 1 & 2)	434-91795 & 436-91995, respectively (Fujifilm Wako)	3 & 4	9

Table 9.8. Beckman Coulter quality control material information.

QC material	Name	Product ID	Manufacturer
1	Control Serum 1	ODC0003	Beckman Coulter
2	Control Serum 2	ODC0004	Beckman Coulter
3	WAKO Control Serum I	410-00104	Fujifilm Wako
4	WAKO Control Serum II	416-00204	Fujifilm Wako
5	Glycerol control	GY1369	Randox
7	HDL / LDL Control Serum 1	ODC0005	Beckman Coulter
8	HDL / LDL Control Serum 2		
11	Ketone Control 1 (human assayed sera L2)	HS2611	Randox
12	Ketone Control 2 (human assayed sera L3)	HS2611	Randox

9.1.2. Molecular biology studies

9.1.2.1. RNA-sequencing

9.1.2.1.1. Sample preparation and RNA-sequencing

The Oxford Genomics Centre performed all sample preparation, library generation and RNA-sequencing. Briefly, RNA was quantified using RiboGreen (Invitrogen) on the FLUOstar OPTIMA plate reader (BMG Labtech Ltd, Aylesbury, UK) and size profile and integrity analysed using the RNA ScreenTape system on the 2200 or 4200 TapeStation (Agilent Technologies). Input material was normalised to 100 ng prior to library preparation. Polyadenylated transcript enrichment and strand specific library preparation was completed using NEBNext ultra II mRNA kit (NEB) following manufacturer's instructions. Libraries were amplified (14 cycles) on a Tetrad (Bio-Rad) using in-house unique dual-indexing primers (Lamble *et al.*, 2013). Individual libraries were normalised using Qubit, size profiles were analysed on the 2200 or 4200 TapeStation and pooled accordingly. The pooled library was diluted to 10 nM, denatured and further diluted prior to loading on the sequencer. Paired end sequencing was performed using a NovaSeq6000 platform (Illumina, NovaSeq 6000 S2/S4 reagent kit v1.5, 300 cycles).

9.1.2.1.2. Differential gene expression analysis

RNA-sequencing data files were processed by Dr Michelle Simon at MRCH. Briefly, RNA-sequencing reads were aligned to the mouse genome (mm10) using TopHat (Trapnell *et al.*, 2012). The read counts for each gene were calculated from the aligned reads using HTSeq (Anders, Pyl and Huber, 2015), and used to calculate CPM (counts per million per kilo-base) and RPKM (reads per million per kilo-base) for each sample. Differentially expressed genes, using RPKM were identified using EdgeR with default parameters (Robinson, McCarthy and Smyth, 2010). Gene expression was plotted using ggplot2 in R (Wickham, 2016). Genomic annotations were provided by Ensembl_v79 (Buniello *et al.*, 2019). Exon usage was analysed using Subreads in R (Liao, Smyth and Shi, 2019).

9.1.2.2. ChIP-sequencing

9.1.2.2.1. Sample preparation

Active Motif Inc. prepared chromatin, performed chromatin immunoprecipitation (ChIP) reactions, generated and sequenced libraries, and performed basic data analysis. In brief, cell pellets were fixed with 1% (v/v) formaldehyde for 15 minutes and quenched with 0.125 M glycine. Chromatin was isolated by adding lysis buffer, followed by disruption with a dounce homogenizer. Lysates were sonicated and DNA sheared to an average length of 300-500 bp with an EpiShear probe sonicator (cat. 53051, Active Motif Inc.). Genomic DNA (input) was prepared by treating aliquots of chromatin with RNase and proteinase K for de-crosslinking, followed by solid-phase reversible-immobilization bead clean-up (Beckman Coulter) and quantitation by Clariostar (BMG Labtech, Ortenberg, Germany).

An aliquot of chromatin (40 µg) was precleared with protein A agarose beads (Invitrogen). Genomic DNA regions of interest were isolated using 6 µg of antibody against HA-tag (cat. ab9110, lot GR3413592-1, Abcam). Complexes were washed, eluted from the beads with SDS buffer, and subjected to RNAse and proteinase K treatment. Crosslinks were reversed by incubation overnight at 65°C, and ChIP DNA was purified by phenol-chloroform extraction and ethanol precipitation. Subsequently, qPCR reactions were performed in triplicate on specific genomic regions using SYBR green supermix (Bio-Rad). The resulting signals were normalized for primer efficiency by carrying out qPCR for each primer pair using input DNA.

9.1.2.2.2. ChIP-sequencing

Custom Illumina sequencing libraries (paired-read adapter oligonucleotides described by (Bentley *et al.*, 2008)) were prepared from ChIP and input DNAs using an automated Apollo 342 system (Wafergen Biosystems/TaKaRa Bio). After PCR amplification, DNA libraries were quantified and sequenced on Illumina's NextSeq 500 (75-nucleotide reads, single-end). Reads were aligned to the human or mouse genome (hg38 or mm10) using the Burrows-Wheeler aligner algorithm (default settings) (Li and Durbin, 2009). Duplicate reads were removed, and only uniquely mapped reads (mapping quality ≥ 25) were used for further analysis. Alignments were extended *in silico* at their 3'-ends to a length of 200 bp (average genomic fragment length in the size-selected library) and assigned to 32-nucleotide bins along the genome. The resulting histograms (genomic "signal maps") were stored in bigWig files. Peak locations were determined using the model-based analysis of ChIP-sequencing (MACS) algorithm v2.1.0, with a cut-off $p<1x10^{-7}$ (Zhang *et al.*, 2008). Peaks that were on the ENCODE

blacklist of known false ChIP-sequencing peaks were removed. Signal maps and peak locations were used as input data to Active Motif's proprietary analysis program, which creates Excel tables containing detailed information on sample comparison, peak metrics, peak locations, and gene annotations.

9.1.2.2.3. HA antibody validation

Before running a full ChIP-sequencing analysis, Active Motif performed antibody validation. ChIP reactions were carried out using 30 µg chromatin per sample with the anti-HA-tag antibody. The ChIP DNAs were processed into standard Illumina ChIP-sequencing libraries and sequenced to generate ≥10 million reads and aligned to human or mouse genome (hg38 or mm10) (described in 9.1.2.2.2). Signal maps capturing fragment densities along the genome were generated and visualized in the integrated genome browser. In addition, MACS peak finding was performed to identify the most significant peaks.

9.2. Results

9.2.1. Chapter 3 – Prioritising the role of potentially functional coding SNPs within the *TBX15* gene

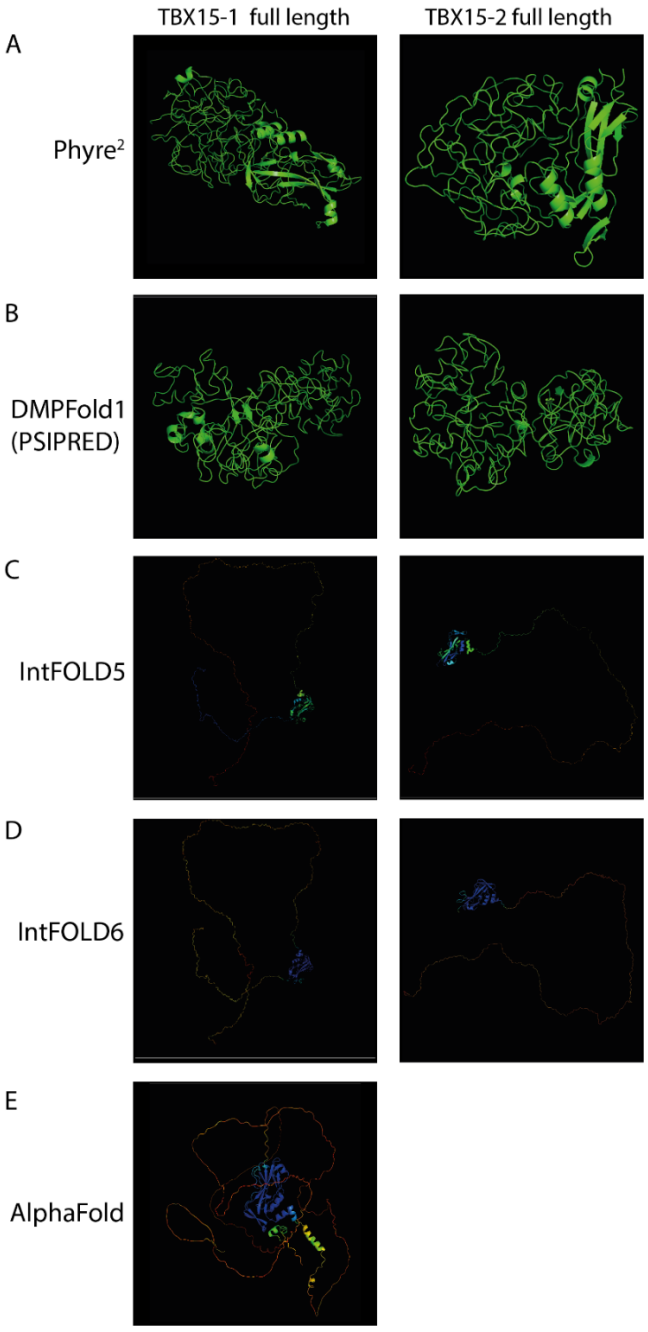

Figure 9.1 Comparison of full-length 3D TBX15 protein models between several homology modelling servers. TBX15-1 (602aa) and TBX15-2 (496aa) models using several servers. A. Phyre v2.0, B. DMPFold v1.0, C. IntFOLD v5.0, D. IntFOLD v6.0 and E. AlphaFold v2.0. DMPFold v1.0 can only process sequences up to 500 amino acids in length, for the full length TBX15-202 sequence residues 1-500 were modelled. For C-E residues were coloured by residue accuracy predictions using reverse colour scheme - blue high accuracy, through green, yellow and orange to red low accuracy: IntFOLD v5.0/6.0 residue accuracy predictions (Angstroms), and AlphaFold v2.0 per-residue confidence.

Table 9.9. Associated scores for full-length 3D TBX15 protein models. IntFOLD v5.0 and v6.0 produced scores between 0-1: scores <0.2 indicate incorrectly modelled regions, scores >0.4 indicate models close to native structure of template. This is combined with a p-value that represents probability of incorrect models: p<0.001 (certain=less than 1/1000 incorrect models), p<0.01 (high=less than 1/100 incorrect models), p<0.05 (medium=less than 1/20 incorrect models), p<0.1 (low=less than 1/10 incorrect models), p≥0.1 (uncertain=more than 1/10 incorrect models). AlphaFold v2.0 produced a per-residue confidence score (pLDDT) between 0 and 100. Very high (pLDDT>90), confident (pLDDT≤90>70), low (pLDDT≤70>50), very low (pLDDT≤50). Phyre v2.0 confidence represents the probability (0-100) that the model is a true homology match to template, % sequence ID between model and template (above 30% is considered a good match, although low % ID models with high confidence can still be useful). DMPfold v1.0 does not provide "scoring" information for models.

Server	TBX15 model	PDB model used as template	Score	p-value (confidence)
Phyre v2.0	TBX15-2	4a04B (TBX1)	61% sequence ID	100% confidence
	TBX15-1	4a04B (TBX1)	61% sequence ID	100% confidence
	TBX15-X2	2DM3 (IgG of palladin)	<5% sequence ID	0% confidence
DMPfold v1.0	TBX15-2	N/A (not provided)	N/A (not provided)	N/A (not provided)
	TBX15-1 (residues 1-500 only)	N/A (not provided)	N/A (not provided)	N/A (not provided)
	TBX15-X2	N/A (not provided)	N/A (not provided)	N/A (not provided)
IntFOLD v5.0	TBX15-2	N/A (no templates used)	0.3327	5.946E-2 (low)
	TBX15-1	1h6fB (TBX3), 2x6uA (TBX5)	0.3135	1.155E-1 (uncertain)
	TBX15-X2	1pclA (Pectate Lyases)	0.2732	3.2724E-1 (uncertain)
IntFOLD v6.0	TBX15-2	1h6fB (TBX3)	0.4042	2.738E-1 (uncertain)
	TBX15-1	1h6fB (TBX3), 2x6uA (TBX5)	0.3747	4.129E-1 (uncertain)
	TBX15-X2	N/A (no templates used)	0.3216	7.27E-1 (uncertain)
AlphaFold v2.0	TBX15-1	N/A (*ab initio* modelling)	Residues 109-302 pLDDT >70 Remaining residues pLDDT <70	N/A

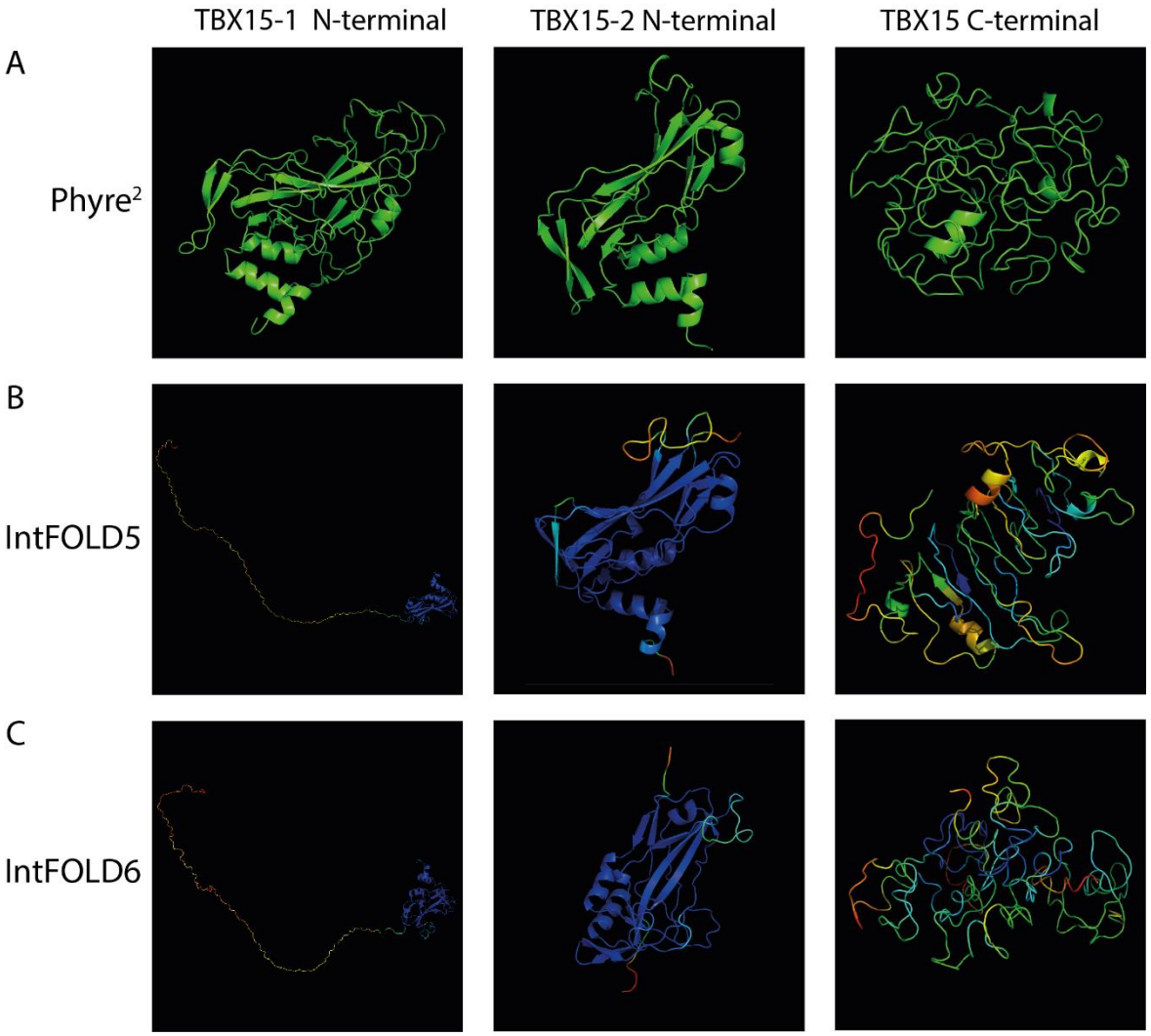

Figure 9.2. Comparison of 3D TBX15 N- and C-terminal protein models between several homology modelling servers. A. Phyre v2.0, B. IntFOLD v5.0, C. IntFOLD v6.0, For B and C residues were coloured by residue accuracy predictions using reverse colour scheme - blue high accuracy, through green, yellow and orange to red low accuracy: IntFOLD v5.0/6.0 residue accuracy predictions (Angstroms).

Table 9.10. Associated scores for 3D TBX15 N-terminal and C-terminal protein models. IntFOLD v5.0 and v6.0 produced scores between 0-1: scores <0.2 indicate incorrectly modelled regions, scores >0.4 indicate models close to native structure of template. This is combined with a p-value that represents probability of incorrect models: p<0.001 (certain=less than 1/1000 incorrect models), p<0.01 (high=less than 1/100 incorrect models), p<0.05 (medium=less than 1/20 incorrect models), p<0.1 (low=less than 1/10 incorrect models), p≥0.1 (uncertain=more than 1/10 incorrect models). Phyre v2.0 confidence represents the probability (0-100) that the model is a true homology match to template, % sequence ID between model and template (above 30% is considered a good match, although low % ID models with high confidence can still be useful).

Server	TBX15 model	PDB model used as template	Score	p-value (confidence)
Phyre v2.0	TBX15-2 N-terminal	4a04B (TBX1)	61% sequence ID	100% confidence
	TBX15-1 N-terminal	4a04B (TBX1)	61% sequence ID	100% confidence
	TBX15-2/1 C-terminal	5gxwB (Importin)	<5% sequence ID	1% confidence
IntFOLD v5.0	TBX15-2 N-terminal	1h6fB (TBX3), 2x6uA (TBX5)	0.5393	3.486E-8 (certain)
	TBX15-1 N-terminal	1h6fB (TBX3), 5t1jA (T-bet), 2x6uA (TBX5)	0.42323	6.005E-5 (certain)
	TBX15-2/1 C-terminal	7vobC (SAM enzyme BslE)	0.2703	4.006E-1 (uncertain)
IntFOLD v6.0	TBX15-2 N-terminal	2x6uA (TBX5)	0.6429	2.904E-13
	TBX15-1 N-terminal	1h6fB (TBX3), 2x6uA (TBX5)	0.5029	3.123E-2 (medium)
	TBX15-1/1 C-terminal	N/A (no templates used)	0.3511	5.521E-1

9.2.2. Chapter 4 – Characterising the function of *Tbx15 in vivo*

Table 9.11. Female *Tbx15*$^{+/-}$ echo-MRI body composition over 4 to 24 weeks. All data was analysed by repeated measures two-way ANOVA with post-hoc Šídák's multiple comparisons, per sex and diet. Interaction (time x genotype); significant values (p<0.05) highlighted in bold. High-fat diet: *Tbx15*$^{+/+}$ (n=18), -*Tbx15*$^{+/-}$ (n=22), low-fat diet: *Tbx15*$^{+/+}$ (n=18), *Tbx15*$^{+/-}$ (n=22).

	High-fat diet						**Low-fat diet**					
	Bodyweight		**Fat Mass**		**Lean Mass**		**Bodyweight**		**Fat Mass**		**Lean Mass**	
Interaction	0.8947		0.5595		**0.0162**		0.0660		**0.0011**		**0.0281**	
Time	**<0.0001**		**<0.0001**		**<0.0001**		**<0.0001**		**<0.0001**		**<0.0001**	
Genotype	0.9415		0.9573		0.6541		**0.0326**		**0.0329**		0.1619	
Post-hoc analysis (adjusted P value)												
Weeks	**Diff means**	**P-value**	**Diff means**	**P-value**	**Diff means**	**P-value**	**Diff means**	**P-value**	**Diff means**	**P-value**	**Diff means**	**P-value**
4	-0.1661	>0.9999	0.03500	>0.9999	-0.1967	0.9998	0.2577	0.9998	0.1579	0.9104	0.1160	>0.9999
6	0.5383	0.9719	0.6076	0.5326	-0.7169	0.6303	0.9611	0.1003	0.1814	0.9936	0.7993	0.0879
8	0.1180	>0.9999	0.4184	0.9986	-0.1377	>0.9999	0.8369	0.4473	0.2866	0.9630	0.5027	0.8371
10	0.6193	>0.9999	0.8722	0.9936	-0.4692	0.9119	1.045	0.1802	0.1971	0.9983	0.9033	0.2951
12	0.3415	>0.9999	0.5134	>0.9999	-0.3403	0.9937	0.4708	0.9681	0.1235	>0.9999	0.3069	0.9957
14	-0.5401	>0.9999	-0.5054	>0.9999	0.003081	>0.9999	0.7259	0.7028	0.1951	0.9991	0.5511	0.7775
16	-0.0693	>0.9999	-0.1124	>0.9999	-0.005758	>0.9999	1.355	0.0712	0.7974	0.0559	0.4904	0.8557
18	-0.6226	>0.9999	-0.7039	>0.9999	-0.03955	>0.9999	1.159	0.3611	0.8595	0.3206	0.3034	0.9957
20	-0.2106	>0.9999	-0.4092	>0.9999	0.09298	>0.9999	1.093	0.5902	0.8231	0.5165	0.3195	0.9884
22	-0.7793	>0.9999	-0.8038	>0.9999	0.06293	>0.9999	1.282	0.4570	1.076	0.2270	0.2579	0.9994
24	-0.1881	>0.9999	-0.4598	>0.9999	0.1848	>0.9999	1.145	0.6618	0.9386	0.4241	0.1728	>0.9999

Table 9.12. Male *Tbx15*$^{+/-}$ echo-MRI body composition over 4 to 24 weeks. All data was analysed by repeated measures two-way ANOVA with post-hoc Šídák's multiple comparisons, per sex and diet. Interaction (time x genotype); significant values (p<0.05) highlighted in bold. High-fat diet: *Tbx15*$^{+/+}$ (n=21), *Tbx15*$^{+/-}$ (n=17), low-fat diet: *Tbx15*$^{+/+}$ (n=21), *Tbx15*$^{+/-}$ (n=14).

	High-fat diet						**Low-fat diet**					
	Bodyweight		**Fat Mass**		**Lean Mass**		**Bodyweight**		**Fat Mass**		**Lean Mass**	
Interaction	0.6853		0.5674		0.9740		0.1105		**0.0014**		0.9827	
Time	**<0.0001**		**<0.0001**		**<0.0001**		**<0.0001**		**<0.0001**		**<0.0001**	
Genotype	0.3346		0.4715		0.4100		**0.0226**		0.1414		0.1796	
Post-hoc analysis (adjusted P value)												
Weeks	**Diff means**	**P-value**	**Diff means**	**P-value**	**Diff means**	**P-value**	**Diff means**	**P-value**	**Diff means**	**P-value**	**Diff means**	**P-value**
4	-0.6607	0.9315	-0.2943	0.8636	-0.6589	0.8115	0.7321	0.9008	-0.1005	0.9992	0.6921	0.7630
6	-0.2036	>0.9999	0.1433	>0.9999	-0.5016	0.9941	0.8886	0.5712	-0.007381	>0.9999	0.9600	0.4291
8	-0.3576	>0.9999	-0.2558	>0.9999	-0.3956	0.9998	0.8931	0.5852	0.08500	>0.9999	0.9181	0.5613
10	-0.9032	0.9998	-0.3336	>0.9999	-0.4313	0.9997	1.171	0.3838	0.2426	0.9996	0.9021	0.7750
12	-1.319	0.9980	-0.9258	0.9995	-0.1154	>0.9999	1.424	0.2206	0.4443	0.9942	0.6343	0.9851
14	-1.599	0.9928	-1.121	0.9980	-0.5946	0.9985	1.520	0.1992	0.7748	0.8523	0.7376	0.9322
16	-1.807	0.9799	-1.364	0.9815	-0.5719	0.9994	1.907	0.1734	0.9193	0.9039	0.8505	0.9070
18	-1.789	0.9765	-1.377	0.9602	-0.5077	0.9999	1.616	0.4088	1.201	0.7042	0.4286	0.9994
20	-1.782	0.9184	-1.167	0.9290	-0.7157	0.9959	2.127	0.1906	1.454	0.5981	0.5602	0.9977
22	-1.636	0.8955	-0.7625	0.9879	-0.8105	0.9926	2.101	0.3605	1.445	0.7509	0.6331	0.9946
24	-1.269	0.9798	0.2052	>0.9999	-0.8028	0.9925	2.161	0.3054	1.765	0.5230	0.3474	>0.9999

Table 9.13. Female *Tbx15*^{H156N} echo-MRI body composition over 4 to 24 weeks. All data was analysed by repeated measures two-way ANOVA with post-hoc Šídák's multiple comparisons, per sex and diet. Interaction (time x genotype); significant values (p<0.05) highlighted in bold. High-fat diet: *Tbx15*$^{+/+}$ (n=23), *Tbx15*$^{+/H156N}$ (n=27), *Tbx15*$^{H156N/H156N}$ (n=16), low-fat diet: *Tbx15*$^{+/+}$ (n=23), *Tbx15*$^{+/H156N}$ (n=23), *Tbx15*$^{H156N/H156N}$ (n=15).

		High-fat diet						**Low-fat diet**					
		Bodyweight		**Fat Mass**		**Lean Mass**		**Bodyweight**		**Fat Mass**		**Lean Mass**	
Interaction		0.9902		0.9697		**<0.0001**		0.9946		0.9621		0.6944	
Time		**<0.0001**		**<0.0001**		**<0.0001**		**<0.0001**		**<0.0001**		**<0.0001**	
Genotype		0.9520		0.9779		**0.0190**		0.3881		0.1372		0.5240	
Post-hoc analysis (adjusted P value)													
Weeks	**Comparison**	**Diff means**	**p-value**	**Diff means**	**p-value**	**Diff means**	**p-value**	**Diff means**	**p-value**	**Diff means**	**p-value**	**Diff means**	**p-value**
4	+/+ vs +/H156N	0.4398	0.4011	0.09994	0.8058	0.3287	0.4642	-0.6439	0.3825	-0.2487	0.2461	-0.2283	0.8030
	+/+ vs H156N/H156N	0.08921	0.9660	0.06207	0.9303	0.1696	0.8491	-0.9045	0.2145	-0.07672	0.8607	-0.2819	0.7836
	+/H156N vs H156N/H156N	-0.3506	0.6374	-0.03787	0.9723	-0.1591	0.8944	-0.2606	0.8268	0.1720	0.3916	-0.05362	0.9883
6	+/+ vs +/H156N	-0.03486	0.9959	0.1571	0.8666	-0.7810	0.0661	-0.5365	0.3503	-0.1243	0.7369	-0.2696	0.7822
	+/+ vs H156N/H156N	-0.3172	0.7934	-0.1503	0.9076	-0.3114	0.7420	-0.5903	0.3771	-0.6413	**0.0420**	0.2805	0.7843
	+/H156N vs H156N/H156N	-0.2823	0.8369	-0.3074	0.5936	0.4695	0.4654	-0.05380	0.9889	-0.5170	0.1181	0.5501	0.3575
8	+/+ vs +/H156N	-0.1796	0.9551	-0.1214	0.9688	-0.8419	0.0929	-0.5191	0.3710	-0.2630	0.3239	-0.3909	0.5330
	+/+ vs H156N/H156N	-0.5057	0.8187	-0.2316	0.9224	-0.2846	0.7974	-0.5666	0.3619	-0.6121	**0.0429**	0.1517	0.9427
	+/H156N vs H156N/H156N	-0.3261	0.9255	-0.1103	0.9817	0.5573	0.4177	-0.04745	0.9909	-0.3491	0.3093	0.5426	0.4679
10	+/+ vs +/H156N	-0.1352	0.9885	0.1789	0.9750	-1.130	**0.0204**	-0.4048	0.5809	-0.2830	0.2672	-0.2661	0.7717
	+/+ vs H156N/H156N	-0.2135	0.9737	0.04375	0.9985	-0.4378	0.6117	-0.3624	0.6786	-0.6840	**0.0267**	0.4056	0.6908
	+/H156N vs H156N/H156N	-0.07838	0.9970	-0.1351	0.9879	0.6922	0.3109	0.04235	0.9936	-0.4009	0.2122	0.6717	0.3734
12	+/+ vs +/H156N	-0.07237	0.9978	0.02224	0.9998	-0.8429	0.1431	-0.5352	0.4093	-0.3439	0.3114	-0.6596	0.1630
	+/+ vs H156N/H156N	-0.5891	0.8999	-0.3536	0.9502	-0.1183	0.9703	-0.3849	0.6817	-0.5128	0.1128	0.3194	0.8044

	+/H156N vs H156N/H156N	-0.5167	0.9318	-0.3759	0.9518	0.7246	0.3653	0.1503	0.9349	-0.1689	0.7577	0.9790	0.1643
14	+/+ vs +/H156N	-0.1918	0.9871	-0.2400	0.9758	-1.157	**0.0444**	-0.8552	0.2568	-0.5609	0.1811	-0.1852	0.8868
	+/+ vs H156N/H156N	-0.8827	0.8072	-0.7030	0.8299	-0.4759	0.5821	-0.6440	0.5473	-0.6744	0.1247	0.2381	0.9062
	+/H156N vs H156N/H156N	-0.6909	0.8941	-0.4630	0.9319	0.6814	0.2668	0.2112	0.9213	-0.1135	0.9206	0.4233	0.7100
16	+/+ vs +/H156N	-0.06142	0.9990	-0.1083	0.9964	-1.320	**0.0290**	-0.7083	0.4864	-0.5278	0.4054	-0.1570	0.9156
	+/+ vs H156N/H156N	-1.009	0.8427	-0.7264	0.8857	-0.5741	0.5192	-0.5929	0.7349	-0.7126	0.3702	0.3109	0.8369
	+/H156N vs H156N/H156N	-0.9475	0.8732	-0.6181	0.9235	0.7457	0.3139	0.1154	0.9872	-0.1848	0.9216	0.4679	0.6581
18	+/+ vs +/H156N	-0.8663	0.8367	-0.7999	0.8359	-1.746	**0.0044**	-1.040	0.2788	-0.7322	0.2681	-0.2617	0.8170
	+/+ vs H156N/H156N	-1.029	0.8711	-0.6226	0.9347	-0.8514	0.3009	-1.209	0.3395	-1.017	0.1495	0.09730	0.9854
	+/H156N vs H156N/H156N	-0.1629	0.9969	0.1773	0.9953	0.8942	0.2647	-0.1692	0.9778	-0.2852	0.8400	0.3590	0.8163
20	+/+ vs +/H156N	-0.2880	0.9809	-0.1276	0.9954	-1.777	**0.0049**	-0.6657	0.6663	-0.4861	0.6582	-0.07478	0.9843
	+/+ vs H156N/H156N	-0.4770	0.9727	-0.08671	0.9987	-0.7829	0.4374	-0.8644	0.5980	-0.8181	0.3514	0.1644	0.9592
	+/H156N vs H156N/H156N	-0.1891	0.9960	0.04086	0.9997	0.9940	0.2547	-0.1987	0.9712	-0.3320	0.7960	0.2392	0.9118
22	+/+ vs +/H156N	-0.7584	0.8797	-0.6644	0.8813	-1.785	**0.0050**	-0.6261	0.7195	-0.5678	0.6117	0.01000	0.9997
	+/+ vs H156N/H156N	-0.1012	0.9990	0.4436	0.9706	-0.9233	0.4983	-0.5693	0.8298	-0.7023	0.5235	0.4186	0.7731
	+/H156N vs H156N/H156N	0.6572	0.9578	1.108	0.8371	0.8618	0.5379	0.05675	0.9980	-0.1345	0.9731	0.4086	0.7608
24	+/+ vs +/H156N	-0.5673	0.9328	-0.6288	0.8886	-1.755	**0.0066**	-0.8109	0.6438	-0.6261	0.6058	-0.1896	0.9050
	+/+ vs H156N/H156N	0.6816	0.9506	0.9075	0.8723	-0.7105	0.5354	-0.4427	0.9021	-0.7603	0.5476	0.4729	0.7158
	+/H156N vs H156N/H156N	1.249	0.8522	1.536	0.6955	1.045	0.2806	0.3682	0.9310	-0.1342	0.9791	0.6625	0.4969

Table 9.14. Male *Tbx15*^{H156N} echo-MRI body composition over 4 to 24 weeks. All data was analysed by repeated measures two-way ANOVA with post-hoc Šídák's multiple comparisons, per sex and diet. Interaction (time x genotype); significant values (p<0.05) highlighted in bold. High-fat diet *Tbx15*$^{+/+}$ (n=21), *Tbx15*$^{+/H156N}$ (n=23), *Tbx15*$^{H156N/H156N}$ (n=21), low-fat diet *Tbx15*$^{+/+}$ (n=21), *Tbx15*$^{+/H156N}$ (n=20), *Tbx15*$^{H156N/H156N}$ (n=20).

		High-fat diet						**Low-fat diet**					
		Bodyweight		**Fat Mass**		**Lean Mass**		**Bodyweight**		**Fat Mass**		**Lean Mass**	
Interaction		0.1351		0.0749		**<0.0001**		0.4415		**0.0093**		0.8940	
Time		**<0.0001**		**<0.0001**		**<0.0001**		**<0.0001**		**<0.0001**		**<0.0001**	
Genotype		0.7019		0.0966		**0.0131**		0.3697		0.3740		0.5307	
Post-hoc analysis (adjusted P value)													
Weeks		**Diff means**	**p-value**	**Diff means**	**p-value**	**Diff means**	**p-value**	**Diff means**	**p-value**	**Diff means**	**p-value**	**Diff means**	**p-value**
4	+/+ vs +/H156N	0.5690	0.6121	-0.2391	0.2014	0.6809	0.3797	-0.02979	0.9986	-0.04950	0.8779	-0.2641	0.8927
	+/+ vs H156N/H156N	0.6850	0.5516	0.08089	0.8016	0.6071	0.5037	-0.4003	0.7719	-0.05050	0.8899	-0.3506	0.7831
	+/H156N vs H156N/H156N	0.1160	0.9802	0.3200	0.0717	-0.07377	0.9891	-0.3705	0.8400	-0.001000	>0.9999	-0.08650	0.9885
6	+/+ vs +/H156N	0.1628	0.9368	0.3918	0.5877	-1.385	**0.0094**	0.05717	0.9933	0.008833	0.9987	-0.8957	0.3147
	+/+ vs H156N/H156N	0.4874	0.4724	0.6932	0.1912	-0.1855	0.9235	-0.2453	0.8705	-0.2462	0.4917	-0.5687	0.5687
	+/H156N vs H156N/H156N	0.3246	0.6706	0.3014	0.6554	1.200	0.0711	-0.3025	0.7756	-0.2550	0.4701	0.3270	0.7931
8	+/+ vs +/H156N	0.06178	0.9956	0.6790	0.6081	-2.122	**0.0012**	0.3788	0.7306	-0.2013	0.7584	-0.1786	0.9559
	+/+ vs H156N/H156N	1.047	0.1681	1.795	**0.0229**	-0.8355	0.3956	-0.5872	0.4871	-0.5063	0.2429	-0.2201	0.9311
	+/H156N vs H156N/H156N	0.9848	0.2690	1.116	0.2646	1.287	0.1888	-0.9660	0.0901	-0.3050	0.5624	-0.04150	0.9972
10	+/+ vs +/H156N	0.9000	0.5948	1.323	0.3426	-1.972	**0.0028**	0.3374	0.8647	-0.1411	0.9395	-0.1382	0.9773
	+/+ vs H156N/H156N	1.180	0.2437	1.982	0.0808	-0.7043	0.5387	-0.07057	0.9918	-0.4596	0.5157	-0.3377	0.8875
	+/H156N vs H156N/H156N	0.2795	0.9328	0.6594	0.7910	1.267	0.2429	-0.4080	0.7077	-0.3185	0.6925	-0.1995	0.9454
12	+/+ vs +/H156N	1.199	0.4957	1.277	0.3869	-1.991	**0.0037**	0.4404	0.8505	0.2861	0.8991	-0.5254	0.7729
	+/+ vs H156N/H156N	0.9868	0.4927	1.778	0.1555	-0.6514	0.5374	-0.3626	0.8604	-0.5589	0.5785	-0.2354	0.9460
	+/H156N vs H156N/H156N	-0.2122	0.9749	0.5010	0.8825	1.340	0.1877	-0.8030	0.4386	-0.8450	0.3428	0.2900	0.9056

14	+/+ vs +/H156N	0.6399	0.8228	1.400	0.3409	-2.147	**0.0048**	0.3128	0.9235	0.1941	0.9574	-0.7375	0.6218
	+/+ vs H156N/H156N	1.460	0.2375	2.236	0.0838	-1.042	0.3520	-0.5042	0.7679	-0.5239	0.6700	-0.2580	0.9379
	+/H156N vs H156N/H156N	0.8197	0.7191	0.8358	0.7409	1.105	0.4150	-0.8170	0.4843	-0.7180	0.5465	0.4795	0.7994
16	+/+ vs +/H156N	0.9013	0.7037	0.8667	0.6071	-2.065	**0.0088**	0.6960	0.7394	0.3652	0.8965	-0.7564	0.5975
	+/+ vs H156N/H156N	0.5324	0.7868	1.393	0.1537	-1.196	0.2858	-0.5995	0.7798	-0.7673	0.5910	-0.2969	0.9271
	+/H156N vs H156N/H156N	-0.3688	0.9380	0.5259	0.8530	0.8691	0.6032	-1.296	0.2678	-1.133	0.3267	0.4595	0.8100
18	+/+ vs +/H156N	0.05520	0.9985	0.2538	0.9407	-2.551	**0.0040**	0.7429	0.7400	0.6796	0.7346	-0.9034	0.5012
	+/+ vs H156N/H156N	0.2795	0.9305	1.228	0.1662	-0.8922	0.5168	-0.7376	0.7143	-0.7564	0.6723	-0.2334	0.9546
	+/H156N vs H156N/H156N	0.2243	0.9751	0.9740	0.4878	1.659	0.2132	-1.481	0.1954	-1.436	0.2142	0.6700	0.6672
20	+/+ vs +/H156N	0.3112	0.9450	0.3901	0.7910	-2.369	**0.0117**	1.086	0.6263	1.239	0.4680	-1.166	0.3412
	+/+ vs H156N/H156N	0.1002	0.9874	1.066	0.1001	-1.296	0.2792	-0.4762	0.8966	-0.5024	0.8641	-0.3602	0.9032
	+/H156N vs H156N/H156N	-0.2110	0.9733	0.6755	0.5404	1.073	0.5432	-1.562	0.2748	-1.742	0.2131	0.8060	0.5830
22	+/+ vs +/H156N	-0.2229	0.9631	-0.003775	>0.9999	-2.506	**0.0034**	1.397	0.4372	1.243	0.4780	-1.111	0.3846
	+/+ vs H156N/H156N	0.1503	0.9663	1.210	0.0856	-1.398	0.2069	-0.1906	0.9819	-0.2964	0.9539	-0.7235	0.7245
	+/H156N vs H156N/H156N	0.3731	0.9089	1.214	0.1315	1.108	0.4929	-1.588	0.2734	-1.540	0.3525	0.3875	0.9153
24	+/+ vs +/H156N	-1.103	0.4242	-0.2615	0.9153	-2.741	**0.0020**	1.394	0.4337	2.163	0.1923	-1.206	0.3504
	+/+ vs H156N/H156N	-0.1162	0.9856	1.378	0.0817	-1.498	0.2265	-0.1829	0.9823	0.9822	0.6490	-0.8840	0.5410
	+/H156N vs H156N/H156N	0.9868	0.6056	1.640	**0.0333**	1.243	0.4601	-1.577	0.2851	-1.181	0.5989	0.3215	0.9310

Table 9.15. Female *Tbx15*^{M566R} echo-MRI body composition over 4 to 24 weeks. All data was analysed by repeated measures two-way ANOVA with post-hoc Šídák's multiple comparisons, per sex and diet. Interaction (time x genotype); significant values (p<0.05) highlighted in bold. High-fat diet: *Tbx15*$^{+/+}$ (n=22), *Tbx15*$^{+/M566R}$ (n=22), *Tbx15* $^{M566R/M566R}$ (n=21), low-fat diet: *Tbx15*$^{+/+}$ (n=20), *Tbx15*$^{+/M566R}$ (n=21), *Tbx15* $^{M566R/M566R}$ (n=22).

		High-fat diet						Low-fat diet					
		Bodyweight		**Fat Mass**		**Lean Mass**		**Bodyweight**		**Fat Mass**		**Lean Mass**	
Interaction		0.9966		0.9974		0.7826		0.0813		**0.0245**		0.9417	
Time		**<0.0001**		**<0.0001**		**<0.0001**		**<0.0001**		**<0.0001**		**<0.0001**	
Genotype		0.5514		0.7229		0.3145		0.1668		0.1122		0.5665	
Post-hoc analysis (adjusted P-value)													
Weeks	**Comparison**	**Diff means**	**P-value**	**Diff means**	**P-value**	**Diff means**	**P-value**	**Diff means**	**P-value**	**Diff means**	**P-value**	**Diff means**	**P-value**
4	+/+ vs +/M566R	-0.4714	0.6628	-0.3109	0.3806	-0.1809	0.8452	0.1511	0.9624	0.07179	0.9105	0.06860	0.9835
	+/+ vs M566R/M566R	-0.7223	0.3603	-0.3818	0.2630	-0.3648	0.5130	0.4866	0.6830	0.1848	0.5755	0.3078	0.7260
	+/M566R vs M566R/M566R	-0.2510	0.9046	-0.07087	0.9658	-0.1839	0.8580	0.3355	0.8268	0.1130	0.7683	0.2392	0.8223
6	+/+ vs +/M566R	-0.6527	0.3282	-0.1168	0.9556	-0.5823	0.1373	0.3094	0.7246	0.3263	0.1822	0.01324	0.9991
	+/+ vs M566R/M566R	-0.9985	0.1305	-0.6488	0.3522	-0.3554	0.5457	0.4998	0.3026	0.3125	0.2819	0.1516	0.8578
	+/M566R vs M566R/M566R	-0.3458	0.7749	-0.5320	0.4965	0.2268	0.7351	0.1904	0.8813	-0.01383	0.9971	0.1384	0.8858
8	+/+ vs +/M566R	-1.085	0.2412	-0.4377	0.7486	-0.6623	**0.0440**	0.1014	0.9494	0.1337	0.8070	-0.00588	0.9998
	+/+ vs M566R/M566R	-0.9364	0.4211	-0.5429	0.6740	-0.4115	0.3193	0.4340	0.2755	0.3847	0.2768	0.07286	0.9648
	+/M566R vs M566R/M566R	0.1491	0.9795	-0.1051	0.9871	0.2507	0.5961	0.3326	0.5877	0.2511	0.5130	0.07874	0.9532
10	+/+ vs +/M566R	-0.4682	0.8500	-0.3482	0.9127	-0.1532	0.8018	-0.1110	0.9410	0.2080	0.5784	-0.3896	0.4651
	+/+ vs M566R/M566R	-0.5945	0.7633	-0.5440	0.7832	0.003030	>0.9999	0.4367	0.2922	0.3684	0.2773	0.02900	0.9942
	+/M566R vs M566R/M566R	-0.1263	0.9900	-0.1959	0.9745	0.1562	0.8056	0.5477	0.2605	0.1604	0.7309	0.4186	0.3058
12	+/+ vs +/M566R	-0.5927	0.8572	-0.2836	0.9589	-0.3382	0.3985	-0.1869	0.8988	0.1411	0.8021	-0.2725	0.6838
	+/+ vs M566R/M566R	-0.4870	0.9018	-0.2484	0.9677	-0.2511	0.6757	0.4191	0.4481	0.4043	0.1649	0.05259	0.9807
	+/M566R vs M566R/M566R	0.1058	0.9963	0.03524	0.9995	0.08712	0.9571	0.6060	0.3033	0.2632	0.4776	0.3250	0.5354

14	+/+ vs +/M566R	-1.420	0.5699	-0.9918	0.7223	-0.3309	0.4619	-0.003000	>0.9999	0.1114	0.9296	-0.1840	0.8286
	+/+ vs M566R/M566R	-1.075	0.6915	-0.8820	0.7475	-0.1451	0.8780	0.5056	0.3832	0.4241	0.2877	0.1923	0.7491
	+/M566R vs M566R/M566R	0.3452	0.9722	0.1098	0.9965	0.1858	0.8121	0.5086	0.5392	0.3127	0.5427	0.3763	0.4508
16	+/+ vs +/M566R	-1.961	0.4183	-1.370	0.5848	-0.5123	0.1961	-0.2754	0.8881	-0.0287	0.9965	-0.2656	0.7300
	+/+ vs M566R/M566R	-1.221	0.6882	-0.8562	0.7977	-0.2569	0.7258	0.8015	0.1801	0.7815	**0.0241**	0.07518	0.9609
	+/M566R vs M566R/M566R	0.7408	0.8994	0.5138	0.9370	0.2554	0.7223	1.077	0.1746	0.8103	0.0699	0.3408	0.6032
18	+/+ vs +/M566R	-1.273	0.7178	-0.8668	0.8228	-0.4164	0.3749	-0.4890	0.6246	-0.1182	0.9484	-0.2102	0.7812
	+/+ vs M566R/M566R	-1.386	0.6100	-1.029	0.7105	-0.3538	0.5563	0.4500	0.5443	0.4611	0.3913	-0.02305	0.9957
	+/M566R vs M566R/M566R	-0.1132	0.9978	-0.1618	0.9941	0.06253	0.9824	0.9390	0.2124	0.5794	0.2830	0.1871	0.8316
20	+/+ vs +/M566R	-1.376	0.6773	-0.6768	0.8768	-0.7336	0.1792	-0.7479	0.4548	-0.4369	0.6079	-0.2593	0.7087
	+/+ vs M566R/M566R	-1.418	0.6475	-0.9266	0.7734	-0.5550	0.3704	0.5377	0.5719	0.5215	0.4051	0.04173	0.9896
	+/M566R vs M566R/M566R	-0.04208	0.9997	-0.2498	0.9858	0.1786	0.9011	1.286	0.1132	0.9583	0.1068	0.3011	0.6351
22	+/+ vs +/M566R	-1.689	0.5487	-1.231	0.6298	-0.4164	0.5263	-0.7230	0.4760	-0.2236	0.8910	-0.4835	0.3979
	+/+ vs M566R/M566R	-1.334	0.6849	-1.041	0.7157	-0.2334	0.8320	0.5594	0.5701	0.6235	0.3398	-0.009955	0.9993
	+/M566R vs M566R/M566R	0.3556	0.9773	0.1898	0.9905	0.1830	0.8983	1.282	0.1394	0.8472	0.1965	0.4736	0.4277
24	+/+ vs +/M566R	-1.232	0.7005	-0.7295	0.8211	-0.3418	0.6475	-0.5762	0.7152	-0.3022	0.8640	-0.1262	0.9299
	+/+ vs M566R/M566R	-0.9639	0.8077	-0.3169	0.9597	-0.2747	0.7891	0.9054	0.2621	0.8344	0.2098	0.1086	0.9171
	+/M566R vs M566R/M566R	0.2684	0.9859	0.4126	0.9444	0.06708	0.9852	1.482	0.1225	1.137	0.1277	0.2348	0.7776

Table 9.16. Male *Tbx15*^{M566R} echo-MRI body composition over 4 to 24 weeks. All data was analysed by repeated measures two-way ANOVA with post-hoc Šídák's multiple comparisons, per sex and diet. Interaction (time x genotype); significant values (p<0.05) highlighted in bold. High-fat diet: *Tbx15*$^{+/+}$ (n=22), *Tbx15*$^{+/M566R}$ (n=22), *Tbx15*$^{M566R/M566R}$ (n=18), low-fat diet: *Tbx15*$^{+/+}$ (n=22), *Tbx15*$^{+/M566R}$ (n=21), *Tbx15* $^{M566R/M566R}$ (n=17).

		High-fat diet						**Low-fat diets**					
		Body weight		Fat Mass		Lean Mass		Body weight		Fat Mass		Lean Mass	
Interaction		0.5704		0.5248		0.0875		**0.0082**		0.3014		0.3510	
Time		**<0.0001**		**<0.0001**		**<0.0001**		**<0.0001**		**<0.0001**		**<0.0001**	
Genotype		0.5277		0.1137		0.9329		0.8563		0.5165		0.3531	
Post-hoc analysis (adjusted P-value)													
Weeks	**Comparison**	**Diff means**	**P-value**	**Diff means**	**P-value**	**Diff means**	**P-value**	**Diff means**	**P-value**	**Diff means**	**P-value**	**Diff means**	**P-value**
4	+/+ vs +/M566R	1.211	0.5418	0.2645	0.4949	0.8082	0.6382	-0.4389	0.8527	-0.03619	0.9505	-0.3401	0.8648
	+/+ vs M566R/M566R	-0.3303	0.9412	-0.07803	0.9447	-0.2715	0.9314	1.657	0.2097	0.1547	0.5204	1.467	0.1760
	+/M566R vs M566R/M566R	-1.541	0.3631	-0.3426	0.3304	-1.080	0.4434	2.096	0.1059	0.1909	0.3648	1.807	0.0941
6	+/+ vs +/M566R	0.5945	0.6849	0.7064	0.3723	-0.1482	0.9458	0.02799	0.9983	0.01297	0.9979	0.00548	>0.9999
	+/+ vs M566R/M566R	1.240	0.2552	0.7683	0.4341	0.5794	0.4591	0.2658	0.8176	-0.07404	0.9356	0.2726	0.6993
	+/M566R vs M566R/M566R	0.6459	0.6801	0.06192	0.9937	0.7276	0.3547	0.2378	0.8797	-0.08700	0.9122	0.2672	0.7743
8	+/+ vs +/M566R	1.679	0.2448	1.963	0.0618	-0.3373	0.7828	-0.08489	0.9826	-0.08823	0.9521	0.01727	0.9992
	+/+ vs M566R/M566R	1.274	0.5257	1.210	0.4756	-0.03626	0.9975	0.2039	0.8784	-0.09021	0.9512	0.4037	0.5459
	+/M566R vs M566R/M566R	-0.4046	0.9331	-0.7533	0.7310	0.3010	0.8638	0.2888	0.8104	-0.00199	>0.9999	0.3865	0.6059
10	+/+ vs +/M566R	1.222	0.5959	1.775	0.2426	-0.4409	0.7145	-0.2789	0.8919	-0.1384	0.9539	-0.1009	0.9844
	+/+ vs M566R/M566R	0.8516	0.8009	1.269	0.5523	-0.4506	0.7421	0.2718	0.8766	-0.3785	0.6503	0.6628	0.3297
	+/M566R vs M566R/M566R	-0.3703	0.9631	-0.5060	0.9183	-0.00965	0.9999	0.5506	0.6070	-0.2401	0.8725	0.7636	0.3357
12	+/+ vs +/M566R	1.627	0.4604	2.098	0.1445	-0.5241	0.6664	0.05697	0.9964	-0.09736	0.9860	0.1291	0.9802
	+/+ vs M566R/M566R	0.5898	0.9037	1.128	0.5920	-0.5927	0.6335	0.4001	0.8528	-0.3343	0.8445	0.7258	0.4043
	+/M566R vs M566R/M566R	-1.037	0.7628	-0.9696	0.7265	-0.06859	0.9944	0.3431	0.8912	-0.2369	0.9283	0.5967	0.6025
14	+/+ vs +/M566R	1.298	0.6143	1.744	0.1984	-0.3464	0.8607	0.04736	0.9980	0.1444	0.9803	0.1978	0.9483

	+/+ vs M566R/M566R	0.9197	0.7739	1.167	0.5144	-0.2303	0.9434	-0.06866	0.9957	-0.7793	0.4930	0.7460	0.3869
	+/M566R vs M566R/M566R	-0.3785	0.9651	-0.5765	0.8750	0.1161	0.9865	-0.1160	0.9888	-0.9237	0.4371	0.5482	0.6376
16	+/+ vs +/M566R	1.823	0.3729	1.876	0.0683	-0.06500	0.9953	0.3719	0.9139	0.4321	0.8781	-0.1452	0.9738
	+/+ vs M566R/M566R	1.491	0.4924	1.423	0.2201	-0.00732	>0.9999	-0.07484	0.9966	-0.8467	0.5432	0.9533	0.1913
	+/M566R vs M566R/M566R	-0.3325	0.9737	-0.4532	0.8846	0.05768	0.9970	-0.4467	0.8869	-1.279	0.3431	1.099	0.1988
18	+/+ vs +/M566R	1.440	0.4856	1.584	0.0573	-0.00454	>0.9999	0.8790	0.6398	0.8223	0.6307	0.1494	0.9706
	+/+ vs M566R/M566R	0.7287	0.8175	0.9057	0.3663	-0.4725	0.7874	0.09693	0.9956	-0.5749	0.7847	0.5263	0.5555
	+/M566R vs M566R/M566R	-0.7117	0.8663	-0.6784	0.6493	-0.4680	0.8298	-0.7821	0.7517	-1.397	0.3096	0.3769	0.8159
20	+/+ vs +/M566R	0.7386	0.7863	1.527	0.1351	-0.3036	0.9075	1.127	0.4715	0.9289	0.5492	0.2935	0.8704
	+/+ vs M566R/M566R	0.6544	0.7702	0.9361	0.2208	-0.05823	0.9960	0.06246	0.9981	-0.4458	0.8689	0.4896	0.5739
	+/M566R vs M566R/M566R	-0.08419	0.9968	-0.5908	0.7360	0.2454	0.9492	-1.065	0.5863	-1.375	0.3412	0.1960	0.9365
22	+/+ vs +/M566R	0.7391	0.7737	0.9959	0.1668	-0.2509	0.9396	0.9557	0.6227	0.6383	0.7531	0.4100	0.7721
	+/+ vs M566R/M566R	0.2218	0.9695	0.8089	0.3432	-0.5932	0.6649	0.2250	0.9810	-0.3157	0.9356	0.4548	0.6760
	+/M566R vs M566R/M566R	-0.5173	0.8751	-0.1870	0.9463	-0.3423	0.9043	-0.7306	0.8136	-0.9540	0.5845	0.04482	0.9971
24	+/+ vs +/M566R	0.6509	0.8397	0.9058	0.2516	-0.2014	0.9637	1.448	0.3734	0.8584	0.6314	0.6842	0.5322
	+/+ vs M566R/M566R	0.3357	0.9371	0.6847	0.4619	-0.3323	0.8880	0.3978	0.9530	-0.4002	0.9186	0.6929	0.4673
	+/M566R vs M566R/M566R	-0.3152	0.9546	-0.2211	0.9225	-0.1309	0.9856	-1.050	0.7132	-1.259	0.4608	0.008683	>0.9999

Table 9.17. *Tbx15*$^{+/-}$ intraperitoneal glucose tolerance tests at 13 weeks. All data was analysed by repeated measures two-way ANOVA with post-hoc Šídák's multiple comparisons, per sex and diet. Interaction (time x genotype); significant values (p<0.05) highlighted in bold. Female high-fat diet: *Tbx15*$^{+/+}$ (n=18), -*Tbx15*$^{+/-}$ (n=22), low-fat diet: *Tbx15*$^{+/+}$ (n=18), *Tbx15*$^{+/-}$ (n=22), male high-fat diet: *Tbx15*$^{+/+}$ (n=21), *Tbx15*$^{+/-}$ (n=17), low-fat diet: *Tbx15*$^{+/+}$ (n=21), *Tbx15*$^{+/-}$ (n=14).

	Female				**Male**			
	High-fat diet		**Low-fat diet**		**High-fat diet**		**Low-fat diet**	
Interaction	0.7414		0.3480		0.3349		0.8717	
Time	**<0.0001**		**<0.0001**		**<0.0001**		**<0.0001**	
Genotype	0.9494		**0.0403**		0.4500		0.4716	
Post-hoc analysis (adjust P value)								
Time	**Diff means**	**P-value**	**Diff means**	**P-value**	**Diff means**	**P-value**	**Diff means**	**P-value**
0 min	-0.1510	0.9959	-0.7897	0.1965	-0.4815	0.9659	0.4690	0.4690
30 min	0.6813	0.9919	-2.331	0.3290	0.4910	0.9989	0.5976	0.5976
60 min	0.4136	0.9983	-1.396	0.4372	-2.413	0.7731	1.598	1.598
120 min	-0.6970	0.8970	-0.4865	0.7478	-2.714	0.7663	0.3262	0.3262

Table 9.18. *Tbx15*$^{+/-}$ fasted blood glucose and area under the curve from intraperitoneal glucose tolerance tests. All data was analysed by two-tailed unpaired t-tests, per sex and diet; significant values (p<0.05) highlighted in bold. Female high-fat diet: *Tbx15*$^{+/+}$ (n=18), *Tbx15*$^{+/-}$ (n=22), low-fat diet: *Tbx15*$^{+/+}$ (n=18), *Tbx15*$^{+/-}$ (n=22), male high-fat diet: *Tbx15*$^{+/+}$ (n=21), *Tbx15*$^{+/-}$ (n=17), low-fat diet: *Tbx15*$^{+/+}$ (n=21), *Tbx15*$^{+/-}$ (n=14).

	Female				**Male**			
	High-fat diet		**Low-fat diet**		**High-fat diet**		**Low-fat diet**	
	Diff means	**P-value**	**Diff means**	**P-value**	**Diff means**	**P-value**	**Diff means**	**P-value**
Fasted glucose	0.1510	0.7433	0.7897	0.0533	0.4815	0.5644	-0.4690	0.2833
AUC	-34.08	0.7809	66.92	0.4780	124.7	0.5081	-50.27	0.7460

Table 9.19. *Tbx15*$^{+/-}$ intraperitoneal insulin sensitivity tests at 17 weeks. All data analysed by repeated measures two-way ANOVA with post-hoc Šídák's multiple comparisons, per sex and diet. Interaction (time x genotype); significant values (p<0.05) highlighted in bold. Female high-fat diet: *Tbx15*$^{+/+}$ (n=18), -*Tbx15*$^{+/-}$ (n=22), low-fat diet: *Tbx15*$^{+/+}$ (n=18), *Tbx15*$^{+/-}$ (n=22). Male high-fat diet: *Tbx15*$^{+/+}$ (n=21), *Tbx15*$^{+/-}$ (n=17), low-fat diet: *Tbx15*$^{+/+}$ (n=21), *Tbx15*$^{+/-}$ (n=14).

	Female		**Male**	
	High-fat diet	**Low-fat diet**	**High-fat diet**	**Low-fat diet**
Interaction	0.2510	0.5535	0.6164	0.2072
Time	**<0.0001**	**<0.0001**	**<0.0001**	**<0.0001**
Genotype	0.2978	0.6098	0.8332	0.7660
Post-hoc analysis (adjust P value)				
0 min	0.2506	>0.9999	0.9994	0.8854
15 min	0.6880	0.9963	0.9999	0.7833
30 min	0.9997	0.9051	0.9973	0.9911
45 min	>0.9999	0.9983	0.9987	0.9985
60 min	>0.9999	0.9101	>0.9999	0.9533
90 min	0.8376	0.9938	0.9972	>0.9999

Table 9.20. *Tbx15*$^{+/-}$ area under the curve from intraperitoneal insulin sensitivity tests. Data was analysed by two-tailed unpaired t-tests, per sex and diet; significant values (p<0.05) highlighted in bold. Female high-fat diet: *Tbx15*$^{+/+}$ (n=18), *Tbx15*$^{+/-}$ (n=22), low-fat diet: *Tbx15*$^{+/+}$ (n=18), *Tbx15*$^{+/-}$ (n=22), male high-fat diet: *Tbx15*$^{+/+}$ (n=21), *Tbx15*$^{+/-}$ (n=17), low-fat diet: *Tbx15*$^{+/+}$ (n=21), *Tbx15*$^{+/-}$ (n=14).

	Female				**Male**			
	High-fat diet		**Low-fat diet**		**High-fat diet**		**Low-fat diet**	
	Diff means	**P-value**	**Diff means**	**P-value**	**Diff means**	**P-value**	**Diff means**	**P-value**
AUC	49.37	0.3680	40.33	0.4993	-20.49	0.8697	-55.58	0.5386

Table 9.21. *Tbx15*^{H156N} intraperitoneal glucose tolerance tests at 13 weeks. All data was analysed by repeated measures two-way ANOVA with post-hoc Šídák's multiple comparisons, per sex and diet. Interaction (time x genotype); significant values (p<0.05) highlighted in bold. Female high-fat diet: *Tbx15*$^{+/+}$ (n=23), *Tbx15*$^{+/H156N}$ (n=27), *Tbx15*$^{H156N/H156N}$ (n=16), low-fat diet: *Tbx15*$^{+/+}$ (n=23), *Tbx15*$^{+/H156N}$ (n=23), *Tbx15*$^{H156N/H156N}$ (n=15). Male high-fat diet: *Tbx15*$^{+/+}$ (n=21), *Tbx15*$^{+/H156N}$ (n=23), *Tbx15*$^{H156N/H156N}$ (n=21), low-fat diet: *Tbx15*$^{+/+}$ (n=19), *Tbx15*$^{+/H156N}$ (n=19), *Tbx15*$^{H156N/H156N}$ (n=20). Two *Tbx15*$^{+/+}$ and one *Tbx15*$^{+/H156N}$ LFD males were not included in testing due to fighting-induce wounds (identified after overnight fast).

		Female				**Male**			
		High-fat diet		**Low-fat diet**		**High-fat diet**		**Low-fat diet**	
Interaction		0.7174		0.7483		0.2482		0.4525	
Time		**<0.0001**		**<0.0001**		**<0.0001**		**<0.0001**	
Genotype		0.3057		0.2726		0.2671		0.5035	
Post-hoc analysis (adjust P value)									
Time	**Comparison**	**Diff means**	**P-value**	**Diff means**	**P-value**	**Diff means**	**P-value**	**Diff means**	**P-value**
0 min	+/+ vs +/H156N	0.3619	0.3699	0.6348	0.0938	1.294	0.0635	-0.4887	0.3485
	+/+ vs H156N/H156N	0.1271	0.9402	0.4278	0.4402	0.2400	0.9360	-0.06368	0.9788
	+/H156N vs H156N/H156N	-0.2348	0.8070	-0.2070	0.7968	-1.054	0.1811	0.4250	0.4262
30 min	+/+ vs +/H156N	1.234	0.8022	1.839	0.5054	1.073	0.8239	1.523	0.7163
	+/+ vs H156N/H156N	-1.948	0.5595	0.5603	0.9408	2.254	0.5190	1.163	0.7656
	+/H156N vs H156N/H156N	-3.182	0.1949	-1.279	0.6427	1.181	0.7795	-0.3600	0.9761
60 min	+/+ vs +/H156N	1.720	0.6507	1.343	0.2098	1.728	0.6891	2.711	0.2453
	+/+ vs H156N/H156N	-0.1708	0.9954	1.081	0.4858	-0.6357	0.9510	0.7605	0.8905
	+/H156N vs H156N/H156N	-1.891	0.5538	-0.2623	0.9419	-2.364	0.5102	-1.950	0.4395
120 min	+/+ vs +/H156N	0.9429	0.5267	0.1478	0.9350	3.803	0.0597	1.088	0.6379
	+/+ vs H156N/H156N	-0.3688	0.9137	0.3017	0.7647	0.7065	0.9047	0.2129	0.9855
	+/H156N vs H156N/H156N	-1.312	0.1738	0.1539	0.9219	-3.096	0.2113	-0.8750	0.7124

Table 9.22. *Tbx15*^{H156N} fasted blood glucose and area under the curve analysis from intraperitoneal glucose tolerance tests. All data was analysed by one-way ANOVA with post-hoc Tukey's multiple comparisons, per sex and diet; significant values (p<0.05) highlighted in bold. Female high-fat diet: *Tbx15*$^{+/+}$ (n=23), *Tbx15*$^{+/H156N}$ (n=27), *Tbx15*$^{H156N/H156N}$ (n=16), low-fat diet: *Tbx15*$^{+/+}$ (n=23), *Tbx15*$^{+/H156N}$ (n=23), *Tbx15*$^{H156N/H156N}$ (n=15), male high-fat diet: *Tbx15*$^{+/+}$ (n=21), *Tbx15*$^{+/H156N}$ (n=23), *Tbx15*$^{H156N/H156N}$ (n=21), low-fat diet: *Tbx15*$^{+/+}$ (n=19), *Tbx15*$^{+/H156N}$ (n=19), *Tbx15*$^{H156N/H156N}$ (n=20), Two *Tbx15*$^{+/+}$ and one *Tbx15*$^{+/H156N}$ LFD males were not included in testing due to fighting-induce wounds (identified after overnight fast).

		Female				**Male**			
		High-fat diet		**Low-fat diet**		**High-fat diet**		**Low-fat diet**	
Fasted glucose	**Genotype**	0.4565		0.1035		0.0772		0.2931	
	Post-hoc analysis (adjusted P value)								
	Comparison	**Diff means**	**P-value**	**Diff means**	**P-value**	**Diff means**	**P-value**	**Diff means**	**P-value**
	+/+ vs +/H156N	0.3619	0.4345	0.6348	0.0905	1.294	0.0846	-0.4887	0.3242
	+/+ vs H156N/H156N	0.1271	0.9254	0.4278	0.4110	0.2400	0.9184	-0.06368	0.9806
	+/H156N vs H156N/H156N	-0.2348	0.7562	-0.2070	0.8097	-1.054	0.1966	0.4250	0.4152
Area under curve	**Genotype**	0.4889		0.6934		0.8629		0.2355	
	Post-hoc analysis (adjusted P value)								
	Comparison	**Diff means**	**P-value**	**Diff means**	**P-value**	**Diff means**	**P-value**	**Diff means**	**P-value**
	+/+ vs +/H156N	104.9	0.7573	72.10	0.6749	88.13	0.8522	251.5	0.2204
	+/+ vs H156N/H156N	-90.37	0.8577	47.46	0.8735	35.05	0.9761	82.15	0.8470
	+/H156N vs H156N/H156N	-195.3	0.4716	-24.64	0.9641	-53.07	0.9449	-169.4	0.4887

Table 9.23. *Tbx15*^{H156N} intraperitoneal insulin sensitivity tests at 17 weeks. All data analysed by repeated measures two-way ANOVA with post-hoc Šídák's multiple comparisons, per sex and diet, interaction (time x genotype); significant values (p<0.05) highlighted in bold. Female high-fat diet (HFD): *Tbx15*$^{+/+}$ (n=23), *Tbx15*$^{+/H156N}$ (n=16), *Tbx15*$^{H156N/H156N}$ (n=13), low-fat diet (LFD): *Tbx15*$^{+/+}$ (n=23), *Tbx15*$^{+/H156N}$ (n=15), *Tbx15*$^{H156N/H156N}$ (n=14). Male HFD: *Tbx15*$^{+/+}$ (n=20), *Tbx15*$^{+/H156N}$ (n=13), *Tbx15*$^{H156N/H156N}$ (n=20), LFD: *Tbx15*$^{+/+}$ (n=19), *Tbx15*$^{+/H156N}$ (n=15), *Tbx15*$^{H156N/H156N}$ (n=18). 11 *Tbx15*$^{+/H156N}$ and three *Tbx15*$^{H156N/H156N}$ HFD female, eight *Tbx15*$^{+/H156N}$ and one *Tbx15*$^{H156N/H156N}$ LFD female, one *Tbx15*$^{+/+}$, 13 *Tbx15*$^{+/H156N}$ and one *Tbx15*$^{H156N/H156N}$ HFD male, and two *Tbx15*$^{+/+}$, five *Tbx15*$^{+/H156N}$ and two *Tbx15*$^{H156N/H156N}$ LFD male mice were excluded from testing due to incorrect insulin product at time of testing.

		Female		**Male**	
		HFD	**LFD**	**HFD**	**LFD**
Interaction		0.0962	0.2658	0.5031	**0.0436**
Time		**<0.0001**	**<0.0001**	**<0.0001**	**<0.0001**
Genotype		0.5267	0.2718	0.7606	0.7781
Post-hoc analysis (adjusted p-value)					
0 min	+/+ vs +/H156N	0.3186	0.8850	0.7638	0.1280
	+/+ vs H156N/H156N	0.9385	0.6439	0.9232	0.1630
	+/H156N vs H156N/H156N	0.8366	0.9546	0.8769	0.9526
15 min	+/+ vs +/H156N	0.6874	0.2366	0.9530	0.5842
	+/+ vs H156N/H156N	0.9307	0.9221	0.9973	0.3282
	+/H156N vs H156N/H156N	0.9333	0.0575	0.9659	0.9838
30 min	+/+ vs +/H156N	0.9513	0.1066	0.7863	0.9778
	+/+ vs H156N/H156N	0.7409	0.5162	0.9668	0.5607
	+/H156N vs H156N/H156N	0.6560	0.3730	0.8735	0.8318
45 min	+/+ vs +/H156N	0.6632	0.4871	0.5510	0.5323
	+/+ vs H156N/H156N	0.9830	0.8676	0.9839	0.8732
	+/H156N vs H156N/H156N	0.9540	0.6984	0.6281	0.7419
60 min	+/+ vs +/H156N	0.1358	0.4812	0.3875	0.7360
	+/+ vs H156N/H156N	0.9936	0.9241	0.9103	0.7094
	+/H156N vs H156N/H156N	0.4345	0.6440	0.5825	0.9974
90 min	+/+ vs +/H156N	0.1880	0.2889	0.5620	0.8994
	+/+ vs H156N/H156N	0.9141	0.4634	0.9995	>0.9999
	+/H156N vs H156N/H156N	0.3567	0.9126	0.5714	0.8993

Table 9.24. *Tbx15*^{H156N} area above the curve analysis from intraperitoneal insulin sensitivity tests. All data was analysed by one-way ANOVA with post-hoc Tukey's multiple comparisons, per sex and diet; significant values (p<0.05) highlighted in bold. Female high-fat diet (HFD): *Tbx15*$^{+/+}$ (n=23), *Tbx15*$^{+/H156N}$ (n=16), *Tbx15*$^{H156N/H156N}$ (n=13), low-fat diet (LFD): *Tbx15*$^{+/+}$ (n=23), *Tbx15*$^{+/H156N}$ (n=15), *Tbx15*$^{H156N/H156N}$ (n=14). Male HFD: *Tbx15*$^{+/+}$ (n=20), *Tbx15*$^{+/H156N}$ (n=13), *Tbx15*$^{H156N/H156N}$ (n=20), LFD: *Tbx15*$^{+/+}$ (n=19), *Tbx15*$^{+/H156N}$ (n=15), *Tbx15*$^{H156N/H156N}$ (n=18). 11 *Tbx15*$^{+/H156N}$ and three *Tbx15*$^{H156N/H156N}$ HFD female, eight *Tbx15*$^{+/H156N}$ and one *Tbx15*$^{H156N/H156N}$ LFD female, one *Tbx15*$^{+/+}$, 13 *Tbx15*$^{+/H156N}$ and one *Tbx15*$^{H156N/H156N}$ HFD male, and two *Tbx15*$^{+/+}$, five *Tbx15*$^{+/H156N}$ and two *Tbx15*$^{H156N/H156N}$ LFD male mice were excluded from testing due to incorrect insulin product at time of testing.

		Female				**Male**			
		High-fat diet		**Low-fat diet**		**High-fat diet**		**Low-fat diet**	
Area above the curve	**Genotype**	0.4976		0.6138		0.6751		0.8380	
	Post-hoc analysis (adjusted P value)								
	Comparison	**Diff means**	**P-value**	**Diff means**	**P-value**	**Diff means**	**P-value**	**Diff means**	**P-value**
	+/+ vs +/H156N	77.54	0.4653	-83.92	0.5952	150.8	0.6601	-50.49	0.8284
	+/+ vs H156N/H156N	27.97	0.9231	-45.86	0.8551	25.85	0.9815	-30.17	0.9284
	+/H156N vs H156N/H156N	-49.57	0.8069	38.07	0.9172	-125.0	0.7546	20.32	0.9706

Table 9.25. *Tbx15*^{M566R} intraperitoneal glucose tolerance tests at 13 weeks. All data was analysed by repeated measures two-way ANOVA with post-hoc Šídák's multiple comparisons, per sex and diet. Interaction (time x genotype); significant values (p<0.05) highlighted in bold. Female high-fat diet: *Tbx15*$^{+/+}$ (n=22), *Tbx15*$^{+/M566R}$ (n=22), *Tbx15* $^{M566R/M566R}$ (n=21), low-fat diet: *Tbx15*$^{+/+}$ (n=20), *Tbx15*$^{+/M566R}$ (n=21), *Tbx15* $^{M566R/M566R}$ (n=22), male high-fat diet: *Tbx15*$^{+/+}$ (n=22), *Tbx15*$^{+/M566R}$ (n=22), *Tbx15*$^{M566R/M566R}$ (n=18), low-fat diet: *Tbx15*$^{+/+}$ (n=22), *Tbx15*$^{+/M566R}$ (n=21), *Tbx15* $^{M566R/M566R}$ (n=17).

		Female				**Male**			
		High-fat diet		**Low-fat diet**		**High-fat diet**		**Low-fat diet**	
Interaction		0.9628		0.8445		0.1527		0.4149	
Time		**<0.0001**		**<0.0001**		**<0.0001**		**<0.0001**	
Genotype		0.5357		0.6965		0.0958		0.1654	
Post-hoc analysis (adjust P value)									
Time	**Comparison**	**Diff means**	**P-value**	**Diff means**	**P-value**	**Diff means**	**P-value**	**Diff means**	**P-value**
0 min	**+/+ vs +/M566R**	-0.1000	0.9435	-0.5012	0.4222	2.082	**0.0497**	0.03636	0.9953
	+/+ vs M566R/M566R	-0.6152	0.3885	-0.03864	0.9934	0.1421	0.9883	0.08182	0.9806
	+/M566R vs M566R/M566R	-0.5152	0.4936	0.4626	0.4911	-1.940	0.0508	0.04545	0.9936
30 min	**+/+ vs +/M566R**	0.07727	0.9988	0.2569	0.9796	4.659	**0.0198**	1.291	0.7659
	+/+ vs M566R/M566R	-1.408	0.7208	-0.3505	0.9697	0.7091	0.8931	3.382	0.2763
	+/M566R vs M566R/M566R	-1.485	0.6739	-0.6074	0.9072	-3.950	0.0748	2.091	0.4881
60 min	**+/+ vs +/M566R**	-0.4409	0.9332	-1.301	0.2673	0.8227	0.8678	1.886	0.4805
	+/+ vs M566R/M566R	-0.8301	0.8326	-0.9105	0.3694	-1.517	0.7336	2.508	0.3358
	+/M566R vs M566R/M566R	-0.3892	0.9524	0.3903	0.8924	-2.340	0.4291	0.6219	0.8732
120 min	**+/+ vs +/M566R**	-0.7818	0.5345	-0.09214	0.9792	3.209	0.2520	0.06364	0.9948
	+/+ vs M566R/M566R	-1.121	0.2763	-0.3168	0.7313	2.444	0.6076	1.286	0.1285
	+/M566R vs M566R/M566R	-0.3387	0.9291	-0.2247	0.9035	-0.7653	0.9293	1.223	0.1698

Table 9.26. *Tbx15*^{M566R} fasted blood glucose and area under the curve from intraperitoneal glucose tolerance tests. All data was analysed by one-way ANOVA with post-hoc Tukey's multiple comparisons, per sex and diet; significant values (p<0.05) highlighted in bold. Female high-fat diet: *Tbx15*$^{+/+}$ (n=22), *Tbx15*$^{+/M566R}$ (n=22), *Tbx15* $^{M566R/M566R}$ (n=21), low-fat diet: *Tbx15*$^{+/+}$ (n=20), *Tbx15*$^{+/M566R}$ (n=21), *Tbx15* $^{M566R/M566R}$ (n=22), male high-fat diet: *Tbx15*$^{+/+}$ (n=22), *Tbx15*$^{+/M566R}$ (n=22), *Tbx15*$^{M566R/M566R}$ (n=18), low-fat diet: *Tbx15*$^{+/+}$ (n=22), *Tbx15*$^{+/M566R}$ (n=21), *Tbx15* $^{M566R/M566R}$ (n=17).

		Female				**Male**			
		High-fat diet		**Low-fat diet**		**High-fat diet**		**Low-fat diet**	
Fasted glucose	**Genotype**	0.2804		0.3576		**0.0318**		0.9815	
	Post-hoc analysis (adjusted P value)								
		Diff means	**P-value**	**Diff means**	**P-value**	**Diff means**	**P-value**	**Diff means**	**P-value**
	+/+ vs +/M566R	-0.1000	0.9667	-0.5012	0.4083	2.082	**0.0456**	0.03636	0.9953
	+/+ vs M566R/M566R	-0.6152	0.2948	-0.03864	0.9945	0.1421	0.9859	0.08182	0.9796
	+/M566R vs M566R/M566R	-0.5152	0.4221	0.4626	0.4486	-1.940	0.0810	0.04545	0.9937
Area under curve	**Genotype**	0.8969		0.7738		0.8751		0.2035	
	Post-hoc analysis (adjusted P value)								
		Diff means	**P-value**	**Diff means**	**P-value**	**Diff means**	**P-value**	**Diff means**	**P-value**
	+/+ vs +/M566R	-30.61	0.9591	-15.25	0.9811	61.53	0.8699	121.7	0.6035
	+/+ vs M566R/M566R	-52.20	0.8883	-55.81	0.7706	18.46	0.9884	244.4	0.1773
	+/M566R vs M566R/M566R	-21.59	0.9799	-40.56	0.8680	-43.07	0.9371	122.7	0.6390

Table 9.27. *Tbx15*$^{+/-}$ DEXA at 23 weeks under recoverable anaesthesia. All data was analysed by unpaired t-tests per sex and diet; significant values (p<0.05) highlighted in bold. BMD (bone mineral density), BMC (bone mineral content). Female high-fat diet: *Tbx15*$^{+/+}$ (n=18), *Tbx15*$^{+/-}$ (n=22), low-fat diet: *Tbx15*$^{+/+}$ (n=18), *Tbx15*$^{+/-}$ (n=22), male high-fat diet: *Tbx15*$^{+/+}$ (n=21), *Tbx15*$^{+/-}$ (n=17), low-fat diet: *Tbx15*$^{+/+}$ (n=21), *Tbx15*$^{+/-}$ (n=14).

	Female				**Male**			
	High-fat diet		**Low-fat diet**		**High-fat diet**		**Low-fat diet**	
	Diff means	**P-value**	**Diff means**	**P-value**	**Diff means**	**P-value**	**Diff means**	**P-value**
Bodyweight	0.3090	0.8501	-1.163	0.0668	1.206	0.3326	-2.115	**0.0340**
Fat mass	0.5847	0.6641	-0.9146	**0.0413**	0.2582	0.7399	-1.568	0.1065
Lean Mass	-0.3788	0.4568	-0.2026	0.5346	0.9498	0.3348	-0.6072	0.3962
Fat mass %	0.9253	0.5475	-2.690	0.0508	-0.5720	0.6512	-2.914	0.2232
BMD	0.000891	0.2661	-0.00117	0.1860	0.001655	0.2207	0.000579	0.5790
BMC	0.02190	0.2631	-0.0102	0.4674	-0.00029	0.9927	-0.02061	0.1316

Table 9.28. Female *Tbx15^{H156N}* DEXA at 24 weeks under terminal anaesthesia. All data was analysed by one-way ANOVA with post-hoc Tukey's multiple comparisons, per diet, significant values (p<0.05) highlighted in bold. BMD (bone mineral density), BMC (bone mineral content). High-fat diet: *Tbx15$^{+/+}$* (n=23), *Tbx15$^{+/H156N}$* (n=27), *Tbx15$^{H156N/H156N}$* (n=16), low-fat diet: *Tbx15$^{+/+}$* (n=23), *Tbx15$^{+/H156N}$* (n=23), *Tbx15$^{H156N/H156N}$* (n=15).

High-fat diet

	Bodyweight		**Fat Mass**		**Lean Mass**		**Fat Mass %**		**BMD**		**BMC**	
Genotype	0.7550		0.6249		0.6272		0.3109		0.7590		0.8608	
Post-hoc analysis (adjusted P-value)												
Comparison	**Diff means**	**P-value**	**Diff means**	**P-value**	**Diff means**	**P-value**	**Diff means**	**P-value**	**Diff means**	**P-value**	**Diff means**	**P-value**
+/+ vs +/H156N	0.04945	0.9996	0.6565	0.8869	-0.5813	0.6213	1.819	0.4504	0.0003784	0.7707	0.01121	0.8483
+/+ vs H156N/H156N	1.369	0.7784	1.569	0.5964	-0.1489	0.9763	2.431	0.3406	0.00004810	0.9968	0.005383	0.9715
+/H156N vs H156N/H156N	1.319	0.7805	0.9125	0.8291	0.4324	0.8072	0.6127	0.9284	-0.0003303	0.8514	-0.005831	0.9646
Low-fat diet												
	Bodyweight		**Fat Mass**		**Lean Mass**		**Fat Mass %**		**BMD**		**BMC**	
Genotype	0.6781		0.7068		0.7128		0.6132		0.1121		0.2146	
Post-hoc analysis (adjusted P-value)												
Comparison	**Diff means**	**P-value**	**Diff means**	**P-value**	**Diff means**	**P-value**	**Diff means**	**P-value**	**Diff means**	**P-value**	**Diff means**	**P-value**
+/+ vs +/H156N	-0.4309	0.8519	-0.1870	0.9480	-0.2783	0.6893	-0.7870	0.8748	-0.0003565	0.8459	0.004435	0.9296
+/+ vs H156N/H156N	-0.7786	0.6629	-0.5629	0.6842	-0.1490	0.9188	-1.781	0.5852	0.001163	0.2539	0.02359	0.2062
+/H156N vs H156N/H156N	-0.3477	0.9207	-0.3759	0.8436	0.1293	0.9382	-0.9936	0.8452	0.001520	0.1007	0.01915	0.3490

Table 9.29. Male *Tbx15^{H156N}* DEXA at 24 weeks under terminal anaesthesia. All data was analysed by one-way ANOVA with post-hoc Tukey's multiple comparisons, per diet, significant values (p<0.05) highlighted in bold. BMD (bone mineral density), BMC (bone mineral content). High-fat diet: *Tbx15$^{+/+}$* (n=21), *Tbx15$^{+/H156N}$* (n=23), *Tbx15$^{H156N/H156N}$* (n=21), low-fat diet: *Tbx15$^{+/+}$* (n=21), *Tbx15$^{+/H156N}$* (n=20), *Tbx15$^{H156N/H156N}$* (n=20).

High-fat diet

	Bodyweight		**Fat Mass**		**Lean Mass**		**Fat Mass %**		**BMD**		**BMC**	
Genotype	0.6492		**0.0364**		0.0962		**0.0231**		0.3360		0.4596	
Post-hoc analysis (adjusted P-value)												
Comparison	**Diff means**	**P-value**	**Diff means**	**P-value**	**Diff means**	**P-value**	**Diff means**	**P-value**	**Diff means**	**P-value**	**Diff means**	**P-value**
+/+ vs +/H156N	-0.4043	0.8837	1.255	0.1551	-1.486	0.1107	2.827	0.0570	-0.001193	0.3179	0.01530	0.4702
+/+ vs H156N/H156N	0.4005	0.8906	1.750	**0.0346**	-1.296	0.1983	3.137	**0.0355**	-0.0008314	0.5838	0.01277	0.6038
+/H156N vs H156N/H156N	0.8048	0.6220	0.4948	0.7469	0.1901	0.9640	0.3091	0.9653	0.0003617	0.9004	-0.002534	0.9797

Low-fat diet

	Bodyweight		**Fat Mass**		**Lean Mass**		**Fat Mass %**		**BMD**		**BMC**	
Genotype	0.2229		0.3403		0.6942		0.3853		0.9643		0.4967	
Post-hoc analysis (adjusted P-value)												
Comparison	**Diff means**	**P-value**	**Diff means**	**P-value**	**Diff means**	**P-value**	**Diff means**	**P-value**	**Diff means**	**P-value**	**Diff means**	**P-value**
+/+ vs +/H156N	1.681	0.2647	1.334	0.4214	0.4431	0.6752	2.653	0.4959	0.0001640	0.9842	0.007731	0.8363
+/+ vs H156N/H156N	0.09698	0.9955	-0.06310	0.9980	0.1581	0.9509	-0.3467	0.9879	-0.00009595	0.9946	0.01613	0.4638
+/H156N vs H156N/H156N	-1.584	0.3147	-1.398	0.3968	-0.2850	0.8527	-3.000	0.4181	-0.0002600	0.9616	0.008400	0.8140

Table 9.30. Female *Tbx15*^{M566R} DEXA at 23 weeks under recoverable anaesthesia. All data was analysed by one-way ANOVA with post-hoc Tukey's multiple comparisons, per diet, significant values (p<0.05) highlighted in bold. BMD (bone mineral density), BMC (bone mineral content). High-fat diet: *Tbx15*$^{+/+}$ (n=22), *Tbx15*$^{+/M566R}$ (n=22), *Tbx15* $^{M566R/M566R}$ (n=21), low-fat diet: *Tbx15*$^{+/+}$ (n=20), *Tbx15*$^{+/M566R}$ (n=21), *Tbx15* $^{M566R/M566R}$ (n=22).

High-fat diet

	Bodyweight		**Fat Mass**		**Lean Mass**		**Fat Mass %**		**BMD**		**BMC**	
Genotype	0.6642		0.7867		0.5671		0.9576		0.3694		0.2835	
Post-hoc analysis (adjusted P-value)												
Comparison	**Diff means**	**P-value**	**Diff means**	**P-value**	**Diff means**	**P-value**	**Diff means**	**P-value**	**Diff means**	**P-value**	**Diff means**	**P-value**
+/+ vs +/M566R	-1.365	0.6626	-0.7707	0.8368	-0.5154	0.5924	0.07029	0.9989	0.0004545	0.9710	-0.01688	0.9242
+/+ vs M566R/M566R	-1.051	0.7873	-0.8575	0.8063	-0.4569	0.6684	-0.3698	0.9710	-0.002200	0.5139	-0.06964	0.2785
+/M566R vs M566R/M566R	0.3141	0.9788	-0.08683	0.9978	0.05844	0.9934	-0.4401	0.9592	-0.002655	0.3816	-0.05275	0.4764
Low-fat diet												
	Bodyweight		**Fat Mass**		**Lean Mass**		**Fat Mass %**		**BMD**		**BMC**	
Genotype	0.1163		**0.0427**		0.8965		0.0550		0.8558		0.0672	
Post-hoc analysis (adjusted P-value)												
Comparison	**Diff means**	**P-value**	**Diff means**	**P-value**	**Diff means**	**P-value**	**Diff means**	**P-value**	**Diff means**	**P-value**	**Diff means**	**P-value**
+/+ vs +/M566R	-0.6329	0.5926	-0.7334	0.3592	0.1643	0.9223	-2.180	0.4018	-0.0004160	0.8430	-0.02713	0.1641
+/+ vs M566R/M566R	0.6986	0.5219	0.6062	0.4868	-0.01299	0.9995	1.864	0.5041	-0.0001895	0.9643	0.004767	0.9426
+/M566R vs M566R/M566R	1.331	0.0962	1.340	**0.0329**	-0.1772	0.9059	4.043	**0.0430**	0.0002264	0.9482	0.03190	0.0758

Table 9.31 Male *Tbx15*^{M566R} DEXA at 23 weeks under recoverable anaesthesia. All data was analysed by one-way ANOVA with post-hoc Tukey's multiple comparisons, per diet, significant values (p<0.05) highlighted in bold. BMD (bone mineral density), BMC (bone mineral content). High-fat diet: *Tbx15*$^{+/+}$ (n=22), *Tbx15*$^{+/M566R}$ (n=22), *Tbx15*$^{M566R/M566R}$ (n=18), low-fat diet: *Tbx15*$^{+/+}$ (n=22), *Tbx15*$^{+/M566R}$ (n=21), *Tbx15* $^{M566R/M566R}$ (n=17).

High-fat diet

	Bodyweight		**Fat Mass**		**Lean Mass**		**Fat Mass %**		**BMD**		**BMC**	
Genotype	0.7975		0.6335		0.9769		0.7798		0.6047		0.8617	
Post-hoc analysis (adjusted P-value)												
Comparison	**Diff means**	**P-value**	**Diff means**	**P-value**	**Diff means**	**P-value**	**Diff means**	**P-value**	**Diff means**	**P-value**	**Diff means**	**P-value**
+/+ vs +/M566R	0.6900	0.7814	0.5459	0.6132	0.05983	0.9960	0.4875	0.8218	-0.001177	0.5800	-0.009609	0.8669
+/+ vs M566R/M566R	0.4101	0.9243	0.1897	0.9478	-0.09955	0.9901	-0.04135	0.9987	-0.0007237	0.8297	-0.008239	0.9097
+/M566R vs M566R/M566R	-0.2799	0.9640	-0.3562	0.8282	-0.1594	0.9748	-0.5288	0.8123	0.0004535	0.9292	0.001370	0.9974

Low-fat diet

	Bodyweight		**Fat Mass**		**Lean Mass**		**Fat Mass %**		**BMD**		**BMC**	
Genotype	0.5743		0.5133		0.3513		0.4340		0.9547		0.3189	
Post-hoc analysis (adjusted P-value)												
Comparison	**Diff means**	**P-value**	**Diff means**	**P-value**	**Diff means**	**P-value**	**Diff means**	**P-value**	**Diff means**	**P-value**	**Diff means**	**P-value**
+/+ vs +/M566R	1.135	0.5665	0.4414	0.8777	0.5949	0.5397	0.1137	0.9978	0.0003297	0.9502	0.02293	0.3118
+/+ vs M566R/M566R	0.2655	0.9723	-0.6819	0.7581	0.8145	0.3595	-2.138	0.5033	0.0001596	0.9894	0.005257	0.9455
+/M566R vs M566R/M566R	-0.8694	0.7458	-1.123	0.4822	0.2196	0.9283	-2.252	0.4747	-0.0001700	0.9882	-0.01767	0.5420

Table 9.32. *Tbx15*$^{+/-}$ terminal measurements. All data was analysed by unpaired t-tests per sex and diet; significant values (p<0.05) highlighted in bold. Female high-fat diet: *Tbx15*$^{+/+}$ (n=18), *Tbx15*$^{+/-}$ (n=22), low-fat diet: *Tbx15*$^{+/+}$ (n=18), *Tbx15*$^{+/-}$ (n=22), male high-fat diet: *Tbx15*$^{+/+}$ (n=21), *Tbx15*$^{+/-}$ (n=17), low-fat diet: *Tbx15*$^{+/+}$ (n=21), *Tbx15*$^{+/-}$ (n=14).

	Female				**Male**			
	High-fat diet		**Low-fat diet**		**High-fat diet**		**Low-fat diet**	
	Diff means	**p-value**	**Diff means**	**p-value**	**Diff means**	**p-value**	**Diff means**	**p-value**
Bodyweight	0.2873	0.8617	**-1.339**	**0.0351**	1.075	0.3891	-2.194	**0.0421**
Length	-0.3061	**0.0013**	-0.04444	0.7209	0.1345	0.1081	-0.04524	0.7060
gWAT:iWAT ratio	0.01061	0.9541	0.02929	0.8635	-0.03599	0.7939	-0.3533	0.0548

Table 9.33. *Tbx15*$^{+/-}$ terminal depot weights. All data was analysed by multiple unpaired t-tests (two-stage step-up (Benjamini, Krieger, and Yekutieli) (false discovery rate 5%)) per sex and diet; significant values (p<0.05 and q<0.05) highlighted in bold. Female high-fat diet: *Tbx15*$^{+/+}$ (n=18), *Tbx15*$^{+/-}$ (n=22), low-fat diet: *Tbx15*$^{+/+}$ (n=18), *Tbx15*$^{+/-}$ (n=22), male high-fat diet: *Tbx15*$^{+/+}$ (n=21), *Tbx15*$^{+/-}$ (n=17), low-fat diet: *Tbx15*$^{+/+}$ (n=21), *Tbx15*$^{+/-}$ (n=14).

	Female						**Male**					
	High-fat diet			**Low-fat diet**			**High-fat diet**			**Low-fat diet**		
	Diff means	**p-value**	**q-value**	**Diff means**	**p-value**	**q-value**	**Diff means**	**p-value**	**q-value**	**Diff means**	**p-value**	**q-value**
Depots												
gWAT	-0.3740	0.075582	0.458026	0.1673	**0.016295**	**0.044882**	0.1326	0.242680	0.735319	0.2727	**0.018697**	0.113306
mWAT	-0.08467	0.583874	0.589713	0.07597	**0.016606**	**0.044882**	-0.05391	0.534343	0.809529	0.1197	0.050586	0.153274
Liver	0.09049	0.303097	0.555747	0.07077	0.083527	0.101235	-0.05273	0.736618	0.892781	0.01945	0.718158	0.725340
pWAT	0.09701	0.366830	0.555747	0.02282	0.163419	0.165053	0.1202	0.149957	0.735319	0.08073	0.123951	0.250381
BAT	-0.01896	0.345566	0.555747	0.01298	**0.023358**	**0.044882**	0.001978	0.934984	0.944334	0.01484	0.373792	0.566295
iWAT	-0.1090	0.576446	0.589713	0.09660	**0.029625**	**0.044882**	0.1476	0.481930	0.809529	0.05805	0.531634	0.644341
Depots adjusted for body weight												
gWAT/BW	-0.8132	**0.004071**	**0.024672**	0.5860	**0.018231**	0.094550	0.4443	0.193523	0.586374	0.6617	**0.026914**	0.163097
mWAT/BW	-0.1915	0.437636	0.530415	0.2147	**0.035300**	0.094550	-0.07384	0.663216	0.834552	0.2190	0.096424	0.194777
Liver/BW	0.2128	0.108086	0.327500	0.07921	0.512132	0.517254	-0.05462	0.826289	0.834552	-0.1938	0.056300	0.170589
pWAT/BW	0.2794	0.225255	0.341261	0.07532	0.260372	0.315571	0.3008	0.077712	0.470934	0.1933	0.202317	0.306510
BAT/BW	-0.04258	0.181519	0.341261	0.03825	0.050835	0.094550	0.01381	0.766385	0.834552	0.01286	0.756175	0.834000
iWAT/BW	-0.2685	0.539531	0.544926	0.3562	0.062409	0.094550	0.3907	0.346830	0.700597	0.05857	0.825743	0.834000

Table 9.34. Female *Tbx15^{H156N}* terminal measurements. All data was analysed by one-way ANOVA with post-hoc Tukey's multiple comparisons, per diet; significant values (p<0.05) highlighted in bold. High-fat diet: *Tbx15$^{+/+}$* (n=23), *Tbx15$^{+/H156N}$* (n=27), *Tbx15$^{H156N/H156N}$* (n=16), low-fat diet: *Tbx15$^{+/+}$* (n=23), *Tbx15$^{+/H156N}$* (n=23), *Tbx15$^{H156N/H156N}$* (n=15).

	High-fat diet						**Low-fat diet**					
	Bodyweight		**Length**		**gWAT:iWAT ratio**		**Bodyweight**		**Length**		**gWAT:iWAT ratio**	
Genotype	0.7550		0.0566		0.1224		0.6781		0.8574		0.0638	
Post-hoc analysis (adjusted P-value)												
Comparison	**Diff means**	**P-value**	**Diff means**	**P-value**	**Diff means**	**P-value**	**Diff means**	**P-value**	**Diff means**	**P-value**	**Diff means**	**P-value**
+/+ vs +/H156N	0.04945	0.9996	0.1865	0.0543	0.1918	0.1113	-0.4309	0.8519	-0.02609	0.9431	-0.04125	0.8449
+/+ vs H156N/H156N	1.369	0.7784	0.1524	0.2188	0.06234	0.8325	-0.7786	0.6629	-0.04928	0.8481	-0.1962	0.0581
+/H156N vs H156N/H156N	1.319	0.7805	-0.03403	0.9204	-0.1295	0.4357	-0.3477	0.9207	-0.02319	0.9641	-0.1550	0.1631

Table 9.35. Male *Tbx15^{H156N}* terminal measurements. All data was analysed by one-way ANOVA with post-hoc Tukey's multiple comparisons, per diet; significant values (p<0.05) highlighted in bold. High-fat diet: *Tbx15$^{+/+}$* (n=21), *Tbx15$^{+/H156N}$* (n=23), *Tbx15$^{H156N/H156N}$* (n=21), low-fat diet: *Tbx15$^{+/+}$* (n=21), *Tbx15$^{+/H156N}$* (n=20), *Tbx15$^{H156N/H156N}$* (n=20).

	High-fat diet						**Low-fat diet**					
	Bodyweight		**Length**		**gWAT:iWAT ratio**		**Bodyweight**		**Length**		**gWAT:iWAT ratio**	
Genotype	0.6492		0.5106		0.3633		0.2229		**0.0162**		0.1763	
Post-hoc analysis (adjusted P-value)												
Comparison	**Diff means**	**P-value**	**Diff means**	**P-value**	**Diff means**	**P-value**	**Diff means**	**P-value**	**Diff means**	**P-value**	**Diff means**	**P-value**
+/+ vs +/H156N	-0.4043	0.8837	-0.06739	0.5005	0.06087	0.3935	1.681	0.2647	0.3700	**0.0123**	0.3979	0.1563
+/+ vs H156N/H156N	0.4005	0.8906	-0.05000	0.6932	0.007345	0.9869	0.09698	0.9955	0.1421	0.5049	0.2455	0.4852
+/H156N vs H156N/H156N	0.8048	0.6220	0.01739	0.9554	-0.05353	0.4930	-1.584	0.3147	-0.2279	0.1862	-0.1525	0.7596

Table 9.36. *Tbx15*^{H156N} terminal depot weights. All data was analysed by repeated measures two-way ANOVA with post-hoc Šídák's multiple comparisons, per sex and diet, interaction (Depot x Genotype); significant values (p<0.05) highlighted in bold. Female high-fat diet: *Tbx15*$^{+/+}$ (n=23), *Tbx15*$^{+/H156N}$ (n=27), *Tbx15*$^{H156N/H156N}$ (n=16), low-fat diet: *Tbx15*$^{+/+}$ (n=23), *Tbx15*$^{+/H156N}$ (n=23), *Tbx15*$^{H156N/H156N}$ (n=15), male high-fat diet: *Tbx15*$^{+/+}$ (n=21), *Tbx15*$^{+/H156N}$ (n=23), *Tbx15*$^{H156N/H156N}$ (n=21), low-fat diet: *Tbx15*$^{+/+}$ (n=21), *Tbx15*$^{+/H156N}$ (n=20), *Tbx15*$^{H156N/H156N}$ (n=20).

		Female				**Male**			
		High-fat diet		**Low-fat diet**		**High-fat diet**		**Low-fat diet**	
Raw values									
Interaction		0.5771		0.8665		0.1494		0.2593	
Depot		**<0.0001**		**<0.0001**		**<0.0001**		**<0.0001**	
Genotype		0.7833		0.6213		0.0828		0.3324	
Post-hoc analysis (adjusted p-value)									
	Comparison	**Diff means**	**P-value**	**Diff means**	**P-value**	**Diff means**	**P-value**	**Diff means**	**P-value**
gWAT	+/+ vs +/H156N	-0.03130	0.9938	-0.04410	0.9166	0.08929	0.7663	0.2228	0.3434
	+/+ vs H156N/H156N	0.1846	0.8690	-0.1582	0.5338	0.1417	0.5203	-0.05070	0.9425
	+/H156N vs H156N/H156N	0.2159	0.8070	-0.1141	0.6623	0.05244	0.8582	-0.2735	0.2533
mWAT	+/+ vs +/H156N	-0.03481	0.9788	-0.03619	0.7360	0.09004	0.3382	0.1117	0.3323
	+/+ vs H156N/H156N	-0.01221	0.9986	-0.05327	0.6253	0.06281	0.4923	0.03530	0.8763
	+/H156N vs H156N/H156N	0.02260	0.9948	-0.01708	0.9385	-0.02723	0.8905	-0.07638	0.5643
Liver	+/+ vs +/H156N	-0.06300	0.8290	-0.02320	0.9004	0.01520	0.9944	0.1073	0.4579
	+/+ vs H156N/H156N	-0.04834	0.8994	-0.06298	0.6378	0.05812	0.8847	0.05069	0.7974
	+/H156N vs H156N/H156N	0.01466	0.9926	-0.03979	0.7851	0.04292	0.9520	-0.05659	0.7322
pWAT	+/+ vs +/H156N	0.1203	0.1234	-0.01541	0.2253	0.09972	0.0623	0.1573	**0.0048**
	+/+ vs H156N/H156N	0.08990	0.3639	-0.006582	0.8138	0.06745	0.2519	0.08006	0.3005
	+/H156N vs H156N/H156N	-0.03040	0.8514	0.008827	0.7286	-0.03228	0.6582	-0.07724	0.1910
BAT	+/+ vs +/H156N	-0.01605	0.8057	-0.001561	0.9811	-0.008617	0.8459	0.02455	0.5138
	+/+ vs H156N/H156N	-0.01163	0.9207	-0.01210	0.3376	-0.01771	0.5622	-0.003096	0.9900
	+/H156N vs H156N/H156N	0.004429	0.9885	-0.01054	0.4717	-0.009089	0.8654	-0.02765	0.4857
iWAT	+/+ vs +/H156N	-0.3923	0.3946	-0.03234	0.9311	-0.1726	0.5060	-0.02053	0.9892
	+/+ vs H156N/H156N	0.003096	>0.9999	-0.04761	0.9222	0.2238	0.3017	-0.08238	0.8092
	+/H156N vs H156N/H156N	0.3954	0.5302	-0.01526	0.9893	0.3964	**0.0087**	-0.06186	0.8959

Adjusted for bodyweight									
Interaction		0.2992		0.7780		0.2013		0.1898	
Depot		**<0.0001**		**<0.0001**		**<0.0001**		**<0.0001**	
Genotype		0.6151		0.5460		0.0852		0.3849	
Post-hoc analysis (adjusted p-value)									
	Comparison	**Diff means**	**P-value**	**Diff means**	**P-value**	**Diff means**	**P-value**	**Diff means**	**P-value**
gWAT/BW	+/+ vs +/H156N	-0.1077	0.9605	-0.2126	0.8099	0.1847	0.8186	0.5198	0.3716
	+/+ vs H156N/H156N	0.1810	0.9222	-0.5617	0.4388	0.2568	0.6759	-0.1582	0.9125
	+/H156N vs H156N/H156N	0.2887	0.7759	-0.3490	0.6748	0.07209	0.9590	-0.6780	0.2815
mWAT/BW	+/+ vs +/H156N	-0.07462	0.9613	-0.1370	0.5499	0.2332	0.1641	0.2108	0.4130
	+/+ vs H156N/H156N	-0.07432	0.9784	-0.1515	0.5304	0.09699	0.7088	0.08583	0.8297
	+/H156N vs H156N/H156N	0.0003009	>0.9999	-0.01452	0.9928	-0.1362	0.5028	-0.1250	0.7277
Liver/BW	+/+ vs +/H156N	-0.1250	0.6830	-0.05087	0.9167	0.1147	0.9024	0.1088	0.7606
	+/+ vs H156N/H156N	-0.2155	0.3091	-0.1248	0.6343	0.08338	0.9280	0.1228	0.6144
	+/H156N vs H156N/H156N	-0.09049	0.8597	-0.07388	0.8525	-0.03137	0.9910	0.01400	0.9932
pWAT/BW	+/+ vs +/H156N	0.2978	0.0644	-0.05870	0.2300	0.2261	**0.0375**	0.4437	**0.0054**
	+/+ vs H156N/H156N	0.1815	0.4380	-0.01325	0.9348	0.1328	0.3245	0.2407	0.2713
	+/H156N vs H156N/H156N	-0.1163	0.5469	0.04545	0.5428	-0.09335	0.4550	-0.2030	0.2487
BAT/BW	+/+ vs +/H156N	-0.01325	0.9377	-0.001739	0.9978	-0.01255	0.9050	0.04395	0.6733
	+/+ vs H156N/H156N	-0.01446	0.9414	-0.03765	0.3098	-0.04530	0.3824	-0.01055	0.9784
	+/H156N vs H156N/H156N	-0.001204	0.9996	-0.03591	0.4125	-0.03275	0.6096	-0.05450	0.6082
iWAT/BW	+/+ vs +/H156N	-0.9062	0.2612	-0.1711	0.8241	-0.3157	0.5530	-0.1684	0.8884
	+/+ vs H156N/H156N	-0.08458	0.9922	-0.09989	0.9640	0.4235	0.3481	-0.2719	0.6957
	+/H156N vs H156N/H156N	0.8216	0.4100	0.07119	0.9782	0.7392	**0.0071**	-0.1035	0.9535

Table 9.37. Female *Tbx15*^{M566R} terminal measurements. All data was analysed by one-way ANOVA with post-hoc Tukey's multiple comparisons, per diet; significant values (p<0.05) highlighted in bold. High-fat diet: *Tbx15*$^{+/+}$ (n=22), *Tbx15*$^{+/M566R}$ (n=22), *Tbx15* $^{M566R/M566R}$ (n=21), low-fat diet: *Tbx15*$^{+/+}$ (n=20), *Tbx15*$^{+/M566R}$ (n=21), *Tbx15* $^{M566R/M566R}$ (n=22).

	High-fat diet						**Low-fat diet**					
	Bodyweight		**Length**		**gWAT:iWAT ratio**		**Bodyweight**		**Length**		**gWAT:iWAT ratio**	
Genotype	0.4524		0.2831		0.8043		0.1715		0.5866		0.3509	
Post-hoc analysis (adjusted P-value)												
Comparison	**Diff means**	**P-value**	**Diff means**	**P-value**	**Diff means**	**P-value**	**Diff means**	**P-value**	**Diff means**	**P-value**	**Diff means**	**P-value**
+/+ vs +/M566R	-1.887	0.4317	-0.1091	0.3274	-0.002146	0.9995	-0.3682	0.8629	-0.03595	0.9364	-0.07334	0.6348
+/+ vs M566R/M566R	-1.262	0.6903	-0.1019	0.3847	0.04243	0.8417	0.9143	0.4005	0.06773	0.7886	-0.1151	0.3234
+/M566R vs M566R/M566R	0.6248	0.9127	0.007143	0.9952	0.04458	0.8269	1.283	0.1631	0.1037	0.5673	-0.04176	0.8560

Table 9.38. Male *Tbx15*^{M566R} terminal measurements. All data was analysed by one-way ANOVA with post-hoc Tukey's multiple comparisons, per diet; significant values (p<0.05) highlighted in bold. High-fat diet: *Tbx15*$^{+/+}$ (n=22), *Tbx15*$^{+/M566R}$ (n=22), *Tbx15*$^{M566R/M566R}$ (n=18), low-fat diet: *Tbx15*$^{+/+}$ (n=22), *Tbx15*$^{+/M566R}$ (n=21), *Tbx15* $^{M566R/M566R}$ (n=17).

	High-fat diet						**Low-fat diet**					
	Bodyweight		**Length**		**gWAT:iWAT ratio**		**Body weight**		**Length**		**gWAT:iWAT ratio**	
Genotype	0.8201		0.8079		0.5290		0.4136		0.5060		0.4412	
Post-hoc analysis (adjusted P-value)												
Comparison	**Diff means**	**P-value**	**Diff means**	**P-value**	**Diff means**	**P-value**	**Diff means**	**P-value**	**Diff means**	**P-value**	**Diff means**	**P-value**
+/+ vs +/M566R	0.5559	0.8500	-0.05455	0.8060	0.09135	0.8881	1.460	0.3797	0.03463	0.8967	-0.08891	0.5072
+/+ vs M566R/M566R	0.5811	0.8523	-0.01212	0.9904	-0.1432	0.7697	0.7122	0.8113	0.09626	0.4762	-0.09130	0.5276
+/M566R vs M566R/M566R	0.02520	0.9997	0.04242	0.8890	-0.2346	0.4986	-0.7476	0.7980	0.06162	0.7402	-0.002390	0.9996

Table 9.39. *Tbx15*^{M566R} terminal depot measurements. All data was analysed by repeated measures two-way ANOVA with post-hoc Šídák's multiple comparisons, per sex and diet, interaction (Depot x Genotype); significant values (p<0.05) highlighted in bold. Female high-fat diet: *Tbx15*$^{+/+}$ (n=22), *Tbx15*$^{+/M566R}$ (n=22), *Tbx15* $^{M566R/M566R}$ (n=21), low-fat diet: *Tbx15*$^{+/+}$ (n=20), *Tbx15*$^{+/M566R}$ (n=21), *Tbx15* $^{M566R/M566R}$ (n=22), male high-fat diet: *Tbx15*$^{+/+}$ (n=22), *Tbx15*$^{+/M566R}$ (n=22), *Tbx15*$^{M566R/M566R}$ (n=18), low-fat diet: *Tbx15*$^{+/+}$ (n=22), *Tbx15*$^{+/M566R}$ (n=21), *Tbx15* $^{M566R/M566R}$ (n=17).

		Female				**Male**			
		High-fat diet		**Low-fat diet**		**High-fat diet**		**Low-fat diet**	
Raw values									
Interaction		0.9942		0.3452		0.9507		0.8444	
Depot		**<0.0001**		**<0.0001**		**<0.0001**		**<0.0001**	
Genotype		0.4991		0.2168		0.7401		0.4450	
Post-hoc analysis (adjusted p-value)									
	Comparison	**Diff means**	**P-value**	**Diff means**	**P-value**	**Diff means**	**P-value**	**Diff means**	**P-value**
gWAT	+/+ vs +/M566R	-0.2383	0.3998	-0.03173	0.9449	-0.01401	0.9865	0.1118	0.6032
	+/+ vs M566R/M566R	-0.2355	0.4643	0.1391	0.2754	0.09418	0.4416	-0.06803	0.8441
	+/M566R vs M566R/M566R	0.002774	>0.9999	0.1708	0.1924	0.1082	0.4919	-0.1798	0.3604
mWAT	+/+ vs +/M566R	-0.1411	0.6573	-0.009361	0.9748	0.003855	0.9973	0.02449	0.9242
	+/+ vs M566R/M566R	-0.1352	0.6809	0.05664	0.2715	-0.03626	0.8432	-0.05120	0.6855
	+/M566R vs M566R/M566R	0.005849	0.9994	0.06600	0.2703	-0.04011	0.8179	-0.07568	0.4636
Liver	+/+ vs +/M566R	-0.07642	0.7252	-0.002225	0.9981	0.1568	0.5954	0.06998	0.5419
	+/+ vs M566R/M566R	-0.05303	0.8324	0.03208	0.6484	0.1545	0.5534	0.01315	0.9903
	+/M566R vs M566R/M566R	0.02339	0.9719	0.03430	0.7079	-0.002236	0.9999	-0.05684	0.8320
pWAT	+/+ vs +/M566R	-0.06179	0.8483	-0.005239	0.9812	-0.04079	0.9122	0.1017	0.2765
	+/+ vs M566R/M566R	-0.05247	0.8914	0.02709	0.4192	0.001642	0.9998	0.02418	0.9422
	+/M566R vs M566R/M566R	0.009315	0.9957	0.03233	0.3926	0.04243	0.9020	-0.07756	0.5873
BAT	+/+ vs +/M566R	-0.02399	0.5106	-0.006418	0.6376	0.007323	0.8912	0.02168	0.5656
	+/+ vs M566R/M566R	-0.01894	0.6073	-0.0004986	0.9970	0.004619	0.9661	-0.01061	0.8900
	+/M566R vs M566R/M566R	0.005047	0.9748	0.005920	0.7474	-0.002704	0.9870	-0.03228	0.2808
iWAT	+/+ vs +/M566R	-0.2169	0.7940	-0.08119	0.6544	0.1246	0.8693	-0.01620	0.9923
	+/+ vs M566R/M566R	-0.07268	0.9726	0.03085	0.9201	-0.06068	0.9742	-0.1159	0.6797
	+/M566R vs M566R/M566R	0.1443	0.9114	0.1120	0.4625	-0.1853	0.7733	-0.09970	0.7561

Adjusted for bodyweight									
Interaction		0.9999		0.2702		0.9569		0.7768	
Depot		**<0.0001**		**<0.0001**		**<0.0001**		**<0.0001**	
Genotype		0.7665		0.2778		0.9120		0.4456	
Post-hoc analysis (adjusted p-value)									
	Comparison	**Diff means**	**P-value**	**Diff means**	**P-value**	**Diff means**	**P-value**	**Diff means**	**P-value**
gWAT/BW	+/+ vs +/M566R	-0.1339	0.8716	-0.06472	0.9809	-0.1057	0.9136	0.1717	0.8079
	+/+ vs M566R/M566R	-0.2379	0.6880	0.5242	0.2400	0.1742	0.6477	-0.2153	0.7001
	+/M566R vs M566R/M566R	-0.1040	0.9243	0.5890	0.1865	0.2799	0.5538	-0.3870	0.4197
mWAT/BW	+/+ vs +/M566R	-0.1462	0.8327	0.007203	0.9984	-0.02943	0.9762	-0.03148	0.9701
	+/+ vs M566R/M566R	-0.1761	0.7603	0.1664	0.2906	-0.1136	0.7686	-0.1848	0.2851
	+/M566R vs M566R/M566R	-0.02998	0.9939	0.1592	0.3898	-0.08419	0.8639	-0.1533	0.4471
Liver/BW	+/+ vs +/M566R	-0.04723	0.9420	0.05390	0.8092	0.2827	0.5159	0.03839	0.9144
	+/+ vs M566R/M566R	-0.04175	0.9387	-0.005335	0.9979	0.2515	0.5439	0.04177	0.9665
	+/M566R vs M566R/M566R	0.005478	0.9992	-0.05923	0.8143	-0.03128	0.9901	0.003380	0.9998
pWAT/BW	+/+ vs +/M566R	-0.1226	0.8691	-0.008065	0.9969	-0.1021	0.8742	0.2544	0.3317
	+/+ vs M566R/M566R	-0.1316	0.8587	0.09661	0.4950	-0.01984	0.9938	0.08153	0.8971
	+/M566R vs M566R/M566R	-0.009025	0.9992	0.1047	0.5135	0.08222	0.9149	-0.1729	0.6737
BAT/BW	+/+ vs +/M566R	-0.03082	0.6538	-0.01853	0.6878	0.01037	0.9466	0.03486	0.7408
	+/+ vs M566R/M566R	-0.02836	0.6489	-0.01456	0.8601	0.005123	0.9900	-0.03847	0.6960
	+/M566R vs M566R/M566R	0.002459	0.9975	0.003972	0.9907	-0.005250	0.9877	-0.07333	0.2179
iWAT/BW	+/+ vs +/M566R	-0.1678	0.9715	-0.2880	0.6871	0.1954	0.9232	-0.1362	0.9209
	+/+ vs M566R/M566R	0.1058	0.9878	0.09185	0.9517	-0.1685	0.9538	-0.3776	0.5462
	+/M566R vs M566R/M566R	0.2735	0.9259	0.3798	0.5284	-0.3638	0.7983	-0.2414	0.7855

Table 9.40. *Tbx15*$^{+/-}$ blood plasma clinical chemistry. Data analysed by multiple unpaired t-tests (two-stage step-up (Benjamini, Krieger, and Yekutieli) (false discovery rate 5%)) per sex and diet; significant values (p<0.05 and q<0.05) highlighted in bold. ALT (alanine aminotransferase), ALP (alkaline phosphatase), AST (aspartate aminotransferase), CK (creatine kinase), LDH (lactate dehydrogenase), LDL (low density lipoprotein), HDL (high density lipoprotein), FFA (free fatty acids). Female high-fat diet: *Tbx15*$^{+/+}$ (n=18), *Tbx15*$^{+/-}$ (n=22), low-fat diet: *Tbx15*$^{+/+}$ (n=18), *Tbx15*$^{+/-}$ (n=22), male high-fat diet: *Tbx15*$^{+/+}$ (n=21), *Tbx15*$^{+/-}$ (n=17), low-fat diet: *Tbx15*$^{+/+}$ (n=21), *Tbx15*$^{+/-}$ (n=14). The baseline detection limit for uric acid was 45 µmol/L, all values detected as <45 µmol/L in the assay were reported as 45 µmol/L.

	Female						**Male**					
	High-fat diet			**Low-fat diet**			**High-fat diet**			**Low-fat diet**		
Analyte	**Diff means**	**p-value**	**q-value**	**Diff means**	**p-value**	**q-value**	**Diff means**	**p-value**	**q-value**	**Diff means**	**p-value**	**q-value**
Sodium	0.09091	0.992882	0.935111	0.05556	0.995378	>0.99999	-0.6611	0.990903	>0.99999	0.6905	0.942668	0.972477
Potassium	0.2195	0.982810	0.935111	-0.07365	0.993873	>0.99999	0.009244	0.999873	>0.99999	-0.1833	0.984765	0.972477
Chloride	0.4293	0.966395	0.935111	-0.07937	0.993397	>0.99999	-0.6863	0.990557	>0.99999	0.1429	0.988129	0.972477
Urea	0.5722	0.955217	0.935111	0.5786	0.951895	>0.99999	0.2697	0.996288	>0.99999	0.2524	0.979029	0.972477
Glucose	-0.1626	0.987266	0.935111	-0.5651	0.953016	>0.99999	-0.1342	0.998154	>0.99999	0.6929	0.942471	0.972477
Calcium	0.03192	0.997501	0.935111	0.03603	0.997002	>0.99999	0.003137	0.999957	>0.99999	0.03833	0.996814	0.972477
Inorganic Phosphorous	-0.001010	0.999921	0.935111	0.08079	0.993278	>0.99999	-0.1665	0.997708	>0.99999	0.03548	0.997052	0.972477
Total Bilirubin	-0.2990	0.976592	0.935111	0.1825	0.984815	>0.99999	0.06415	0.999117	>0.99999	0.00238	0.999802	0.972477
ALT	0.6566	0.948625	0.935111	2.659	0.781613	>0.99999	-3.204	0.955926	>0.99999	-5.333	0.578591	0.972477
ALP	1.626	0.873198	0.935111	-4.349	0.650215	>0.99999	-5.622	0.922760	>0.99999	-3.095	0.747169	0.972477
Total Protein	0.8364	0.934584	0.935111	0.5635	0.953148	>0.99999	-0.00812	0.999888	>0.99999	1.038	0.913899	0.972477
Albumin	0.1202	0.990588	0.935111	-0.09444	0.992143	>0.99999	-0.2314	0.996816	>0.99999	0.7952	0.933989	0.972477
AST	3.015	0.767310	0.935111	10.26	0.284758	>0.99999	-8.353	0.885454	>0.99999	-6.976	0.467535	0.972477
CK	0.3030	0.976275	0.935111	10.29	0.283643	>0.99999	-26.71	0.645115	>0.99999	-23.45	**0.014744**	0.193591
Amylase	-14.13	0.165845	0.935111	3.778	0.693662	>0.99999	12.99	0.822675	>0.99999	21.10	**0.028221**	0.247027
Total Cholesterol	0.2238	0.982478	0.935111	0.2222	0.981514	>0.99999	0.3167	0.995642	>0.99999	0.1576	0.986902	0.972477
Triglycerides	0.04828	0.996219	0.935111	0.02040	0.998303	>0.99999	-0.00885	0.999878	>0.99999	0.02048	0.998298	0.972477
Uric Acid	61.95	**<0.000001**	**<0.000001**	-8.587	0.370675	>0.99999	-23.34	0.687281	>0.99999	-0.6667	0.944642	0.972477
LDH	19.18	0.060060	0.505505	29.35	**0.002265**	0.061770	-67.02	0.247922	>0.99999	-37.24	**0.000112**	**0.002950**
Iron	-0.5106	0.960035	0.935111	-0.4810	0.960004	>0.99999	-0.6866	0.990553	>0.99999	0.7000	0.941879	0.972477
LDL	0.05657	0.995571	0.935111	0.04865	0.995953	>0.99999	0.1722	0.997631	>0.99999	0.06762	0.994381	0.972477
HDL	0.1206	0.990556	0.935111	0.1605	0.986650	>0.99999	0.1969	0.997291	>0.99999	0.09952	0.991729	0.972477
FFAs	0.1775	0.986100	0.935111	0.08540	0.992896	>0.99999	-0.06118	0.999158	>0.99999	0.1364	0.988663	0.972477
Creatinine	0.5303	0.958494	0.935111	0.1135	0.990558	>0.99999	0.07787	0.998928	>0.99999	0.2286	0.981007	0.972477
Glycerol	36.07	**0.000417**	**0.005263**	12.33	0.198923	>0.99999	-6.039	0.917046	>0.99999	19.88	**0.038620**	0.253541
Ketone Bodies	-0.06374	0.995009	0.935111	0.05373	0.995530	>0.99999	-0.01966	0.999729	>0.99999	-0.00143	0.999881	0.972477
Magnesium	0.03030	0.997627	0.935111	-0.02103	0.998250	>0.99999	-0.04440	0.999389	>0.99999	0.01952	0.998378	0.972477

Table 9.41. *Tbx15*^{H156N} blood plasma clinical chemistry. Female high-fat diet and low-fat diet, and male high-fat diet data was analysed by two-way ANOVA with Tukeys's multiple corrections. Two male LFD samples did not have sufficient volume to run a full analyte panel: one *Tbx15*$^{+/H156N}$ (no ALT, Free Fatty Acids, Glycerol, Ketones or Magnesium) and one *Tbx15*$^{H156N/H156N}$ (no Free Fatty Acids, Glycerol or Ketones), male low-fat diet data was analysed by mixed-effect model (REML) with Tukey's multiple comparisons. Significant values (p<0.05) highlighted in bold. ALT (alanine aminotransferase), ALP (alkaline phosphatase), AST (aspartate aminotransferase), CK (creatine kinase), LDH (lactate dehydrogenase), LDL (low density lipoprotein), and HDL (high density lipoprotein). Female high-fat diet: *Tbx15*$^{+/+}$ (n=23), *Tbx15*$^{+/H156N}$ (n=27), *Tbx15*$^{H156N/H156N}$ (n=16), low-fat diet: *Tbx15*$^{+/+}$ (n=23), *Tbx15*$^{+/H156N}$ (n=23), *Tbx15*$^{H156N/H156N}$ (n=15), male high-fat diet: *Tbx15*$^{+/+}$ (n=21), *Tbx15*$^{+/H156N}$ (n=23), *Tbx15*$^{H156N/H156N}$ (n=21), low-fat diet: *Tbx15*$^{+/+}$ (n=21), *Tbx15*$^{+/H156N}$ (n=20), *Tbx15*$^{H156N/H156N}$ (n=20).

		Female				**Male**			
		High-fat diet		**Low-fat diet**		**High-fat diet**		**Low-fat diet**	
Interaction		**<0.0001**		**<0.0001**		**<0.0001**		**0.0047**	
Analyte		**<0.0001**		**<0.0001**		**<0.0001**		**<0.0001**	
Genotype		**0.0223**		**0.0051**		**0.0333**		0.2319	
Post-hoc analysis (adjusted p-value)									
Analyte	**Comparison**	**Diff means**	**P-value**	**Diff means**	**P-value**	**Diff means**	**P-value**	**Diff means**	**P-value**
Sodium	+/+ vs +/H156N	-0.1143	0.9796	-0.3478	0.8454	-1.055	0.7394	0.6333	0.6871
	+/+ vs H156N/H156N	-0.5842	0.7734	-1.119	0.1570	-1.606	0.4351	0.6333	0.4633
	+/H156N vs H156N/H156N	-0.4699	0.8265	-0.7710	0.4704	-0.5507	0.7735	0.000	>0.9999
Potassium	+/+ vs +/H156N	-0.7274	**0.0043**	-0.1174	0.8175	-0.4464	0.0857	-0.03857	0.9542
	+/+ vs H156N/H156N	-0.2285	0.5378	-0.1464	0.7667	0.08420	0.8886	-0.1436	0.5853
	+/H156N vs H156N/H156N	0.4988	0.1153	-0.02899	0.9894	0.5306	**0.0301**	-0.1050	0.7458
Chloride	+/+ vs +/H156N	0.05797	0.9932	0.3478	0.8188	-0.6324	0.8433	-0.1452	0.9697
	+/+ vs H156N/H156N	-1.421	0.2318	-0.4290	0.7864	-1.165	0.5108	-0.4952	0.6187
	+/H156N vs H156N/H156N	-1.479	0.2180	-0.7768	0.5427	-0.5321	0.7224	-0.3500	0.8452
Urea	+/+ vs +/H156N	0.0009662	>0.9999	0.1174	0.8754	0.1243	0.8966	0.03214	0.9883
	+/+ vs H156N/H156N	0.006522	0.9994	-0.2046	0.7090	0.006710	0.9996	0.4421	0.1116
	+/H156N vs H156N/H156N	0.005556	0.9996	-0.3220	0.4597	-0.1176	0.8760	0.4100	0.1601
Glucose	+/+ vs +/H156N	-0.05539	0.9950	-0.04783	0.9969	-1.368	0.1882	1.548	0.1664
	+/+ vs H156N/H156N	-0.01141	0.9998	-1.780	**0.0098**	-0.5727	0.7680	0.6781	0.6151
	+/H156N vs H156N/H156N	0.04398	0.9983	-1.732	**0.0168**	0.7957	0.6884	-0.8700	0.5131
Calcium	+/+ vs +/H156N	-0.01440	0.8917	0.02391	0.7302	-0.01545	0.9216	0.03262	0.5739
	+/+ vs H156N/H156N	-0.03217	0.4698	-0.03154	0.7038	-0.04403	0.4525	-0.006881	0.9708
	+/H156N vs H156N/H156N	-0.01778	0.7910	-0.05545	0.2908	-0.02857	0.4635	-0.03950	0.4229

Inorganic Phosphorous	+/+ vs +/H156N	-0.3622	**0.0005**	0.02522	0.9594	-0.2549	**0.0232**	0.05243	0.8521
	+/+ vs H156N/H156N	-0.1128	0.3220	-0.09180	0.6828	-0.04035	0.8651	0.1389	0.2691
	+/H156N vs H156N/H156N	0.2494	**0.0094**	-0.1170	0.5592	0.2146	0.0958	0.08650	0.6572
Total Bilirubin	+/+ vs +/H156N	-0.7296	**0.0284**	-0.6565	0.3113	-0.6263	0.0827	-1.153	0.4023
	+/+ vs H156N/H156N	0.03750	0.9844	-0.1780	0.7971	0.1955	0.6882	-0.3081	0.4035
	+/H156N vs H156N/H156N	0.7671	**0.0206**	0.4786	0.5467	0.8217	**0.0090**	0.8450	0.6130
ALT	+/+ vs +/H156N	-123.2	**0.0233**	-70.65	**0.0405**	-9.008	0.9575	-36.90	0.4150
	+/+ vs H156N/H156N	-0.3016	>0.9999	8.939	0.8772	23.25	0.6932	-19.25	0.3798
	+/H156N vs H156N/H156N	122.9	**0.0355**	79.59	**0.0327**	32.25	0.5639	17.65	0.8081
ALP	+/+ vs +/H156N	-1.610	0.8146	-0.3913	0.9963	1.672	0.9246	-7.521	0.6963
	+/+ vs H156N/H156N	-1.370	0.9222	1.310	0.9643	-0.3550	0.9963	-2.121	0.7711
	+/H156N vs H156N/H156N	0.2407	0.9966	1.701	0.9269	-2.027	0.8596	5.400	0.8288
Total Protein	+/+ vs +/H156N	0.01578	0.9997	-0.07391	0.9903	0.1180	0.9855	1.271	0.2798
	+/+ vs H156N/H156N	0.3940	0.8412	-0.2484	0.9194	0.1803	0.9628	0.3962	0.8673
	+/H156N vs H156N/H156N	0.3782	0.8722	-0.1745	0.9458	0.06232	0.9962	-0.8750	0.5037
Albumin	+/+ vs +/H156N	-0.4317	0.4220	0.3043	0.7028	0.2569	0.7966	0.8764	0.1904
	+/+ vs H156N/H156N	0.06712	0.9779	-0.7626	0.0840	0.1234	0.9549	0.2214	0.9145
	+/H156N vs H156N/H156N	0.4988	0.4031	-1.067	**0.0025**	-0.1335	0.9474	-0.6550	0.4134
AST	+/+ vs +/H156N	-162.6	**0.0210**	-148.9	**0.0352**	-51.06	0.2304	-116.6	0.1477
	+/+ vs H156N/H156N	-1.245	0.9996	18.43	0.8945	25.59	0.5203	-28.25	0.3762
	+/H156N vs H156N/H156N	161.3	**0.0421**	167.3	**0.0235**	76.66	**0.0360**	88.35	0.3224
CK	+/+ vs +/H156N	-16.92	0.3296	-6.696	0.9285	-1.061	0.9973	-40.97	0.3152
	+/+ vs H156N/H156N	-35.33	0.1373	-23.54	0.4172	-21.50	0.4034	-24.87	0.3875
	+/H156N vs H156N/H156N	-18.41	0.5804	-16.85	0.6776	-20.44	0.3483	16.10	0.8653
Amylase	+/+ vs +/H156N	-168.2	0.3150	-191.4	**0.0397**	-74.72	0.5016	-72.24	0.5512
	+/+ vs H156N/H156N	-43.89	0.9447	-16.47	0.9390	54.55	0.5816	-79.69	0.5468
	+/H156N vs H156N/H156N	124.4	0.6381	175.0	0.0738	129.3	**0.0297**	-7.450	0.9958
Total Cholesterol	+/+ vs +/H156N	-0.1182	0.8923	0.09696	0.7783	0.2062	0.7585	0.1076	0.9132
	+/+ vs H156N/H156N	0.07666	0.9607	-0.05023	0.9304	0.7918	0.0584	-0.06536	0.9486
	+/H156N vs H156N/H156N	0.1948	0.8180	-0.1472	0.4192	0.5855	0.2055	-0.1730	0.7839
Triglycerides	+/+ vs +/H156N	0.06717	0.8807	-0.1196	0.8427	0.06125	0.7728	0.1237	0.7010
	+/+ vs H156N/H156N	0.08337	0.8323	0.2154	0.5164	0.1286	0.2536	0.2137	0.3329
	+/H156N vs H156N/H156N	0.01620	0.9942	0.3350	0.2162	0.06739	0.5454	0.09000	0.7215

Uric Acid	+/+ vs +/H156N	-5.702	0.7109	3.261	0.7860	4.237	0.7050	-3.481	0.6830
	+/+ vs H156N/H156N	-0.8016	0.9899	-6.148	0.6091	-6.212	0.6496	0.06905	0.9997
	+/H156N vs H156N/H156N	4.900	0.7986	-9.409	0.3113	-10.45	0.3114	3.550	0.6923
LDH	+/+ vs +/H156N	-568.9	**0.0439**	-205.7	0.1513	-315.2	0.2749	-277.0	0.2504
	+/+ vs H156N/H156N	48.93	0.9495	97.95	0.5270	196.5	0.3173	-87.37	0.5540
	+/H156N vs H156N/H156N	617.8	**0.0331**	303.6	**0.0287**	511.6	**0.0353**	189.6	0.5143
Iron	+/+ vs +/H156N	-2.666	0.1544	0.1087	0.9923	0.5162	0.9148	0.2588	0.9777
	+/+ vs H156N/H156N	-0.9582	0.8717	-0.9217	0.6740	1.044	0.7074	0.7438	0.6926
	+/H156N vs H156N/H156N	1.708	0.6242	-1.030	0.6430	0.5280	0.9242	0.4850	0.8919
LDL	+/+ vs +/H156N	-0.04457	0.8183	0.02913	0.7623	0.06962	0.7669	-0.03798	0.8783
	+/+ vs H156N/H156N	-0.005245	0.9971	0.02748	0.7615	0.2456	0.0809	-0.01798	0.9599
	+/H156N vs H156N/H156N	0.03933	0.8855	-0.001652	0.9984	0.1760	0.2557	0.02000	0.9621
HDL	+/+ vs +/H156N	-0.01705	0.9944	0.07957	0.7397	0.1690	0.6025	0.1318	0.7348
	+/+ vs H156N/H156N	0.07052	0.9282	-0.09759	0.6251	0.4131	0.1395	-0.05619	0.9174
	+/H156N vs H156N/H156N	0.08757	0.9145	-0.1772	0.1228	0.2441	0.4746	-0.1880	0.5274
Free Fatty Acids	+/+ vs +/H156N	0.07528	0.3492	-0.01478	0.9326	0.0004743	>0.9999	0.02221	0.8636
	+/+ vs H156N/H156N	0.05253	0.5463	0.003188	0.9972	0.009004	0.9477	-0.007268	0.9793
	+/H156N vs H156N/H156N	-0.02275	0.9063	0.01797	0.9132	0.008530	0.9728	-0.02947	0.7103
Creatinine	+/+ vs +/H156N	-0.1565	0.8575	-0.6739	0.4049	-0.2172	0.9073	-0.1164	0.9555
	+/+ vs H156N/H156N	-0.1003	0.9730	0.09246	0.9676	0.1188	0.9594	-0.1064	0.9569
	+/H156N vs H156N/H156N	0.05625	0.9903	0.7664	0.3693	0.3360	0.7686	0.01000	0.9996
Glycerol	+/+ vs +/H156N	98.17	0.3311	-74.04	0.7077	44.01	0.6723	65.63	0.7299
	+/+ vs H156N/H156N	65.99	0.7134	76.48	0.6477	69.42	0.3438	105.5	0.3718
	+/H156N vs H156N/H156N	-32.17	0.9009	150.5	0.1939	25.42	0.7712	39.84	0.8623
Ketone Bodies	+/+ vs +/H156N	-0.001288	0.9998	0.07609	0.3907	-0.02275	0.9097	-0.01955	0.6190
	+/+ vs H156N/H156N	0.02318	0.9316	0.1300	0.0537	0.01968	0.9072	-0.009549	0.8946
	+/H156N vs H156N/H156N	0.02447	0.8775	0.05394	0.3984	0.04242	0.6671	0.01000	0.9083
Magnesium	+/+ vs +/H156N	-0.01512	0.6207	-0.01739	0.6254	-0.01312	0.7688	0.01516	0.5918
	+/+ vs H156N/H156N	-0.02269	0.3690	-0.04899	0.0543	-0.01087	0.8646	0.02345	0.2548
	+/H156N vs H156N/H156N	-0.007569	0.9051	-0.03159	0.3646	0.002257	0.9948	0.008289	0.8776

Table 9.42. *Tbx15*^{M566R} blood plasma clinical chemistry analysis. Female LFD, and male HFD and LFD data was analysed by two-way ANOVA with Tukey's multiple corrections. One female HFD *Tbx15*$^{+/+}$ sample did not have sufficient volume to run a full analyte panel (no total protein or uric acid); female HFD data was analysed by mixed-effect model (REML) with Tukey's multiple comparisons. Significant values (p<0.05) highlighted in bold. ALT (alanine aminotransferase), ALP (alkaline phosphatase), AST (aspartate aminotransferase), CK (creatine kinase), LDH (lactate dehydrogenase), LDL (low density lipoprotein), and HDL (high density lipoprotein). Female high-fat diet: *Tbx15*$^{+/+}$ (n=22), *Tbx15*$^{+/M566R}$ (n=22), *Tbx15* $^{M566R/M566R}$ (n=21), low-fat diet: *Tbx15*$^{+/+}$ (n=20), *Tbx15*$^{+/M566R}$ (n=21), *Tbx15* $^{M566R/M566R}$ (n=22), male high-fat diet: *Tbx15*$^{+/+}$ (n=22), *Tbx15*$^{+/M566R}$ (n=22), *Tbx15*$^{M566R/M566R}$ (n=18), low-fat diet: *Tbx15*$^{+/+}$ (n=22), *Tbx15*$^{+/M566R}$ (n=21), *Tbx15* $^{M566R/M566R}$ (n=17).

		Female				**Male**			
		High-fat diet		**Low-fat diet**		**High-fat diet**		**Low-fat diet**	
Interaction		0.9570		0.3175		>0.9999		0.8820	
Analyte		**<0.0001**		**<0.0001**		**<0.0001**		**<0.0001**	
Genotype		0.7196		0.6368		0.7161		0.3491	
Post-hoc analysis (adjusted p-value)									
Analyte	**Comparison**	**Diff means**	**P-value**	**Diff means**	**P-value**	**Diff means**	**P-value**	**Diff means**	**P-value**
Sodium	+/+ vs +/M566R	0.6364	0.5119	0.2429	0.8952	-0.8636	**0.0465**	-0.3810	0.5647
	+/+ vs M566R/M566R	0.6948	0.4816	0.6909	0.5645	-1.510	**0.0004**	0.3529	0.7617
	+/M566R vs M566R/M566R	0.05844	0.9940	0.4481	0.8073	-0.6465	0.1281	0.7339	0.3080
Potassium	+/+ vs +/M566R	0.1623	0.1336	-0.03340	0.9296	0.1318	0.3124	0.04654	0.8402
	+/+ vs M566R/M566R	0.09628	0.5395	0.005318	0.9981	0.3086	**0.0015**	-0.006684	0.9968
	+/M566R vs M566R/M566R	-0.06600	0.6449	0.03872	0.8887	0.1768	**0.0471**	-0.05322	0.8313
Chloride	+/+ vs +/M566R	1.045	0.1226	-0.1286	0.9648	-0.7727	0.1570	-0.2706	0.7288
	+/+ vs M566R/M566R	0.6385	0.3764	0.2091	0.9094	-1.227	**0.0228**	0.03476	0.9977
	+/M566R vs M566R/M566R	-0.4069	0.7312	0.3377	0.8310	-0.4545	0.3950	0.3053	0.8396
Urea	+/+ vs +/M566R	-0.1864	0.7441	0.000	>0.9999	0.02273	0.9933	0.1723	0.7929
	+/+ vs M566R/M566R	-0.08009	0.9450	0.2409	0.7294	-0.2364	0.3671	-0.1241	0.8700
	+/M566R vs M566R/M566R	0.1063	0.8959	0.2409	0.6774	-0.2591	0.4963	-0.2964	0.5528
Glucose	+/+ vs +/M566R	-1.591	**0.0488**	0.4088	0.7529	1.214	0.2469	0.5721	0.8098
	+/+ vs M566R/M566R	-1.760	**0.0210**	0.8805	0.1993	2.258	**0.0127**	0.08048	0.9977
	+/M566R vs M566R/M566R	-0.1693	0.9335	0.4716	0.6747	1.044	0.3328	-0.4916	0.9332
Calcium	+/+ vs +/M566R	-0.008636	0.8142	0.01943	0.2066	0.01091	0.6897	0.02749	0.0948
	+/+ vs M566R/M566R	-0.01132	0.7526	0.01255	0.7153	0.004394	0.9515	0.003316	0.9844
	+/M566R vs M566R/M566R	-0.002684	0.9838	-0.006883	0.9215	-0.006515	0.9033	-0.02417	0.4122

Inorganic Phosphorous	+/+ vs +/M566R	0.1482	0.7579	0.1266	0.6982	-0.2114	0.4040	-0.002359	>0.9999
	+/+ vs M566R/M566R	0.2998	0.3119	0.2258	0.3229	-0.05944	0.9308	0.2401	0.3975
	+/M566R vs M566R/M566R	0.1517	0.6600	0.09918	0.7887	0.1519	0.7068	0.2425	0.2692
Total Bilirubin	+/+ vs +/M566R	-0.1636	0.3156	-0.07286	0.7359	0.004545	0.9977	-0.4736	0.6115
	+/+ vs M566R/M566R	-0.1251	0.2066	0.07000	0.7309	0.003535	0.9987	-1.266	0.5889
	+/M566R vs M566R/M566R	0.03853	0.9336	0.1429	0.3393	-0.001010	0.9999	-0.7927	0.8308
ALT	+/+ vs +/M566R	-11.82	0.7734	-1.538	0.9165	9.455	0.9639	-26.21	0.4474
	+/+ vs M566R/M566R	-5.918	0.9192	3.427	0.5252	-21.24	0.8779	-22.97	0.3558
	+/M566R vs M566R/M566R	5.900	0.9510	4.965	0.2502	-30.70	0.7964	3.244	0.9915
ALP	+/+ vs +/M566R	-0.2727	0.9964	2.307	0.8906	6.455	0.4723	-3.846	0.7619
	+/+ vs M566R/M566R	-1.067	0.9442	5.586	0.5366	3.965	0.7526	-12.58	0.1488
	+/M566R vs M566R/M566R	-0.7944	0.9618	3.279	0.7895	-2.490	0.8095	-8.734	0.5235
Total Protein	+/+ vs +/M566R	-0.4071	0.8792	-0.2512	0.9181	1.759	**0.0145**	0.4950	0.7742
	+/+ vs M566R/M566R	-0.7476	0.6061	0.06136	0.9940	0.8101	0.5080	0.02219	0.9998
	+/M566R vs M566R/M566R	-0.3405	0.9139	0.3126	0.8592	-0.9490	0.3473	-0.4728	0.9116
Albumin	+/+ vs +/M566R	-0.1182	0.9575	-0.4369	0.3442	0.5364	0.2734	0.2013	0.8960
	+/+ vs M566R/M566R	-0.4606	0.3895	0.01136	0.9994	0.2470	0.7914	-0.4155	0.7300
	+/M566R vs M566R/M566R	-0.3424	0.5988	0.4483	0.2866	-0.2894	0.7224	-0.6168	0.5639
AST	+/+ vs +/M566R	-13.50	0.6411	-2.569	0.9089	8.727	0.9344	-45.53	0.5698
	+/+ vs M566R/M566R	-2.885	0.9712	5.186	0.5493	-25.29	0.7302	-30.67	0.3985
	+/M566R vs M566R/M566R	10.61	0.8146	7.755	0.2215	-34.02	0.6048	14.85	0.9519
CK	+/+ vs +/M566R	48.82	0.0562	31.32	0.6628	-12.55	0.8776	-59.54	0.4771
	+/+ vs M566R/M566R	58.79	**0.0177**	7.336	0.9839	-0.8333	0.9991	-14.93	0.8440
	+/M566R vs M566R/M566R	9.968	0.7325	-23.98	0.7533	11.71	0.8934	44.61	0.6586
Amylase	+/+ vs +/M566R	-5.409	0.9188	-26.33	0.4279	-24.05	0.1696	-2.749	0.9953
	+/+ vs M566R/M566R	8.117	0.8193	-34.63	0.1037	-2.864	0.9798	-47.04	0.1384
	+/M566R vs M566R/M566R	13.53	0.5876	-8.299	0.9383	21.18	0.3563	-44.29	0.3958
Total Cholesterol	+/+ vs +/M566R	-0.03000	0.9931	0.04402	0.8785	0.7145	**0.0275**	0.2337	0.5982
	+/+ vs M566R/M566R	-0.1908	0.7307	0.1654	0.0828	0.4395	0.3593	0.2044	0.7621
	+/M566R vs M566R/M566R	-0.1608	0.8297	0.1214	0.3291	-0.2750	0.6109	-0.02930	0.9954
Triglycerides	+/+ vs +/M566R	-0.04591	0.6430	0.0009762	0.9988	0.01545	0.9140	0.01173	0.8877
	+/+ vs M566R/M566R	-0.08149	0.2122	0.01505	0.7426	0.003687	0.9946	0.008930	0.9443
	+/M566R vs M566R/M566R	-0.03558	0.6521	0.01407	0.7755	-0.01177	0.9427	-0.002801	0.9957

Uric Acid	+/+ vs +/M566R	0.9416	0.9856	0.1238	0.9979	0.5455	0.9972	-2.896	0.5771
	+/+ vs M566R/M566R	-7.810	0.4604	-1.991	0.7281	2.742	0.9313	-6.829	0.3689
	+/M566R vs M566R/M566R	-8.751	0.4153	-2.115	0.6542	2.197	0.9574	-3.933	0.7623
LDH	+/+ vs +/M566R	4.227	0.9959	-31.43	0.2029	15.82	0.9961	-122.8	0.5985
	+/+ vs M566R/M566R	11.60	0.9561	18.81	0.6434	-157.4	0.8324	-127.3	0.2870
	+/M566R vs M566R/M566R	7.374	0.9886	50.24	0.0501	-173.2	0.8128	-4.490	0.9995
Iron	+/+ vs +/M566R	-1.332	0.3201	-0.9831	0.5633	2.245	0.2947	-0.3238	0.9677
	+/+ vs M566R/M566R	-0.8764	0.7399	0.1368	0.9897	1.379	0.5751	1.000	0.6301
	+/M566R vs M566R/M566R	0.4554	0.9227	1.120	0.5064	-0.8667	0.8065	1.324	0.5694
LDL	+/+ vs +/M566R	-0.02182	0.9532	0.01074	0.9015	0.2836	**0.0228**	0.03758	0.8291
	+/+ vs M566R/M566R	-0.03987	0.8425	0.02914	0.2613	0.1688	0.3317	0.04973	0.8018
	+/M566R vs M566R/M566R	-0.01805	0.9698	0.01840	0.6662	-0.1148	0.5415	0.01216	0.9883
HDL	+/+ vs +/M566R	-0.001364	>0.9999	0.04110	0.8023	0.2841	0.0630	0.1670	0.5550
	+/+ vs M566R/M566R	-0.1124	0.7330	0.1344	0.0565	0.1478	0.6322	0.1326	0.7765
	+/M566R vs M566R/M566R	-0.1111	0.7877	0.09327	0.2935	-0.1363	0.6258	-0.03440	0.9868
Free Fatty Acids	+/+ vs +/M566R	-0.02955	0.8308	0.001190	0.9981	0.03318	0.6586	0.01708	0.8137
	+/+ vs M566R/M566R	-0.06777	0.3678	-0.02636	0.4890	0.005606	0.9887	-0.008636	0.9586
	+/M566R vs M566R/M566R	-0.03823	0.4795	-0.02755	0.4385	-0.02758	0.6597	-0.02571	0.7059
Creatinine	+/+ vs +/M566R	0.6136	0.5318	-0.3314	0.8694	-0.3864	0.5820	-0.2734	0.8902
	+/+ vs M566R/M566R	0.2870	0.8260	0.02182	0.9992	-0.6424	0.2836	0.4762	0.6761
	+/M566R vs M566R/M566R	-0.3266	0.7652	0.3532	0.7669	-0.2561	0.8733	0.7496	0.3685
Glycerol	+/+ vs +/M566R	17.23	0.7261	6.110	0.8966	2.136	0.9874	1.171	0.9954
	+/+ vs M566R/M566R	11.61	0.8490	14.35	0.6063	-31.56	0.2433	11.11	0.7526
	+/M566R vs M566R/M566R	-5.621	0.9621	8.236	0.7497	-33.70	0.2375	9.944	0.7828
Ketone Bodies	+/+ vs +/M566R	0.01636	0.9178	0.004167	0.9970	-0.01500	0.9732	-0.03818	0.2815
	+/+ vs M566R/M566R	-0.03000	0.7856	-0.06432	0.5964	-0.05985	0.4474	-0.01406	0.8621
	+/M566R vs M566R/M566R	-0.04636	0.4220	-0.06848	0.4825	-0.04485	0.7682	0.02412	0.7350
Magnesium	+/+ vs +/M566R	-0.01318	0.8700	0.02819	0.4004	-0.01000	0.9027	-0.005433	0.9703
	+/+ vs M566R/M566R	0.0005195	0.9998	0.03291	0.2815	-0.002323	0.9937	0.01644	0.7660
	+/M566R vs M566R/M566R	0.01370	0.8250	0.004719	0.9699	0.007677	0.9455	0.02188	0.6071

Table 9.43. *Tbx15*$^{+/-}$ average adipocyte cell area. All data was analysed by repeated measures two-way ANOVA with post-hoc Šídák's multiple comparisons, per sex and diet, interaction (Depot x Genotype); significant values (p<0.05) highlighted in bold. Female high-fat diet: *Tbx15*$^{+/+}$ (n=4), *Tbx15*$^{+/-}$ (n=4), low-fat diet: *Tbx15*$^{+/+}$ (n=4), *Tbx15*$^{+/-}$ (n=4), male high-fat diet: *Tbx15*$^{+/+}$ (n=4), *Tbx15*$^{+/-}$ (n=4), low-fat diet: *Tbx15*$^{+/+}$ (n=4), *Tbx15*$^{+/-}$ (n=4).

	Female				**Male**			
	High-fat diet		**Low-fat diet**		**High-fat diet**		**Low-fat diet**	
Interaction	0.0517		0.9856		0.7344		0.9004	
Depot	**0.0005**		**<0.0001**		**0.0002**		**0.0025**	
Genotype	0.8259		0.7861		0.2074		0.5837	
Post-hoc analysis (adjust P value)								
Depot	**Diff means**	**p-value**	**Diff means**	**p-value**	**Diff means**	**p-value**	**Diff means**	**p-value**
gWAT	-159.7	0.9916	75.37	0.9984	160.7	0.9892	148.8	0.9989
mWAT	29.67	>0.9999	26.56	0.9999	183.5	0.9395	424.0	0.8316
pWAT	-455.5	0.8603	74.13	0.9119	472.3	0.2110	238.8	0.8467
iWAT	935.6	0.4984	55.22	0.9995	260.1	0.7784	49.02	>0.9999

Table 9.44. Female *Tbx15*$^{+/-}$ high-fat diet adipocyte cell area distribution. All data was analysed by multiple unpaired t-tests (two-stage step-up (Benjamini, Krieger, and Yekutieli) (false discovery rate 5%)) per diet and depot; significant values (p<0.05 and q<0.05) highlighted in bold. *Tbx15*$^{+/+}$ (n=4), *Tbx15*$^{+/-}$ (n=4).

Adipocyte size bin (μm²)	gWAT			mWAT			pWAT			iWAT		
	Diff means	p-value	q-value	Diff means	p-value	q-value	Diff means	p-value	q-value	Diff means	p-value	q-value
0-499	-1.045	0.446755	0.928413	0.6225	0.801369	0.911557	-6.375	0.099839	0.183900	-0.8175	0.747685	0.972757
500-999	-0.1050	0.890782	0.947480	1.735	0.536830	0.697879	-4.508	**0.049198**	0.122100	-2.420	0.313260	0.970116
1000-1499	-0.1750	0.698991	0.928413	1.555	0.392675	0.574193	-1.465	0.148903	0.203252	-0.8850	0.461960	0.970116
1500-1999	0.4000	0.073937	0.749728	1.413	0.233738	0.574193	-1.040	**0.028400**	0.086148	0.1650	0.746274	0.972757
2000-2499	0.2975	0.302360	0.928413	0.9300	0.077542	0.574193	-0.1300	0.614659	0.699175	0.5400	0.352457	0.970116
2500-2999	0.2550	0.229579	0.928413	0.6275	0.275458	0.574193	-0.01250	0.957163	>0.999999	0.5500	0.256448	0.970116
3000-3499	0.4125	**0.027694**	0.749728	0.08750	0.899502	0.963190	-0.1100	0.579220	0.687510	0.5650	0.304236	0.970116
3500-3999	0.3600	0.186995	0.928413	0.08000	0.917324	0.963190	0.5725	**0.002842**	0.077587	0.7950	0.228122	0.970116
4000-4499	0.3800	0.082388	0.749728	-0.2000	0.800250	0.911557	0.8050	**0.032740**	0.089382	0.5550	0.310445	0.970116
4500-4999	0.2950	0.210328	0.928413	-0.4600	0.589609	0.731651	0.6775	0.123983	0.203252	0.4550	0.435452	0.970116
5000-5499	0.2700	0.375713	0.928413	-0.5375	0.490894	0.670070	1.010	**0.017136**	0.079267	0.6125	0.269523	0.970116
5500-5999	0.06500	0.696017	0.928413	-0.7075	0.325267	0.574193	0.6000	0.128825	0.203252	0.3625	0.358702	0.970116
6000-6499	0.07500	0.674669	0.928413	-0.5725	0.371480	0.574193	0.5600	0.101044	0.183900	0.4025	0.223462	0.970116
6500-6999	-0.08500	0.613820	0.928413	-0.5725	0.314359	0.574193	0.8400	**0.022531**	0.079267	0.09000	0.793992	0.972757
7000-7499	0.06750	0.646771	0.928413	-0.6100	0.285625	0.574193	0.9575	**0.017435**	0.079267	0.2375	0.349022	0.970116
7500-7999	-0.04750	0.773988	0.928413	-0.3725	0.399622	0.574193	0.7450	0.087096	0.182901	-0.007500	0.976224	>0.999999
8000-8499	0.02250	0.800737	0.928413	-0.4850	0.216818	0.574193	0.9575	**0.017957**	0.079267	0.05000	0.866806	0.972757
8500-8999	0.01500	0.902362	0.947480	-0.2900	0.386903	0.574193	0.8750	**0.016556**	0.079267	-0.1825	0.558153	0.972757
9000-9499	0.1500	0.392048	0.928413	-0.2550	0.299685	0.574193	0.9600	**0.014462**	0.079267	-0.05500	0.852806	0.972757
9500-9999	-0.06500	0.601058	0.928413	-0.2750	0.239948	0.574193	0.7500	**0.023228**	0.079267	0.04500	0.866958	0.972757
10000-10999	-0.05000	0.816187	0.928413	-0.3375	0.377203	0.574193	1.223	0.072024	0.163854	-0.2675	0.615904	0.972757
11000-11999	-0.2450	0.354924	0.928413	-0.2750	0.340133	0.574193	0.8050	0.147764	0.203252	-0.06250	0.890803	0.972757
12000-12999	-0.1025	0.744778	0.928413	-0.1725	0.253287	0.574193	0.6425	0.141170	0.203252	-0.2800	0.449595	0.970116
13000-13999	-0.1800	0.576799	0.928413	-0.1250	0.312625	0.574193	0.4150	0.267208	0.347370	-0.05500	0.868000	0.972757
14000-14999	-0.1650	0.537543	0.928413	-0.1025	0.316412	0.574193	0.2950	0.372620	0.462388	-0.1250	0.600888	0.972757
15000+	-0.7875	0.532803	0.928413	-0.2225	0.316989	0.574193	-0.01000	0.991239	>0.999999	-0.2600	0.706349	0.972757

Table 9.45. Female *Tbx15*$^{+/-}$ low-fat diet adipocyte cell area distribution. All data was analysed by multiple unpaired t-tests (two-stage step-up (Benjamini, Krieger, and Yekutieli) (false discovery rate 5%)) per diet and depot; significant values (p<0.05 and q<0.05) highlighted in bold. *Tbx15*$^{+/+}$ (n=4), *Tbx15*$^{+/-}$ (n=4).

Adipocyte size bin (μm²)	gWAT			mWAT			pWAT			iWAT		
	Diff means	p-value	q-value	Diff means	p-value	q-value	Diff means	p-value	q-value	Diff means	p-value	q-value
0-249	0.1925	0.881672	>0.999999	1.165	0.717914	0.931177	-1.040	0.761820	0.954197	-0.8775	0.732032	>0.999999
250-499	0.3300	0.918190	>0.999999	-1.160	0.812599	0.995433	-0.7000	0.903480	0.954197	-0.1325	0.980079	>0.999999
500-749	0.5100	0.786779	>0.999999	-1.565	0.270121	0.611705	1.220	0.697125	0.954197	0.04750	0.980706	>0.999999
750-999	-0.09500	0.949763	>0.999999	-2.060	0.210462	0.611705	1.195	0.412599	0.954197	-0.07500	0.934747	>0.999999
1000-1249	-0.09000	0.910327	>0.999999	-0.2175	0.912893	>0.999999	0.5425	0.669698	0.954197	-0.2375	0.864971	>0.999999
1250-1499	-0.3750	0.520110	>0.999999	0.08000	0.960774	>0.999999	-0.2525	0.864865	0.954197	0.04500	0.976062	>0.999999
1500-1749	-0.5750	0.184581	>0.999999	0.5675	0.681129	0.931177	-0.4600	0.745120	0.954197	-0.1650	0.892463	>0.999999
1750-1999	-0.2650	0.620599	>0.999999	0.6500	0.515721	0.758110	-0.6150	0.696336	0.954197	0.03250	0.975107	>0.999999
2000-2249	-0.3950	0.462873	>0.999999	0.4975	0.475124	0.748321	-0.9475	0.508555	0.954197	0.1675	0.848137	>0.999999
2250-2499	-0.4300	0.557308	>0.999999	0.5150	0.302161	0.611705	-0.5200	0.655865	0.954197	0.2000	0.770457	>0.999999
2500-2749	-0.4125	0.542238	>0.999999	0.3450	0.305159	0.611705	-0.2200	0.836197	0.954197	0.1275	0.836444	>0.999999
2750-2999	-0.3300	0.638507	>0.999999	0.2300	0.395572	0.670951	-0.2325	0.769295	0.954197	0.07250	0.887642	>0.999999
3000-3249	-0.09250	0.882558	>0.999999	0.2000	0.334248	0.614181	-0.07750	0.908759	0.954197	0.08500	0.860151	>0.999999
3250-3499	-0.03750	0.947969	>0.999999	0.1775	0.285882	0.611705	0.1925	0.731122	0.954197	0.1275	0.724935	>0.999999
3500-3749	-0.01000	0.986313	>0.999999	0.1325	0.238132	0.611705	0.1425	0.760784	0.954197	0.09000	0.775401	>0.999999
3750-3999	0.02250	0.961884	>0.999999	-0.007500	0.897217	>0.999999	0.04750	0.902848	0.954197	0.06750	0.788393	>0.999999
4000-4249	0.1775	0.689374	>0.999999	0.06500	0.224842	0.611705	0.1800	0.627245	0.954197	0.07000	0.705873	>0.999999
4250-4499	0.1075	0.804102	>0.999999	0.05250	0.183960	0.611705	0.2100	0.532337	0.954197	0.1225	0.409795	>0.999999
4500-4749	0.1625	0.720337	>0.999999	0.04250	0.235544	0.611705	0.1075	0.558064	0.954197	0.07750	0.622275	>0.999999
4750-5999	0.1425	0.680638	>0.999999	0.02750	0.190833	0.611705	0.1725	0.499369	0.954197	0.07000	0.555834	>0.999999
5000+	1.458	0.513134	>0.999999	0.2525	0.145434	0.611705	1.045	0.422771	0.954197	0.08750	0.864786	>0.999999

Table 9.46. Male *Tbx15*$^{+/-}$ high-fat diet adipocyte cell area distribution. All data was analysed by multiple unpaired t-tests (two-stage step-up (Benjamini, Krieger, and Yekutieli) (false discovery rate 5%)) per diet and depot; significant values (p<0.05 and q<0.05) highlighted in bold. *Tbx15*$^{+/+}$ (n=4), *Tbx15*$^{+/-}$ (n=4).

Adipocyte size bin (μm²)	gWAT			mWAT			pWAT			iWAT		
	Diff means	p-value	q-value	Diff means	p-value	q-value	Diff means	p-value	q-value	Diff means	p-value	q-value
0-499	-0.7875	0.500825	0.996180	-2.785	0.085995	0.191984	-1.763	0.445391	0.801749	2.170	0.289258	0.557891
500-999	-1.033	0.220924	0.996180	-1.785	0.098454	0.191984	-0.7175	0.528986	0.818888	-0.3075	0.607731	0.754140
1000-1499	-0.3375	0.620860	0.996180	-1.180	0.093983	0.191984	0.1875	0.646945	0.862939	-1.025	0.078128	0.411967
1500-1999	0.1250	0.836483	0.996180	-0.5175	0.242258	0.300620	0.2650	0.396565	0.801749	-0.9475	0.090542	0.411967
2000-2499	-0.1475	0.754432	0.996180	-0.1625	0.505577	0.575094	0.2000	0.434972	0.801749	-1.188	**0.004487**	0.122494
2500-2999	0.1075	0.747366	0.996180	-0.05000	0.740661	0.808802	0.05500	0.802725	0.949927	-0.6850	**0.035523**	0.411967
3000-3499	0.1575	0.581981	0.996180	0.1825	0.262777	0.311905	0.04750	0.869897	0.949927	-0.3175	0.278369	0.557891
3500-3999	0.04750	0.866213	0.996180	0.05500	0.834540	0.876267	0.2300	0.319567	0.793107	-0.4750	0.066906	0.411967
4000-4499	0.02000	0.941656	0.996180	0.3900	0.231305	0.300620	0.04000	0.860329	0.949927	-0.4250	0.133130	0.436171
4500-4999	0.1750	0.485355	0.996180	0.4125	0.160532	0.233517	-0.2425	0.469889	0.801749	-0.1125	0.708869	0.841397
5000-5499	0.1800	0.381640	0.996180	0.5100	0.140853	0.233517	-0.1300	0.572656	0.822816	0.2200	0.279315	0.557891
5500-5999	0.2050	0.416976	0.996180	0.3950	0.200587	0.273801	-0.01750	0.925828	0.972119	0.2075	0.440518	0.668119
6000-6499	0.01500	0.948743	0.996180	0.4625	0.158808	0.233517	0.05750	0.756293	0.938491	0.2175	0.513750	0.701269
6500-6999	0.1075	0.720631	0.996180	0.4825	0.069968	0.191012	0.1950	0.206163	0.793107	0.4450	0.071082	0.411967
7000-7499	0.1125	0.697700	0.996180	0.4850	0.051317	0.155661	0.1250	0.539926	0.818888	0.1225	0.556710	0.723723
7500-7999	0.2225	0.393844	0.996180	0.4175	**0.032351**	0.144116	-0.07250	0.467083	0.801749	0.1600	0.494357	0.701269
8000-8499	0.1275	0.473240	0.996180	0.3650	**0.038220**	0.144116	0.1975	**0.034750**	0.721393	0.1950	0.342544	0.584467
8500-8999	0.05000	0.813118	0.996180	0.3500	**0.026337**	0.144116	0.1750	0.187913	0.793107	0.1625	0.408025	0.655240
9000-9499	0.08750	0.559062	0.996180	0.3125	**0.042232**	0.144116	0.1400	0.218586	0.793107	0.03000	0.795163	0.891723
9500-9999	-0.01750	0.938079	0.996180	0.2225	**0.041953**	0.144116	0.1850	0.139333	0.793107	0.2150	0.198175	0.531157
10000-10999	0.1375	0.633238	0.996180	0.4475	**0.015381**	0.139970	0.2775	0.269317	0.793107	0.2525	0.117455	0.436171
11000-11999	0.05250	0.851825	0.996180	0.3600	**0.003100**	0.084624	0.2150	0.278322	0.793107	0.2825	0.143793	0.436171
12000-12999	0.06250	0.806174	0.996180	0.1750	0.080501	0.191984	0.06750	0.663799	0.862939	0.02750	0.849260	0.891723
13000-13999	0.08250	0.642731	0.996180	0.1350	**0.010542**	0.139970	0.1725	0.052849	0.721393	0.1250	0.214019	0.531157
14000-14999	0.06250	0.666637	0.996180	0.09500	0.153961	0.233517	0.1200	0.310361	0.793107	0.08750	0.306534	0.557891
15000+	0.1875	0.792979	0.996180	0.2150	0.162521	0.233517	0.4950	0.228659	0.793107	0.08250	0.834893	0.891723

Table 9.47. Male *Tbx15*$^{+/-}$ low-fat diet adipocyte cell area distribution. All data was analysed by multiple unpaired t-tests (two-stage step-up (Benjamini, Krieger, and Yekutieli) (false discovery rate 5%)) per diet and depot; significant values (p<0.05 and q<0.05) highlighted in bold. *Tbx15*$^{+/+}$ (n=4), *Tbx15*$^{+/-}$ (n=4).

Adipocyte size bin (μm²)	gWAT			mWAT			pWAT			iWAT		
	Diff means	p-value	q-value	Diff means	p-value	q-value	Diff means	p-value	q-value	Diff means	p-value	q-value
0-249	-0.4100	0.531082	0.858160	-0.7100	0.632238	0.750439	0.2975	0.926489	>0.999999	-1.205	0.651782	0.741402
250-499	-1.453	0.482792	0.858160	-2.950	0.461205	0.750439	0.7100	0.898304	>0.999999	-5.175	0.331215	0.625704
500-749	-0.8925	0.590389	0.895423	-2.238	0.377604	0.750439	0.07000	0.981956	>0.999999	-3.380	0.212738	0.625704
750-999	-1.010	0.534385	0.858160	-1.208	0.363957	0.750439	-0.2875	0.858864	>0.999999	-1.450	0.410672	0.625704
1000-1249	-0.7975	0.517594	0.858160	-0.08250	0.744846	0.829653	-0.3325	0.768712	>0.999999	-0.05500	0.959525	>0.999999
1250-1499	-0.6925	0.438169	0.858160	0.3525	0.510702	0.750439	-0.1300	0.807269	>0.999999	0.1100	0.929447	>0.999999
1500-1749	-0.3625	0.650519	0.934694	0.8050	0.380047	0.750439	-0.4125	0.598735	>0.999999	0.7125	0.521675	0.647351
1750-1999	-0.1300	0.781305	0.964785	0.6875	0.493326	0.750439	-0.2000	0.794288	>0.999999	0.8100	0.458013	0.625704
2000-2249	0.03000	0.930913	0.977458	0.6125	0.506716	0.750439	-0.3550	0.614916	>0.999999	0.7875	0.352771	0.625704
2250-2499	0.2050	0.466688	0.858160	0.6950	0.414421	0.750439	-0.1500	0.810373	>0.999999	0.7925	0.317703	0.625704
2500-2749	0.3650	0.287974	0.858160	0.7250	0.340745	0.750439	-0.02500	0.970408	>0.999999	0.6800	0.319135	0.625704
2750-2999	0.5850	0.213701	0.858160	0.6025	0.353212	0.750439	-0.2050	0.748697	>0.999999	0.6375	0.342742	0.625704
3000-3249	0.6475	0.104746	0.858160	0.4075	0.498739	0.750439	0.09000	0.888029	>0.999999	0.4575	0.400943	0.625704
3250-3499	0.2800	0.525948	0.858160	0.4200	0.419827	0.750439	0.1150	0.839604	>0.999999	0.5525	0.395420	0.625704
3500-3749	0.4350	0.319862	0.858160	0.2225	0.605798	0.750439	-0.1225	0.854286	>0.999999	0.5650	0.340090	0.625704
3750-3999	0.3875	0.446099	0.858160	0.2900	0.413380	0.750439	-0.1100	0.856402	>0.999999	0.4575	0.316275	0.625704
4000-4249	0.3850	0.461414	0.858160	0.2775	0.340012	0.750439	-0.02750	0.963696	>0.999999	0.3200	0.418456	0.625704
4250-4499	0.3200	0.518270	0.858160	0.2425	0.391278	0.750439	-0.05750	0.914881	>0.999999	0.4825	0.283245	0.625704
4500-4749	0.3875	0.371676	0.858160	0.1150	0.625023	0.750439	0.005000	0.991946	>0.999999	0.4425	0.349551	0.625704
4750-5999	0.1750	0.695229	0.948987	0.1125	0.623225	0.750439	-0.03000	0.944448	>0.999999	0.2225	0.560507	0.665297
5000-5999	1.240	0.364358	0.858160	0.3725	0.534168	0.750439	-0.05250	0.974907	>0.999999	1.105	0.427554	0.625704
6000-6999	0.6775	0.532562	0.858160	0.07000	0.839020	0.880971	0.1600	0.903634	>0.999999	0.6150	0.498885	0.647351
7000-7999	0.2225	0.812823	0.964785	0.1400	0.545186	0.750439	0.2300	0.809729	>0.999999	0.5800	0.364877	0.625704
8000-8999	-0.07750	0.909627	0.977458	0.08000	0.562022	0.750439	0.2125	0.739502	>0.999999	0.2500	0.458391	0.625704
9000-9999	-0.1100	0.849939	0.966805	-0.02750	0.759756	0.829653	0.2125	0.610760	>0.999999	0.2175	0.448303	0.625704
10000+	-0.4000	0.812278	0.964785	0.1700	0.369366	0.750439	0.3900	0.638673	>0.999999	0.4750	0.396600	0.625704

9.2.3. Chapter 5 – Identifying the TBX15 transcriptional network

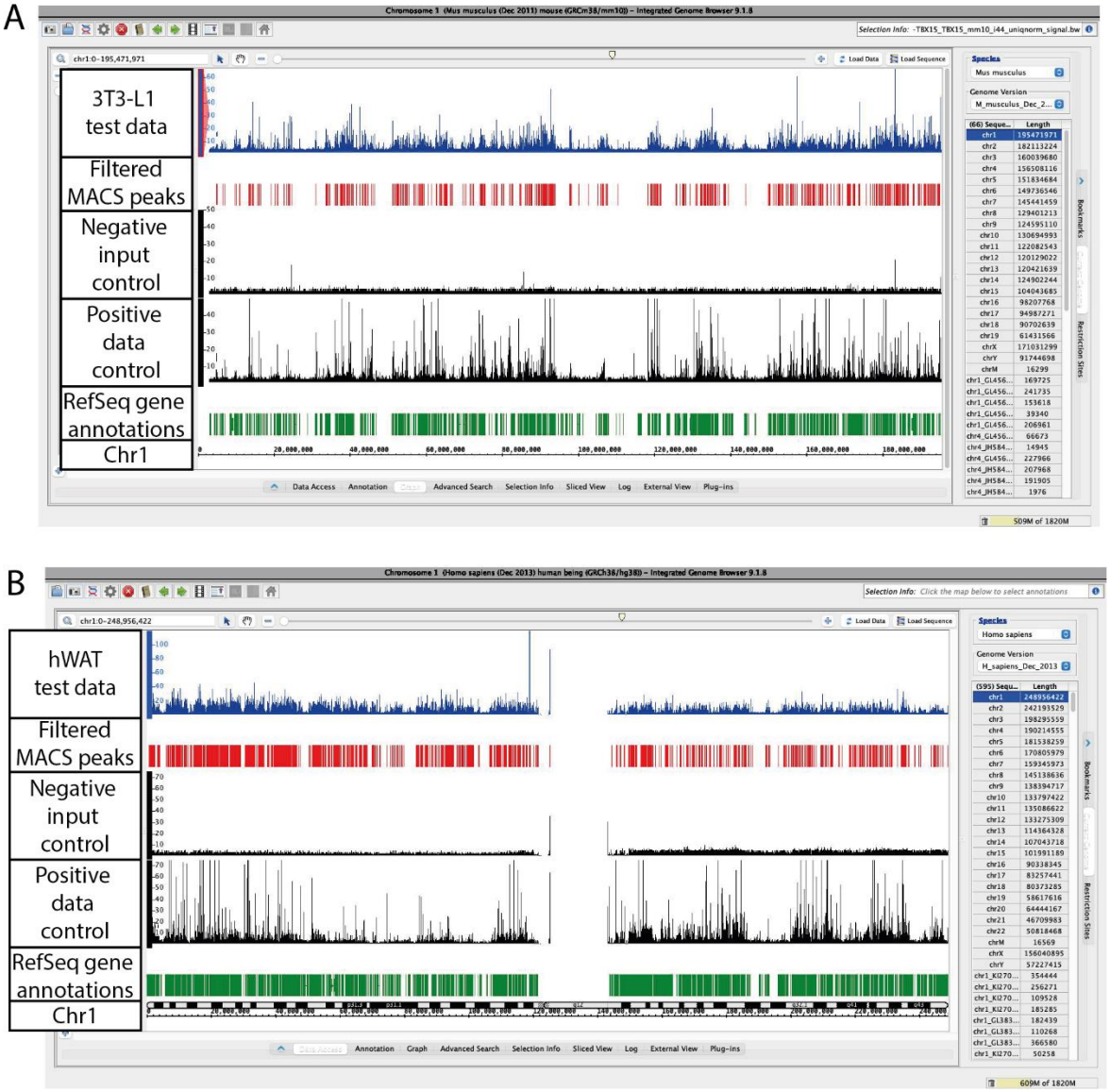

Figure 9.3. TBX15-HA ChIP-sequencing sample validation. A-B. Example integrated genome browser visualisation of ChIP fragments for 3T3-L1 (mouse) (A) and hWAT (human) (B). Top track (blue) shows test TBX15-HA data, second track (red) shows location of filtered MACS peaks, third and fourth tracks (black) show a negative "input control" and positive "assay control" (unrelated data) for illustration only, fifth track (green) shows RefSeq gene annotation, chromosome 1 co-ordinates are shown in the bottom track. Where applicable, y-axes were adjusted for comparison of scales; HA antibody qualification experiments and data visualisation produced by Active Motif Inc.

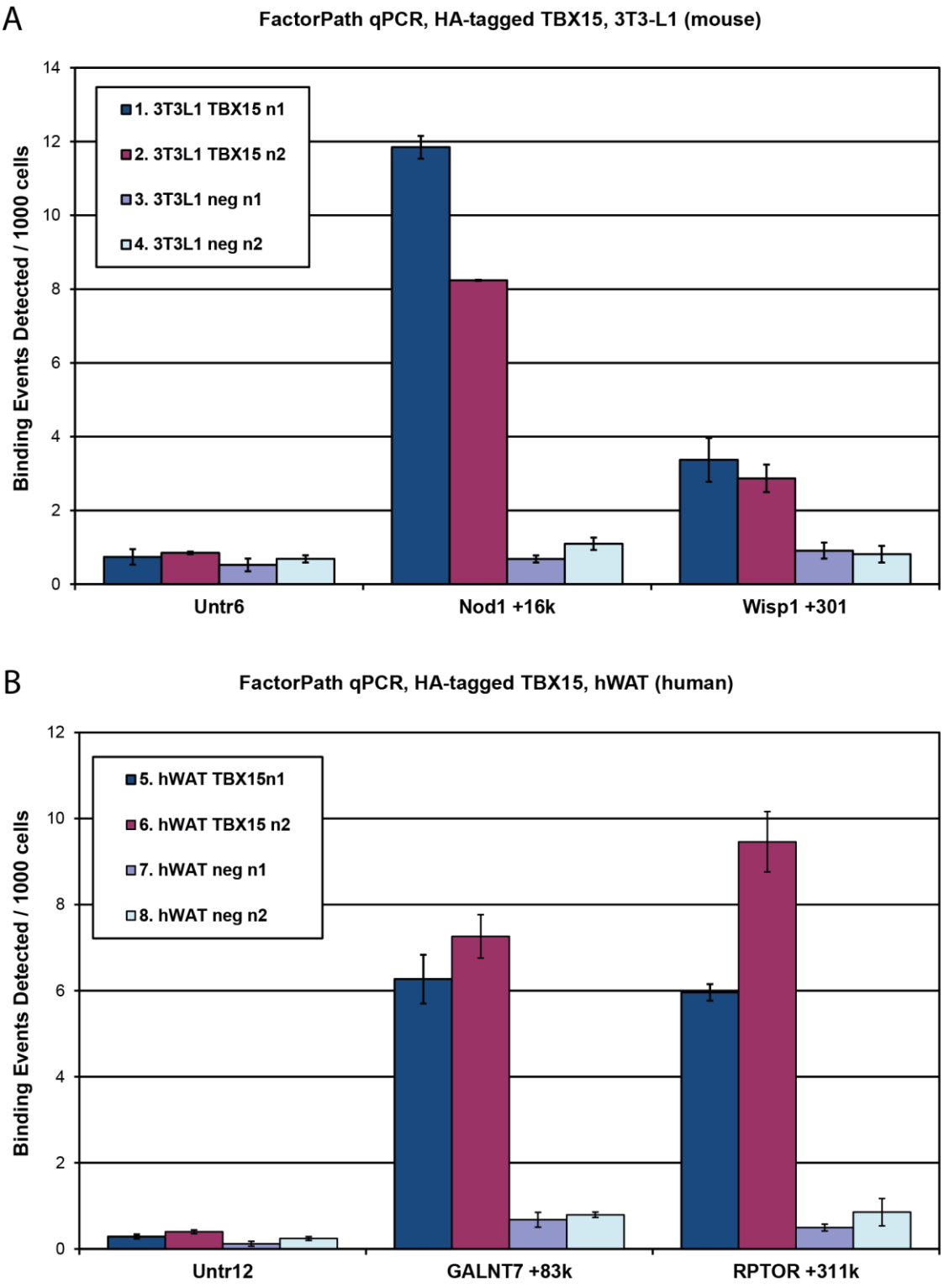

Figure 9.4. FactorPath qPCR validation of TBX15-HA samples A. 3T3-L1 samples validated for negative PCR control in gene desert region of chromosome 6 (Untr6), and positive controls for *Nod1* (nucleotide-binding oligomerization domain-containing protein 1) and *Wisp1* (Wnt1-inducible signalling pathway protein-1). B. hWAT samples validated for negative PCR control in gene desert region of chromosome 12 (Untr12), and positive controls for *GALNT7* (polypeptide N-acetylgalactosaminyltransferase 7) and *RPTOR* (regulatory associated protein of MTOR complex 1); qPCR validation experiments and data visualisation produced by Active Motif Inc.

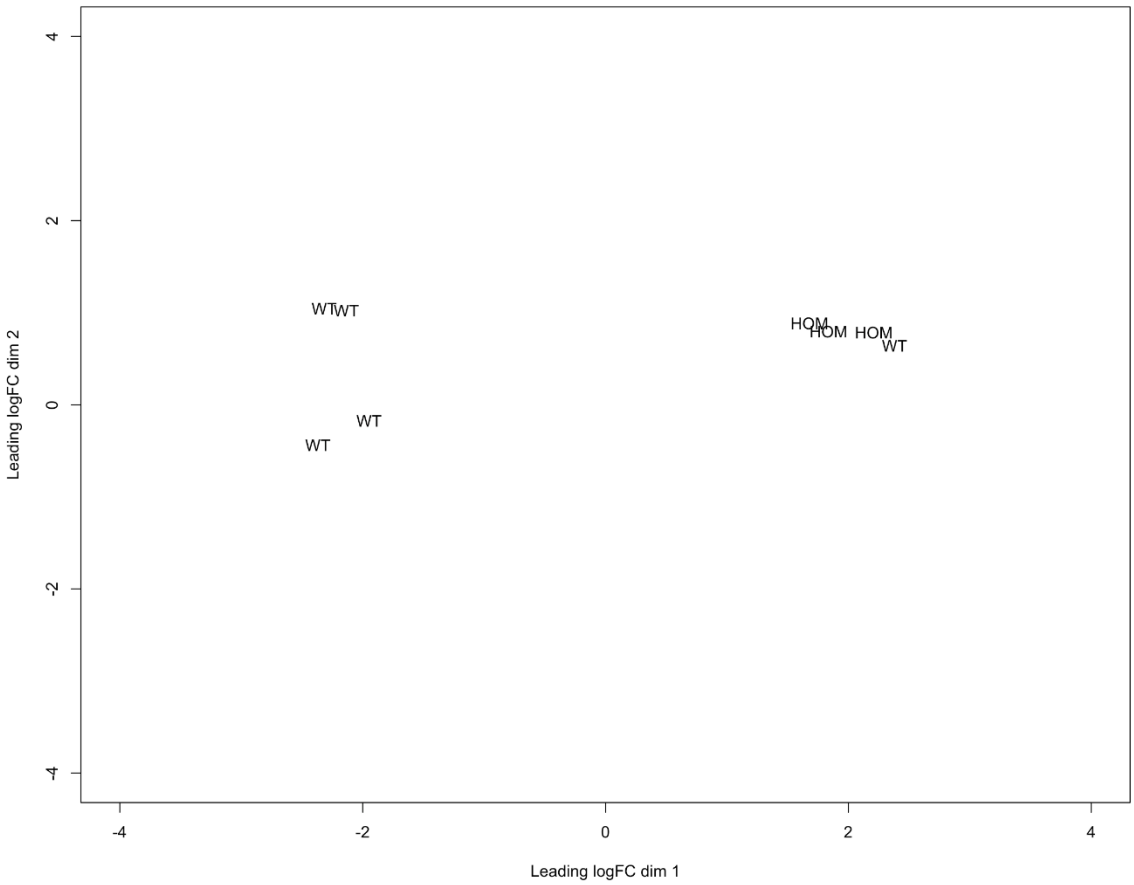

Figure 9.5. Principal component analysis of female *Tbx15*$^{-/-}$ adipose tissues. Principal component analysis of female wild-type *Tbx15*$^{+/+}$ (WT; n=5) and homozygous *Tbx15*$^{-/-}$ (HOM; n=4) inguinal white adipose tissues. One WT sample (ID: TBX15-KO-B6N-IC/10.1d) clustered with HOM samples in principal components 1 and 2. Quality control and plot produced by Dr. Michelle Simon.

9.2.4. Chapter 6 – Identifying p.H156N perturbations of the TBX15 transcriptional network

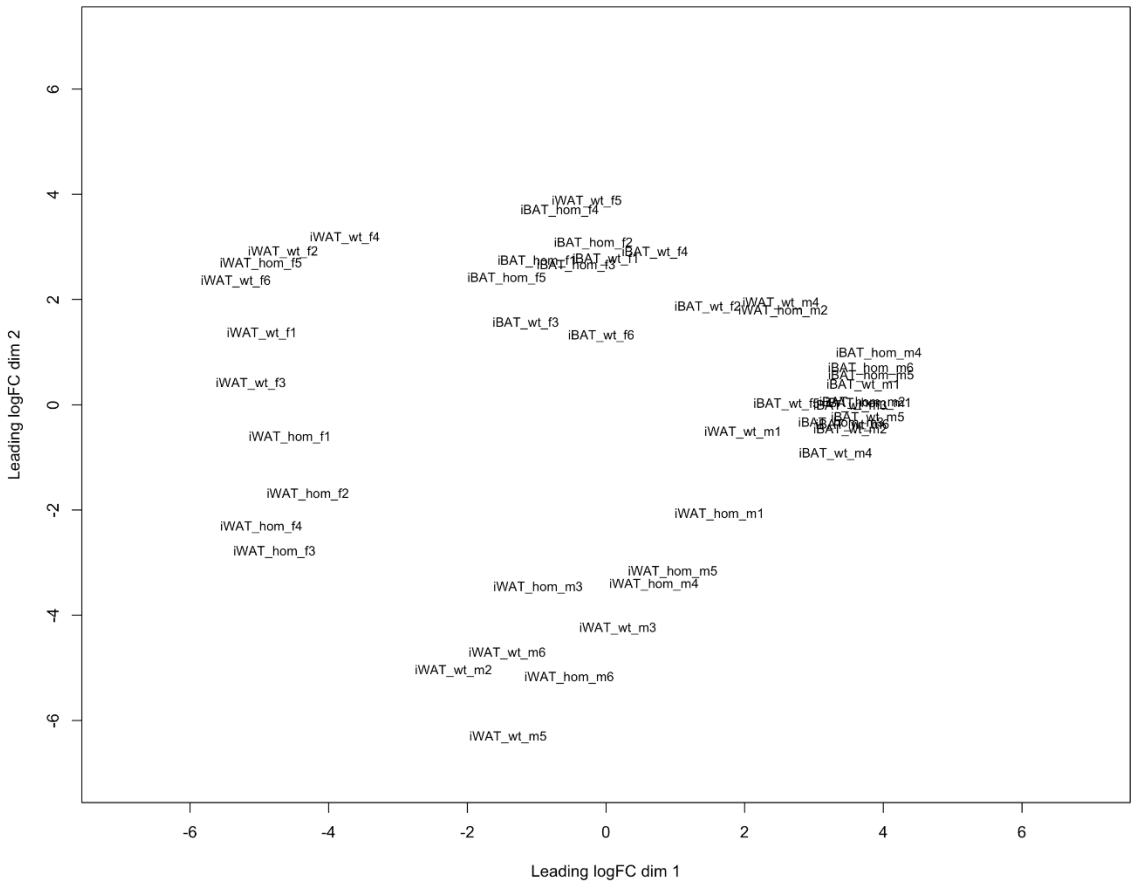

Figure 9.6. Principal component analysis of *Tbx15*$^{H156N/H156N}$ adipose tissues. Principal component analysis of inguinal white adipose tissue (iWAT) and brown adipose tissue (BAT) from female wild-type *Tbx15*$^{+/+}$ (iWAT_wt_f and BAT_wt_f, respectively; n=6) and homozygous *Tbx15*$^{H156N/H156N}$ (iWAT_hom_f and BAT_hom_f, respectively; n=5) and male wild-type *Tbx15*$^{+/+}$ (iWAT_wt_m and BAT_wt_m, respectively; n=6) and homozygous *Tbx15*$^{H156N/H156N}$ (iWAT_hom_m and BAT_hom_m, respectively; n=6). Quality control and plot produced by Dr. Michelle Simon.